

Institute for Basic Science

**NUCLEAR THEORY  
IN THE SUPERCOMPUTING ERA – 2018  
(NTSE-2018)**

**International Conference**

**Daejeon, Republic of Korea, October 29 – November 2, 2018**

**PROCEEDINGS**

Editors A. M. Shirokov and A. I. Mazur

Khabarovsk, Russia  
Pacific National University  
2019

УДК 539.14  
ББК В38я431

N 91

N 91

**Nuclear** Theory in the Supercomputing Era – 2018 (NTSE-2018): International Conference. Daejeon, Republic of Korea, October 29 – November 2, 2018. Proceedings. Eds. A. M. Shirokov and A. I. Mazur. — Khabarovsk, Russia: Pacific National University, 2019. — 322 p.

ISBN 978-5-7389-3043-0

The primary motivation for the series of International Conferences “Nuclear Theory in the Supercomputing Era (NTSE)” (<http://www.ntse.khb.ru>) was the rapid growth of supercomputers and the impact they, along with theoretical and algorithmic developments, are having on nuclear theory. The first conferences in this series, “Horizons of Innovative Theories, Experiments, and Supercomputing in Nuclear Physics” (HITES-2012) and NTSE-2012, were hosted respectively by the Louisiana State University in New Orleans, Louisiana, USA in June 4–7, 2012 and by the Pacific National University, Khabarovsk, Russia in June 18–22, 2012. These conferences were proceeded later under the common title NTSE. The NTSE-2013 was hosted by the Iowa State University, Ames, Iowa, USA in May 13–17, 2013 and celebrated the 70th birthday of Professor James Vary. The NTSE-2014 and the NTSE-2016 was hosted by the Pacific National University, Khabarovsk, Russia in June 23–27, 2014 and September 19–23, 2016 respectively.

These proceedings includes talks presented at the NTSE-2018 Conference hosted by the Institute for Basic Science in the city of Daejeon, Republic of Korea, from October 29th through November 2nd, 2018. The Conference was sponsored by the Institute for Basic Science (Republic of Korea), Rare Isotope Science Project (Republic of Korea), Korea Institute of Science and Technology Information (Republic of Korea), Center for High Energy Astrophysics (Republic of Korea), Pacific National University (Khabarovsk, Russia) and by the RAON Users Association (Republic of Korea).

The contributions to the NTSE-2018 Proceedings published here, are also available online at <http://www.ntse.khb.ru/2018/Proc/>.

УДК 539.14  
ББК В38я431

ISBN 978-5-7389-3043-0

©Pacific National University, 2019

## Preface

The International Conference on Nuclear Theory in the Supercomputing Era — 2018 (NTSE-2018) brought together experts in nuclear theory and high-performance computing in the city of Daejeon, Republic of Korea, from October 29th through November 2nd, 2018. This conference series was started in 2012 by the NTSE-2012 and HITES-2012 conferences which were proceeded later under the common title NTSE. The NTSE conferences focus on forefront challenges in physics, namely the fundamentals of nuclear structure and reactions, the origin of the strong inter-nucleon interactions from QCD, and computational nuclear physics with leadership class supercomputer facilities to provide forefront simulations leading to new discoveries.

The conference welcomed many young scientists, including graduate students in nuclear physics, computational science and applied mathematics. All participants together made the conference a great success.

The conference topics,

- (1) *Ab initio* nuclear structure;
- (2) Microscopic approaches to nuclear reactions;
- (3) Origin and properties of the strong interactions; and
- (4) Computational science and applied mathematics,

reflect current world-wide research interests and encompass a broad area of fundamental physics and high-performance computing.

We would like to express our appreciation to all participants of the NTSE-2018 conference, to all contributors to these proceedings, to all members of the Scientific Advisory Committee and to the NTSE-2018 sponsors.

The organizing committee:

Youngman Kim (Chair), Institute for Basic Science, Republic of Korea  
Kihyeon Cho, Korea Institute of Science and Technology Information, Republic of Korea  
Kyujin Kwak, Ulsan National Institute of Science and Technology, Republic of Korea  
Alexander Mazur, Pacific National University, Russia  
Ik Jae Shin (Scientific secretary), Institute for Basic Science, Republic of Korea  
Andrey Shirokov (Vice Chair), Moscow State University, Russia  
James Vary (Vice Chair), Iowa State University, USA

**NTSE-2018 Scientific Advisory Committee:**

- **James Vary (Chair)**, Iowa State University, USA
- **Bruce Barrett**, University of Arizona, USA
- **Leonid Blokhintsev**, Moscow State University, Russia
- **Stanley J. Brodsky**, SLAC-Stanford, USA
- **Mark Caprio**, University of Notre Dame, USA
- **David Dean**, Oak Ridge National Laboratory, USA
- **Jerry Draayer**, Louisiana State University, USA
- **Victor Efros**, Russian Research Centre Kurchatov Institute, Russia
- **Charlotte Elster**, Ohio University, USA
- **Evgeny Epelbaum**, University of Bochum, Germany
- **Morten Hjorth-Jensen**, University of Oslo, Norway and Michigan State University, USA
- **Youngman Kim**, Institute for Basic Science, South Korea
- **Ruprecht Machleidt**, University of Idaho, USA
- **Pieter Maris**, Iowa State University, USA
- **Alexander Mazur**, Pacific National University, Russia
- **Alexander Motovilov**, Joint Institute for Nuclear Research, Russia
- **Takashi Nakatsukasa**, University of Tsukuba, Japan
- **Petr Navrátil**, TRIUMF, Canada
- **Witold Nazarewicz**, Michigan State University, USA
- **Esmond Ng**, Lawrence Berkeley National Laboratory, USA
- **Giuseppina Orlandini**, Università di Trento, Italy
- **Takaharu Otsuka**, University of Tokyo, Japan
- **Wayne Polyzou**, University of Iowa, USA
- **Sophia Quaglioni**, Lawrence Livermore National Laboratory, USA
- **Robert Roth**, Technische Universität Darmstadt, Germany
- **Kimiko Sekiguchi**, Tohoku University, Japan

- **Andrey Shirokov**, Moscow State University, Russia
- **Masha Sosonkina**, Old Dominion University, USA
- **Furong Xu**, Peking University, China
- **Xingbo Zhao**, Institute of Modern Physics, China

### NTSE-2018 Organizing Committee:

- **Youngman Kim (Chair)**, Institute for Basic Science, Republic of Korea
- **Kihyeon Cho**, Korea Institute of Science and Technology Information, Republic of Korea
- **Kyujin Kwak**, Ulsan National Institute of Science and Technology, Republic of Korea
- **Alexander Mazur**, Pacific National University, Russia
- **Ik Jae Shin (Scientific secretary)**, Institute for Basic Science, Republic of Korea
- **Andrey Shirokov (Vice Chair)**, Moscow State University, Russia
- **James Vary (Vice Chair)**, Iowa State University, USA

International Conference  
Nuclear Theory in the Supercomputing Era — 2018  
(NTSE-2018)



PROGRAM

**Sunday, October 28.** *Hotel ICC 1F.*

16:30–19:00 *Registration*

**Monday, October 29.** *Auditorium, IBS Science Culture Center 2F.*

8:00–9:00 *Registration*

**Chair: James P. Vary**

9:00–9:10 *Conference opening*

9:10–9:40 **Youngman Kim:** Daejeon16 *NN* interaction

9:40–10:10 **Ruprecht Machleidt:** What is wrong with our current nuclear forces?

10:10–10:30 **Mario Sánchez:** The two-nucleon system within chiral effective field theory

10:30–11:00 *Coffee break*

**Chair: Jerry Draayer**

11:00–11:30 **Ulf-G. Meißner:** Towards nuclear physics as precision science

11:30–12:00 **Dean Lee:** Applications of lattice effective field theory to nuclear forces and structure

12:00–12:30 **Andreas Ekström:** Statistical analysis and optimization of chiral forces

12:30–14:00 *Lunch*

**Chair: Nadezda Smirnova**

14:00–14:30 **Thomas Neff:** Cluster states in  $^{12}\text{C}$  and neighboring nuclei

14:30–15:00 **Alexander Volya:** Interplay of single-particle and cluster degrees of freedom in atomic nuclei

15:00–15:30 **Yury Tchuvil'sky:** Nuclear clustering, step to a supercomputing approach

15:30–15:50 **Dmitry Rodkin:** *Ab initio* description of one-nucleon resonances and halo states in light nuclei

15:50–16:20 *Coffee break*

**Chair: Thomas Neff**

16:20–16:40 **Seonghyun Kim:** Calculation of ground-state energy for light nuclei with the Strutinsky's method

16:40–17:00 **Eun Jin In:** Nuclear mass table in deformed relativistic continuum Hartree-Bogoliubov theory

17:00–17:20 **Kyoungsu Heo:** Extended optical model analyses of  $^{11}\text{Be} + ^{197}\text{Au}$  System with dynamical polarization potential

17:20–17:40 **Jounghwa Lee:** A semi-empirical model for calculating fission product yields

19:00 *Welcome party*

**Tuesday, October 30.** Auditorium, IBS Science Culture Center 2F.

<i>Chair: Ulf-G. Meißner</i>	
8:30–9:00	<b>Young Kwan Kwon:</b> Status of RAON
9:00–9:30	<b>Nir Barnea:</b> <i>Ab initio</i> calculation of nuclear structure effects in muonic atoms
9:30–10:00	<b>Wei Zuo:</b> Three-body force effect on the Properties of nuclear matter
10:00–10:30	<b>Francesca Sammarruca:</b> Correlations in nuclei and nuclear matter
10:30–11:00	<i>Coffee break</i>
<i>Chair: Ruprecht Machleidt</i>	
11:00–11:30	<b>Esmond G. Ng:</b> Scientific discovery through exascale computing
11:30–12:00	<b>Kihyeon Cho:</b> Nuclear theory in the 5th supercomputing era
12:00–12:30	<b>Stefan Wild:</b> Optimization problems in nuclear theory
12:30–14:00	<i>Lunch</i>
<i>Chair: Kimiko Sekiguchi</i>	
14:00–14:30	<b>Witold Nazarewicz:</b> Quantified nuclear density functional theory
14:30–15:00	<b>Chang Ho Hyun:</b> Novel Framework of Nuclear EDF
15:00–15:30	<b>Feng Pan:</b> Algebraic solution of the isovector pairing problem
15:30–16:00	<b>Myung Ki Cheoun:</b> Competence of pairing correlations and deformation in the nuclear structure
16:00–16:30	<i>Coffee break</i>
<i>Chair: Furong Xu</i>	
16:30–17:00	<b>Chong Qi:</b> Large-scale shell model calculations of heavy nuclei
17:00–17:30	<b>Ionel Stetcu:</b> Modeling fission dynamics with leadership class computing capabilities
17:30–18:00	<b>Jun Terasaki:</b> Examination of consistency of QRPA approach to double-beta decay

**Wednesday, October 31.** Auditorium, IBS Science Culture Center 2F.

<i>Chair: Francesca Sammarruca</i>	
9:00–9:30	<b>Petr Navrátil:</b> Nuclear structure and dynamics from chiral forces
9:30–10:00	<b>Charlotte Elster:</b> Nucleon-nucleus elastic scattering using <i>ab initio</i> folding potentials based on NCSM nonlocal one-body densities
10:00–10:30	<b>Bruce R. Barrett:</b> Microscopically calculated shell-model effective two-body matrix elements in the <i>sd</i> shell
10:30–11:00	<b>Seung-Woo Hong:</b> Science opportunities with RAON
11:30–13:00	<i>Lunch</i>
13:00–18:00	<i>Excursion</i>
18:30	<i>Conference dinner</i>

Thursday, November 1. Auditorium, IBS Science Culture Center 2F.

<i>Chair: Petr Navrátil</i>	
8:30–9:00	<b>Kimiko Sekiguchi:</b> Approach to three-nucleon forces via three- and four-nucleon scattering
9:00–9:30	<b>Roman Skibiński:</b> Nucleon-deuteron scattering with chiral semilocal coordinatespace and momentum-space regularized interactions
9:30–10:00	<b>Andreas Nogga:</b> Faddeev–Yakubovsky and Jacobi-no-core-shell model results for light hypernuclei
10:00–10:30	<b>Kacper W. Topolnicki:</b> ${}^3\text{H}$ and ${}^3\text{He}$ bound state calculations without angular momentum decomposition
10:30–11:00	<i>Coffee break</i>
<i>Chair: Charlotte Elster</i>	
11:00–11:30	<b>Rimantas Lazauskas:</b> On the solution of the Faddeev–Yakubovsky equations for five nucleon systems
11:30–12:00	<b>Alexander K. Motovilov:</b> Unphysical energy sheets and resonances in the Friedrichs–Faddeev model
12:00–12:30	<b>Sergey L. Yakovlev:</b> <i>Ab initio</i> scattering calculation in three-body Coulomb systems: $e^+ - \text{H}$ , $e^- - \text{H}$ and $e^+ - \text{He}^+$
12:30–14:00	<i>Lunch</i>
<i>Chair: Dean Lee</i>	
14:00–14:30	<b>Evgeny Epelbaum:</b> High-precision nuclear forces from chiral EFT: Where do we stand?
14:30–15:00	<b>James P. Vary:</b> No-core shell model with chiral effective field theory interactions
15:00–15:30	<b>Furong Xu:</b> <i>Ab initio</i> calculations of nuclear resonances
15:30–16:00	<b>Shung-Ichi Ando:</b> The $S_{E1}$ factor of radiative alpha capture on ${}^{12}\text{C}$ in cluster effective field theory
16:00–16:30	<i>Coffee break</i>
<i>Chair: Witold Nazarewicz</i>	
16:30–17:00	<b>Luigi Coraggio:</b> Chiral three-body forces and the monopole component of effective shell-model hamiltonians
17:00–17:30	<b>Carlo Barbieri:</b> Recent advances for computational self-consistent Green’s function theory in nuclear physics
17:30–18:00	<b>Noritaka Shimizu:</b> Large-scale shell model calculations and chiral doublet bands in ${}^{128}\text{Cs}$

**Friday, November 2.** *Conference Room, IBS Science Culture Center 2F.*

<i>Chair: Alexander Volya</i>	
8:30–9:00	<b>Tobias Frederico:</b> The relativistic dynamics in Minkowski space: exploring hadron structure
9:00–9:30	<b>Vladimir Karmanov:</b> Bound states of relativistic origin
9:30–10:00	<b>Xingbo Zhao:</b> Light-front approach to a chiral nucleon-pion Lagrangian
10:00–10:30	<b>Chandan Mondal:</b> Basis light-front quantization approach for the nucleon
10:30–11:00	<i>Coffee break</i>
<i>Chair: Nir Barnea</i>	
11:00–11:30	<b>Mark A. Caprio:</b> Predictions for nuclear rotational structure from <i>ab initio</i> calculations
11:30–12:00	<b>Gaute Hagen:</b> A solution to the puzzle of quenched beta-decays
12:00–12:30	<b>Nadezda Smirnova:</b> Isospin-symmetry breaking correction to Fermi beta-decay
12:30–14:00	<i>Lunch</i>
<i>Chair: Esmond G. Ng</i>	
14:00–14:30	<b>Jerry Draayer:</b> Symmetry adapted no-core shell-model calculations for probing the structure of atomic nuclei
14:30–15:00	<b>Anna McCoy:</b> Convergence in the <i>ab initio</i> symplectic no-core configuration interaction framework
15:00–15:30	<b>Takashi Abe:</b> No-core Monte Carlo shell model calculations with Daejeon16 <i>NN</i> interaction
15:30–16:00	<b>Kevin Fosse:</b> Neutron-rich helium isotopes: complex made simple
16:00–16:30	<i>Coffee break</i>
<i>Chair: Youngman Kim</i>	
16:30–17:00	<b>Alexander I. Mazur:</b> Description of continuum states within no-core shell model. Single-state HORSE method
17:00–17:30	<b>Igor A. Mazur:</b> Elastic $n-{}^6\text{He}$ scattering and ${}^7\text{He}$ resonant states in single-state HORSE method
17:30–18:00	<b>Andrey Shirokov:</b> Tetraneutron resonance
18:00–18:10	<i>Conference closing</i>

# Contents

<i>Preface</i> .....	3
<i>NTSE-2018 Scientific Advisory Committee</i> .....	4
<i>NTSE-2018 Organizing Committee</i> .....	5
<i>Program of International Conference on Nuclear Theory in the Supercomputing Era — 2018 (NTSE-2018)</i> .....	6
Invited talks:	
<u>Y. Kim</u> , I. J. Shin, A. M. Shirokov, M. Sosonkina, P. Maris and J. P. Vary, <i>Daejeon16 NN interaction</i> .....	15
<u>R. Machleidt</u> , <i>What is wrong with our current nuclear forces?</i> .....	21
<u>Ulf-G. Meißner</u> , <i>Towards nuclear physics as precision science</i> .....	28
<u>Dean Lee</u> , <i>Recent advances in nuclear lattice simulations</i> .....	45
<u>W. Zuo</u> , <i>Three-body force effect on the properties of nuclear matter</i> .....	52
<u>F. Sammarruca</u> , L. E. Marcucci, M. Viviani and R. Machleidt, <i>Correlations in nuclear matter and nuclei</i> .....	64
<u>Feng Pan</u> , Kristina D. Launey and Jerry P. Draayer, <i>Algebraic solution of the isovector pairing problem</i> .....	73
<u>Chong Qi</u> , <i>Large-scale shell model calculations of heavy nuclei</i> .....	83
<u>I. Stetcu</u> , A. Bulgac, S. Jin, K. J. Roche and N. Schunk, <i>Modeling fission dynamics with leadership class computing capabilities</i> .....	91
<u>J. Terasaki</u> , <i>Examination of consistency of QRPA approach to double-beta decay</i> .....	100
<u>Kimiko Sekiguchi</u> , <i>Experimental approach to three-nucleon forces via three- and four-nucleon scattering</i> .....	108
<u>R. Skibiński</u> , J. Golak, A. Grassi, V. Soloviov, K. Topolnicki, V. Urbaneych, Yu. Volkotrub, H. Witała, <i>Nucleon-deuteron scattering with chiral semilocal coordinate space and momentum space regularized interactions</i> .....	115
<u>K. Topolnicki</u> , J. Golak, R. Skibiński, H. Witała, Yu. Volkotrub, V. Soloviov, A. Grassi, <i><math>^3\text{H}</math> and <math>^3\text{He}</math> bound state calculations without angular momentum decomposition</i> .....	122
<u>Alexander K. Motovilov</u> , <i>Unphysical sheets and resonances for the Friedrichs-Faddeev model</i> .....	127
V. A. Gradusov, V. A. Roudnev, E. A. Yarevsky and <u>S. L. Yakovlev</u> , <i>Ab initio scattering calculation in three-body Coulomb systems: <math>e^+ - \text{H}</math>, <math>e^- - \bar{\text{H}}</math> and <math>e^+ - \text{He}^+</math></i> .....	137

<u>Evgeny Epelbaum</u> , <i>Towards high-precision nuclear forces from chiral effective field theory</i> .....	150
Pieter Maris, Ik Jae Shin and <u>James P. Vary</u> , <i>Ab initio structure of p-shell nuclei with Chiral Effective Field Theory and Daejeon16 interactions</i> .....	168
S. J. Dai, <u>F. R. Xu</u> , J. G. Li, B. S. Hu and Z. H. Sun, <i>Continuum effect in resonant excitation spectra of weakly-bound nuclei</i> .....	183
<u>L. Coraggio</u> and Y. Z. Ma, <i>Shell-model study of calcium isotopic chain starting from chiral two- and three-body potentials</i> .....	192
<u>Tobias Frederico</u> , Dyana C. Duarte, Wayne de Paula, Emanuel Ydrefors, Shaoyang Jia and Pieter Maris, <i>Towards Minkowski space solutions of Dyson–Schwinger equations through un-Wick rotation</i> .....	199
<u>V. A. Karmanov</u> , J. Carbonell and H. Sazdjian, <i>Bound states of relativistic nature</i> .....	212
Weijie Du, Yang Li, <u>Xingbo Zhao</u> and James P. Vary, <i>Dynamical nucleon-pion system via basis light-front quantization</i> .....	224
<u>Chandan Mondal</u> , Siqi Xu, Jiangshan Lan, Xingbo Zhao, Yang Li, Henry Lamm and James P. Vary, <i>Nucleon form factors from basis light-front quantization</i> ..	239
<u>M. A. Caprio</u> , P. J. Fasano, J. P. Vary, P. Maris and J. Hartley, <i>Robust ab initio predictions for nuclear rotational structure in the Be isotopes</i> .....	250
<u>Nadezda A. Smirnova</u> and Latsamy Xayavong, <i>Isospin-symmetry breaking correction to superallowed <math>0^+ \rightarrow 0^+</math> <math>\beta</math>-decay</i> .....	263
<u>J. P. Draayer</u> , K. D. Launey, T. Dytrych, R. B. Baker, A. C. Dreyfuss, D. Kekejian and G. H. Sargsyan, <i>Symmetry-adapted no-core shell-model calculations for probing the structure of atomic nuclei</i> .....	279
<u>Anna E. McCoy</u> , Mark A. Caprio and Tomáš Dytrych, <i>Convergence in the symplectic no-core configuration interaction framework</i> .....	293
<u>Takashi Abe</u> , <i>Alpha-cluster structure from no-core Monte Carlo shell model</i> .....	301
<u>I. A. Mazur</u> , A. M. Shirokov, I. J. Shin, A. I. Mazur, Y. Kim, P. Maris and J. P. Vary, <i>Elastic <math>n</math>-<math>^6\text{He}</math> scattering and <math>^7\text{He}</math> resonant states in the no-core shell model</i> .....	310
Alphabetic list of the NTSE-2018 participants.....	319

International Conference  
**NUCLEAR THEORY**  
**IN THE SUPERCOMPUTING ERA – 2018**  
**(NTSE-2018)**

**INVITED TALKS**



# Daejeon16 $NN$ Interaction

Y. Kim<sup>a</sup>, I. J. Shin<sup>a</sup>, A. M. Shirokov<sup>b,c</sup>, M. Sosonkina<sup>d</sup>,  
P. Maris<sup>e</sup> and J. P. Vary<sup>e</sup>

<sup>a</sup>Rare Isotope Science Project, Institute for Basic Science, Daejeon 34047, Korea

<sup>b</sup>Skobeltsyn Institute of Nuclear Physics, Moscow State University, Moscow 119991, Russia

<sup>c</sup>Department of Physics, Pacific National University, Khabarovsk 680035, Russia

<sup>d</sup>Department of Modeling, Simulation and Visualization Engineering, Old Dominion University, Norfolk, VA 23529, USA

<sup>e</sup>Department of Physics and Astronomy, Iowa State University, Ames, IA 50011, USA

## Abstract

We have developed a realistic nucleon-nucleon ( $NN$ ) interaction, dubbed Daejeon16. We start from a SRG (similarity renormalization group) evolved chiral N3LO interaction. We then apply PETs (phase-equivalent transformations) to the SRG-evolved interaction. It turned out that the obtained in such a way Daejeon16  $NN$  interaction provides a good description of various observables in light nuclei without  $NNN$  forces. In this contribution, we present our new results for some selected nuclei using the *ab initio* no-core shell model (NCSM) with the Daejeon16 interaction. One of the interesting results is that the *ab initio* NCSM with Daejeon16 clearly demonstrates the phenomenon of parity inversion in  $^{11}\text{Be}$ , i. e., the ground state in  $^{11}\text{Be}$  has the spin-parity  $1/2^+$  in experiments contrary to the expectation from the conventional shell model.

**Keywords:** *No-core shell model; NN interaction; parity inversion*

## 1 Introduction

As the advent of new rare isotope (RI) facilities such as FAIR, FRIB, HIRFL, NICA, RAON, etc., we have much more opportunities to resolve big questions in science. Nuclear theory for rare isotopes should be timely developed to face new precise observables from the forthcoming RI facilities which can produce exotic nuclei near the nuclear drip line. Thanks to the rapid developments of high performance supercomputers, we have a good chance to conduct a rigorous study of nuclear structures and reactions using fundamental (or realistic) nuclear interactions based on quantum chromodynamics (QCD). Several promising *ab initio* methods have been developed for nuclear structure and reactions [1–5].

The *ab initio* theory requires a high-quality realistic inter-nucleon interaction to provide predictions for binding energies, spectra and other observables in nuclei with

---

*Proceedings of the International Conference ‘Nuclear Theory in the Supercomputing Era — 2018’ (NTSE-2018), Daejeon, South Korea, October 29 – November 2, 2018, eds. A. M. Shirokov and A. I. Mazur. Pacific National University, Khabarovsk, Russia, 2019, p. 15.*

<http://www.ntse.khb.ru/files/uploads/2018/proceedings/Kim.pdf>.

mass up to  $A \sim 20$  and selected heavier nuclear systems around closed shells. Therefore, it is important to develop realistic nucleon-nucleon ( $NN$ ) interactions with better convergence that require less computational resources. In Ref. [6], we developed a realistic  $NN$  interaction, dubbed Daejeon16, starting from a chiral N3LO interaction which is SRG (similarity renormalization group) evolved. Then, we apply PETs (phase-equivalent transformations) to the SRG-evolved interaction. It turned out that Daejeon16 provides a good description of various observables in light nuclei without  $NNN$  forces and also generates rapid convergence in *ab initio* calculations.

In this short write-up, after a brief description of Daejeon16, we present some recent results from *ab initio* nuclear studies using the Daejeon16  $NN$  interaction, with an emphasis on the ground-state parity inversion in  $^{11}\text{Be}$ .

## 2 Daejeon16 and applications

Nuclei are composed of nucleons (protons and neutrons) and their properties such as the binding energy and radius are largely governed by the nuclear force, i. e., the strong interaction. Therefore, nuclear forces are at the core of the nuclear structure studies. Meson exchange theory has been successfully applied to obtain realistic nuclear potentials such as CD-Bonn, Argonne V18, etc. A bit more down to the mother theory of the nuclear force, i. e., QCD, nuclear interactions from the chiral effective field have been developed: N2LO, N3LO, etc. For *ab initio* nuclear studies, the JISP16 interaction [7], which is phenomenological, has been widely used. Here, JISP stands for  $J$ -matrix Inverse Scattering Potential. Recently, a new nuclear force dubbed ‘Daejeon16’ has been developed from a N3LO  $NN$  interaction. Daejeon is a city in Korea where a next generation RI facility called RAON will be built and 16 is from  $^{16}\text{O}$  which is the heaviest nucleus used in fitting process. In Ref. [6], the authors start from Idaho N3LO  $NN$  interaction and apply to it PETs which preserve scattering phase shifts and bound state energy of the two-nucleon system (deuteron). The optimal set of PET parameters is determined to describe the binding energies of  $^3\text{H}$ ,  $^4\text{He}$ ,  $^6\text{Li}$ ,  $^8\text{He}$ ,  $^{10}\text{B}$ ,  $^{12}\text{C}$  and  $^{16}\text{O}$  nuclei and excitation energies of a few narrow excited states: the two lowest excited states with  $(J^\pi, T) = (3^+, 0)$  and  $(0^+, 1)$  in  $^6\text{Li}$  and the first excited states  $(1^+, 0)$  in  $^{10}\text{B}$  and  $(2^+, 0)$  in  $^{12}\text{C}$ . For a sketch about the procedure to obtain JISP16 and Daejeon16, we refer to Fig. 1.

It turned out that the Daejeon16 works well for light  $p$ -shell nuclei compared with other established interactions such as JISP16, for instance see Fig. 2.

Now, we move on to some recent results using the Daejeon16 interaction.

### 2.1 Parity inversion in $^{11}\text{Be}$

$^{11}\text{Be}$  shows an interesting feature which is opposite to the expectation from the conventional shell model. Experimentally, the ground state of  $^{11}\text{Be}$  is  $1/2^+$  [9], while it was expected to be a  $1/2^-$  state in the conventional shell model. To tackle the issue of the parity inversion in  $^{11}\text{Be}$ , we evaluate the spectrum of  $^{11}\text{Be}$  using the *ab initio* no-core shell model (NCSM) with the Daejeon16 interaction and extrapolate the results to the infinite basis space using the method of Ref. [8]. For the two lowest-lying states, we obtain

$$1/2^+ : -65.22(7) \text{ MeV}, \quad 1/2^- : -64.63(2) \text{ MeV}.$$

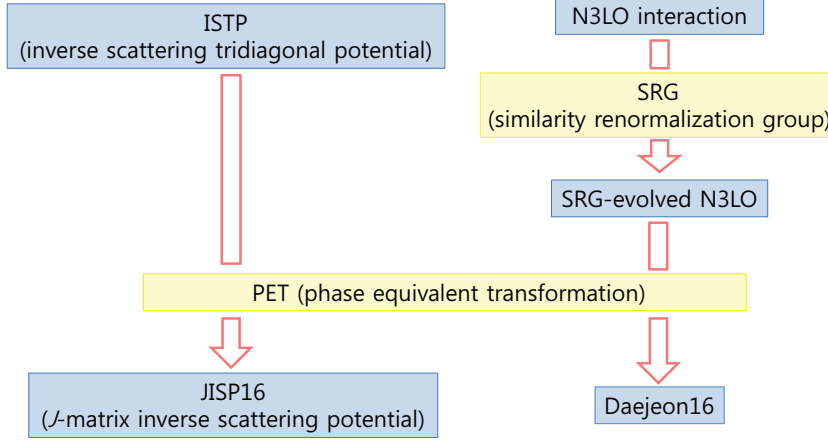


Figure 1: A sketch of the procedure to obtain Daejeon16 compared with JISP16.

The numbers in parenthesis show the uncertainties of the extrapolations of the energies. This result is compared with the experiment and with the one from JISP16 in Fig. 3, which shows that the *ab initio* NCSM with Daejeon16 successfully reproduces the parity inversion in  $^{11}\text{Be}$ . Note that the JISP16 is unable to reproduce the

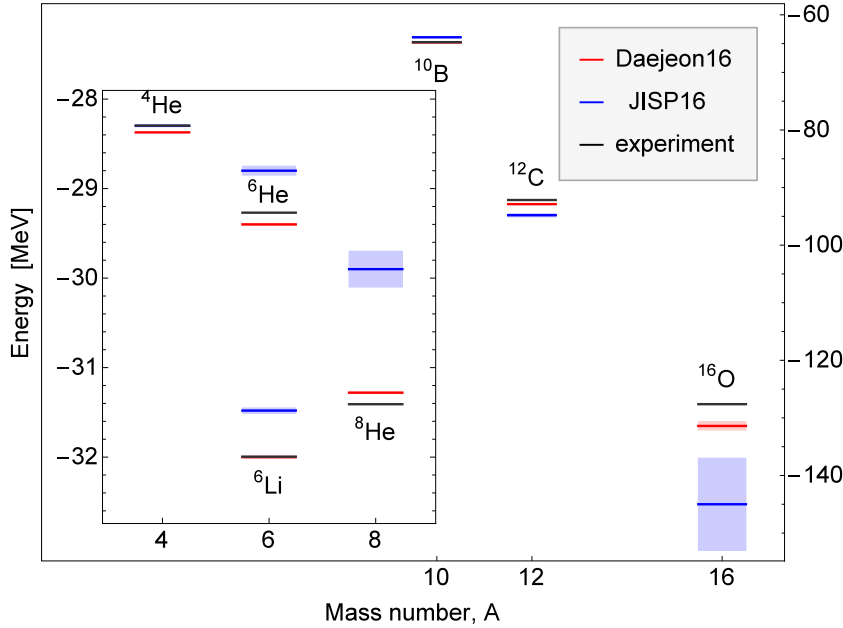


Figure 2: The ground state energies of several *p*-shell nuclei using Daejeon16 and JISP16 compared with experiment. The calculations were performed within the NCSM and extrapolated to the infinite basis space using the methods of Ref. [8]; the shaded areas show the uncertainties of the extrapolations. It is noted that all shown nuclei were used to PET fitting as mentioned in the text.

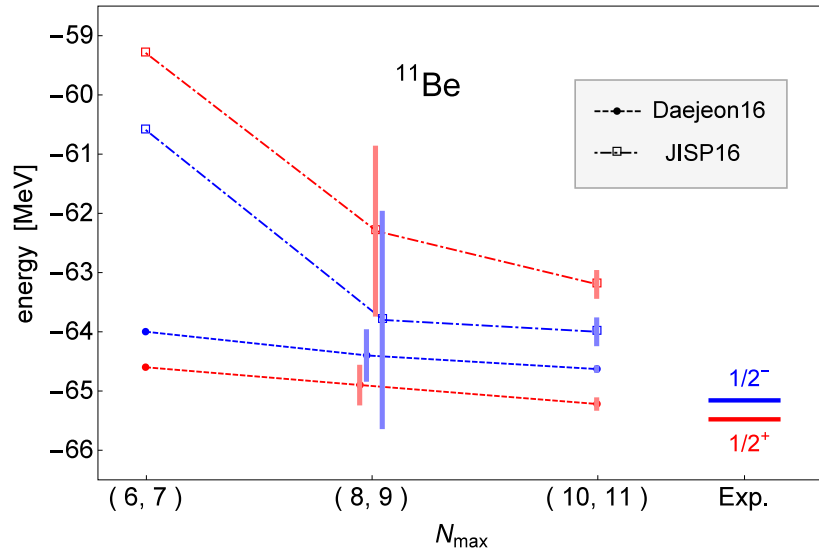


Figure 3: Energies of the ground and first-excited states of  $^{11}\text{Be}$  calculated within the *ab initio* NCSM with Daejeon16 and JISP16. The values are obtained using extrapolation B [8] for each highest  $N_{\max}$  at the variational minima and the error bars are given as the differences with the previous  $N_{\max}$  extrapolation. Experimental values are taken from Refs. [9, 10].

parity inversion (the current evaluation of the uncertainties of the JISP16 results is yet preliminary).

For an earlier study of the parity inversion in *ab initio* nuclear theory, we refer to Ref. [11].

## 2.2 Deep learning for *ab initio* nuclear theory

Recently, we proposed a feed-forward artificial neural network (ANN) method as an extrapolation tool for *ab initio* nuclear theory [12, 13]. Using the *ab initio* NCSM with Daejeon16 and the feed-forward ANN method, we predicted the ground-state energy and the ground-state point-proton root-mean-square (rms) radius of  $^6\text{Li}$ . We observed that our results are nearly converged at  $N_{\max} = 70$  (ground-state energy) and  $N_{\max} = 90$  (ground-state point-proton rms radius). Therefore, we concluded that the designed ANNs are sufficient to produce results for these two very different observables utilizing the NCSM results obtained in small basis spaces that exhibit the independence of basis space parameters in the limit of extremely large matrices [12, 13].

Before closing this Section, we refer to Refs. [14, 15], where resonance states such as tetra-neutron and  $^5\text{He}$  were studied in the framework of the single-state harmonic oscillator representation of scattering equations and the *ab initio* NCSM with Daejeon16 and some other modern  $NN$  interactions.

### 3 Summary

In this contribution, we briefly introduced the Daejeon16 *NN* interaction. We then presented some of interesting results from the *ab initio* NCSM studies with Daejeon16 and some other *NN* interactions such as JISP16. A remarkable result is that the parity inversion in  $^{11}\text{Be}$  is successfully reproduced in our study with Daejeon16.

We will continue to use Daejeon16 and some other modern *NN* interactions for various *ab initio* nuclear studies to be well-prepared for the forthcoming RI facilities.

### Acknowledgments

This work is supported in part by the U.S. Department of Energy under Grants No. DESC00018223 (SciDAC/NUCLEI) and No. DE-FG02-87ER40371, by the Russian Science Foundation under Grant No. 16-12-10048, by the Rare Isotope Science Project of Institute for Basic Science funded by Ministry of Science and ICT and National Research Foundation of Korea (2013M7A1A1075764), and the Ames Laboratory, operated for the U.S. Department of Energy under Contract No. DE-AC02-07CH11358 by Iowa State University.

### References

- [1] S. C. Pieper and R. B. Wiringa, *Annu. Rev. Nucl. Part. Sci.* **51**, 53 (2001).
- [2] K. Kowalski, D. J. Dean, M. Hjorth-Jensen, T. Papenbrock and P. Piecuch, *Phys. Rev. Lett.* **92**, 132501 (2004).
- [3] B. R. Barrett, P. Navrátil and J. P. Vary, *Prog. Part. Nucl. Phys.* **69**, 131 (2013).
- [4] E. Epelbaum, H. Krebs, D. Lee and U. G. Meißner, *Phys. Rev. Lett.* **106**, 192501 (2011).
- [5] P. Navrátil, S. Quaglioni, I. Stetcu and B. R. Barrett, *J. Phys. G* **36**, 083101 (2009).
- [6] A. M. Shirokov, I. J. Shin, Y. Kim, M. Sosonkina, P. Maris and J. P. Vary, *Phys. Lett. B* **761**, 87 (2016).
- [7] A. M. Shirokov, J. P. Vary, A. I. Mazur and T. A. Weber, *Phys. Lett. B* **644**, 33 (2007).
- [8] P. Maris, J. P. Vary and A. M. Shirokov, *Phys. Rev. C* **79**, 014308 (2009).
- [9] J. H. Kelley, E. Kwan, J. E. Purcell, C. G. Sheu and H. R. Weller, *Nucl. Phys. A* **880**, 88 (2012).
- [10] M. Wang, G. Audi, F. G. Kondev, W. J. Huang, S. Naimi and X. Xu, *Chin. Phys. C* **41**, 030003 (2017).
- [11] A. Calci, P. Navrátil, R. Roth, J. Dohet-Eraly, S. Quaglioni and G. Hupin, *Phys. Rev. Lett.* **117**, 242501 (2016).

- 
- [12] G. A. Negroita, G. R. Luecke, J. P. Vary, P. Maris, A. M. Shirokov, I. J. Shin, Y. Kim, E. G. Ng and C. Yang, in *Proc. Ninth Int. Conf. Comput. Logics, Algebras, Programming, Tools, and Benchmarking COMPUTATION TOOLS 2018, Barcelona, Spain, February 18–22, 2018*. IARIA, 2018, p. 20, arXiv:1803.03215 [physics.comp-ph] (2018).
- [13] G. A. Negroita, J. P. Vary, G. R. Luecke, P. Maris, A. M. Shirokov, I. J. Shin, Y. Kim, E. G. Ng, C. Yang, M. Lockner and G. M. Prabhu, *Phys. Rev. C* **99**, 054308 (2019).
- [14] A. M. Shirokov, Y. Kim, A. I. Mazur, I. A. Mazur, I. J. Shin and J. P. Vary, *AIP Conf. Proc.* **2038**, 020038 (2018).
- [15] A. M. Shirokov, A. I. Mazur, I. A. Mazur, E. A. Mazur, I. J. Shin, Y. Kim, L. D. Blokhintsev and J. P. Vary, *Phys. Rev. C* **98**, 044624 (2018).

# What Is Wrong with Our Current Nuclear Forces?

R. Machleidt

*Department of Physics, University of Idaho, Moscow, Idaho 83844, USA*

## Abstract

I discuss *ab initio* predictions for light and intermediate-mass nuclei as well as nuclear matter. Problems and open issues are outlined and an attempt is made to relate them to specific deficiencies of the chiral two- and many-nucleon forces currently in use. In particular, I identify the softness of the  $NN$  potential (due to non-locality) as one important factor for the improvement of microscopic predictions. This finding is very much in tune with the recent investigation by Lu *et al.* (arXiv:1812.10928) where — within a simple, but realistic model — it is shown that proper nuclear matter saturation requires a considerable amount of non-locality in the  $NN$  interaction.

**Keywords:** *Chiral effective field theory; two-nucleon forces; many-body forces; nuclear matter saturation*

One of the most fundamental aims in theoretical nuclear physics is to understand nuclear structure and reactions in terms of the basic forces between nucleons. In spite of intensive efforts for half a century [1], this goal has not been achieved. Why? Microscopic nuclear structure has essentially two ingredients: quantum many-body theory (QMBT) and nuclear forces. Thus, the reason for the failure can be that either our QMBT methods are wrong or our forces are deficient — or both. Over the past two decades, a large number of many-body approaches have been developed, refined, and tested [2–5], with the result that all of them generate essentially the same predictions when applied with the same forces. Hence, QMBT seems to be under control and the failure is most likely due to persistent problems with nuclear forces. Therefore, the focus of the rest of this paper is on nuclear interactions.

As discussed in numerous review papers [6–8], chiral effective field theory (EFT) is presently perceived to be the best approach to nuclear forces since it generates the forces needed (two- and many-body forces) on an equal footing and in a systematic way.

Consequently, a large number of applications of chiral two-nucleon forces (2NFs) together with chiral three-nucleon forces (3NFs) [and in some cases even four-nucleon forces (4NFs)] have been conducted in recent years. These investigations include few-nucleon reactions [9–14], the structure of light- and medium-mass nuclei [15–23], infinite matter at zero temperature [6, 24–33] and finite temperature [34, 35], and nuclear dynamics and response functions [36–42]. Although satisfactory predictions have been obtained in many cases, specific problems persist. Among them is the

---

*Proceedings of the International Conference ‘Nuclear Theory in the Supercomputing Era — 2018’ (NTSE-2018), Daejeon, South Korea, October 29 – November 2, 2018, eds. A. M. Shirokov and A. I. Mazur. Pacific National University, Khabarovsk, Russia, 2019, p. 21.*

<http://www.ntse.khb.ru/files/uploads/2018/proceedings/Machleidt.pdf>.

problem of describing the properties of medium-mass nuclei. For these nuclei, typically, the predicted radii are too small [43], while binding energies turn out to be too large [44]. This has led some groups to fit the forces directly to the properties of those medium-mass nuclei [45]. However, the resulting  $NN$  potential, which has become known as  $NNLO_{\text{sat}}$  [45], reproduces  $NN$  data only up to 35 MeV. Thus, the apparent success of this potential comes, in part, at the expenses of a satisfactory description of  $NN$  scattering above 35 MeV, which is not an acceptable solution of the problem. The idea of the *ab initio* approach is that the 2NF is fixed by two-nucleon data and the 3NF by three-nucleon data, with no further adjustments allowed. Applications in systems with  $A > 3$  are then true predictions.

A recent study [22] has provided an indication for how to overcome the overbinding problem: In Ref. [25], a nucleon-nucleon potential denoted by 1.8/2.0(EM) (which fits the  $NN$  data up to 290 MeV laboratory energy) was constructed to be extremely soft. Together with appropriate 3NFs (fit to the  ${}^3\text{H}$  binding energy and the  ${}^4\text{He}$  charge radius) it was used to calculate the ground-state properties of closed shell nuclei ranging from  ${}^4\text{He}$  to  ${}^{78}\text{Ni}$  [22]. The ground-state energies were reproduced very well, while the radii came out slightly too small. In another investigation [23], in which the same forces were applied, the structure of the light Tin isotopes were studied, reproducing both the binding energy and the small splitting between the lowest  $J^\pi = 7/2^+$  and  $5/2^+$  states of  ${}^{100}\text{Sn}$ . Moreover, in Ref. [25] it had been demonstrated that the 2NF + 3NF combination used in the above-cited calculations of finite nuclei reproduces nuclear matter saturation correctly. Thus, not surprisingly, there is a firm link between nuclear saturation and the ground-state properties of medium-mass and heavy nuclei.

Although, for reasons to be discussed below, these calculations do not provide a true solution to the radius and overbinding problem, they do give us a clue for how to overcome these problems: The 2NF has to be extremely soft, in fact, the 2NF should be such that applying it alone leads to substantial overbinding. Then adding a repulsive density-dependent 3NF contribution makes it possible to bring about the correct nuclear matter saturation [25].

In theory, one may also think of other ways to explain nuclear saturation. Namely, opposite to the above scheme, one may start from a relatively repulsive 2NF, leading to underbinding, and then adding an attractive, density-dependent 3NF contribution. An example for this scenario is the combination of the Argonne V18 (AV18) 2NF [46] plus the Urbana IX 3NF [47]. However, the nuclear matter saturation density *and energy* could not be reproduced by this combination [48] and medium-mass nuclei are severely underbound [49]. Similar problems occur, when AV18 is combined with the Illinois-7 3NF [49, 50]. So, it appears that the combination of repulsive 2NF plus attractive 3NF does not work in reality.

Thus, overbinding the many-body system by the 2NF and creating saturation by the 3NF contribution appears to be the only working approach. On a historical note, we mention that this is also the way how a quantitative explanation of nuclear saturation was achieved, *for the first time*, applying the so-called Dirac–Brueckner–Hartree–Fock approach [51–57], see Fig. 1.

However, the investigations of Refs. [22, 23, 25] can only be perceived as test calculations, because they are not fully consistent. The 2NF used in [22, 23, 25] is very soft because it is renormalization group (RG) evolved from a harder potential. But, to preserve the attraction created by the softness of the potential, the induced 3NF

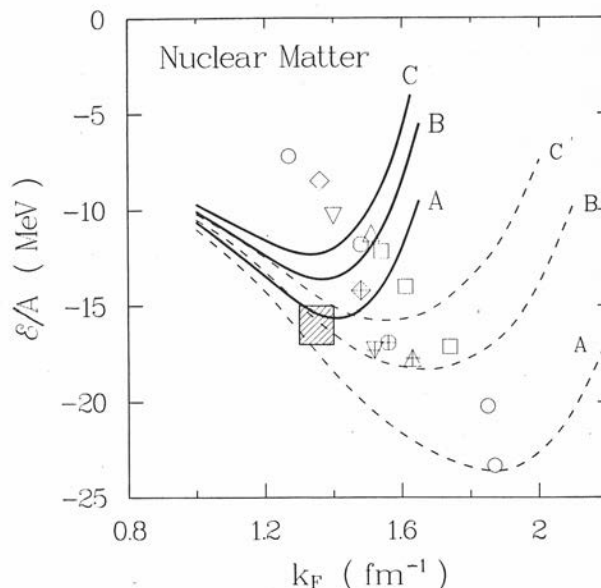


Figure 1: Ground state energy per particle of symmetric nuclear matter,  $\mathcal{E}/A$ , as a function of the Fermi momentum,  $k_F$ . The dashed lines are the predictions from 2NFs while the solid lines include the 3NF effects as generated by the Dirac–Brueckner–Hartree–Fock approach. Symbols denoted the saturation points from a variety of 2NFs. The shaded box represents the approximate empirical saturation energy and density. Taken from Ref. [52].

is left out. Or, in other words, the RG evolved potential is treated like an original potential. This was useful and insightful as a test calculation to show the principle, but it cannot be viewed as a fully consistent procedure. What we need now are fully consistent calculations, which take into account the above observations. For this,  $NN$  potentials are required that are soft from the outset. Therefore, recently, such  $NN$  potentials have been constructed through all order from leading-order (LO) to next-to-next-to-next-to-next-to-leading order ( $N^4LO$ ) [58].

There are many ways to quantify the softness of a  $NN$  potential. Weinberg eigenvalues have proven to be excellent for this purpose [59]. Other, simpler parameters are the  $D$ -state probability of the deuteron,  $P_D$ , with low  $P_D$  being a sign of softness. The triton binding energy,  $B_t$ , as predicted by the 2NF alone, is also a good indicator for smoothness. Based upon the experiences with the potentials used in Refs. [22, 23, 25],  $P_D < 4.5\%$  and  $B_t > 8.0$  MeV is desirable for the necessary softness of the 2NF. The soft  $NN$  potentials of Ref. [58] complemented by suitable 3NFs are generating promising nuclear matter predictions [60, 61], cf. Fig. 2.

The softness of these potentials can be clearly attributed to their non-local character. This finding is very much in tune with the recent investigation of Ref. [62] where — within a simple, but realistic model — it is shown that proper nuclear matter saturation requires a considerable amount of non-locality in the  $NN$  interaction.

It is now of interest to apply these new interactions in systematic studies of intermediate-mass nuclei to see if the anticipated improvements of the microscopic

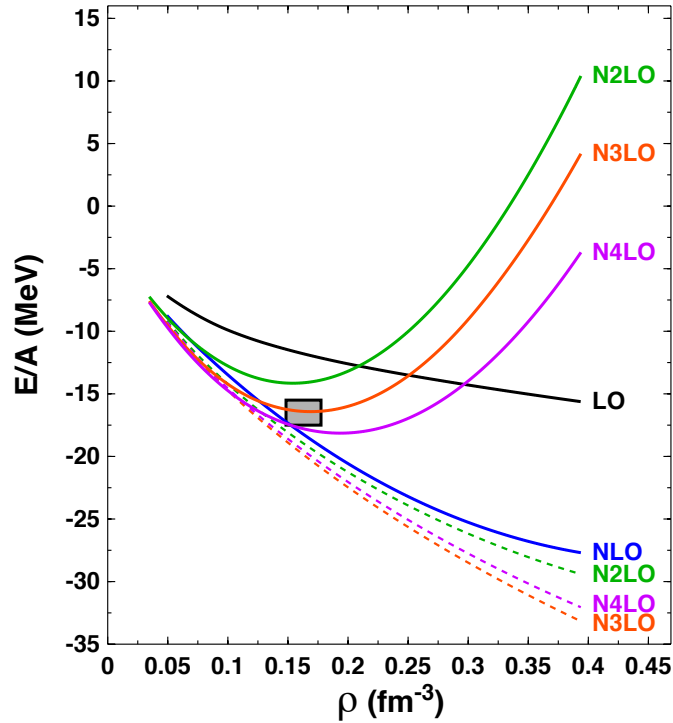


Figure 2: Ground state energy per particle of symmetric nuclear matter,  $E/A$ , as a function of density,  $\rho$ , from chiral 2NFs (dotted lines) and chiral 2NFs + 3NFs (solid lines) at the denoted orders of chiral EFT. Note that at LO and NLO, the 3NFs vanish. The grey box represents the approximate empirical saturation energy and density. Taken from Ref. [61].

predictions do occur.

This research is supported in part by the US Department of Energy under Grant No. DE-FG02-03ER41270.

## References

- [1] J. W. Negele, Phys. Rev. C **1**, 1260 (1970).
- [2] B. R. Barrett, P. Navrátil and J. P. Vary, Prog. Part. Nucl. Phys. **69**, 131 (2013).
- [3] G. Hagen, T. Papenbrock, M. Hjorth-Jensen and D. J. Dean, Rep. Prog. Phys. **77**, 096302 (2014).
- [4] J. Carlson, S. Gandolfi, F. Pederiva, S. C. Pieper, R. Schiavilla, K. E. Schmidt and R. B. Wiringa, Rev. Mod. Phys. **87**, 1067 (2015).
- [5] H. Hergert, S. K. Bogner, T. D. Morris, A. Schwenk and K. Tsukiyama, Phys. Rep. **621**, 165 (2016).

- 
- [6] R. Machleidt and F. Sammarruca, *Phys. Scr.* **91**, 083007 (2016).
- [7] R. Machleidt and D. R. Entem, *Phys. Rep.* **503**, 1 (2011).
- [8] E. Epelbaum, H.-W. Hammer and U.-G. Meißner, *Rev. Mod. Phys.* **81**, 1773 (2009).
- [9] E. Epelbaum, A. Nogga, W. Glöckle, H. Kamada, U.-G. Meißner and H. Witala, *Phys. Rev. C* **66**, 064001 (2002).
- [10] P. Navratil, R. Roth and S. Quaglioni, *Phys. Rev. C* **82**, 034609 (2010).
- [11] M. Viviani, L. Girlanda, A. Kievsky and L. E. Marcucci, *Phys. Rev. Lett.* **111**, 172302 (2013).
- [12] J. Golak *et al.*, *Eur. Phys. J. A* **50**, 177 (2014).
- [13] N. Kalantar-Nayestanaki, E. Epelbaum, J. G. Messchendorp and A. Nogga, *Rep. Prog. Phys.* **75**, 016301 (2012).
- [14] P. Navratil, S. Quaglioni, G. Hupin, C. Romero-Redondo and A. Calci, *Phys. Scr.* **91**, 053002 (2016).
- [15] H. Hagen, M. Hjorth-Jensen, G. R. Jansen, R. Machleidt and T. Papenbrock, *Phys. Rev. Lett.* **108**, 242501 (2012).
- [16] H. Hagen, M. Hjorth-Jensen, G. R. Jansen, R. Machleidt and T. Papenbrock, *Phys. Rev. Lett.* **109**, 032502 (2012).
- [17] A. Gezerlis, I. Tews, E. Epelbaum, S. Gandolfi, K. Hebeler, A. Nogga and A. Schwenk, *Phys. Rev. Lett.* **111**, 032501 (2013).
- [18] H. Hergert, S. K. Bogner, S. Binder, A. Calci, J. Langhammer, R. Roth and A. Schwenk, *Phys. Rev. C* **87**, 034307 (2013).
- [19] V. Somà, A. Cipollone, C. Barbieri, P. Navratil and T. Duget, *Phys. Rev. C* **89**, 061301(R) (2014).
- [20] K. Hebeler, J. D. Holt, J. Menéndez and A. Schwenk, *Annu. Rev. Nucl. Part. Sci.* **65**, 457 (2015).
- [21] G. Hagen *et al.*, *Nature Phys.* **12**, 186 (2015).
- [22] J. Simonis, S. R. Stroberg, K. Hebeler, J. D. Holt and A. Schwenk, *Phys. Rev. C* **96**, 014303 (2017).
- [23] T. D. Morris, J. Simonis, S. R. Stroberg, C. Stumpf, G. Hagen, J. D. Holt, G. R. Jansen, T. Papenbrock, R. Roth and A. Schwenk, *Phys. Rev. Lett.* **120**, 152503 (2018).
- [24] K. Hebeler and A. Schwenk, *Phys. Rev. C* **82**, 014314 (2010).
- [25] K. Hebeler, S. K. Bogner, R. J. Furnstahl, A. Nogga and A. Schwenk, *Phys. Rev. C* **83**, 031301(R) (2011).

- 
- [26] G. Baardsen, A. Ekström, G. Hagen and M. Hjorth-Jensen, *Phys. Rev. C* **88**, 054312 (2013).
- [27] G. Hagen, T. Papenbrock, A. Ekström, K. A. Wendt, G. Baardsen, S. Gandolfi, M. Hjorth-Jensen and C. J. Horowitz, *Phys. Rev. C* **89**, 014319 (2014).
- [28] L. Coraggio, J. W. Holt, N. Itaco, R. Machleidt and F. Sammarruca, *Phys. Rev. C* **87**, 014322 (2013).
- [29] L. Coraggio, J. W. Holt, N. Itaco, R. Machleidt, L. E. Marcucci and F. Sammarruca, *Phys. Rev. C* **89**, 044321 (2014).
- [30] F. Sammarruca, L. Coraggio, J. W. Holt, N. Itaco, R. Machleidt and L. E. Marcucci, *Phys. Rev. C* **91**, 054311 (2015).
- [31] C. Drischler, A. Carbone, K. Hebeler and A. Schwenk, *Phys. Rev. C* **94**, 054307 (2016).
- [32] I. Tews, S. Gandolfi, A. Gezerlis and A. Schwenk, *Phys. Rev. C* **93**, 024305 (2016).
- [33] J. W. Holt and N. Kaiser, *Phys. Rev. C* **95**, 034326 (2017).
- [34] C. Wellenhofer, J. W. Holt, N. Kaiser and W. Weise, *Phys. Rev. C* **89**, 064009 (2014).
- [35] C. Wellenhofer, J. W. Holt and N. Kaiser, *Phys. Rev. C* **92**, 015801 (2015).
- [36] S. Bacca, K. Hally, C. J. Pethick and A. Schwenk, *Phys. Rev. C* **80**, 032802 (2009).
- [37] A. Bartl, C. J. Pethick and A. Schwenk, *Phys. Rev. Lett.* **113**, 081101 (2014).
- [38] E. Rrapaj, J. W. Holt, A. Bartl, S. Reddy and A. Schwenk, *Phys. Rev. C* **91**, 035806 (2015).
- [39] M. Buraczynski and A. Gezerlis, *Phys. Rev. Lett.* **116**, 152501 (2016).
- [40] J. W. Holt, N. Kaiser and G. A. Miller, *Phys. Rev. C* **93**, 064603 (2016).
- [41] J. Birkhan *et al.*, *Phys. Rev. Lett.* **118**, 252501 (2017).
- [42] J. Rotureau, P. Danielewicz, G. Hagen, F. Nunes and T. Papenbrock, *Phys. Rev. C* **95**, 024315 (2017).
- [43] V. Lapoux, V. Somà, C. Barbieri, H. Hergert, J. D. Holt and S. R. Stroberg, *Phys. Rev. Lett.* **117**, 052501 (2016).
- [44] S. Binder, J. Langhammer, A. Calci and R. Roth, *Phys. Lett. B* **736**, 119 (2014).
- [45] A. Ekström *et al.*, *Phys. Rev. C* **91**, 051301 (2015).
- [46] R. B. Wiringa, V. G. J. Stoks and R. Schiavilla, *Phys. Rev. C* **51**, 38 (1995).
- [47] B. S. Pudliner, V. R. Pandharipande, J. Carlson and R. B. Wiringa, *Phys. Rev. Lett.* **74**, 4396 (1995).

- 
- [48] A. Akmal, V. R. Pandharipande and D. G. Ravenhall, *Phys. Rev. C* **58**, 1804 (1998).
- [49] D. Lonardoni, A. Lovato, S. C. Pieper and R. B. Wiringa, *Phys. Rev. C* **96**, 024326 (2017).
- [50] S. C. Pieper, *AIP Conf. Proc.* **1011**, 143 (2008).
- [51] R. Brockmann and R. Machleidt, *Phys. Lett. B* **149**, 283 (1984).
- [52] R. Machleidt, *Adv. Nucl. Phys.* **19**, 189 (1989).
- [53] R. Brockmann and R. Machleidt, *Phys. Rev. C* **42**, 1965 (1990).
- [54] D. Alonso and F. Sammarruca, *Phys. Rev. C* **67**, 054301 (2003).
- [55] F. Sammarruca, arXiv:0807.0263 [nucl-th] (2008).
- [56] F. Sammarruca, B. Chen, L. Coraggio, N. Itaco and R. Machleidt, *Phys. Rev. C* **86**, 054317 (2012).
- [57] H. Muether, F. Sammarruca and Z. Ma, *Int. J. Mod. Phys. E* **26**, 173001 (2017).
- [58] D. R. Entem, R. Machleidt and Y. Nosyk, *Phys. Rev. C* **96**, 024004 (2017).
- [59] J. Hoppe, C. Drischler, R. J. Furnstahl, K. Hebeler and A. Schwenk, *Phys. Rev. C* **96**, 054002 (2017).
- [60] C. Drischler, K. Hebeler and A. Schwenk, *Phys. Rev. Lett.* **122**, 042501 (2019).
- [61] F. Sammarruca, L. E. Marcucci, L. Coraggio, J. W. Holt, N. Itaco and R. Machleidt, arXiv:1807.06640 [nucl-th] (2018).
- [62] B. N. Lu, N. Li, S. Elhatisari, D. Lee, E. Epelbaum and U.-G. Meißner, arXiv:1812.10928 [nucl-th] (2018).

# Towards Nuclear Physics as Precision Science

Ulf-G. Meißner

*Helmholtz-Institut für Strahlen- und Kernphysik and Bethe Center for Theoretical Physics,  
Universität Bonn, D-53115 Bonn, Germany  
Institute for Advanced Simulation and Institut für Kernphysik, Forschungszentrum Jülich,  
D-52425 Jülich, Germany  
Tbilisi State University, 0186 Tbilisi, Georgia*

## Abstract

I discuss the foundations of Nuclear Lattice Effective Field Theory and discuss a number of applications to nuclear structure and reactions, including  $\alpha$ - $\alpha$  scattering, clustering in nuclei and the first steps towards calculations beyond next-to-next-to-leading order.

**Keywords:** *Effective field theory, nuclear forces, lattice, Monte Carlo methods*

## 1 Introduction: The big picture

Nuclear physics is an important part of the Standard Model (SM) of the strong, electromagnetic and weak interactions. While only about 5% of the energy-matter content of the Universe is a visible matter, this mostly comes in the form of atomic nuclei and is the stuff we are made off. In a way, the precise understanding of the formation of strongly interacting composites in forms of hadrons and nuclei can be seen as the last frontier of the SM. Furthermore, precision calculations in nuclear physics may open the door to unravel physics beyond the SM, e. g., through the electric dipole moments of light nuclei or neutrinoless  $\beta\beta$ -decay. Last but not least, as the generation of elements in the Big Bang and in stars exhibits some fine-tunings, the variation of the fundamental constants of the SM gives access to the multiverse and thus allows to investigate the anthropic view of the Universe.

Nuclear Lattice Effective Field Theory (NLEFT) combines the successful description of the forces between two, three and four nucleons in the continuum (see Evgeny Epelbaum's contribution to these Proceedings [1]), as initiated by Weinberg [2, 3], with stochastic methods to numerically exactly solve the nuclear  $A$ -body problems. NLEFT also allows to perform *ab initio* studies of nuclear reactions. This is an important feature as nuclear structure and reactions should be considered together. In the following, I will briefly outline some basic ingredients and a number of results obtained in this framework. More recent developments will be given in Dean Lee's contribution to these Proceedings [4].

---

*Proceedings of the International Conference 'Nuclear Theory in the Supercomputing Era — 2018' (NTSE-2018), Daejeon, South Korea, October 29 – November 2, 2018, eds. A. M. Shirokov and A. I. Mazur. Pacific National University, Khabarovsk, Russia, 2019, p. 28.*

<http://www.ntse.khb.ru/files/uploads/2018/proceedings/Meissner.pdf>.

## 2 Basics of nuclear lattice simulations

Nuclear lattice simulations or NLEFT is a new method to investigate the nuclear few- and many-body problem. In this approach, the Euclidean space-time is represented by a discrete hyper-cubic volume,  $V = L \times L \times L \times L_t$ , with the spatial (temporal) length  $L$  ( $L_t$ ) and corresponding lattice spacings  $a$  and  $a_t$ , respectively. The nucleons are considered as the basic constituents and are placed on the lattice sites, see a schematic pictorial in the left panel of Fig. 1. The interactions between the nucleons are given by the same chiral EFT potentials as in the continuum, for a review see, e. g., Ref. [5] simply adapted to the lattice formulation, see, e. g., Ref. [6]. The Coulomb interaction between the protons can also straightforwardly be included [7]. The chiral  $NN$  interactions obey a power counting, where the leading order (LO) consists of the static one-pion exchange and two four-nucleon contact terms. At higher orders, two-pion exchange, corrections to the one-pion exchange as well as contact interactions with an even number of derivatives appear. The latter are accompanied by low-energy constants (LECs) that must be fitted to the nucleon-nucleon scattering data. At the next-to-next-to-leading order (N<sup>2</sup>LO), the three-nucleon forces appear that contain two new LECs, that must be fitted to a three-nucleon system or three-nucleon scattering data. On the lattice, the finite lattice spacing entails an UV cut-off, as the maximal momentum is given by  $p_{\max} = \pi/a$ . For the most commonly used value of the lattice spacing,  $a \simeq 2$  fm, one has  $p_{\max} = 314$  MeV, which corresponds to a very soft interaction. Monte Carlo (MC) methods can then be used to numerically exactly solve the  $A$ -body problem for a given set of  $NN$  and  $NNN$  interactions. A very important ingredient in these simulations is the approximate Wigner  $SU(4)$  symmetry of the nuclear interactions, that is crucial in suppressing the malicious sign oscillations that plague fermion MC studies at finite baryonic density [8, 9]. The remaining sign oscillations are caused by  $SU(4)$  non-symmetric contact terms as well as by the one-pion-exchange. For more details, see the review [10] and the upcoming textbook [11].

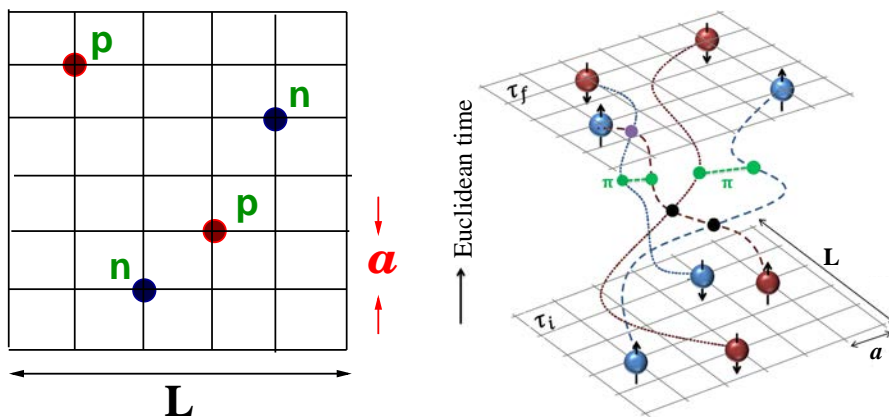


Figure 1: Left panel: Neutrons and protons on a space-time lattice with spatial length  $L$  and lattice spacing  $a$ . Right panel: Evolution of a  ${}^4\text{He}$  nucleus in Euclidean time.

The central object of NLEFT is the  $A$ -nucleon correlation function,

$$Z_A(t) = \langle \Psi_A | \exp(-tH) | \Psi_A \rangle, \quad (1)$$

with  $t$  being the Euclidean time and  $\Psi_A$  being a Slater determinant of  $A$  free nucleons or a more sophisticated correlated initial/final state. From the transient energy

$$E_A(t) = -\frac{d}{dt} \ln Z_A(t) \quad (2)$$

one can infer the ground state energy of the  $A$ -nucleon system via

$$E_A^0 = \lim_{t \rightarrow \infty} E_A(t). \quad (3)$$

Similarly, the expectation value of any normal-ordered operator follows from

$$Z_A^{\mathcal{O}} = \langle \Psi_A | \exp(-tH/2) \mathcal{O} \exp(-tH/2) | \Psi_A \rangle \quad (4)$$

in the limit of infinite Euclidean time,

$$\lim_{t \rightarrow \infty} (Z_A^{\mathcal{O}}(t)/Z_A(t)) = \langle \Psi_A | \mathcal{O} | \Psi_A \rangle. \quad (5)$$

Excited state properties can also be extracted. In order to compute the low-lying excited states of a given nucleus, the Euclidean time projection method is generalized to a multi-channel calculation [12]. The Euclidean time evolution of a  ${}^4\text{He}$  nucleus is depicted in the right panel of Fig. 1. Initial states are either properly antisymmetrized free standing waves of four particles or more complex correlated configurations. With the help of auxiliary fields, the multi-nucleon interactions and the pion exchanges can be mapped onto insertions on a single nucleon world-line, which makes such a computation most accessible for parallel computing. One major advantage of this approach is that all possible configurations are sampled, in particular also four nucleons, on one lattice site. This already lets one suspect that clustering will emerge naturally in this approach.

## 3 Results from nuclear lattice simulations

### 3.1 General remarks

Before discussing results obtained using NLEFT, a few general remarks are in order. As already stressed, nuclear structure and reactions dynamics should be treated on the same footing. This has important implications for the simulations. While originally all LECs have been determined in few-nucleon systems, which has led to a number of intriguing results, it was realized later that nucleus-nucleus collisions should also be used for determining some LECs as this appears to be advantageous in pinning down more precisely the three- and higher-body forces. Furthermore, the framework of nuclear lattice simulations could only be established as a novel quantum many-body method since one was able to solve problems that before could not be mastered in the well established schemes based on the same chiral forces.

Most results in NLEFT have been obtained with an NNLO action that involves a Gaussian smearing of the two LO contact interactions, with the smearing parameter

fixed from the average  $S$ -wave  $np$  effective range. The canonical lattice had a coarse lattice spacing of  $a = 1.97$  fm and  $L \simeq 10 \dots 16$  fm depending on the nucleus or system under investigation. For such a coarse lattice, the NLO and NNLO corrections can be treated as perturbations, in particular, the contribution from the two-pion exchange can be absorbed in the LECs of the  $4N$  operators. At this order, one has 11 LECs related to  $np$ ,  $nn$  and  $pp$  scattering as well as two  $3N$  LECs. The  $2N$  LECs were determined from fits to the  $np$  phase shifts using the spherical wall method [13] and its refinement [14] as well as to the  $nn$  and  $pp$  scattering lengths. The  $3N$  LECs were determined from a fit to the triton binding energy and the spin-doublet neutron-deuteron scattering phase shift. The first non-trivial prediction is then the  ${}^3\text{He}$ - ${}^3\text{H}$  binding energy difference [7,15] which comes out as 0.78(5) MeV close to the empirical value of 0.76 MeV. Ground state energies up to  ${}^{28}\text{Si}$  can now be calculated with a few percent accuracy and an error of about 1%, see Refs. [16,17]. Note, however, that at this order there is still some residual lattice spacing dependence when  $a$  is varied between 1 and 2 fm, see Refs. [18,19]. An effective four-nucleon operator has been utilized to overcome this effect. This residual lattice spacing dependence, however, disappears at NNNLO as than the  $np$  phase shifts are independent on  $a$  for  $a$  varying between 1 and 2 fm within uncertainties as recently shown in Ref. [20].

Excited states can be computed with a comparable accuracy. In Fig. 2, the LO calculation of the first two  $0^+$  states in  ${}^{12}\text{C}$  is shown, starting from various initial states (plane waves and alpha cluster states) [21]. One set of these initial states directly gives the ground state (left panel), whereas the other set first traces out the first excitation with the same quantum numbers as shown by the intermediate plateau (right panel). This is the famous Hoyle state [22]. The thermalization of various initial states with growing Euclidean time to almost the same energy gives a

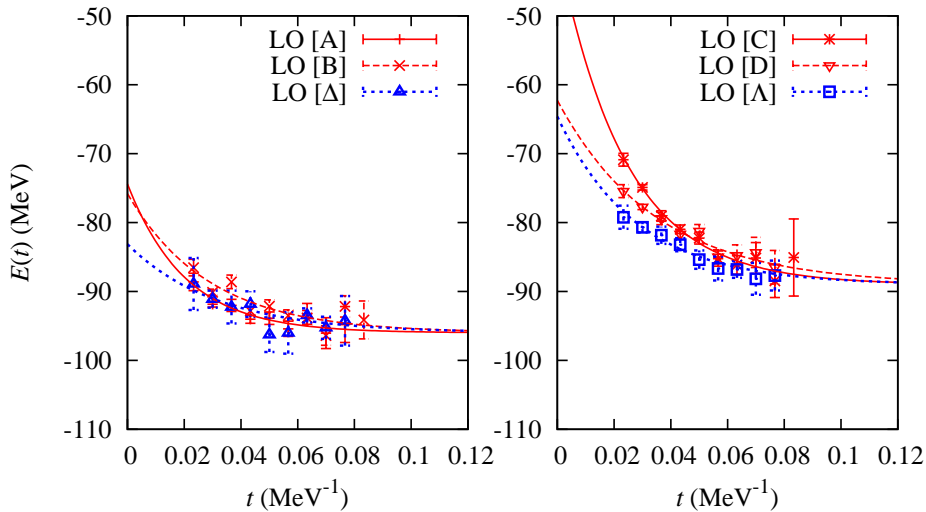


Figure 2: Results for the lowest  $0^+$  states in  ${}^{12}\text{C}$  at LO. The left panel shows the results using various initial states, each of which approaches the ground state energy with increasing Euclidean time  $t$ . The right panel shows the results using other initial states. These trace out an intermediate plateau at an energy  $\sim 7$  MeV above the ground state.

handle on the systematic uncertainties inherent to the simulations. For more details, see, e. g., Ref. [17].

Using this framework, a number of interesting results has been obtained, such as the first *ab initio* calculation of the Hoyle state in  $^{12}\text{C}$  [12,21], the study of the triple-alpha process under variations of some fundamental constants [23,24], the calculation of the ground state energies of the alpha-cluster nuclei up to  $^{28}\text{Si}$  with an accuracy of about 1% [16], an *ab initio* calculation of the spectrum and structure of  $^{16}\text{O}$  [25], and the first ever microscopic calculation of alpha-alpha scattering [26]. However, the employed NNLO action works well for alpha-type nuclei, but is less precise for other systems. Therefore, new forms of smearing including also the pion-exchange as well as a non-local distribution of lattice creation and annihilation operators have been employed to gain further insight. Based on these improved LO actions, it was found that nuclear physics is near a quantum phase transition from a Bose gas to the nuclear liquid, where the first alpha-cluster nuclei are formed [27]. Another important observation in that paper is related to the degree of locality of the contact interactions, that appears to play a major role when going to larger nuclei and nuclear or neutron matter, as recently emphasized in Ref. [28]. Furthermore, isotopic chains from H to O could be calculated and new insights into nuclear clustering was obtained recently, including also a new algorithm that for the first time allows to calculate density distributions in nuclei and the corresponding form factors [29]. Some selected topics from this rich spectrum of results will be discussed in what follows. Most of these results have been obtained on supercomputers like JUGENE and JUQUEEN at the Forschungszentrum Jülich. The CPU scaling is approximately quadratic in atomic number, so nuclei up to  $A \simeq 40$  have been investigated. Going to larger nuclei requires more fine-tuned actions to suppress the remaining sign oscillations.

### 3.2 *Ab initio* calculation of alpha-alpha scattering

Let us now consider the  $\alpha$ - $\alpha$  scattering as a prototypical nuclear reaction. This is related to the facts that processes involving  $\alpha$ -type nuclei comprise a major part of stellar nucleosynthesis, and control the production of certain elements in stars. Also, *ab initio* calculations of scattering and reactions suffer from exponential or factorial scaling with the number of nucleons in the clusters, so therefore it was not possible so far to perform an *ab initio* calculation of  $\alpha$ - $\alpha$  scattering. It is thus a challenging task to use the lattice to tackle such type of processes. We note that on the lattice one only has discrete energy levels, and therefore a direct calculation of scattering processes appears impossible. This hurdle can be overcome by the so-called adiabatic projection method, that splits the problem of the calculation of scattering and inelastic reactions into two parts. First, using the Euclidean time projection method, one constructs a low-energy cluster Hamiltonian, called the adiabatic Hamiltonian. In the second step, one then computes scattering phase shifts or reaction amplitudes using this adiabatic Hamiltonian. The method was developed and refined in Refs. [30–34] and resembles in the methodology the Hamiltonian matrix approach combining the no-core shell model with the resonating group method, see, e. g., Refs. [35–37]. In more detail, the construction of a low-energy effective theory for clusters proceeds as follows: One uses initial states as a direct product of two clusters located on the lattice, parameterized

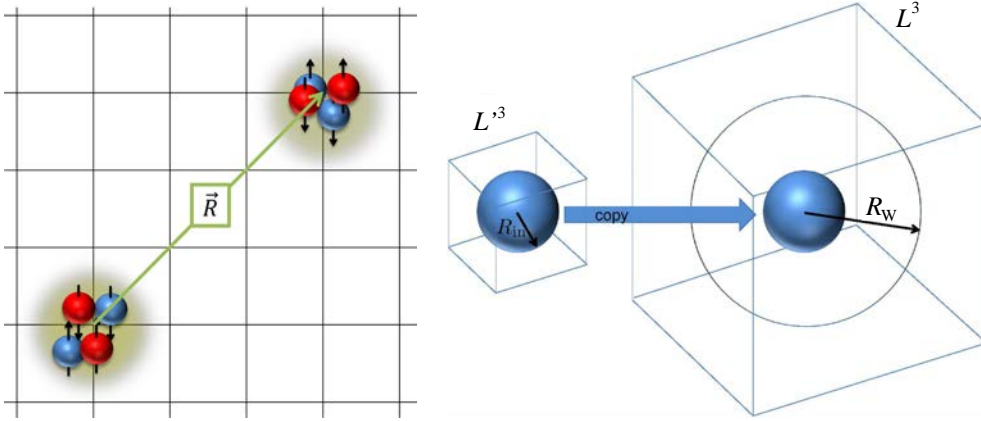


Figure 3: Left panel: A two-dimensional picture of the two-cluster initial state  $|\vec{R}\rangle$  separated by the displacement vector  $\vec{R}$ . Right panel: A sketch of the lattices for the cluster-cluster calculations in the overlapping and in the noninteracting regions.  $R_{in}$  is the largest radial distance where the full adiabatic Hamiltonian is matched to the effective free cluster Hamiltonian without introducing any systematic errors.  $R_W$  indicates the radius of the spherical wall as discussed in the text.

by the relative separation between the clusters, as shown in the left panel of Fig. 3,

$$|\vec{R}\rangle = \sum_{\vec{r}} |\vec{r} + \vec{R}\rangle \otimes \vec{r}. \quad (6)$$

These are projected in Euclidean time with the chiral EFT Hamiltonian  $H$ ,  $|\vec{R}\rangle_\tau = \exp(-H\tau)|\vec{R}\rangle$ . These so-called dressed cluster states include all possible interaction effects such as polarizations as well as deformations and, of course, the Pauli principle. The adiabatic Hamiltonian is then given by  $[H_\tau]_{\vec{R}\vec{R}'} = {}_\tau\langle\vec{R}|H|\vec{R}'\rangle_\tau$ . In general, this Hamiltonian needs to be normalized, which requires left and right multiplication with the corresponding norm matrices. What concerns the strong interactions, it can be shown that asymptotically, the adiabatic Hamiltonian is nothing but the free Hamiltonian for two clusters, eventually supplemented by infinite-range interactions as the Coulomb one. The underlying simulations can be simplified considerably by employing the so-called radial Hamiltonian based on the lattice version of angular momentum projection and binning the lattice points in rings of a given width. Further, the long-range Coulomb interaction can also be included exactly. For that, one performs first simulations in small box with a volume  $L^3 \sim (16 \text{ fm})^3$ , with all interactions switched on. This is supplemented by a second set of simulations in a large box with a volume of about  $L^3 \sim (120 \text{ fm})^3$ , where the strong interactions are turned off and the long-range Coulomb interaction is included by imposing Coulomb boundary conditions on a spherical wall with radius  $R_W \simeq 40 \text{ fm}$ , see the right panel of Fig. 3. In that way, all effects of the strong and the electromagnetic interactions are included.

Using the same NNLO Hamiltonian as for the studies of the spectrum and structure of  $^{12}\text{C}$  and  $^{16}\text{O}$ , the  $S$ - and  $D$ -wave phase shifts have been computed in Ref. [26], as shown in Fig. 4. At LO in the employed counting, the Coulomb interaction is not included, so both the  $S$ - and  $D$ -wave phase shifts are off the data. This is visibly

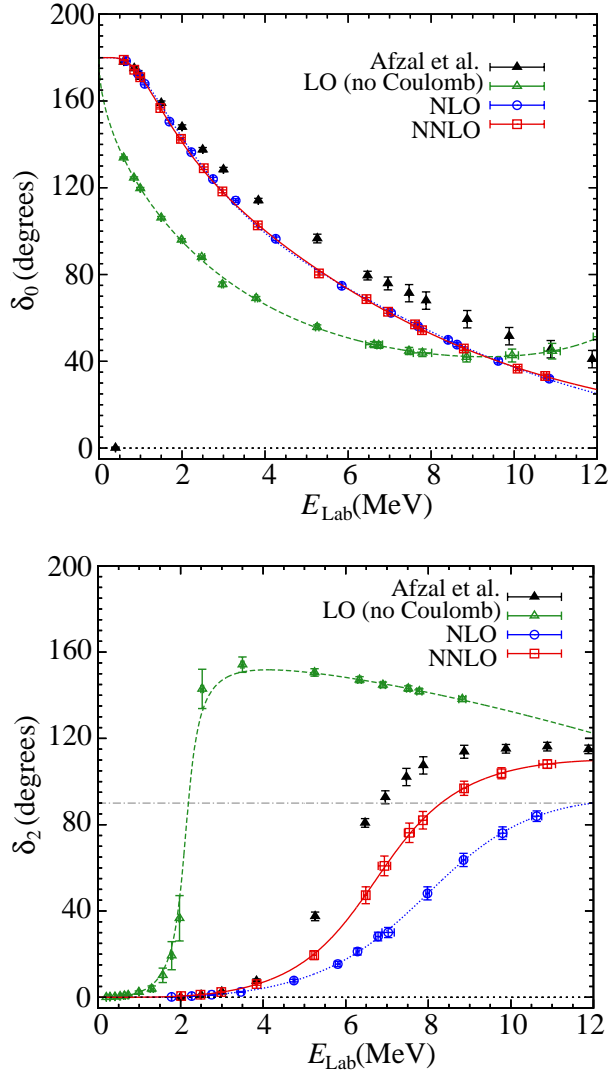


Figure 4: Upper panel:  $S$ -wave  $\alpha$ - $\alpha$  phase shifts  $\delta_0$ . Bottom panel:  $D$ -wave  $\alpha$ - $\alpha$  phase shifts  $\delta_2$ . Shown are the NLEFT LO (green triangles), NLO (blue circles) and NNLO (red squares) results. The data (black triangles with error bars) are from Ref. [38].

improved at NLO and further at NNLO for the  $D$ -wave. The small NNLO corrections in the  $S$ -wave are due to the coarse lattice spacing. Overall, one finds a good description of the scattering data. In the  $S$ -wave, we find a bound state corresponding to  ${}^8\text{Be}$  that is bound by  $-0.11(1)$  MeV, whereas in nature this nucleus is unbound by  $+0.09$  MeV. This deviation of about 200 keV reflects the precision of the calculation. In the  $D$ -wave at NNLO, the resonance parameters are  $E_R^{\text{NNLO}} = 3.27(12)$  MeV and  $\Gamma_R^{\text{NNLO}} = 2.09(16)$  MeV, not far off the empirical data of  $2.92(18)$  MeV and  $1.35(50)$  MeV, respectively. Maybe the most significant result of this study is the fact that the computational time scales quadratically with the number of nucleons in the two clusters,  $t_{\text{CPU}} \sim (A_1 + A_2)^2$ , with  $A_i$  being the number of nucleons in the cluster  $i$  ( $i = 1, 2$ ). This means that the computational time for the so-called holy grail of nuclear astrophysics, the radiative alpha capture on  ${}^{12}\text{C}$  at stellar energies (given by the Gamow peak),  $\alpha + {}^{12}\text{C} \rightarrow {}^{16}\text{O} + \gamma$ , is in reach, requiring only 8 times

as much CPU time as the computation of elastic  $\alpha$ - $\alpha$  scattering (twice the number of nucleons and two channels). Before doing that, however, the chiral forces should be worked out to N3LO so as to reach the required accuracy.

### 3.3 New insights into nuclear clustering

Clustering in nuclei is an old but ever fascinating topic, introduced by Wheeler in 1937 in this seminal paper on “Molecular Viewpoints in Nuclear Structure” [39]. The most prominent type of clustering is the observation of  $\alpha$ -particle substructures in light and medium-mass nuclei, and its eventual disappearance as the atomic number increases. There have been many works on alpha clustering, here I just mention recent work on alpha clustering employing density functional methods by the Peking group [40] as well as work by the Paris–Zagreb group [41]. For a recent review, see, e. g., Ref. [42].

As already mentioned above, alpha clustering emerges naturally in NLEFT and a number of intriguing results on alpha-type nuclei and clustering have already been obtained, such as the first *ab initio* calculation of the Hoyle state or the observation that nuclear physics is close to a quantum phase transition from a Bose gas of  $\alpha$ 's to a nuclear liquid for  $\alpha$ -type nuclei. However, when adding extra neutrons and/or protons, the precision of the calculations quickly deteriorates due to the remaining sign oscillations. To overcome this, a new LO action with smeared SU(4) local and non-local symmetric contact interactions as well as smeared one-pion exchange was constructed in Ref. [29]. The non-local smearing distributes any nucleon creation and/or annihilation operator over the six neighboring lattice sites as depicted in the left panel of Fig. 5,

$$a_{\text{NL}}^{(\dagger)}(\mathbf{n}) = a^{(\dagger)}(\mathbf{n}) + s_{\text{NL}} \sum_{\langle \mathbf{n}' \mathbf{n} \rangle} a^{(\dagger)}(\mathbf{n}'), \quad (7)$$

where  $s_{\text{NL}}$  is a real parameter, and the notation  $\sum_{\langle \mathbf{n}' \mathbf{n} \rangle}$  represents the summation over nearest-neighbor lattice sites of the site  $\mathbf{n}$ . While this smearing was originally designed to just suppress the remaining sign oscillations when extra neutrons and/or protons are added to alpha-type nuclei, it turned out to work much better. For that, consider a LO action that is SU(4) symmetric with local and non-local smearing as well as smeared one-pion exchange. This action has three LECs, the strength of the SU(4)-symmetric contact term, the parameter related to the degree of locality of the interaction and the above-mentioned  $s_{\text{NL}}$ . Fitting these to the average  $np$   $S$ -wave scattering lengths and effective ranges and also to the  $\alpha$ - $\alpha$   $S$ -wave scattering length, one can predict the isotope chains from hydrogen to oxygen as shown in the right panel of Fig. 5. These have an accuracy of 0.7 MeV per nucleon or better. This is quite amazing given this highly simplified LO action. Clearly, NLO effects (and higher orders) need to be accounted for to achieve, e. g., a better description of the  $^1S_0$   $np$  phase.

Using this action, one can also obtain deeper insight into nuclear clustering. For that, define as probes of alpha clusters the quantities

$$\rho_4 = \sum_{\mathbf{n}} : \rho^4(\mathbf{n})/4! : \quad \text{and} \quad \rho_3 = \sum_{\mathbf{n}} : \rho^3(\mathbf{n})/3! : . \quad (8)$$

Here,  $\rho_4$  couples to the center of the  $\alpha$ -cluster while  $\rho_3$  gets contributions from a wider portion of the alpha-particle wave function and thus these can be used for “measuring” cluster properties. Note that  $\rho_3$  and  $\rho_4$  depend on the regulator, the

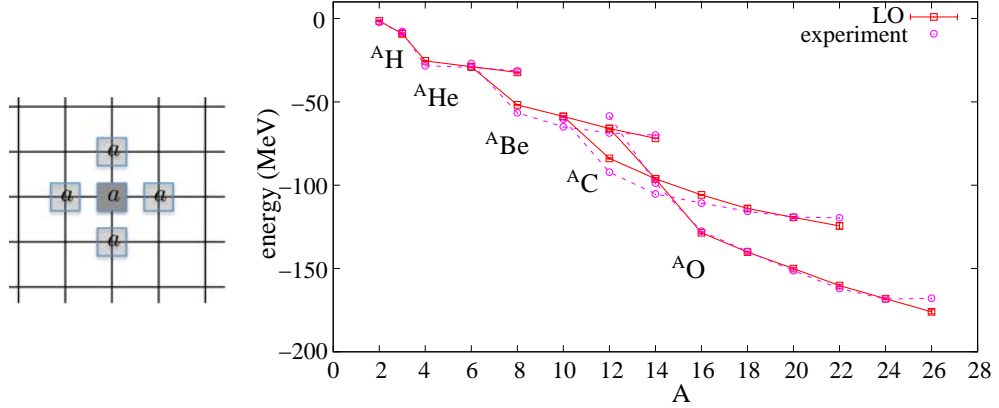


Figure 5: Left panel: Two-dimensional illustration of the non-local smearing of a nucleon creation/annihilation operator over the neighboring lattice sites. Right panel: The ground state energies versus the number of nucleons  $A$  for the hydrogen, helium, beryllium, carbon, and oxygen isotopes (NLEFT: squares with error bars, experiment: circles). The errors are one-standard deviation error bars associated with the stochastic errors and the extrapolation to an infinite number of time steps.

lattice spacing  $a$ , but not on the nucleus. However, the ratios  $\rho_3/\rho_{3,\alpha}$  and  $\rho_4/\rho_{4,\alpha}$  are free from short-distance ambiguities. If properly defined, the effective number of alpha clusters should be greater than or equal to  $N_\alpha$ . A value equal to  $N_\alpha$  indicates that the alpha clusters are behaving as indivisible objects, and the nucleus can be regarded as a compound fluid of alpha particles and neutrons. If the effective number is significantly greater than  $N_\alpha$ , then the description in terms of individual alpha clusters breaks down and the system behaves more as a nuclear liquid of protons and neutrons. The behavior is shown in the left panel of Fig. 6, where it is seen that, for the oxygen isotope chain, the entanglement between the clusters leads to the expectation values of  $\rho_3/\rho_{3,\alpha}$  and  $\rho_4/\rho_{4,\alpha}$  much larger than 4. This shows that the transition from cluster-like states in light systems to nuclear liquid-like states in heavier systems should not be viewed as a simple suppression of multi-nucleon short-distance correlations, but rather as an increasing *entanglement* of the nucleons involved in the multi-nucleon correlations.

Another important development of Ref. [29] was the formulation of the so-called pinhole algorithm, see the right panel of Fig. 6. In general, auxiliary field quantum MC calculations involve states that are superpositions of many different center-of-mass (cm) positions, so a direct calculation of density distributions of nucleons in a nucleus is not possible. This can be overcome by inserting a screen with pinholes with spin and isospin labels that allows nucleons with corresponding spin and isospin to pass. In that way, one measures the  $A$ -body density operator

$$\rho_{i_1, j_1, \dots, i_A, j_A}(\mathbf{n}_1, \dots, \mathbf{n}_A) = : \rho_{i_1, j_1}(\mathbf{n}_1) \dots \rho_{i_A, j_A}(\mathbf{n}_A) : \quad (9)$$

MC sampling of the amplitude

$$A_{i_1, j_1, \dots, i_A, j_A}(\mathbf{n}_1, \dots, \mathbf{n}_A, L_t) = \langle \psi(\tau/2) | \rho_{i_1, j_1, \dots, i_A, j_A}(\mathbf{n}_1, \dots, \mathbf{n}_A) | \psi(\tau/2) \rangle \quad (10)$$

then allows to measure the proton and neutron densities as well as more complicated

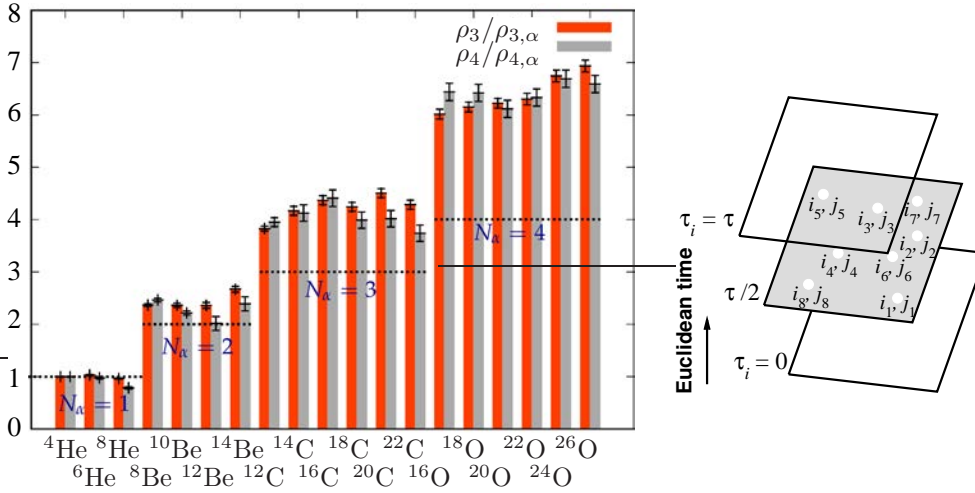


Figure 6: Left panel: The ratios  $\rho_3/\rho_{3,\alpha}$  and  $\rho_4/\rho_{4,\alpha}$  for the helium, beryllium, carbon and oxygen isotopes. For orientation, we also indicate by the dashed lines the expected number of  $\alpha$ -clusters,  $N_\alpha$ . Right panel: Sketch of the pinhole locations and spin-isospin indices at time  $t = L_t a_t / 2$ .

two-, three- or higher-body correlations of nucleons within a given nucleus. This is because the pinhole sheet allows one to determine the cm of a given nucleus given simply by the minimal distance to all nucleons. Further, the resolution of this method is  $a/A$  because the cm position  $\mathbf{r}_{\text{cm}}$  is an integer  $\mathbf{n}_{\text{cm}}$  times  $a/A$ . Results for the proton and neutron distributions in the isotopes  $^{12,14,16}\text{C}$  are shown in the upper panel of Fig. 7. The proton size of  $r_E^p = 0.84$  fm [43, 44] is accounted for and asymptotic properties for the volume dependence of  $N$ -body bound states [45] have been used. Upon the Fourier-transformation of these densities, one can obtain the corresponding elastic form factor. This is shown in the bottom panel of Fig. 7 for  $^{12}\text{C}$ . Given the simplicity of the underlying Hamiltonian, the agreement is quite satisfactory. This paves the way for detailed nuclear structure studies.

### 3.4 Fine-tunings and the multiverse

In nuclear physics, we observe a number of so-called fine-tunings, for some reviews and recent works, see, e. g., Refs. [47–51]. A prominent example is the lightest nucleus, the deuteron. It is bound by a mere 2 MeV, just one tenth of percent of its total mass. Also, the aforementioned Hoyle state must be very closely placed to the triple-alpha threshold, in nature the energy difference is just 380 keV, much less than typical nuclear excitation energies of a few MeV. This close proximity is required so that in hot, old stars a sufficient amount of carbon and also oxygen is generated [22]. It is therefore natural to ask how much the SM fundamental parameters can be detuned so that this resonance condition is no longer viable? First, however, we must find out what the relevant parameters are. Nuclear binding is a delicate balance between the attractive strong and the repulsive electromagnetic interactions. The latter are given in terms of Sommerfeld’s fine-structure constant,  $\alpha_{\text{EM}} \simeq 1/137$ . As concerns the strong interaction, the strong coupling constant  $\alpha_S$  is intimately tied to

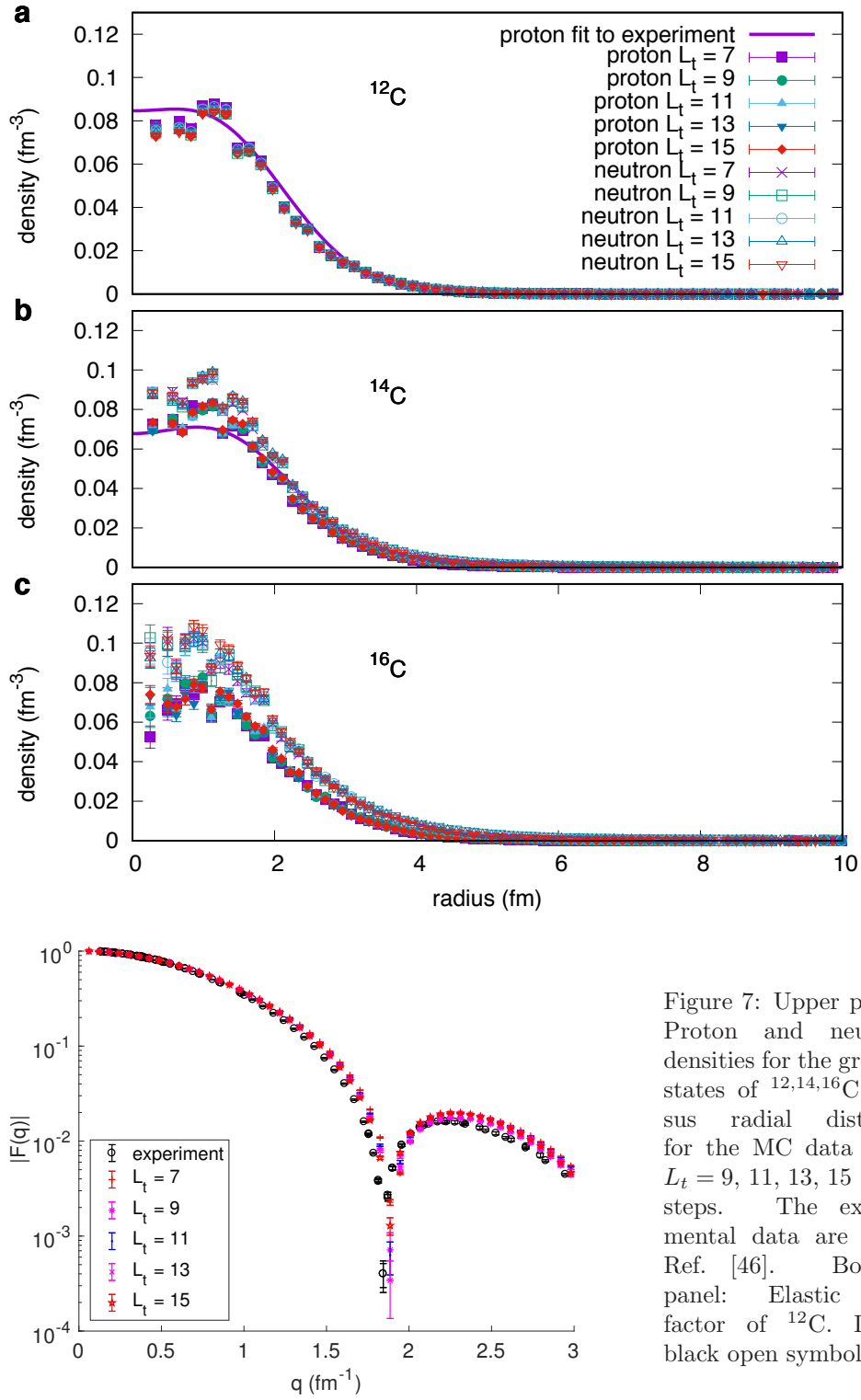


Figure 7: Upper panel: Proton and neutron densities for the ground states of  $^{12,14,16}\text{C}$  versus radial distance for the MC data with  $L_t = 9, 11, 13, 15$  time steps. The experimental data are from Ref. [46]. Bottom panel: Elastic form factor of  $^{12}\text{C}$ . Data: black open symbols.

the nucleon mass because of dimensional transmutation, and therefore the small light quark masses  $m_u, m_d$  are the relevant parameters that control nuclear binding. This appears at first counter-intuitive, as the major part of the nucleon mass is given by gluon field energy by means of the trace anomaly, while the light quark contribution to the nucleon mass is given by the so-called pion-nucleon  $\sigma$ -term,  $\sigma_{\pi N} = 59(3)$  MeV [52]. However, the quark mass values of a few MeV (which are, of course, scale- and scheme-dependent) are of the same size as the nuclear binding energy per nucleon,  $E/A$ , so that these are the pertinent strong interaction parameters. To be more precise, the rate of the triple-alpha process is given by  $r_{3\alpha} \sim \Gamma_\gamma \exp(-\Delta E/kT)$ , with  $k$  being the Boltzmann constant,  $T$  is the temperature,  $\Gamma_\gamma$  is the width of the Hoyle state and  $\Delta E = E_{12}^* - 3E_\alpha = 379.47(18)$  keV, where  $E^*$  is the energy of the Hoyle state. The question now is how much can the  $\Delta E$  be changed so that there is still enough  $^{12}\text{C}$  and  $^{16}\text{O}$  produced in the stars? This was answered in a calculation of the element generation in stars by varying  $\Delta E$  but no other parameter. It turned out that the allowed variation is  $\delta|\Delta E| \lesssim 100$  keV [53, 54], which does not appear to be any form of fine-tuning. Note that very recent stellar simulations appear to soften this envelope [55]. However, one still has to make the connection to the fundamental parameters of the SM. While this can be done for the electromagnetic interactions in cluster-type models as used, e. g., in Ref. [53], the variation of the quark masses requires a more microscopic framework as provided by chiral EFT. This is depicted for the quark mass dependence of the LO  $NN$  force in the upper panel of Fig. 8. Here, the quark mass and pion mass dependences can be used synonymously, as the Gell-Mann–Oakes–Renner relation,  $M_\pi^2 \sim m_u + m_d$ , is fulfilled to better than 94% in QCD [56]. As can be seen from this figure, there are explicit (through the pion propagator) and implicit (through the pion-nucleon coupling, the nucleon mass and the four-nucleon couplings) pion mass dependences. All this can be accounted for systematically and precisely using chiral EFT. Coming back to the triple alpha-process, nuclear lattice simulations are the appropriate tool to study its dependence on the fundamental parameters, for details see Refs. [23, 24]. For that, one has to translate the condition  $\delta|\Delta E| \lesssim 100$  keV into a constraint for the quark masses (and similarly for the fine-structure constant). For the quark masses, it reads (for fixed  $\alpha_{\text{EM}}$ )

$$\left| \left( 0.571(14)\bar{A}_s + 0.934(11)\bar{A}_t - 0.069(6) \right) \frac{\delta m_q}{m_q} \right| < 0.0015, \quad (11)$$

with the average light quark mass (as the strong isospin breaking plays no role here)  $m_q = (m_u + m_d)/2$ ,  $\bar{A}_{s,t} \equiv \partial a_{s,t}^{-1} / \partial M_\pi |_{M_\pi^{\text{phys}}}$ , where  $a_s$  and  $a_t$  denote the singlet and the triplet  $NN$  scattering length, respectively. Independently of the precise values of these two quantities, it can be shown that the various fine-tunings in the triple-alpha process (the closeness of the  $^8\text{Be}$  binding energy to the  $2\alpha$  threshold and the closeness of the Hoyle state to the  $3\alpha$  threshold) are indeed correlated. This had been speculated before [58] but could only be worked out precisely using NLEFT. Bounds on  $\bar{A}_{s,t}$  had been obtained earlier based on resonance saturation of  $4N$  operators [59] in Ref. [57] (see also Ref. [60]) as shown by the black cross in the bottom panel of Fig. 8. The fairly large uncertainty can eventually be overcome using lattice QCD to calculate these quantities. In the plane of  $\bar{A}_s$ - $\bar{A}_t$ , varying the quark mass leads to diagonal bands whose widths depends on the assumed variations. This is shown for variations of  $\delta m_q/m_q$  of 0.5, 1 and 5% by the three different bands. Clearly, a smaller

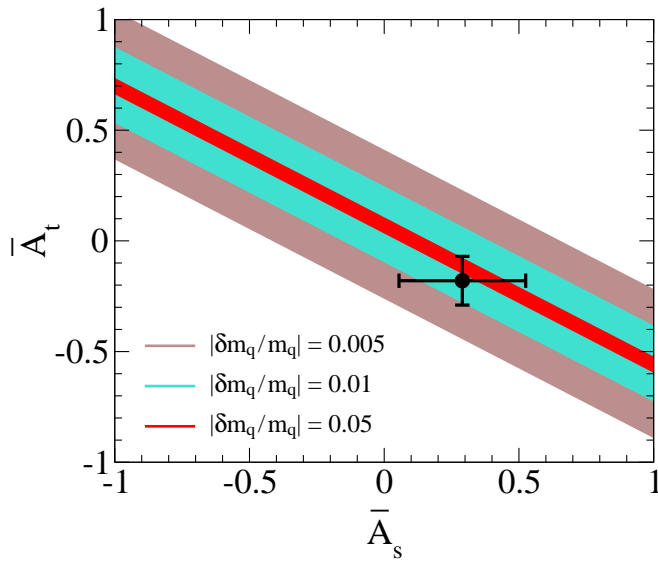
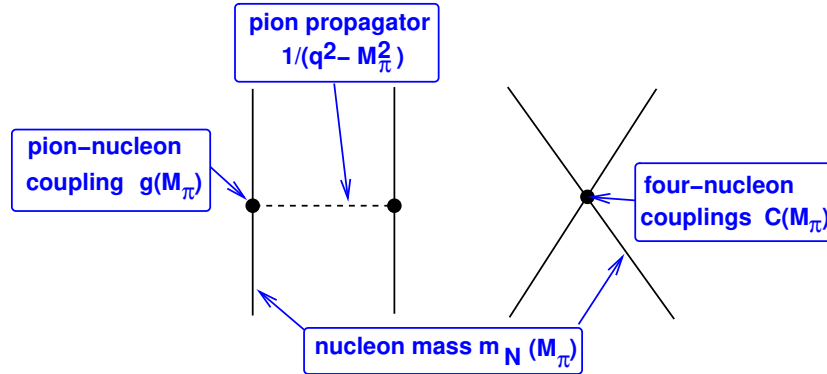


Figure 8: Upper panel: Schematic drawing of the quark mass dependence in the two-nucleon force. Bottom panel: “Survivability bands” for carbon-oxygen based life due to 0.5% (broad outer band), 1% (medium band) and 5% (narrow inner band) changes in  $m_q$  in terms of the input parameters  $\bar{A}_s$  and  $\bar{A}_t$ . The black cross denotes the results of the N2LO analysis from [57].

variation leads to a broader band. If one focuses on the central value of  $\bar{A}_{s,t}$ , one finds that the  $m_q$  variations of 2–3% are allowed so that the abovementioned condition is fulfilled. The large uncertainties in  $\bar{A}_{s,t}$  do not allow for a more precise statement. For  $\alpha_{EM}$ , no such uncertainties are present and it can be stated with certainty that it can be varied by at most 2.5%. Also, no other bounds are found if one varies both the quark masses and the fine-structure constant at the same time. This is clearly a stronger fine-tuning as for  $|\Delta E|$  and its consequences for our anthropic view of the Universe are discussed in Ref. [61]. Lattice QCD can be used to tighten the bounds on  $\bar{A}_{s,t}$ , for the state-of-the-art see Ref. [62].

## 4 Summary and outlook

Let me briefly summarize the main messages of this talk:

- Chiral EFT for nuclear forces provides a precise framework for  $2N$  and  $3N$

forces with small uncertainties, as discussed by Evgeny Epelbaum [1] in these Proceedings. The nuclear forces from chiral EFT can also be formulated for varying strong and electromagnetic forces, which is a necessary requirement to study various fine-tunings in nuclear physics.

- Nuclear lattice simulations are a new quantum many-body approach that is based on the successful continuum nuclear chiral EFT. Already a number of intriguing results have been obtained based on NLEFT. In particular, the clustering emerges naturally and  $\alpha$ -cluster nuclei are well described. Further, with an improved chiral action based on non-local smearing, neutron- and proton-rich nuclei can also be studied. With the invention of the pinhole algorithm, the calculation of charge densities and form factors has become possible. Furthermore, a fine-tuning in nuclear reactions can be studied.
- Various bridges to the lattice QCD studies need to be explored, in particular, in pinning down some of the LECs related to multi-nucleon forces or the quark mass dependence of multi-nucleon operators.
- Finally, it must be said that many open issues in nuclear structure and reaction physics can now be addressed in a truly quantitative manner. For example, the “holy grail” of nuclear astrophysics [63], the *ab initio calculation* of the reaction  ${}^4\text{He} + {}^{12}\text{C} \rightarrow {}^{16}\text{O} + \gamma$ , is in reach.

More recent developments in NLEFT will be covered in Dean Lee’s contribution [4].

## Acknowledgements

I thank the organizers for giving me an opportunity to present these thoughts at this interesting workshop. I am grateful to all my collaborators, who have contributed to my understanding of the issues discussed here. Partial financial support by the CAS (2018DM0034), DFG (TRR 110), and VolkswagenStiftung (grant no. 93562) is gratefully acknowledged.

## References

- [1] E. Epelbaum, *see these Proceedings*, p. 150, <http://www.ntse.khb.ru/files/uploads/2018/proceedings/Epelbaum.pdf>.
- [2] S. Weinberg, Phys. Lett. B **251**, 288 (1990).
- [3] S. Weinberg, Nucl. Phys. B **363**, 3 (1991).
- [4] D. Lee, *see these Proceedings*, p. 45, <http://www.ntse.khb.ru/files/uploads/2018/proceedings/Lee.pdf>.
- [5] E. Epelbaum, H.-W. Hammer and U.-G. Meißner, Rev. Mod. Phys. **81**, 1773 (2009).
- [6] B. Borasoy, E. Epelbaum, H. Krebs, D. Lee and U.-G. Meißner, Eur. Phys. J. A **31**, 105 (2007).

- 
- [7] E. Epelbaum, H. Krebs, D. Lee and U.-G. Meißner, Eur. Phys. J. A **45**, 335 (2010).
- [8] E. Wigner, Phys. Rev. **51**, 106 (1937).
- [9] J. W. Chen, D. Lee and T. Schäfer, Phys. Rev. Lett. **93**, 242302 (2004).
- [10] D. Lee, Prog. Part. Nucl. Phys. **63**, 117 (2009).
- [11] T. A. Lähde and U.-G. Meißner, *Nuclear lattice effective field theory: An introduction*. Springer-Verlag, Heidelberg (*in print*).
- [12] E. Epelbaum, H. Krebs, D. Lee and U.-G. Meißner, Phys. Rev. Lett. **106**, 192501 (2011).
- [13] B. Borasoy, E. Epelbaum, H. Krebs, D. Lee and U.-G. Meißner, Eur. Phys. J. A **35**, 343 (2008).
- [14] B. N. Lu, T. A. Lähde, D. Lee and U.-G. Meißner, Phys. Lett. B **760**, 309 (2016).
- [15] E. Epelbaum, H. Krebs, D. Lee and U.-G. Meißner, Phys. Rev. Lett. **104**, 142501 (2010).
- [16] T. A. Lähde, E. Epelbaum, H. Krebs, D. Lee, U.-G. Meißner and G. Rupak, Phys. Lett. B **732**, 110 (2014).
- [17] T. A. Lähde *et al.*, J. Phys. G **42**, 034012 (2015).
- [18] J. M. Alarcon *et al.*, Eur. Phys. J. A **53**, 83 (2017).
- [19] N. Klein, S. Elhatisari, T. A. Lähde, D. Lee and U.-G. Meißner, Eur. Phys. J. A **54**, 121 (2018).
- [20] N. Li, S. Elhatisari, E. Epelbaum, D. Lee, B. N. Lu and U.-G. Meißner, Phys. Rev. C **98**, 044002 (2018).
- [21] E. Epelbaum, H. Krebs, T. A. Lähde, D. Lee and U.-G. Meißner, Phys. Rev. Lett. **109**, 252501 (2012).
- [22] F. Hoyle, Astrophys. J. Suppl. **1**, 121 (1954).
- [23] E. Epelbaum, H. Krebs, T. A. Lähde, D. Lee and U.-G. Meißner, Phys. Rev. Lett. **110**, 112502 (2013).
- [24] E. Epelbaum, H. Krebs, T. A. Lähde, D. Lee and U.-G. Meißner, Eur. Phys. J. A **49**, 82 (2013).
- [25] E. Epelbaum *et al.*, Phys. Rev. Lett. **112**, 102501 (2014).
- [26] S. Elhatisari *et al.*, Nature **528**, 111 (2015).
- [27] S. Elhatisari *et al.*, Phys. Rev. Lett. **117**, 132501 (2016).
- [28] B. N. Lu, N. Li, S. Elhatisari, D. Lee, E. Epelbaum and U.-G. Meißner, arXiv:1812.10928 [nucl-th] (2018).

- 
- [29] S. Elhatisari *et al.*, Phys. Rev. Lett. **119**, 222505 (2017).
- [30] G. Rupak and D. Lee, Phys. Rev. Lett. **111**, 032502 (2013).
- [31] M. Pine, D. Lee and G. Rupak, Eur. Phys. J. A **49**, 151 (2013).
- [32] S. Elhatisari and D. Lee, Phys. Rev. C **90**, 064001 (2014).
- [33] A. Rokash, M. Pine, S. Elhatisari, D. Lee, E. Epelbaum and H. Krebs, Phys. Rev. C **92**, 054612 (2015).
- [34] S. Elhatisari, D. Lee, U. G. Meißner and G. Rupak, Eur. Phys. J. A **52**, 174 (2016).
- [35] P. Navrátil and S. Quaglioni, Phys. Rev. C **83**, 044609 (2011).
- [36] P. Navrátil, R. Roth and S. Quaglioni, Phys. Lett. B **704**, 379 (2011).
- [37] P. Navrátil and S. Quaglioni, Phys. Rev. Lett. **108**, 042503 (2012).
- [38] S. A. Afzal, A. A. Z. Ahmad and S. Ali, Rev. Mod. Phys. **41**, 247 (1969).
- [39] J. A. Wheeler, Phys. Rev. **52**, 1083 (1937).
- [40] P. W. Zhao, N. Itagaki and J. Meng, Phys. Rev. Lett. **115**, 022501 (2015).
- [41] J.-P. Ebran, E. Khan, T. Niksic and D. Vretenar, Nature **487**, 341 (2012).
- [42] M. Freer, H. Horiuchi, Y. Kanada-En'yo, D. Lee and U. G. Meißner, Rev. Mod. Phys. **90**, 035004 (2018).
- [43] M. A. Belushkin, H.-W. Hammer and U.-G. Meißner, Phys. Rev. C **75**, 035202 (2007).
- [44] R. Pohl *et al.*, Nature **466**, 213 (2010).
- [45] S. König and D. Lee, Phys. Lett. B **779**, 9 (2018).
- [46] F. J. Kline, H. Crannell, J. T. O' Brien, J. Mccarthy and R. R. Whitney, Nucl. Phys. A **209**, 381 (1973).
- [47] C. J. Hogan, Rev. Mod. Phys. **72**, 1149 (2000).
- [48] R. L. Jaffe, A. Jenkins and I. Kimchi, Phys. Rev. D **79**, 065014 (2009).
- [49] L. A. Barnes, Publ. Astron. Soc. Austral. **29**, 529 (2012).
- [50] A. N. Schellekens, Rev. Mod. Phys. **85**, 1491 (2013).
- [51] J. F. Donoghue, Annu. Rev. Nucl. Part. Sci. **66**, 1 (2016).
- [52] M. Hoferichter, J. Ruiz de Elvira, B. Kubis and U.-G. Meißner, Phys. Rev. Lett. **115**, 092301 (2015).
- [53] H. Oberhummer, A. Csoto and H. Schlattl, Science **289**, 88 (2000).
- [54] H. Schlattl, A. Heger, H. Oberhummer, T. Rauscher and A. Csoto, Astrophys. Space Sci. **291**, 27 (2004).

- [55] L. Huang, F. C. Adams and E. Grohs, *Astropart. Phys.* **105**, 13 (2019).
- [56] G. Colangelo, J. Gasser and H. Leutwyler, *Phys. Rev. Lett.* **86**, 5008 (2001).
- [57] J. C. Berengut *et al.*, *Phys. Rev. D* **87**, 085018 (2013).
- [58] S. Weinberg, *Facing up*. Harvard University Press, Cambridge, MA, 2001.
- [59] E. Epelbaum, U.-G. Meißner, W. Gloeckle and C. Elster, *Phys. Rev. C* **65**, 044001 (2002).
- [60] P. F. Bedaque, T. Luu and L. Platter, *Phys. Rev.* **C83**, 045803 (2011).
- [61] U.-G. Meißner, *Sci. Bull.* **60**, 43 (2015).
- [62] V. Baru, E. Epelbaum and A. A. Filin, *Phys. Rev. C* **94**, 014001 (2016).
- [63] W. A. Fowler, *Rev. Mod. Phys.* **56**, 149 (1984).

# Recent Advances in Nuclear Lattice Simulations

Dean Lee

*Facility for Rare Isotope Beams and Department of Physics and Astronomy, Michigan State University, East Lansing, MI 48824, USA*

## Abstract

We review several recent results in the area of nuclear lattice simulations based on chiral effective field theory by the Nuclear Lattice EFT Collaboration. The topics we cover are lattice interactions with improved rotational properties and a computational method called eigenvector continuation.

**Keywords:** *Lattice simulations; effective field theory; nuclear forces; nuclear theory*

## 1 Introduction

Chiral effective field theory (EFT) describes the low-energy interactions of nucleons. It consists of an expansion in powers of momenta and factors of the pion mass near the chiral limit where the light quarks are massless; see Ref. [1] for a review of chiral EFT. Terms with a total of  $n$  powers of nucleon momenta or factors of the pion masses are labelled as order  $Q^n$ . The leading order (LO) interactions are at order  $Q^0$ , the next-to-leading order (NLO) interactions correspond to order  $Q^2$ , next-to-next-to-leading order (N2LO) terms are  $Q^3$ , and next-to-next-to-next-to-leading order (N3LO) are  $Q^4$ . In this Proceedings article we review two recent results using chiral EFT by the Nuclear Lattice EFT Collaboration. See also the contribution by Ulf-G. Meißner in the same Proceedings volume [2] for other recent results.

## 2 Improved lattice interactions

Nuclear lattice simulations using chiral EFT have been used to describe the structure and scattering of atomic nuclei [3–5]. However the treatment of nuclear forces at higher orders in the chiral expansion are difficult on the lattice due to the breaking of rotational invariance produced by the nonzero lattice spacing [6, 7].

In Ref. [8] we solve these problems with a new set of short-range chiral EFT interactions on the lattice that decomposes more easily into spin channels. The key idea is to define smeared annihilation and creation operators. This procedure gives us better rotational symmetry properties when taking spatial derivatives as finite differences. We start with  $a_{i,j}(\mathbf{n})$ , the nucleonic annihilation operator on lattice site  $\mathbf{n}$

---

*Proceedings of the International Conference ‘Nuclear Theory in the Supercomputing Era — 2018’ (NTSE-2018), Daejeon, South Korea, October 29 – November 2, 2018, eds. A. M. Shirokov and A. I. Mazur. Pacific National University, Khabarovsk, Russia, 2019, p. 45.*

<http://www.ntse.khb.ru/files/uploads/2018/proceedings/Lee.pdf>.

with spin  $i$  and isospin  $j$ . To this we add neighboring lattice operator with relative weight,  $s_{\text{NL}}$ , to define the smeared annihilation operator

$$a_{i,j}^{\text{sNL}}(\mathbf{n}) = a_{i,j}(\mathbf{n}) + s_{\text{NL}} \sum_{|\mathbf{n}'|=1} a_{i,j}(\mathbf{n} + \mathbf{n}'). \quad (1)$$

Next we form bilinear functions of the annihilation operators with various spin and isospin quantum numbers,  $S, S_z, I, I_z$ ,

$$[a(\mathbf{n}) a(\mathbf{n}')]_{S,S_z,I,I_z}^{\text{sNL}} = \sum_{i,j,i',j'} a_{i,j}^{\text{sNL}}(\mathbf{n}) M_{ii'}(S, S_z) M_{jj'}(I, I_z) a_{i',j'}^{\text{sNL}}(\mathbf{n}'). \quad (2)$$

We introduce orbital angular momentum using solid spherical harmonics,

$$R_{L,L_z}(\mathbf{r}) = \sqrt{\frac{4\pi}{2L+1}} r^L Y_{L,L_z}(\theta, \phi), \quad (3)$$

that are written as functions of the lattice derivatives of one of the annihilation operators,

$$P_{S,S_z,L,L_z,I,I_z}^{2M,s_{\text{NL}}}(\mathbf{n}) = [a(\mathbf{n}) \nabla_{1/2}^{2M} R_{L,L_z}^*(\nabla) a(\mathbf{n})]_{S,S_z,I,I_z}^{\text{sNL}}. \quad (4)$$

We then project onto the selected spin and orbital angular momentum using Clebsch-Gordan coefficients,

$$O_{S,L,J,J_z,I,I_z}^{2M,s_{\text{NL}}}(\mathbf{n}) = \sum_{S_z,L_z} \langle SS_z LL_z | JJ_z \rangle P_{S,S_z,L,L_z,I,I_z}^{2M,s_{\text{NL}}}(\mathbf{n}). \quad (5)$$

We present in Ref. [8] results for the neutron-proton system up to next-to-next-to-next-to-leading order for lattice spacings of 1.97, 1.64, 1.32, and 0.99 fm. In Fig. 1 we show results for the neutron-proton scattering phase shifts and mixing angles versus the relative momenta for the lattice spacing  $a = 1.32$  fm, and in Fig. 2 we show neutron-proton scattering phase shifts and mixing angles for the lattice spacing  $a = 0.99$  fm. The blue, green and red bands signify the estimated uncertainties at NLO, N2LO and N3LO respectively. The black solid line and diamonds denote phase shift or mixing angle from the Nijmegen partial wave analysis and lattice calculation at N3LO, respectively. These results show marked improvement over previous studies of chiral EFT interactions on the lattice.

### 3 Eigenvector continuation

In nuclear theory and other fields of quantum theory we often would like to find the extremal eigenvalues and eigenvectors of a Hamiltonian matrix in a vector space that is extremely large, so large that linear algebra operations on general vectors cannot be done. Monte Carlo methods are well suited to overcome this problem, however stochastic methods fail when severe sign oscillations appear and there is strong cancellation between positive and negative amplitudes.

We present in Ref. [9] a new technique called eigenvector continuation (EC) that can improve the reach of Monte Carlo methods. The main idea is that while an eigenvector inhabits a linear space with very many dimensions, the eigenvector trajectory generated by smooth changes of the Hamiltonian matrix can be well approximated by a low-dimensional manifold. This statement is proven using analytic continuation.

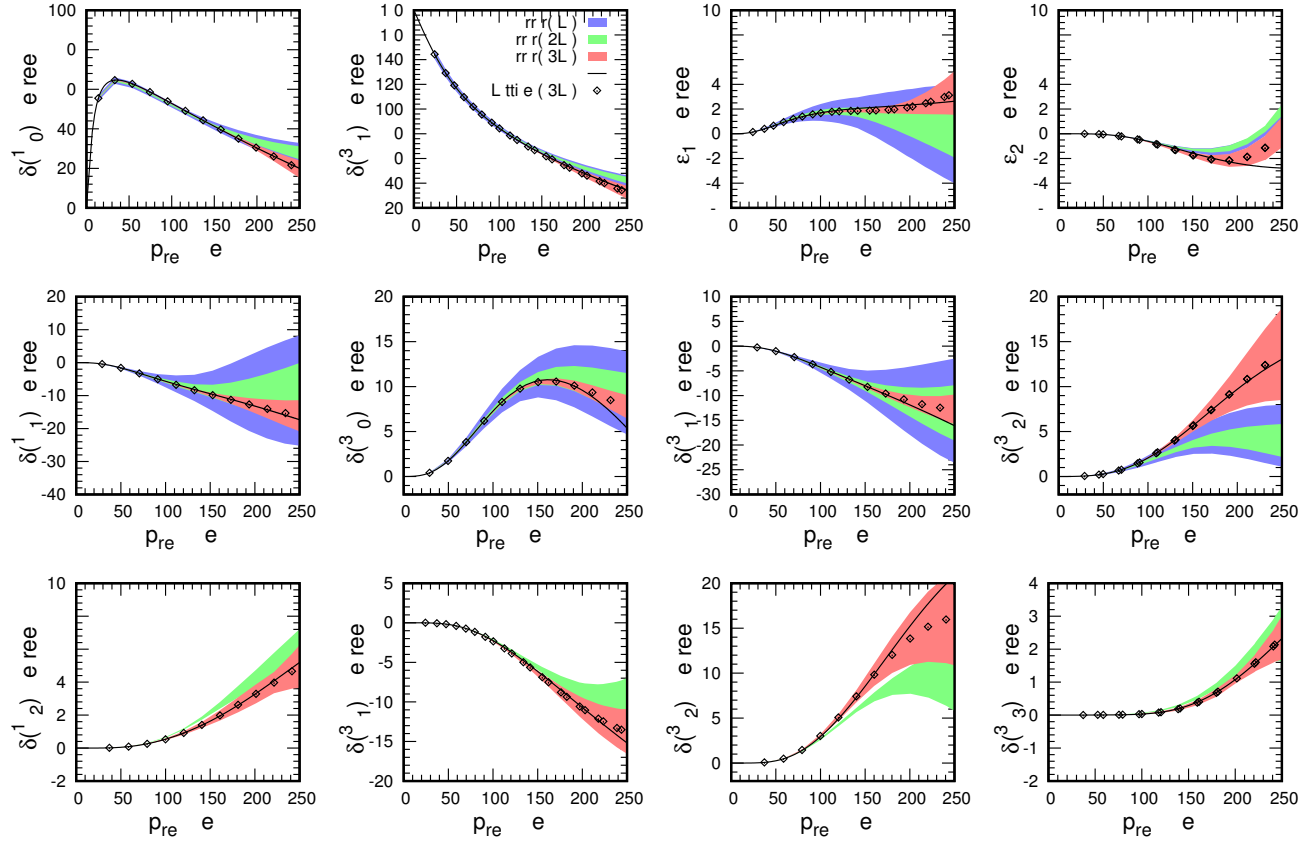


Figure 1: Results for the neutron-proton scattering phase shifts and mixing angles versus the relative momenta for the lattice spacing  $a = 1.32$  fm. The blue, green and red bands signify the estimated uncertainties at NLO, N2LO and N3LO respectively. The black solid line and diamonds denote phase shifts or mixing angles from the Nijmegen partial wave analysis and lattice calculation at N3LO, respectively.

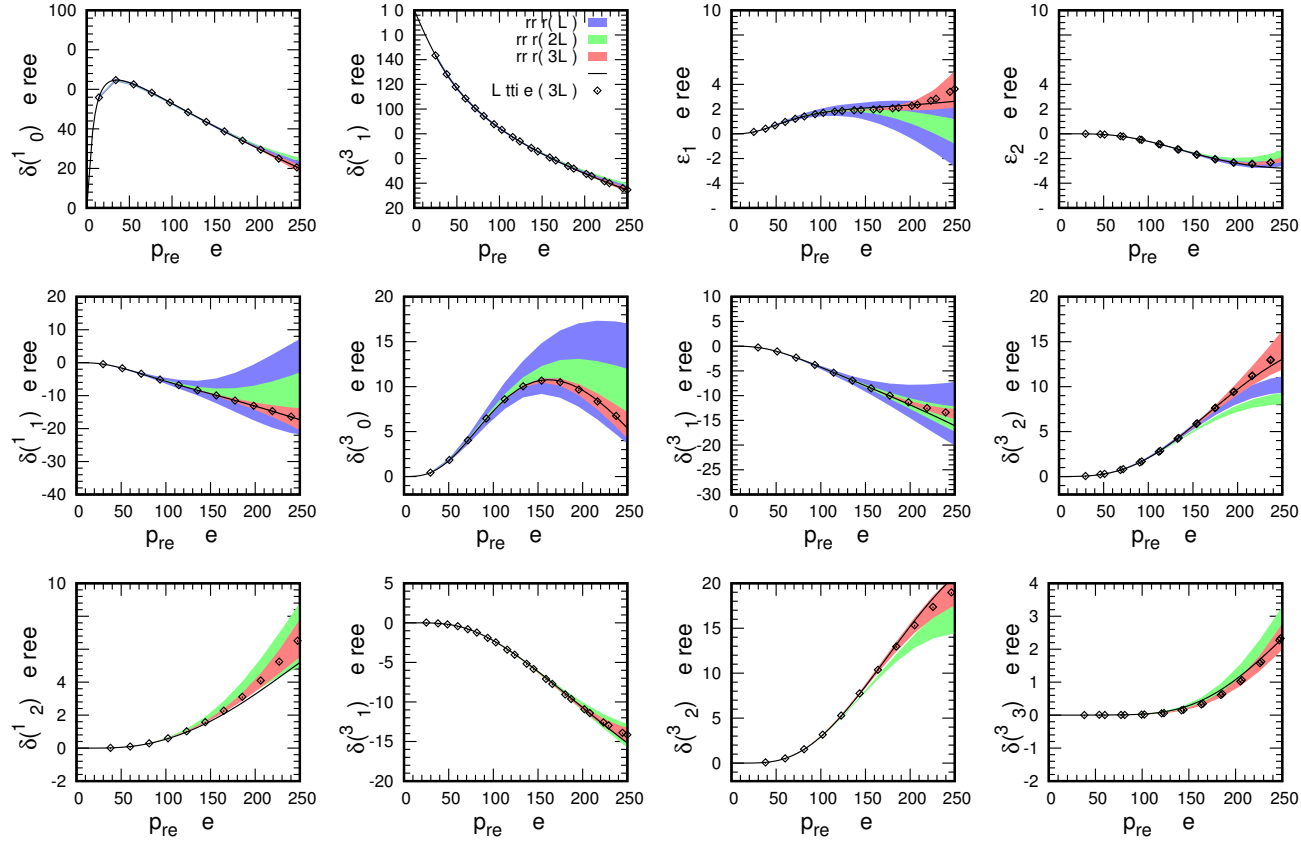


Figure 2: Results for the neutron-proton scattering phase shifts and mixing angles versus the relative momenta for the lattice spacing  $a = 0.99$  fm. The blue, green and red bands signify the estimated uncertainties at NLO, N2LO and N3LO respectively. The black solid line and diamonds denote phase shifts or mixing angles from the Nijmegen partial wave analysis and lattice calculation at N3LO, respectively.

Suppose that the Hamiltonian  $H(c)$  depends smoothly on some control parameter  $c$ . Let  $c_\odot$  be the target value of the parameter where we wish to compute the ground state wave function  $|\Psi_0(c_\odot)\rangle$ . The EC method is variational calculations where the variational subspace consists of eigenvectors  $|\Psi_0(c)\rangle$  for different values of  $c$ . The computational advantage is clear when the direct calculation of  $|\Psi_0(c_\odot)\rangle$  is not possible but we can use values of  $c$  where the Monte Carlo simulations are accurate and reliable.

We assume that  $H(c)$  is Hermitian for real  $c$  and thus diagonalizable. Hence we can define  $|\Psi_0(c)\rangle$  so that it also has no singularities on the real axis. We now expand  $|\Psi_0(c)\rangle$  as a power series about the point  $c = 0$ . The coefficients for  $c^n$  are  $|\Psi_0^{(n)}(0)\rangle/n!$ , where the superscript  $(n)$  indicates the  $n^{\text{th}}$  derivative. An analogous series expansion can be applied to the eigenvalue  $E_0(c)$ . These series converge for all  $|c| < |z|$ , where  $z$  and its complex conjugate  $\bar{z}$  are the closest singularities to  $c = 0$  in the complex plane. Although the series expansion about  $c = 0$  fails to converge for  $|c| > |z|$ , we can define an analytic extension by constructing a new series about another point  $c = w$ , where  $w$  is real and  $|w| < |z|$ .

For this new series the coefficients of  $(c - w)^n$  are  $|\Psi_0^{(n)}(w)\rangle/n!$ . We can use the original series to express each  $|\Psi_0^{(n)}(w)\rangle$  in terms of  $|\Psi_0^{(m)}(0)\rangle$ . In this way we can approximate  $|\Psi_0(c)\rangle$  to arbitrary accuracy as a linear combination of the vectors  $|\Psi_0^{(n)}(0)\rangle$  in the region  $|c - w| < |z - w|$  centered at  $w$ . This process of analytic continuation is illustrated in Fig. 3. By applying this analytic continuation repeatedly, we can reach any value of  $c$  and express any  $|\Psi_0(c)\rangle$  to any desired accuracy as a linear combination of a finite number of vectors  $|\Psi_0^{(n)}(0)\rangle$ . The number of required vectors is determined by the number of different expansion centers needed in the analytic continuation and the rate of convergence of each series expansion. This explains

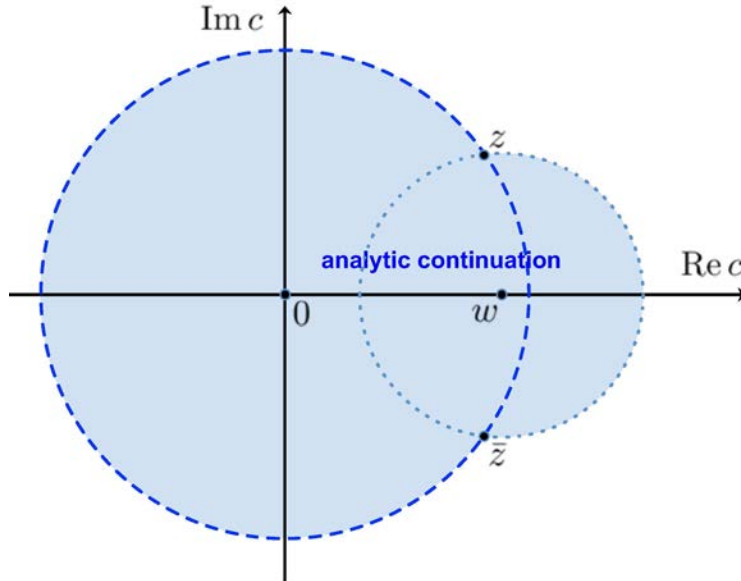


Figure 3: Analytic continuation of the wave function  $|\Psi_0(c)\rangle$  beyond the nearest singularity at  $z$  and  $\bar{z}$ .

Table 1: EC results for the ground state energy for six and fourteen neutrons using sampling data  $g_A^2 = c_1, c_2, c_3$ , where  $c_1 = 0.25$ ,  $c_2 = 0.60$ , and  $c_3 = 0.95$ . For comparison we also show the direct calculation results.

$g_A^2$ values	$E_0$ , 6 neutrons (MeV)	$E_0$ , 14 neutrons (MeV)
$c_1$	14.0(4)	48.8(6)
$c_2$	13.7(4)	48.5(7)
$c_3$	13.8(6)	48.8(8)
$c_2, c_3$	13.7(4)	48.4(7)
$c_3, c_1$	13.8(4)	48.8(6)
$c_1, c_2$	13.7(4)	48.4(7)
$c_1, c_2, c_3$	13.7(4)	48.4(7)
direct calculation	$12^{(+3)}_{(-4)}$	$42^{(+7)}_{(-15)}$

why the trajectory traced out by  $|\Psi_0(c)\rangle$  can be approximated by a manifold with a small number of linearly-independent directions.

In Ref. [9] we consider simulations of the neutron matter at the leading order using the leading order interaction described in Ref. [10]. This particular lattice action is plagued by large sign oscillations due to the one-pion exchange interaction, which is parameterized by the coupling  $g_A^2$ . The systems we calculate are the ground state energies of 6 and 14 neutrons on a  $4 \times 4 \times 4$  lattice with spatial lattice spacing 1.97 fm and time lattice spacing 1.32 fm. We first attempt to compute the ground state energies by direct calculation. The errors are quite large due to sign oscillations. For 6 neutrons the ground state energy is  $E_0 = 12^{(+3)}_{(-4)}$  MeV, and for 14 neutrons  $E_0 = 42^{(+7)}_{(-15)}$  MeV.

Next we use the EC for the values  $g_A^2 = c_1, c_2, c_3$ , where  $c_1 = 0.25$ ,  $c_2 = 0.60$ , and  $c_3 = 0.95$ . We use Monte Carlo simulations to calculate the ground state eigenvectors for  $c_1, c_2, c_3$ . In Table 1 we show the EC results using just one of the three vectors, two of the vectors, or all three vectors. The error bars are estimates of the stochastic error and extrapolation error in the projection time. For comparison we also show the direct calculation results. The EC results are consistent with the direct calculation results, though with an error bar that is smaller by an order of magnitude. The EC approach is now being developed for all interactions that produce sign oscillations in the nuclear lattice simulations.

## 4 Acknowledgements

I thank my wonderful collaborators José M. Alarcón, Serdar Elhatisari, Evgeny Epelbaum, Dillon Frame, Rongzheng He, Ilse Ipsen, Nico Klein, Hermann Krebs, Timo A. Lähde, Daniel Lee, Ning Li, Bing-Nan Lu, Thomas Luu, Ulf-G. Meißner, and Ermal Rrapaj, for their insight, work, and determination that made the collaborative work reported here possible. Partial support provided by the U.S. Department of Energy (DE-SC0018638 and DE-AC52-06NA25396). The computational resources were provided by the Julich Supercomputing Centre at Forschungszentrum Jülich, Oak Ridge Leadership Computing Facility, RWTH Aachen, and Michigan State University.

## References

- [1] E. Epelbaum, H. W. Hammer and U.-G. Meißner, *Rev. Mod. Phys.* **81**, 1773 (2009).
- [2] U.-G. Meißner, *see these Proceedings*, p. 28,  
<http://www.ntse.khb.ru/files/uploads/2018/proceedings/Meissner.pdf>.
- [3] E. Epelbaum, H. Krebs, D. Lee and U.-G. Meißner, *Phys. Rev. Lett.* **106**, 192501 (2011).
- [4] E. Epelbaum, H. Krebs, T. A. Lähde, D. Lee and U.-G. Meißner, *Phys. Rev. Lett.* **109**, 252501 (2012).
- [5] S. Elhatisari, D. Lee, G. Rupak, E. Epelbaum, H. Krebs, T. A. Lähde, T. Luu and U.-G. Meißner, *Nature* **528**, 111 (2015).
- [6] J. M. Alarcón *et al.*, *Eur. Phys. J. A* **53**, 83 (2017).
- [7] N. Klein, S. Elhatisari, T. A. Lähde, D. Lee and U.-G. Meißner, *Eur. Phys. J. A* **54**, 121 (2018).
- [8] N. Li, S. Elhatisari, E. Epelbaum, D. Lee, B. N. Lu and U.-G. Meißner, *Phys. Rev. C* **98**, 044002 (2018).
- [9] D. Frame, R. He, I. Ipsen, D. Lee, D. Lee and E. Rrapaj, *Phys. Rev. Lett.* **121**, 032501 (2018).
- [10] D. Lee, *Lecture Notes Phys.* **936**, 237 (2017).

# Three-Body Force Effect on the Properties of Nuclear Matter

W. Zuo

*Institute of Modern Physics, Chinese Academy of Sciences, Lanzhou 730000, China  
School of Nuclear Science and Technology, University of Chinese Academy of Sciences,  
Beijing 100049, China*

## Abstract

We give a review of our research work on the equation of state and single particle properties of nuclear matter within the framework of the extended Brueckner–Hartree–Fock approach. We discuss especially the three-body force (TBF) effect. The TBF effect has been shown to be necessary for describing the saturation properties of nuclear matter in nonrelativistic microscopic framework. As for asymmetric nuclear matter, the TBF turns out to result in a strong stiffening of the density dependence of symmetry energy at supra-saturation densities. Within the framework of the Brueckner theory, the TBF may lead to a rearrangement contribution to the single-particle (s.p.) potentials, which enhances significantly the repulsion and momentum-dependence of the s.p. potentials at high densities and high momenta.

**Keywords:** *Nuclear matter; equation of state; symmetry energy; Brueckner–Hartree–Fock approach; three-body force*

## 1 Introduction

One of the most important issues in nuclear physics is to constrain experimentally and theoretically the equation of state (EOS) and single-particle (s.p.) properties of nuclear matter [1–3], especially the density dependence of symmetry energy, which not only plays an essential role in predicting the properties of heavy nuclei and neutron-rich nuclei [4–7], but is also crucial for understanding many phenomena in nuclear astrophysics [8–11]. For instance, it has been shown by theoretical investigations [5, 6] that the neutron-skin thickness of heavy nuclei is correlated strongly with the density dependence of symmetry energy around the saturation density. In Ref. [7], the effect of symmetry energy on the  $\alpha$ -decay energies of superheavy nuclei has been explored and the symmetry energy turns out to play a decisive role in explaining the experimentally observed enhancement of the stability against  $\alpha$ -decay with increasing the mass number along an isotope chain for the synthesized superheavy nuclei not around shell closures. Concerning nuclear astrophysics, the EOS of nuclear matter

---

*Proceedings of the International Conference ‘Nuclear Theory in the Supercomputing Era — 2018’ (NTSE-2018), Daejeon, South Korea, October 29 – November 2, 2018, eds. A. M. Shirokov and A. I. Mazur. Pacific National University, Khabarovsk, Russia, 2019, p. 52.*

<http://www.ntse.khb.ru/files/uploads/2018/proceedings/Zuo.pdf>.

is the basic input for the Tolman–Oppenheimer–Volkov (TOV) equation, and plays an extremely important role in modeling structure of neutron stars [12, 13]. The high-density behavior of symmetry energy determines the proton fraction in  $\beta$ -stable ( $n, p, e, \mu$ ) neutron star matter [14], and thus is crucial for understanding the cooling mechanism via neutrino emission in the inner part of neutron stars [15].

In recent years, the properties of asymmetric nuclear matter have been investigated extensively within various many-body approaches, including both *ab initio* and phenomenological methods. In a phenomenological many-body framework such as the Skyrme–Hartree–Fock approach, the nucleon–nucleon ( $NN$ ) correlations in nuclear medium have been incorporated implicitly in the parameters of the adopted effective interactions, and the predicted high-density behavior of symmetry energy using different parameter sets may differ essentially and even may appear opposite [5]. In the *ab initio* approaches based on realistic  $NN$  interactions which are determined by experimental  $NN$  phase shifts, the nuclear correlations are taken into account using various approximation schemes for the exact nuclear many-body problem. Almost all *ab initio* approaches are able to reproduce more or less the empirical value of symmetry energy at the empirical saturation density and predict a monotonically increasing symmetry energy as a function of density, however, the stiffness of the density dependence of symmetry energy obtained by adopting different approaches and/or different  $NN$  interactions may become significantly different at high densities [16–18].

We have studied the the EOS and s.p. properties of asymmetric nuclear matter within the framework of the Brueckner–Hartree–Fock (BHF) approach extended to include a microscopic three-body force (TBF). In the present paper, we shall give a review of our research work concerning the properties of nuclear matter, and we shall discuss especially the TBF effect on the properties of asymmetric nuclear matter.

## 2 Theoretical approaches

The EOS and s.p. properties of nuclear matter can be predicted within the frameworks of various *ab initio* approaches. In our investigation, the BHF approach has been adopted, which is based on the Brueckner–Bethe–Goldstone (BBG) theory [19]. The extensions of the BBG scheme to the asymmetric nuclear matter and to include a microscopic TBF can be found in Refs. [14, 20] and Refs. [21, 22], respectively. Here we simply give a brief review for completeness. The key point of the BHF approach is the reaction  $G$ -matrix, which satisfies the following isospin-dependent Bethe–Goldstone (BG) equation,

$$G(\rho, \beta, \omega) = v + v \sum_{k_1 k_2} \frac{|k_1 k_2\rangle Q(k_1, k_2) \langle k_1 k_2|}{\omega - \epsilon(k_1) - \epsilon(k_2)} G(\rho, \beta, \omega), \quad (1)$$

where  $k_i \equiv (\vec{k}_i, \sigma_i, \tau_i)$  denotes the momentum and the  $z$ -components of spin and isospin of a nucleon, respectively;  $v$  is a realistic  $NN$  interaction;  $\omega$  is the starting energy;  $Q(k_1, k_2)$  is the Pauli operator. The isospin asymmetry parameter is defined as  $\beta = (\rho_n - \rho_p)/\rho$ , where  $\rho$ ,  $\rho_n$ , and  $\rho_p$  denote the total, the neutron and the proton densities, respectively. For the interaction  $v$  in our calculation, we adopt some realistic two-body interaction (i. e., the Argonne  $V_{18}$  interaction [23] or the Bonn potential [24]) plus the corresponding microscopic TBF [22, 25] constructed in a consistent way with the adopted two-body interaction by using the meson-exchange current approach [21].

The s.p. energy is given by  $\epsilon(k) = \hbar^2 k^2 / (2m) + U_{BHF}(k)$ . In solving the BG equation, the continuous choice [26] is adopted for the auxiliary potential  $U_{BHF}$  since it has been shown to provide a much faster convergence of the hole-line expansion than the gap choice [27]. Under the continuous choice, the s.p. potential describes physically at the lowest BHF level the nuclear mean field felt by a nucleon in nuclear medium, and it can be obtained from the real part of the on-shell  $G$ -matrix,

$$U_{BHF}(k) = \sum_{k'} n(k') \text{Re} \langle k k' | G(\epsilon(k) + \epsilon(k')) | k k' \rangle_A. \quad (2)$$

In the BHF approximation, the EOS of asymmetric nuclear matter (i. e., the energy per nucleon of asymmetric nuclear matter as a function of density  $\rho$  and isospin asymmetry  $\beta$ ) is given by

$$E_A(\rho, \beta) = \frac{3}{5} \frac{\hbar^2}{2m} \left[ \left( \frac{1-\beta}{2} \right)^{5/3} + \left( \frac{1+\beta}{2} \right)^{5/3} \right] (3\pi^2 \rho)^{2/3} + \frac{1}{2\rho} \text{Re} \sum_{\tau, \tau'} \sum_{k \leq k_F^\tau, k' \leq k_F^{\tau'}} \langle k k' | G(\rho, \beta; \epsilon(k) + \epsilon(k')) | k k' \rangle_A, \quad (3)$$

where the first term is the contribution of the kinetic part and the second term is the potential part.

As is well known, a nonrelativistic *ab initio* model of rigid nucleons interacting via realistic two-body forces fitting in-vacuum  $NN$  scattering data is not able to reproduce the empirical saturation properties of nuclear matter. Within the framework of the BHF approach, the saturation points predicted by various  $NN$  interactions are shown to locate in a narrow band (Coester band) which is far away from the empirical point [17, 28]. There are two different ways to introduce the medium effects and to solve the above problem. One is to adopt a relativistic theory, such as the Dirac-BHF method [24], suggesting that nucleons propagate in nuclear medium as *dressed* Dirac spinors which may incorporate a special class of TBF (i. e., the TBF involving the virtual excitations of nucleon-antinucleon pairs) and respond for the main relativistic contribution to the nuclear matter EOS [22, 29, 30]. The other is to introduce TBFs in nonrelativistic approaches. Up to now, several different kinds of TBF models have been applied in the BHF calculations. One is the semi-phenomenological TBF model, such as the Urbana TBF [31], in which few adjustable parameters are usually determined by fitting the observed triton binding energies and/or the empirical saturation properties of symmetric nuclear matter. Another kind of TBF models adopted in the BHF calculations is the microscopic one [21, 22, 25] based on the meson exchange theory for  $NN$  interactions. In the microscopic TBF model, there is no adjustable parameter in the sense that the meson parameters are essentially determined self-consistently by the corresponding two-body force. The classical parts of the microscopic TBF model associated with the  $\pi$  and  $\rho$  meson exchanges have been developed during a long period by several authors [32–34]. The extension to include the  $\sigma$  and  $\omega$  exchanges as well as the associated virtual nucleon-antinucleon pair excitations have been done by Grangé *et al.* [21]. Further improvement and development of the model have been achieved in Refs. [22, 25]. In recent years, nuclear TBF has also been developed systematically within the framework of the chiral effective field theory [35].

In order to include the TBF contribution into the two-body BG equation and to avoid the in-medium three-body Faddeev problem, we have reduced the TBF to an effectively equivalent two-body interaction according to a standard and extensively adopted scheme [21]. In the  $r$ -space, the equivalent two-body force  $V_3^{\text{eff}}$  reads:

$$\begin{aligned} \langle \vec{r}'_1 \vec{r}'_2 | V_3^{\text{eff}} | \vec{r}_1 \vec{r}_2 \rangle = & \frac{1}{4} \text{Tr} \sum_n \int d\vec{r}_3 d\vec{r}'_3 \phi_n^*(\vec{r}'_3) (1 - \eta(r'_{13})) (1 - \eta(r'_{23})) \\ & \times W_3(\vec{r}'_1 \vec{r}'_2 \vec{r}'_3 | \vec{r}_1 \vec{r}_2 \vec{r}_3) \phi_n(\vec{r}_3) (1 - \eta(r_{13})) (1 - \eta(r_{23})). \end{aligned} \quad (4)$$

The justification of the above approximation can be found in Refs. [21, 33]. In this averaging scheme, the direct and most important single-exchange TBF contributions are taken into account.

As well known, at the lowest mean field approximation, the BHF approach has two problems in predicting nuclear s.p. properties. First, the predicted optical potential at the saturation density is shown to be too deep as compared to its empirical value [26], and the Hugenholtz–Van Hove (HVH) theorem is destroyed seriously. The solution of this problem is to go beyond the lowest order approximation by taking into account the effect of ground state (g.s.) correlations [26, 36]. The contribution of the g.s. correlations can be obtained according to the hole-line expansion of the mass operator,

$$M(k, \omega) = M_1(k, \omega) + M_2(k, \omega) + M_3(k, \omega) + \dots, \quad (5)$$

where  $M_1(k, \omega)$  corresponds to the lowest-order BHF contribution and its on-shell value describes the nuclear mean field  $U_{\text{BHF}}$  at the lowest-order BHF approximation. The second-order contribution  $M_2$  is called Pauli rearrangement term and it gives the dominant contribution of the g.s. correlations.

Second, at the lowest-order BHF approximation, the predicted potential at high densities and high momenta is too attractive and its momentum dependence turns out to be too weak for describing the experimental elliptic flow data [37]. In order to solve these two problems, we have improved the Brueckner calculation of the s.p. properties in two aspects. The first is to extend the calculation of the effect of g.s. correlations to asymmetric nuclear matter [20]. The second is to take into account the TBF-induced rearrangement contribution in calculating the s.p. properties as shown in Ref. [38] where the TBF rearrangement term has been derived,

$$U_{\text{TBF}}(k) \approx \frac{1}{2} \sum_{k_1 k_2} n_{k_1} n_{k_2} \left\langle k_1 k_2 \left| \frac{\delta V_3^{\text{eff}}}{\delta n_k} \right| k_1 k_2 \right\rangle_A. \quad (6)$$

### 3 EOS of symmetric nuclear matter

We display in Fig. 1 the EOS of symmetric nuclear matter predicted within different *ab initio* theoretical frameworks including the BHF approach [22, 25], the many-body variational method [39], and the relativistic Dirac–Brueckner–Hartree–Fock (DBHF) theory [24]. In the figure, the box indicates the location of the empirical saturation point; other symbols indicate the predicted saturation points. It is clear that without TBF, the saturation points obtained within the two nonrelativistic frameworks (i. e., the BHF and variational approaches) are far away from the empirical one. At low densities well below the saturation density, the TBF effect is reasonably small. At

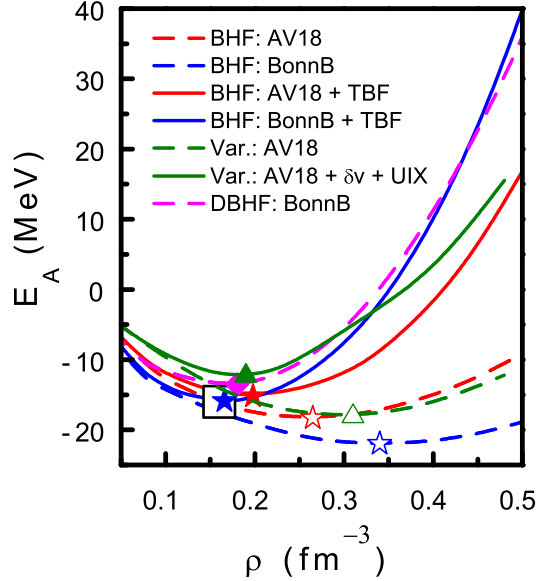


Figure 1: EOS of symmetric nuclear matter predicted by different microscopic approaches. The results of the BHF approach are taken from Refs. [22] and [25]. The DBHF prediction is taken from Ref. [24]. The results of the variational approach are from Ref. [39]. The dashed curves are obtained by purely two-body interactions; the solid ones are the results by the two-body interactions plus various TBFs.

supra-saturation densities, the TBF provides a repulsive contribution to the nuclear EOS, and its repulsion increases monotonically as a function of density. It is worth stressing that inclusion of the TBF contribution improves remarkably the saturation points predicted by the two nonrelativistic *ab initio* approaches, indicating that the TBF is necessary for reproducing the empirical saturation properties of nuclear matter in a non-relativistic microscopic framework.

Within the BHF framework, by including the TBFs, the calculated saturation density may be improved significantly from  $0.265\text{fm}^{-3}$  and  $0.33\text{fm}^{-3}$  to  $0.167\text{fm}^{-3}$  and  $0.19\text{fm}^{-3}$ , respectively when the AV18 and BonnB interactions are adopted as the two-body interaction. The latter two values are compatible with the empirical value and the DBHF prediction of roughly  $0.18\text{fm}^{-3}$ . Concerning the relativistic effect in the DBHF approach, it has been shown quantitatively in Refs. [22, 25] that the main relativistic correction to the EOS of nuclear matter can be reproduced by the TBF component involving the virtual excitations of nucleon-antinucleon pairs due to the  $2\sigma$ -meson exchange.

## 4 EOS of asymmetric nuclear matter

The isovector part of the EOS of nuclear matter (i. e., the difference between the energy per nucleon of asymmetric nuclear matter and that of symmetric nuclear matter) as a function of  $\beta^2$  at four typical densities,  $\rho = 0.085, 0.17, 0.34$  and  $0.45 \text{ fm}^{-3}$ , is reported in Fig. 2. It is clearly seen that the isovector part of the EOS fulfills satisfactorily a linear dependence on  $\beta^2$  in the whole asymmetry range of  $0 \leq \beta \leq 1$ , i. e.,

$$E_A(\rho, \beta) - E_A(\rho, 0) = E_{sym}(\rho)\beta^2. \quad (7)$$

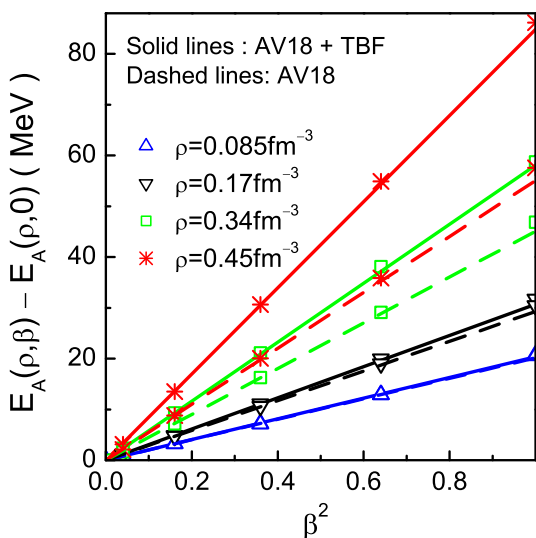


Figure 2: Isovector part of EOS of asymmetric nuclear matter. Different symbols show predictions by the BHF approach for four different densities, and the lines are the corresponding linear fits. Taken from Ref. [22].

Both the TBF effect and the thermal effect do not destroy the linear dependence of  $E_A(\rho, \beta)$  on  $\beta^2$  [22, 40]. The symmetry energy  $E_{sym}(\rho)$  is defined generally as

$$E_{sym}(\rho) = \frac{1}{2} [\partial^2 E_A / \partial \beta^2]_{\beta=0}. \quad (8)$$

The linear  $\beta^2$  dependence of  $E_A(\rho, \beta)$  predicted within the framework of different *ab initio* many-body approaches and by using various  $NN$  interactions provides a microscopic support for the empirical  $\beta^2$  law extracted from the nuclear mass table, and extends its validity up to the highest asymmetry and to high densities well above the saturation density. The above simple  $\beta^2$  law of  $E_A(\rho, \beta)$  may lead to several important consequences. First, it implies that the isovector part of the EOS of asymmetric nuclear matter at a given density is determined essentially by the symmetry energy. Second, the symmetry energy can be calculated directly as the difference between the EOS of pure neutron matter and that of symmetric nuclear matter, i. e.,  $E_{sym}(\rho) = E_A(\rho, 1) - E_A(\rho, 0)$ . Third, due to the linear  $\beta^2$  dependence of  $E_A(\rho, \beta)$ , the difference of the neutron and proton chemical potentials in neutron star matter can be explicitly related to the symmetry energy:  $\mu_n - \mu_p = 4\beta E_{sym}$ .

## 5 High-density behavior of symmetry energy

We show in Fig. 3 the density dependence of symmetry energy predicted within three different *ab initio* theoretical frameworks, including the BHF approach [22, 25], the variational method [39], and the DBHF theory [41]. It is worthy of notice that the predicted symmetry energy increases monotonically as a function of density regardless of the adopted *ab initio* approach and/or the realistic  $NN$  interaction. At subsaturation densities, the difference between different predictions has been shown to be quite small [3], and the TBF effect is seen to be reasonably weak; whereas the high-density behaviors of symmetry energy predicted by three different *ab initio* approaches may become significantly different. In the BHF calculations, the inclusion of the TBF

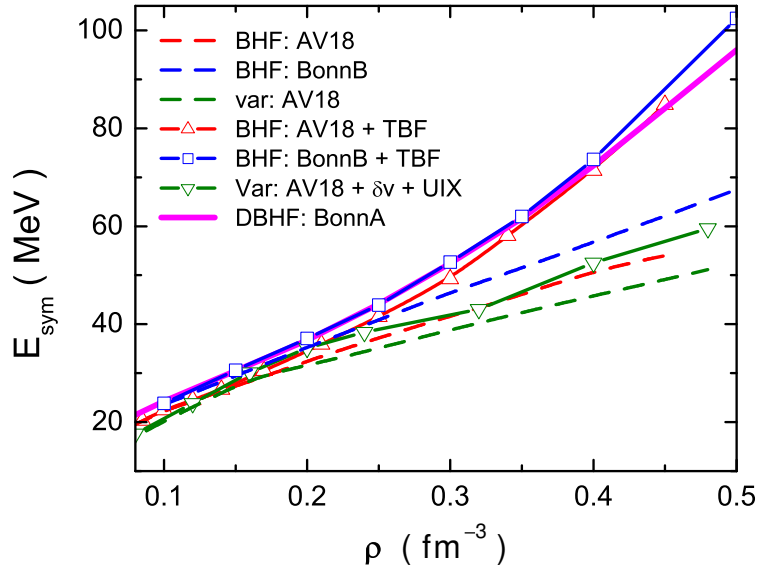


Figure 3: Symmetry energy vs density predicted within three different *ab initio* theoretical frameworks: the BHF [22, 25], the variational approach [39], and the DBHF [41].

results in that the predicted symmetry energy almost completely coincides with the DBHF prediction up to  $\rho = 0.5 \text{ fm}^{-3}$ . Within the two nonrelativistic *ab initio* frameworks, the TBF effect on the symmetry energy is repulsive, and the inclusion of the TBFs leads to a stiffening of the density dependence of symmetry energy at supra-saturation densities. It is worth noting that the TBF symmetry energy repulsion at high densities within the BHF framework is much stronger than that within the variational framework. At high densities well above the saturation density, the TBF effect may even enlarge remarkably the discrepancy between the BHF and variational predictions. To clarify this problem, further investigation is necessary.

## 6 Single particle potential in nuclear matter

In our calculation of the s.p. potential, we take into account three different contributions, i. e., the leading-order contribution  $U_{\text{BHF}}$  corresponding to the lowest-order BHF s.p. potential, the Pauli rearrangement contribution  $U_2$  due to the effect of g.s. correlations in nuclear medium, and the rearrangement contribution  $U_{\text{TBF}}$  induced by the TBF. The full s.p. potential is the sum of these contributions,

$$U(k) = U_{\text{BHF}}(k) + U_2(k) + U_{\text{TBF}}(k). \quad (9)$$

We show in Fig. 4 these three contributions to the symmetric nuclear matter at three typical densities of  $\rho = 0.085, 0.17, \text{ and } 0.34 \text{ fm}^{-3}$ . The lowest-order BHF s.p. potential  $U_{\text{BHF}}$  is seen to be strongly attractive at low momenta, and its attraction increases as a function of density. The g.s. correlations lead to a repulsive contribution  $U_2$  which is much smaller in magnitude than the lowest-order BHF contribution  $U_{\text{BHF}}$ . It is

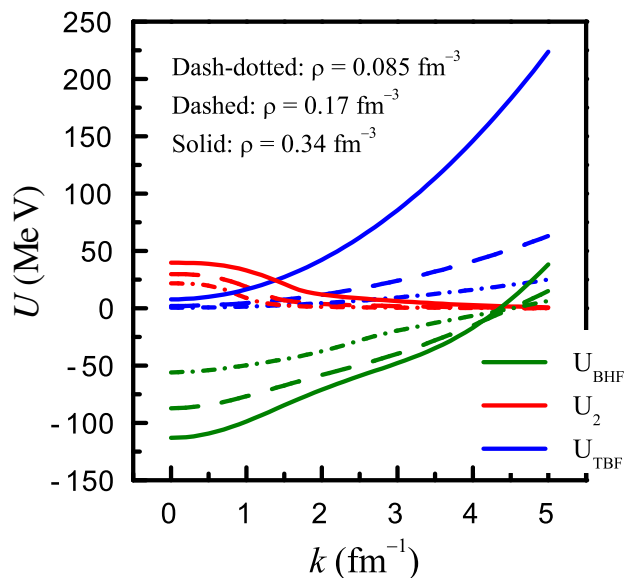


Figure 4: Three different contributions,  $U_{\text{BHF}}$ ,  $U_2$  and  $U_{\text{TBF}}$ , to symmetric nuclear matter at three densities. Taken from Ref. [42].

clearly seen that the contribution of g.s. correlations modifies the s.p. potential mainly at low momenta around and below the Fermi surface, and it decreases rapidly around the Fermi momentum and vanishes at high momenta well above the Fermi momentum. As discussed in Ref. [38], the inclusion of the effect of g.s. correlations cannot provide any appreciable improvement of the *high-momentum* behavior of the BHF s.p. potential at high densities. The TBF-induced rearrangement contribution  $U_{\text{TBF}}$  is repulsive, and it turns out to be completely different from the Pauli rearrangement contribution  $U_2$ . At low densities and/or low momenta well below the Fermi momentum, the TBF rearrangement potential  $U_{\text{TBF}}$  is fairly small. However, the  $U_{\text{TBF}}$  increases monotonically and rapidly as a function of density and momentum. At high densities and high momenta, it becomes strongly repulsive and momentum-dependent. Such a strongly repulsive and momentum-dependent rearrangement potential induced by the TBF is necessary for improving the *high-momentum* behavior of the lowest-order BHF s.p. potential which has been shown to be too attractive at high densities and whose momentum dependence turns out to be too weak to describe the experimental elliptic flow data in heavy-ion collisions at high energies [37].

Now let us discuss briefly the isospin dependence of the nucleon s.p. potentials in asymmetric nuclear matter. In asymmetric nuclear matter ( $\beta > 0$ ), the neutron potential  $U^n$  becomes different from the proton one  $U^p$ . At relatively low momenta, the neutron s.p. potential  $U_{\text{BHF}}^n$  at the lowest-order BHF approximation becomes less attractive while the proton one becomes more attractive as the asymmetry  $\beta$  increases. The different  $\beta$ -dependence of the neutron and proton potentials stems essentially from the isospin  $T = 0$  neutron-proton short-range correlations in the  $SD$  channel [14,20]. As discussed in Ref. [20], the contribution of the g.s. correlations may destroy the linear  $\beta$ -dependence fulfilled at the lowest-order BHF approximation by the neutron and proton potentials at a fixed momentum. The isospin dependence of the TBF rearrangement potentials has been shown to be relatively weak in magnitude as compared to the lowest-order BHF potentials [38].

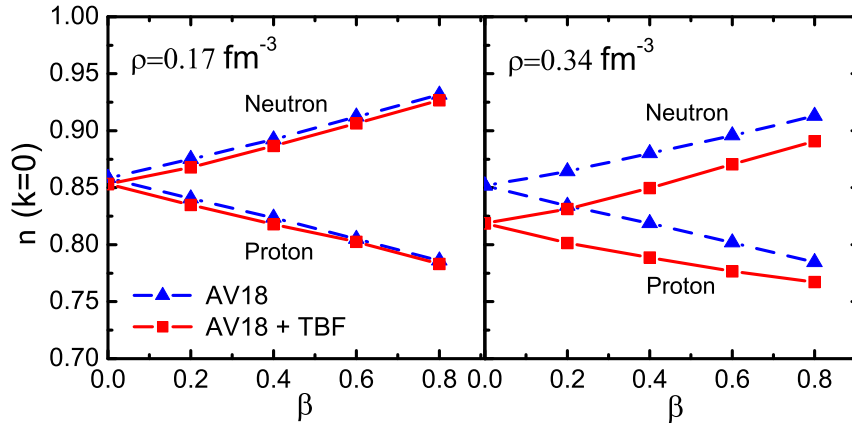


Figure 5: Neutron and proton momentum distributions at zero momentum in asymmetric nuclear matter vs isospin asymmetry  $\beta$  for two densities,  $0.17 \text{ fm}^{-3}$  (left panel) and  $0.34 \text{ fm}^{-3}$  (right panel). Taken from Ref. [43].

## 7 Nucleon momentum distribution

Nucleon momentum distribution measures the strength of the dynamical  $NN$  correlations in a nuclear many-body system. Its information not only plays a significant role in understanding the nature of  $NN$  interactions, but is also crucial for testing the validity of the physical picture of independent particle motion in the mean field theory or in the standard shell model. In order to discuss the isospin dependence and the TBF effect clearly, we report in Fig. 5 the predicted proton and neutron momentum distributions at zero momentum  $k = 0$  as functions of asymmetry  $\beta$  in two cases with and without considering the TBF [43]. It is clearly seen that the neutron and proton momentum distributions become different in asymmetric nuclear matter at  $\beta > 0$ . At a higher asymmetry, the neutron Fermi sea tends to be more occupied while the proton Fermi sea becomes less occupied. One may notice that the neutron (proton) occupation probability at zero momentum increases (decreases) almost linearly as a function of asymmetry  $\beta$ , which indicates that the short-range tensor correlations between neutrons and protons become stronger (weaker) for proton (neutron) at a higher asymmetry. At low densities around and below the saturation densities, the TBF effect is negligibly small. However, at high densities well above the saturation density, the TBF may lead to an overall enhancement of the depletion of the neutron and proton hole states, which is expected since the TBF induces extra short-range correlations in dense nuclear medium.

## 8 Summary

In summary, we have reviewed part of our research work on the EOS and the s.p. properties of nuclear matter within the framework of the Brueckner approach extended to include a microscopic TBF. We have discussed especially the TBF effects and compared our results with the predictions of different *ab initio* approaches. TBF provides a repulsive contribution to the EOS of nuclear matter, and is shown to be

necessary for reproducing the empirical saturation properties of nuclear matter within the framework of a nonrelativistic *ab initio* approach. The EOS of asymmetric nuclear matter turns out to fulfill satisfactorily a linear dependence on  $\beta^2$  in the whole asymmetry range of  $0 \leq \beta \leq 1$ . Both the TBF and the thermal effect do not destroy the  $\beta^2$  law fulfilled by the EOS of asymmetric nuclear matter. The symmetry energy predicted by three different *ab initio* approaches and/or different realistic  $NN$  interactions is shown to increase monotonically as a function of density. In the non-relativistic approaches, the TBF may lead to a strong enhancement of the stiffness of symmetry energy at high densities. The TBF symmetry energy repulsion at high densities is found to be much stronger within the BHF than that within the variational framework.

In predicting the s.p. properties, we have improved the Brueckner calculation in two aspects. The first one is to extend the calculation of the g.s. correlation effect to the asymmetric nuclear matter. Second, we include the TBF-induced rearrangement contribution in our calculations. Both improvements are shown to be necessary for predicting reliably the s.p. properties of nuclear matter within the Brueckner approach. Especially, the TBF rearrangement potential turns out to be strongly repulsive and momentum-dependent at high densities and momenta, which is necessary for improving the large-density and high-momentum behavior of the s.p. potentials. At high densities well above the saturation density, the TBF effect leads to an overall enhancement of the depletion of nuclear Fermi sea since the TBF may induce extra short-range correlations in dense nuclear medium.

The work is partly supported by the National Natural Science Foundation of China (11435014, 11175219) and the 973 Program of China (2013CB834405).

## References

- [1] B. A. Li, L. C. Chen and C. M. Ko, Phys. Rep. **464**, 113 (2008) *and reference therein*.
- [2] P. Danielewicz, R. Lacey and W. G. Lynch, Science **298**, 1592 (2002).
- [3] W. Zuo, I. Bombaci and U. Lombardo, Eur. Phys. J. A **50**, 12 (2014).
- [4] I. Tanihata, Nucl. Phys. A **616**, 56c (1997).
- [5] L.W. Chen, C.M. Ko and B.A. Li, Phys. Rev C **72**, 064309 (2005).
- [6] J. M. Dong *et al.*, Phys. Rev. C **85**, 034308 (2012).
- [7] J. M. Dong, W. Zuo, W. Scheid, Phys. Rev. Lett. **107**, 012501 (2011).
- [8] A. W. Steiner *et al.*, Phys. Rep. **411**, 325 (2005).
- [9] M. Baldo and C. Maieron, J. Phys. G **34**, R243 (2007).
- [10] W. Zuo, A. Li, Z. H. Li and U. Lombardo, Phys. Rev. C **70**, 055802 (2004); A. Li, G. F. Burgio, U. Lombardo and W. Zuo, *ibid.* **74**, 055801 (2006).
- [11] J. M. Lattimer and M. Prakash, Science **304**, 536 (2004).
- [12] M. Baldo, I. Bombaci and G. F. Burgio, Astron. Astrophys. **328**, 274 (1997).

- 
- [13] X. R. Zhou, G. F. Burgio, U. Lombardo, H.-J. Schulze and W. Zuo, Phys. Rev. C **69**, 018801 (2004).
- [14] I. Bombaci and U. Lombardo, Phys. Rev. C **44**, 1892 (1991).
- [15] J. M. Lattimer, C. J. Pethick, M. Prakash and P. Haensel, Phys. Rev. Lett. **66**, 2701 (1991).
- [16] A. E. L. Dieperink, Y. Dewulf, D. Van Neck, M. Waroquier and V. Rodin, Phys. Rev. C **68**, 064307 (2003).
- [17] Z. H. Li, U. Lombardo, H. J. Schulze, W. Zuo, L. W. Chen and H. R. Ma, Phys. Rev. C **74**, 047304 (2006).
- [18] P. Gögelein, E. N. E. van Dalen, Kh. Gad, Kh. S. A. Hassaneen and M. Mütter, Phys. Rev. C **79**, 024308 (2009).
- [19] B. D. Day, Rev. Mod. Phys. **39**, 719 (1967).
- [20] W. Zuo, I. Bombaci and U. Lombardo, Phys. Rev. C **60**, 024605 (1999).
- [21] P. Grangé, A. Lejeune, M. Martzolf and J. F. Mathiot, Phys. Rev. C **40**, 1040 (1989).
- [22] W. Zuo, A. Lejeune, U. Lombardo and J. F. Mathiot, Nucl. Phys. A **706**, 418 (2002); Eur. Phys. J. A **14**, 469 (2002).
- [23] R. B. Wiringa, V. G. J. Stoks and R. Schiavilla, Phys. Rev. C **51**, 38 (1995).
- [24] R. Machleidt, K. Holinde and Ch. Elster, Phys. Rep. **149**, 1 (1987); R. Machleidt, Adv. Nucl. Phys. **19**, 189 (1989); R. Brockmann and R. Machleidt, Phys. Rev. C **42**, 1965 (1990).
- [25] Z. H. Li, U. Lombardo, H. J. Schulze and W. Zuo, Phys. Rev. C **77**, 034316 (2008).
- [26] J. P. Jeukenne, A. Lejeune and C. Mahaux, Phys. Rep. **25**, 83 (1976).
- [27] H. Q. Song, M. Baldo, G. Giansiracusa and U. Lombardo, Phys. Rev. Lett. **81**, 1584 (1998).
- [28] F. Coester, S. Cohen, B. Day and C. M. Vincent, Phys. Rev. C **1**, 769 (1970); F. Coester, B. Day and A. Goodman, *ibid.* **5**, 1135 (1972).
- [29] C. Fuchs and H. H. Wolter, Eur. Phys. J. A **30**, 5 (2006).
- [30] G. E. Brown, W. Weise, G. Baym, J. Speth, Comments Nucl. Part. Phys. **17**, 39 (1987).
- [31] J. Carlson, V. R. Pandharipande and R. B. Wiringa, Nucl. Phys. A **401**, 59 (1983).
- [32] B. Loiseau, Y. Nogami and C. K. Ross, Nucl. Phys. A **165**, 601 (1971); M. Martzolf, B. Loiseau and P. Grange, Phys. Lett. B **92**, 46 (1980).

- [33] S. A. Coon, M. D. Scadron, P. C. McNamee, B. R. Barrett, D.W. E. Blatt and B. H. J. McKellar, Nucl. Phys. A **317**, 242 (1979); S. A. Coon and W. Glöckle, Phys. Rev. C **23**, 1790 (1981); R. G. Ellis, S. A. Coon and B. H. J. McKellar, Nucl. Phys. A **438**, 631 (1985).
- [34] A. Stadler, J. Adam, H. Henning and P. U. Sauer, Phys. Rev. C **51**, 2896 (1995).
- [35] E. Epelbaum, H. W. Hammer and U.-G. Meißner, Rev. Mod. Phys. **81**, 1773 (2009); R. Machleidt and D. R. Entem, Phys. Rep. **503**, 1 (2011).
- [36] M. Baldo *et al.*, Phys. Lett. B **209**, 135 (1988); M. Baldo *et al.*, Phys. Rev. C **41**, 1748 (1990).
- [37] P. Danielewicz, Nucl. Phys. A **673**, 375 (2000).
- [38] W. Zuo, U. Lombardo, H. J. Schulze and Z. H. Li, Phys. Rev. C **74**, 014317 (2006).
- [39] A. Akmal, V. R. Pandharipande and D. G. Ravenhall, Phys. Rev. C **58**, 1804 (1998).
- [40] W. Zuo, Z. H. Li, A. Li and G. C. Lu, Phys. Rev. C **69**, 064001 (2004).
- [41] E. N. E. van Dalen, C. Fuchs and A. Faessler, Nucl. Phys. A **744**, 227 (2004); Phys. Rev. C **72**, 065803 (2005).
- [42] W. Zuo, Nucl. Phys. A **834**, 574c (2010).
- [43] P. Yin, J. Y. Li, P. Wang and W. Zuo, Phys. Rev. C **87**, 014314 (2013).

# Correlations in Nuclear Matter and Nuclei

F. Sammarruca<sup>a</sup>, L. E. Marcucci<sup>b,c</sup>, M. Viviani<sup>c</sup>  
and R. Machleidt<sup>a</sup>

<sup>a</sup>*Department of Physics, University of Idaho, Moscow, ID 83844, USA*

<sup>b</sup>*Dipartimento di Fisica “Enrico Fermi”, Università di Pisa, Largo Bruno Pontecorvo 3, I-56127 Pisa, Italy*

<sup>c</sup>*Istituto Nazionale di Fisica Nucleare, Sezione di Pisa, Largo Bruno Pontecorvo 3, I-56127 Pisa, Italy*

## Abstract

This contribution addresses momentum distributions in  $A = 2, 3$  systems, with particular emphasis on high momentum components. The latter carry information on the short-range nuclear dynamics. We show predictions obtained with state-of-the-art chiral interactions and compare with those obtained with traditional, phenomenological or meson-theoretic, potentials. Model dependence is discussed, along with other aspects such as the impact of three-nucleon forces on the predictions.

**Keywords:** *Momentum distribution; short-range correlations; chiral nuclear interactions*

## 1 Introduction

The nuclear force has short-range repulsive and intermediate-range attractive components. Naturally, these features strongly limit the validity of a mean-field picture. Short-range correlations (SRC) refer to the nucleon dynamics at short distances and are responsible for the high-momentum components of nuclear wave functions.

An additional motivation for studying this important aspect of nucleon dynamics is provided by the lively experimental program aimed at extracting the SRC information via inclusive electron scattering at high momentum transfer or coincidence experiments involving knock-out of a nucleon pair [1–10].

In this contribution, we will first address high-momentum distributions and SRC in the deuteron, reviewing and updating one of our previous investigations [11]. We will then present a subselection of our most recent results [12] for momentum distributions and SRC in  $^3\text{He}$ .

We conclude with some thoughts on the meaning and implications of measuring SRC. In future work, a careful consideration should be given to the approximations typically applied in order to extract the SRC information from high-momentum transfer electron scattering data.

---

*Proceedings of the International Conference ‘Nuclear Theory in the Supercomputing Era — 2018’ (NTSE-2018), Daejeon, South Korea, October 29 – November 2, 2018, eds. A. M. Shirokov and A. I. Mazur. Pacific National University, Khabarovsk, Russia, 2019, p. 64.*

<http://www.ntse.khb.ru/files/uploads/2018/proceedings/Sammarruca.pdf>

## 2 High-momentum distributions in the deuteron

Deuteron momentum distributions in the context of SRC were studied in Ref. [11] using local and non-local realistic two-nucleon ( $2N$ ) interactions. Those included: purely phenomenological local potentials, such as the Argonne  $v_{18}$  [13] (AV18) or the Nijmegen II [14] models, non-local meson-theoretic models, such as the charge dependent Bonn (CDBonn) potential [15], and state-of-the-art non-local chiral potentials [16–18]. In the study of Ref. [11], it was concluded that predictions of high-momentum distributions in the deuteron with non-local meson-exchange forces *or* state-of-the-art chiral forces are systematically lower than those obtained with the local AV18 or Nijmegen II potentials.

The analysis of Ref. [11] highlights non-localities in the tensor force as the source of differences in SRC among the various predictions. We recall that the presence of non-locality in the tensor force has been determined since a long time to be a desirable feature in nuclear structure calculations (see, for instance, Refs. [19–21].)

In Fig. 1 we show the deuteron momentum distributions  $\rho(k)$ , defined as the Fourier transform squared of the coordinate-space deuteron wave function. On the left side of the figure, we show the results, with focus on high-momentum components, obtained with the latest chiral interactions of Ref. [22] from the leading to fifth order ( $N^4$ LO). On the right side of the figure, we show for comparison the same quantities calculated as in Ref. [11] with the older chiral potentials of Refs. [16–18]. We note that the convergence pattern shows improvement from the use of the new potentials.

We define the integrated probability of SRC in the deuteron as in Ref. [11], i. e.,

$$a_{2N}(d) = 4\pi \int_{k_{min}}^{\infty} \rho(k) k^2 dk, \quad (1)$$

where  $k_{min}$  is taken to be  $1.4 \text{ fm}^{-1}$ . This definition was adopted in Ref. [1], where the choice of the lower integration limit was suggested by the onset of scaling of

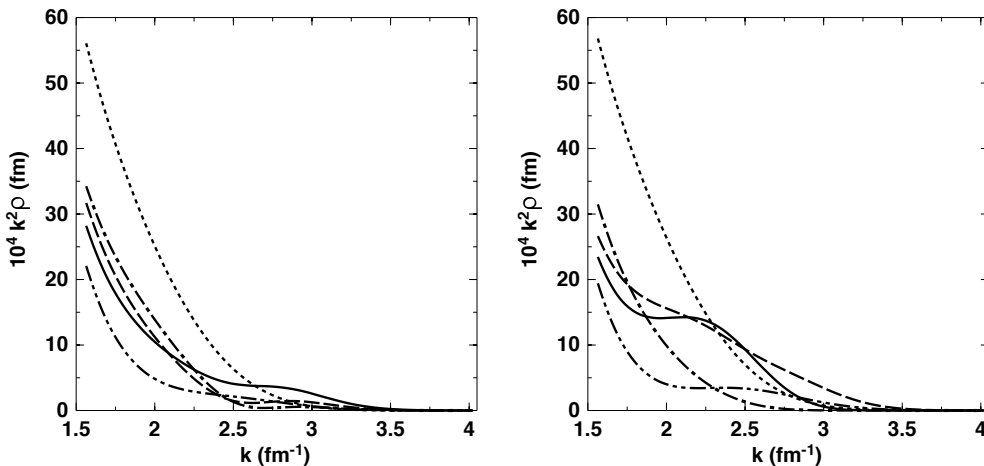


Figure 1: Left: Momentum distributions in the deuteron predicted with the chiral potentials of Ref. [22] at LO (dotted), NLO (dash-double dot),  $N^2$ LO (dash-dot),  $N^3$ LO (dash),  $N^4$ LO (solid). The cutoff is fixed at  $\Lambda = 500 \text{ MeV}$ . Right: Predictions taken from Ref. [11] are obtained using the chiral potentials of Refs. [16–18].

Table 1: Probabilities of SRCs as defined in Eq. (1) and deuteron  $D$ -state percentage for the chiral interactions considered in the left panel of Fig. 1. The values in parenthesis, given for comparison, are taken from Ref. [11] and correspond to the distributions shown in the right panel of Fig. 1. The cutoff  $\Lambda$  is equal to 500 MeV in all cases.

Model	$a_{2N}(d)$	$P_D$
LO	0.046 (0.047)	0.0729 (0.0757)
NLO	0.015 (0.015)	0.0340 (0.0313)
N <sup>2</sup> LO	0.026 (0.022)	0.0449 (0.0417)
N <sup>3</sup> LO	0.024 (0.030)	0.0415 (0.0451)
N <sup>4</sup> LO	0.024 (0.026)	0.0410 (0.0414)

electron scattering cross section, which should signal the dominance of scattering from a strongly correlated nucleon. The absolute per-nucleon SRC probability in a nucleus  $A$  can be deduced if the absolute per-nucleon probability in  ${}^3\text{He}$  and the deuteron are calculated or estimated. More precisely,

$$a_{2N}(A) = a_2(A/{}^3\text{He}) a_{2N}({}^3\text{He}) \quad \text{and} \quad a_{2N}({}^3\text{He}) = a_2({}^3\text{He}/d) a_{2N}(d), \quad (2)$$

where  $a_2(A_1/A_2)$  is the SRC probability for nucleus  $A_1$  relative to nucleus  $A_2$ . The probability in the deuteron was taken to be equal to  $0.041 \pm 0.008$  in Ref. [2]. We list in Table 1 the integrated probabilities  $a_{2N}(d)$  defined in Eq. (1), calculated integrating the curves of Fig. 1 (left panel). As an additional, related information, we also show the corresponding  $D$ -state percentage. In fact, deuteron  $D$ -state probabilities are larger with stronger short-range central and tensor components of the nuclear force which, for the non-local chiral interactions and, generally, for non-local interactions, are softer than for the local AV18 potential. The values in parenthesis correspond to the distributions displayed on the right of Fig. 1, i. e., obtained with the older chiral potentials of Refs. [16–18]. As the table shows, there are huge variations between the LO and the NLO cases, and still large differences between the NLO and N<sup>2</sup>LO. Variations at higher orders indicate a clear convergence pattern, definitely improved by the use of the newest potentials. Finally we notice that the deuteron integrated probabilities  $a_{2N}(d)$  display significant model-dependence, as the corresponding values obtained with the AV18 and the CDBonn potentials are 0.042 and 0.032, respectively.

### 3 Momentum distributions in ${}^3\text{He}$

In this Section, we show and discuss a subselection of results from Ref. [12] for momentum distributions in  ${}^3\text{He}$ . We refer the reader to Ref. [12] for an extensive and detailed presentation of the formalism as well as additional predictions.

Note that the Hyperspherical Harmonics (HH) method is used to solve the  $A = 3$  quantum mechanical problem. This method has the great advantage of being applicable in both coordinate- and momentum-space, with no restriction on the choice

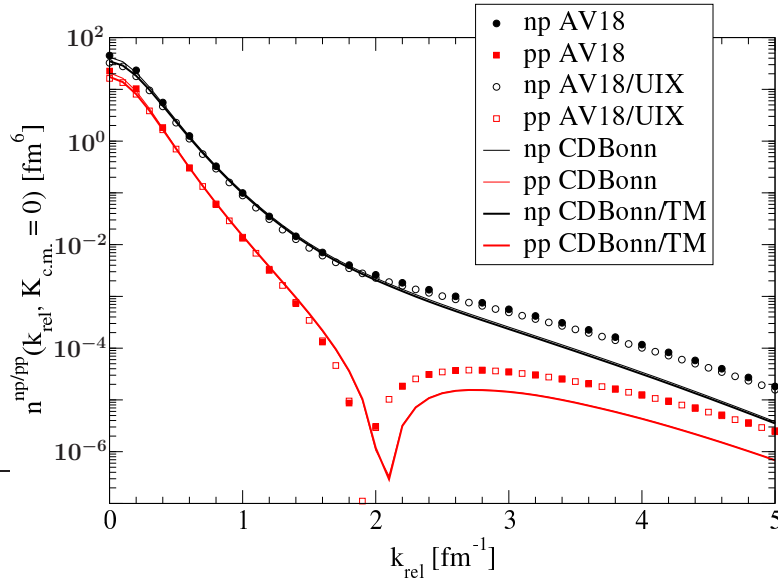


Figure 2: The  $2N$  momentum distributions  $n^{np/pp}(k_{rel}, K_{c.m.} = 0)$  in  ${}^3\text{He}$  calculated using the AV18, AV18/UIX, CDBonn and CDBonn/TM  $2N$  and  $3N$  interaction models. The thin and thick lines essentially overlap.

of the nuclear potential model, which can be local or non-local. The starting point are the so-called Jacobi coordinates, which are defined in the coordinate space as in Refs. [23, 24].

We first explore the model-dependence of the  $2N$  momentum distributions, by comparing predictions based on the CDBonn potential without or with the Tucson–Melbourne (TM) [25] three-nucleon ( $3N$ ) force with those based on the AV18, without or with the UIX  $3N$  force [26]. In Fig. 2 we show results for the  $n^{np/pp}(k_{rel}, K_{c.m.} = 0)$ , namely, we have selected the “back-to-back” (BB) configuration for the nucleon pair. We observe that the results with CDBonn/TM and those with AV18/UIX are substantially different from each other, especially in the high- $k_{rel}$  tails, confirming consistency with our earlier observations about the deuteron. Furthermore, the  $3N$  force contributions are barely appreciable on the logarithmic scale of the plot.

We now turn our attention to the  $2N$  momentum distributions obtained with the  $2N$  chiral potentials without or with the  $3N$  forces, obtained as discussed in Ref. [12]. We begin with studying the order-by-order pattern, using the  $\Lambda = 500$  MeV cutoff as an example. The results obtained with the other values of  $\Lambda$  display a similar behavior. In Fig. 3 we show the BB  $np$  momentum distribution  $n^{np}(k_{rel}, K_{c.m.} = 0)$  obtained using only the  $2N$  force at LO, NLO, N2LO, N3LO and N4LO. The figure reveals that the LO curve has a distinctly different behavior at small  $k_{rel}$  compared with the other curves, which suggests that the asymptotic part of the wave function at LO is significantly different than at the higher orders. Figure 4 displays the same predictions but for the  $pp$  pair, also BB. As we can see, similar remarks apply to the  $pp$  case as well. We also observe that the N3LO and N4LO curves are very similar up to  $k_{rel} \simeq 2.2 \text{ fm}^{-1}$ , indicating satisfactory order-by-order convergence at least in the region where the distributions still have non-negligible size.

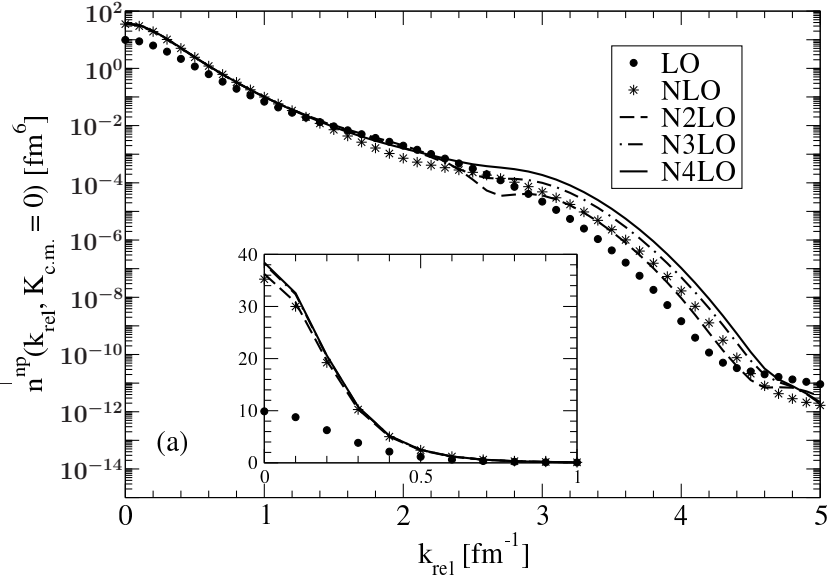


Figure 3: The  $np$  momentum distributions  $n^{np}(k_{rel}, K_{c.m.} = 0)$  in  ${}^3\text{He}$  calculated using only  $2N$  chiral interactions with  $\Lambda = 500$  MeV. The different chiral orders are labelled as in the text. In the inset we show the small  $k_{rel}$  range ( $k_{rel} \leq 1 \text{ fm}^{-1}$ ) on a linear scale.

The BB  $2N$  momentum distributions  $n^{np}(k_{rel}, K_{c.m.} = 0)$  and  $n^{pp}(k_{rel}, K_{c.m.} = 0)$  calculated with and without  $3N$  interaction, at different chiral order and for different values of the cutoff  $\Lambda$ , are shown in Figs. 5 and 6, respectively. The cutoff dependence is negligible below  $k_{rel} \simeq 2.2\text{--}2.5 \text{ fm}^{-1}$ , and increasingly strong above that.

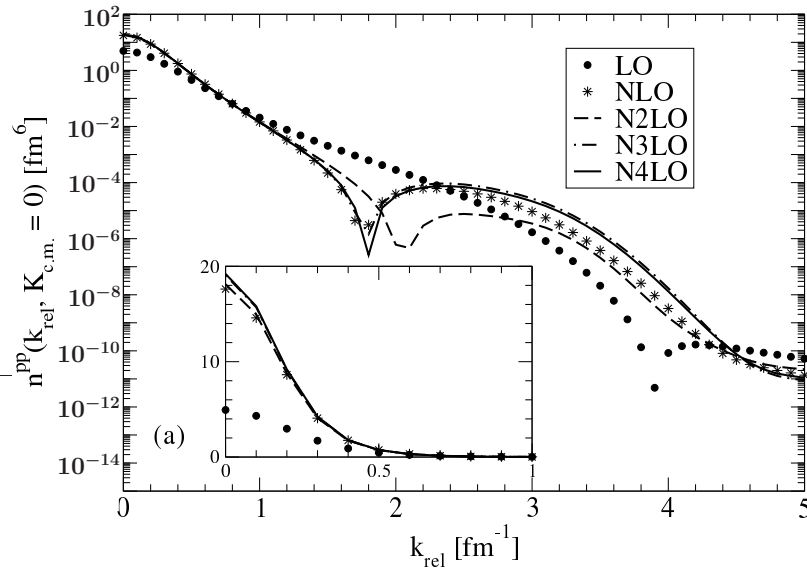


Figure 4: Same as Fig. 3 but for the  $pp$  pair.

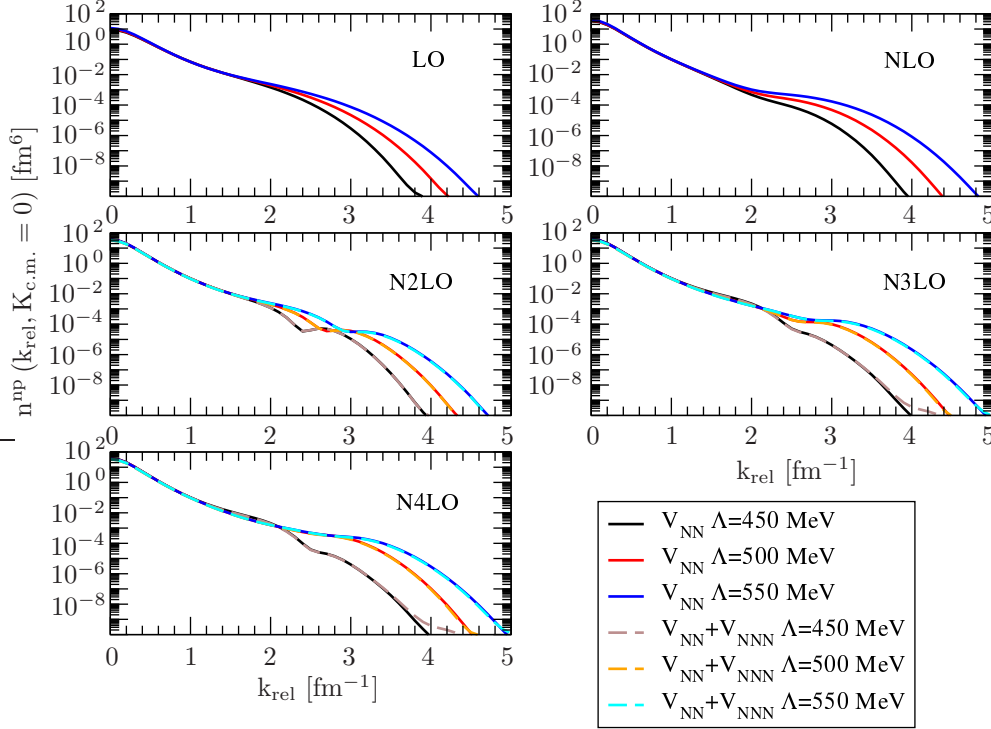
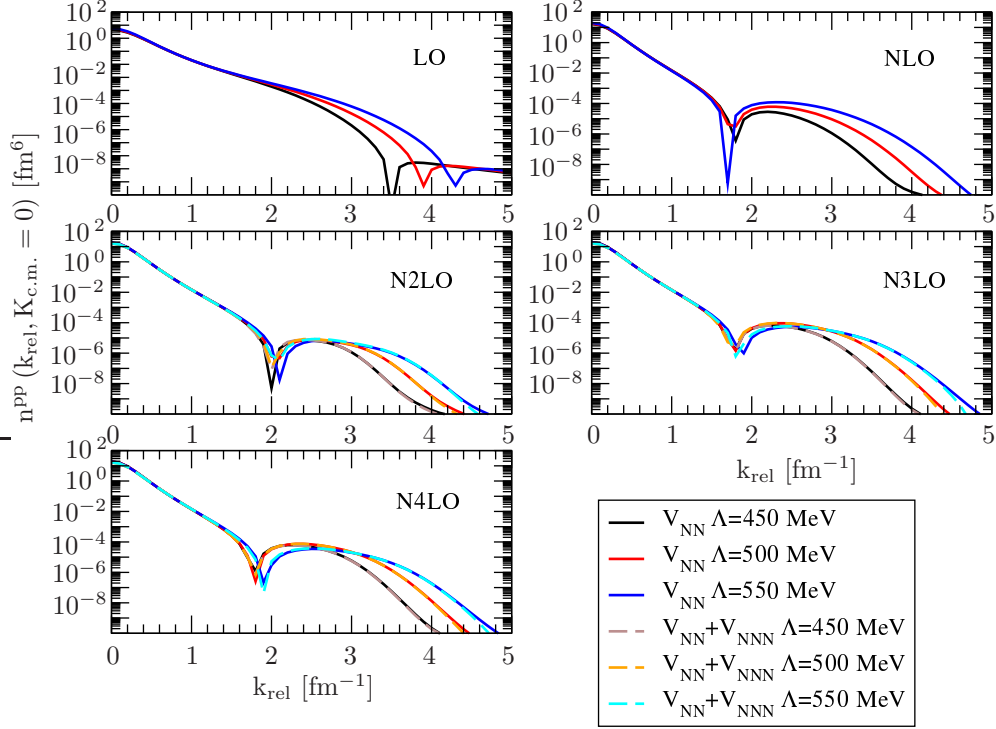


Figure 5: The  $np$  momentum distributions  $n^{np}(k_{rel}, K_{c.m.} = 0)$  in  ${}^3\text{He}$  calculated using only  $2N$  (solid lines) and  $2N + 3N$  (dashed lines) chiral interactions, at different chiral order and for three values of the cutoff  $\Lambda = 450, 500, 550$  MeV. In all panels, the lines from bottom to top correspond to the lower to higher values of  $\Lambda$ . Our approach to the construction of the leading  $3N$  force is described in Ref. [12].

Furthermore, the  $3N$  force contributions are visible only for  $k_{rel} \geq 3.0\text{--}3.5$  fm<sup>-1</sup>. Note, however, that above  $k_{rel} \simeq 2.5$  fm<sup>-1</sup> all momentum distributions are so small that the differences are of no practical relevance.

As noted for the deuteron case, the momentum distributions calculated with chiral interactions die out at a faster rate than those obtained with phenomenological potentials, a feature which may be expected given the softer nature of chiral forces. While this is a correct observation within the spectrum of interactions considered here, it is important to note that the chiral nature of an interaction does not necessarily bring the additional softness. To support this statement, we refer to Ref. [27], where predictions for single-nucleon and  $2N$  momentum distributions in  $A \leq 16$  are shown. In that work, it is concluded that, when *local* chiral interactions are employed, the resulting momentum distributions are *consistent* with those obtained from local phenomenological potentials. In fact, the local  $2N$  chiral interactions (at N2LO) applied in Ref. [27] and developed in Refs. [28, 29] predict a  $D$ -state probability for the deuteron ranging between 5.5 and 6.1%, values which are typical for the “hardest” local potentials.

Therefore, once again, the local vs non-local nature of the  $2N$  force (by far the largest contribution to our predicted momentum distributions), is a major factor in

Figure 6: Same as Fig. 5 but for the  $pp$  pair.

determining the theoretical momentum distributions in nuclei and, particularly, their short-range part.

## 4 Conclusions and outlook

We have discussed predictions for the  $2N$  momentum distributions in the deuteron and  ${}^3\text{He}$ . Our predictions are based on the state-of-the-art chiral  $2N$  potentials, including (or not) the leading chiral  $3N$  force. Also, for the purpose of comparison, we have considered older potentials plus an appropriate  $3N$  force, either fully phenomenological or based on meson theory. One of the main motivations was to explore the short-range few-nucleon dynamics as predicted by these diverse interactions. One of our findings is that, regardless the  $2N$  force model, the contribution from the  $3N$  forces is weak.

We find a significant model dependence, especially in the high-momentum tails of the momentum distributions, with both phenomenological and chiral potentials. We have explored the cutoff dependence and found that it can be significant. This is the case, though, in the region where the momentum becomes larger than the cutoff values themselves.

Although potentials based on chiral EFT may be expected to produce weaker SRC than purely phenomenological or meson-exchange ones, the local vs non-local nature of the underlying  $2N$  force appears to be a major factor in the observed model dependence. We find this to be an important issue, extensively debated in

the literature of the 1990's [19–21] and now re-emerging along with new stimulating discussions around electron scattering measurements.

The  $2N$  potentials considered here have an established success record with low-energy predictions, such as the structure of light and medium-mass nuclei as well as the properties of nuclear matter. But, as shown above, they differ considerably in their high-momentum components. Note that there is no physical reason why the off-shell behavior of, say, AV18, should be preferable as compared to other potentials. In fact, on the fundamental grounds, the off-shell behavior is not an observable. High momentum transfer reactions are easier to analyze using one-body currents of the impulse approximation, suitable with harder  $2N$  potentials, whereas the use of soft, non-local potentials, complicates the currents necessary to describe high momentum transfer experiments [30]. One should carefully consider, for instance, to which extent analyses of quasielastic electron scattering in terms of external radiation graphs [30], without gauge-invariance preserving terms, may cause a sensitivity to the (otherwise unobservable) off-shell behavior.

## Acknowledgments

The work of F.S. and R.M. was supported by the U.S. Department of Energy, Office of Science, Office of Basic Energy Sciences, under Award Number DE-FG02-03ER41270. Computational resources provided by the INFN-Pisa Computer Center are gratefully acknowledged.

## References

- [1] K. S. Egiyan *et al.*, Phys. Rev. Lett. **96**, 082501 (2006) *and references therein*.
- [2] K. Sh. Egiyan *et al.*, CLAS-NOTE 2005-004 (2005), [https://misportal.jlab.org/ul/physics/Hall-B/clas/index.cfm?note\\_year=2005](https://misportal.jlab.org/ul/physics/Hall-B/clas/index.cfm?note_year=2005).
- [3] K. Sh. Egiyan *et al.*, Phys. Rev. C **68**, 014313 (2003).
- [4] M. McGauley and M. M. Sargsian, arXiv:1102.3973v3 [nucl-th] (2012).
- [5] E. Piasetzky, M. Sargsian, L. Frankfurt, M. Strikman and J. W. Watson, Phys. Rev. Lett. **97**, 162504 (2006).
- [6] A. Tang *et al.*, Phys. Rev. Lett. **90**, 042301 (2003).
- [7] I. Korover *et al.* (Jefferson Lab Hall A Collaboration), Phys. Rev. Lett. **113**, 022501 (2014).
- [8] R. Shneor *et al.* (Jefferson Lab Hall A Collaboration), Phys. Rev. Lett. **99**, 072501 (2007).
- [9] R. Subedi *et al.*, Science **320**, 1476 (2008).
- [10] H. Baghdasaryan *et al.* (CLAS Collaboration), Phys. Rev. Lett. **105**, 222501 (2010).
- [11] F. Sammarruca, Phys. Rev. C **92**, 044003 (2015).

- [12] L. E. Marcucci, F. Sammarruca, M. Viviani and R. Machleidt, *Phys. Rev. C* **99**, 034003 (2019).
- [13] R. B. Wiringa, V. G. J. Stoks and R. Schiavilla, *Phys. Rev. C* **51**, 38 (1995).
- [14] V. G. J. Stoks, R. A. M. Klomp, C. P. F. Terheggen and J. J. de Swart, *Phys. Rev. C* **49**, 2950 (1994).
- [15] R. Machleidt, *Phys. Rev. C* **63**, 024001 (2001).
- [16] D. R. Entem and R. Machleidt, *Phys. Rev. C* **68**, 041001(R) (2003).
- [17] E. Marji, A. Canul, Q. MacPherson, R. Winzer, Ch. Zeoli, D. R. Entem and R. Machleidt, *Phys. Rev. C* **88**, 054002 (2013).
- [18] R. Machleidt and D. R. Entem, *Phys. Rep.* **503**, 1 (2011).
- [19] R. Machleidt, F. Sammarruca and Y. Song, *Phys. Rev. C* **53**, R1483(R) (1996).
- [20] A. Polls, H. Mütter, R. Machleidt and M. Hjorth-Jensen, *Phys. Lett. B* **432**, 1 (1998).
- [21] H. Mütter and A. Polls, *Phys. Rev. C* **61**, 014304 (1999).
- [22] D. R. Entem, R. Machleidt and Y. Nosyk, *Phys. Rev. C* **96**, 024004 (2017).
- [23] M. Viviani, L. E. Marcucci, S. Rosati, A. Kievsky and L. Girlanda, *Few-Body Syst.* **39**, 159 (2006).
- [24] A. Kievsky, S. Rosati, M. Viviani, L. E. Marcucci and L. Girlanda, *J. Phys. G* **35**, 063101 (2008).
- [25] S. A. Coon and H. K. Han, *Few-Body Syst.* **30**, 131 (2001).
- [26] B. S. Pudliner, V. R. Pandharipande, J. Carlson and R. B. Wiringa, *Phys. Rev. Lett.* **74**, 4396 (1995).
- [27] D. Lonardoni, S. Gandolfi, X. B. Wang and J. Carlson, *Phys. Rev. C* **98**, 014322 (2018).
- [28] A. Gezerlis, I. Tews, E. Epelbaum, S. Gandolfi, K. Hebeler, A. Nogga and A. Schwenk, *Phys. Rev. Lett.* **111**, 032501 (2013).
- [29] A. Gezerlis, I. Tews, E. Epelbaum, M. Freunek, S. Gandolfi, K. Hebeler, A. Nogga and A. Schwenk, *Phys. Rev. C* **90**, 054323 (2014).
- [30] O. Hen, G. A. Miller, E. Piasetzky and L. B. Weinstein, *Rev. Mod. Phys.* **89**, 045002 (2017).

# Algebraic Solution of the Isovector Pairing Problem

Feng Pan<sup>a,b</sup>, Kristina D. Launey<sup>b</sup> and Jerry P. Draayer<sup>b</sup>

<sup>a</sup>*Department of Physics, Liaoning Normal University, Dalian 116029, China*

<sup>b</sup>*Department of Physics and Astronomy, Louisiana State University, Baton Rouge, LA 70803-4001, USA*

## Abstract

A simple and effective algebraic isospin projection procedure for constructing basis vectors of irreducible representations of  $O(5) \supset O_T(3) \otimes O_N(2)$  from those in the canonical  $O(5) \supset SU_\Lambda(2) \otimes SU_I(2)$  basis is outlined, which is useful in dealing with the isovector pairing problem. The expansion coefficients are components of null-space vectors of the projection matrix. Explicit formulae for evaluating  $O_T(3)$ -reduced matrix elements of  $O(5)$  generators are derived.

**Keywords:** *Isovector pairing; proton-neutron quasi-spin group; dynamical symmetry*

## 1 Introduction

The proton-neutron quasi-spin group generated by an  $O(5)$  algebra is very useful in dealing with nucleon pairing problems in a shell model framework [1–5]. Due to its importance in nuclear spectroscopy, irreducible representations (irreps) of  $O(5)$  have been studied in various ways. The most natural basis for irreps of  $O(5)$  may be the branching multiplicity-free canonical one with  $O(5) \supset O(4)$ , where  $O(4)$  is locally isomorphic to  $SU_\Lambda(2) \otimes SU_I(2)$ , of which the construction of the basis vectors was presented in Refs. [6–8]. The matrix representations of  $O(5) \supset SU_\Lambda(2) \otimes SU_I(2)$  were provided in Refs. [6–9]. Since the isospin is approximately conserved in the charge-independent isovector pairing problem, it is more convenient to adopt the non-canonical  $O(5) \supset O_T(3) \otimes O_N(2)$  basis for this case, where  $O_T(3)$  is the isospin group, and  $O_N(2) \sim U_N(1)$  is related with the number of nucleons in the system. The main problem is that the reduction  $O(5) \downarrow O_T(3) \otimes O_N(2)$  is no longer branching multiplicity-free in general. Basis vectors of  $O(5)$  irreps in the  $O(5) \supset O_T(3) \otimes O_N(2)$  basis can be either expanded in terms of those in the  $O(5) \supset SU_\Lambda(2) \otimes SU_I(2)$  or constructed by using tensor coupling methods directly, for which various attempts were made [6, 10–15]. A recent survey on the subject with relevant references is provided in Refs. [16, 17]. Though various procedures for the construction of basis vectors of  $O(5)$  irreps in the  $O(5) \supset O_T(3) \otimes O_N(2)$  were provided in these works, only cases up to the branching multiplicity three were obtained explicitly

---

*Proceedings of the International Conference ‘Nuclear Theory in the Supercomputing Era — 2018’ (NTSE-2018), Daejeon, South Korea, October 29 – November 2, 2018, eds. A. M. Shirokov and A. I. Mazur. Pacific National University, Khabarovsk, Russia, 2019, p. 73.*

<http://www.ntse.khb.ru/files/uploads/2018/proceedings/Pan.pdf>.

in the past. Moreover, though there are closed expressions of the expansion coefficients (overlaps) [13] of the basis vectors of  $O(5) \supset O_T(3) \otimes O_{\mathcal{N}}(2)$  in terms of those of  $O(5) \supset SU_{\Lambda}(2) \otimes SU_I(2)$  for any irrep of  $O(5)$ , a triple sum is involved. Especially, the basis vectors of  $O(5) \supset O_T(3) \otimes O_{\mathcal{N}}(2)$  obtained in all previous works [6, 10–15] are non-orthogonal with respect to the branching multiplicity label, of which direct computation will be CPU time consuming.

## 2 $O(5)$ in the $O_T(3) \otimes O_{\mathcal{N}}(2)$ basis

The generators of  $O(5)$  in the  $O(5) \supset O_T(3) \times O_{\mathcal{N}}(2)$  basis may be expressed as

$$\begin{aligned} A_1^\dagger &= \nu_+, & A_{-1}^\dagger &= \tau_+, & A_1 &= \nu_-, & A_{-1} &= \tau_-, \\ A_0^\dagger &= U_{\frac{1}{2}\frac{1}{2}}, & A_0 &= -U_{-\frac{1}{2}-\frac{1}{2}}, & T_+ &= -\sqrt{2}U_{\frac{1}{2}-\frac{1}{2}}, & T_- &= -\sqrt{2}U_{-\frac{1}{2}\frac{1}{2}}, \\ T_0 &= \nu_0 - \tau_0, & \hat{\mathcal{N}} &= \nu_0 + \tau_0, \end{aligned} \quad (1)$$

where  $\{T_+, T_-, T_0\}$  generate the subgroup  $O_T(3)$ , and  $\hat{\mathcal{N}}$  generates the  $O_{\mathcal{N}}(2)$ .  $\hat{\mathcal{N}} = \frac{\hat{n}}{2} - \Omega$ , where  $\Omega = \sum_j (j + 1/2)$  and the sum runs over all single-particle orbits considered, and  $\hat{n}$  is the total number operator of valence nucleons, which is used in the isovector pairing model [1–5]. Moreover,  $\{\nu_+ = A_1^\dagger, \nu_- = A_1, \nu_0 = \hat{n}_\pi/2 - \Omega/2\}$  and  $\{\tau_+ = A_{-1}^\dagger, \tau_- = A_{-1}, \tau_0 = \hat{n}_\nu/2 - \Omega/2\}$ , where  $\hat{n}_\pi$  and  $\hat{n}_\nu$  are valence neutron and proton number operator, respectively, generate the  $SU_{\Lambda}(2) \otimes SU_I(2)$  related to the quasispin of protons and neutrons with  $\Lambda = (\Omega - v_\pi)/2$  and  $I = (\Omega - v_\nu)/2$ , where  $v_\pi$  and  $v_\nu$  are proton and neutron seniority numbers, respectively. The matrix elements of the double-tensor  $\mathbf{U}$  introduced in Eq. (1) under the  $O(5) \supset SU_{\Lambda}(2) \otimes SU_I(2)$  basis were given in Refs. [6–9].

For a given irrep  $(v_1, v_2)$  of  $O(5)$ , the basis vectors of  $O(5) \supset SU_{\Lambda}(2) \otimes SU_I(2)$  are denoted as

$$\left| \begin{array}{c} (v_1, v_2) \\ \Lambda = \frac{1}{2}(u_1 + u_2), I = \frac{1}{2}(u_1 - u_2) \\ m_{\Lambda}, \quad m_I \end{array} \right\rangle, \quad (2)$$

where  $m_{\Lambda}$  and  $m_I$  are quantum number of  $\nu_0$  and  $\tau_0$ , respectively,  $u_1 = v_1 - q$  and  $u_2 = v_2 - p$  with  $p = 0, 1, \dots, 2v_2$ , and  $q = 0, 1, \dots, v_1 - v_2$ .

As can be observed from Eq. (1), the basis vectors of  $O(5) \supset SU_{\Lambda}(2) \otimes SU_I(2)$  given in Eq. (2) are also eigenstates of  $T_0$  and  $\hat{\mathcal{N}}$  with eigenvalues

$$M_T = m_{\Lambda} - m_I, \quad \mathcal{N} = m_{\Lambda} + m_I. \quad (3)$$

For a given irrep  $(v_1, v_2)$  of  $O(5)$ , all possible basis vectors of  $O(5) \supset SU_{\Lambda}(2) \otimes SU_I(2) \supset U_{\Lambda}(1) \otimes U_I(1)$  shown in Eq. (2) restricted by the conditions (3) form a complete set for the fixed  $M_T$  and  $\mathcal{N}$ . Therefore, the basis vectors of  $O(5) \supset O_T(3) \otimes O_{\mathcal{N}}(2)$  can be expanded in terms of them with the restriction on the quantum numbers  $m_{\Lambda} = \frac{1}{2}(\mathcal{N} + M_T)$  and  $m_I = \frac{1}{2}(\mathcal{N} - M_T)$ . In constructing the basis vectors of  $O(5) \supset O_T(3) \otimes O_{\mathcal{N}}(2)$  for the irrep  $(v_1, v_2)$  of  $O(5)$  with fixed  $\mathcal{N}$ , there is a freedom to choose a specific basis vector of  $O(5) \supset O_T(3) \otimes O_{\mathcal{N}}(2)$  with isospin  $T$  and the quantum number of the third component of the isospin  $M_T$ . Practically, it is convenient to choose the highest or the lowest weight state of  $O_T(3)$  with  $M_T = T$  or  $M_T = -T$ . Here, we choose the highest weight state of  $O_T(3)$  with  $M_T = T$  as a

reference state with

$$\left| \begin{array}{c} (v_1, v_2) \\ \zeta \ T = M_T, \mathcal{N} \end{array} \right\rangle, \quad (4)$$

where  $\zeta$  is the multiplicity label needed in the reduction  $(v_1, v_2) \downarrow (T, \mathcal{N})$  of  $O(5) \supset O_T(3) \otimes O_{\mathcal{N}}(2)$ . Thus, the vectors (4) should satisfy

$$T_+ \left| \begin{array}{c} (v_1, v_2) \\ \zeta \ T = M_T, \mathcal{N} \end{array} \right\rangle = 0. \quad (5)$$

Once the basis vector (4) for the highest weight state of  $O_T(3)$  with  $M_T = T$  is known, the basis vector of  $O(5) \supset O_T(3) \otimes O_{\mathcal{N}}(2)$  for any  $M_T$  can be expressed in the standard way as

$$\left| \begin{array}{c} (v_1, v_2) \\ \zeta \ T, M_T, \mathcal{N} \end{array} \right\rangle = \sqrt{\frac{(T + M_T)!}{(2T)!(T - M_T)!}} (T_-)^{T - M_T} \left| \begin{array}{c} (v_1, v_2) \\ \zeta \ T, M_T = T, \mathcal{N} \end{array} \right\rangle. \quad (6)$$

In order to find all basis vectors of  $O(5) \supset SU_{\Lambda}(2) \otimes SU_I(2)$  with fixed  $M_T > 0$  and  $\mathcal{N}$  in the irrep  $(v_1, v_2)$  of  $O(5)$ , one suffices to consider possible irreps  $(\Lambda, I)$  of  $SU_{\Lambda}(2) \otimes SU_I(2)$  embedded in the canonical chain satisfying the condition (3). According to the restrictions  $M_T = m_{\Lambda} - m_I$ ,  $\mathcal{N} = m_{\Lambda} + m_I$  and the reduction rules, we find that the following basis vectors are all possible ones within the  $O(5)$  irrep  $(v_1, v_2)$  with  $M_T \geq 0$  for fixed  $\mathcal{N}$ :

$$\left| \begin{array}{c} (v_1, v_2) \\ \Lambda, \quad I \\ \frac{1}{2}(\mathcal{N} + M_T), \quad \frac{1}{2}(\mathcal{N} - M_T) \end{array} \right\rangle \quad (7)$$

with the restrictions

$$\frac{1}{2}|\mathcal{N} + M_T| \leq \Lambda \leq \frac{1}{2}(v_1 + v_2), \quad \frac{1}{2}|\mathcal{N} - M_T| \leq I \leq \frac{1}{2}(v_1 - v_2). \quad (8)$$

Hence, the basis vectors of  $O(5) \supset O_T(3) \otimes O_{\mathcal{N}}(2)$  may be expanded in terms of vectors (7) as

$$\begin{aligned} \left| \begin{array}{c} (v_1, v_2) \\ \zeta \ T = M_T, \mathcal{N} \end{array} \right\rangle &= \sum_{q=0}^{v_1 - v_2} \sum_{p=\text{Max}[0, q - v_1 + v_2 + |\mathcal{N} - T|]}^{\text{Min}[v_1 + v_2 - q - |\mathcal{N} + T|, 2v_2]} c_{p,q}^{(\zeta)} \\ &\times \left| \begin{array}{c} (v_1, v_2) \\ \Lambda = \frac{1}{2}(v_1 + v_2 - p - q), \quad I = \frac{1}{2}(v_1 - v_2 + p - q) \\ \frac{1}{2}(\mathcal{N} + T), \quad \frac{1}{2}(\mathcal{N} - T) \end{array} \right\rangle, \quad (9) \end{aligned}$$

where the summations should also be restricted by the condition that  $v_1 + v_2 - p - q - |\mathcal{N} + T|$  are even numbers,  $\zeta$  is the multiplicity label needed in the reduction  $(v_1, v_2) \downarrow (\mathcal{N}, T)$ , and  $\{c_{pq}^{(\zeta)} \equiv c_{pq}^{(\zeta)}((v_1, v_2), \mathcal{N}, T)\}$  are the expansion coefficients, which must satisfy

$$-\sqrt{\frac{1}{2}}T_+ \left| \begin{array}{c} (v_1, v_2) \\ \zeta \ T = M_T, \mathcal{N} \end{array} \right\rangle = U_{\frac{1}{2} - \frac{1}{2}} \left| \begin{array}{c} (v_1, v_2) \\ \zeta \ T = M_T, \mathcal{N} \end{array} \right\rangle = 0. \quad (10)$$

By using the explicit matrix elements of  $\mathbf{U}$  in the  $O(5) \supset SU_\Lambda(2) \otimes SU_I(2)$  basis provided in Refs. [6–9], Eq. (10) leads to the following four-term relation to determine the expansion coefficients  $\{c_{p,q}^{(\zeta)}\}$ :

$$\begin{aligned}
& c_{p,q+1}^{(\zeta)} (-1)^{2\mathcal{N}-2q+2v_1} \\
& \times \left[ \frac{(1+q)(2v_1-q+2)(v_1+v_2-q+1)(v_1+v_2-p-q+T+\mathcal{N}+1)(v_1-v_2+T-\mathcal{N}+p-q+1)(v_1-v_2-q)}{(v_1+v_2-p-q)(v_1-v_2+p-q)} \right]^{\frac{1}{2}} \\
& + c_{p+1,q}^{(\zeta)} (-1)^{v_1+v_2+\mathcal{N}-p-q+T} \\
& \times \left[ \frac{(1+p)(2v_2-p)(v_1+v_2-p+1)(v_1+v_2+T+\mathcal{N}-p-q+1)(v_1-v_2+p+2)(v_1-v_2-T+\mathcal{N}+p-q+1)}{(v_1+v_2-p-q)(v_1-v_2+p-q+2)} \right]^{\frac{1}{2}} \\
& + c_{p-1,q}^{(\zeta)} (-1)^{v_1-v_2+\mathcal{N}+p-q-T} \\
& \times \left[ \frac{p(2v_2-p+1)(v_1+v_2-p+2)(v_1+v_2-T-\mathcal{N}-p-q+1)(v_1-v_2+p+1)(v_1-v_2+T-\mathcal{N}+p-q+1)}{(v_1+v_2-p-q+2)(v_1-v_2+p-q)} \right]^{\frac{1}{2}} \\
& + c_{p,q-1}^{(\zeta)} \\
& \times \left[ \frac{q(2v_1-q+3)(v_1+v_2-q+2)(v_1+v_2-T-\mathcal{N}-p-q+1)(v_1-v_2-T+\mathcal{N}+p-q+1)(v_1-v_2-q+1)}{(v_1+v_2-p-q+2)(v_1-v_2+p-q+2)} \right]^{\frac{1}{2}} = 0.
\end{aligned} \tag{11}$$

Accordingly, one can construct a matrix equation equivalent to Eq. (11),

$$\mathbf{P}((v_1, v_2), \mathcal{N}, T) \mathbf{c}^{(\zeta)} = \Lambda \mathbf{c}^{(\zeta)}. \tag{12}$$

Entries of the isospin projection matrix  $\mathbf{P}((v_1, v_2), \mathcal{N}, T)$  can easily be read out from Eq. (11) and the eigenvector  $\mathbf{c}^{(\zeta)} \equiv \mathbf{c}^{(\zeta)}((v_1, v_2), \mathcal{N}, T)$ , which transpose is arranged as  $(\mathbf{c}^{(\zeta)})^T = (c_{0,0}^{(\zeta)}, c_{1,0}^{(\zeta)}, c_{2,0}^{(\zeta)}, \dots, c_{0,1}^{(\zeta)}, c_{1,1}^{(\zeta)}, \dots)$ . The components of the eigenvector  $\mathbf{c}^{(\zeta)}$  corresponding to  $\Lambda = 0$  provide the expansion coefficients  $\{c_{p,q}^{(\zeta)}\}$  of Eq. (9). Once the matrix  $\mathbf{P}((v_1, v_2), \mathcal{N}, T)$  is constructed, it can be verified that the number of  $\Lambda = 0$  solutions of Eq. (12) equals exactly to the number of rows of  $\mathbf{P}((v_1, v_2), \mathcal{N}, T)$  with all entries zero. Actually, the eigenvectors  $\mathbf{c}^{(\zeta)}((v_1, v_2), T, \mathcal{N})$  belong to the null-space of  $\mathbf{P}((v_1, v_2), \mathcal{N}, T)$ . Since there are many ways to find null-space vectors of a matrix, to find solutions of Eq. (12) with  $\Lambda = 0$  becomes practically easy. Furthermore,  $(\mathbf{c}^{(\zeta')})^T \cdot \mathbf{c}^{(\zeta)} \neq 0$  when the multiplicity is greater than 1 mainly because the projection matrix  $\mathbf{P}((v_1, v_2), \mathcal{N}, T)$  is nonsymmetric. Therefore, the  $O(5) \supset O_T(3) \otimes O_{\mathcal{N}}(2)$  basis vectors (9) constructed from the expansion coefficients obtained according to Eq. (11) are also non-orthogonal with respect to the multiplicity label  $\zeta$  in general. The Gram–Schmidt process may be adopted in order to construct orthonormalized basis vectors of  $O(5) \supset O_T(3) \otimes O_{\mathcal{N}}(2)$ . Nevertheless, in the Wolfram Mathematica, the built-in function NullSpace of a matrix with non-integer entries generates orthonormalized null-space vectors automatically, with which the Gram–Schmidt orthogonalization can be avoid. In the following, we use  $\tilde{\mathbf{c}}^{(\zeta)}$  to denote the orthonormalized null-space vectors of  $N[\mathbf{P}((v_1, v_2), \mathcal{N}, T)]$  with respect to the multiplicity label  $\zeta$  obtained from the Wolfram Mathematica numerically, where  $N[\mathbf{P}]$  means to take  $\mathbf{P}$  with numerical valued entries with a default precision.

The CPU time cost and memory space needed for a computer to solve the null-space problem (12) depend mainly on the number of terms  $d(\mathcal{N}, T)$  needed in the expansion (9), which equals to the number of columns of  $\mathbf{P}((v_1, v_2), \mathcal{N}, T)$ . Generally, it would take the CPU time on the order of  $O(d^3)$  with a unit inversely proportional to the CPU frequency, and the memory space on the order of  $O(d^2)$  bytes. When  $v_1$  and  $v_2$  are integers, for example, we observe from Eq. (9) that the maximal number

of terms occurs in the  $T = \mathcal{N} = 0$  case. In such extreme case, the upper bound of the number of terms involved in the expansion can be estimated as

$$d(\mathcal{N} = 0, T = 0) \leq \sum_{q=0}^{v_1-v_2} \sum_{p=\text{Max}[0, q-v_1+v_2]}^{\text{Min}[v_1+v_2-q, 2v_2]} 1 = (1 + v_1 - v_2)(2v_2 + 1), \quad (13)$$

which shows that  $\text{Max}[d(\mathcal{N}, T)] \leq d(\mathcal{N} = 0, T = 0)$  increases with  $v_1$  linearly and with  $v_2$  quadratically.

### 3 Matrix elements of the isovector pairing operators in the $O(5) \supset O_T(3) \otimes O_{\mathcal{N}}(2)$ basis

Once the orthonormalized expansion coefficients  $\{\tilde{c}^{(\zeta)}\}$  are obtained according to the isospin projection shown in the previous section, one can easily calculate matrix elements of  $O(5)$  generators  $\{A_{\mu}^{\dagger}, A_{\mu}, T_{\mu}, \mathcal{N}\}$  ( $\mu = -1, 0, 1$ ) given in Eq. (1) in the  $O_T(3) \otimes O_{\mathcal{N}}(2)$  basis. Since the matrix elements of  $\{T_{\mu}, \mathcal{N}\}$  are well-known, depend only on  $T$  or  $\mathcal{N}$ , and are irrelevant to the irrep of  $O(5)$  and the multiplicity label  $\zeta$ , only the formulae of matrix elements of the isovector pairing operator  $A_{\mu}^{\dagger}$  and  $A_{\mu}$  in the  $O(5) \supset O_T(3) \otimes O_{\mathcal{N}}(2)$  basis will be provided.

In the  $O(5) \supset O_T(3) \otimes O_{\mathcal{N}}(2)$  basis, the pair creation operators  $\mathcal{A}_{\mu}^{+}$  with  $\{\mathcal{A}_1^{+} = -A_1^{\dagger}, \mathcal{A}_0^{+} = A_0^{\dagger}, \mathcal{A}_{-1}^{+} = A_{-1}^{\dagger}\}$  and the pair annihilation operators  $\mathcal{A}_{\mu}$  with  $\{\mathcal{A}_1 = A_{-1}, \mathcal{A}_0 = -A_0, \mathcal{A}_{-1} = -A_1\}$  are  $T = 1$  irreducible tensor operators of  $O_T(3)$  satisfying the following conjugation relation [18]:

$$\mathcal{A}_{\mu} = (-1)^{1-\mu} (\mathcal{A}_{-\mu}^{+})^{\dagger}. \quad (14)$$

These  $T = 1$  irreducible tensor operators shift  $\mathcal{N}$  by one unit, while  $A_1^{\dagger} = \nu_{+}$ ,  $A_0^{\dagger} = U_{\frac{1}{2}\frac{1}{2}}$ , and  $A_{-1}^{\dagger} = \tau_{+}$  in the  $O(5) \supset SU_{\Lambda}(2) \otimes SU_I(2)$  basis shown in Refs. [6–9]. Using the Wigner–Eckart theorem for matrix elements of  $O(5) \supset O_T(3) \otimes O_{\mathcal{N}}(2)$ , we have

$$\begin{aligned} & \left\langle \begin{matrix} (v_1, v_2) \\ \zeta' T' M_T', \mathcal{N}' \end{matrix} \left| \mathcal{A}_{\mu}^{+} \right| \begin{matrix} (v_1, v_2) \\ \zeta T M_T, \mathcal{N} \end{matrix} \right\rangle \\ &= \delta_{\mathcal{N}', \mathcal{N}+1} \langle T M_T, 1\mu | T' M_T' \rangle \left\langle \begin{matrix} (v_1, v_2) \\ \zeta' T', \mathcal{N}'+1 \end{matrix} \left\| \mathcal{A}^{+} \right\| \begin{matrix} (v_1, v_2) \\ \zeta T, \mathcal{N} \end{matrix} \right\rangle, \quad (15) \end{aligned}$$

where  $\langle T M_T, 1\mu | T' M_T' \rangle$  is the Clebsch–Gordan coefficient of  $O_T(3)$ , and

$$\left\langle \begin{matrix} (v_1, v_2) \\ \zeta' T', \mathcal{N}' \end{matrix} \left\| \mathcal{A}^{+} \right\| \begin{matrix} (v_1, v_2) \\ \zeta T, \mathcal{N} \end{matrix} \right\rangle$$

is the  $O_T(3)$ -reduced matrix element. In the calculation, we ensure that  $T'$  is always involved in the  $O_T(3)$  coupling  $T \otimes 1$ , and  $M_T' = M_T + \mu$  is always satisfied. By using Eq. (9) and the expressions of  $A_{\mu}^{\dagger}$  in terms of the generators of  $O(5)$  in the  $SU_{\Lambda}(2) \otimes SU_I(2)$  basis shown in Eq. (1), the left-hand-side of Eq. (15) can be

expressed in terms of expansion coefficients  $\tilde{c}^{(\zeta)}$  and the matrix elements of  $O(5)$  generators in the  $SU_\Lambda(2) \otimes SU_I(2)$  basis. In the following, we list nonzero  $O_T(3)$ -reduced matrix elements of  $\mathcal{A}^\dagger$  derived in this way:

$$\left\langle \begin{matrix} (v_1, v_2) \\ \zeta' T+1, \mathcal{N}+1 \end{matrix} \left\| \mathcal{A}^+ \right\| \begin{matrix} (v_1, v_2) \\ \zeta T, \mathcal{N} \end{matrix} \right\rangle = -\frac{1}{2} \sum_{q,p} \tilde{c}_{p,q}^{(\zeta')}(\mathcal{N}+1, T+1) \tilde{c}_{p,q}^{(\zeta)}(\mathcal{N}, T) \\ \times \sqrt{(v_1+v_2-p-q-\mathcal{N}-T)(v_1+v_2-p-q+\mathcal{N}+T+2)},$$

$$\left\langle \begin{matrix} (v_1, v_2) \\ \zeta' T, \mathcal{N}+1 \end{matrix} \left\| \mathcal{A}^+ \right\| \begin{matrix} (v_1, v_2) \\ \zeta T, \mathcal{N} \end{matrix} \right\rangle \\ = \sqrt{\frac{T+1}{8T}} \sum_{q,p} \tilde{c}_{q,t}^{(\zeta)}(\mathcal{N}, T) \left( \tilde{c}_{p,q-1}^{(\zeta')}(\mathcal{N}+1, T) (-1)^{2\mathcal{N}-2q+2v_1+1} \right. \\ \times \left[ \frac{q(2v_1-q+3)(v_1-v_2+p-q+\mathcal{N}-T+2)(v_1+v_2-p-q+T+\mathcal{N}+2)(v_1-v_2-q+1)(v_1+v_2-q+2)}{(v_1-v_2+p-q+1)(v_1-v_2+p-q+2)(v_1+v_2-p-q+1)(v_1+v_2-p-q+2)} \right]^{\frac{1}{2}} \\ \left. + \tilde{c}_{p-1,q}^{(\zeta)}(\mathcal{N}+1, T) (-1)^{v_1+v_2+\mathcal{N}-p-q+T} \right. \\ \times \left[ \frac{p(2v_2-p+2)(v_1-v_2+p-q-\mathcal{N}+T)(v_1+v_2-p-q+T+\mathcal{N}+2)(v_1-v_2+p+1)(v_1+v_2-p+2)}{(v_1-v_2+p-q+1)(v_1-v_2+p-q)(v_1+v_2-p-q+1)(v_1+v_2-p-q+2)} \right]^{\frac{1}{2}} \\ \left. + \tilde{c}_{p+1,q}^{(\zeta)}(\mathcal{N}+1, T) (-1)^{v_1-v_2+\mathcal{N}+p-q-T} \right. \\ \times \left[ \frac{(p+1)(2v_2-p)(v_1-v_2+\mathcal{N}-T+p-q+2)(v_1+v_2-T-\mathcal{N}-p-q)(v_1-v_2+p+2)(v_1+v_2-p+1)}{(v_1-v_2+p-q+1)(v_1-v_2+p-q+2)(v_1+v_2-p-q)(v_1+v_2-p-q+1)} \right]^{\frac{1}{2}} \\ \left. + \tilde{c}_{p,q+1}^{(\zeta)}(\mathcal{N}+1, T) \right. \\ \times \left. \left[ \frac{(q+1)(2v_1-q+2)(v_1-v_2-T+\mathcal{N}+p-q)(v_1+v_2-T-\mathcal{N}-p-q)(v_1-v_2-q)(v_1+v_2-q+1)}{(v_1-v_2+p-q)(v_1-v_2+p-q+1)(v_1+v_2-p-q)(v_1+v_2-p-q+1)} \right]^{\frac{1}{2}} \right)$$

for  $T \geq \frac{1}{2}$ , and

$$\left\langle \begin{matrix} (v_1, v_2) \\ \zeta' T-1, \mathcal{N}+1 \end{matrix} \left\| \mathcal{A}^+ \right\| \begin{matrix} (v_1, v_2) \\ \zeta T, \mathcal{N} \end{matrix} \right\rangle \\ = \frac{1}{2} \sqrt{\frac{2T+1}{2T-1}} \sum_{q,p} \tilde{c}_{p,q}^{(\zeta')}(\mathcal{N}+1, T-1) \tilde{c}_{p,q}^{(\zeta)}(\mathcal{N}, T) \\ \times \sqrt{(v_1-v_2+p-q-\mathcal{N}+T)(v_1-v_2+p-q+\mathcal{N}-T+2)} \quad (16)$$

for  $T \geq 1$ . The other non-zero reduced matrix elements of  $\mathcal{A}$  can be obtained by the conjugation relation:

$$\left\langle \begin{matrix} (v_1, v_2) \\ \zeta' T', \mathcal{N}' \end{matrix} \left\| \mathcal{A} \right\| \begin{matrix} (v_1, v_2) \\ \zeta T, \mathcal{N} \end{matrix} \right\rangle = (-1)^{T'-T+1} \sqrt{\frac{2T+1}{2T'+1}} \left\langle \begin{matrix} (v_1, v_2) \\ \zeta T, \mathcal{N} \end{matrix} \left\| \mathcal{A}^+ \right\| \begin{matrix} (v_1, v_2) \\ \zeta' T', \mathcal{N}' \end{matrix} \right\rangle. \quad (17)$$

## 4 Applications to the isovector pairing model

In the spherical shell model, we consider  $n$  valence nucleons with  $J = 0$  and  $T = 1$  pairing interactions in  $p$  single-particle orbits. In general, the spherical shell model is the mean-field plus the isovector pairing interaction Hamiltonian may be written as [5]

$$\hat{H} = \sum_j \epsilon_j n_j - G_\pi A_{+1}^\dagger A_{+1} - G_{\pi\nu} A_0^\dagger A_0 - G_\nu A_{-1}^\dagger A_{-1}, \quad (18)$$

where  $\epsilon_j$  is the single particle energy of the  $j$ -orbit,  $G_\pi > 0$ ,  $G_\nu > 0$ , and  $G_{\pi\nu} > 0$  are proton-proton ( $pp$ ), neutron-neutron ( $nn$ ), and neutron-proton ( $np$ ) pairing interaction strengths, respectively,  $n_j = \sum_{mm_t} a_{jm,m_t}^\dagger a_{jm,m_t}$  is the valence nucleon number operator in the  $j$ -orbit, and  $a_{jm,m_t}^\dagger$  ( $a_{jm,m_t}$ ) is the creation (annihilation) operator for a valence nucleon in the state with angular momentum  $j$ , angular momentum projection  $m$ , and isospin projection  $m_t = 1/2, -1/2$ . When  $G_\pi = G_\nu = G_{\pi\nu} = G$ , the isospin is a good quantum number. In this isospin conserving-case, the Hamiltonian (18) is exactly solvable [18, 19]. Since neutron and proton single-particle energies in the  $j$ -orbit are the same, it is expected that  $G_\pi = G_\nu = G$  may be approximately satisfied, while, in general,  $G_{\pi\nu} \neq G$  and the Bethe ansatz method used in Ref. [18, 19] will no longer be useful. In such a case, the Hamiltonian (18) may be diagonalized in the  $O(5) \supset O_T(3) \otimes O_{\mathcal{N}}(2)$  basis [20–23]. For the sake of simplicity, in the following, we consider the degenerate case with  $\epsilon_j = \epsilon \forall j$  when the first term in Eq. (18) becomes a constant for a fixed number of nucleons  $n$ , and is neglected. Thus, the Hamiltonian can be expressed as

$$\hat{H}_P = -G \mathcal{A}^+ \cdot \mathcal{A}, \quad (19)$$

where  $G_\pi = G_\nu = G_{\pi\nu} = G$  is assumed. The Hamiltonian (19) is  $O_T(3)$  invariant and can be expressed as

$$\hat{H}_{O_T(3)} = \hat{H}_P = -G \mathcal{A}^+ \cdot \mathcal{A} = -\frac{1}{2}G \left( C_2(O(5)) - \hat{\mathcal{N}}(\hat{\mathcal{N}} - 3) - \mathbf{T} \cdot \mathbf{T} \right), \quad (20)$$

which is diagonal in the  $O(5) \supset O_T(3) \otimes O_{\mathcal{N}}(2)$  basis:

$$\begin{aligned} & \hat{H}_{O_T(3)} \left| \begin{matrix} (v_1, v_2) \\ \zeta T, M_T, \mathcal{N} \end{matrix} \right\rangle \\ &= -\frac{1}{2}G \left( v_1(v_1 + 3) + v_2(v_2 + 1) - \mathcal{N}(\mathcal{N} - 3) - T(T + 1) \right) \left| \begin{matrix} (v_1, v_2) \\ \zeta T, M_T, \mathcal{N} \end{matrix} \right\rangle. \end{aligned} \quad (21)$$

In this case, the labels of the  $O(5)$  irrep  $(v_1, v_2)$  are related to the seniority of nucleons  $v$  and the reduced isospin  $t$  with  $v_1 = \Omega - v/2$  and  $v_2 = t$ , where  $v$  and  $t$  indicate that there are  $v$  nucleons coupled to the isospin  $t$ , which are not included in the  $J = 0$  and  $T = 1$  pairs. One can also directly calculate matrix elements of  $\mathcal{A}^+ \cdot \mathcal{A}$  in the  $O(5) \supset O_T(3) \otimes O_{\mathcal{N}}(2)$  basis using the matrix elements of  $\mathcal{A}^+$  provided in the previous Section,

$$\left\langle \begin{matrix} (v_1, v_2) \\ \zeta T, M_T, \mathcal{N} \end{matrix} \left| \mathcal{A}^+ \cdot \mathcal{A} \right| \begin{matrix} (v_1, v_2) \\ \zeta T, M_T, \mathcal{N} \end{matrix} \right\rangle = \sum_{\zeta' T'} \left| \left\langle \begin{matrix} (v_1, v_2) \\ \zeta T, \mathcal{N} \end{matrix} \left\| \mathcal{A}^+ \right\| \begin{matrix} (v_1, v_2) \\ \zeta' T', \mathcal{N} - 1 \end{matrix} \right\rangle \right|^2, \quad (22)$$

where the relation (17) is used to check that the results shown in the previous Section are indeed valid.

Moreover, besides the  $O_T(3)$  isospin dynamical symmetry limit case shown above, there is the well known  $SU_\Lambda(2) \otimes SU_I(2)$  quasispin dynamical symmetry limit for any value of  $G_\pi$  and  $G_\nu$  when  $G_{\pi\nu} = 0$ , where  $\Lambda$  and  $I$  are the quasi-spin of the proton and neutron pairing, respectively. In this case, the pairing interaction part of Eq. (18)

$$\hat{H}_{SU_\Lambda(2) \otimes SU_I(2)} = -G_\pi A_{+1}^\dagger A_{+1} - G_\nu A_{-1}^\dagger A_{-1} \quad (23)$$

is diagonal in the  $O(5) \supset SU_\Lambda(2) \otimes SU_I(2)$  basis,

$$\begin{aligned} & \hat{H}_{SU_\Lambda(2) \otimes SU_I(2)} \left| \begin{array}{c} (v_1, v_2) \\ \Lambda, I \\ m_\Lambda, m_I \end{array} \right\rangle \\ &= \left( -G_\pi(\Lambda(\Lambda+1) - m_\Lambda(m_\Lambda+1)) - G_\nu(I(I+1) - m_I(m_I+1)) \right) \left| \begin{array}{c} (v_1, v_2) \\ \Lambda, I \\ m_\Lambda, m_I \end{array} \right\rangle, \quad (24) \end{aligned}$$

where  $\Lambda = (\Omega - v_\pi)/2$  and  $I = (\Omega - v_\nu)/2$  and  $v_\pi$  ( $v_\nu$ ) is the proton (neutron) seniority,  $m_\Lambda = n_\pi/2 - \Omega/2$ ,  $m_I = n_\nu/2 - \Omega/2$  and  $n_\pi$  ( $n_\nu$ ) is the number of valence protons (neutrons), which shows that the Hamiltonian (23) is still block diagonal with respect to the  $O(5)$  irrep labeled by  $(v_1, v_2)$ , though the interpretation of  $(v_1, v_2)$  in terms of  $v$  and  $t$  is no longer appropriate in this case due to the fact that the isospin symmetry is broken.

For other values of the pairing interaction strengths, the pairing interaction part of the Hamiltonian (18) can be only diagonalized in any basis of  $O(5)$  and the eigenstates may be expanded in terms of either the basis vectors of  $O(5) \supset O_T(3) \otimes O_N(2)$  or those of  $O(5) \supset SU_\Lambda(2) \otimes SU_I(2)$ . The parameter rectangle of the pure isovector pairing Hamiltonian is illustrated in Fig. 1, which shows that the pure isovector pairing Hamiltonian may be diagonalized in the  $O(5) \supset O_T(3) \otimes O_N(2)$  basis, except the  $G_{\pi\nu} = 0$  case indicated by the left leg of the rectangle with the  $SU_\Lambda(2) \otimes SU_I(2)$  quasispin dynamical symmetry.

## 5 Summary

In this talk, a simple and effective algebraic isospin projection procedure for constructing basis vectors of the irreducible representations of the non-canonical

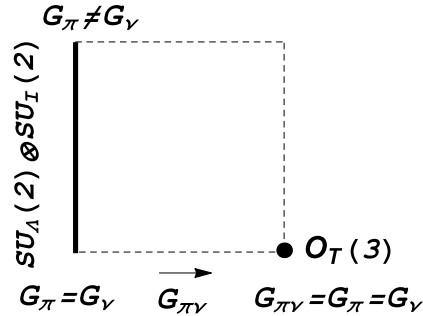


Figure 1: The parameter rectangle of the isovector pairing Hamiltonian, where the left leg marked by the solid line represents the Hamiltonian with arbitrary values of  $G_\pi$  and  $G_\nu$  and  $G_{\pi\nu} = 0$  corresponding to the  $SU_\Lambda(2) \otimes SU_I(2)$  quasispin dynamical symmetry, and the vertex marked by the solid dot represents the Hamiltonian with  $G_\pi = G_\nu = G_{\pi\nu}$  corresponding to the  $O_T(3)$  isospin dynamical symmetry. The Hamiltonian for other values of the parameters shown by the other area of the rectangle may be diagonalized in either the  $O(5) \supset SU_\Lambda(2) \otimes SU_I(2)$  or the  $O(5) \supset O_T(3) \otimes O_N(2)$  basis.

$O(5) \supset O_T(3) \otimes O_N(2)$  basis from those of the canonical  $O(5) \supset SU_\Lambda(2) \otimes SU_I(2)$  basis is presented. The main content of this talk is based on our recent work [24], where more detailed results are provided. It is shown that the expansion coefficients can be obtained as components of the null-space vectors of the projection matrix, where there are only four nonzero elements in each row in general. There are currently available well-optimized algorithms for computing the null-space vectors of a matrix, for example, the Wolfram Mathematica providing the null-space vectors which are orthonormalized. Hence, an evaluation of the expansion coefficients of the orthonormal basis vectors of  $O(5) \supset O_T(3) \otimes O_N(2)$  in terms of the basis of the canonical chain becomes straightforward. The advantage of this work lies in the fact that the basis vectors of  $O(5) \supset O_T(3) \otimes O_N(2)$  thus obtained are orthonormalized with respect to the  $O(5) \downarrow O_T(3) \otimes O_N(2)$  branching multiplicity label  $\zeta$  for any irrep of  $O(5)$ . Explicit formulae for evaluating  $O_T(3)$ -reduced matrix elements of  $O(5)$  generators are derived.

For the general non-degenerate case of the Hamiltonian (18) when there are  $p$  non-degenerate orbits, one needs to diagonalize the Hamiltonian in the  $\bigotimes_{i=1}^p O_i(5)$  subspace, where the matrix elements of the isovector pairing operators provided in this talk are useful. Thus, one can further analyze the isospin symmetry breaking effects in the Hamiltonian (18) with  $G_\pi \neq G_\nu \neq G_{\pi\nu}$  as was done for the specific cases in Refs. [20–23], which is also helpful for understanding the  $np$ -pairing effect in  $N \sim Z$  nuclei [25].

## Acknowledgments

Support from the National Natural Science Foundation of China (11675071 and 11375080), the U. S. National Science Foundation (OIA-1738287 and ACI-1713690), U. S. Department of Energy (DE-SC0005248), the Southeastern Universities Research Association, the China–U. S. Theory Institute for Physics with Exotic Nuclei (CUSTIPEN) (DE-SC0009971), and the LSU-LNNU joint research program (9961) is acknowledged.

## References

- [1] K. Helmers, Nucl. Phys. **23**, 594 (1961).
- [2] A. K. Kerman, Ann. Phys. **12**, 300 (1961).
- [3] M. Ichimura, Prog. Theor. Phys. **33**, 215 (1965).
- [4] J. N. Ginocchio, Nucl. Phys. **74**, 321 (1965).
- [5] K. T. Hecht, Phys. Rev. **139**, B794 (1965).
- [6] K. T. Hecht, Nucl. Phys. **63**, 214 (1965).
- [7] R. T. Sharp and S. C. Pieper, J. Math. Phys. **9**, 663 (1968).
- [8] N. Kemmer, D. L. Pursey and S. A. Williams, J. Math. Phys. **9**, 1224 (1968).
- [9] F. Pan, Chin. Phys. **11**, 870 (1991).

- [10] R. P. Hemenger and K. T. Hecht, Nucl. Phys. A **145**, 468 (1970).
- [11] K. Ahmed and R. T. Sharp, J. Math. Phys. **11**, 1112 (1970).
- [12] Yu F. Smirnov and V. N. Tolstoy, Rep. Math. Phys. **4**, 97 (1973).
- [13] S. Ališauskas, J. Phys. A **17**, 2899 (1984).
- [14] K. T. Hecht and J. P. Elliott, Nucl. Phys. A **438**, 29 (1985).
- [15] Q.-Z. Han, H.-Z. Sun and J.-J. Wang, Commun. Theor. Phys. **20**, 201 (1993).
- [16] M. A. Caprio, K. D. Sviratcheva and A. E. McCoy, J. Math. Phys. **51**, 093518 (2010).
- [17] M. A. Caprio, J. Phys. Conf. Ser. **237**, 012009 (2010).
- [18] F. Pan and J. P. Draayer, Phys. Rev. C **66**, 044314 (2002).
- [19] J. Dukelsky, V. G. Gueorguiev, P. Van Isacker, S. Dimitrova, B. Errea and S. Lerma H., Phys. Rev. Lett. **96**, 072503 (2006).
- [20] K. D. Sviratcheva, A. I. Georgieva and J. P. Draayer, J. Phys. G **29**, 1281 (2003).
- [21] K. D. Sviratcheva, A. I. Georgieva and J. P. Draayer, Phys. Rev. C **69**, 024313 (2004).
- [22] K. D. Sviratcheva, A. I. Georgieva and J. P. Draayer, Phys. Rev. C **70**, 064302 (2004).
- [23] K. D. Sviratcheva, J. P. Draayer and J. P. Vary, Phys. Rev. C **73**, 034324 (2006).
- [24] F. Pan, X. Ding, K. D. Launey and J. P. Draayer, Nucl. Phys. A **974**, 86 (2018).
- [25] S. Frauendorf and A. O. Macchiavelli, Prog. Part. Nucl. Phys. **78**, 24 (2014).

# Large-Scale Shell Model Calculations of Heavy Nuclei

Chong Qi

*Department of physics, KTH Royal institute of Technology, SE-10691, Stockholm*

## Abstract

In this contribution I describe briefly the application of the shell model configuration interaction approach to intermediate-mass and heavy nuclei at KTH. I focus in particular on the technical side of the development which enables us not only to perform large-scale full-configuration interaction calculations but also to solve efficiently the nuclear pairing Hamiltonian in a truncated space defined by seniority.

**Keywords:** *Nuclear shell model; truncation; pairing; collective motion*

## 1 Introduction

In the talk I present systematic calculations of the spectroscopy and transition properties of intermediate-mass and heavy nuclei around doubly magic  $^{100}\text{Sn}$  as well as around  $^{208}\text{Pb}$  by using the large-scale configuration interaction shell model approach with realistic interactions. Those nuclei are of interest to us partially due to the fact that they are the longest isotopic chains that can be studied by the nuclear shell model. We hope they can provide excellent background to study the competition of single-particle and two-body excitations. In particular, we studied the yrast spectra of Te isotopes which show a vibrational-like equally-spaced pattern but a few known  $E2$  transitions show anomalous rotational-like behaviour, which cannot be reproduced by collective models [1–6]. Moreover, the calculated  $B(E2)$  values for neutron-deficient and heavier Te isotopes show contrasting different behaviours along the yrast line. This may be related to the enhanced neutron-proton correlation when approaching  $N = 50$ . In general, the deviations between theory and experiment concerning the excitation energies and electromagnetic properties of low-lying  $0^+$  and  $2^+$  excited states and isomeric states may provide a constraint on our understanding of nuclear interaction and a hint on possible quantum phase transition. We have measured the lifetimes of the first excited  $2^+$  and  $4^+$  states in the neutron-deficient nuclide  $^{172}\text{Pt}$  [7]. We have also done several large-scale shell model calculations with realistic nucleon-nucleon interactions for Pt, Os and W isotopes between  $N = 82$  and  $94$  by considering either  $^{132}\text{Sn}$  or  $^{146}\text{Gd}$  as the inert cores. A striking feature we found is that the ratio  $B(E2; 4_1^+ \rightarrow 2_1^+)/B(E2; 2_1^+ \rightarrow g.s.) = 0.55(19)$  is unusually low. In

---

*Proceedings of the International Conference ‘Nuclear Theory in the Supercomputing Era — 2018’ (NTSE-2018), Daejeon, South Korea, October 29 – November 2, 2018, eds. A. M. Shirokov and A. I. Mazur. Pacific National University, Khabarovsk, Russia, 2019, p. 83.*

<http://www.ntse.khb.ru/files/uploads/2018/proceedings/Qi.pdf>.

addition, a few other neutron-deficient W, Os, and Pt nuclei in this region feature the same effect [8].

In this talk I also illustrate the application of the importance-truncation approach, which is based on the monopole Hamiltonian, to neutron deficient Pb isotopes [9]. For those nuclei, the full shell-model results also agree well with our generalized seniority and nucleon-pair-approximation truncation calculations. We have developed an angular momentum projection technique to derive the analytic wave functions and energy expressions for those states in the simplified single- $j$  case [10].

In this Proceeding, I would like to focus on some technical details of our efforts at KTH, Stockholm in developing the shell model algorithm and its possible various applications. In addition to large-scale full and truncated configuration interaction calculations, one of our primary interests is to apply the model to solve the pairing Hamiltonian in large model space efficiently.

## 2 Shell model approach

The shell model we refer to, deals with residual interaction between valence particles around the Fermi surface, which is mostly supposed to be of a two-body nature. The effective Hamiltonians in terms of single-particle energies and two-body matrix elements can be written as follows,

$$H_{eff} = \sum_{\alpha} \varepsilon_{\alpha} \hat{N}_{\alpha} + \frac{1}{4} \sum_{\alpha\beta\delta\gamma JT} \langle \alpha\beta | V | \gamma\delta \rangle_{JT} A_{JT;\alpha\beta}^{\dagger} A_{JT;\delta\gamma}, \quad (1)$$

where we assume that the effective Hamiltonian conserves isospin symmetry,  $\alpha = \{nljt\}$  denotes the single-particle orbitals and  $\varepsilon_{\alpha}$  stands for the corresponding single-particle energies.  $\hat{N}_{\alpha} = \sum_{j_z, t_z} a_{\alpha, j_z, t_z}^{\dagger} a_{\alpha, j_z, t_z}$  is the particle number operator.  $\langle \alpha\beta | V | \gamma\delta \rangle_{JT}$  are the two-body matrix elements coupled to spin  $J$  and isospin  $T$ .  $A_{JT}$  ( $A_{JT}^{\dagger}$ ) is the fermion pair annihilation (creation) operator.

The pairing matrix elements refer to those with  $J = 0$  and  $\alpha$  and  $\beta$  (as well as  $\delta$  and  $\gamma$ ) corresponding to time reversal orbitals. One has

$$H_P = \sum_{\alpha} \varepsilon_{\alpha} \hat{N}_{\alpha} + \frac{1}{4} \sum_{\alpha\bar{\alpha}\gamma\bar{\gamma}T} \langle \alpha\bar{\alpha} | V | \gamma\bar{\gamma} \rangle_{J=0T} A_{JT;\alpha\bar{\alpha}}^{\dagger} A_{JT;\gamma\bar{\gamma}}. \quad (2)$$

In most mean field approaches, usually the proton-proton and neutron-neutron pairing are considered only. The neutron and proton pair can couple to both  $T = 1$  (isovector) and  $T = 0$  (isoscalar). The importance of neutron-proton correlation may also become important in  $N \sim Z$  nuclei. In relation to that, there is a long-standing quest for a possible existence of the  $np$  pairing in  $N \sim Z$  nuclei (see recent discussions in Refs. [11–15]).

The monopole Hamiltonian determines average energy of eigenstates in a given configuration. The monopole interaction itself does not induce any mixture between different configurations, however it can change significantly the (effective) mean field and drive the evolution of the shell structure. The monopole interaction  $V_m$  is the angular momentum averaged effects of the two-body interaction,

$$V_{m,\alpha\beta} = \frac{\sum_J (2J+1) V_{\alpha\beta\alpha\beta}^J}{\sum_J (2J+1) [1 - \delta_{\alpha\beta} (-1)^J]} = \frac{\sum_J (2J+1) V_{\alpha\beta\alpha\beta}^J}{(2j_{\alpha} + 1)} \frac{1 + \delta_{\alpha\beta}}{2j_{\beta} + 1 - \delta_{\alpha\beta}}. \quad (3)$$

The strong mixture of the wave function is mainly induced by the residual  $J = 0$  pairing and the  $QQ$  neutron-proton interaction in the multipole Hamiltonian. However, a tricky issue one often get confused is that the diagonal matrix elements of the pairing Hamiltonian (with  $\alpha = \gamma$ ) also contribute significantly to the monopole interaction.

The number of orbitals one can include is strongly restricted due to the computational limitation. Extensive studies of the algorithm optimizations and possible truncation or approximation methods have been carried out. State-of-the-art configuration interaction algorithms are able to diagonalize matrices with dimensions up to  $2 \times 10^{10}$  with the shell model codes like KSHELL and Redstick. Truncations often have to be applied in order to reduce the sizes of the shell-model bases. The simplest way of the truncation is to restrict the maximal/minimal numbers of particles in different orbitals. This method is applied to both the no-core (often being referred to as  $N_{\max}$ ) and empirical shell model ( $np-nh$ ) calculations. We studied in Ref. [1] the structure and electromagnetic transition properties of light Sn isotopes within the large  $gds_{11/2}$  model space by restricting to four the maximal number of neutrons that can be excited out of the  $g_{9/2}$  orbital. However, the convergence can be very slow if there is no clear shell or subshell closure or if the single-particle structure is significantly modified by the monopole interaction, as it happens in neutron-rich light nuclei (see, e. g., Ref. [16]).

One can evaluate the importance of a given basis vector  $\psi_i$  within a partition through the perturbation measure  $R_i = |\langle \psi_i | H_{eff} | \psi_c \rangle| / (\epsilon_i - \epsilon_c)$  where  $\psi_c$  is the chosen reference state with the unperturbed energy  $\epsilon_c$ . It is expected that the basis vectors with larger  $R_i$  should play larger role in the given state dominated by the reference basis state  $\psi_c$  used to define the truncation scheme. The off-diagonal matrix elements  $\langle \psi_i | H_{eff} | \psi_c \rangle$  are relatively weak in comparison to the diagonal ones. The most important configurations may be selected by considering the unperturbed energy difference  $r_i = \epsilon_i - \epsilon_c$ . A truncated model space can thus be defined by taking the vectors with smallest  $r_i$ . The challenge here is that the truncated bases may not conserve angular momentum. An angular momentum conserved correlated basis truncation approach was introduced in Ref. [17]. We are implementing this method in the widely distributed shell-model code NuShellX by replacing its projection subroutine with our new correlated basis method.

An importance truncation can be introduced based on the total monopole energy by considering the multipole Hamiltonian as a perturbation. The idea behind is again that the Hamiltonian is dominated by the diagonal monopole channel. One can evaluate the total monopole energy of a given partition  $\mathcal{P}$  as

$$E_{\mathcal{P}}^m = \sum_{\alpha} \varepsilon_{\alpha} N_{\mathcal{P};\alpha} + \sum_{\alpha \leq \beta} V_{m;\alpha\beta} \frac{N_{\mathcal{P};\alpha} (N_{\mathcal{P};\beta} - \delta_{\alpha\beta})}{1 + \delta_{\alpha\beta}}, \quad (4)$$

where  $N_{\mathcal{P};\alpha}$  denotes the particle distributions within a given partition  $\mathcal{P}$ . One can order all partitions according to the monopole energy  $E_{\mathcal{P}}^m$  and consider the lowest ones for a given truncation calculation. Moreover, it is expected that the pairing correlation should play a significant role governing the structure of the lowest-lying states of the semi-magic Pb isotopes. This model was applied in our calculations of Pb isotopes [9]. Convergence is mostly achieved at  $d/D \sim 0.1$ , i. e., by considering only 10% of the total M-scheme bases. This method is very easy to implement and it preserves the simplicity of the M-scheme algorithm.

We have also done pair-truncated shell-model calculations with collective pairs as building blocks in Refs. [9, 14, 18] for both the standard shell model and continuum shell model in the complex energy plane.

### 3 Exact diagonalization of pairing Hamiltonian

The pairing Hamiltonian is usually solved using the simple BCS or the HFB approach which both violate the conservation of the number of particles. Particle-number-conserved pairing calculations can be done within the Richardson approach (see, e.g., Ref. [19]) or utilizing the exact diagonalization in a way similar to the shell model [16, 20]. The Richardson approach can be applied to very large (infinite) systems but is limited to Hamiltonians of a certain form. On the other hand, the exact diagonalization can be done for a general Hamiltonian but the number of orbitals one can include is limited. This limitation makes it difficult to perform realistic calculations and to compare the results with those from the BCS or similar approaches. In addition, it limits the application of the model to the  $\alpha$  decay or pair transfer reaction calculations. This is one of the challenges we have been trying to resolve in the past few years. We have developed a very efficient and robust solver for the Richardson equation which will be publicly available soon. We have also developed two large-scale exact diagonalizers: one is based on our large-scale shell model code and parallelized using MPI + OpenMP hybrid algorithm; the other one uses only OpenMP parallelization which can be easily combined with existing mean field codes to replace the problematic BCS solver.

We have developed a seniority truncation approach for the M-scheme shell model algorithms. For systems comprising the particles of the same kind, the low-lying states can be well described within the seniority scheme. This is related to the fact that the  $T = 1$  two-body matrix elements are dominated by the  $J = 0$  pairing interactions. The seniority is related to the number of particles that are not paired to  $J = 0$ . The seniority coupling has shown a remarkable success in describing the spectroscopy and electromagnetic transition properties of semi-magic nuclei with spherical symmetry. Our recent studies on the seniority coupling scheme may be found in Refs. [21–26]. The standard seniority coupling cannot be utilized within the M-scheme shell model code where the angular momentum conservation is not considered at the basis vector level. On the other hand, we can define a seniority-like M-scheme pair. We set this ‘seniority’ to zero if all particle pairs can be coupled to  $M = 0$  that is all orbitals have their time reversal partners. The seniority in our M-scheme refers then to the number of particles that have no time reversal partners.

One can derive the exact solution of the pairing Hamiltonian by diagonalizing the matrix spanned by the seniority  $v = 0$ , spin  $I = 0$  states which represent only a tiny part of the total wave function. Our second code is designed in such a way that it works only in the  $v = 0$  or low seniority cases but in a very simple and efficient way. If only the seniority  $v = 0$  states are considered, there is ONLY one basis vector for each shell model partition. This allows us to generate the  $v = 0$  basis in a way similar to the M-scheme shell model. We take one time reversal orbital pair as one binary bit which is represented as ‘1’ if the orbital is occupied. So, the combination problem of generating all possible M-scheme vectors with a fixed number of identical pairs  $N$  in  $M$  time reversal states is equal to generating binary integers consisting of the same  $N$  number of digit ‘1’ and  $M - N$  number of digit ‘0’. As an example,

for three pairs in six doubly degenerate orbitals, an obvious basis would be ‘000111’ which is easy to generate and which has the minimum value. The basis with maximum value can also be generated simply. Then we have a two-step mechanism to generate the rest basis vectors: For an input binary integer, first, find the first two adjacent bits with the binary pattern ‘01’ and turn them to ‘10’; second, move all digit ‘1’ on the lower side of the turned ‘10’ to the lowermost. The next larger integer is then generated. The iteration should start from the minimum as input and be stopped when the output is equal to the maximum.

We take again the above system as an example: the two-step mechanism starts from the vector 000111 with the minimum value; the first ‘01’ appears at the third bit, we turn ‘01’ to ‘10’ and ‘000111’ is turned to ‘001011’; since all digit ‘1’ is on the lowermost, the output is ‘001011’. From this basis, we can generate ‘001101’ and ‘001110’. For the basis ‘001110’, we flip the first ‘01’ which changes the basis to ‘010110’. However, on the lower side of the fourth bit, there are two digits ‘1’ at the second and the third bit which should be moved to the lowermost, so the final output is ‘010011’. This simple mechanism allows us to generate a large-scale basis in a very efficient manner which was actually a bottleneck for us before.

A remarkable feature is that the algorithm works also in the case of degenerate systems which allow more than one pair in a single orbital. In such situations, we at first represent an orbital with degeneracy  $D$  as  $D/2$  continuous bits. One can, of course, generate the basis in the same way as above. We have a complete M-scheme basis for which the solution will be eigenstates of the spherical pairing Hamiltonian. However, one should bear in mind that the dimension of such a M-scheme-like basis set can be orders of magnitude larger than the J-scheme-like seniority-zero basis which makes the calculations much less efficient.

To overcome this problem, we label the bits from the same degenerate orbital as a subgroup. Inside each subgroup, since all particles are indistinguishable, we just need one vector to represent different combination of bits, and the easiest choice is to put all digit ‘1’ on the lowermost side. For example, ‘000111’ can represent uniquely the vector for a system with three pairs in a 12-fold orbital. All the rest will be neglected. In other words, we will do not flip the ‘01’ within a given subgroup.

The basis vectors generated with the above algorithm are ordered accordingly to their values. This also allows us to identify the non-zero Hamiltonian matrix elements in an efficient way. For a given vector  $|\phi_i\rangle$  we first generate a subbasis set from the operation  $\phi_j = H|\phi_i\rangle$ . The indices of the subbasis  $\phi_j$  can be determined then by matching their values with those from the original basis set using standard searching algorithms. It can be quite efficient since the basis vectors are ordered.

With the code described above, one can readily solve a half-filled system with up to 36–38 doubly-degenerate orbitals and 18–19 pairs (with dimensions  $9 \times 10^9 - 3.5 \times 10^{10}$ ). The corresponding shell-model space dimensions are around  $4 \times 10^{20} - 7 \times 10^{21}$ ) which is a problem formidable to solve.

The code works efficiently on PC, and now we are combing the code with publicly available Hartree–Fock (HF) mean field codes for realistic calculations. One of our concerns is the contribution of the pairing matrix elements to the monopole energy.

Let us consider a simple system with  $N$  pairs of identical particles in a single- $j$  shell. The total energy can be obtained as

$$E = N(N - 1)G - N\Omega G, \quad (5)$$

where  $G$  is the pair coupling constant and  $\Omega = j + 1/2$ . The first linear term on the right hand side corresponds to the contribution of the pairing to the monopole channel or the mean field, and the second term defines the pairing correlation energy

$$E_{\text{corr}} = N(N - \Omega)G. \quad (6)$$

This aspect looks simple but should be properly taken into account when the pairing Hamiltonian is solved exactly to evaluate the pairing correlation or to be compared with the BCS approach. For a system involving equally-spaced doubly-degenerate orbitals, we showed that the total energy can be also rather well approximated as [20]

$$E(N) \simeq N(N - 1)\mathcal{G} + NE_2, \quad (7)$$

where  $\mathcal{G}$  is a coefficient related to the pairing strength and level density. One has

$$\begin{aligned} E_{\text{corr}}(N) &\simeq N(N - 1)\mathcal{G} + NE_2 - N(N + 1) + NG \\ &= N(N - 1)(\mathcal{G} - 1) + N(E_2 - 2 + G), \end{aligned} \quad (8)$$

where the first and the second terms define the Pauli blocking effect and the correlation energy of a single pair, respectively.

As discussed above, the diagonal channel of the full pairing Hamiltonian contributes significantly to the total binding energy, which may result in an over-counting problem and has to be removed from the exact solution of the pairing Hamiltonian in the mean field applications. In some cases, the diagonal matrix elements are removed in analogy to the BCS approach, and the following Hamiltonian is diagonalized,

$$H' = \sum_{\alpha} \varepsilon \hat{n}_{\alpha} - \sum_{\alpha \neq \beta} G_{\alpha\beta} a_{\alpha}^{\dagger} a_{\bar{\alpha}}^{\dagger} a_{\beta} a_{\bar{\beta}}, \quad (9)$$

where  $\alpha$  runs again over the time-reversal orbits with quantum numbers  $j_{\alpha}$  and  $|m_{\alpha}|$  within the HF configuration. In this way one excludes the renormalization effect of the single-particle energy from the diagonal pairing matrix elements. The disadvantage is that the rotational symmetry is not conserved at the two-body level.

The *de facto* standard approach to extract the correlation energy is to take the difference between the total energy  $E$  and the energy of the lowest, unperturbed HF configuration as

$$E_{\text{corr}} = E - E_{HF}, \quad (10)$$

where  $E_{\text{corr}}$  is the (negative) correlation energy and  $E_{HF}$  is the HF energy which provides the upper bound for the total energy and is the starting point for various post-HF calculations of the correlation. One can define in a straightforward way the correlation energy as

$$E_{\text{corr}}^{(1)} = E_{gs} - \sum_{\alpha} [2\varepsilon_{\alpha} - G_{\alpha\alpha}], \quad (11)$$

where  $E_{gs}$  is the lowest energy.  $G_{\alpha\alpha}$  are the corresponding diagonal matrix elements.

Now we introduce a different definition for the correlation energy based properly on the definition of the monopole interaction. If only the pairing interaction is considered for the particle-particle channel, we have  $V_{jjjj}^{J=0} = -\Omega_j G_{jj}$  and  $V_{jj} = -G_{jj}/2j$ . Thus one can define an alternate way to calculate the correlation energy as

$$E_{\text{corr}}^{(2)} = E - \sum_{j \in HF} \left[ n_j \varepsilon_j - \frac{G_{jj}}{2j} \frac{n_j(n_j - 1)}{2} \right], \quad (12)$$

where  $j$  runs over all single- $j$  levels within the HF configuration.

$E_{\text{corr}}^{(1)}$  and  $E_{\text{corr}}^{(2)}$  would be identical if all single-particle levels within the HF configuration are fully occupied. However, it should be emphasized that  $E_{\text{corr}}^{(2)}$  gives a stronger (negative) correlation energy than  $E_{\text{corr}}^{(1)}$  if the last orbital is only partially occupied (with  $N = 1$  to  $\Omega - 1$  pairs). The deviation is

$$E_{\text{corr}}^{(2)} - E_{\text{corr}}^{(1)} = -N_k(\Omega_k - N_k) \frac{G_{kk}}{\Omega_k - 1/2}, \quad (13)$$

where  $k$  corresponds to the last occupied orbital and  $N_k(\Omega_k - N_k) = (\Omega_k u_k v_k)^2$ . This deviation is related to the fundamental difference between the coupling of particles in the two schemes: The particles are constrained to pair to zero angular momentum with its time reversed partner in the former case but there is no such constraint in the second case. This is the reason why  $E_{\text{corr}}^{(2)}$  predicts more correlation energy than the first case. With the pairing correlation energy thus defined, we can perform now a systematic study of nuclear masses.

## 4 Summary

In this talk, I presented our recent works on the configuration-interaction shell-model calculations of the spectroscopy and transition properties of intermediate-mass and heavy nuclei. In this contribution to the Proceedings, I started by introducing the basic framework of the nuclear shell model and of the monopole channel of the effective Hamiltonian. A simple truncation scheme can be established by considering configurations with the lowest monopole energies, which I refer to as the importance-truncation approach. A seniority-like truncation has also been introduced, which allows to apply the large-scale shell model algorithm to the problem of solving the standard pairing Hamiltonians. We introduced a simple but efficient way to generate the basis for the paired states and for calculating the non-zero Hamiltonian matrix elements. We also discussed different ways to exclude the pairing contribution to the monopole interaction in order to utilize our thus developed exact pairing solver in realistic mean field calculations.

## Acknowledgement

This work is supported by the Swedish Research Council (VR) under grants Nos. 621-2012-3805 and 621-2013-4323 and by the Göran Gustafsson foundation. Computational support provided by the Swedish National Infrastructure for Computing (SNIC) at PDC, KTH, Stockholm is acknowledged.

## References

- [1] T. Back, C. Qi, B. Cederwall, R. Liotta, F. G. Moradi, A. Johnson, R. Wyss and R. Wadsworth, *Phys. Rev. C* **87**, 031306 (2013).
- [2] O. Möller, N. Warr, J. Jolie, A. Dewald, A. Fitzler, A. Linnemann, K. O. Zell, P. E. Garrett and S. W. Yates, *Phys. Rev. C* **71**, 064324 (2005).

- 
- [3] M. Saxena *et al.*, Phys. Rev. C **90**, 024316 (2014).
  - [4] C. Qi, Phys. Rev. C **94**, 034310 (2016).
  - [5] M. Doncel *et al.*, Phys. Rev. C **96**, 051304 (2017).
  - [6] M. Doncel *et al.*, Phys. Rev. C **95**, 044321 (2017).
  - [7] B. Cederwall *et al.*, Phys. Rev. Lett., **121**, 022502 (2018).
  - [8] T. Grahn *et al.*, Phys. Rev. C **94**, 044327 (2016).
  - [9] C. Qi, L. Y. Jia and G. J. Fu, Phys. Rev. C **94**, 014312 (2016).
  - [10] Y. Qian and C. Qi, Phys. Rev. C **98**, 061303 (2018).
  - [11] B. Cederwall *et al.*, Nature **469**, 68 (2011).
  - [12] S. Frauendorf and A. O. Macchiavelli, Prog. Part. Nucl. Phys. **78**, 24 (2014).
  - [13] C. Qi, J. Blomqvist, T. Bäck, B. Cederwall, A. Johnson, R. J. Liotta and R. Wyss, Phys. Rev. C **84**, 021301 (2011).
  - [14] Z. X. Xu, C. Qi, J. Blomqvist, R. J. Liotta and R. Wyss, Nucl. Phys. A **77**, 51 (2012).
  - [15] C. Qi and R. Wyss, Phys. Scr. **91**, 013009 (2016).
  - [16] Z. X. Xu and C. Qi, Phys. Lett. B **724**, 247 (2013).
  - [17] L. F. Jiao, Z. H. Sun, Z. X. Xu, F. R. Xu and C. Qi, Phys. Rev. C **90**, 024306 (2014).
  - [18] H. Jiang, C. Qi, Y. Lei, R. Liotta, R. Wyss and Y. M. Zhao, Phys. Rev. C **88**, 044332 (2013).
  - [19] C. Qi and T. Chen, Phys. Rev. C **92**, 051304 (2015).
  - [20] S. Changizi, C. Qi and R. Wyss, Nucl. Phys. A **940**, 210 (2015).
  - [21] C. Qi, X. B. Wang, Z. X. Xu, R. J. Liotta, R. Wyss and F. R. Xu, Phys. Rev. C **82**, 014304 (2010).
  - [22] C. Qi, Phys. Rev. C **83**, 014307 (2011).
  - [23] C. Qi, Z. X. Xu and R. J. Liotta, Nucl. Phys. A **884**, 21 (2012).
  - [24] C. Qi, Phys. Lett. B **717**, 436 (2012).
  - [25] C. Qi, Phys. Lett. B **773**, 619 (2017).
  - [26] L. Y. Jia and C. Qi, Phys. Rev. C **94**, 044312 (2016).

# Modeling Fission Dynamics with Leadership Class Computing Capabilities

I. Stetcu<sup>a</sup>, A. Bulgac<sup>b</sup>, S. Jin<sup>b</sup>, K. J. Roche<sup>b,c</sup> and N. Schunk<sup>d</sup>

<sup>a</sup>*Los Alamos National Laboratory, Los Alamos, New Mexico, 87545, USA*

<sup>b</sup>*University of Washington, Seattle, Washington 98195-1560, USA*

<sup>c</sup>*Pacific Northwest National Laboratory, Richland, Washington 99352, USA*

<sup>d</sup>*Lawrence Livermore National Laboratory, Livermore, California 94551, USA*

## Abstract

In this contribution, we present a snapshot of recent progress in the microscopic description of low-energy nuclear fission using the time-dependent density functional theory approach, made possible by the latest advances in computational infrastructure. Independent of the choice of the nuclear energy density functional, our investigations show that the collective motion is highly dissipative, with little trace of inertial dynamics, due to the one-dissipation mechanism alone. This finding justifies the validity of using the overdamped collective motion approach. We also briefly discuss the inclusion, in a quantum-mechanical unitary approach, of fluctuations and dissipation. These two components are indispensable to the description of observed distributions (e. g., mass, charge, total kinetic energy). Thus, as the next generation leadership-class computers are being deployed, the fully microscopical description of fission observables and their distributions is within reach.

**Keywords:** *Fission; density functional theory*

## 1 Introduction

Two major developments in theory and computational resources created the favorable conditions for achieving a microscopic description of nuclear fission almost eighty years after its discovery in 1939 by Hahn and Strassmann [1]. The density functional theory (DFT) provides the only microscopic framework suitable for description of heavy nuclei and feasible on today's computers. Instead of computing the full many-body wave function, one can determine only the one-body density within the DFT, the highly successful approach pioneered by Kohn, Hohenberg and Sham [2, 3] for many-electron systems in chemistry and condensed matter physics. Within the extension to time-dependent DFT [4–6], the fission dynamics becomes computationally manageable and, hence, a microscopic description feasible. To study quantum dynamics, we implemented on leadership class computers the real-time DFT extension, explicitly including the dynamics of the crucial pairing correlations [6]. At the moment, we are concentrating on obtaining average properties of fission fragments (FFs)

---

*Proceedings of the International Conference 'Nuclear Theory in the Supercomputing Era — 2018' (NTSE-2018), Daejeon, South Korea, October 29 – November 2, 2018, eds. A. M. Shirokov and A. I. Mazur. Pacific National University, Khabarovsk, Russia, 2019, p. 91.*

<http://www.ntse.khb.ru/files/uploads/2018/proceedings/Stetcu.pdf>.

produced during the process, before neutron, gamma and beta emissions, with a plan to describe distributions of relevant observables in the near future. The broad goals of our investigations are to provide a microscopic understanding of the fission process, and to help guide other models used in applications.

In practical applications ranging from energy production to global security, understanding and accurately predicting the distribution of prompt neutron and gamma observables is essential. Hence, phenomenological codes, like FREYA [7] at Livermore and CGMF [8, 9] at Los Alamos, have been developed. In such approaches, the fission fragments are treated as compound nuclei, whose de-excitation via neutron and gamma emission can be modeled using Weisskopf [10] or Hauser–Feshbach [11] formalisms. Input into these models usually comes from direct experimental data, like measured mass, charge and total kinetic energy distributions. However, for other important input quantities, only indirect information can be extracted. For example, if one can compute the total excitation energy available in FFs from the energy balance of the reaction, an additional information on the number of neutrons emitted as a function of the FF mass has been used in order to parameterize the total energy sharing between FFs. This type of data is available for a limited number of reactions, usually spontaneous fission of select actinides and fission induced by thermal neutrons. Much fewer data are available at higher incident neutron energies, although the existing data [12] illustrates an interesting property: the entire additional excitation energy brought by the neutron is stored in the heavy fragment. Current modeling capabilities do not take this feature into account given the lack of experimental data necessary to parameterize the energy dependence.

The FF spin distributions are important in the description of prompt gamma properties. A direct measurement of the angular momenta cannot be performed, but model-dependent attempts to extract average values have been made in the past from other fission observables like isomer production ratios [13, 14], gamma-ray de-excitation feeding patterns of the ground-state bands [15] and angular anisotropy of prompt-fission gamma rays [16]. The information such experiments provide is sparse, often limited to even-even isotopes. In addition, even for a simple case of thermal neutron capture, the simulations do not produce an excellent agreement with experimental data [17].

Existing theoretical models of fission based on random-walks on an energy surface [18], Langevin approach with fluctuations and dissipation [19], or more microscopic approaches like DFT + time-dependent generator coordinator method [20] do not produce fully separated FFs and can be plagued by the adiabatic approximation, which inherently produces “cold” fragments. Our time-dependent superfluid local density approximation (TD-SLDA) is the only framework in which the FFs can be fully separated, and an important information (e. g., the energy sharing or FF spins) could be extracted. Such simulations require significant computational resources, but can be also useful in providing microscopic support for existing theoretical approaches to fission, that can be more practical in the sense of requiring limited computational power.

In this contribution, we review our previous investigations of the fission of the  $^{240}\text{Pu}$  nucleus. Since the TD-SLDA can only provide average quantities, we briefly discuss introducing fluctuations and dissipations in the evolution, so that the full distributions can be calculated in the near future.

## 2 Theoretical framework

In mean-field theories, the ground state of a quantum system is described by a single Slater determinant, constructed from particle states for closed-shell nuclei or quasiparticle states for open-shell nuclei. Densities and current densities are computed from this single Slater determinant, and the ground state energy is computed by minimizing a density energy functional, which is formally equivalent to solving the self-consistent Hartree–Fock–Bogoliubov or Bogoliubov–de Gennes equations for the (quasi-)particle wave functions:

$$\begin{pmatrix} h_{\uparrow\uparrow} - \mu & h_{\uparrow\downarrow} & 0 & \Delta \\ h_{\downarrow\uparrow} & h_{\downarrow\downarrow} - \mu & -\Delta & 0 \\ 0 & -\Delta^* & -(h_{\uparrow\uparrow}^* - \mu) & -h_{\uparrow\downarrow}^* \\ \Delta^* & 0 & -h_{\downarrow\uparrow}^* & -(h_{\downarrow\downarrow}^* - \mu) \end{pmatrix} \begin{pmatrix} u_{k\uparrow} \\ u_{k\downarrow} \\ v_{k\uparrow} \\ v_{k\downarrow} \end{pmatrix} = E_k \begin{pmatrix} u_{k\uparrow} \\ u_{k\downarrow} \\ v_{k\uparrow} \\ v_{k\downarrow} \end{pmatrix}, \quad (1)$$

where  $u_{k\uparrow(\downarrow)}$  and  $v_{k\uparrow(\downarrow)}$  are the up (down) components of the quasiparticle wave functions (qpwfs), with the dependence on the spacial coordinates not shown explicitly,  $E_k$  is the corresponding quasiparticle energy, and  $\mu$  is the chemical potential needed to impose a constraint on the desired number of particles. The one-body Hamiltonian  $h$  is a function of the densities and current densities and can include external fields (and, in particular, additional constraints). The superfluid local density approximation (SLDA) reduces Eq. (1) to the usual Hartree–Fock equations when the pairing field is zero (the so-called normal systems). In the case of nuclear systems, two different coupled equations, one for protons and one for neutrons, need to be solved.

The dynamics is obtained by following in time the evolution of the qpwfs by solving the time-dependent Schrödinger-like equations,

$$i\hbar \frac{\partial}{\partial t} \begin{pmatrix} u_{k\uparrow} \\ u_{k\downarrow} \\ v_{k\uparrow} \\ v_{k\downarrow} \end{pmatrix} = \begin{pmatrix} h_{\uparrow\uparrow} - \mu & h_{\uparrow\downarrow} & 0 & \Delta \\ h_{\downarrow\uparrow} & h_{\downarrow\downarrow} - \mu & -\Delta & 0 \\ 0 & -\Delta^* & -(h_{\uparrow\uparrow}^* - \mu) & -h_{\uparrow\downarrow}^* \\ \Delta^* & 0 & -h_{\downarrow\uparrow}^* & -(h_{\downarrow\downarrow}^* - \mu) \end{pmatrix} \begin{pmatrix} u_{k\uparrow} \\ u_{k\downarrow} \\ v_{k\uparrow} \\ v_{k\downarrow} \end{pmatrix}, \quad (2)$$

where, for simplicity, in addition to the spatial coordinate  $\vec{r}$ , we have also suppressed the time coordinate  $t$ . At each time  $t$ , the one-body Hamiltonian and the pairing field depend on the densities and currents constructed from the qpwfs at the same time  $t$ .

The TD-SLDA can treat both linear response (equivalent to QRPA) and large amplitude collective motion (e. g., fission). However, during the time evolution, the underlying solutions are single Slater determinants, even in the case of fission shown in Fig. 1, when two fragments are formed. In DFT, in general, densities are the quantities of interest and not the many-body wave functions.

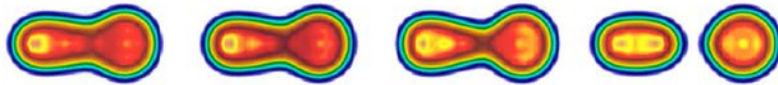


Figure 1: Evolution from a compact configuration to one where the two fragments are fully separated.

### 3 Numerical details

In our implementation, both the SLDA and TD-SLDA equations (1) and (2) are discretized on rectangular lattices, the former providing initial conditions for the latter. While the dimensions of the matrices involved are very large, this discretization allows us to obtain solutions without any symmetry restrictions (arbitrary deformations) and to describe accurately the continuum components of the qpwfs.

Less demanding numerical methods that allow the extraction of densities and currents without the full diagonalization of Eq. (1) exist. We have implemented one such method efficiently on GPU machines [21]. However, in order to start the time evolution, the full initial eigenvector is required at  $t = 0$ . Therefore, the initial qpwfs are obtained by a full diagonalization of the HFB matrix, using the package SCALapack. Assuming  $N_x$ ,  $N_y$  and  $N_z$  lattice points in  $x$ ,  $y$  and  $z$  directions respectively, the basis states used to diagonalize the full HFB matrix are given generically by

$$\Phi_{i_x, i_y, i_z}(\vec{r}) = \phi_{i_x}(x) \phi_{i_y}(y) \phi_{i_z}(z), \quad (3)$$

where

$$\phi_{i_x}(x) = \frac{1}{N} \exp\left(-\frac{i\pi(x - x_{i_x})}{dx}\right) \frac{\sin \frac{\pi(x - x_{i_x})}{dx}}{\sin \frac{\pi(x - x_{i_x})}{N_x dx}}, \quad (4)$$

with  $dx$  being the lattice constant in  $x$  direction and  $i_x = 0, \dots, N_x - 1$  is the location on the lattice, and similarly for the  $y$  and  $z$  directions. Each component is expanded using the basis states (3), so that the total dimension is  $4N_x N_y N_z$ . The matrix elements of all operators can be analytically calculated in this basis. Because of the spin-orbit contribution, the matrix in Eq. (1) is complex Hermitian. Note that the phase factor included in Eq. (4) is necessary to ensure compatibility with the fast Fourier transforms computed with the FFTW package (on CPUs or its cuda implementation). This discrete variable representation basis is optimal for numerically representing wave functions in nuclear physics [22], and SLDA in particular.

The time evolution of the nuclear system formally represented by Eq. (2) is simulated using the fifth order Adams–Bashford–Milne numerical method [23]. This approach reduces the number of applications of the Hamiltonian at each time step to only two, although the errors are of the order  $\mathcal{O}(\Delta t^5)$ , where  $\Delta t$  is the numerical integration step in time. The derivatives are efficiently calculated via Fourier transforms, using GPU accelerators. It is well known that on systems with GPUs, the bottleneck could be the need to transfer often large amounts of data between CPUs and GPUs. We minimize the amount of data exchanged by only transferring the densities for reduction over CPUs using MPI calls. This ensures almost perfect weak and strong scaling properties. At this moment, the bottleneck for the time-dependent code is only restricted by the communications between MPI processes. We will publish a more detailed analysis of the scaling properties of the code in an upcoming manuscript, which will accompany the release of both the static and dynamic codes as open sources. The advantage brought by GPU acceleration is remarkable, providing a speedup factor of 9.4x with respect to the CPU version only of the code, when the two are compared on the same number of processors. The CPU and hybrid CPU+GPU versions of the codes have the same design, the only difference being the use of GPUs to accelerate numerically intensive portions of the code, like the time integration and calculation of densities. Compared with other time dependent

state-of-the-art codes in the literature, our simulations solve three to four orders of magnitude more partial differential equations, being about 100 times faster than other approaches. This significant improvement over other simulations is a consequence of the less demanding while accurate time-integration algorithm, as well as the efficient use of GPUs to accelerate the calculations, in particular, the use of accurate Fast Fourier transforms for spatial derivatives. The first application of these codes have been to linear response [24] and relativistic Coulomb excitation of heavy nuclei [25], but the main focus of our work has been devoted to fission.

The evolution in time follows the system from a compact shape to two fully separated fragments. When the fragments are fully separated, we split the box into two, and compute the properties of each fragment in its half of the box. The total kinetic energy (TKE) is calculated by adding each FF kinetic energy and the Coulomb interaction between the fragments, as TKE is defined at infinite distance between fragments. We can also compute the total energy of each fragment, and then calculate the FF excitation energy by subtracting the ground state energy computed in an independent minimization for each FF.

## 4 Fission fragment properties from fission dynamics

In our first simulations of the fission of  $^{240}\text{Pu}$  [26], our initial states in the evolution were chosen from beyond the fission barrier, a few MeVs above the zero-temperature potential energy surface. Those states were obtained with a mix of shape constraints and external potentials that would induce a mass asymmetry. The constraints and external potential were then removed adiabatically, and the dynamics of the system followed from a compact initial configuration to two fully separated fragments, as shown in Fig. 1. For this first calculation, the SLy4 parameterization of the Skyrme functional was chosen. However, because the potential energy surface and the fission barrier properties in particular are not well described with this functional, it was found that the evolution time from the saddle to the scission can be extremely large [26] as this particular functional facilitates the conversion between multiple collective degrees of freedom. It was also found that the saddle-to-scission time is particularly sensitive to the pairing correlations, which is to be expected as the pairing interaction facilitates fission at low energies [27–29]. Finally, results obtained in TD-SLDA are consistent with expectations that the light fragment emerges deformed, while the heavy fragment is close to spherical shape with very weak or collapsed pairing field, as it is expected to be close to a closed shell configuration.

In Ref. [26], only four distinct initial conditions have been used to compute the FF properties. Hence, one of natural and frequently asked questions was about the impact the particular initial conditions have on the final results. In a more recent investigation of Ref. [30], we have started with a larger number of initial conditions considering different points on the potential energy surface. In this case, we have used functionals that better describe the potential energy surfaces of actinides, in particular, the SKM\* and recently developed SeaLL1 density functionals. The initial conditions were chosen to have a large spread in quadrupole deformation ( $Q_{20}$ ) and mass asymmetry ( $Q_{30}$ ), but similar initial excitation energies with respect to the ground state, as shown in Fig. 2. The two sets of initial conditions shown in Fig. 2 have excitation energies around 7.9 MeV (red) and 2.6 MeV (blue), respectively.

The results of the two sets of calculations are summarized in Table 1. Despite the

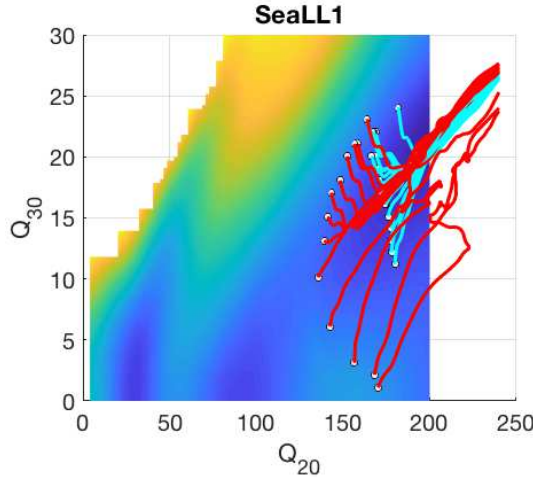


Figure 2: Evolution from compact to separated shapes in the  $(Q_{20}, Q_{30})$  plane, for the SeaLL1 nuclear density functional. These trajectories start around 7.9 MeV (red) and 2.6 MeV (blue) excitation energies, with a standard deviation of about 1.7 and 1.8 MeV, respectively.  $Q_{20}$  is in the units of  $b$  and  $Q_{30}$  is in the units of  $b^{3/2}$ .

relatively large spread in the shape of the initial state, the fragments are produced with a relatively small dispersion in all observables, as illustrated by the focusing of the different trajectories in Fig. 2. The TD-SLDA can only provide an average path for the evolution, following to a large extent the minimum on the potential energy surface. Very similar FF characteristics are thus obtained within TD-SLDA, if no fluctuations (and dissipation) are included.

An interesting feature of the evolution is the fact that the collective energy flow, defined as

$$E_{\text{coll.flow}} = \int d^3\vec{r} \frac{\vec{j}^2(\vec{r}, t)}{2M_N\rho(\vec{r}, t)}, \quad (5)$$

where  $\vec{j}(\vec{r}, t) = \frac{i\hbar}{2} \sum_k (v_k^*(\vec{r}, t) \vec{\nabla} v_k(\vec{r}, t) - v_k(\vec{r}, t) \vec{\nabla} v_k^*(\vec{r}, t))$  is the current density, and  $\rho(\vec{r}, t) = \sum_k |v_k(\vec{r}, t)|^2$  is the particle number density, remains almost constant throughout the saddle-to-scission evolution, and at a very low (1–2 MeV) value. Hence, the motion from the saddle to the scission is strongly dissipative, because the one-body dissipation included in TD-SLDA is strong. This finding is at odds with adiabatic approaches, where one expects a full conversion of the collective energy potential surface into a collective flow energy of about 15 to 20 MeV from the saddle to the scission, and in line with the hypothesis of overdamped collective motion, as assumed in the work by Randrup *et al.* [31].

Fluctuations and dissipations have been introduced recently in a quantum-mechanical fully-unitary approach [32]. The fluctuations are modeled by introducing

Table 1: The excitation energy of the initial state used in TD-SLDA evolution, TKE, charge, mass and excitation energy of the heavy FF for the trajectories shown in Fig. 2. We record the standard deviation for each quantity in parentheses.

$E_{ini}^*$ (MeV)	TKE (MeV)	$Z_H$	$A_H$	$E_H^*$ (MeV)
7.9(1.7)	177.8(3.1)	53.2(0.4)	136.6(0.8)	17.1(3.0)
2.6 (1.8)	178.0(2.3)	52.9(0.4)	135.8(0.6)	19.5(3.8)

a “stochastic” velocity field  $\vec{u}(\vec{r}, t)$ , see Ref. [32] for details. This additional field induces heating in the system, which has to be counterbalanced by a dissipation term to the evolution of the form  $\gamma[\rho(\vec{r}, t)]\dot{\rho}(\vec{r}, t)$ , with a density-dependent strength  $\gamma$ . This addition ensures that the energy of the system is conserved on average. The strength of the friction term is connected to the strength of the stochastic field, similar to the Einstein’s fluctuation-dissipation theorem.

The resources necessary to run simulations that include fluctuations and dissipation in TD-SLDA are considerable. Hence, for the first test that also allow us to experiment with the strength of fluctuation and dissipation terms, this approach has been implemented in the nuclear quantum hydrodynamic equations using a phenomenological nuclear energy density functional [32]. The hydrodynamic equations do not include the shell effects and stationary states with broken left-right symmetry have always higher energies than states with unbroken left-right symmetry. In applications to the spontaneous fission of  $^{258}\text{Fm}$ , the widths of the simulated distributions are in good agreement with observed experimental distributions [32]. The fluctuations and dissipation have been also implemented in the full TD-SLDA equations and illustrated in Ref. [32]. Calculations of the full distribution of fission observables are thus within reach, even with the current computational power available on leadership capabilities available today (and in the near future).

## 5 Conclusions

Current computing capabilities put us in the position to be able to envision a complete microscopic model for fission in the next few years. TD-SLDA is an effective tool in answering qualitative and quantitative questions regarding the dynamics of the fission process. This is also the only method that can offer a guidance on properties that simply cannot be described in alternate approaches. This includes the excitation energy sharing mechanism between the fission fragments and its behavior with increasing the incident neutron energy. Within the TD-SLDA one can also investigate the physics of scission neutrons, that make the subject of heated debate in the community, and the distribution of the angular momenta. In the future, we will obtain trends with the incident energy of the incoming neutrons from TD-SLDA calculations and will use them as an input in phenomenological calculations of prompt fission neutron and gamma-ray emission.

## Acknowledgments

The work of AB and SJ was supported by U.S. Department of Energy, Office of Science, Grant No. DE-FG02-97ER41014 and in part by NNSA cooperative agreement DE-NA0003841. The TDDFT calculations have been performed by SJ at the OLCF Titan and Piz Daint and for generating initial configurations for direct input into the TDDFT code at OLCF Titan and NERSC Edison. This research used resources of the Oak Ridge Leadership Computing Facility, which is a U.S. DOE Office of Science User Facility supported under Contract No. DE-AC05-00OR22725 and of the National Energy Research Scientific computing Center, which is supported by the Office of Science of the U.S. Department of Energy under Contract No. DE-AC02-05CH11231. We acknowledge PRACE for awarding us access to resource Piz Daint

based at the Swiss National Supercomputing Centre (CSCS), decision No. 2016153479. The work of KJR is supported by U.S. DOE Office of Advanced Scientific Computing Research and was conducted at Pacific Northwest National Laboratory and University of Washington. The work of NS was supported by the Scientific Discovery through Advanced Computing (SciDAC) program funded by the U.S. Department of Energy, Office of Science, Advanced Scientific Computing Research and Nuclear Physics, and it was partly performed under the auspices of the U.S. Department of Energy by the Lawrence Livermore National Laboratory under Contract DE-AC52-07NA27344. NS performed the calculations of the initial configurations, of the ground state and the finite temperature properties of the FFs under the auspices of the U.S. Department of Energy by the Lawrence Livermore National Laboratory under Contract DE-AC52-07NA27344. Some of the calculations reported here have been performed with computing support from the Lawrence Livermore National Laboratory (LLNL) Institutional Computing Grand Challenge program. The work of IS was performed at Los Alamos National Laboratory, under the auspices of the National Nuclear Security Administration of the U.S. Department of Energy. Numerical development of the fluctuations and dissipation code in a hydrodynamic approach and some calculations have been performed on Kodiak of the Institutional Computing Program at Los Alamos National Laboratory.

## References

- [1] O. Hahn and F. Strassmann, *Naturwis.* **27**, 11 (1939).
- [2] P. Hohenberg and W. Kohn, *Phys. Rev.* **136**, B864 (1964).
- [3] W. Kohn and L. J. Sham, *Phys. Rev.* **140**, A1133 (1965).
- [4] E. Runge and E. K. U. Gross, *Phys. Rev. Lett.* **52**, 997 (1984).
- [5] L. N. Oliveira, E. K. U. Gross and W. Kohn, *Phys. Rev. Lett.* **60**, 2430 (1988).
- [6] A. Bulgac, *Annu. Rev. Nucl. Part. Sci.* **63**, 97 (2013).
- [7] J. Verbeke, J. Randrup and R. Vogt, *Comput. Phys. Commun.* **222**, 263 (2018).
- [8] B. Becker, P. Talou, T. Kawano, Y. Danon and I. Stetcu, *Phys. Rev. C* **87**, 014617 (2013).
- [9] P. Talou, T. Kawano and I. Stetcu, *CGMF documentation. Tech. rep. LA-UR-14-24031*. Los Alamos National Laboratory, Los Alamos, 2014.
- [10] J. M. Blatt and V. F. Weisskopf, *Theoretical nuclear physics*. Wiley, New York, 1952.
- [11] W. Hauser and H. Feshbach, *Phys. Rev.* **87**, 366 (1952).
- [12] A. A. Naqvi, F. Käppeler, F. Dickmann and R. Müller, *Phys. Rev. C* **34**, 218 (1986).
- [13] S. S. Kapoor and R. Ramanna, *Phys. Rev.* **133**, B598 (1964).
- [14] H. Naik, S. P. Dange and R. J. Singh, *Phys. Rev. C* **71**, 014304 (2005).

- [15] J. B. Wilhelmy, E. Cheifetz, R. C. Jared, S. G. Thompson, H. R. Bowman and J. O. Rasmussen, *Phys. Rev. C* **5**, 2041 (1972).
- [16] M. M. Hoffman, *Phys. Rev.* **133**, B714 (1964).
- [17] I. Stetcu, P. Talou, T. Kawano and M. Jandel, *Phys. Rev. C* **88**, 044603 (2013).
- [18] P. Möller, D. G. Madland, A. J. Sierk and A. Iwamoto, *Nature* **409**, 785 (2001).
- [19] A. J. Sierk, *Phys. Rev. C* **96**, 034603 (2017).
- [20] N. Schunck and L. M. Robledo, *Rep. Prog. Phys.* **79**, 116301 (2016).
- [21] S. Jin, A. Bulgac, K. Roche and G. Wlazłowski, *Phys. Rev. C* **95**, 044302 (2017).
- [22] A. Bulgac and M. M. Forbes, *Phys. Rev. C* **87**, 051301(R) (2013).
- [23] R. W. Hamming, *Numerical methods for scientists and engineers*. Dover, 1986.
- [24] I. Stetcu, A. Bulgac, P. Magierski and K. J. Roche, *Phys. Rev. C* **84**, 051309(R) (2011).
- [25] I. Stetcu, C. A. Bertulani, A. Bulgac, P. Magierski and K. J. Roche, *Phys. Rev. Lett.* **114**, 012701 (2015).
- [26] A. Bulgac, P. Magierski, K. J. Roche and I. Stetcu, *Phys. Rev. Lett.* **116**, 122504 (2016).
- [27] G. F. Bertsch, F. Barranco and R. A. Broglia, in *Windsurfing the Fermi sea: Proc. Int. Conf. and Symposium on Unified Concepts of Many-Body Problems in honor of Gerry Brown's 60th birthday, September 4-6, 1986, Stony Brook, USA*, eds. T. T. S. Kuo and J. Speth. North-Holland, Amsterdam, 1987, p. 33.
- [28] F. Barranco, R. A. Broglia and G. F. Bertsch, *Phys. Rev. Lett.* **60**, 507 (1988).
- [29] G. F. Bertsch and A. Bulgac, *Phys. Rev. Lett.* **79**, 3539 (1997).
- [30] A. Bulgac, S. Jin, K. J. Roche, N. Schunck and I. Stetcu, *Phys. Rev. C* **100**, 034615 (2019).
- [31] J. Randrup, P. Möller and A. J. Sierk, *Phys. Rev. C* **84**, 034613 (2011).
- [32] A. Bulgac, S. Jin and I. Stetcu, *Phys. Rev. C* **100**, 014615 (2019).

# Examination of Consistency of QRPA Approach to Double-Beta Decay

J. Terasaki

*Institute of Experimental and Applied Physics, Czech Technical University in Prague, Horská 3a/22, 128 00, Prague 2, Czech Republic*

## Abstract

Determination of the neutrino mass scale is a major subject of modern physics. I calculate the nuclear matrix element of the neutrinoless double- $\beta$  decay of  $^{48}\text{Ca}$  and derive the reduced half-life, which makes a relation between the half-life and the effective neutrino mass. The nuclear wave functions are obtained by the quasiparticle random-phase approximation. The reduced half-life of a few nuclear species are shown along with those of other groups. My value of reduced half-life is much larger than the majority of values of other groups. The charge-change transition density is examined by comparing the calculated transition strength function with that extracted by the charge-change reactions. The data are reproduced successfully using the appropriate transition operator and my charge-change transition density.

**Keywords:** *Neutrinoless double- $\beta$  decay; effective neutrino mass; nuclear matrix element; QRPA*

## 1 Introduction

Nuclear theory plays two indispensable roles in neutrino physics. One is a calculation of the cross section of the  $\nu$ -nucleus scattering [1] in relation to the neutrino-oscillation experiments, and another is a calculation of the nuclear matrix element (NME) and phase-space factor of the neutrinoless double- $\beta$  ( $0\nu\beta\beta$ ) decay for determining the effective neutrino mass. The half-life of this decay is a function of the NME, phase-space factor, and the effective neutrino mass, thus, a reliable predictive calculation of these theoretical quantities are necessary.  $^{48}\text{Ca}$  is the lightest candidate of the mother nuclei for the experiments. The nuclear wave functions cannot be obtained without an approximation. On the other hand, the values of the phase-space factor are established for relatively light candidate nuclei because accurate wave functions of the emitted particles can be used. It is a well-known problem that the calculated NME of the  $0\nu\beta\beta$  decay is distributed in a region of a factor of 2–3 systematically depending on the theoretical methods [2]. The number of calculations increased in the past decade, however this uncertainty factor does not change. The NME also affects the future plans of the experimental facilities for observing the  $0\nu\beta\beta$  decay

---

*Proceedings of the International Conference ‘Nuclear Theory in the Supercomputing Era — 2018’ (NTSE-2018), Daejeon, South Korea, October 29 – November 2, 2018, eds. A. M. Shirokov and A. I. Mazur. Pacific National University, Khabarovsk, Russia, 2019, p. 100.*

<http://www.ntse.khb.ru/files/uploads/2018/proceedings/Terasaki.pdf>.

because the NME affects an amount of the detector materials necessary for the aimed effective neutrino masses [3].

The reason for the discrepancy of the calculated NMEs is not yet clarified. The shell model includes high-order particle-hole correlations, but the single-particle space is limited to one major shell in most of the calculations. The quasiparticle random-phase approximation is not constrained by this limit, but its applicability is limited to nuclei in which the effects of high-order particle-hole correlations are small. Under this circumstance, the appropriate effective  $g_A$ , the axial-vector current coupling, is not yet established. Thus, the key point of the NME study is how the reliability of the calculation is shown.

Operators for calculating the  $0\nu\beta\beta$  NME are the neutrino potential and the charge-change operators of the Gamow–Teller (GT), Fermi, and the tensor types. The last one has only a small contribution, and it is neglected in my calculations. The GT transition density associated with  $J^\pi = 1^+$  is an ingredient of the NME calculation. This transition density is also included in the charge-change strength function, which can be extracted from the experimental cross sections using the impulse approximation and an extrapolation to the limit of vanishing momentum transfer [4]. There are experimental charge-change strength functions obtained in this manner from the  $^{48}\text{Ca}(p, n)^{48}\text{Sc}$  and  $^{48}\text{Ti}(n, p)^{48}\text{Sc}$  reactions [5]. In this paper, I show that these data can be reproduced by my QRPA calculation. However, this reproduction is not trivial because the experimental data do not satisfy the GT sum rule. This problem is resolved by introducing an isovector spin-monopole operator in addition to the usual GT operator. By this test, the validity of my charge-change transition density is proven indirectly.

## 2 Nuclear matrix element of neutrinoless double- $\beta$ decay

The effective neutrino mass is defined by

$$\langle m_\nu \rangle = \left| \sum_{i=1,2,3} U_{ei}^2 m_i \right|, \quad (1)$$

where  $U_{ei}$  is the matrix element of the Pontecorvo–Maki–Nakagawa–Sakata (PMNS) matrix [6] with  $i$  denoting the eigenstate of mass  $m_i$ . Suffix  $e$  stands for the electron flavor. The half-life to the  $0\nu\beta\beta$  decay  $T_{1/2}^{(0\nu)}$  and  $\langle m_\nu \rangle$  are related as [7]

$$T_{1/2}^{(0\nu)} = \frac{R_{1/2}^{(0\nu)}}{\langle m_\nu \rangle^2}, \quad (2)$$

$$R_{1/2}^{(0\nu)} = \frac{(m_e c^2)^2}{G_{0\nu} g_A^4 |M^{(0\nu)}|^2}, \quad (3)$$

where  $G_{0\nu}$  is the phase-space factor,  $g_A$  is the axial-vector current coupling,  $M^{(0\nu)}$  is the NME, and  $m_e$  is the electron mass. I call  $R_{1/2}^{(0\nu)}$  a reduced half-life.

The  $0\nu\beta\beta$ -decay NME  $M^{(0\nu)}$  is obtained by calculating

$$M^{(0\nu)} = M_{GT}^{(0\nu)} - \frac{g_V^2}{g_A^2} M_F^{(0\nu)}. \quad (4)$$

$M_{GT}^{(0\nu)}$  is the GT NME, and  $M_F^{(0\nu)}$  is the Fermi NME. The vector current coupling  $g_V$  is 1; this coupling is thought to be a physical constant. An effective value is used for  $g_A$  (see below). Those NMEs can be written as

$$M_{GT}^{(0\nu)} = \sum_K \sum_{a_I^K a_F^K} \sum_{pn p' n'} V_{pp', nn'}^{GT(0\nu)}(\bar{E}_a) \langle F | c_p^\dagger c_n | a_F^K \rangle \langle a_F^K | a_I^K \rangle \langle a_I^K | c_{p'}^\dagger c_{n'} | I \rangle, \quad (5)$$

$$M_F^{(0\nu)} = \sum_K \sum_{a_I^K a_F^K} \sum_{pn p' n'} V_{pp', nn'}^{F(0\nu)}(\bar{E}_a) \langle F | c_p^\dagger c_n | a_F^K \rangle \langle a_F^K | a_I^K \rangle \langle a_I^K | c_{p'}^\dagger c_{n'} | I \rangle. \quad (6)$$

The initial and final states of the  $0\nu\beta\beta$  decay are denoted by  $|I\rangle$  and  $|F\rangle$ , respectively, and the states of the intermediate nucleus are  $|a_F^K\rangle$  and  $|a_I^K\rangle$ . The states  $\{|a_F^K\rangle\}$  are obtained by QRPA<sup>1</sup> based on  $|F\rangle$ , and  $\{|a_I^K\rangle\}$  are obtained by QRPA based on  $|I\rangle$ .  $K$  is a component of the nuclear angular momentum projected on the symmetry axis; in my calculation, the axial symmetry of the nuclear density distribution is assumed. The indexes  $p$  and  $p'$  denote the proton states, and  $n$  and  $n'$  denote the neutron states.  $c_i^\dagger$  and  $c_i$  are respectively the creation and annihilation operators of a particle in the state  $i$ .  $\langle F | c_p^\dagger c_n | a_F^K \rangle$  and  $\langle a_F^K | c_{p'}^\dagger c_{n'} | I \rangle$  are the transition-density matrices of the charge change.  $V_{pp', nn'}^{GT(0\nu)}(\bar{E}_a)$  and  $V_{pp', nn'}^{F(0\nu)}(\bar{E}_a)$  are the two-body transition matrix elements:

$$V_{pp', nn'}^{GT(0\nu)}(\bar{E}_a) = \langle pp' | h_+(r_{12}, \bar{E}_a) \boldsymbol{\sigma}(1) \cdot \boldsymbol{\sigma}(2) \tau^-(1) \tau^-(2) | nn' \rangle, \quad (7)$$

$$V_{pp', nn'}^{F(0\nu)}(\bar{E}_a) = \langle pp' | h_+(r_{12}, \bar{E}_a) \tau^-(1) \tau^-(2) | nn' \rangle. \quad (8)$$

The operators of the spin and charge change from neutron to proton are denoted by  $\boldsymbol{\sigma}$  and  $\tau^-$ , respectively. Their argument distinguishes the two particles that the operators act on. The neutrino potential is given by

$$h_+(r_{12}, \bar{E}_a) \simeq \frac{R}{r_{12}} \frac{2}{\pi} \left\{ \sin\left(\frac{c}{\hbar} \bar{\mu}_a m_e r_{12}\right) \text{ci}\left(\frac{c}{\hbar} \bar{\mu}_a m_e r_{12}\right) \right. \quad (9)$$

$$\left. - \cos\left(\frac{c}{\hbar} \bar{\mu}_a m_e r_{12}\right) \text{si}\left(\frac{c}{\hbar} \bar{\mu}_a m_e r_{12}\right) \right\}, \quad (10)$$

$$\bar{\mu}_a = \frac{1}{m_e c^2} (\bar{E}_a - \bar{M}). \quad (11)$$

This neutrino potential is derived by neglecting the effective neutrino mass compared to the major momentum transfer by the propagating neutrino [7].  $R$  is the root-mean-square radius of nucleus,  $r_{12}$  is the distance variable between two particles, and  $\bar{E}_a$  is the average energy of the intermediate states (the closure approximation).  $R = 1.1 A^{1/3}$  fm with the mass number  $A$  and  $\bar{\mu}_a = 18.51$  [7] are used in our calculations. In Eq. (10), the functions

$$\text{si}(x) = - \int_x^\infty \frac{\sin(t)}{t} dt, \quad \text{ci}(x) = - \int_x^\infty \frac{\cos(t)}{t} dt \quad (12)$$

are used.

The interaction used for obtaining the nuclear states is the Skyrme SkM\* [9] and volume contact pairing interactions. The QRPA equation was solved in the matrix

---

<sup>1</sup>The proton-neutron QRPA [8] is used. I call it the QRPA for simplicity in this paper.

Table 1: NME of  $0\nu\beta\beta$  decay of  $^{48}\text{Ca}$ , specific terms, effective  $g_A$  used for the calculation, and reduced half-life.

$M^{(0\nu)}$	$M_{GT}^{(0\nu)}$	$M_F^{(0\nu)}$	$g_A$	$R_{1/2}^{(0\nu)}$ ( $10^{12}$ MeV $^2$ yr)
3.054	1.723	-0.319	0.49	19.572

formulation. Table 1 shows the obtained NME, GT and Fermi terms, effective  $g_A$ , and the reduced half-life of the  $0\nu\beta\beta$  decay of  $^{48}\text{Ca}$ . The effective  $g_A = 0.49$  was determined so as to reproduce the measured half-life to the  $2\nu\beta\beta$  decay [10]. This value of  $g_A$  is much smaller than the bare value of approximately 1.27. Figure 1

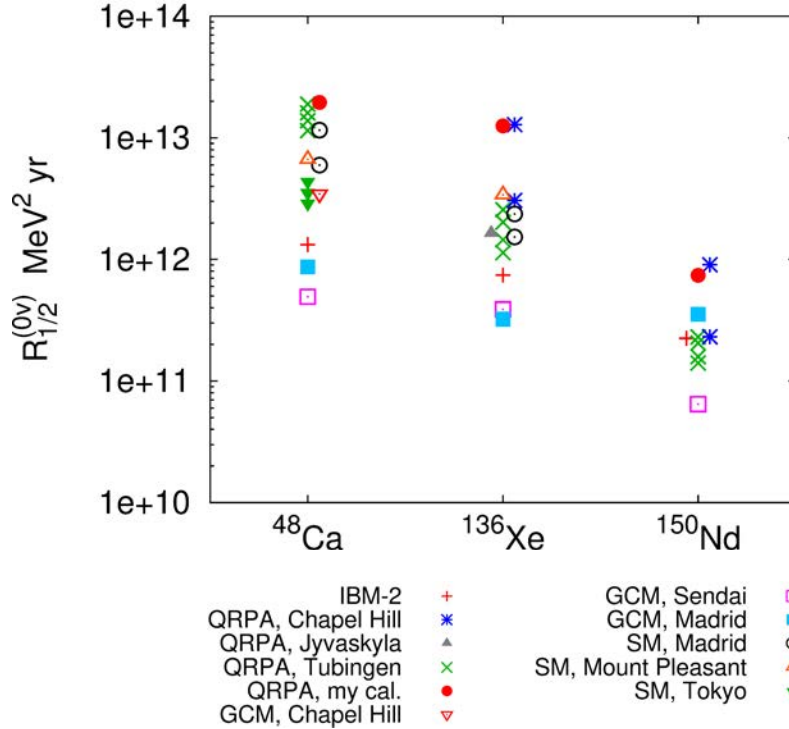


Figure 1: Reduced half-life of  $^{48}\text{Ca}$ ,  $^{136}\text{Xe}$ , and  $^{150}\text{Nd}$  obtained by several groups. The references are as follows.  $^{48}\text{Ca}$ : [11] (QRPA Tübingen), [12] (SM, Mount Pleasant), [13] (SM, Tokyo), [14] (IBM-2), [15] (GCM, Madrid), [16] (GCM, Sendai), [17] (SM, Madrid), [18] (GCM, Chapel Hill), [19] (QRPA, my calculation);  $^{136}\text{Xe}$ : [14] (IBM-2), [11] (QRPA, Tübingen), [20] (QRPA, Chapel Hill), [16] (GCM, Sendai), [15] (GCM, Madrid), [17] (SM, Madrid), [12] (SM, Mount Pleasant), [21] (QRPA, Jyväskylä), [22] (QRPA, my calculation);  $^{150}\text{Nd}$ : [14] (IBM-1), [23] (QRPA, Tübingen), [20] (QRPA, Chapel Hill), [16] (GCM, Sendai), [15] (GCM, Madrid), [24, 25] (QRPA, my calculation). SM, GCM, and IBM stand for the shell model, generator coordinate method, and interacting boson model, respectively. The effective  $g_A$  is not unified.

illustrates the reduced half-life of three nuclear species obtained by several groups including my values, which are much higher than the majority of the results of other groups. This result implies that the half-life is predicted by my calculation to be much longer than that of other groups. Test of reliability of my calculation is quite important.

### 3 Charge-change strength function

The experimental GT strength function of  $^{48}\text{Ca}(p, n)^{48}\text{Sc}$  and  $\text{GT}^+$  [ $\tau^+ = (\tau^-)^\dagger$  is used] strength function of  $^{48}\text{Ti}(n, p)^{48}\text{Sc}$  are drawn in Fig. 2 together with my theoretical strength functions obtained by calculating

$$S_{\text{GT}^-}(E) = \frac{1}{\pi} \sum_{a_I^K} \frac{\delta |\langle a_I^K | \sigma \tau^- | I \rangle|^2}{[E - E(a_I^K)]^2 + \delta^2}. \quad (13)$$

$E(a_I^K)$  is the energy of the state  $|a_I^K\rangle$ , and  $\delta$  is a small constant for smoothing. The transition operator  $\sigma \tau^-$  is the one-body operator. The summation includes all states of  $^{48}\text{Sc}$  for which the transition matrix element does not vanish. The  $\text{GT}^+$  strength function can be calculated analogously using  $|F\rangle$  and  $|a_F^K\rangle$ . The calculated strength functions apparently overestimate the data, however these results satisfy the GT sum rule,

$$\int_0^\infty dE S_{\text{GT}^-}(E) |_{(Z, N) \rightarrow (Z+1, N-1)} - \int_0^\infty dE S_{\text{GT}^+}(E) |_{(Z, N) \rightarrow (Z-1, N+1)} = 3(N - Z). \quad (14)$$

For the initial nucleus  $^{48}\text{Ca}$ , the first term provides the value of 24.638 while the second term is equal to  $-0.633$  resulting in the sum-rule value of 24.005. For the initial nucleus  $^{48}\text{Ti}$ , I obtain respectively 15.257 and  $-3.268$  and thus the value of 11.989 for the sum rule. The exact values are respectively 24 and 12 for these two nuclei. The sum of the experimental charge-change transition strengths of  $^{48}\text{Ca}(p, n)^{48}\text{Sc}$

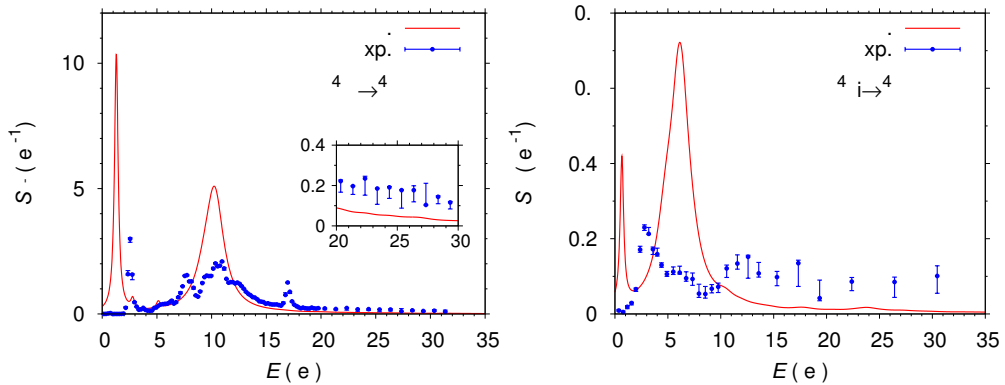


Figure 2: Charge-change strength functions of  $^{48}\text{Ca}(p, n)^{48}\text{Sc}$  (left) and  $^{48}\text{Ti}(n, p)^{48}\text{Sc}$  (right). Symbols are the experimental data of Ref. [5], solid lines are the results of my calculations. The inset in the left panel is a magnification of the high-energy region.

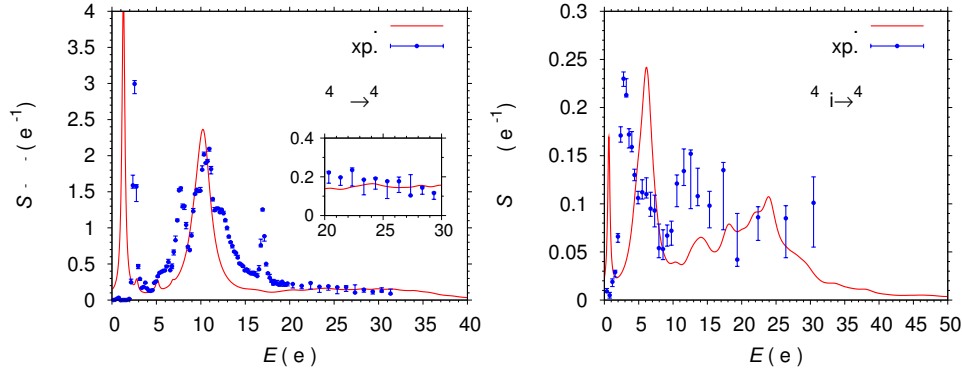


Figure 3: The same as Fig. 2 but for the transition operator  $O_{\pm}$ .

is  $64 \pm 9$  % of the sum-rule [5]. The tail of the experimental strength function (left panel of Fig. 2) converges to zero, indicating that there is no strength in the higher-energy region. Thus, it is implied by the data, that this transition involves not only the GT operator  $\sigma\tau^-$  but also other ones. A possible candidate is the isovector spin-monopole operator  $r^2\sigma\tau^-$  [26,27]. This operator causes a two- $\hbar\omega$  jump and can explain the strength distribution in the higher-energy region where  $\sigma\tau^-$  cannot create the strength, see the right panel in Fig. 2. The possible contribution of the isovector spin-monopole operator has been already mentioned in Ref. [5].

I introduce the transition operator [19]

$$O_{\pm} = \sigma\tau^{\pm} + \alpha_{\pm}r^2\sigma\tau^{\pm}, \quad (15)$$

and determine  $\alpha_{\pm}$  so as to reproduce the experimental strength functions in the two- $\hbar\omega$ -jump region; those values are  $\alpha_- = -0.03 \text{ fm}^{-2}$  for  $^{48}\text{Ca} \rightarrow ^{48}\text{Sc}$  and  $\alpha_+ = -0.0253 \text{ fm}^{-2}$  for  $^{48}\text{Ti} \rightarrow ^{48}\text{Sc}$ . The strength functions of  $O_{\pm}$  are drawn in Fig. 3 together with the experimental data. The description of the data is improved significantly. Therefore, the contribution of the isovector spin-monopole operator is a reasonable explanation to the observed charge-change transitions. It is stressed that my transition density is confirmed indirectly through this reproduction of the data.

The calculated strength function of  $O_{\pm}$  up to 12 MeV ( $^{48}\text{Ca}$ ) or 10 MeV ( $^{48}\text{Ti}$ ) is lowered compared to that of the GT operator. This change can be understood by rewriting  $O_{\pm}$  as

$$O_{\pm} = \{1 + \alpha_{\pm}\langle r^2 \rangle_{nf_{7/2}} + \alpha_{\pm}(r^2 - \langle r^2 \rangle_{nf_{7/2}})\} \sigma\tau^{\pm}, \quad (16)$$

where  $\langle r^2 \rangle_{nf_{7/2}}$  is the expectation value of  $r^2$  with respect to the specified neutron state. The operator  $\alpha_{\pm}(r^2 - \langle r^2 \rangle_{nf_{7/2}})$  is the two- $\hbar\omega$  component in a good approximation [27]. Since  $\alpha_{\pm}$  are negative, the zero- $\hbar\omega$  component  $1 + \alpha_{\pm}\langle r^2 \rangle_{nf_{7/2}}$  is hindered.

## 4 Summary

I have calculated the NME of the  $0\nu\beta\beta$  decay of  $^{48}\text{Ca} \rightarrow ^{48}\text{Ti}$  using the QRPA, and the reduced half-life was obtained. My result predicts much longer half-life of  $^{48}\text{Ca}$  to that decay compared to those predicted by other groups. Check of the transition

density has been made indirectly by reproducing the charge-change strength functions obtained by the  $(n, p)$  and  $(p, n)$  reactions. As a by-product, it has been shown that the transition operator of that charge-change reaction includes the isovector spin-monopole operator.

In this paper, I omitted the discussions on the two-neutrino double- $\beta$  ( $2\nu\beta\beta$ ) decay and the detail of the method to determine the strength of the proton-neutron ( $pn$ ) pairing interaction [19]. The strength of the isoscalar  $pn$  pairing interaction is determined by an identity derived under the closure approximation, and the effective  $g_A$  is determined so as to reproduce the measured half-life to the  $2\nu\beta\beta$  decay. The convergence of the  $0\nu\beta\beta$  NME was also checked with respect to the single-particle space. Thus, my calculation does not have a free parameter.

## Acknowledgments

Numerical calculations of this paper were performed by the K computer at the RIKEN Center for Computational Science through the program of High Performance Computing Infrastructure in 2017–2018 and 2018–2019 (hp170288). The computer Coma at the Center for Computational Sciences, University of Tsukuba was also used through the Multidisciplinary Cooperative Research Program of this center in 2016 (TKBNDFT) and 2017 (DBTHEORY). Furthermore, the computer Oakforest-PACS at the Joint Center for Advanced High Performance Computing was used through the above program of the Center for Computational Sciences, University of Tsukuba in 2018 (xg18i006). This study is supported by the European Regional Development Fund-Project “Engineering applications of microworld physics” (No. CZ.02.1.01/0.0/0.0/16\_019/0000766).

## References

- [1] C. Barbieri, *Recent (computational and non) advances for self-consistent Green’s function theory in nuclear physics*, talk given at the Int. Conf. ‘Nuclear Theory in the Supercomputing Era — 2018’ (NTSE-2018), October 29 – November 2, 2018, Daejeon, South Korea, <http://ntse.khb.ru/files/uploads/2018/presentations/Barbieri.pdf>.
- [2] J. Engel and J. Menéndez, *Rep. Prog. Phys.* **80**, 046301 (2017).
- [3] A. S. Barabash, *Front. Phys.*, **6**,160 (2019).
- [4] M. Ichimura, H. Sakai and T. Wakasa, *Prog. Part. Nucl. Phys.* **56**, 446 (2006).
- [5] K. Yako *et al.*, *Phys. Rev. Lett.* **103**, 012503 (2009).
- [6] B. Pontecorvo, *Sov. Phys. JETP* **7**, 172 (1958).
- [7] M. Doi, T. Kotani and E. Takasugi, *Prog. Theor. Phys. Suppl.* **83**, 1 (1985).
- [8] J. A. Halbleib Sr. and R. A. Sorensen, *Nucl. Phys. A* **98**, 542 (1967).
- [9] J. Bartel, P. Quentin, M. Brack, C. Guet and H.-B. Håkansson, *Nucl. Phys. A* **386**, 79 (1982).

- [10] A. S. Barabash, in *Proc. Workshop on Calculation of Double-Beta-Decay Matrix Elements (MEDEX'13), Prague, June 11–14, 2013*, eds. O. Civitarese, I. Stekl and J. Suhonen. AIP Publishing, 2013, p. 11.
- [11] F. Šimkovic, V. Rodin, A. Faessler and P. Vogel, *Phys. Rev. C* **87**, 045501 (2013).
- [12] M. Horoi and A. Neacsu, *Phys. Rev. C* **93**, 024308 (2016).
- [13] Y. Iwata, N. Shimizu, T. Otsuka, Y. Utsuno, J. Menéndez, M. Homma and T. Abe, *Phys. Rev. Lett.* **116**, 112502 (2016).
- [14] J. Barea, J. Kotila and F. Iachello, *Phys. Rev. C* **91**, 034304 (2015).
- [15] N. L. Vaquero, T. R. Rodríguez and J. L. Egido, *Phys. Rev. Lett.* **111**, 142501 (2013).
- [16] J. M. Yao, L. S. Song, K. Hagino, P. Ring and J. Meng, *Phys. Rev. C* **91**, 024316 (2015).
- [17] J. Menéndez, A. Poves, E. Caurier and F. Nowacki, *Nucl. Phys. A* **818**, 139 (2009).
- [18] C. F. Jiao, J. Engel and J. D. Holt, *Phys. Rev. C* **96**, 054310 (2017).
- [19] J. Terasaki, *Phys. Rev. C* **97**, 034304 (2018).
- [20] M. T. Mustonen and J. Engel, *Phys. Rev. C* **87**, 064302 (2013).
- [21] J. Hyvärinen and J. Suhonen, *Phys. Rev. C* **91**, 024613 (2015).
- [22] J. Terasaki and Y. Iwata, *Phys. Rev. C* **100**, 034325 (2019).
- [23] D.-L. Fang, A. Faessler and F. Šimkovic, *Phys. Rev. C* **92**, 044301 (2015).
- [24] J. Terasaki, *Phys. Rev. C* **91**, 034318 (2015).
- [25] J. Terasaki, *Phys. Rev. C* **93**, 024317 (2016).
- [26] O. Civitarese and J. Suhonen, *Phys. Rev. C* **89**, 044319 (2014).
- [27] I. Hamamoto and H. Sagawa, *Phys. Rev. C* **62**, 024319 (2000).

# Experimental Approach to Three-Nucleon Forces via Three- and Four-Nucleon Scattering

Kimiko Sekiguchi

*Department of Physics, Tohoku University, JAPAN*

## Abstract

Few-nucleon scattering offers a good opportunities to study dynamical aspects of three-nucleon forces, that are momentum, spin and isospin dependent. In this contribution, the experimental results of deuteron-proton elastic scattering obtained in the course of the study are presented. The data are compared with the state-of-the-art theoretical predictions based on the realistic bare nuclear potentials. Recently the experimental study has been extended to the proton- $^3\text{He}$  scattering in which the isospin  $T = 3/2$  channel in 3NFs could be investigated.

**Keywords:** *Three-nucleon force, nucleon-deuteron scattering, proton- $^3\text{He}$  scattering*

## 1 Introduction

One of the main interests of nuclear physics is to understand the forces acting between nuclear constituents. Importance of the three-nucleon force (3NF) in the nuclear Hamiltonian has been studied in few-nucleon systems as well as in many-nucleon systems [1–3].

The nucleon-deuteron ( $Nd$ ) scattering — a scattering process in the the three-nucleon ( $3N$ ) system — offers a good opportunity to study dynamical aspects of 3NFs, which are momentum, spin and isospin dependent, since it provides not only cross sections but also a variety of spin observables at different incident nucleon energies. A direct comparison between the experimental data and rigorous numerical calculations in terms of Faddeev theory based on realistic bare nuclear potentials provides information on 3NFs. Indeed, the last two decades have witnessed extensive experimental and theoretical investigations of the  $Nd$  scattering performed in a wide range of incoming nucleon energies up to  $E \sim 300$  MeV/nucleon.

The four-nucleon ( $4N$ ) systems could also play an important role for the study of 3NFs. The 3NF effects are expected to be sizable in the  $4N$  system. In addition, while the  $Nd$  scattering is essentially a pure isospin  $T = 1/2$  state, tests of the  $T = 3/2$  channel in any 3NF can be performed in a  $4N$  system such as proton- $^3\text{He}$  scattering. Note, an importance of the study of isospin dependence of the 3NF has been pronounced for understanding of nuclear system with larger-isospin asymmetry [4, 5]. In

---

*Proceedings of the International Conference ‘Nuclear Theory in the Supercomputing Era — 2018’ (NTSE-2018), Daejeon, South Korea, October 29 – November 2, 2018, eds. A. M. Shirokov and A. I. Mazur. Pacific National University, Khabarovsk, Russia, 2019, p. 108.*

<http://www.ntse.khb.ru/files/uploads/2018/proceedings/Sekiguchi.pdf>.

recent years, there has been a large progress in solving the  $4N$  scattering problem with realistic Hamiltonians even above the four-nucleon breakup threshold energies [6, 7], which opens up new possibilities to approaching to properties of  $3NF$ s.

With the aim of exploring the  $3NF$ s, experimental programs of deuteron-proton ( $dp$ ) scattering as well as proton- $^3\text{He}$  ( $p + ^3\text{He}$ ) scattering using polarized beams and target systems are in progress at RIKEN, RCNP Osaka University, and CYRIC Tohoku University in Japan. In this contribution we introduce recently conducted experiments and present results of comparison between the experimental data and theoretical predictions based on realistic bare nuclear potentials.

## 2 Experimental results for $dp$ scattering

Experiments on the  $dp$  scattering were performed at the RIKEN Accelerator Facility using the polarized deuteron beams at the incident energies up to 135 MeV/nucleon. The measured observables are the cross sections, all deuteron analyzing powers ( $iT_{11}$ ,  $T_{20}$ ,  $T_{21}$ , and  $T_{22}$ ), and the deuteron to proton polarization transfer coefficients [8]. Later the experiments were extended to the RIKEN RI Beam Factory (RIBF). All deuteron analyzing powers were obtained at the energies of 190, 250, and 294 MeV/nucleon [9–11].

In Fig. 1 some representative experimental results for the  $dp$  and  $nd$  elastic scattering are compared with the Faddeev calculations with and w/o the  $3NF$ s. The red (blue) bands are the calculations with (without) the Tucson–Melbourne99 (TM99)  $3NF$  [12], which is a version of the Tucson–Melbourne  $3NF$  [13] more consistent with the chiral symmetry [14, 15], based on modern  $NN$  potentials, i. e., CD Bonn, AV18, Nijmegen I and II. The solid lines are the calculations based on the AV18 potential and including the Urbana IX  $3NF$  [16].

specific features are seen in the dependence on scattering angles in the center-of-mass system,  $\theta_{c.m.}$ . At the forward angles,  $\theta_{c.m.} \lesssim 80^\circ$ , the theoretical calculations based on various  $NN$  potentials are well converged and the predicted  $3NF$  effects are very small. The experimental data are well described by the calculations except for the very forward angles. This discrepancy comes from the fact that the calculations shown in the figure do not take into account the Coulomb interactions between protons [17]. At the angles  $\theta_{c.m.} \gtrsim 80^\circ$ , clear discrepancies between the data and the calculations based on the  $NN$  potentials are found. They become larger with the incident energy. At the angles around  $\theta_{c.m.} = 80^\circ\text{--}120^\circ$ , the discrepancies are explained by taking into account the  $2\pi$ -exchange-type  $3NF$  models (TM99 and Urbana IX). At the backward angles,  $\theta_{c.m.} \gtrsim 120^\circ$ , with increasing the incident energy, the differences appear between the experimental data and even the calculations including the  $3NF$  potentials and are seen up to the very backward angle,  $\theta_{c.m.} \sim 180^\circ$ , at a higher energy of 250 MeV/nucleon. Since these features are more pronounced as going to higher energies [18, 19], the relativistic effects were estimated by using the Lorentz-boosted  $NN$  potentials with the TM99 [20]. However, the relativistic effects have turned out to be small and only slightly alter the cross sections [10].

For the vector analyzing power  $iT_{11}$ , the discrepancies between the data and the predictions based on  $2NF$ s (blue bands) are seen at the angles  $\theta_{c.m.} \sim 120^\circ$ . At 135 and 190 MeV/nucleon, the data agree well with the predictions with the  $3NF$ s, while at 250 MeV/nucleon, a discrepancy is seen at the backward angles  $\theta_{c.m.} \gtrsim 120^\circ$ . The tensor analyzing power  $T_{22}$  reveals a different energy dependence than that of  $iT_{11}$ .

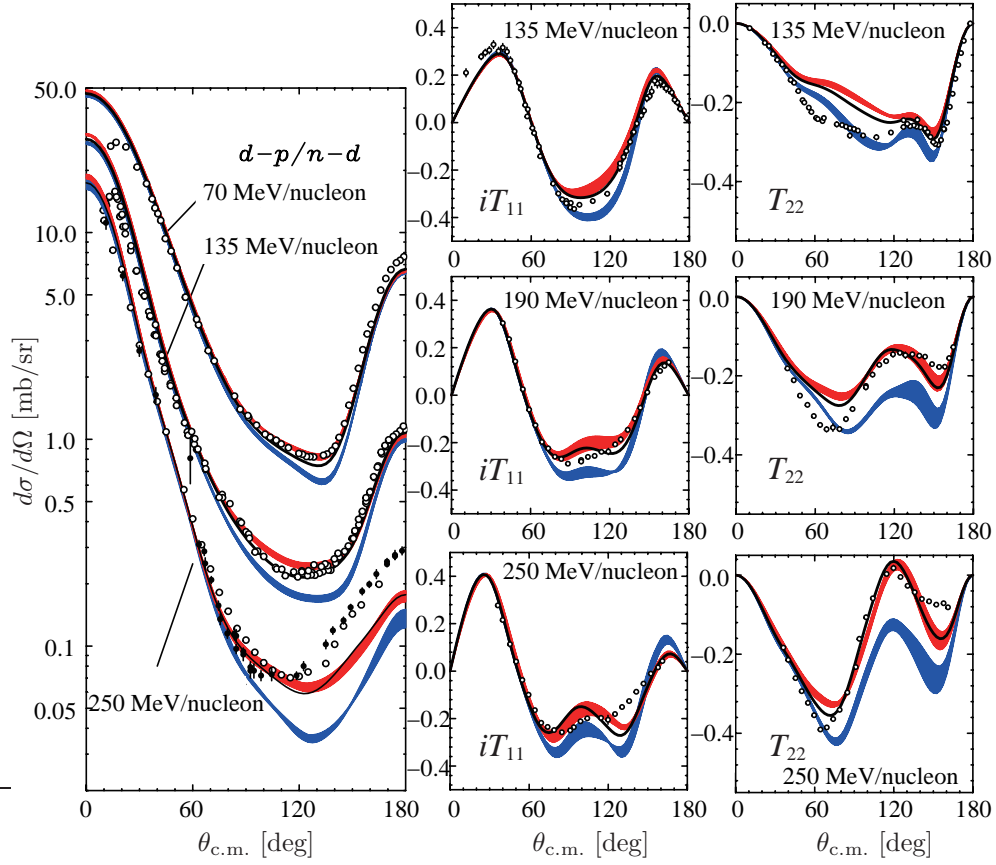


Figure 1: Differential cross section and deuteron analyzing powers  $iT_{11}$ ,  $T_{22}$  for elastic  $Nd$  scattering. The red (blue) bands are the calculations with (w/o) TM99 3NF based on the modern  $NN$  potentials, namely CD Bonn, AV18, Nijmegen I and II. The solid lines are the calculations based on the AV18 potential with inclusion of Urbana IX 3NF. For the cross sections, the open circles at 70 and 135 MeV/nucleon are the  $dp$  data from Refs. [8]. The open and solid circles at 250 MeV/nucleon are the  $pd$  and  $nd$  data, respectively, from Refs. [18]. For the deuteron analyzing powers, the data at 70 and 135 MeV/nucleon are from Refs. [8]. The data at 250 MeV/nucleon are taken at the RIBF [9].

At 135 MeV/nucleon, adding the 3NFs worsens the description of data in a large angular region. It is contrary to what happens at 190 and 250 MeV/nucleon, where large 3NF effects are supported by the measured data. The results of comparison show that the 3NF is definitely needed in the  $Nd$  elastic scattering. However the spin-dependent parts of the 3NF may be deficient.

It is interesting to see how the potentials of the chiral effective field theory ( $\chi$ EFT) describe the deuteron analyzing powers for the  $dp$  elastic scattering. In Fig. 2, the data are compared with the calculations based on the  $\chi$ EFT N4LO  $NN$  potentials [21]. For the cross section, a large difference is seen at the backward angles, that is quite similar to the results shown in Fig. 1. The vector analyzing power  $iT_{11}$  data are well

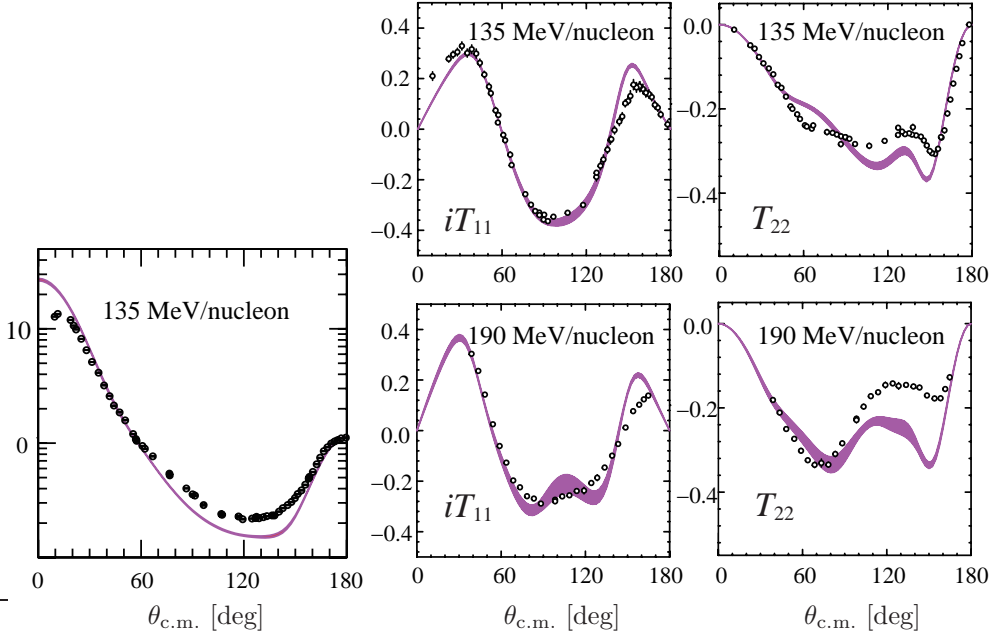


Figure 2: Differential cross section and deuteron analyzing powers  $iT_{11}$ ,  $T_{22}$  for the elastic  $Nd$  scattering. The bands are the calculations based on the  $\chi$ EFT N4LO  $NN$  potentials.

described by the  $\chi$ EFT N4LO  $NN$  potentials, while large discrepancies are found for the tensor analyzing power  $T_{22}$ . In order to see how  $\chi$ EFT 3NFs describe the data, the theoretical treatments are now in progress [22].

### 3 Experiment on $p + {}^3\text{He}$ scattering

Following the experiments on the  $dp$  scattering, we proceeded to the experiments on the  $p + {}^3\text{He}$  scattering at energies around 100 MeV/nucleon. The experiment consisted of two measurements. The measurement of the cross section and proton analyzing power was performed by using a 65 MeV polarized proton beam at RCNP, Osaka University. The measurement of the  ${}^3\text{He}$  analyzing power at an incident proton energy of 70 MeV was performed by using the newly constructed  ${}^3\text{He}$  target [23] at Cyclotron Radioisotope Center (CYRIC), Tohoku University. Both measurements covered a wide angular range in the center-of-mass system. In Fig. 3, a part of the data is compared with rigorous numerical four-nucleon calculations in terms of the Alt–Grassberger–Sandhas equation based on modern  $NN$  potentials (CD Bonn and INOY04 [24]) [25]. The clear discrepancies are found in the  ${}^3\text{He}$  analyzing power at the angles 80–120° in the center-of-mass system. The data analysis is now in progress.

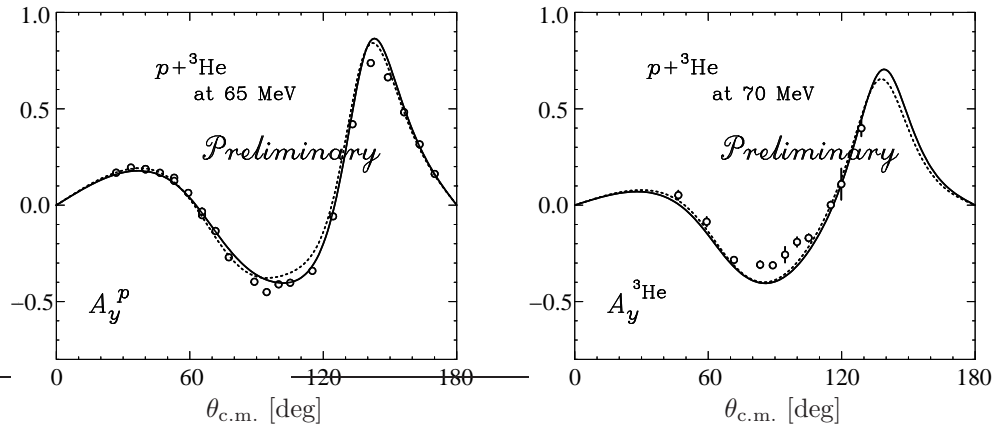


Figure 3: Proton analyzing power (left) and  ${}^3\text{He}$  analyzing power (right) for the  $p + {}^3\text{He}$  elastic scattering. The data for the proton analyzing power were taken with a polarized proton beam at 65 MeV; those for the  ${}^3\text{He}$  analyzing power at 70 MeV were obtained using a polarized  ${}^3\text{He}$  target. The solid (dotted) lines are the calculations based on the INOY04 (CD Bonn)  $NN$  potential.

## 4 Summary

The few-nucleon scattering provides rich sources to explore the properties of 3NFs that are momentum, spin and isospin dependent. The last two decades have witnessed an extensive study of the  $Nd$  scattering, that is an example of scattering in a three-nucleon system, both from theory and experiment. The experiments performed with polarized deuteron beams at RIKEN are presented and recent achievements in the study of 3NFs via  $dp$  scattering are discussed. The energy and angular dependent results for the cross sections as well as the polarization observables show that clear signatures of the 3NF effects are found in the cross section. Meanwhile the spin-dependent parts of the 3NFs may be deficient. In order to obtain a consistent understanding of the effects of three-nucleon forces in the 3N scattering, a further investigation is necessary. It would be interesting to see how well new theoretical approaches, e. g., an addition of the 3NFs other than that of the  $2\pi$ -exchange type, and the potentials based on the chiral effective field theory, will be able to describe these data.

The 3NF effects could also be sizable in the four-nucleon scattering systems, such as the  $p + {}^3\text{He}$  scattering, where tests of the isospin  $T = 3/2$  channel in 3NFs can be performed. As the first step, we have conducted experiments on the  $p + {}^3\text{He}$  elastic scattering at around 65 MeV. The obtained data would provide a valuable source of information on the 3NFs including their isospin dependences.

## Acknowledgments

The author would like to thank the collaborators for the experiments performed at RIKEN RI Beam Factory, RCNP Osaka University, and CYRIC Tohoku University.

She is also grateful for the strong supports from the theorists, H. Witała, W. Glöckle, H. Kamada, J. Golak, A. Nogga, R. Skibiński, P. U. Sauer, A. Deltuva, and A. C. Fonseca.

## References

- [1] W. Glöckle, H. Witała, D. Hüber, H. Kamada and J. Golak, Phys. Rep. **274**, 107 (1996).
- [2] H.-W. Hammer, A. Nogga and A. Schwenk, Rev. Mod. Phys. **85** 197 (2013) *and references therein*.
- [3] N. Kalantar-Nayestanaki, E. Epelbaum, J. G. Messchendorp and A. Nogga, Rep. Prog. Phys. **75**, 016301 (2012).
- [4] S. C. Pieper, V. R. Pandharipande, R. B. Wiringa and J. Carlson, Phys. Rev. C. **64**, 014001 (2001).
- [5] S. Gandolfi, J. Carlson, S. Reddy, A. W. Steiner and R. B. Wiringa, Eur. Phys. J. A **50**, 10 (2014).
- [6] A. Deltuva and A. C. Fonseca, Phys. Rev. C **87**, 054002 (2013).
- [7] M. Viviani, L. Girlanda, A. Kievsky and L. E. Marcucci, Phys. Rev. Lett. **111**, 172302 (2013).
- [8] N. Sakamoto *et al.*, Phys. Lett. B **367**, 60 (1996); H. Sakai *et al.*, Phys. Rev. Lett. **84**, 5288 (2000); K. Sekiguchi *et al.*, Phys. Rev. C **65**, 034003 (2002); K. Sekiguchi *et al.*, *ibid.* **70**, 014001 (2004); K. Sekiguchi *et al.*, Phys. Rev. Lett **95**, 162301 (2005).
- [9] K. Sekiguchi *et al.*, Phys. Rev. C **83**, 061001(R) (2011).
- [10] K. Sekiguchi *et al.*, Phys. Rev. C **89**, 064007 (2014).
- [11] K. Sekiguchi *et al.*, Phys. Rev. C **96**, 064001 (2017).
- [12] S. A. Coon and H. K. Han, Few-Body Syst. **30**, 131 (2001).
- [13] S. A. Coon and W. Glöckle, Phys. Rev. C **23**, 1790 (1981).
- [14] J. L. Friar, D. Hüber and U. van Kolck, Phys. Rev. C **59**, 53 (1999).
- [15] D. Hüber, J. L. Friar, A. Nogga, H. Witała and U. van Kolck, Few-Body Syst. **30**, 95 (2001).
- [16] B. S. Pudliner, V. R. Pandharipande, J. Carlson, S. C. Pieper and R. B. Wiringa, Phys. Rev. C **56**, 1720 (1997).
- [17] A. Deltuva, A. C. Fonseca and P. U. Sauer, Phys. Rev. C **71**, 054005 (2005).
- [18] K. Hatanaka *et al.*, Phys. Rev. C **66**, 044002 (2002); Y. Maeda *et al.*, *ibid.* **76**, 014004 (2007).

- 
- [19] A. Ramazani-Moghaddam-Arani *et al.*, Phys. Rev. C **78**, 014006 (2008).
- [20] H. Witała, J. Gólał, R. Skibiński, W. Glöckle, H. Kamada and W. N. Polyzou, Phys. Rev. C **83**, 044001 (2011); Erratum: *ibid.* **88**, 069904(E) (2013).
- [21] S. Binder *et al.*, Phys. Rev. C **93**, 044002 (2016).
- [22] E. Epelbaum, *private communications*.
- [23] Y. Wada, Ph.D. thesis, Tohoku University, 2017.
- [24] P. Doleschall, Phys. Rev. C **69**, 054001 (2004).
- [25] A. Deltuva, *private communications*.

# Nucleon-Deuteron Scattering with Chiral Semilocal Coordinate Space and Momentum Space Regularized Interactions

R. Skibiński, J. Gólał, A. Grassi, V. Soloviov, K. Topolnicki,  
V. Urbanevych, Yu. Volkotrub and H. Witała

*M. Smoluchowski Institute of Physics, Jagiellonian University, PL30-348 Kraków, Poland*

## Abstract

The nucleon-deuteron elastic scattering reaction is investigated using two chiral models of the two-body interaction with semilocal regularization proposed by E. Epelbaum *et al.* and by P. Reinert *et al.* In particular, we give predictions for the differential cross section and the deuteron tensor analyzing power  $T_{22}$  at energies of the incoming nucleon up to 200 MeV. Both models deliver a qualitatively similar description of the nucleon-deuteron elastic scattering data. However, we find the model by P. Reinert *et al.* to be less sensitive to the values of regularization parameters used. For this interaction the long-standing problem of the cut-off dependence of three-nucleon predictions is practically absent, as the uncertainty of studied observables related to regularization parameters remains below 1% at most of the scattering angles. Only in the worst case of  $T_{22}$  at  $E = 200$  MeV and for specific scattering angles this uncertainty amounts to 7%.

**Keywords:** *Nuclear forces; chiral effective field theory; nucleon-deuteron scattering; few-body systems*

## 1 Introduction

The Chiral Effective Field Theory ( $\chi$ EFT) has dominated studies of the nuclear forces since the beginning of the 21st century. The ideas introduced by S. Weinberg [1–3], J. Gasser and H. Leutwyler [4, 5], C. Ordóñez and U. van Kolck [6], and many others (see Refs. [7, 8] for a historical background and a general introduction to the  $\chi$ EFT), resulted in various models of the nuclear interaction [9–14]. The two recent models from this group are the chiral interaction with semilocal regularization performed in the coordinate space (SCS) [12, 13] and the chiral interaction with semilocal regularization applied in the momentum space (SMS) [14]. The nucleon-nucleon ( $NN$ ) interaction has been derived completely up to the fifth order of the chiral expansion (N4LO) in both models. Additionally, in the SMS interaction also some terms from the sixth order of the chiral expansion have been incorporated. This, together with other improvements introduced to the SMS model, has resulted in the best  $NN$  data

---

*Proceedings of the International Conference ‘Nuclear Theory in the Supercomputing Era — 2018’ (NTSE-2018), Daejeon, South Korea, October 29 – November 2, 2018, eds. A. M. Shirokov and A. I. Mazur. Pacific National University, Khabarovsk, Russia, 2019, p. 115.*

<http://www.ntse.khb.ru/files/uploads/2018/proceedings/Skibinski.pdf>.

description obtained so far, achieving  $\chi^2/data \approx 1$  (see Ref. [14] for more specific values, which depend on the energy range, isospin channel, order of chiral expansion and values of regulator parameters).

The applications of both models beyond the two-nucleon system are ongoing. They are more advanced for the SCS interaction which has been already used to study the nucleon-deuteron scattering and properties of the light and medium mass nuclei [15–18] as well as to investigate the deuteron and  $^3\text{He}$  photodisintegrations, the nucleon-deuteron radiative capture, and muon capture in the deuteron and  $^3\text{He}$  [19]. Summarizing these studies one can conclude that the SCS interaction shows its good quality also in many-nucleon systems. Using only the two-body interaction, a nice convergence with respect to the chiral order is observed for all observables. The cut-off dependence, i. e., the dependence on the regulator parameter value, is small, however for the nucleon-deuteron scattering at higher energies and the energies of nuclear states it is not negligible. The three-nucleon interaction consistent with the SCS two-body force has been applied so far only up to the next-to-next-to-leading order (N2LO) to study elastic nucleon-deuteron scattering and structure of chosen nuclei. At this order of chiral expansion, where only the leading contributions to the three-nucleon interaction are present, the SCS model describes data with a precision similar to the semi-phenomenological models, like the combination of the AV18  $NN$  force [20] with the Urbana IX three-nucleon interaction [21] discussed in detail, e. g., in Ref. [22]. Combining the chiral N2LO three-nucleon force with the N4LO two-nucleon interactions does not change that picture [18]. This shows that to improve the data description, the three-nucleon force at higher orders of chiral expansion has to be included. Unfortunately, an explicit regularization of the chiral three-nucleon force in the coordinate space is very challenging and has not been done beyond the N2LO order yet. The regularization in the momentum space gives more hope. While currently the three-nucleon force consistent with the  $NN$  interaction with the semilocal regularization in the momentum space is under construction, the application of the two-body interaction [14] is a first step towards obtaining a complete (i. e.,  $NN + 3N + 4N + \dots$ ) chiral interaction at higher orders of the chiral expansion.

In this contribution, we focus on the nucleon-deuteron elastic scattering process and would like to test the dependence of the predictions for the differential cross section and the deuteron tensor analyzing power  $T_{22}$  on the regulator values used in the SCS and the SMS interactions.

## 2 Formalism

The nucleon-deuteron scattering can be described within the formalism of Faddeev equations [23, 24]. In practical applications, we solve the Faddeev equation for an auxiliary state  $T|\phi\rangle$ ,

$$T|\phi\rangle = tP|\phi\rangle + (1+tG_0)V_4^{(1)}(1+P)|\phi\rangle + tPG_0T|\phi\rangle + (1+tG_0)V_4^{(1)}(1+P)G_0T|\phi\rangle, \quad (1)$$

and from its solutions all physical observables for elastic nucleon-deuteron scattering and the deuteron breakup reaction are obtained [25]. The ingredients of Eq. (1) are the off-the-energy shell  $NN$   $t$ -matrix  $t$  related to the  $NN$  interaction via the Lippmann–Schwinger equation, the three-body permutation operator  $P$ , the free  $3N$  propagator  $G_0$ , and the initial channel state  $|\phi\rangle$  composed of a momentum eigenstate

of the projectile nucleon and a deuteron. On top of the two-nucleon forces also a three-nucleon force is included, and  $V_4^{(1)}$  is that part of it which is symmetrical under the exchange of nucleons 2 and 3. Equation (1) accounts for an infinite sequence of two-body and three-body rescattering processes with free propagations in between. In Ref. [23] the path to the cross section and spin observables is described in detail.

We solve Eq. (1) in the partial wave basis and take into account all two-body channels up to the  $2N$  total angular momentum  $j_{max} = 5$  and the  $3N$  total angular momentum  $J_{max} = \frac{25}{2}$ . This number of partial waves is sufficient to achieve the convergence of predictions at both presented here energies. Since the consistent three-nucleon interaction is not available for the SMS model, we restrict ourselves only to the  $NN$  interaction and set  $V_4^{(1)} = 0$ . Thus we will not discuss the importance of the three-nucleon interaction for the nucleon-deuteron elastic scattering reaction.

### 3 Results

In the following we compare the cut-off dependence of our predictions for the differential cross section and the deuteron tensor analyzing power  $T_{22}$  obtained with two semilocal regularized interactions at N4LO. We choose two kinetic energies of the incoming nucleon in the laboratory (lab) system:  $E = 65$  MeV and  $E = 200$  MeV. While the first one is well within the range of applicability of chiral forces at the order used, for the second one it is expected that contributions from the higher orders of the chiral expansion can still play some role. We refer the reader to Ref. [26] for a more detailed discussion based on the analysis of the truncation errors.

The differential cross section at  $E = 65$  MeV is shown in Fig. 1. It is clear that at

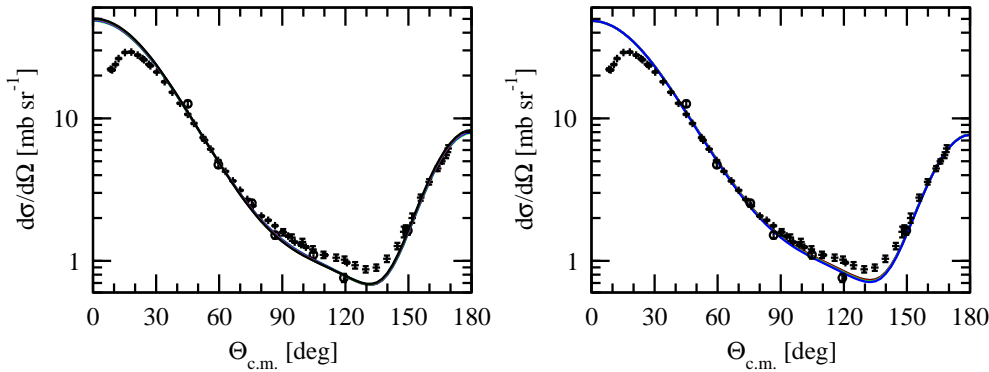


Figure 1: Differential cross sections for the elastic nucleon-deuteron scattering at the incoming nucleon energy in the lab system  $E = 65$  MeV. The predictions have been obtained with the N4LO SCS potential (left) and the N4LO SMS force (right). In the left panel, curves are the predictions obtained with the following values of the regulator parameter  $R$ : 1.2 fm (black), 1.1 fm (dark green), 1.0 fm (magenta), 0.9 fm (blue), and 0.8 fm (green). In the right panel, curves are the predictions obtained with the following values of the regulator parameter  $\Lambda$ : 400 MeV (black), 450 MeV (red), 500 MeV (green), and 550 MeV (blue). The experimental data are taken from Refs. [27] (pluses) and [28] (circles).

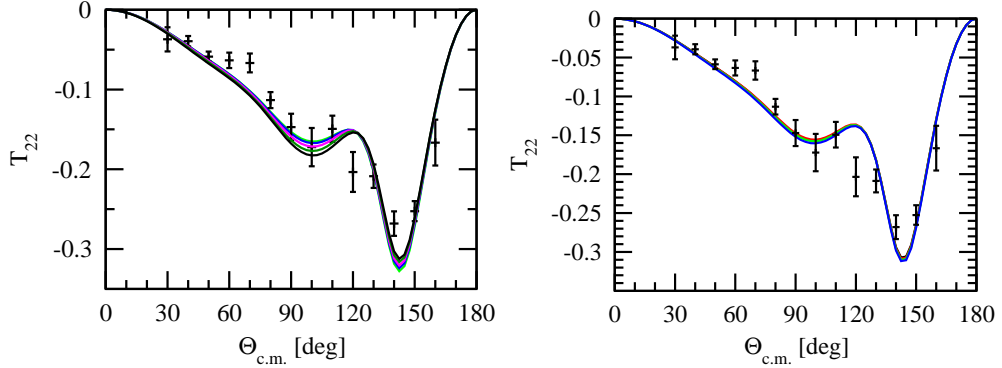


Figure 2: Deuteron tensor analyzing power  $T_{22}$  for the elastic nucleon-deuteron scattering at the incoming nucleon energy in the lab system  $E = 65$  MeV. Curves are the same as in Fig. 1. The experimental data are taken from Ref. [29].

this energy the dependence of the predictions on the regulator parameters is insignificant for both potentials. All predictions are close to each other and the maximal difference between them for all scattering angles is smaller than the experimental uncertainties. The observed discrepancy with data in the minimum of the cross section stems from neglecting three-nucleon forces in calculations presented here.

Another picture is observed at the same energy,  $E = 65$  MeV, for the deuteron tensor analyzing power  $T_{22}$ , see Fig. 2. Here the predicted magnitude of the  $T_{22}$  clearly depends on the value of the regulator  $R$  used for the SCS model. This dependence is especially strong at both minima of the  $T_{22}$  seen around scattering angles  $\theta_{c.m.} = 100^\circ$  and  $\theta_{c.m.} = 145^\circ$ . The spread of predictions amounts up to 10% for the first minimum and up to 5% for the latter one and predictions obtained with  $R = 0.8$  fm and  $R = 1.2$  fm are the extreme ones for both minima. The SMS interaction predictions are much less sensitive to the value of the cut-off parameter. Here at the minimum around  $\theta_{c.m.} = 100^\circ$  the spread of predicted values of  $T_{22}$  is 3% and at the minimum around  $\theta_{c.m.} = 145^\circ$  it amounts up to approximately 1.3%.

The cut-off dependence grows with energy. This is shown for the cross section at  $E = 200$  MeV in Fig. 3 and for the deuteron tensor analyzing power  $T_{22}$  at the same energy in Fig. 4. At such a high energy, the cut-off dependence is seen already for the cross section when the SCS potential is used. Using various values of the regulator  $R$  leads to substantially different predictions not only near the minimum of the cross section but nearly for all scattering angles. The SMS model works much better at this energy and we observe only a tiny cut-off dependence in the minimum of the cross section. The SCS potential fails also for the  $T_{22}$ , especially at the scattering angles  $60^\circ \leq \theta_{c.m.} \leq 150^\circ$ . At  $\theta_{c.m.} = 110^\circ$  the spread of predictions exceeds 65%. The SMS potential delivers a much more stable description in this case. While the cut-off dependence of predictions is also seen in the range  $60^\circ \leq \theta_{c.m.} \leq 150^\circ$ , it is much smaller and at  $\theta_{c.m.} = 110^\circ$  predictions differ by less than 7%. Outside the  $60^\circ \leq \theta_{c.m.} \leq 150^\circ$  range, the predictions based on various values of regulators remain practically the same for both models of the interaction used.

Summarizing, we can confirm that the newest chiral interaction derived by the Bochum group [14] preserves its high quality when moving from two- to three-nucleon

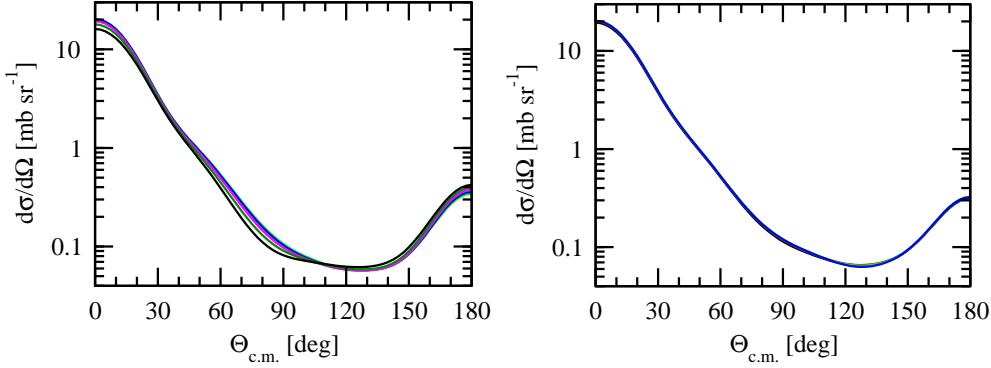


Figure 3: Differential cross section for the elastic nucleon-deuteron scattering at the incoming nucleon energy in the lab system  $E = 200$  MeV. Curves are the same as in Fig. 1.

system. We found that for this model the predictions for the elastic nucleon-deuteron scattering practically do not depend (at N4LO) on the value of regulator used. This property eliminates one of the most important difficulties in practical applications of the chiral forces in many-nucleon systems and in the detailed analysis of the data and properties of nuclear forces. The lack of the cut-off dependence also reduces the theoretical uncertainties present in studying various secondary effects like, i. e., the role of many-nucleon forces. A study of the cut-off dependence of the three- and many-body observables including the consistent SMS three-nucleon force is in progress.

## Acknowledgements

We would like to thank E. Epelbaum and P. Reinert and other members of the LENPIC Collaboration for helpful discussions. This work was supported by the Polish

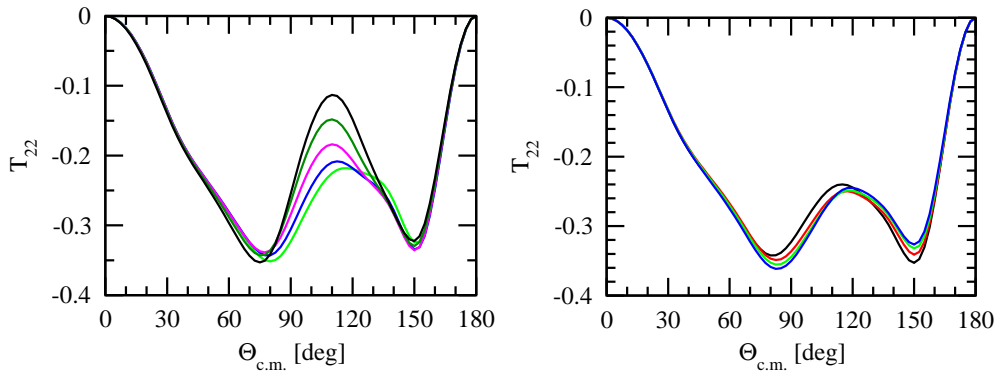


Figure 4: Deuteron tensor analyzing power  $T_{22}$  for the elastic nucleon-deuteron scattering at the incoming nucleon energy in the lab system  $E = 200$  MeV. Curves are the same as in Fig. 1.

National Science Centre under Grants No. 2016/22/M/ST2/00173 and No. 2016/21/D/ST2/01120. Numerical calculations were performed on the super-computer cluster of the JSC, Jülich, Germany.

## References

- [1] S. Weinberg, *Physica A* **96**, 327 (1979).
- [2] S. Weinberg, *Phys. Lett. B* **251**, 288 (1990).
- [3] S. Weinberg, *Nucl. Phys. B* **363**, 3 (1991).
- [4] J. Gasser and H. Leutwyler, *Ann. Phys. (NY)* **158**, 142 (1984).
- [5] J. Gasser and H. Leutwyler, *Nucl. Phys. B* **250**, 465 (1985).
- [6] C. Ordóñez and U. van Kolck, *Phys. Lett. B* **291**, 459 (1992).
- [7] E. Epelbaum, H.-W. Hammer and U.-G. Meißner, *Rev. Mod. Phys.* **81**, 1773 (2009).
- [8] E. Epelbaum, *Lectures given at the 2009 Joliot-Curie school, Lacanau, France, 27.09–3.10.2009*; arXiv:1001.3229 [nucl-th] (2010).
- [9] E. Epelbaum *et al.*, *Nucl. Phys. A* **637**, 107 (1998).
- [10] E. Epelbaum *et al.*, *Nucl. Phys. A* **671**, 295 (2000).
- [11] E. Epelbaum *et al.*, *Phys. Rev. C* **66**, 064001 (2002).
- [12] E. Epelbaum, H. Krebs and U.-G. Meißner, *Phys. Rev. Lett.* **115**, 122301 (2015).
- [13] E. Epelbaum, H. Krebs and U.-G. Meißner, *Eur. Phys. J. A* **51**, 53 (2015).
- [14] P. Reinert, H. Krebs and E. Epelbaum, *Eur. Phys. J. A* **54**, 86 (2018).
- [15] S. Binder *et al.*, *Phys. Rev. C* **93**, 044002 (2016).
- [16] S. Binder *et al.*, *Phys. Rev. C* **98**, 014002 (2018).
- [17] E. Epelbaum *et al.*, *Phys. Rev. C* **99**, 024313 (2019).
- [18] H. Witała *et al.*, *Few-Body Syst.* **60**, 19 (2019).
- [19] R. Skibiński *et al.*, *Phys. Rev. C* **93**, 064002 (2016).
- [20] R. B. Wiringa, V. G. J. Stoks and R. Schiavilla, *Phys. Rev. C* **51**, 38 (1995).
- [21] B. S. Pudliner *et al.*, *Phys. Rev. C* **56**, 1720 (1997).
- [22] H. Witała *et al.*, *Phys. Rev. C* **63**, 024007 (2001).
- [23] W. Glöckle, H. Witała, D. Hüber, H. Kamada and J. Golak, *Phys. Rep.* **274**, 107 (1996).

- 
- [24] W. Glöckle, *The quantum-mechanical few-body problem*. Springer-Verlag, Berlin, 1983.
- [25] D. Hüber, H. Kamada, H. Witała and W. Glöckle, *Acta Phys. Polon. B* **28**, 167 (1997).
- [26] R. Skibiński, Yu. Volkotrub, J. Golak, K. Topolnicki and H. Witała, *Phys. Rev. C* **98**, 014001 (2018).
- [27] S. Shimizu *et al.*, *Phys. Rev. C* **52**, 1193 (1995).
- [28] H. Rühl *et al.*, *Nucl. Phys. A* **524**, 377 (1991).
- [29] H. Witała *et al.*, *Few-Body Syst.* **15**, 67 (1993).

# ${}^3\text{H}$ and ${}^3\text{He}$ Bound State Calculations without Angular Momentum Decomposition

K. Topolnicki, J. Golak, R. Skibiński, H. Witała,  
Yu. Volkotrub, V. Soloviov and A. Grassi

*M. Smoluchowski Institute of Physics, Jagiellonian University, PL-30348 Kraków, Poland*

## Abstract

Recent advances in the so-called “three dimensional” ( $3D$ ) formalism made it possible to perform numerically efficient calculations of the three-nucleon ( $3N$ ) bound states that utilize  $3N$  forces. In this paper we present results related to the  ${}^3\text{H}$  bound state. We also discuss our way of incorporating the Coulomb forces in  $3D$  calculations of the  ${}^3\text{He}$  bound state.

**Keywords:** *Few-nucleon forces; three-nucleon system; bound states*

## 1 Introduction

An introduction to the  $3D$  approach can be found in Ref. [1]. In this approach, few-nucleon calculations are carried out without using the partial wave decomposition and instead the three-dimensional momentum degrees of freedom of the nucleons are used. Some previous work related to the  $3N$  bound state was reported in Refs. [2,3]. Below we provide a brief summary of the formalism used in these papers.

The starting point of the calculation is the operator form of the Faddeev component  $|\psi\rangle$  of the  $3N$  bound state  $|\Psi\rangle$  [3,4]:

$$\langle \mathbf{p}\mathbf{q}; \left(t\frac{1}{2}\right)TM_T | \psi \rangle = \sum_{i=1}^8 \psi_{tT}^{(i)}(\mathbf{p}, \mathbf{q}, \hat{\mathbf{p}} \cdot \hat{\mathbf{q}}) \check{O}_i(\mathbf{p}, \mathbf{q}) |\chi^m\rangle. \quad (1)$$

In Eq. (1),  $\psi_{tT}^{(i)}(\mathbf{p}, \mathbf{q}, \hat{\mathbf{p}} \cdot \hat{\mathbf{q}})$  are scalar functions that effectively define the Faddeev component  $|\psi\rangle$ ,  $\check{O}_i(\mathbf{p}, \mathbf{q})$  are operators in the spin space of the  $3N$  system (they are listed in Ref. [3]),  $|(t\frac{1}{2})TM_T\rangle$  is a  $3N$  isospin state in which the isospins of two nucleons are coupled to  $t$  and then further coupled with the isospin of the third particle to the total isospin  $T$  with projection  $M_T$ . Finally  $\mathbf{p}, \mathbf{q}$  are Jacobi momenta and  $|\chi^m\rangle$  is a  $3N$  spin state (given explicitly in Ref. [3]).

The operator form (1) is plugged into the Faddeev equation (note that we use a version of the Faddeev equation without the two nucleon transition operator):

$$|\psi\rangle = \check{G}_0(E) \left( \check{V} + \check{V}^{(1)} \right) (\check{1} + \check{P}) |\psi\rangle, \quad (2)$$

---

*Proceedings of the International Conference ‘Nuclear Theory in the Supercomputing Era — 2018’ (NTSE-2018), Daejeon, South Korea, October 29 – November 2, 2018, eds. A. M. Shirokov and A. I. Mazur. Pacific National University, Khabarovsk, Russia, 2019, p. 122.*

<http://www.ntse.khb.ru/files/uploads/2018/proceedings/Topolnicki.pdf>.

where  $\check{V}$  is the two-nucleon ( $2N$ ) potential acting between particles 2 and 3,  $\check{V}^{(1)}$  is a part of the  $3N$  potential that is symmetric with respect to the exchange of particles 2 and 3,  $\check{G}_0(E)$  is the free propagator for energy  $E$  and finally  $\check{P} = \check{P}_{12}\check{P}_{23} + \check{P}_{13}\check{P}_{23}$  is an operator composed from transpositions  $\check{P}_{ij}$ . After removing the spin dependencies from the resulting equations, Eq. (2) is transformed into

$$\check{A}(E)\psi = \psi, \quad (3)$$

where the energy-dependent operator  $\check{A}(E)$  acts in a linear space spanned by the scalar functions  $\psi (\equiv \psi_{iT}^{(i)}(p, q, \hat{\mathbf{p}} \cdot \hat{\mathbf{q}}))$  that appear in Eq. (1). In practice a slightly different equation is solved:

$$\check{A}(E)\psi = \lambda\psi, \quad (4)$$

and various values of the energy  $E$  are checked looking for the one that yields  $\lambda = 1$ , so the corresponding energy is the bound state energy. The resulting scalar functions  $\psi$  can be used to reconstruct the Faddeev component.

The full bound state wave function of the  $3N$  system  $|\Psi\rangle$  is related to the Faddeev component  $|\psi\rangle$  via

$$|\Psi\rangle = (\check{1} + \check{P})|\psi\rangle. \quad (5)$$

The operator form (1) can also be used to represent the full bound state function  $|\Psi\rangle$  where it will be defined by a different set of scalar functions  $\Psi (\equiv \Psi_{iT}^{(i)}(p, q, \hat{\mathbf{p}} \cdot \hat{\mathbf{q}}))$ . The operator forms of  $|\Psi\rangle$  and  $|\psi\rangle$  can be inserted into Eq. (5) and the spin dependencies can be removed. This results in the following equation:

$$\Psi = \check{B}\psi, \quad (6)$$

where the operator  $\check{B}$  acts in a linear space spanned by the scalar functions that define the Faddeev component.

## 2 Numerical results

We show in Figs. 1 and 2 selected scalar functions ( $\psi^{(1)}, \Psi^{(1)}$  and  $\psi^{(2)}, \Psi^{(2)}$ , respectively) for the Faddeev component  $|\psi\rangle$  and the full bound state function  $|\Psi\rangle$  of  ${}^3\text{H}$ . These results were obtained using the same  $2N$  and  $3N$  potentials as in Ref. [3].

In order to verify our solutions, all plots related to the Faddeev component  $|\psi\rangle$  also contain the functions

$$\beta = \check{A}\psi. \quad (7)$$

Since the functions  $\psi$  satisfy Eq. (4) with  $\lambda \approx 1$ , the two functions,  $\psi$  and  $\beta$ , should overlap. Additionally all plots related to the full  $3N$  bound state function  $|\Psi\rangle$  also contain functions

$$\frac{1}{3}\zeta = \frac{1}{3}\check{B}|\Psi\rangle. \quad (8)$$

Since the operator  $\check{B}$  is directly related to  $\check{1} + \check{P}$ , acting with this operator on the Faddeev scalar functions twice results in a multiplying factor of 3. It can be expected that  $\Psi = \frac{1}{3}\zeta$ .

The calculations presented in Figs. 1 and 2 both benefit from the new method of implementing the  $3N$  forces described in Ref. [5]. That paper also contains results related to the  ${}^3\text{He}$  bound state with a screened Coulomb potential from Ref. [6]. The

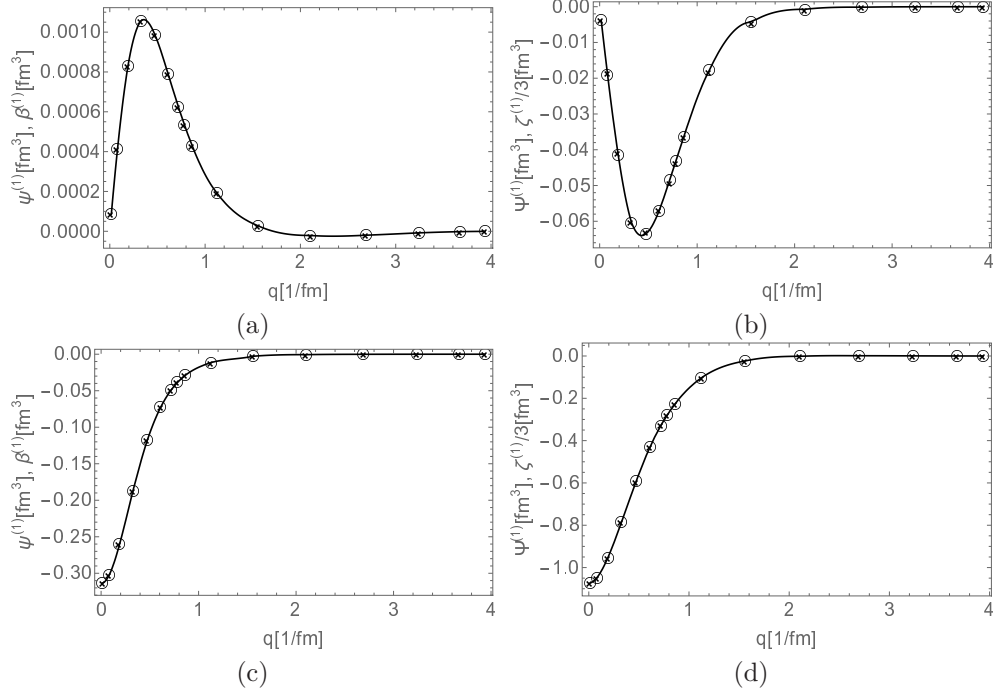


Figure 1: Selected scalar functions for the Faddeev component of the  ${}^3\text{H}$  bound state are shown in the first column, panels (a), (c). The values of the  $\psi$  (circles) and  $\beta$  (crosses) functions practically overlap, verifying the solution. Chosen scalar functions for the full bound state of  ${}^3\text{H}$  are shown in the second column, panels (b), (d). The values of the  $\Psi$  (circles) and  $\frac{1}{3}\zeta$  (crosses) functions practically overlap, again verifying the obtained solution. All plots show the  $t = 0$ ,  $T = \frac{1}{2}$  components with  $p = 0.355851 \text{ fm}^{-1}$ ,  $\hat{\mathbf{p}} \cdot \hat{\mathbf{q}} = -0.950676$ . The presented calculations used an improved implementation of the  $3N$  force from Ref. [5], and the resulting value of the bound state energy is  $-8.62 \text{ MeV}$ .

implementation of the Coulomb interaction in  $3D$  calculations is straightforward and requires only modifications in certain sets of integration points. The value of the bound state energy for  ${}^3\text{He}$  obtained in Ref. [5] is  $-7.73 \text{ MeV}$ .

### 3 Summary

The new implementation of the  $3N$  force in  $3D$  calculations described in Ref. [5] makes it possible to test a wide variety of nuclear interactions. Although the calculations presented in Ref. [5] were carried out with a small number of grid points for the scalar functions, the results are encouraging and we plan future calculations with a larger number of integration points. This will require adaptation of our code to an efficient use of the JURECA booster computer at the Jülich Supercomputing Center. This will increase the precision of the  $3D$  calculations and allow us to test the newest versions of two- and three-nucleon forces.

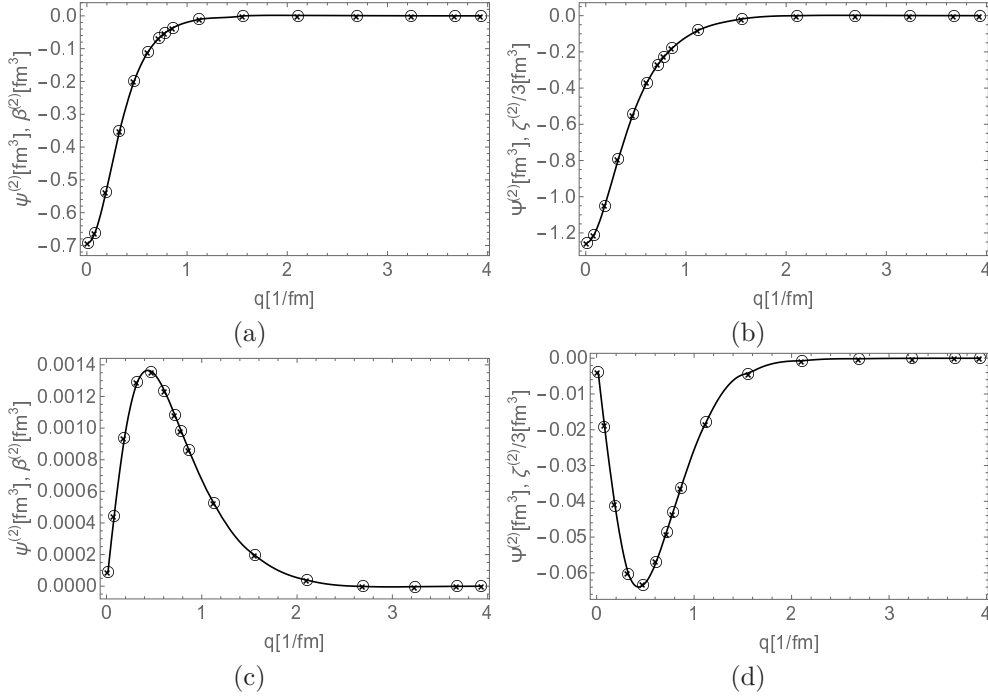


Figure 2: Selected scalar functions for the Faddeev component of the  ${}^3\text{H}$  bound state are shown in the first column, panels (a), (c). The values of the  $\psi$  (circles) and  $\beta$  (crosses) functions practically overlap, verifying the solution. Chosen scalar functions for the full bound state of  ${}^3\text{H}$  are shown in the second column, panels (b), (d). The values of the  $\Psi$  (circles) and  $\frac{1}{3}\zeta$  (crosses) functions practically overlap, again verifying the obtained solution. All plots show the  $t = 1, T = \frac{1}{2}$  components with  $p = 0.355851 \text{ fm}^{-1}$ ,  $\hat{\mathbf{p}} \cdot \hat{\mathbf{q}} = -0.950676$ . The presented calculations used an improved implementation of the 3N force from Ref. [5], and the resulting value of the bound state energy is  $-8.62 \text{ MeV}$ .

## Acknowledgments

The project was financed from the resources of the National Science Center, Poland, under grants 2016/22/M/ST2/00173 and 2016/21/D/ST2/01120. The numerical calculations were performed on the supercomputing clusters of the Jülich Supercomputing Center, Jülich, Germany.

## References

- [1] H. Witała, J. Gólał, R. Skibiński and K. Topolnicki, *J. Phys. G* **41**, 094011 (2014).
- [2] W. Glöckle, Ch. Elster, J. Gólał, R. Skibiński, H. Witała and H. Kamada, *Few-Body Syst.* **47**, 25 (2010).
- [3] J. Gólał, K. Topolnicki, R. Skibiński, W. Glöckle, H. Kamada and A. Nogga, *Few-Body Syst.* **54**, 2427 (2013).

- [4] I. Fachruddin, W. Glöckle, Ch. Elster and A. Nogga, Phys. Rev. C **69**, 064002 (2004).
- [5] K. Topolnicki, Phys. Rev. C **99**, 044004 (2019).
- [6] M. Rodríguez-Gallardo, A. Deltuva, E. Cravo, R. Crespo, A. C. Fonseca, Phys. Rev. C **78**, 034602 (2008).

# Unphysical Sheets and Resonances for the Friedrichs–Faddeev Model

Alexander K. Motovilov

*Bogoliubov Laboratory of Theoretical Physics, JINR, 6 Joliot-Curie, 141980 Dubna, Russia  
Dubna State University, 19 Universitetskaya, 141980 Dubna, Russia*

## Abstract

The Friedrichs–Faddeev model is considered in the case where the kernel of the potential operator is holomorphic in both arguments on a certain complex domain. For this model, we, first, derive representations for the transition operator and scattering matrix continued on unphysical energy sheet(s) that explicitly express them in terms of the same operators exclusively on the physical sheet. Then the Friedrichs–Faddeev Hamiltonian becomes subject to a complex deformation. We show that, in the case under consideration, the deformation resonances (non-real eigenvalues of the deformed Hamiltonian) are nothing but the scattering matrix resonances, i. e., they represent the poles of the scattering matrix analytically continued on the respective unphysical energy sheet.

**Keywords:** *Friedrichs–Faddeev model; complex deformation; resonances; unphysical sheets*

## 1 Introduction

Assume that  $\mathfrak{h}$  is a Hilbert space and let  $\Delta = (a, b)$ , where  $-\infty \leq a < b \leq \infty$ . Denote by  $L_2(\Delta, \mathfrak{h})$  the Hilbert space of  $\mathfrak{h}$ -valued functions of  $\lambda \in (a, b)$  with the scalar product

$$\langle f, g \rangle = \int_a^b d\lambda \langle f(\lambda), g(\lambda) \rangle_{\mathfrak{h}},$$

where  $\langle \cdot, \cdot \rangle_{\mathfrak{h}}$  stands for the scalar product in  $\mathfrak{h}$ . The Hamiltonian of the Friedrichs–Faddeev model has the form

$$H = H_0 + V \tag{1.1}$$

with  $H_0$  being the operator of multiplication by an independent variable in  $L_2(\Delta, \mathfrak{h})$ ,

$$(H_0 f)(\lambda) = \lambda f(\lambda), \quad \lambda \in \Delta, \quad f \in L_2(\Delta, \mathfrak{h}), \tag{1.2}$$

and  $V$  being an integral operator,

$$(Vf)(\lambda) = \int_a^b V(\lambda, \mu) f(\mu) d\mu. \tag{1.3}$$

---

*Proceedings of the International Conference ‘Nuclear Theory in the Supercomputing Era — 2018’ (NTSE-2018), Daejeon, South Korea, October 29 – November 2, 2018, eds. A. M. Shirokov and A. I. Mazur. Pacific National University, Khabarovsk, Russia, 2019, p. 127.*

<http://www.ntse.khb.ru/files/uploads/2018/proceedings/Motovilov.pdf>.

It is assumed that, for every  $\lambda, \mu \in \Delta$ , the quantity  $V(\lambda, \mu)$  is a bounded linear operator on  $\mathfrak{h}$  such that  $V(\lambda, \mu) = V(\mu, \lambda)^*$ , and, in addition,  $V$  is a Hölder continuous operator-valued function of  $\lambda, \mu \in \overline{\Delta}$ . Furthermore, one requires

$$V(a, \mu) = V(b, \mu) = V(\lambda, a) = V(\lambda, b) = 0 \quad \text{in the case of finite } a \text{ or/and } b \quad (1.4)$$

or imposes suitable requirements on the rate of decreasing of  $V(\lambda, \mu)$  as  $|\lambda|, |\mu| \rightarrow \infty$  in the case of infinite  $a$  or/and  $b$ .

In its starting form the model (1.1)–(1.4) was introduced by K. Friedrichs [1] who considered the Hamiltonian

$$H_\epsilon = H_0 + \epsilon V, \quad \epsilon > 0, \quad (1.5)$$

with  $H_0$  and  $V$  given by (1.2) and (1.3) in the simplest case of one-dimensional internal Hilbert space  $\mathfrak{h} = \mathbb{C}$  and  $\Delta = (-1, 1)$ . The spectrum of the (self-adjoint) operator  $H_0$  is absolutely continuous and, in this case, coincides with the segment  $[-1, 1]$ . Friedrichs studied variation of the continuous spectrum of  $H_0$  under the perturbation  $\epsilon V$ . He has succeeded to prove that, if  $\epsilon$  is sufficiently small, then the spectrum of  $H_\epsilon$  remains absolutely continuous and still fills the segment  $[-1, 1]$ . In Ref. [2], Friedrichs has extended this result to the case of arbitrary finite- or infinite-dimensional Hilbert space  $\mathfrak{h}$  and arbitrary finite or infinite end points  $a$  and  $b$ . More precisely, he has proven that, if  $\epsilon > 0$  is small enough, then the perturbed operator (1.5) is unitarily equivalent to the unperturbed one,  $H_0$ , and, hence, the spectrum of  $H_\epsilon$  is absolutely continuous and fills the set  $\overline{\Delta}$ .

O. A. Ladyzhenskaya and L. D. Faddeev have dropped in Ref. [3] the assumption of smallness of the perturbation  $V$  and studied the model Hamiltonian (1.1)–(1.4) with not small  $\epsilon$  at  $V$ . However, instead of the smallness, they required compactness of the values of  $V(\lambda, \mu)$  as operators on  $\mathfrak{h}$  for all  $\lambda, \mu \in \Delta$ . Detail proofs for the results of Ref. [3] are presented by Faddeev in Ref. [4]. As a matter of fact, the paper [4] contains a complete version of the scattering theory for the model (1.1)–(1.4). Furthermore, the paper [4] may be viewed as a relatively simple introduction to the approach used by Faddeev in his celebrated study [5] of the three-body problem. Also notice that the typical two-body Schrödinger operator may be reduced to the Friedrichs–Faddeev model with  $a = 0$ ,  $b = +\infty$  and  $\mathfrak{h} = L_2(S^2)$ , where  $S^2$  is the unit sphere in  $\mathbb{R}^3$  (see Ref. [4]; cf. Ref. [6, Section 3]).

Faddeev’s in-depth study [4] of the Hamiltonian (1.1)–(1.4) is the main reason why this Hamiltonian is often referred to as the Friedrichs–Faddeev model. In addition, the double naming allows to distinguish the model (1.1)–(1.4) from another popular model due to Friedrichs contained in Ref. [2]. The second model from Ref. [2] involves a  $2 \times 2$  block matrix Hamiltonian and works well, in particular, in the theory of Feshbach resonances (see, e.g., Refs. [7, 8] and references therein). For later results just on the Friedrichs–Faddeev model and its generalizations, see Refs. [9–13].

In the present work, we adopt the ideas and approach from the previous works of the author [14, 15] in order to study the structure of the  $T$ - and  $S$ -matrices for the Friedrichs–Faddeev model continued on unphysical energy sheets neighboring the physical one. Namely, we obtain representations that explicitly express the continued  $T$ - and  $S$ -matrices in terms of the same operators considered exclusively on the physical sheet (see Lemmas 2.2 and 2.3 below). The obtained representations show, in particular, that a resonance on an unphysical sheet under consideration corresponds

to the energy  $z$  in the physical sheet where the scattering matrix has the zero eigenvalue.

We perform a complex deformation of the Friedrichs–Faddeev Hamiltonian. (Notice that the “usual” complex scaling [16, 17] may be understood as a particular case of the complex deformation, see Ref. [6, Section 3].) A complex discrete spectrum of the complexly-deformed Hamiltonian is interpreted as resonances. We show that these resonances are simultaneously the poles of the continued scattering (and  $T$ -) matrix on the unphysical sheet(s), that is, they are resonances in the sense of scattering theory. Recall that, in general, to prove the equivalence of the scaling resonances and scattering matrix resonances is a rather hard job (see Ref. [18]). In contrast, in the case of the Friedrichs–Faddeev model, the proof of such an equivalence is quite easy and illustrative.

Throughout the article, we denote by  $\sigma(T)$  the spectrum of a closed linear operator  $T$ . Notation  $T^*$  is used for the adjoint of  $T$ .  $T$  is called self-adjoint (Hermitian) if  $T^* = T$ . Notations  $\sigma_p(T)$  and  $\sigma_c(T)$  are used for the point and continuous spectra of  $T$ , respectively. By  $I_{\mathfrak{R}}$  we denote the identity operator on a vector space  $\mathfrak{R}$ ; the index  $\mathfrak{R}$  is omitted if no confusion arises. Notation  $\mathbb{C}^+ = \{z \in \mathbb{C} \mid \text{Im}z > 0\}$  ( $\mathbb{C}^- = \{z \in \mathbb{C} \mid \text{Im}z < 0\}$ ) is used for the upper (lower) halfplane of the complex plane  $\mathbb{C}$ .

The present paper represents a conference version of the work [6].

## 2 Structure of the $T$ - and $S$ -matrices on unphysical energy sheets

We consider the model (1.1)–(1.4) in the case where for each  $\lambda, \mu \in (a, b)$  the value of  $V(\lambda, \mu)$  is a compact operator in  $\mathfrak{h}$ . We assume, in addition, that the function  $V(\lambda, \mu)$  admits analytic continuation both in  $\lambda$  and  $\mu$  onto a domain  $\Omega \subset \mathbb{C}$  containing  $\Delta$ . More precisely, we suppose that

$$V(\lambda, \mu) \text{ is compact and holomorphic in both } \lambda, \mu \in \Omega, \quad \Omega \supset (a, b). \quad (2.1)$$

Also we assume that  $V(\lambda, \mu) = V(\mu, \lambda)^*$  for real  $\lambda, \mu \in \Delta$  (which is needed for the self-adjointness of  $V$ ). Surely, this implies  $V(\lambda, \mu) = V(\mu^*, \lambda^*)^*$  for any  $\lambda, \mu \in \Omega$  such that their conjugates  $\lambda^*, \mu^* \in \Omega$  and, hence, the domain  $\Omega$  should be mirror-symmetric with respect to the real axis.

Following Refs. [2, 4] one imposes some natural requirements on the rate of decreasing of  $V(\lambda, \mu)$  as  $|\lambda|, |\mu| \rightarrow \infty$  in the case of  $a = -\infty$  or/and  $b = +\infty$ . To unify the consideration, we simply assume that

$$\|V(\lambda, \mu)\| \leq K(1 + |\lambda| + |\mu|)^{-(1+\eta_1)}, \quad \eta_1 > 0; \quad (2.2)$$

$$\|V(\lambda + \alpha, \mu + \beta) - V(\lambda, \mu)\| \leq K(1 + |\lambda| + |\mu|)^{-(1+\eta_1)}(|\alpha|^{\eta_2} + |\beta|^{\eta_2}), \quad \eta_2 > 1/2, \quad (2.3)$$

with some  $K > 0$  for any  $\lambda, \mu \in \Omega$  and any  $\alpha, \beta$  such that  $\lambda + \alpha \in \Omega, \mu + \beta \in \Omega$ . Since  $V(\lambda, \mu)$  is holomorphic in both  $\lambda \in \Omega$  and  $\mu \in \Omega$ , the requirement (2.3) with  $\eta_2 < 1$  is essential only in the neighborhoods of the finite end points  $a$  and/or  $b$ . Otherwise, one may replace  $\eta_2$  with unity.

We use the standard notations for the resolvents,

$$R_0(z) := (H_0 - z)^{-1}, \quad R(z) := (H - z)^{-1},$$

and for the transition operator,

$$T(z) := V - VR(z)V. \quad (2.4)$$

Since, at least for  $z \notin \sigma(H_0) \cup \sigma(H)$ ,

$$R(z) = R_0(z) - R_0(z)T(z)R_0(z), \quad (2.5)$$

the study of the spectral problem for the perturbed Hamiltonian  $H = H_0 + V$  is reduced to the study of the transition operator ( $T$ -matrix)  $T(z)$ , the kernel of which is less singular than that of the resolvent  $R(z)$ .

From [4, Theorem 3.1] it follows that the kernel  $T(\lambda, \mu, z)$  is a well-behaved function of  $\lambda, \mu \in \Delta$  and  $z$  on the complex plane  $\mathbb{C}$  punctured at  $\sigma_p(H)$  and cut along  $[a, b]$ . Moreover,  $T(\lambda, \mu, z)$  is of the same class (2.2), (2.3) as  $V(\lambda, \mu)$  but with  $\eta_1$  and  $\eta_2$  replaced by positive  $\eta'_1 < \eta_1$  and  $\eta'_2 < \eta_2$  which may be chosen arbitrary close to  $\eta_1$  and  $\eta_2$ , respectively. The kernel  $T(\lambda, \mu, z)$  has limits

$$T(\lambda, \mu, E \pm i0), \quad E \in \Delta \setminus \sigma_p(H).$$

In our case, these limits are smooth in  $\lambda, \mu \in \Delta \setminus \sigma_p(H)$ . The scattering matrix for the pair  $(H_0, H)$  reads as

$$S_+(E) = I_{\mathfrak{h}} - 2\pi i T(E, E, E + i0), \quad E \in (a, b) \setminus \sigma_p(H).$$

Due to requirements (1.4) and (2.3) the point spectrum  $\sigma_p(H)$  of  $H$  represents a finite set of eigenvalues with finite multiplicities (see Ref. [4]; cf. Ref. [12]).

Recall that the  $T(\lambda, \mu, z)$  satisfies the following two Lippmann–Schwinger equations:

$$T(\lambda, \mu, z) = V(\lambda, \mu) - \int_a^b d\nu \frac{V(\lambda, \nu) T(\nu, \mu, z)}{\nu - z}, \quad (2.6)$$

$$T(\lambda, \mu, z) = V(\lambda, \mu) - \int_a^b d\nu \frac{T(\lambda, \nu, z) V(\nu, \mu)}{\nu - z}, \quad (2.7)$$

$$z \notin (a, b), \quad \lambda, \mu \in (a, b)$$

Substituting  $T(\nu, \mu, z)$  in the r.h.s. part of Eq. (2.6) by the r.h.s. part of Eq. (2.7), one obtains

$$\begin{aligned} T(\lambda, \mu, z) = & V(\lambda, \mu) - \int_a^b d\nu \frac{V(\lambda, \nu) V(\nu, \mu)}{\nu - z} \\ & + \int_a^b d\nu_1 \int_a^b d\nu_2 \frac{V(\lambda, \nu_1) T(\nu_1, \nu_2, z) V(\nu_2, \mu)}{(\nu_1 - z)(\nu_2 - z)}, \quad z \notin [a, b]. \end{aligned} \quad (2.8)$$

Since  $V(\lambda, \mu)$  is analytic in both  $\lambda, \mu \in \Omega$ , one easily concludes from Eq. (2.8) that the kernel  $T(\lambda, \mu, z)$  possesses the same holomorphy property. More detail statement is as follows.

**Proposition 2.1.** *If  $z \notin (a, b) \cup \sigma_p(H)$ , the function  $T(\lambda, \mu, z)$  is holomorphic in both  $\lambda \in \Omega$  and  $\mu \in \Omega$ . One can replace the interval  $(a, b)$  in Eqs. (2.6) and (2.7) by an arbitrary piecewise smooth Jordan contour  $\gamma \subset \Omega$  obtained from  $(a, b)$  by continuous transformation provided that the end points are fixed and the point  $z$  is avoided during the transformation  $(a, b) \rightarrow \gamma$ .*

For the sake of simplicity, in the following we usually assume that the numbers  $a, b \in \mathbb{R}$  are finite.

Now consider a smooth Jordan contour  $\gamma \subset \Omega \cap \mathbb{C}^\pm$  obtained from the interval  $(a, b)$  by a continuous transformation with the fixed end points  $a$  and  $b$ . From the Proposition 2.1 it follows that Eq. (2.6) can be equivalently written as

$$T(\lambda, \mu, z) = V(\lambda, \mu) - \int_{\gamma} d\nu \frac{V(\lambda, \nu) T(\nu, \mu, z)}{\nu - z}, \quad (2.9)$$

$$\lambda, \mu \in \Omega, \quad z \in \mathbb{C} \setminus \Omega_{\gamma},$$

where the set  $\Omega_{\gamma} \subset \mathbb{C}$  is confined by (and containing) the segment  $[a, b]$  and the curve  $\gamma$  (see Fig. 1). By applying to Eq. (2.9) the Faddeev’s approach of Ref. [4], one can prove that a solution  $T(\lambda, \mu, z)$  exists and is analytic on  $z$  for any

$$z \notin \sigma_p(H) \cup \overline{\gamma} \cup \sigma_{\text{res}}(\gamma), \quad (2.10)$$

where  $\sigma_{\text{res}}(\gamma)$  is a discrete set located inside  $\Omega_{\gamma}$ ; the overlining in  $\overline{\gamma}$  means the closure, that is,  $\overline{\gamma} = \gamma \cup \{a\} \cup \{b\}$ . Because of the holomorphy of  $V(\lambda, \mu)$  in  $\lambda, \mu \in \Omega$ , the solution  $T(\lambda, \mu, z)$  remains analytic in  $\lambda, \mu \in \Omega$  for any  $z \in \mathbb{C}$  satisfying (2.10). The points of  $\sigma_{\text{res}}(\gamma)$  (resonances) correspond to the poles of the solution  $T(z)$ , which residues are finite rank operators. Hence, Eq. (2.9) allows one to pull the argument  $z$  of  $T(z)$  from  $\mathbb{C}^+$  to  $\mathbb{C}^-$  at least into the interior of the set  $\Omega_{\gamma}$ . Of course, the points of  $\sigma_{\text{res}}(\gamma)$  should be avoided during this procedure.

It turns out, however, that, after such a continuation, the solution  $T(\lambda, \mu, z)$  for  $z \in \Omega \cap \mathbb{C}^-$  is taken on an unphysical sheet of the Riemann energy surface of  $T$ . This unphysical sheet is attached to the physical sheet along the upper rim of the cut of  $\mathbb{C}$  through the interval  $(a, b)$  and we denote it by  $\Pi_-$ . Thus, it is necessary to use a different notation, say,  $T'(\lambda, \mu, z)$  for the continuation of the kernel of  $T$  on  $\Pi_-$  (in order to distinguish it from  $T(z)$  at the same  $z$  on the physical energy sheet). By the

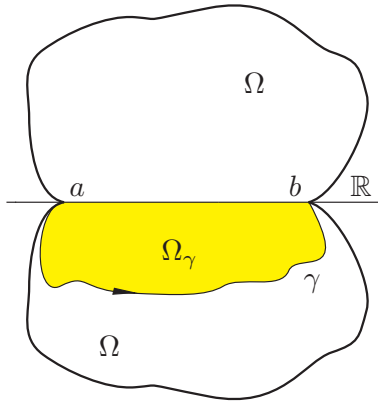


Figure 1: Domain  $\Omega$  where the kernel  $V(\lambda, \mu)$  is holomorphic both in  $\lambda$  and  $\mu$ . The set  $\Omega_{\gamma}$  is bounded by (and contains both) the Jordan contour  $\gamma$  and the segment  $[a, b]$ .

way, this kernel will coincide with the original one, that is,  $T'(\lambda, \mu, z) = T(\lambda, \mu, z)$ , provided  $z \in \mathbb{C} \setminus (\Omega_\gamma \cup \sigma_p(H))$ .

The amazing thing is that the continued equation (2.9) may be solved explicitly. To show this, let us assume that  $z \in \Omega_\gamma \setminus (\overline{\gamma} \cup \sigma_{\text{res}}(\gamma))$  and perform a two-step transformation of the contour  $\gamma$  (see Fig. 1) in the way shown in Fig. 2.

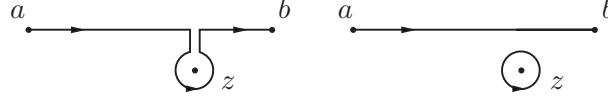


Figure 2: Two steps in transformation of the contour  $\gamma$  back to  $(a, b)$ .

By performing such a transformation and computing the residue at  $\nu = z$ , one obtains from Eq. (2.9) the following equation for the unphysical-sheet values  $T'(\lambda, \mu, z)$  of  $T$ :

$$T'(\lambda, \mu, z) = V(\lambda, \mu) - 2\pi i V(\lambda, z) T'(z, \mu, z) - \int_a^b d\nu \frac{V(\lambda, \nu) T'(\nu, \mu, z)}{\nu - z}, \quad (2.11)$$

$$\lambda, \mu \in \Omega, \quad z \in \Omega \cap \mathbb{C}^-.$$

Adopting the standard terminology of scattering theory one calls the kernel  $T'(z, \mu, z)$  “half-on-shell” since its first argument equals the spectral parameter (energy)  $z$ . Similarly, the kernel  $T'(z, z, z)$  is called “(completely) on-shell”, whereas the kernel  $T'(\lambda, \mu, z)$  with arbitrary admissible values of  $\lambda$  and  $\mu$  is called “off-shell”. Surely, the adjectives “off-shell”, “half-on-shell”, and “on-shell” may be applied to any function of the complex arguments  $\lambda$ ,  $\mu$ , and  $z$ .

By transferring all the entries in Eq. (2.11) with the off-shell kernel  $T'$  to the l.h.s. one obtains:

$$T'(\lambda, \mu, z) + \int_a^b d\nu \frac{V(\lambda, \nu) T'(\nu, \mu, z)}{\nu - z} = V(\lambda, \mu) - 2\pi i V(\lambda, z) T'(z, \mu, z), \quad (2.12)$$

$$\lambda, \mu \in \Omega, \quad z \in \Omega \cap \mathbb{C}^-.$$

Meanwhile, for  $z$  on the physical sheet we have:  $(I + VR_0(z))^{-1}V = T(z)$ ,  $z \notin \sigma_p(H)$ . This allows to rewrite Eq. (2.12) in the form

$$T'(\lambda, \mu, z) = T(\lambda, \mu, z) - 2\pi i T(\lambda, z, z) T'(z, \mu, z), \quad (2.13)$$

where the absence of the the prime in notation of the entry  $T(\cdot, \mu, z)$  means that this entry is taken for  $z$  on the physical energy sheet. Now by setting  $\lambda = z$  in Eq. (2.13), one gets

$$T'(z, \mu, z) = T(z, \mu, z) - 2\pi i T(z, z, z) T'(z, \mu, z). \quad (2.14)$$

From Eq. (2.14) it follows that

$$S_-(z) T'(z, \mu, z) = T(z, \mu, z), \quad (2.15)$$

where

$$S_-(z) := I_{\mathfrak{h}} + 2\pi i T(z, z, z), \quad z \in \Omega \cap \mathbb{C}^-, \quad (2.16)$$

is just the scattering matrix for the values of  $z$  in the lower half-plane. We emphasize that the values of  $z$  in Eq. (2.16) are taken on the physical sheet. From Eq. (2.15) it follows that

$$T'(z, \mu, z) = S_-(z)^{-1} T(z, \mu, z), \quad (2.17)$$

of course, under the condition that the inverse  $S_-(z)^{-1}$  exists. That is,  $z$  in Eq. (2.17) should be such that  $S_-(z)$  does not have eigenvalue zero. Combining Eqs. (2.13) and (2.17), one finally obtains

$$T'(\lambda, \mu, z) = T(\lambda, \mu, z) - 2\pi i T(\lambda, z, z) S_-(z)^{-1} T(z, \mu, z). \quad (2.18)$$

All the entries on the r.h.s. part of Eq. (2.18) are taken for the same  $z$  as on the l.h.s. part but on the physical sheet. Thus, the representation (2.18) discloses the structure of the analytically continued transition operator  $T'(z) = T(z)|_{\Pi_-}$  on the unphysical sheet  $\Pi_-$  exclusively in terms of the physical sheet.

An analytic continuation of  $T(\lambda, \mu, z)$  from the lower half-plane  $\mathbb{C}^-$  to the part  $\Omega \cap \mathbb{C}^+$  of the unphysical energy sheet  $\Pi_+$  attached to the physical sheet along the lower rim of the cut  $(a, b)$  may be performed exactly in the same way. As a result, one arrives at the following statement that works for both sheets  $\Pi_\ell$  where the number  $\ell = \pm 1$  in the subscript is identified with the corresponding sign  $\pm$  in the previous notation  $\Pi_\pm$ .

**Lemma 2.2.** *The transition operator  $T(z)$  admits a meromorphic continuation (as an operator-valued function of the energy  $z$ ) through the cut along the interval  $(a, b)$  both from the upper,  $\mathbb{C}^+$ , and lower,  $\mathbb{C}^-$ , half-planes to the respective parts*

$$\Omega_- := \Omega \cap \mathbb{C}^- \text{ and } \Omega_+ := \Omega \cap \mathbb{C}^+$$

of the unphysical sheets  $\Pi_{-1}$  and  $\Pi_{+1}$  attached to the physical sheet along the upper and lower rims of the above cut. The kernel of the continued operator  $T(z)|_{\Pi_\ell \cap \Omega_\ell}$ ,  $\ell = \pm 1$ , is given by the equality

$$T(\lambda, \mu, z)|_{z \in \Pi_\ell \cap \Omega_\ell} = (T(\lambda, \mu, z) + 2\pi i \ell T(\lambda, z, z) S_\ell(z)^{-1} T(z, \mu, z))|_{z \in \Omega_\ell}, \quad (2.19)$$

$$z \in \Omega_\ell \setminus \sigma_{\text{res}}^\ell, \quad (2.20)$$

with all the entries on the r.h.s. part, including the scattering matrix

$$S_\ell(z) = I_{\mathfrak{h}} - 2\pi i \ell T(z, z, z), \quad (2.21)$$

being taken for the same  $z$  on the physical sheet. Notation  $\sigma_{\text{res}}^\ell$  is used for the set of all those points  $\zeta \in \Omega \cap \mathbb{C}^\ell$  where  $S_\ell(\zeta)$  has eigenvalue zero.

It is worth mentioning that some further analytic properties of  $V(\lambda, \mu)$  outside  $\Omega$  should be known in order to decide whether  $\Pi_-$  and  $\Pi_+$  represent the same (“second”) unphysical sheet or they are really different sheets of the energy Riemann surface (cf. Ref. [14]).

Continuation formula for the scattering matrix is a simple corollary to Lemma 2.2.

**Lemma 2.3.** *An analytic continuation of the scattering matrix  $S_{-\ell}(z)$ ,  $\ell = \pm 1$ , to the unphysical sheet  $\Pi_\ell$  is given by*

$$S_{-\ell}(z)|_{z \in \Pi_\ell \cap \Omega_\ell} = S_\ell(z)^{-1}|_{z \in \Omega_\ell}, \quad z \notin \sigma_{\text{res}}^\ell, \quad (2.22)$$

where the r.h.s. part is taken for  $z$  on the physical sheet.

### 3 Equivalence of the deformation and scattering resonances in the Friedrichs–Faddeev model

From now on we consider a family of the Friedrichs–Faddeev Hamiltonians

$$H_\gamma = H_{0,\gamma} + V_\gamma$$

associated with smooth Jordan curves  $\gamma \subset \Omega$  obtained by continuous transformation from the interval  $(a, b)$ , with the end points  $a, b$  fixed during the transformation. As before, the notation  $\Omega$  is used for the holomorphy domain of  $V(\lambda, \mu)$  in  $\lambda, \mu$ . The domain  $\Omega$  may or may not include the points  $a$  and/or  $b$ . The entries  $H_{0,\gamma}$  and  $V_\gamma$  are given by

$$(H_{0,\gamma}f)(\lambda) = \lambda f(\lambda) \quad \text{and} \quad (V_\gamma f)(\lambda) = \int_\gamma V(\lambda, \mu) f(\mu) d\mu, \quad \lambda \in \gamma.$$

It is assumed that  $f \in L_2(\gamma, \mathfrak{h})$  where  $L_2(\gamma, \mathfrak{h})$  is the Hilbert space of  $\mathfrak{h}$ -valued functions of the variable  $\lambda \in \gamma$  with the scalar product

$$\langle f, g \rangle_\gamma = \int_\gamma |d\lambda| \langle f(\lambda), g(\lambda) \rangle_{\mathfrak{h}}.$$

Notice once again that the standard complex scaling [16, 17] of a two-body Hamiltonian may be viewed as a particular case of the complex deformation of the Friedrichs–Faddeev model (see Ref. [6, Section 3]).

Assume, for simplicity, like in Section 2, that both  $a$  and  $b$  are finite real numbers and let  $V(\lambda, \mu)$  be also as in Section 2. As usually, for the resolvent  $R_\gamma(z) = (H_\gamma - z)^{-1}$  of the operator  $H_\gamma$  we have

$$R_\gamma(z) = R_{0,\gamma}(z) - R_{0,\gamma}(z) T_\gamma(z) R_{0,\gamma}(z), \quad (3.1)$$

where  $R_{0,\gamma}(z)$  is the resolvent of  $H_{0,\gamma}$ ,

$$R_{0,\gamma}(z) = (H_{0,\gamma} - z)^{-1}, \quad z \notin \sigma(H_{0,\gamma}),$$

and

$$T_\gamma(z) = V_\gamma - V_\gamma (H_\gamma - z)^{-1} V_\gamma, \quad z \notin \sigma(H_\gamma) \quad (3.2)$$

is the transition operator for the pair  $(H_{0,\gamma}, H_\gamma)$ .

Clearly,  $H_{0,\gamma}$  is a normal operator on  $\mathfrak{H}_\gamma$ . Its spectrum is purely absolutely continuous and fills the curve  $\bar{\gamma}$ . From Eq. (3.1) it immediately follows that the discrete eigenvalues of  $H_\gamma$  are associated just with the poles of the operator-valued function  $T_\gamma(z)$ .

Suppose that the above Jordan contour  $\gamma$  lies entirely in  $\Omega_- = \Omega \cap \mathbb{C}^-$  (or entirely in  $\Omega_+ = \Omega \cap \mathbb{C}^+$ ) and let  $\Omega_\gamma$  be again the set in  $\mathbb{C}$  confined by (and containing) the interval  $[a, b]$  and the curve  $\gamma$  (see Fig. 1).

**Lemma 3.1.** *The following equality holds:  $\sigma(H_\gamma) \setminus \Omega_\gamma = \sigma_p(H) \setminus \bar{\Delta}$ , which means that the spectrum of  $H_\gamma$  outside  $\Omega_\gamma$  is purely real and coincides with the corresponding eigenvalue set of  $H$ . Furthermore,  $\sigma_p(H_\gamma) \cap \Delta = \sigma_p(H) \cap \Delta$ , i. e., the eigenvalues of  $H_\gamma$  lying on  $\Delta$  do not depend on the (smooth) Jordan contour  $\gamma$ . Finally, the spectrum of  $H_\gamma$  inside  $\Omega_\gamma$  consists of the scattering-matrix resonances.*

We skip a detail justification of this assertion and refer the reader to the proof of the corresponding statement in Ref. [6, Proposition 4.1]. Here we only notice that the proof in Ref. [6] is reduced to the observation that the kernels of the  $T$ -matrices (3.2) and (2.4) possess the property

$$T_\gamma(\lambda, \mu, z) = T(\lambda, \mu, z) \quad \text{whenever} \quad \lambda, \mu \in \gamma, \quad z \in \mathbb{C} \setminus \Omega_\gamma \quad (\text{and } z \notin \sigma_p(H)).$$

Then, by the uniqueness principle for the analytic continuation, one concludes that, for  $z$  inside  $\Omega_\gamma$ , the kernel  $T_\gamma(\lambda, \mu, z)$  represents just the analytic continuation of  $T(\lambda, \mu, \cdot)$  to the interior of  $\Omega_\gamma$  belonging already to the unphysical sheet. Hence, the poles of  $T_\gamma(z)$  within  $\Omega_\gamma$  represent resonances of the original Friedrichs–Faddeev Hamiltonian (the one associated with the interval  $(a, b)$ ). This also means that the positions of the resonances inside  $\Omega_\gamma$  are stable in the sense that they do not depend on  $\gamma$ .

## Conclusion

In this work we have studied the Friedrichs–Faddeev model with an analytic potential kernel  $V(\lambda, \mu)$ . We have found that the transition operator and the scattering matrix for this model, analytically continued on unphysical energy sheets, admit explicit representations in terms of the same operators considered exclusively on the physical sheet. A resonance on the unphysical sheet  $\Pi_\ell$ ,  $\ell = \pm 1$ , or, more precisely, in the domain  $\Pi_\ell \cap \Omega_\ell$ , is a point, for the copy  $z$  of which on the physical sheet the scattering matrix  $S_\ell(z)$  has eigenvalue zero, i. e.,

$$S_\ell(z) \mathcal{A} = 0 \quad \text{for a non-zero } \mathcal{A} \in \mathfrak{h}.$$

We have also shown that, for the Friedrichs–Faddeev model under consideration, the deformation resonances are nothing else but the scattering matrix resonances.

## Acknowledgments

This work was supported by the Heisenberg–Landau Program and by the Russian Foundation for Basic Research.

## References

- [1] K. Friedrichs, *Math. Ann.* **115**, 249 (1938).
- [2] K. O. Friedrichs, *Comm. Pure Appl. Math.* **1**, 361 (1948).
- [3] O. A. Ladyzhenskaya and L. D. Faddeev, *Dokl. Akad. Nauk SSSR* **120**, 1187 (1958).
- [4] L. D. Faddeev, *Am. Math. Soc. Transl.* **62**, 177 (1967).
- [5] L. D. Faddeev, *Trudy Mat. Inst. Steklov.* **69**, 3 (1963).
- [6] A. K. Motovilov, *Few-Body Syst.* **60**, 21 (2019).

- 
- [7] M. Gadella and G. P. Pronko, *Fortschr. Phys.* **59**, 795 (2011).
  - [8] S. Albeverio and A. K. Motovilov, arXiv:1712.05770 [math.SP] (2017); *to be published in Math. Notes*.
  - [9] B. S. Pavlov and S. B. Petras, *Funct. Anal. Appl.* **4**, 136 (1970).
  - [10] S. N. Lakaev, *Comment. Math. Univ. Carolinae* **27**, 341 (1986).
  - [11] S. N. Lakaev, *J. Soviet Math.* **45**, 1540 (1989).
  - [12] E. M. Dyn'kin, S. N. Naboko and S. I. Yakovlev, *St. Petersburg Math. J.* **3**, 299 (1992).
  - [13] H. Isozaki and S. Richard, *Ann. Henri Poincaré* **13**, 1469 (2012).
  - [14] A. K. Motovilov, *Theor. Math. Phys.* **95**, 692 (1993).
  - [15] A. K. Motovilov, *Math. Nachr.* **187**, 147 (1997).
  - [16] E. Balslev and J. M. Combes, *Commun. Math. Phys.* **22**, 280 (1971).
  - [17] M. Reed and B. Simon, *Methods of modern mathematical physics I: Functional analysis*. Academic Press, New York, 1980.
  - [18] G. A. Hagedorn, *Commun. Math. Phys.* **65**, 181 (1979).

# *Ab Initio* Scattering Calculation in Three-Body Coulomb Systems: $e^+ - \text{H}$ , $e^- - \bar{\text{H}}$ and $e^+ - \text{He}^+$

V. A. Gradusov, V. A. Roudnev, E. A. Yarevsky  
and S. L. Yakovlev

*Department of Computational Physics, St. Petersburg State University,  
7/9 Universitetskaya nab., St. Petersburg, 199034, Russia*

## Abstract

We present the results of our detailed calculations of scattering characteristics in  $e^- e^+ \bar{p}$  ( $e^- e^+ p$ ) and  $e^+ e^- \text{He}^{++}$  systems with zero total orbital momentum by direct solving the Faddeev–Mercuriev equations in the differential form. We calculate all possible cross-sections in the low-energy region which admits up to seven open channels including the rearrangement channels of ground and excited states of antihydrogen, positronium and helium ion formations. All sharp resonances of the systems obtained and approved previously by a number of authors are clearly reproduced in the calculated cross sections. Alternatively, the exterior complex scaling approach has been used for calculating resonant energies. It confirmed the existence of reported by other authors broad resonances in the  $e^+ e^- \text{He}^{++}$  system. Prominent oscillations of Gailitis–Damburg type have been found in cross sections for energies above the threshold corresponding to  $n = 2$  state of antihydrogen.

**Keywords:** *Faddeev–Mercuriev equations; positron scattering; antihydrogen formation; Gailitis–Damburg oscillations*

## 1 Introduction

Study of electron and positron scattering off light atomic targets (like (anti)hydrogen atom and helium cation) is of fundamental importance for atomic physics. These colliding systems represent genuine three-body Coulombic systems with variety of channels, rich resonant structure of scattering cross sections and the fundamental rearrangement phenomenon of positronium (electron-positron bound state) formation. For such a case the solution methods should be capable of representing the solution for all the asymptotic fragmentations accurately. The Faddeev equations [1] and their generalization to the long-range Coulomb case, the so-called Faddeev–Mercuriev (FM) equations [2], were designed especially to fulfill this requirement. This generalization is based on the Coulomb potential splitting into the interior and the long range tail parts leading to the mathematically rigorous boundary value problem, which solution

---

*Proceedings of the International Conference ‘Nuclear Theory in the Supercomputing Era — 2018’ (NTSE-2018), Daejeon, South Korea, October 29 – November 2, 2018, eds. A. M. Shirokov and A. I. Mazur. Pacific National University, Khabarovsk, Russia, 2019, p. 137.*

<http://www.ntse.khb.ru/files/uploads/2018/proceedings/Yakovlev.pdf>.

is strictly equivalent to the solution of the Schrödinger equation [1]. This approach suits the computationally difficult detailed low-energy elastic and reactive scattering calculations in three-body Coulomb systems perfectly [3–5].

Here, the formalism of FM equations is used to calculate the  $S$ -wave cross sections in  $e^-e^+\bar{p}$  ( $e^-e^+p$ ) and  $e^+e^-\text{He}^{++}$  systems in the low-energy region for all open channels. Even though there are many calculations available in the literature [3, 4, 6–17], there is still some lack of high-precision and detailed results especially for the  $e^+e^-\text{He}^{++}$  system, which is one of the motivations for performing this research. Besides, a special emphasis is made on the antihydrogen formation by antiproton impact of positronium which is currently used in experiments on antimatter at CERN (see Ref. [18] and references therein).

The paper is organized as follows. In Section 2, we give the necessary portion of the three-body FM equations formalism and briefly describe the respective solution technique in the case of zero total orbital momentum of the system. Section 3 contains results of calculations of low-energy reactive scattering in  $e^-e^+\bar{p}$  ( $e^-e^+p$ ) and  $e^+e^-\text{He}^{++}$  systems. The last Section concludes the paper.

We use atomic units throughout the paper. The magnitude of a vector  $\mathbf{x}$  is denoted by  $x$ , i. e.,  $x = |\mathbf{x}|$ , and  $\hat{\mathbf{x}} = \mathbf{x}/x$  stands for the unit vector. The set of indices  $\{\alpha, \beta, \gamma\}$  runs over the set  $\{1, 2, 3\}$  enumerating particles and is also used for identifying the complementary pair of particles since the pair of particles  $\beta\gamma$  in the partition  $\{\alpha(\beta\gamma)\}$  is uniquely determined by the particle  $\alpha$ .

## 2 Theory and numerical solution

We consider a system of three spinless nonrelativistic charged particles of masses  $m_\alpha$  and charges  $Z_\alpha$ ,  $\alpha = 1, 2, 3$ . Standard Jacobi coordinates are defined for a partition  $\alpha(\beta\gamma)$  as the relative position vectors between the particles of the pair  $\beta\gamma$  and between their center of mass and the particle  $\alpha$ . In applications, it is convenient to use the reduced Jacobi coordinates  $\mathbf{x}_\alpha, \mathbf{y}_\alpha$  which are Jacobi vectors scaled by the factors  $\sqrt{2\mu_\alpha}$  and  $\sqrt{2\mu_{\alpha(\beta\gamma)}}$ , respectively, where the reduced masses are given by

$$\mu_\alpha = \frac{m_\beta m_\gamma}{m_\beta + m_\gamma}, \quad \mu_{\alpha(\beta\gamma)} = \frac{m_\alpha(m_\beta + m_\gamma)}{m_\alpha + m_\beta + m_\gamma}. \quad (1)$$

The reduced Jacobi vectors for different choices of  $\alpha$  are related by an orthogonal transformation,

$$\mathbf{x}_\beta = c_{\beta\alpha} \mathbf{x}_\alpha + s_{\beta\alpha} \mathbf{y}_\alpha, \quad \mathbf{y}_\beta = -s_{\beta\alpha} \mathbf{x}_\alpha + c_{\beta\alpha} \mathbf{y}_\alpha, \quad (2)$$

where

$$c_{\beta\alpha} = - \left[ \frac{m_\beta m_\alpha}{(M - m_\beta)(M - m_\alpha)} \right]^{1/2}, \quad s_{\beta\alpha} = (-1)^{\beta-\alpha} \text{sgn}(\alpha - \beta) (1 - c_{\beta\alpha}^2)^{1/2},$$

and  $M = \sum_\alpha m_\alpha$ . In what follows, it is assumed that the  $\beta$  Jacobi vectors are represented through the  $\alpha$  vectors via Eq. (2).

In the reduced Jacobi coordinates, the FM equations for three charged particles [1]

read

$$\{T_\alpha + V_\alpha(x_\alpha) + \sum_{\beta \neq \alpha} V_\beta^{(1)}(x_\beta, y_\beta) - E\} \psi_\alpha(\mathbf{x}_\alpha, \mathbf{y}_\alpha) = -V_\alpha^{(s)}(x_\alpha, y_\alpha) \sum_{\beta \neq \alpha} \psi_\beta(\mathbf{x}_\beta, \mathbf{y}_\beta). \quad (3)$$

Here  $T_\alpha \equiv -\Delta_{\mathbf{x}_\alpha} - \Delta_{\mathbf{y}_\alpha}$  are the kinetic energy operators. In this paper, the potentials  $V_\alpha$  represent the pairwise Coulomb interaction  $V_\alpha(x_\alpha) = \sqrt{2\mu_\alpha} Z_\beta Z_\gamma / x_\alpha$  ( $\beta, \gamma \neq \alpha$ ), although, generally, a short-range (decreasing as  $1/x_\alpha^2$  or faster as  $x_\alpha \rightarrow \infty$ ) potential can also be included in the formalism. The potentials  $V_\alpha$  are split into the interior (short-range)  $V_\alpha^{(s)}$  and the tail (long-range) parts  $V_\alpha^{(l)}$ ,

$$V_\alpha(x_\alpha) = V_\alpha^{(s)}(x_\alpha, y_\alpha) + V_\alpha^{(l)}(x_\alpha, y_\alpha). \quad (4)$$

Equations (3) can be summed up leading to the Schrödinger equation for the wave function  $\Psi = \sum_\alpha \psi_\alpha$ , where  $\psi_\alpha$  are the components of the wave function given by the solution of Eqs. (3).

Splitting Eq. (4) for the potentials in general case is done in the three-body configuration space by the Merkuriev cut-off function  $\chi_\alpha$  [1],

$$V_\alpha^{(s)}(x_\alpha, y_\alpha) = \chi_\alpha(x_\alpha, y_\alpha) V_\alpha(x_\alpha). \quad (5)$$

This splitting confines the short-range part of the potential to the regions in the three-body configuration space corresponding to the three-body collision point (particles are close to each other) and the binary configuration ( $x_\alpha \ll y_\alpha$  when  $y_\alpha \rightarrow \infty$ ). The form of the cut-off function can be rather arbitrary within some general requirements [2, 5]. In the paper [19], we have shown, that for the energies below the breakup threshold, it is practical to confine the cut-off function to the two-body configuration space. Thus in this paper, for actual calculations we use the cut-off function of the form

$$\chi_\alpha(x_\alpha) = 2/\{1 + \exp[(x_\alpha/x_{0\alpha})^{2.01}]\}, \quad (6)$$

where  $x_{0\alpha}$  is a parameter. With this smoothed Heaviside step function, the split potentials  $V_\alpha^{(s,1)}$  become two-body quantities  $V_\alpha^{(s,1)} = V_\alpha^{(s,1)}(x_\alpha)$ .

The splitting procedure makes the properties of the FM equations for Coulomb potentials as appropriate for scattering problems as the standard Faddeev equations in the case of short-range potentials [4]. With the described above choice of the short-range part of the potential  $V^{(s)}$ , the right-hand side of each Eq. (3) is confined to the vicinity of the three-body collision point [20], which is the key property of the FM equations. It leads to the asymptotic uncoupling of the set of FM equations and, accordingly, the asymptotics of each component  $\psi_\alpha$  for energies below the breakup threshold contains only the terms corresponding to the binary configurations of pairing  $\alpha$  [4, 20].

The total orbital momentum is an integral of motion for the three-particle system. This makes it possible to reduce the set of FM equations by projecting Eq. (3) onto a subspace of a given total angular momentum [14]. In this article we consider the case of zero total orbital momentum of the system. The kinetic energy operator in the left-hand side of Eq. (3) on the subspace of zero total orbital momentum has the form

$$T_\alpha = -\frac{\partial^2}{\partial y_\alpha^2} - \frac{2}{y_\alpha} \frac{\partial}{\partial y_\alpha} - \frac{\partial^2}{\partial x_\alpha^2} - \frac{2}{x_\alpha} \frac{\partial}{\partial x_\alpha} - \left( \frac{1}{y_\alpha^2} + \frac{1}{x_\alpha^2} \right) \frac{\partial}{\partial z_\alpha} (1 - z_\alpha^2) \frac{\partial}{\partial z_\alpha}, \quad (7)$$

where  $z_\alpha \equiv \cos(\hat{\mathbf{x}}_\alpha \cdot \hat{\mathbf{y}}_\alpha)$ . The corresponding projection of the component  $\psi_\alpha$  depends only on the coordinates  $X_\alpha = \{x_\alpha, y_\alpha, z_\alpha\}$  in the plane containing all three particles. By choosing the coordinate system appropriately, its asymptotics for energies  $E$  below the three-body ionization threshold can be written as

$$\begin{aligned} \psi_\alpha(X_\alpha) \sim & -\frac{\phi_{n_0\ell_0}(x_\alpha)}{x_\alpha y_\alpha} Y_{\ell_0 0}(\theta_\alpha, 0) e^{-i\vartheta_{\ell_0}(y_\alpha, p_{n_0})} \delta_{\alpha, \alpha_0} \\ & + \sum_{n\ell} \frac{\phi_{n\ell}(x_\alpha)}{x_\alpha y_\alpha} Y_{\ell 0}(\theta_\alpha, 0) \sqrt{\frac{p_{n_0}}{p_n}} S_{n\ell, n_0\ell_0} e^{+i\vartheta_\ell(y_\alpha, p_n)}, \quad (8) \end{aligned}$$

where the set of indices  $\{n\ell\}$  specifies various two-body Coulomb bound states in the pair  $\alpha$  (that is, binary scattering channels  $\{\alpha; n\ell\}$ ) with the wave function  $\phi_{n\ell}(x_\alpha) Y_{\ell m}(\hat{\mathbf{x}})/x_\alpha$  and the energy  $\varepsilon_n$ . Here  $Y_{\ell m}(\hat{\mathbf{x}})$  stands for the standard spherical harmonic function. The momentum  $p_n$  of the outgoing particle is determined by the energy conservation condition  $E = p_n^2 + \varepsilon_n$ . The Coulomb distorted wave phase  $\vartheta_\ell(y_\alpha, p_n) \equiv p_n y_\alpha - \eta_n \log(2p_n y_\alpha) - \ell\pi/2 + \sigma_n$ , where  $\sigma_n = \arg \Gamma(1 + i\eta_n)$  and the Sommerfeld parameter is defined as  $\eta_n \equiv Z_\alpha(Z_\beta + Z_\gamma)\sqrt{2m_\alpha(\beta\gamma)}/(2p_n)$ . Finally,  $S_{n\ell, n_0\ell_0}$  are the  $S$ -matrix elements.

To reduce the computational cost of solving the system of FM equations (3), several modifications has been done. First, since the potential  $V_3$  is repulsive and the corresponding two-body Hamiltonian does not support any bound state, this potential is included in the left-hand side of Eqs. (3), thus reducing the number of these equations from 3 to 2. Formally, it is done by setting  $\chi_3 = 0$ . Secondly, the asymptotic particle-atom Coulomb potential  $V_\alpha^{\text{eff}}(y_\alpha) = 2p_n\eta_n/y_\alpha$  is introduced explicitly in Eqs. (3) for treating the asymptotic Coulomb singularity,

$$\begin{aligned} \{T_\alpha + V_\alpha(x_\alpha) + V_\alpha^{\text{eff}}(y_\alpha) - E\} \psi_\alpha(X_\alpha) = & -V_\alpha^{(s)}(x_\alpha) \psi_\beta(X_\beta) \\ & - [V_\beta^{(1)}(x_\beta) + V_3(x_3) - V_\alpha^{\text{eff}}(y_\alpha)] \psi_\alpha(X_\alpha), \quad (9) \end{aligned}$$

where  $\beta \neq \alpha = 1, 2$ . After that the Coulomb singularity can be effectively inverted [21]. Another modification is done to make the solutions of Eqs. (3) to be real functions. This is achieved by using the asymptotic conditions with standing waves instead of conditions (8).

The FM equations are solved by the spline collocation method [22] in a box  $[0, R_\alpha^x] \times [0, R_\alpha^y] \times [-1, 1]$  for each component  $\psi_\alpha$ . As a basis set for expanding the components, we use products of basis functions in the space of quintic Hermite splines  $S_5^3$  (splines of degree 5 with 2 continuous derivatives) in each coordinate. Each basis function is local and nonzero only on two adjoining intervals of the grid. As a result, the matrix of the system of linear equations for expansion coefficients is sparse. It is solved by the Arnoldi iterations in GMRES variant [23] with right preconditioning by the discretized version of the operators in the left-hand side of the system of FM equations. To invert the preconditioner, we use the algorithm which is known as the ‘‘tensor trick’’ or matrix decomposition method [22, 24, 25]. It provides a fast diagonalization of the matrix using its tensor product structure. For a more detailed description of our computational method, we refer the reader to Ref. [21].

### 3 Results

#### 3.1 Scattering in $e^-e^+\bar{p}$ and $e^+e^-p$ systems

The positron-hydrogen atom scattering is the simplest example of positron-atom scattering process. Many calculations are available in the literature [3, 7, 9–13, 15, 16, 18]. The renewed interest in studying reactions involving the positron, electron and (anti)proton is motivated by experiments on antimatter ongoing at CERN [18]. The reaction of the antihydrogen production via the antiproton ( $\bar{p}$ ) impact on positronium atom (Ps, the bound state of  $e^+$  and  $e^-$ ) plays the key role in antimatter formation. Due to the symmetry of particle charges, the cross sections in  $e^+e^-p$  and  $e^-e^+\bar{p}$  systems are identical. Below in this section we refer to the  $e^+e^-p$  system.

By solving the FM equations, we have calculated the cross sections for all possible scattering processes in the  $e^+e^-p$  system in the total energy range between the energies of the atomic states  $\bar{H}(n=1)$  and  $\bar{H}(n=3)$ , i. e., from  $-0.49973$  a.u. to  $-0.05553$  a.u. with the step in energy of  $0.0007$  a.u. Within this energy interval, the elastic scattering, excitation and rearrangement processes leading to the  $\bar{H}(n=1, 2)$  and Ps( $n=1, 2$ ) atomic states are possible. The energies of these atomic states form the thresholds for scattering channels. The maximal number of open channels in the energy interval between the Ps( $n=2$ ) and  $\bar{H}(n=3)$  states equals to 6. The accuracy of our calculations guarantees that the uncertainties of the obtained cross sections are less than 1%. A calculation of all cross sections for each energy value from this interval requires a time of approximately 3 hours on a SMP node with 32 cores and 20 Gb RAM. We have a system of 3,241,020 linear equations and the respective matrix has 432 nonzero elements in a row.

We compare our results in Table 1 with tabulated results of other authors and present some additional cross sections for further references. In this Table and in the text below we use shortcuts  $\bar{H}(n)$  and  $\bar{H}(n, \ell)$  for the atomic states with the principal quantum number  $n$  and the orbital momentum  $\ell$ . Some of all possible 36 cross sections for the collision processes with  $e^- - \bar{H}$  and  $\bar{p} - \text{Ps}$  configurations in the entrance and final channels are presented in Fig. 1.

The antihydrogen production cross sections in the energy region between the  $\bar{H}(2)$  and  $\bar{H}(3)$  thresholds are studied in detail in a recent work [18]. These cross sections are compared with our results in Fig. 2. The resonances manifest themselves in Figs. 1 and 2 as peaks in some of the calculated cross sections. The resonance energies found by different methods [26–29] are known with a good accuracy. We mark their positions in the figures by vertical dashed lines. All resonances are clearly seen in the calculated cross sections. The  $\bar{p} + \text{Ps}(1, s) \rightarrow \bar{p} + \text{Ps}(1, s)$  and  $e^- + \bar{H}(2, s) \rightarrow e^- + \bar{H}(2, p)$  cross sections as well as the  $e^- + \bar{H}(2, s) \rightarrow e^- + \bar{H}(2, s)$  cross section not shown in the figure, have sharp minima which also look like resonances but do not coincide with any of the known resonance positions. We agree with the interpretation of these minima suggested in Ref. [10] where they were associated with the Ramsauer–Townsend effect.

A special attention should be paid to the oscillations of the cross sections just above the  $\bar{H}(2)$  threshold in Fig. 2. We give more detailed plots of the  $\bar{p} + \text{Ps}(1) \rightarrow e^- + \bar{H}(1)$  and  $\bar{p} + \text{Ps}(1) \rightarrow e^- + \bar{H}(2)$  cross sections in the energy region above this threshold in Fig. 3. Prominent oscillations of both cross sections and their character suggest to associate these oscillations with the phenomenon predicted in Refs. [30, 31]. According to Refs. [30, 31], the energy position  $E_n$  of the  $n$ th maximum of the oscillations follows

Table 1: Our results for scattering cross sections in the  $e^-e^+\bar{p}$  system in comparison with that of other authors (energies are given relative to the  $\bar{H}(1)$  threshold at  $-0.49973$  a.u.).

$E$ , a.u.	0.27026	0.28140	0.32017	0.36145	0.385	0.40	0.415	0.42
$\sigma_{e^- + \bar{H}(1) \rightarrow e^- + \bar{H}(1)}$	0.0353	0.0417	0.0634	0.0836	0.0944	0.100	0.105	0.107
[10]			0.0651	0.0844		0.100		
[3]	0.0372	0.0429	0.0649	0.0866	0.090	0.096	0.099	0.101
[9]		0.0431	0.0650	0.0856				
$\sigma_{e^- + \bar{H}(1) \rightarrow \bar{p} + \text{Ps}(1)}$	0.00412	0.00430	0.00487	0.00562	0.00565	0.00572	0.00575	0.00574
[10]			0.00490	0.00567		0.00581		
[3]	0.00410	0.00439	0.00487	0.00557				
[9]		0.00422	0.00481	0.00554				
$\sigma_{\bar{p} + \text{Ps}(1) \rightarrow \bar{p} + \text{Ps}(1)}$	3.49	7.06	9.87	8.31	7.11	6.44	5.82	5.62
[10]			9.87	8.32		6.45		
[3]	3.500	7.060	9.866	8.312	7.09	6.44	5.83	5.63
[9]		6.936	9.868	8.332				
$\sigma_{\bar{p} + \text{Ps}(1) \rightarrow e^- + \bar{H}(1)}$	0.0272	0.0191	0.0111	0.0091	0.00806	0.00763	0.00724	0.00709
[3]	0.0274	0.0195	0.0111	0.0091	0.00815	0.00780	0.00729	0.00715
$\sigma_{e^- + \bar{H}(1) \rightarrow e^- + \bar{H}(2,s)}$					0.000662	0.00137	0.00206	0.00228
$\sigma_{e^- + \bar{H}(1) \rightarrow e^- + \bar{H}(2,p)}$					0.000399	0.000236	0.000421	0.000582
$\sigma_{e^- + \bar{H}(2,s) \rightarrow \bar{p} + \text{Ps}(1,s)}$					1.26	0.576	0.477	0.475
$\sigma_{e^- + \bar{H}(2,s) \rightarrow e^- + \bar{H}(1,s)}$					0.0249	0.0217	0.0212	0.0212
$\sigma_{\bar{p} + \text{Ps}(1) \rightarrow e^- + \bar{H}(2,s)}$					0.0476	0.0484	0.0581	0.0631
$\sigma_{\bar{p} + \text{Ps}(1) \rightarrow e^- + \bar{H}(2,p)}$					0.0390	0.0484	0.0512	0.0519

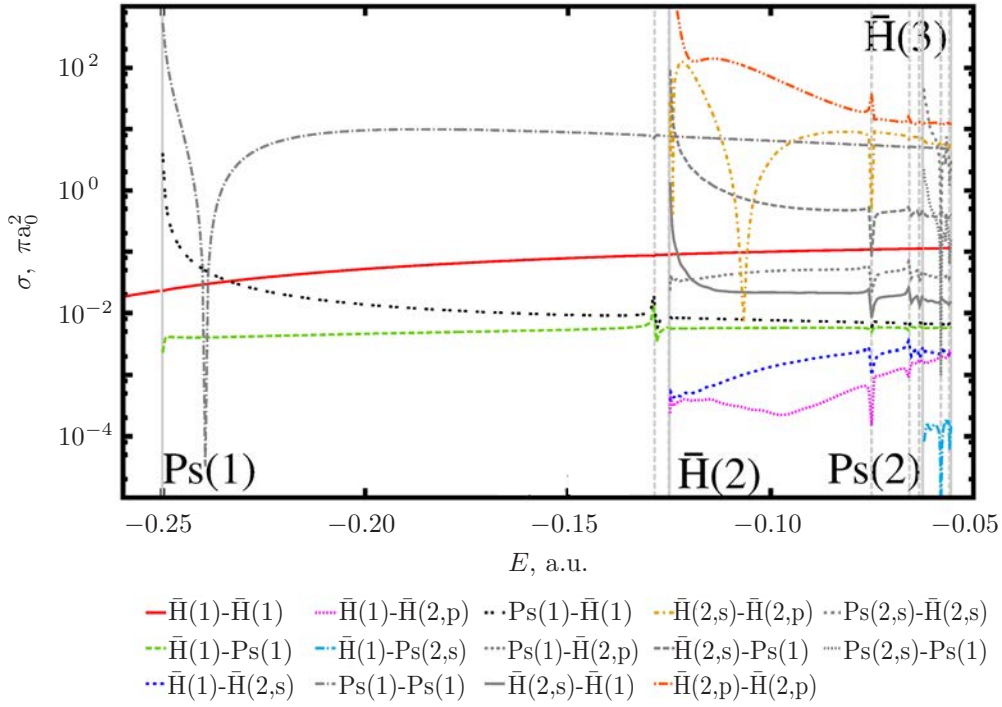


Figure 1: Cross sections in the  $e^-e^+\bar{p}$  system. Vertical solid lines show the binary thresholds, vertical dashed lines mark resonances positions. We use the notation  $\text{Ps}(n_1, \ell_1) - \bar{\text{H}}(n_2, \ell_2)$  to specify the reaction  $\bar{p} + \text{Ps}(n_1, \ell_1) \rightarrow e^- + \bar{\text{H}}(n_2, \ell_2)$  and similar notations for other reactions.

the rule

$$\log(E_n - E_{\text{th}}) = An + B, \quad (10)$$

where  $A$  and  $B$  are constants and  $E_{\text{th}}$  is the threshold energy. We plot the respective quantities for the  $\bar{p} + \text{Ps}(1) \rightarrow e^- + \bar{\text{H}}(1)$  and  $\bar{p} + \text{Ps}(1) \rightarrow e^- + \bar{\text{H}}(2)$  cross section oscillations near the threshold in panels (c)–(e) in Fig. 3. Clearly, the linear spacing of  $\log(E_n - E_{\text{th}})$  is nearly perfect in both cases of rearrangement cross sections except for the last points. The latter probably indicate the range of validity of approximations made in Ref. [30,31] leading to Eq. (10). As for the  $\bar{p} + \text{Ps}(2) \rightarrow e^- + \bar{\text{H}}(n \leq 2)$  cross section behavior shown in the right panel of Fig. 2, we obviously cannot make such a quantitative analysis as of the above threshold oscillations. Nevertheless, we can agree with Ref. [18] that there is an oscillation at the energy close to  $-0.06194$  a.u., which was also found earlier in Ref. [32]. It should be noted that the elastic cross section oscillations for the  $\text{Ps} - p$  scattering above the  $\text{Ps}(2)$  threshold were also found recently in Ref. [33].

### 3.2 Scattering in $e^+e^-\text{He}^{++}$ system

The scattering of positron by positive helium ion is an example of the positron–atomic target scattering in which the asymptotic Coulomb interaction is present in one of

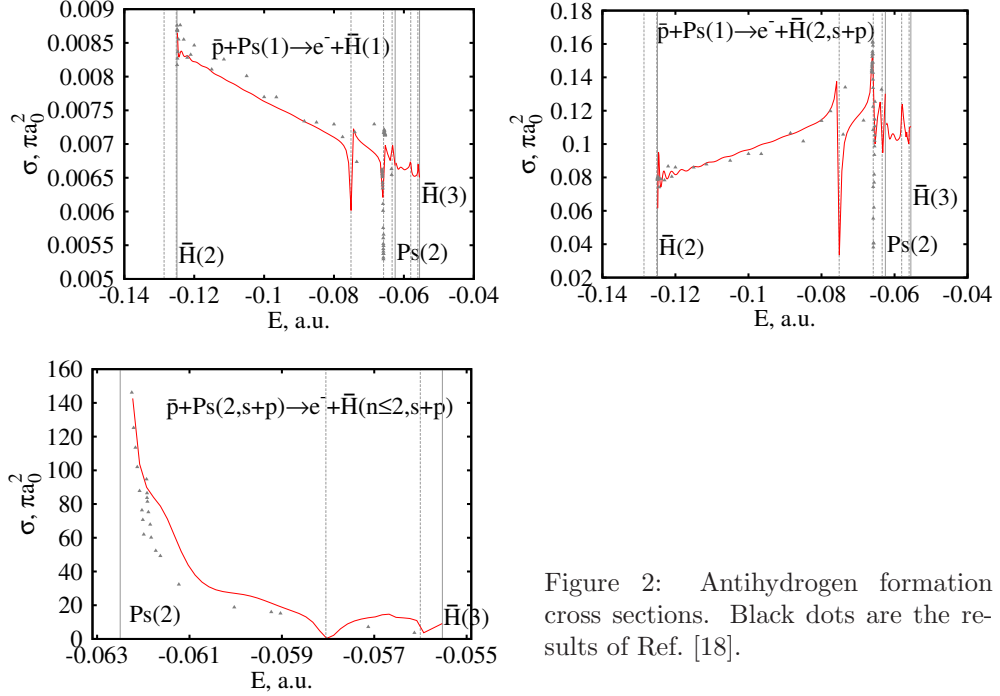


Figure 2: Antihydrogen formation cross sections. Black dots are the results of Ref. [18].

the configurations. There is a number of respective calculations in a wide energy region [34–36]. However, to the best of our knowledge, there is lack of published results of calculations in the low-energy region. In this work, by solving the FM equations, we have calculated cross sections for all possible scattering processes in the  $e^+e^-He^{++}$  system in the entire energy range between the energy thresholds of the  $He^+(1)$  and  $He^+(4)$  states, i. e., from  $-1.9997$  a.u. to  $-0.12496$  a.u. with the step in energy of  $0.0007$  a.u. In this energy interval, the elastic, excitation and rearrangement processes leading to the  $He^+(n = 1, 2, 3)$  and  $Ps(n = 1)$  atomic states are possible. As in the previous case, the accuracy of our calculations guarantees that the uncertainties of the obtained cross sections are not exceeding 1%.

The calculated 11 of all 49 cross sections are given in Table 2. The energy dependences of the cross sections for the reactions  $e^+ - He^+ \rightarrow e^+ - He^+$ ,  $e^+ - He^+ \rightarrow He^{++} - Ps$  and  $He^{++} - Ps \rightarrow He^{++} - Ps$ ,  $He^{++} - Ps \rightarrow e^+ - He^+$  are displayed in Fig. 4.

Resonance energies in the  $e^+e^-He^{++}$  system are far lesser-known, there is a number of disagreements between the published results, see, e. g., Refs. [37–39] and references therein. Most of the authors agree that there are two broad resonances at the energies of  $-0.371$  a.u. and  $-0.188$  a.u. [38] and one narrow resonance slightly below the positronium ground state formation threshold at  $-0.250$  a.u. [38, 39]. The positions of these resonances are marked in Fig. 4 by dashed vertical lines (the dashed vertical line at  $-0.250$  a.u. almost coincides with the vertical line showing the positronium ground state threshold and is not visible). We do not see a usual singular behavior of the cross sections in the vicinity of the narrow resonance. However, at the same time, one can see that the  $e^+ + He^+(1) \rightarrow He^{++} + Ps(1)$  cross section does not follow the well-known law of threshold behavior at the  $Ps(1)$  threshold at  $-0.25$  a.u. The

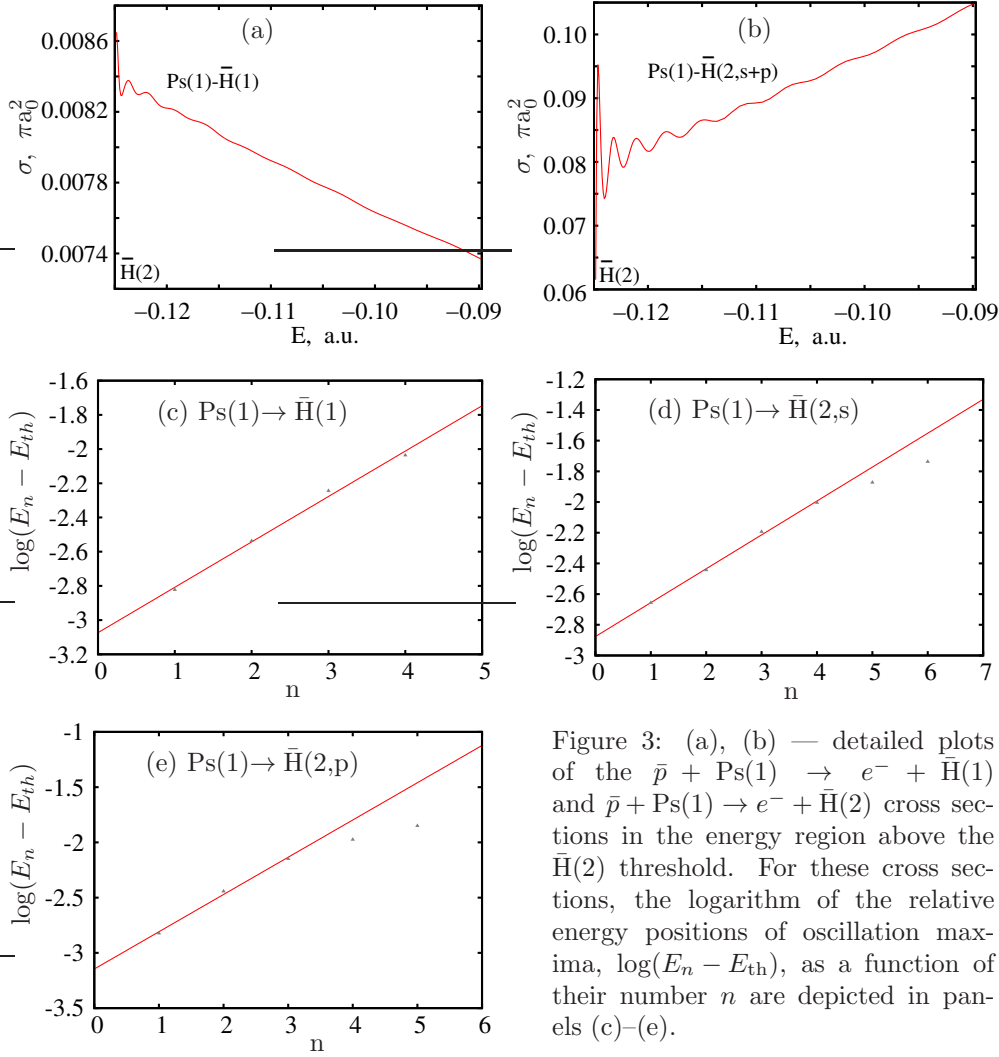


Figure 3: (a), (b) — detailed plots of the  $\bar{p} + \text{Ps}(1) \rightarrow e^- + \bar{\text{H}}(1)$  and  $\bar{p} + \text{Ps}(1) \rightarrow e^- + \bar{\text{H}}(2)$  cross sections in the energy region above the  $\bar{\text{H}}(2)$  threshold. For these cross sections, the logarithm of the relative energy positions of oscillation maxima,  $\log(E_n - E_{th})$ , as a function of their number  $n$  are depicted in panels (c)–(e).

cross section should tend to zero linearly as  $p \rightarrow 0$  where  $p$  is the relative momentum between the target and the projectile [40], but it grows up to some constant value instead. This anomalous behavior can be a sign of a resonance. The broad resonances are not manifested in the cross sections as expected.

To check the existence of the broad resonances, we have used another approach based on the complex rotation method [41] applied to the Schrödinger equation. We have found these broad resonances; their positions and widths are given in Table 3 and compared with the results of Ref. [38].

The sharp local minimum is seen again in the  $\text{He}^{++} + \text{Ps}(1) \rightarrow \text{He}^{++} + \text{Ps}(1)$  cross section for the direct process with neutral target. As in the previous Subsection, we associate this minimum with the Ramsauer–Townsend effect.

Table 2: Scattering cross sections in the  $e^+e^-He^{++}$  system (energies are given relative to the  $He^+(1)$  threshold at  $-1.9997$  a.u.). We use a notation  $a(b)$  for  $a \cdot 10^b$ .

$E$ , a.u.	1.55	1.60	1.65	1.70	1.77	1.80	1.83	1.86
$\sigma_{e^++He^+(1) \rightarrow e^++He^+(1)}$	0.000855	0.00101	0.00116	0.00133	0.00158	0.00168	0.00178	0.00188
$\sigma_{e^++He^+(1) \rightarrow e^++He^+(2,s)}$	$\sim 1(-9)$	$\sim 1(-8)$	$2(-7)$	$6(-7)$	$2.6(-6)$	$4.4(-6)$	$6.9(-6)$	$1.1(-5)$
$\sigma_{e^++He^+(1) \rightarrow e^++He^+(2,p)}$	$\sim 1(-10)$	$\sim 1(-8)$	$3(-7)$	$2.5(-6)$	$1.1(-5)$	$1.8(-5)$	$2.6(-5)$	$3.6(-5)$
$\sigma_{e^++He^+(1) \rightarrow He^{++}+Ps(1)}$					$1(-7)$	$1(-7)$	$2(-7)$	$3(-7)$
$\sigma_{He^{++}+Ps(1) \rightarrow He^{++}+Ps(1)}$					20.6	19.6	8.82	3.00
$\sigma_{He^{++}+Ps(1) \rightarrow e^++He^+(2,s)}$					0.366	0.102	0.0433	0.0199
$\sigma_{He^{++}+Ps(1) \rightarrow e^++He^+(2,p)}$					0.0944	0.0214	0.00876	0.00584
$\sigma_{e^++He^+(2,s) \rightarrow e^++He^+(2,s)}$	1.12	3.35	6.64	6.63	5.11	4.59	4.10	3.66
$\sigma_{e^++He^+(2,p) \rightarrow e^++He^+(2,s)}$	5.34	4.57	2.76	1.35	0.866	0.832	0.820	0.815
$\sigma_{e^++He^+(3,s) \rightarrow e^++He^+(3,s)}$						9.87	18.4	11.7
$\sigma_{e^++He^+(3,s) \rightarrow e^++He^+(3,p)}$						15.7	1.62	1.21

Table 3: Energies of broad resonances in the  $e^+e^-He^{++}$  system and their widths,  $(E_r, \Gamma)$  (in a.u.).

Present work	$(-0.3704, 0.1297)$	$(-0.1857, 0.0395)$
[38]	$(-0.3705, 0.1294)$	$(-0.1856, 0.0393)$

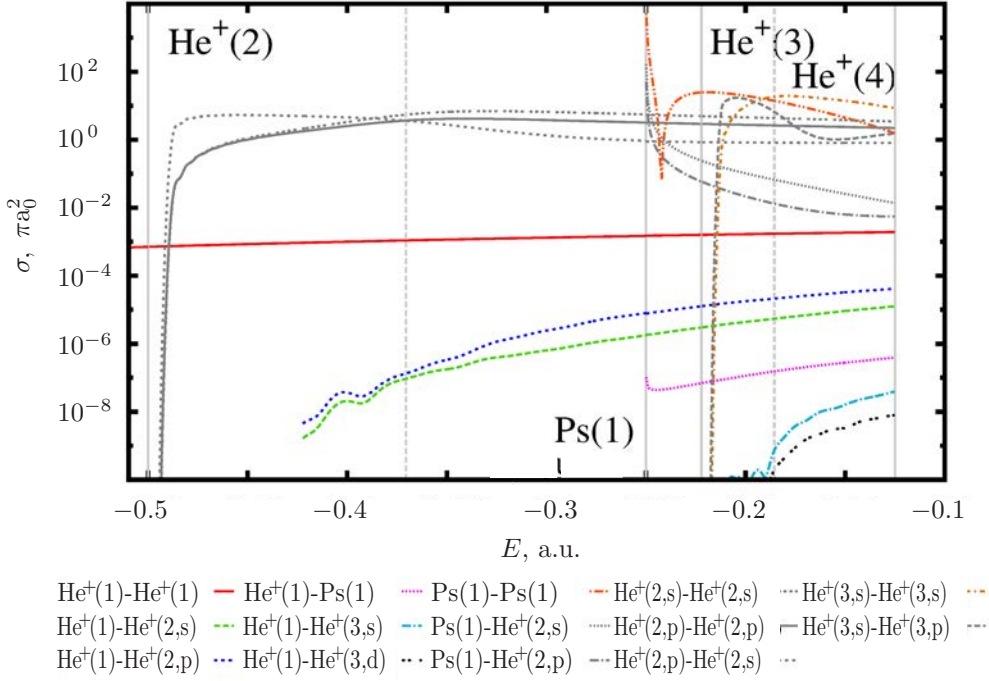


Figure 4: Cross sections in the  $e^-e^+\text{He}^+$  system. Vertical solid lines show the binary thresholds, vertical dashed lines mark resonance positions. We use the notation  $\text{Ps}(n_1, \ell_1)\text{-He}^+(n_2, \ell_2)$  to specify the reaction  $\text{He}^{++} + \text{Ps}(n_1, \ell_1) \rightarrow e^+ + \text{He}^+(n_2, \ell_2)$  and similar notations for other reactions.

## 4 Conclusions

In this paper, detailed calculations of low-energy reactive scattering in the  $e^-e^+\bar{p}$  and  $e^+e^-\text{He}^{++}$  systems in the case of zero total orbital momentum have been performed with the use of the FM equations in the total orbital momentum representation.

The calculated cross sections in the  $e^-e^+\bar{p}$  system reproduce all known resonant peaks. The Gailitis–Damburg oscillations of the  $\bar{p} + \text{Ps}(1) \rightarrow e^- + \bar{\text{H}}(1)$  and  $\bar{p} + \text{Ps}(1) \rightarrow e^- + \bar{\text{H}}(2)$  cross sections just above the  $\bar{\text{H}}(2)$  threshold are discovered and the theory of the energy distribution of the oscillation maxima with respect to the threshold is verified.

The two known broad resonances [38] in the  $e^+e^-\text{He}^{++}$  system do not contribute to the cross section. We suggest to explain the anomalous threshold behavior of the  $e^+ + \text{He}^+(1) \rightarrow \text{He}^{++} + \text{Ps}(1)$  cross section by the existence of the narrow resonance found in Refs. [38, 39].

We have demonstrated that the formalism of FM equations is efficient for calculating elastic and reactive scattering in three-body atomic systems. The extension of the current approach to nonzero total orbital momentum case is now in progress.

## Acknowledgments

This work is supported by the Russian Foundation for Basic Research grant No. 18-02-00492. The calculations were performed using the resources of the Computational Center of St. Petersburg State University.

## References

- [1] L. D. Faddeev and S. P. Merkuriev, *Quantum scattering theory for several particle systems*. Kluwer, Dordrech, 1993.
- [2] S. P. Merkuriev, *Ann. Phys.* **130**, 395 (1980).
- [3] C.-Y. Hu, *J. Phys. B* **32**, 3077 (1999).
- [4] Z. Papp, C.-Y. Hu, Z. T. Hlousek, B. Konya and S. L. Yakovlev, *Phys. Rev. A* **63**, 062721 (2001).
- [5] A. A. Kvitsinsky, J. Carbonell and C. Gignoux, *Phys. Rev. A* **46**, 1310 (1992).
- [6] A. K. Bhatia, A. Temkin and H. Eiserike, *Phys. Rev. A* **9**, 219 (1974).
- [7] J. W. Humberston, P. Van Reeth, M. S. T. Watts and W. E. Meyerhof, *J. Phys. B* **30**, 2477 (1997).
- [8] M. Charlton and J. W. Humberston, *Positron physics*. Cambridge University Press, 2001.
- [9] T. T. Gien, *Phys. Rev. A* **59**, 1238 (1999).
- [10] J. Mitroy and K. Ratnavelu, *J. Phys. B* **28**, 287 (1995).
- [11] A. S. Kadyrov and I. Bray, *Phys. Rev. A* **66**, 012710 (2002).
- [12] A. Igarashi and N. Toshima, *Phys. Rev. A* **50**, 232 (1994).
- [13] S. J. Ward and J. Shertzer, *New J. Phys.* **14**, 025003 (2012).
- [14] A. A. Kvitsinsky, A. Wu and C.-Y. Hu, *J. Phys. B* **28**, 275 (1995).
- [15] S. L. Yakovlev, C.-Y. Hu and D. Caballero, *J. Phys. B* **40**, 1675 (2007).
- [16] R. Lazauskas, *J. Phys. B* **50**, 055201 (2017).
- [17] M. V. Volkov, E. A. Yarevsky and S. L. Yakovlev, *Europhys. Lett.* **110**, 30006 (2015).
- [18] M. Valdes, M. Dufour, R. Lazauskas and P.-A. Hervieux, *Phys. Rev. A* **97**, 012709 (2018).
- [19] V. A. Gradusov, V. A. Roudnev and S. L. Yakovlev, *Atoms* **4**, 9 (2016).
- [20] S. L. Yakovlev and Z. Papp, *Theor. Math. Phys.* **163**, 666 (2010).

- [21] V. A. Gradusov, V. A. Roudnev, E. A. Yarevsky and S. L. Yakovlev, *J. Phys. B* **52**, 055202 (2019).
- [22] N. W. Schellingerhout, L. P. Kok and G. D. Bosveld, *Phys. Rev. A* **40**, 5568 (1989).
- [23] Y. Saad, *Iterative methods for sparse linear systems*. SIAM, 2003.
- [24] B. Bialecki and G. Fairweather, *J. Comput. Appl. Math.* **46**, 369 (1993).
- [25] V. Roudnev and S. Yakovlev, *Comput. Phys. Commun.* **126**, 162 (2000).
- [26] Y. K. Ho and Z.-C. Yan, *Phys. Rev. A* **70**, 032716 (2004).
- [27] K. Varga, J. Mitroy, J. Zs. Mezei and A. T. Kruppa, *Phys. Rev. A* **77**, 044502 (2008).
- [28] R.-M. Yu, Y.-J. Cheng, L.-G. Jiao and Y.-J. Zhou, *Chin. Phys. Lett.* **29**, 053401 (2012).
- [29] M. Umair and S. Jonsell, *J. Phys. B* **47**, 225001 (2014).
- [30] M. Gailitis and R. Damburg, *Sov. Phys. JETP* **17**, 1107 (1963).
- [31] M. Gailitis and R. Damburg, *Proc. Phys. Soc.* **82**, 192 (1963).
- [32] C.-Y. Hu, D. Caballero and Z. Papp, *Phys. Rev. Lett.* **88**, 063401 (2002).
- [33] I. I. Fabrikant, A. W. Bray, A. S. Kadyrov and I. Bray, *Phys. Rev. A* **94**, 012701 (2016).
- [34] B. H. Bransden, C. J. Noble and R. J. Whitehead, *J. Phys. B* **34**, 2267 (2001).
- [35] C. M. Rawlins, A. S. Kadyrov and I. Bray, *Phys. Rev. A* **97**, 012707 (2018).
- [36] Y. Z. Zhang, R. M. Yu, S. X. Li, X. D. Song and L. G. Jiao, *J. Phys. B* **48**, 175206 (2015).
- [37] A. Igarashi and I. Shimamura, *Phys. Rev. A* **56**, 4733 (1997).
- [38] A. Igarashi and I. Shimamura, *Phys. Rev. A* **70**, 012706 (2004).
- [39] M.-M. Liu, H.-L. Han, S.-H. Gu and T.-Y. Shi, *Chin. Phys. Lett.* **29**, 013101 (2012).
- [40] A. I. Baz', Ya. B. Zel'dovich and A. M. Perelomov, *Scattering, reactions and decay in nonrelativistic quantum mechanics*. Israel Program for Scientific Translations, Jerusalem, 1969.
- [41] N. Elander and E. Yarevsky, *Phys. Rev. A* **57**, 3119 (1998).

# Towards High-Precision Nuclear Forces from Chiral Effective Field Theory

Evgeny Epelbaum

*Ruhr-Universität Bochum, Fakultät für Physik und Astronomie, Institut für Theoretische Physik II, D-44780 Bochum, Germany*

## Abstract

Chiral effective field theory is being developed into a precision tool for low-energy nuclear physics. I review the state of the art in the two-nucleon sector, discuss applications to few-nucleon systems and address challenges that will have to be addressed over the coming years.

**Keywords:** *Effective field theory, chiral perturbation theory, nuclear forces, few-nucleon systems*

## 1 Introduction

Chiral effective field theory (EFT) is widely applied to studies of low-energy structure and dynamics of nuclear systems. The method relies on the spontaneously broken approximate  $SU(2)\times SU(2)$  chiral symmetry of QCD and allows one to compute the scattering amplitude of pions, the Nambu–Goldstone bosons of the spontaneously broken axial generators, with themselves and with matter fields via a perturbative expansion in momenta and quark masses, commonly referred to as the chiral expansion [1]. The appealing features of this method lie in its systematic and universal nature, which allows one to establish model-independent perturbative relations between low-energy observables in the Goldstone-boson and single-baryon sectors and low-energy constants (LECs) of the effective chiral Lagrangian.

When applied to self-bound systems such as atomic nuclei, the method outlined above has to be modified appropriately to account for the non-perturbative nature of the problem at hand by resumming certain parts of the scattering amplitude. According to Weinberg [2], the breakdown of perturbation theory is attributed to the appearance of time-ordered diagrams, which would be infrared divergent in the limit of infinitely heavy nucleons and are enhanced relative to their expected chiral order. The quantum mechanical Schrödinger equation provides a simple and natural framework to resum such enhanced contributions to the  $A \geq 2$ -nucleon scattering amplitude as it can be efficiently dealt with using a variety of available *ab initio* continuum methods [3–8], see the contributions of Petr Navrátil [9] and James Vary [10], or lattice simulations [11–13], see the contributions by Ulf-G. Meißner [14] and Dean Lee [15] for selected highlights and exciting new developments along this line. The problem

---

*Proceedings of the International Conference ‘Nuclear Theory in the Supercomputing Era — 2018’ (NTSE-2018), Daejeon, South Korea, October 29 – November 2, 2018, eds. A. M. Shirokov and A. I. Mazur. Pacific National University, Khabarovsk, Russia, 2019, p. 150.*

<http://www.ntse.khb.ru/files/uploads/2018/proceedings/Epelbaum.pdf>.

thus essentially reduces to the derivation of the nuclear forces and currents, defined in terms of the corresponding irreducible (i. e., non-iterative) parts of the amplitude, that are not affected by the above-mentioned enhancement and can be worked out order by order in the chiral expansion. The resulting framework, firmly rooted in the symmetries of QCD, allows one to derive consistent nuclear forces and currents and offers a systematically improvable theoretical approach to few- and many-nucleon systems [16–18].

Contrary to the on-shell scattering amplitudes, the nuclear forces and currents are scheme-dependent quantities, which are affected by unitary transformations or, equivalently, by nonlinear redefinitions of the nucleon field operators. Care is therefore required to maintain consistency between the two- and many-nucleon forces and the current operators, see Section 5 for the discussion. The unitary ambiguity in the resulting nuclear potentials is significantly reduced (but not completely eliminated) by the requirement of their renormalizability<sup>1</sup>. Another complication is related to the regularization of the Schrödinger or Lippmann–Schwinger (LS) equation [19]. Iterations of nuclear potentials in the LS equation generate ultraviolet divergent higher-order contributions to the amplitude, which cannot be made finite by counterterms in the truncated potential. One is, therefore, forced to keep the ultraviolet cutoff  $\Lambda$  finite (of the order of the breakdown scale  $\Lambda_b$ ) [19–21]. As discussed in Section 5, maintaining consistency between nuclear forces and currents in the presence of a finite cutoff is a rather nontrivial task starting from the fourth order in the chiral expansion.

In this contribution I will briefly review the current status of the chiral EFT, discuss a selected application and address the challenges that need to be tackled to develop this approach into a precision tool beyond the two-nucleon system.

## 2 Derivation of nuclear forces and currents

As already pointed out in the Introduction, the nuclear forces and currents are identified with the irreducible parts of the scattering amplitude and can be worked out using a variety of methods including matching to the  $S$ -matrix time-ordered perturbation theory (TOPT) and the method of unitary transformation (UT). The last approach has been pioneered in the fifties of the last century in the context of pion field theory [22, 23] and applied to the effective chiral Lagrangian in Refs. [24, 25]. The derivation of nuclear forces is achieved by performing a UT of the effective pion-nucleon Hamiltonian in the Fock space, which decouples the purely nucleonic subspace from the rest of the Fock space. The corresponding unitary operator is determined perturbatively by using the chiral expansion. The method can be formulated utilizing a diagrammatic language, but the resulting time-ordered-like graphs have a different meaning than the ones arising in the context of TOPT. The importance of any diagram can be estimated by counting the corresponding power  $\nu$  of the chiral expansion parameter  $Q \in \{p/\Lambda_b, M_\pi/\Lambda_b\}$ , where  $M_\pi$  denotes the pion mass and  $p \sim M_\pi$  are three-momenta of the nucleons. For connected diagrams contributing to the  $A$ -nucleon potential with  $B$  insertions of external classical sources, the chiral dimension  $\nu$  is given

---

<sup>1</sup>Contrary to the on-shell  $S$ -matrix, loop contributions to the nuclear forces and currents may contain ultraviolet divergences which cannot be absorbed into the counterterms of the effective Lagrangian, see Section 5. When calculating the scattering amplitude, such divergences cancel against the ones generated by ladder diagrams, which emerge from iterations of the Lippmann–Schwinger equation.

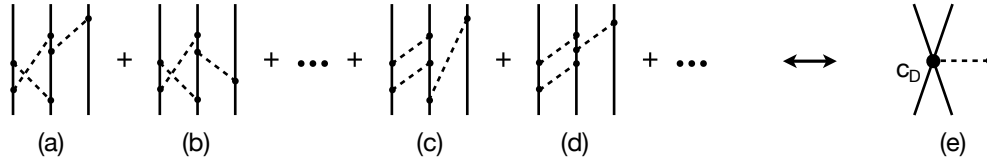


Figure 1: Time-ordered-like diagrams contributing to the two-pion-one-pion-exchange 3NF topology at the fourth order in the chiral expansion (graphs (a)-(d)) along with the one-pion-exchange-contact contribution to the 3NF at the third order. Solid and dashed lines refer to nucleons and pions, respectively. Solid dots and the filled circle denote vertices of dimension  $\Delta = 0$  and  $\Delta = 1$ , respectively.

by [2, 26]

$$\nu = -4 - B + 2(A + L) + \sum_i V_i \Delta_i, \quad (1)$$

where  $L$  is the number of loops and  $V_i$  is the number of vertices of dimension  $\Delta_i$  which appear in the diagram. The dimension of a vertex with  $n_i$  nucleon field operators and  $d_i$  derivatives/ $M_\pi$ -insertions/insertions of the external classical sources is defined according to [2] as

$$\Delta_i = d_i + \frac{1}{2}n_i - 2. \quad (2)$$

The spontaneously broken chiral symmetry permits only interactions with  $\Delta \geq 0$ , so that a finite number of diagrams can be drawn at each finite chiral order  $Q^\nu$ . Notice that for actual calculations in the method of UT, it is more convenient to rewrite Eqs. (1), (2) using different variables as explained in Ref. [27].

As already pointed out above, loop contributions to nuclear potentials can, in general, not be renormalized. The problem is exemplified in Fig. 1 for the fourth-order (i. e.,  $N^3\text{LO}$ ) contribution to the three-nucleon force (3NF) proportional to  $g_A^6$ , with  $g_A$  referring to the nucleon axial-vector constant. To obtain a renormalized expression for the 3NF, the loop integrals should involve only linearly divergent pieces, which can be cancelled by the counterterm in the LEC  $c_D$ . This is only possible if the pion exchange between the pair of the first two nucleons and the last nucleon in diagrams (a)-(d) factorizes out in order to match the expression for diagram (e) at the third chiral order (i. e.,  $N^2\text{LO}$ ). However, evaluating the corresponding diagrams in TOPT, one finds that the pion exchange does, actually, not factorize out. To ensure factorization of the one-pion exchange and enable renormalizability of the 3NF<sup>2</sup>, a broad class of additional unitary transformations in the Fock space has been considered in Refs. [26, 27]. Other types of contributions to the 3NF at  $N^3\text{LO}$  and at the fifth order ( $N^4\text{LO}$ ) in the chiral expansion and to the current operators show similar problems with renormalizability. So far, it was always possible to maintain renormalizability of nuclear forces and current operators, calculated using dimensional regularization (DR), via a suitable choice of additional unitary transformations, see Refs. [27–30] for more details.

Figure 2 visualizes the current state-of-the-art in the derivation of the nuclear Hamiltonian using the heavy-baryon formulation of chiral perturbation theory with

<sup>2</sup>The situation becomes more complicated if cutoff regularization is used instead of dimensional regularization, see the discussion in Section 5.

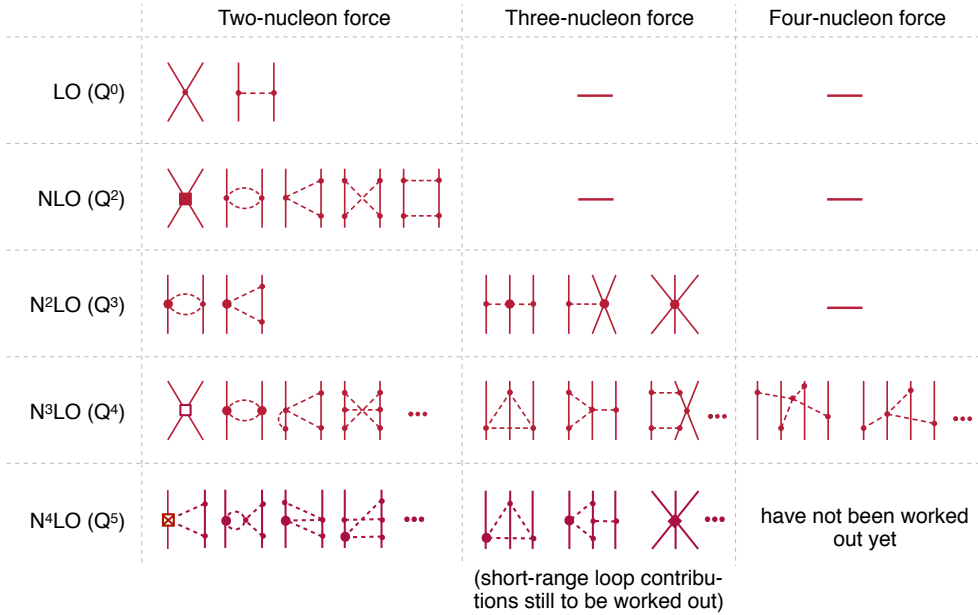


Figure 2: Chiral expansion of the nuclear forces. Solid and dashed lines refer to nucleons and pions. Solid dots, filled circles, filled squares, crossed squares and open squares denotes vertices from the effective chiral Lagrangian of dimension  $\Delta = 0, 1, 2, 3$  and  $4$ , respectively.

pions and nucleons as the only explicit degrees of freedom and utilizing the rules of naive dimensional analysis for few-nucleon contact operators, see Refs. [31–33] for alternative proposals. We remind the reader that all diagrams shown in this and following figures correspond to the irreducible parts of the scattering amplitude and to be understood as series of all possible time-ordered-like graphs for a given topology. As already explained before, the precise meaning of these diagrams and the resulting contributions to the nuclear forces are scheme dependent.

The nucleon-nucleon potential has been calculated to the fifth order (N<sup>4</sup>LO) in the chiral expansion using the dimensional regularization [24, 34–41]. The expressions for the leading and subleading 3NF can be found in Refs. [42–46] and [26, 27], respectively. Apart from the contributions involving  $NN$  contact interactions, which still have to be worked out, the N<sup>4</sup>LO terms in the 3NF can be found in Refs. [29, 47, 48]. The leading contribution to the four-nucleon force (4NF) appears at N<sup>3</sup>LO and has been derived in Refs. [26, 27]. It is important to emphasize that the long-range parts of the nuclear forces are completely determined by the spontaneously broken approximate chiral symmetry of QCD along with the experimental and/or empirical information on the pion-nucleon system needed to determine the relevant LECs in the effective Lagrangian. In this sense, the long-range contributions to the nuclear forces and currents can be regarded as parameter-free predictions. Given that the chiral expansion of the  $NN$  contact operators in the isospin limit contains only contributions at orders  $Q^{2n}$ ,  $n = 0, 1, 2, \dots$ , the N<sup>2</sup>LO and the isospin-invariant N<sup>4</sup>LO corrections to the  $NN$  potential are parameter-free. This also holds true for the N<sup>3</sup>LO contributions to the 3NF and 4NF. For calculations utilizing a formulation of chiral EFT with explicit  $\Delta(1232)$  degrees of freedom see Refs. [49–55].

The chiral power counting offers a natural qualitative explanation of the observed hierarchy of the nuclear forces, and the actual size of the various contributions to observables generally agrees well with the expectations based on naive dimensional analysis (NDA) underlying the chiral power counting. For example, the kinetic energy of the deuteron can naively be expected of the order of  $E_{\text{kin}} \sim M_\pi^2/m_N \sim 20$  MeV, since the pion mass is the only explicit soft scale in the problem. This compares well with the actual findings of  $E_{\text{kin}} \simeq 12 \dots 23$  MeV for the LO ... N<sup>4</sup>LO chiral potentials of Ref. [56, 57] and  $E_{\text{kin}} \simeq 12 \dots 16$  MeV for the LO ... N<sup>4</sup>LO<sup>+</sup><sup>3</sup> potentials of Ref. [58]. For comparison, for the Argonne AV18 potential [60], one finds  $E_{\text{kin}} \simeq 19$  MeV. For <sup>3</sup>H, one can use the following simple considerations to estimate the size of the 3NF. Using phenomenological potentials, one typically finds  $|\langle V_{NN} \rangle|_{\text{3H}} \sim 50$  MeV. Thus, according to the power counting, the 3NF contribution to the <sup>3</sup>H binding energy may be expected of the order of  $Q^3 |\langle V_{NN} \rangle|_{\text{3H}}$ . With  $Q \sim M_\pi/\Lambda_b$  and  $\Lambda_b \simeq 600$  MeV [56], one expects the 3NF to contribute about  $0.013 |\langle V_{NN} \rangle|_{\text{3H}} \sim 650$  keV to the triton binding energy. This matches well with the observed typical underbinding of <sup>3</sup>H in calculations based on the *NN* forces only [61, 62]. Similar estimations may be carried out for the 4NF, for other light nuclei and for nucleon-deuteron scattering observables. In the latter case, assuming  $Q = \max\{p/\Lambda_b, M_\pi/\Lambda_b\}$ , one expects the 3NF effects to be small at low energy, but become more important at higher energies. Again, this expectation is in line with the observed discrepancies between nucleon-deuteron scattering data and calculations based on the *NN* interactions only [61, 62]. Notice, however, that the observed fine tuned nature of the nuclear force, resulting, e. g., in a small value of the deuteron binding energy of  $E_{\text{b},\text{2H}} \simeq 2.224$  MeV, cannot be explained by NDA which actually suggests  $E_{\text{b},\text{2H}} \sim E_{\text{kin},\text{2H}} \sim |\langle V_{NN} \rangle|_{\text{2H}}$ . On the other hand, one observes  $\langle V_{NN} \rangle|_{\text{2H}} \simeq -E_{\text{kin},\text{2H}}$ , so that  $E_{\text{b},\text{2H}} \ll |\langle V_{NN} \rangle|_{\text{2H}}$ . Similar fine tuning also persists for light nuclei.

Nuclear electromagnetic and axial currents have been worked out in chiral EFT completely up through N<sup>3</sup>LO. Figure 3 summarizes the contributions to the electromagnetic charge and current operators derived using the method of UT in Refs. [28, 63, 64] and employing DR for loop integrals. The resulting expressions are, by construction, off-shell consistent with the nuclear forces derived by our group using the same approach. Again, the hierarchy of the *A*-nucleon contributions to the charge and current operators suggested by the chiral power counting is fully in line with empirical findings based on explicit calculations, which show the dominance of single-nucleon contributions for most of the low-energy observables [65, 66]. In particular, the charge operator is strongly dominated by the one-nucleon (1N) term with the “meson-exchange” contributions being suppressed by four powers of the expansion parameter. On the other hand, the power counting suggests that the three-nucleon (3N) charge operator is as important as the two-body one, which can be tested, e. g., by calculating elastic form factors (FFs) of light nuclei. Notice further that up to N<sup>3</sup>LO, the charge operator does not involve any unknown LEC. It is furthermore important to emphasize that the single-nucleon contributions to both the charge and current operators can be expressed in terms of the electromagnetic FFs of the nucleon. Using the available empirical information on the nucleon FFs then allows one to avoid relying on their strict chiral expansion known to converge slowly due to large contributions of vector mesons [67, 68].

---

<sup>3</sup>The “+” sign indicates that we have included four contact interactions in *F* waves from N<sup>5</sup>LO in order to reproduce several sets of very precisely measured proton-proton data at higher energies. The same contact interactions are also included in the N<sup>4</sup>LO potentials of Ref. [59].

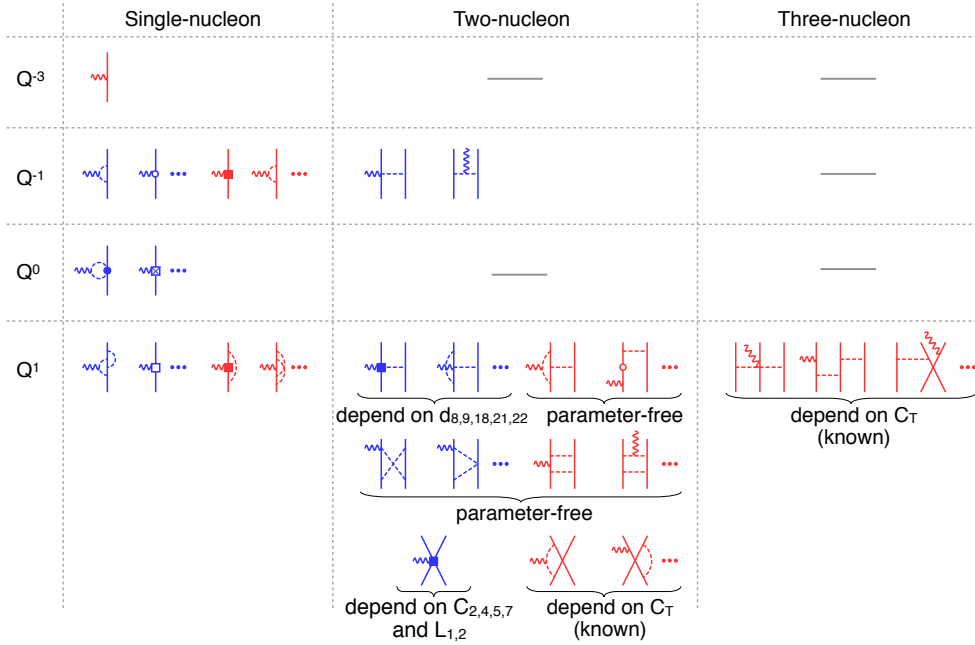


Figure 3: Chiral expansion of the nuclear electromagnetic currents. Red (blue) diagrams show the contributions to the charge (current) operators. Wavy lines refer to photons. For remaining notations see Fig. 2.

The leading contributions to the two-nucleon (2N) current operator emerge from a single pion exchange. The corrections at  $N^3\text{LO}$  include one-loop contributions to the one- and two-pion exchange as well as short-range operators. The third-order pion-nucleon LECs  $d_{18}$  and  $d_{22}$  can be determined from the Goldberger–Treiman discrepancy and the axial radius of the nucleon, while the  $d_{9,21,22}$  contribute to the charged pion photoproduction and the radiative capture reactions [69, 70]. For the explicit form of the pion-nucleon Lagrangian see Ref. [71]. The short-range 2N operators depend, apart from the LECs  $C_i$ , which govern the short-range  $NN$  potential at  $N^2\text{LO}$ , also on two new LECs  $L_{1,2}$ , which can be determined, e. g., from the deuteron magnetic moment and the cross section in the process  $np \rightarrow d\gamma$  [72].

Notice that the expressions for the  $N^3\text{LO}$  contributions to the electromagnetic charge and current operators derived in the method of UT in Refs. [28, 63, 64] differ from the ones calculated by Pastore *et al.* using the TOPT [73–75]. The reader is referred to Ref. [76] for a comprehensive review article, which also addresses the differences between the two approaches.

Recently, these studies have been extended to derive the nuclear axial and pseudoscalar currents up to  $N^3\text{LO}$  using the method of UT [30], see Fig. 4. Interestingly, one observes exactly the opposite pattern as compared to the electromagnetic operators with the dominant contributions to the 1N current, 2N charge and 3N current operators appearing at LO, NLO and  $N^3\text{LO}$ , respectively. In a complete analogy with the electromagnetic currents, the 1N contributions are expressible in terms of the corresponding FFs of the nucleon. The 2N and 3N contributions to the current density are parameter-free at this order, while the long-range one-loop corrections to

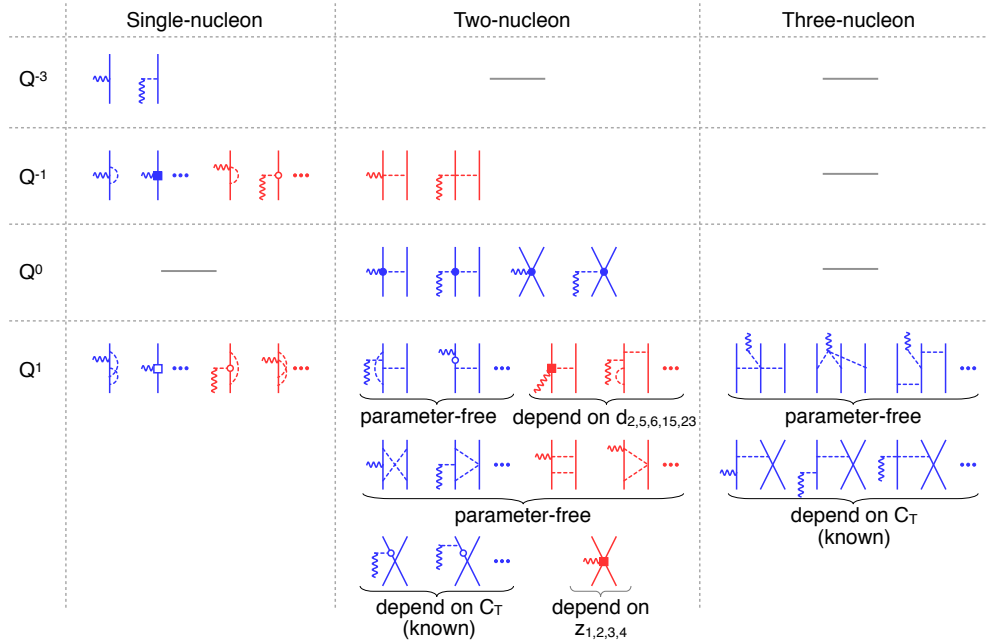


Figure 4: Chiral expansion of the nuclear axial currents. Red (blue) diagrams show the contributions to the charge (current) operators. Wavy lines refer to external axial-vector sources. For remaining notations see Fig. 2.

the 2N charge density depend on a number of poorly known LECs  $d_i$ . In addition, there are four new short-range operators contributing to the 2N charge operator at N<sup>3</sup>LO. Again, we emphasize that our results deviate from the (incomplete) calculation by Baroni *et al.* [77] using TOPT and refer the reader to Ref. [76] for a detailed comparison.

### 3 High-precision chiral two-nucleon potentials

In the previous Section, I briefly reviewed the state of the art in the derivation of nuclear forces and currents. These calculations are carried out using DR to regularize divergent loop integrals. As pointed out in the Introduction, the derived nuclear potentials and current operators are singular at short distances and need to be regularized. To the best of my knowledge, it is not known how to subtract all ultraviolet divergences arising from iterations of the  $NN$  potential in the Lippmann–Schwinger equation. Thus, the cutoff  $\Lambda$  has to be kept finite of the order of the breakdown scale  $\Lambda_b$  [19–21]. In Ref. [56], this scale was estimated to be  $\Lambda_b \sim 600$  MeV. This was confirmed in the Bayesian analysis of Ref. [78], which found that it may even be somewhat larger, see Refs. [79,80] for a related recent work along this line. In practice, even lower values of the cutoff  $\Lambda$  are preferred in order to avoid the appearance of deeply bound states, which would complicate the numerical treatment of the nuclear  $A$ -body problem, and to keep the potentials sufficiently soft in order to facilitate the convergence of many-body methods. It is, therefore,

important to use a regulator, which minimizes the amount of finite-cutoff artifacts. In Ref. [56], we argued that a local regularization of the pion-exchange contributions to the nuclear forces is advantageous compared to the nonlocal regulators used, e. g., in Refs. [25, 81, 82] as it maintains the analytic properties of the potential and does not induce long-range artifacts, see also Refs. [54, 83] for a related discussion. In Refs. [56, 57], a coordinate-space cutoff was employed to regularize the one- and two-pion exchange contributions. However, the implementation of such a regulator in coordinate space has turned out to be technically difficult for the 3NF and current operators. Thus, in Ref. [58], a momentum-space version of the local regulator was introduced by replacing the static propagators of pions exchanged between different nucleons via  $(\vec{q}^2 + M_\pi^2)^{-1} \rightarrow (\vec{q}^2 + M_\pi^2)^{-1} \exp[-(\vec{q}^2 + M_\pi^2)/\Lambda^2]$ , see Ref. [84] for a similar approach. Obviously, the employed regulator does not induce long-range artifacts at any finite order in the  $1/\Lambda$ -expansion. Notice further that the long-range part of the two-pion exchange  $NN$  potential, derived using the DR, does not need to be recalculated using a new regulator. As shown in Ref. [58], the regularization of the two-pion exchange can be easily accounted for using the spectral-function representation. For example, for the central two-pion exchange potential  $V(q)$ , the regularization is achieved via

$$V(q) = \frac{2}{\pi} \int_{2M_\pi}^{\infty} \mu d\mu \frac{\rho(\mu)}{\vec{q}^2 + \mu^2} + \dots \rightarrow \frac{2}{\pi} \int_{2M_\pi}^{\infty} \mu d\mu \frac{\rho(\mu)}{\vec{q}^2 + \mu^2} e^{-\frac{\vec{q}^2 + \mu^2}{2\Lambda^2}} + \dots, \quad (3)$$

where  $\rho(\mu)$  is the corresponding spectral function and the ellipses refer to the contributions polynomial in  $\vec{q}^2$  and  $M_\pi$ . In addition, a final number of (locally regularized) subtraction terms allowed by the power counting are taken into account to ensure that the corresponding long-range potentials and derivatives thereof vanish at the origin. For the contact  $NN$  interactions, a simple non-local cutoff of the Gaussian type  $\exp[-(\vec{p}^2 + \vec{p}'^2)/\Lambda^2]$  with  $\vec{p}$  and  $\vec{p}'$  denoting the initial and final center-of-mass momenta was employed. Using this regularization scheme and adopting the pion-nucleon LECs from the recent analysis in the framework of the Roy–Steiner equations [85, 86], a family of new chiral  $NN$  potentials from LO to  $N^4\text{LO}^+$  was presented in Ref. [58] for the cutoff values  $\Lambda = \{350, 400, 450, 500, 550\}$  MeV. The resulting potentials at  $N^4\text{LO}^+$  are currently the most precise chiral EFT  $NN$  potentials on the market. For the medium cutoff choice of  $\Lambda = 450$  MeV, the description of the neutron-proton and proton-proton scattering data from the 2013 Granada database [87] below  $E_{\text{lab}} = 300$  MeV is essentially perfect at  $N^4\text{LO}^+$  as witnessed by the corresponding  $\chi^2$  values of  $\chi^2/\text{datum} = 1.06$  and  $1.00$ , respectively. The  $N^4\text{LO}^+$  potentials of Ref. [58] thus qualify to be regarded as partial wave analysis (PWA). Distinct features of these potentials in comparison with the other available chiral EFT interactions are summarized in Ref. [88].

As a representative example, we show in Fig. 5 the description of the neutron-proton scattering observables at  $E_{\text{lab}} \simeq 143$  MeV at various orders of the chiral expansion. The truncation bands have been generated using the algorithm formulated in Ref. [56]. For the application of the Bayesian approach for the quantification of truncation errors to the potentials of Ref. [58], see Ref. [88]. One observes excellent convergence of the chiral expansion and a very good agreement with the Nijmegen PWA. These conclusions also hold true for other scattering observables and deuteron properties.

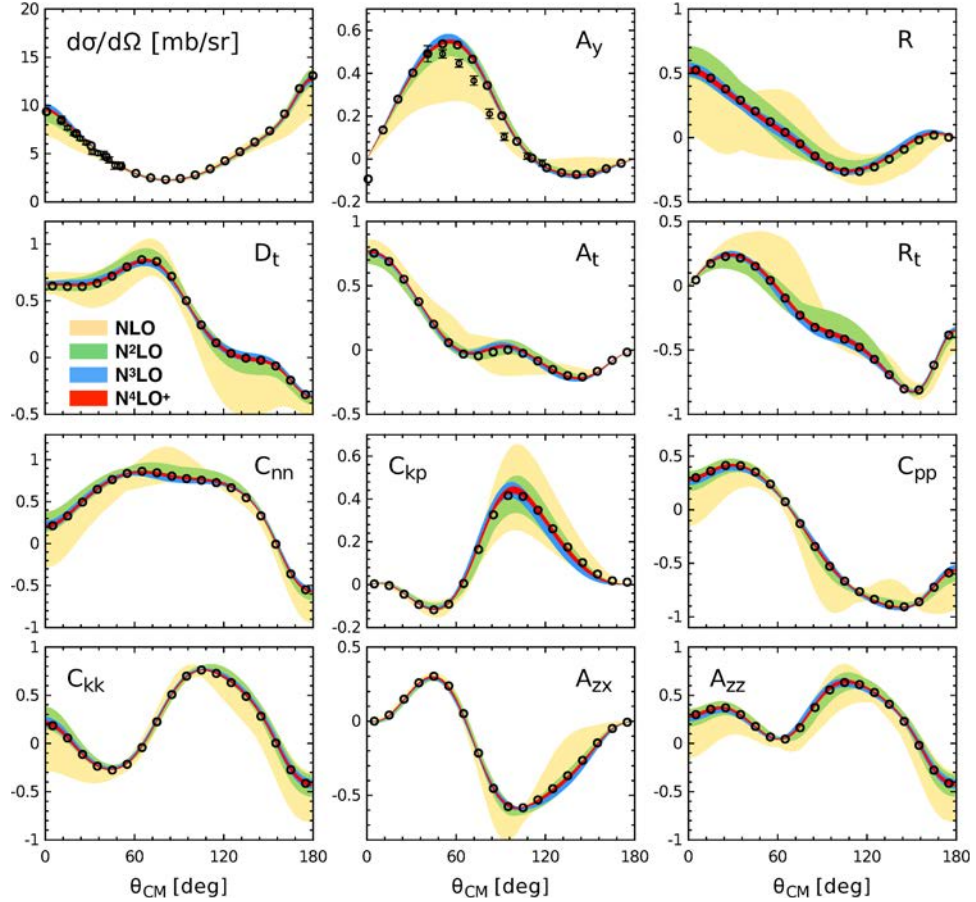


Figure 5: Neutron-proton scattering observables at  $E_{\text{lab}} = 143$  MeV calculated up to  $N^4\text{LO}^+$  using the chiral  $NN$  potentials of Ref. [58] for the cutoff  $\Lambda = 450$  MeV. Data for the cross section are at  $E_{\text{lab}} = 142.8$  MeV and are taken from Ref. [89] and those for the analyzing power  $A_y$  are from Ref. [90]. Bands show the estimated truncation error while open circles are the results of the Nijmegen PWA [91].

## 4 Three-nucleon force

The novel semi-local chiral  $NN$  potentials of Refs. [56–58] have already been explored in nucleon-deuteron scattering and selected nuclei [61, 62, 92–94]. By calculating various few-nucleon observables using the  $NN$  interactions only, a clear discrepancies between experimental data and theoretical results well outside the range of the estimated uncertainties were observed. The magnitude of these discrepancies appears to be consistent with the expected size of the 3NF, which start contributing at  $N^2\text{LO}$ , see Fig. 2.

To perform complete calculations at  $N^2\text{LO}$  and beyond one needs to include the 3NF (and 4NF starting from  $N^3\text{LO}$ ). These have to be regularized in a way *consistent* with the  $NN$  potentials. The precise meaning of the *consistency* in this context will be addressed in the next section. In Ref. [95], we performed calculations of the

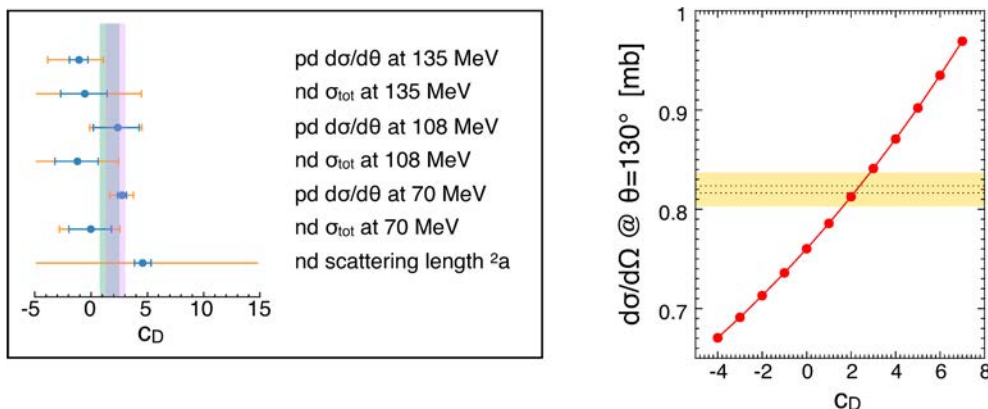


Figure 6: Left: Determination of the LEC  $c_D$  from various  $Nd$  scattering observables as explained in the text for the coordinate-space cutoff  $R = 0.9$  fm. The smaller (blue) error bars correspond to the experimental uncertainty while the larger (orange) error bars also take into account the truncation error at N<sup>2</sup>LO. Right:  $Nd$  cross section in the minimum region ( $\theta = 130^\circ$ ) at  $E_N = 70$  MeV as function of the LEC  $c_D$ . For each  $c_D$  value, the LEC  $c_E$  is adjusted to the  ${}^3\text{H}$  binding energy. Dotted lines show the statistical uncertainty of the experimental data from Ref. [99], while the yellow band also takes into account the quoted systematic uncertainty of 2%.

nucleon-deuteron ( $Nd$ ) scattering and of the ground and low-lying excited states of light nuclei up to  $A = 16$  up through N<sup>2</sup>LO using the semilocal coordinate-space regularized  $NN$  potentials of Refs. [56] together with the 3NF regularized in the same way. Notice that the Faddeev equations are usually solved in the partial wave basis. Partial wave decomposition of arbitrary 3NFs can be accomplished numerically using the machinery developed in Refs. [96,97]. The leading 3NF at N<sup>2</sup>LO depends on two LECs,  $c_D$  and  $c_E$ , which cannot be determined in the  $NN$  system. It is customary to tune the short-range part of the 3NF in such a way that the  ${}^3\text{H}$  and/or  ${}^3\text{He}$  binding energies (BEs) are reproduced. As for the second constraint, different options have been explored including the neutron-deuteron spin-1/2 scattering length  ${}^2a$ , the BE and/or radius of the  $\alpha$ -particle,  $Nd$  scattering observables, selected properties of light and medium-mass nuclei, equation of state for symmetric nuclear matter; see Ref. [98] for a review. In Ref. [95], we have explored the possibility to determine both LECs entirely from the three-nucleon system. Specifically, we used the triton BE to express  $c_E$  as a function of  $c_D$ . To fix the  $c_D$  value, a range of the available differential and total cross section data in elastic  $Nd$  scattering and the doublet scattering length were considered. Notice that the 3NF is well known to have a large impact on the differential cross section in the minimum region (at not too low energies) [3]. Taking into account the estimated theoretical uncertainty from the truncation of the chiral expansion, very precise experimental data of Ref. [99] for the proton-deuteron differential cross section at  $E_N = 70$  MeV were found to impose the strongest constraint on the  $c_D$  value as visualized in Fig. 6. It is important to emphasize that contrary to the scattering length  ${}^2a$  and the  ${}^4\text{He}$  BE, we do not observe any correlations between the triton BE and the cross section minimum in elastic  $Nd$  scattering at the considered energies. In particular, we found that a variation of the  ${}^3\text{H}$  BE used in the fit

effects the value of  $c_E$  but has almost no effect on the value of  $c_D$ . Having determined the LECs  $c_D$  and  $c_E$  as described above, the resulting nuclear Hamiltonian was used to calculate selected  $Nd$  scattering observables and low-lying states in nuclei up to  $A = 16$ . The inclusion of the 3NF was found to improve the agreement with the data for most of the considered observables.

While these results are quite promising, the theoretical uncertainty of the  $N^2\text{LO}$  approximation is still fairly large [95]. At higher chiral orders, the estimated truncation errors are, however, expected to become significantly smaller than the observed deviations between the experimental data and theoretical calculations. This is especially true for the  $Nd$  scattering observables at intermediate energies, see Ref. [61, 62] for examples. Notice that the  $Nd$  scattering observables are known to be not very sensitive to the off-shell behavior of  $NN$  interactions as shown by Faddeev calculations using a variety of essentially phase-equivalent, high-precision phenomenological potentials [3]. This feature persists for the high-precision chiral  $NN$  potentials at  $N^4\text{LO}^+$ . The large discrepancies between the theory and data for spin observables in  $Nd$  scattering [100], therefore, seem to be universal and should presumably be attributed to the deficiencies of the available 3NF models. The 3NF effects at  $N^2\text{LO}$  appear to be qualitatively similar to the ones of the phenomenological models such as the Tucson–Melbourne [101] or Urbana IX [102] 3NFs and are insufficient to resolve the above mentioned discrepancies. The solution of the long-standing 3NF challenge is therefore likely to emerge from corrections to the 3NF beyond  $N^2\text{LO}$ . Based on the experience in the  $NN$  sector [58], the description of  $Nd$  scattering data will likely require pushing the chiral expansion to (at least)  $N^4\text{LO}$ .

## 5 Towards consistent regularization of nuclear forces and currents

To take into account the chiral 3NF in few-body calculations, the resulting expressions, derived using DR as discussed in Section 2, have to be regularized in the way *consistent* with the  $NN$  force. As will be explained below, this poses a nontrivial problem starting from  $N^3\text{LO}$ , where the first loop contributions appear in the 3NF.

As already pointed out above, nuclear potentials and currents are not uniquely defined due to inherent unitary ambiguities. Off-shell behaviors of the 2NF and 3NF must be consistent in order to ensure that iterations of the Lippmann–Schwinger (or Faddeev) equations reproduce the corresponding on-shell contributions to the  $S$ -matrix (up to higher-order corrections), as exemplified in Fig. 7 for one particular contribution to the 3N scattering amplitude. As already mentioned before, all expressions for the nuclear forces and current operators reviewed in Section 2, which are derived using the method of UT and employing DR to regularize the divergent loop integrals, are consistent with each other *provided one also uses DR to regularize the loops from iterations of the integral equation*, see, e. g., the first diagram on the right-hand side of the equation in Fig. 7. However, in practice, regularization of the  $A$ -body Schrödinger equation in the context of nuclear chiral EFT is achieved by introducing a cutoff rather than by using DR. This raises an important question of whether the usage of nuclear potentials, derived in DR and subsequently regularized with a cutoff, still yields results which are consistent in the above-mentioned sense. It is easy to see that this is, generally, not the case by looking at the example shown in

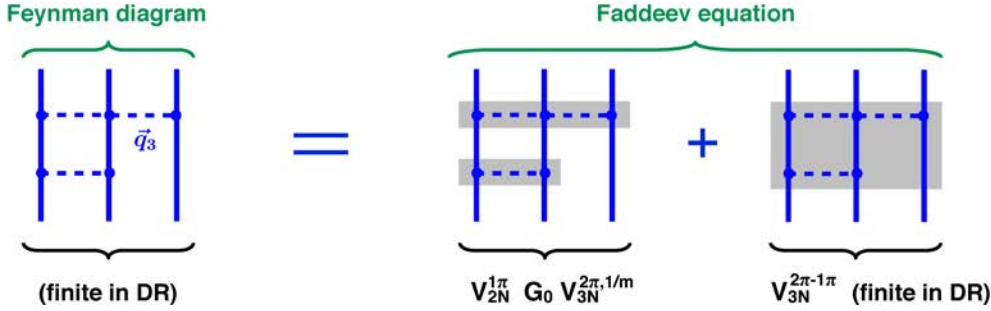


Figure 7: On-shell amplitude from the one-pion-two-pion-exchange Feynman diagram (left) is represented in terms of iterations of the Faddeev equation (right). Gray-shaded rectangles visualize the corresponding two- and three-nucleon potentials.

Fig. 7. The expressions for the two-pion-exchange 3NF proportional to  $g_A^2/m_N$  in the second diagram are given in Eqs. (4.9)–(4.11) of Ref. [46], while the expression for the two-pion-one-pion exchange 3NF proportional to  $g_A^4$  in the last diagram, evaluated in DR, can be found in Eqs. (2.16)–(2.20) of Ref. [45]. The one-pion exchange potential regularized with a local momentum-space cutoff discussed in Section 3 is given in Ref. [58]. Using the same regulator for the two-pion exchange 3NF, one finds that the  $V_{2N}^{1\pi} G_0 V_{3N}^{2\pi, 1/m}$  contribution in Fig. 7 contains linear divergent terms of the kind

$$\sim \Lambda \frac{q_1^i q_3^j}{\bar{q}_3^2 + M_\pi^2}, \quad \sim \Lambda \frac{q_3^i q_3^j}{\bar{q}_3^2 + M_\pi^2}. \quad (4)$$

While the last divergence can be absorbed into the LEC  $c_D$ , the first divergent term violates the chiral symmetry, since it corresponds to a derivative-less coupling of the exchanged pion. No such chiral-symmetry-breaking contribution appears in the 3NF at N<sup>2</sup>LO. On the other hand, the Feynman diagram on the left-hand-side of the equation in Fig. 7 must, of course, be renormalizable not only in the DR but also using the cutoff regularization (provided it respects the chiral symmetry). The issue with the renormalization on the right-hand side of this equation is actually caused by using different regularization schemes when calculating the reducible (i. e., iterative) and irreducible contributions to the amplitude. Re-calculating  $V_{3N}^{2\pi-1\pi}$  using the cutoff regularization instead of DR yields a linearly-divergent contribution, which cancels exactly the problematic divergence given by the first term in Eq. (4), and restores the renormalizability of the scattering amplitude (and the consistency). This example shows that a naive cutoff regularization of the 3NFs, derived using DR, is, in fact, inconsistent starting from N<sup>3</sup>LO. Similar problems appear in calculations involving exchange currents, see Ref. [103] for the discussion and an explicit example.

It is important to emphasize that the above-mentioned problems do not affect calculations in the  $NN$  sector (for the physical value of the quark masses). This is because the chiral symmetry does not impose constraints on the momentum dependence of the  $NN$  contact interactions. It is, therefore, always possible to absorb all appearing ultraviolet divergences into a redefinition of the corresponding LECs. This is different for the contact interactions involving pion fields, which are indeed strongly constrained by the spontaneously broken chiral symmetry of QCD.

Last but not least, it is important to keep in mind that introducing a cutoff in a way compatible with the chiral and gauge symmetries is a rather nontrivial problem. The so-called higher-derivative regularization introduced by Slavnov in [104] provides one a possibility to implement a cutoff in the chirally invariant fashion already at the level of the effective Lagrangian, see Refs. [105–107] for applications in the context of chiral EFT.

## 6 Summary

There have been a remarkable progress in pushing the chiral EFT into a precision tool. This theoretically well-founded approach is firmly rooted in the symmetries of QCD and their breaking pattern. It allows one to address various low-energy hadronic reactions involving pions, nucleons and external sources in a systematically improvable fashion within a unified framework, thus putting nuclear physics onto a solid basis.

In this contribution, I focused mainly on the applications of chiral EFT in the few-nucleon sector. During the past two and a half decades, two-nucleon forces have been worked out completely up through  $N^4\text{LO}$  while the expressions for the 3NF, 4NF as well as the nuclear electromagnetic and axial currents are currently available at  $N^3\text{LO}$ . The last generation chiral  $NN$  potentials of Refs. [58, 59] benefit from the recent analysis of pion-nucleon scattering in the framework of the Roy–Steiner equation [85], which allows one to reconstruct the long-range part of the nuclear force in a parameter-free way. The resulting  $N^4\text{LO}^+$  potentials of Ref. [58] reach the same or even better quality in reproducing the  $NN$  scattering data below the pion production threshold as the phenomenological high-precision potentials, but have  $\sim 40\%$  less adjustable parameters. This reduction signifies the importance of the two-pion exchange, which is completely determined by the spontaneous chiral symmetry of QCD along with the empirical information on the pion-nucleon system. Another important development concerns establishing a simple and reliable approach for estimating truncation errors [56, 57, 78–80], which usually dominate the error budget in chiral EFT, and exploring the other sources of uncertainties [58, 108, 109].

These developments in the  $NN$  sector provide a solid basis for applications to heavier systems and/or processes involving electroweak probes. In contrast to the  $NN$  force, the 3NFs are still poorly understood, and large discrepancies between the theory and data in the three-nucleon continuum pose a long-standing challenge in nuclear physics [100]. While the leading 3NF at  $N^2\text{LO}$  has already been extensively investigated in  $Nd$  scattering and nuclear structure calculations and demonstrated to yield promising results, it is certainly insufficient to resolve the observed discrepancies. To include higher-order contributions to the 3NF (and the nuclear electroweak currents beyond  $N^2\text{LO}$ ), one needs to introduce a regulator in a way *consistent* with the 2NF, which poses a nontrivial problem starting from  $N^3\text{LO}$ . Work along these lines is in progress. Another challenge that will have to be overcome is the determination of the LECs accompanying short-range contributions of the 3NF at  $N^4\text{LO}$ , see Ref. [110] for an exploratory study.

## Acknowledgements

It is a great pleasure to thank all my collaborators, and especially Hermann Krebs and Ulf-G. Meißner, for sharing their insights into various topics discussed in this contribution and useful comments on the manuscript. I also thank the organizers of NTSE-2018 for making this interesting and stimulating workshop possible. This work was supported in part by DFG (SFB/TR 110, “Symmetries and the Emergence of Structure in QCD”) and the BMBF (Grant No. 05P15PCFN1).

## References

- [1] V. Bernard, N. Kaiser and U.-G. Meißner, *Int. J. Mod. Phys. E* **4**, 193 (1995).
- [2] S. Weinberg, *Phys. Lett. B* **251**, 288 (1990).
- [3] W. Glöckle *et al.*, *Phys. Rep.* **274**, 107 (1996).
- [4] B. R. Barrett, P. Navrátil and J. P. Vary, *Prog. Part. Nucl. Phys.* **69**, 131 (2013).
- [5] G. Hagen *et al.*, *Phys. Rev. Lett.* **109**, 032502 (2012).
- [6] H. Hergert *et al.*, *Phys. Rev. C* **87**, 034307 (2013).
- [7] V. Soma, C. Barbieri and T. Duguet, *Phys. Rev. C* **87**, 011303 (2013).
- [8] A. Lovato *et al.*, *Phys. Rev. Lett.* **111**, 092501 (2013).
- [9] P. Navrátil, *Nuclear structure and dynamics from chiral forces*, talk given at the Int. Conf. ‘Nuclear Theory in the Supercomputing Era — 2018’ (NTSE-2018), October 29 – November 2, 2018, Daejeon, South Korea, <http://ntse.khb.ru/files/uploads/2018/presentations/Navratil.pdf>.
- [10] P. Maris, I. J. Shin and J. P. Vary, *see these Proceedings*, p. 168, <http://www.ntse.khb.ru/files/uploads/2018/proceedings/Vary.pdf>.
- [11] D. Lee, *Prog. Part. Nucl. Phys.* **63**, 117 (2009).
- [12] D. Lee, *Lect. Notes Phys.* **936**, 237 (2017).
- [13] T. A. Lähde, U.-G. Meißner, *Lect. Notes Phys.* **957**, 1 (2019).
- [14] U.-G. Meißner, *see these Proceedings*, p. 28, <http://www.ntse.khb.ru/files/uploads/2018/proceedings/Meissner.pdf>.
- [15] D. Lee, *see these Proceedings*, p. 45, <http://www.ntse.khb.ru/files/uploads/2018/proceedings/Lee.pdf>.
- [16] E. Epelbaum, H. W. Hammer and U.-G. Meißner, *Rev. Mod. Phys.* **81**, 1773 (2009).
- [17] E. Epelbaum and U.-G. Meißner, *Annu. Rev. Nucl. Part. Sci.* **62**, 159 (2012).
- [18] R. Machleidt and D. R. Entem, *Phys. Rep.* **503**, 1 (2011).

- 
- [19] G. P. Lepage, nucl-th/9706029 (1997).
- [20] E. Epelbaum and J. Gegelia, Eur. Phys. J. A **41**, 341 (2009).
- [21] E. Epelbaum, A. M. Gasparyan, J. Gegelia and U.-G. Meißner, Eur. Phys. J. A **54**, 186 (2018).
- [22] N. Fukuda, K. Sawada and M. Taketani, Prog. Theor. Phys. **12**, 156 (1954).
- [23] S. Okubo, Prog. Theor. Phys. **12**, 603 (1954).
- [24] E. Epelbaum, W. Glöckle and U.-G. Meißner, Nucl. Phys. A **637**, 107 (1998).
- [25] E. Epelbaum, W. Glöckle and U.-G. Meißner, Nucl. Phys. A **671**, 295 (2000).
- [26] E. Epelbaum, Phys. Lett. B **639**, 456 (2006).
- [27] E. Epelbaum, Eur. Phys. J. A **34**, 197 (2007).
- [28] S. Kölling, E. Epelbaum, H. Krebs and U.-G. Meißner, Phys. Rev. C **84**, 054008 (2011).
- [29] H. Krebs, A. Gasparyan and E. Epelbaum, Phys. Rev. C **85**, 054006 (2012).
- [30] H. Krebs, E. Epelbaum and U.-G. Meißner, Ann. Phys. (NY) **378**, 317 (2017).
- [31] A. Nogga, R. G. E. Timmermans and U. van Kolck, Phys. Rev. C **72**, 054006 (2005).
- [32] M. C. Birse, Phys. Rev. C **74**, 014003 (2006).
- [33] M. P. Valderrama, Int. J. Mod. Phys. E **25**, 1641007 (2016).
- [34] C. Ordonez and U. van Kolck, Phys. Lett. B **291**, 459 (1992).
- [35] J. L. Friar and S. A. Coon, Phys. Rev. C **49**, 1272 (1994).
- [36] N. Kaiser, R. Brockmann and W. Weise, Nucl. Phys. A **625**, 758 (1997).
- [37] N. Kaiser, Phys. Rev. C **61**, 014003 (2000).
- [38] N. Kaiser, Phys. Rev. C **62**, 024001 (2000).
- [39] N. Kaiser, Phys. Rev. C **64**, 057001 (2001).
- [40] N. Kaiser, Phys. Rev. C **65**, 017001 (2002).
- [41] D. R. Entem, N. Kaiser, R. Machleidt and Y. Nosyk, Phys. Rev. C **91**, 014002 (2015).
- [42] U. van Kolck, Phys. Rev. C **49**, 2932 (1994).
- [43] E. Epelbaum *et al.*, Phys. Rev. C **66**, 064001 (2002).
- [44] S. Ishikawa and M. R. Robilotta, Phys. Rev. C **76**, 014006 (2007).
- [45] V. Bernard, E. Epelbaum, H. Krebs and U.-G. Meißner, Phys. Rev. C **77**, 064004 (2008).

- 
- [46] V. Bernard, E. Epelbaum, H. Krebs and U.-G. Meißner, Phys. Rev. C **84**, 054001 (2011).
- [47] H. Krebs, A. Gasparyan and E. Epelbaum, Phys. Rev. C **87**, 054007 (2013).
- [48] L. Girlanda, A. Kievsky and M. Viviani, Phys. Rev. C **84**, 014001 (2011).
- [49] C. Ordonez, L. Ray and U. van Kolck, Phys. Rev. C **53**, 2086 (1996).
- [50] N. Kaiser, S. Gerstendorfer and W. Weise, Nucl. Phys. A **637**, 395 (1998).
- [51] H. Krebs, E. Epelbaum and U.-G. Meißner, Eur. Phys. J. A **32**, 127 (2007).
- [52] E. Epelbaum, H. Krebs and U.-G. Meißner, Nucl. Phys. A **806**, 65 (2008).
- [53] H. Krebs, A. M. Gasparyan and E. Epelbaum, Phys. Rev. C **98**, 014003 (2018).
- [54] M. Piarulli *et al.*, Phys. Rev. C **91**, 024003 (2015).
- [55] A. Ekström, G. Hagen, T. D. Morris, T. Papenbrock and P. D. Schwartz, Phys. Rev. C **97**, 024332 (2018).
- [56] E. Epelbaum, H. Krebs and U.-G. Meißner, Eur. Phys. J. A **51**, 53 (2015).
- [57] E. Epelbaum, H. Krebs and U.-G. Meißner, Phys. Rev. Lett. **115**, 122301 (2015).
- [58] P. Reinert, H. Krebs and E. Epelbaum, Eur. Phys. J. A **54**, 86 (2018).
- [59] D. R. Entem, R. Machleidt and Y. Nosyk, Phys. Rev. C **96**, 024004 (2017).
- [60] R. B. Wiringa, V. G. J. Stoks and R. Schiavilla, Phys. Rev. C **51**, 38 (1995).
- [61] S. Binder *et al.* (LENPIC Collaboration), Phys. Rev. C **93**, 044002 (2016).
- [62] S. Binder *et al.* (LENPIC Collaboration), Phys. Rev. C **98**, 014002 (2018).
- [63] S. Kölling, E. Epelbaum, H. Krebs and U.-G. Meißner, Phys. Rev. C **80**, 045502 (2009).
- [64] H. Krebs, E. Epelbaum and U.-G. Meißner, Few-Body Syst. **60**, 31 (2019).
- [65] H. Arenhovel and M. Sanzone, Few-Body Syst. Suppl. **3**, 1 (1991).
- [66] J. Golak *et al.*, Phys. Rep. **415**, 89 (2005).
- [67] B. Kubis and U.-G. Meißner, Nucl. Phys. A **679**, 698 (2001).
- [68] M. R. Schindler, J. Gegelia and S. Scherer, Eur. Phys. J. A **26**, 1 (2005).
- [69] H. W. Fearing, T. R. Hemmert, R. Lewis and C. Unkmeir, Phys. Rev. C **62**, 054006 (2000).
- [70] A. Gasparyan and M. F. M. Lutz, Nucl. Phys. A **848**, 126 (2010).
- [71] N. Fettes, U.-G. Meißner, M. Mojzis and S. Steininger, Ann. Phys. (NY) **283**, 273 (2000); Erratum: *ibid.* **288**, 249 (2001).
- [72] J. W. Chen, G. Rupak and M. J. Savage, Nucl. Phys. A **653**, 386 (1999).

- [73] S. Pastore, R. Schiavilla and J. L. Goity, Phys. Rev. C **78**, 064002 (2008).
- [74] S. Pastore *et al.*, Phys. Rev. C **80**, 034004 (2009).
- [75] S. Pastore, L. Girlanda, R. Schiavilla and M. Viviani, Phys. Rev. C **84**, 024001 (2011).
- [76] H. Krebs, *Nuclear currents in chiral effective field theory, to be published in Eur. Phys. J. A.*
- [77] A. Baroni *et al.*, Phys. Rev. C **93**, 015501 (2016); Erratum: *ibid.* **93**, 049902 (2016) and *ibid.* **95**, 059901 (2017).
- [78] R. J. Furnstahl, N. Klco, D. R. Phillips and S. Wesolowski, Phys. Rev. C **92**, 024005 (2015).
- [79] J. A. Melendez, S. Wesolowski and R. J. Furnstahl, Phys. Rev. C **96**, 024003 (2017).
- [80] S. Wesolowski, R. J. Furnstahl, J. A. Melendez and D. R. Phillips, J. Phys. G **46**, 045102 (2019).
- [81] E. Epelbaum, W. Glöckle and U.-G. Meißner, Nucl. Phys. A **747**, 362 (2005).
- [82] D. R. Entem and R. Machleidt, Phys. Rev. C **68**, 041001 (2003).
- [83] A. Gezerlis *et al.*, Phys. Rev. C **90**, 054323 (2014).
- [84] T. A. Rijken, Ann. Phys. (NY) **208**, 253 (1991).
- [85] M. Hoferichter, J. Ruiz de Elvira, B. Kubis and U.-G. Meißner, Phys. Rev. Lett. **115**, 192301 (2015).
- [86] M. Hoferichter, J. Ruiz de Elvira, B. Kubis and U.-G. Meißner, Phys. Rep. **625**, 1 (2016).
- [87] R. Navarro Perez, J. E. Amaro and E. Ruiz Arriola, Phys. Rev. C **88**, 064002 (2013); Erratum: *ibid.* **91**, 029901 (2015)].
- [88] E. Epelbaum, *High-precision nuclear forces: Where do we stand?, to be published in Proc. Ninth Int. Workshop on Chiral Dynamics, 17–21 September 2018, Durham, NC, USA.*
- [89] A. J. Bersbach *et al.*, Phys. Rev. D **13**, 535 (1976).
- [90] A. F. Kuckes *et al.*, Phys. Rev. **121**, 1226 (1961).
- [91] V. G. J. Stoks, R. A. M. Klomp, M. C. M. Rentmeester and J. J. de Swart, Phys. Rev. C **48**, 792 (1993).
- [92] R. Skibiński *et al.*, Phys. Rev. C **93**, 064002 (2016).
- [93] H. Witała *et al.*, Few-Body Syst. **57**, 1213 (2016).
- [94] H. Witała *et al.*, Few-Body Syst. **60**, 19 (2019).

- 
- [95] E. Epelbaum *et al.* (LENPIC Collaboration), Phys. Rev. C **99**, 024313 (2019).
- [96] J. Golak *et al.*, Eur. Phys. J. A **43**, 241 (2010).
- [97] K. Hebeler, H. Krebs, E. Epelbaum, J. Golak and R. Skibiński, Phys. Rev. C **91**, 044001 (2015).
- [98] H. W. Hammer, A. Nogga and A. Schwenk, Rev. Mod. Phys. **85**, 197 (2013).
- [99] K. Sekiguchi *et al.*, Phys. Rev. C **65**, 034003 (2002).
- [100] N. Kalantar-Nayestanaki, E. Epelbaum, J. G. Messchendorp and A. Nogga, Rep. Prog. Phys. **75**, 016301 (2012).
- [101] S. A. Coon and H. K. Han, Few-Body Syst. **30**, 131 (2001).
- [102] B. S. Pudliner *et al.*, Phys. Rev. C **56**, 1720 (1997).
- [103] H. Krebs, *Electroweak current in chiral effective field theory, to be published in Proc. Ninth Int. Workshop on Chiral Dynamics, 17–21 September 2018, Durham, NC, USA.*
- [104] A. A. Slavnov, Nucl. Phys. B **31**, 301 (1971).
- [105] D. Djukanovic, M. R. Schindler, J. Gegelia and S. Scherer, Phys. Rev. D **72**, 045002 (2005)
- [106] D. Djukanovic, J. Gegelia, S. Scherer and M. R. Schindler, Few-Body Syst. **41**, 141 (2007).
- [107] J. Behrendt *et al.*, Eur. Phys. J. A **52**, 296 (2016).
- [108] A. Ekström *et al.*, J. Phys. G **42**, 034003 (2015).
- [109] R. Skibiński *et al.*, Phys. Rev. C **98**, 014001 (2018).
- [110] L. Girlanda, A. Kievsky, M. Viviani and L. E. Marcucci, Phys. Rev. C **99**, 054003 (2019).

# *Ab Initio* Structure of $p$ -Shell Nuclei with Chiral Effective Field Theory and Daejeon16 Interactions

Pieter Maris<sup>a</sup>, Ik Jae Shin<sup>b</sup>, and James P. Vary<sup>a</sup>

<sup>a</sup>*Department of Physics and Astronomy, Iowa State University, Ames, IA 50011, USA*

<sup>b</sup>*Rare Isotope Science Project, Institute for Basic Science, Daejeon 34047, Korea*

## Abstract

We present No-Core Full Configuration results for the ground state energies of all particle-stable  $p$ -shell nuclei, as well as the excitation energies of more than 40 narrow states, excluding isobaric analog states. We used the chiral LENPIC nucleon-nucleon plus three-nucleon interaction at  $N^2$ LO with semi-local coordinate space regulators, and also the phenomenological Daejeon16 nucleon-nucleon potential. With simple exponential extrapolations of the total energies of each state, binding energies and spectra are found to be in good agreement with experiment. Both interactions produce a trend towards some overbinding of nuclei at the upper end of the  $p$ -shell.

**Keywords:** *Ab initio nuclear structure; binding energies; spectra*

## 1 Introduction

Recent advances in models of the strong internucleon interactions and in many-body methods to solve, with high precision, the properties of light nuclei have opened new frontiers of fundamental research opportunities. Extensive efforts are underway to continue improving the effective interactions between nucleons based on the strong interactions of QCD and to incorporate improved electroweak operators to better understand the physics of the standard model in a data rich domain. These efforts are also building a foundation for searching for new laws of physics that may be revealed, for example, in experiments seeking to measure neutrinoless double-beta decay. We report here on results for light nuclei that, with their quantified uncertainties, indicate that highly accurate descriptions of the spectroscopy of light nuclei, which provide good agreement with experiment, are becoming available.

We follow an established approach to solve the non-relativistic quantum many-body problem of the structure of light nuclei with realistic strong interactions. The method we adopt is called the No-Core Full Configuration (NCFC) approach [1] that is based on the No-Core Shell Model (NCSM) [2,3] with the improvement of extrapolating finite-basis results to the continuum limit. Both the NCSM and the NCFC

---

*Proceedings of the International Conference ‘Nuclear Theory in the Supercomputing Era — 2018’ (NTSE-2018), Daejeon, South Korea, October 29 – November 2, 2018, eds. A. M. Shirokov and A. I. Mazur. Pacific National University, Khabarovsk, Russia, 2019, p. 168.*

<http://www.ntse.khb.ru/files/uploads/2018/proceedings/Vary.pdf>.

belong to a class of approaches grouped under No-Core Configuration Interaction (NCCI) methods.

For our internucleon interactions, we select two recently developed models. On the one hand, we select the Low Energy Nuclear Physics International Collaboration (LENPIC) [4] nucleon-nucleon ( $NN$ ) plus three-nucleon ( $3N$ ) interactions developed within the framework of chiral effect field theory ( $\chi$ EFT) [5] through Next-to-Next-to Leading Order ( $N^2$ LO) [6–9]. These interactions were recently shown to produce good  $3N$  scattering properties as well as good binding energies of light nuclei [10–12]. On the other hand, we adopt the Daejeon16  $NN$  interaction [13] which is developed from a  $\chi$ EFT approach through Next-to-Next-to-Next-to Leading Order ( $N^3$ LO) [14–16] followed by additional two-body unitary phase-equivalent transformations (PET) [17–20] to reduce its high momentum components and to adjust its off-shell properties to provide good descriptions of selected properties of light nuclei [13].

Our goal here is to compare NCFC results of these two internucleon interactions with each other and with experiment. We focus on the energies of the ground and narrow excited states of the  $p$ -shell nuclei, including states of both parities. Our NCFC results show that, within our extrapolation uncertainties, both internucleon interactions provide good descriptions of the energies of these light nuclei with a noticeable tendency to overbind nuclei at the upper end of the  $p$ -shell. Some of the LENPIC results presented here have appeared in Refs. [12, 21].

## 2 *Ab initio* nuclear structure calculations

A successful theory of atomic nuclei involves two major challenges. The first is to accurately define the internucleon interactions so that results for  $NN$ ,  $3N$  and  $4N$  systems, which can be solved to high accuracy, are in good agreement with experimental data. The second is to develop accurate computational many-body methods to enable calculations of properties of nuclei with atomic number  $A \geq 5$ . We report here on particular combinations of these two elements that provide encouraging results for light nuclei. We begin with a brief description of the NCFC approach.

### 2.1 No-Core Full Configuration approach

In non-relativistic quantum mechanics, we define the dynamics through the many-body Hamiltonian which consists of sums over the relative kinetic energy between pairs of nucleons, the pairwise interactions, three-body interactions, etc., as

$$\hat{\mathbf{H}} = \sum_{i < j} \frac{(\vec{p}_i - \vec{p}_j)^2}{2m A} + \sum_{i < j} V_{ij} + \sum_{i < j < k} V_{ijk} + \dots \quad (1)$$

where  $m$  is the nucleon mass taken here to be equal for protons and neutrons. We then seek the solutions of the many-body eigenvalue equation

$$\hat{\mathbf{H}} \Psi(\vec{r}_1, \dots, \vec{r}_A) = E \Psi(\vec{r}_1, \dots, \vec{r}_A) \quad (2)$$

which yields the eigenenergies  $E$  and the wave functions  $\Psi$  for each state.

In the NCCI nuclear structure calculations, the wave function  $\Psi$  of a nucleus is expanded in an  $A$ -body basis of Slater determinants  $\Phi_k$  of single-particle wave

functions  $\phi_{nljm}(\vec{r})$ . Here,  $n$  ( $l$ ) is the radial (orbital) quantum number,  $j$  is the total angular momentum resulting from orbital motion coupled to the intrinsic nucleon spin, and  $m$  is the projection of the total angular momentum on the  $z$ -axis, the axis of quantization. We construct the Slater determinant basis from separate Slater determinants for the neutrons and the protons in order to retain charge dependence in the basis.

The Hamiltonian  $\hat{H}$  is then evaluated in this Slater determinant basis which results in a Hamiltonian matrix eigenvalue problem. Beyond  $A = 4$  with  $NN$  plus  $3N$  interactions, the Hamiltonian matrix becomes increasingly sparse as  $A$  grows and/or the basis dimension increases. Upon diagonalization, the resulting eigenvalues can be compared with the experimental total binding energies of nuclear states. The resulting wave functions are then employed to evaluate additional observables for comparison with experiments. Electromagnetic moments and transitions, along with weak decays, are among the popular applications of these wave functions.

Following our common practice, we adopt a harmonic oscillator (HO) basis with energy parameter  $\hbar\omega$  for the single-particle wave functions. We truncate the complete (infinite-dimensional) basis with a cutoff in the total number of HO quanta: the basis is limited to Slater determinants with  $\sum_A N_i \leq N_0 + N_{\max}$ , with  $N_0$  the minimal number of quanta for that nucleus (the sum over the HO single-particle quanta  $2n + l$  of the occupied orbitals) and  $N_{\max}$  the truncation parameter. Even (odd) values of  $N_{\max}$  provide results for natural (unnatural) parity. Numerical convergence toward the exact results for a given Hamiltonian is obtained with increasing  $N_{\max}$ , and is marked by approximate  $N_{\max}$  and  $\hbar\omega$  independence. In the NCFC approach we use extrapolations to estimate the binding energy in the complete (infinite-dimensional) space based on a sequence of calculations in finite bases [1, 22–27].

Here, we solve for the eigenvalues of a given nucleus in a sequence of basis spaces defined by the cutoff  $N_{\max}$  and as a function of  $\hbar\omega$ . Subsequently, we use a simple three-parameter exponential form to extrapolate results at a sequence of three  $N_{\max}$  values at fixed  $\hbar\omega$

$$E(N_{\max}) \approx E_{\infty} + a \exp(-bN_{\max}) \quad (3)$$

around the variational minimum in  $\hbar\omega$ . We employ the sensitivity of the extrapolant to the highest  $N_{\max}$  value and its sensitivity to  $\hbar\omega$  to estimate the extrapolation uncertainty for each state's energy, as detailed below where we present our results.

The rate of convergence depends both on the nucleus and on the interaction. For typical realistic interactions, the dimension of the matrix needed to reach a sufficient level of convergence is in the billions, and the number of nonzero matrix elements is in the tens of trillions, which saturates available storage on current High-Performance Computing facilities. All NCFC calculations presented here were performed on the Cray XC30 Edison and Cray XC40 Cori at NERSC and the IBM BG/Q Mira at Argonne National Laboratory, using the code MFDn [28, 29].

## 2.2 Chiral EFT $NN + 3N$ interaction

The  $\chi$ EFT allows us to derive internucleon interactions (and the corresponding electroweak current operators) in a systematic way [5–9, 14–16]. The  $\chi$ EFT expansion is not unique: e. g., different choices for the degrees of freedom, such as whether or not to include  $\Delta$  isobars explicitly, lead to different  $\chi$ EFT interactions. In addition, there is freedom to choose the functional form of regulators.

We adopt the  $\chi$ EFT interactions of the LENPIC collaboration [10–12] which have been developed to describe  $NN$  and nucleon-deuteron scattering and have been applied to the structure of light-mass and medium-mass nuclei. Specifically, we adopt the semi-local coordinate-space regularized  $\chi$ EFT potentials of Refs. [8,9]. The Leading Order (LO) and Next-to-Leading Order (NLO) contributions are given by  $NN$ -only potentials while  $3N$  interactions appear first at  $N^2$ LO in the  $\chi$ EFT expansion [6,7,16]. Four-nucleon forces are even more suppressed and start contributing at  $N^3$ LO. The  $\chi$ EFT power counting thus provides a natural explanation of the observed hierarchy of nuclear forces.

The Low-Energy Constants (LECs) in the  $NN$ -only potentials of Refs. [8,9] have been fitted to  $NN$  scattering data, without any input from nuclei with  $A > 2$ . The  $3N$  interactions at  $N^2$ LO involve two LECs which govern the strength of the one-pion-exchange-contact term and purely contact  $3N$  interaction contributions. Conventionally, these LECs are expressed in terms of two dimensionless parameters  $c_D$  and  $c_E$ . We follow the common practice [6,30–32] and use the  ${}^3\text{H}$  binding energy as one of the observables to provide a correlation between  $c_D$  and  $c_E$ .

A wide range of observables has been considered in the literature to constrain the remaining LEC. In Ref. [12] different ways to fix this LEC in the 3-nucleon sector were explored, and it was shown that it can be reliably determined from the minimum in the differential cross section in elastic nucleon-deuteron scattering at intermediate energies. This allows us to make parameter-free calculations for  $A \geq 4$  nuclei. Here, we present results obtained with the LENPIC interaction having a semi-local coordinate space regulator with  $R = 1.0$  fm. With this regulator, the LEC values for the  $3N$  interactions at  $N^2$ LO are  $c_D = 7.2$  and  $c_E = -0.671$ , as determined in Ref. [12]. Application of these interactions to nucleon-deuteron scattering can be found in Refs. [10,11] for  $NN$ -only potentials, along with selected properties of light- and medium-mass nuclei, and in Ref. [12] including the  $3N$  interactions at  $N^2$ LO.

In order to reduce extrapolation uncertainties by achieving energies of nuclear states closer to convergence in NCSM calculations, we have elected to employ the LENPIC  $NN + 3N$  interaction that has been processed through Similarity Renormalization Group (SRG) evolution [33–35] to a scale of  $\alpha = 0.08$  fm<sup>4</sup> which corresponds to  $\lambda = 1.88$  fm<sup>-1</sup>. This LENPIC  $NN + 3N$  interaction is employed in Ref. [12] and the sensitivity of the NCSM results (i. e. without extrapolation) to  $\alpha$  are shown to be reasonably small for selected nuclear properties including ground state (gs) energies. Sensitivity of NCFC energies for 25  $p$ -shell states to  $\alpha$  with the same LENPIC  $NN + 3N$  interaction is investigated in Ref. [21] and shown to be comparable to or less than the extrapolation uncertainties for this value of the SRG evolution parameter.

This SRG evolution provides a significant reduction in the strong off-diagonal couplings in momentum space of the  $NN$  interaction while, at the same time, inducing contributions to the  $3N$  interaction. It is primarily these reductions in couplings to higher momentum states that facilitate convergence in the NCSM calculations which then lead to reduced uncertainties in the NCFC results.

### 2.3 Daejeon16 $NN$ potential

Our second choice is a pure  $NN$  interaction, Daejeon16 [13], without the addition of a  $3N$  interaction. Daejeon16 was developed from an initial  $\chi$ EFT  $NN$  interaction at  $N^3$ LO [14–16] by SRG evolution to a scale of  $\lambda = 1.5$  fm<sup>-1</sup>.

In addition to SRG evolution, PETs [17–20] were applied so that the resulting Daejeon16  $NN$  interaction provides good descriptions of certain properties of light nuclei. In particular, there are a total of 7 PET parameters chosen to fit estimates of 11 nuclear properties that were obtained in finite basis space NCSM calculations. The estimates of optimal NCSM results were made in anticipation of the corrections that would arise from extrapolation to the full basis limit which would achieve the estimated NCFC results. The selected observables included the binding energies of  ${}^3\text{H}$ ,  ${}^4\text{He}$ ,  ${}^6\text{Li}$ ,  ${}^8\text{He}$ ,  ${}^{10}\text{B}$ ,  ${}^{12}\text{C}$  and  ${}^{16}\text{O}$ . In addition, the PET parameters were chosen to fit the two lowest excited states in  ${}^6\text{Li}$  with  $(J^\pi, T) = (3^+, 0)$  and  $(0^+, 1)$  as well as the first excited  $(1^+, 0)$  in  ${}^{10}\text{B}$  and the first excited  $(2^+, 0)$  in  ${}^{12}\text{C}$ . Some of these observables have been previously determined to be sensitive to  $3N$  interactions, so achieving their accurate descriptions without  $3N$  interactions was a significant milestone.

Throughout the SRG and PET processes, the high-quality descriptions of the two-body data are preserved due to the accurate treatment of unitarity at the level of the  $NN$  interaction. Of course, the off-shell properties of the  $NN$  interactions are modified through these transformations. The PETs that are fitted to properties of light nuclei are attempts to minimize the effects of the neglected  $3N$  and higher-body interactions. Of course, this fitting process cannot completely eliminate the effects of these additional interactions and one expects that nuclear observables will be identified that require higher-body interactions for their accurate description.

### 3 Energies of light nuclei

Here we present our NCFC results for light nuclei from  $A = 4$  through  $A = 16$ . We select results for a total of 22 mostly particle-stable nuclei and include a selection of excited states, both natural and unnatural parity states, that have been experimentally determined to have reasonably narrow widths. Note that we do not anticipate that we can produce NCFC results at the present time that will be as useful for comparing with energies of broad nuclear resonances. Altogether, we report here the energies, spins and parities of a selected set of 74 nuclear states, excluding isobaric analog states. For comparison, we have reported NCFC results on a total of 57(120) states in light nuclei from  $A = 6(3)$  through  $A = 16$  in Ref. [36] (Ref [37]) with the JISP16 interaction [38], though these JISP16 studies did include several isobaric analog states. These extensive studies with JISP16 employed a variety of extrapolation methods and also included electromagnetic observables. In addition, about half of the states we include here were investigated with the LENPIC interactions in Refs. [12] and/or [21] where the dependence on  $\chi\text{EFT}$  truncation order and SRG evolution scale were also investigated.

While we present our theoretical results, along with their uncertainties, in graphical form, it is important to note the limits on the range of  $N_{\text{max}}$  values in the NCSM calculations imposed by the available computational resources. These  $N_{\text{max}}$  limits depend on whether we employ an  $NN + 3N$  interaction or an  $NN$ -only interaction [39, 40]. We therefore choose  $N_{\text{max}}$  limits based both on the limit of overall available computational resources and on estimates of what is required for reasonably small uncertainties. In Table 1 we list the actual  $N_{\text{max}}$  values used for the results presented here.

As mentioned above, we employ a simple three-parameter exponential form to extrapolate the energies to the complete, but infinite-dimensional, basis using a sequence

Table 1: Highest  $N_{\max}$  values used in NCSM calculations for NCFC results presented in this work. The numbers in brackets correspond to the highest  $N_{\max}$  values for states with unnatural parity.

Nucleus	3N	$N_{\max}$	NN	$N_{\max}$	Nucleus	3N	$N_{\max}$	NN	$N_{\max}$
$^4\text{He}$	14		20		$^{11}\text{Be}$	8	(9)		11
$^6\text{He}$	12		18		$^{11}\text{B}$	8			10
$^6\text{Li}$	12		18		$^{12}\text{Be}$	8			10
$^7\text{Li}$	12		16		$^{12}\text{B}$	8			10
$^8\text{He}$	12		16		$^{12}\text{C}$	8			10
$^8\text{Li}$	10		14		$^{13}\text{B}$	8			10
$^8\text{Be}$	10		14		$^{13}\text{C}$	8			10
$^9\text{Li}$	10		12		$^{14}\text{C}$	8			10
$^9\text{Be}$	10	(9)	12	(13)	$^{14}\text{N}$	8			8
$^{10}\text{Be}$	10	(9)	12	(11)	$^{15}\text{N}$	8			8
$^{10}\text{B}$	10	(9)	12	(11)	$^{16}\text{O}$	8			8

of three highest  $N_{\max}$  values from Table 1 at fixed basis parameter  $\hbar\omega$ ,

$$E(N_{\max}, \hbar\omega) \approx E_{\infty}(\hbar\omega) + a(\hbar\omega) \exp(-b(\hbar\omega)N_{\max}). \quad (4)$$

We take as the NCFC extrapolated energy the result at the  $\hbar\omega$  that minimizes the amount of extrapolation,  $|E(N, \hbar\omega) - E_{\infty}^N(\hbar\omega)|$ , with  $N$  signifying the highest  $N_{\max}$  used in that extrapolation, typically at or slightly above the variational minimum in  $\hbar\omega$ . For an estimate of the extrapolation uncertainty, we take the maximum of the following quantities:

- difference with the previous  $N_{\max}$  extrapolation:  $|E_{\infty}^{N-2} - E_{\infty}^N|$ ;
- 20% of the extrapolation:  $0.2 * |E(N, \hbar\omega) - E_{\infty}^N(\hbar\omega)|$ ;
- half of the variation in the extrapolated value,  $0.5 * |\Delta E_{\infty}^N(\hbar\omega)|$ , over a range in  $\hbar\omega$  around the optimal extrapolation; with the range of 7.5 MeV for Daejeon16, and the range of 8 MeV (6 MeV if the extrapolation is at  $\hbar\omega = 16$  MeV) for LENPIC.

While more extensive extrapolation studies have been performed [22–27], we have observed that this simple procedure is reasonably accurate for a range of different states and interactions. In addition, our main thrust here is to apply our methods not only to the gs energies but also to the energies of the excited states. In all cases, we will extrapolate the total energy of each state independent of, for example, the gs energy. This already represents a significant undertaking yet still neglects important energy correlation information. We anticipate that more complete extrapolation analyses will be conducted with these same calculated energies in the future and will lead to refined estimates of converged energies and improved uncertainty estimates.

We present in Figs. 1 and 2 the total energies, spins and parities of the gs and selected excited states of nuclei ranging from  $A = 4$  through  $A = 10$  and from  $A = 11$  to  $A = 16$ , respectively. All of these nuclei are particle-stable, with the exception of

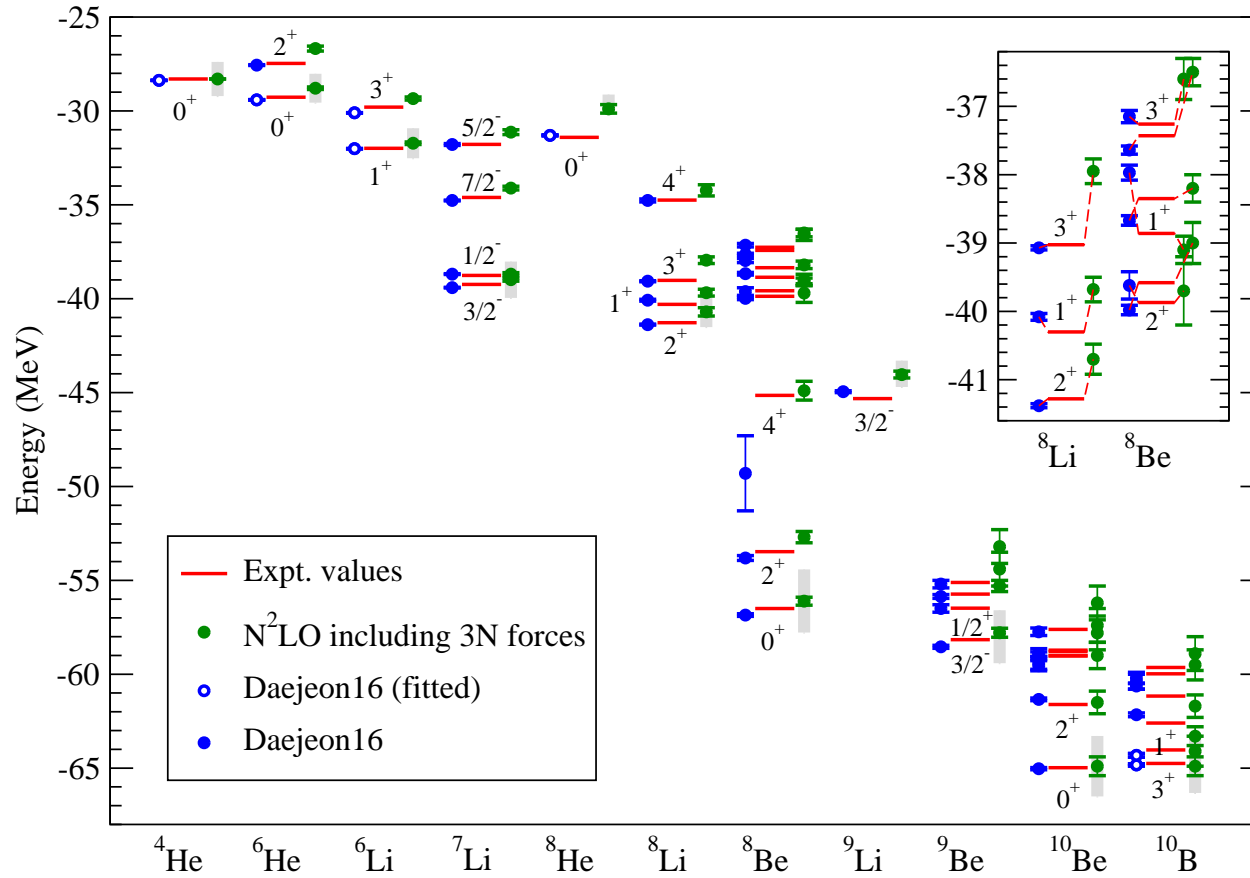


Figure 1: Calculated and experimental energies, spins and parities of the gs and selected excited states of  $A = 4$  through  $A = 10$  nuclei. States employed to determine PET parameters for Daejeon16 [13] are indicated with open symbols; the grey bands indicate examples of uncertainty from truncation at  $N^2\text{LO}$  in the  $\chi\text{EFT}$  expansion [12]. Experimental results are taken from Refs. [41–44].

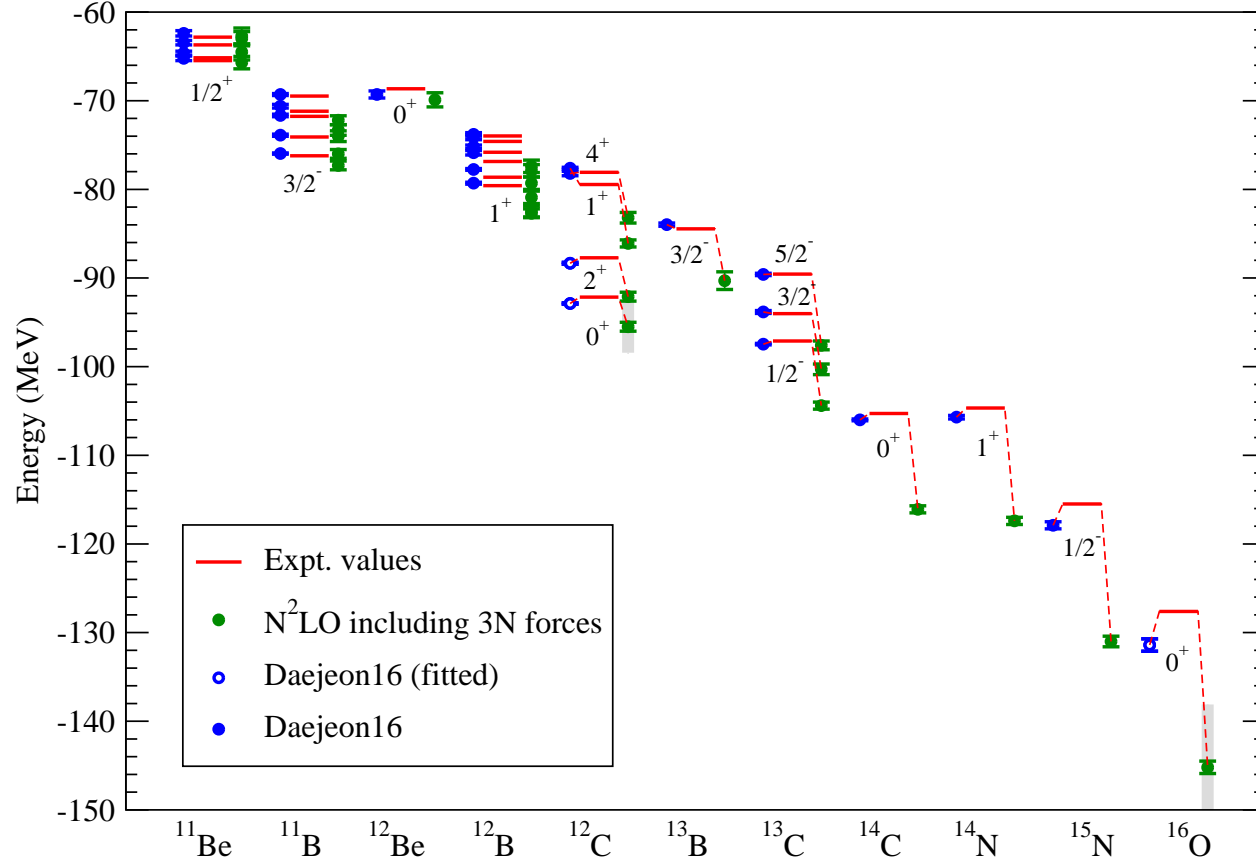


Figure 2: Calculated and experimental energies, spins and parities of the gs and selected excited states of  $A = 11$  through  $A = 16$  nuclei. States employed to determine PET parameters for Daejeon16 [13] are indicated with open symbols; the grey bands indicate examples of uncertainty from truncation at  $\text{N}^2\text{LO}$  in the  $\chi$ EFT expansion [12]. Experimental results are taken from Refs. [41–44].

$^8\text{Be}$ ; furthermore, all of the excited states shown are narrow, with a width that is less than 300 keV, except for the  $2^+$  and  $4^+$  rotational excitations of the gs of  $^8\text{Be}$ .

For each state, we plot the total experimental energy (sometimes referred to as the total interaction energy), and the NCFC energies for the the Daejeon16 potential and for the complete LENPIC  $\text{N}^2\text{LO}$  interaction at  $R = 1.0$  fm, SRG evolved to a scale of  $\alpha = 0.08$  fm $^4$ . The symbols represent the NCFC result from extrapolation to the complete (infinite-dimensional) basis and the error bars represent the estimated extrapolation uncertainty. States employed to determine PET parameters for Daejeon16 [13] are indicated with open symbols: seven states from  $A = 4$  to  $A = 10$ , two states in  $^{12}\text{C}$ , and  $^{16}\text{O}$ . The grey bands indicate examples of uncertainty in the gs energies from truncation at  $\text{N}^2\text{LO}$  in the  $\chi\text{EFT}$  expansion [12]; all of the LECs for the LENPIC interaction were fitted to  $A = 2$  and  $A = 3$  experimental data. The inset in Fig. 1 presents more detail for selected excited states of  $^8\text{Li}$  and  $^8\text{Be}$ .

The first observation from the results in Fig. 1 is the overall good agreement between theory and experiment, within the theoretical uncertainties, for all the states shown. Both interactions give the correct gs spin and parity for all 11 nuclei shown in the lower  $p$ -shell. Furthermore, almost all experimental excited states have a corresponding theoretical state with each of the two interactions. The exception is the first excited  $0^+$  in  $^{10}\text{Be}$ : with Daejeon16 we do obtain this state in our calculated low-lying spectrum, but not with the LENPIC  $\text{N}^2\text{LO}$  interaction (see Fig. 3 below for more details). More significantly, the level orderings of the theory results are nearly all correct to within extrapolation uncertainties. Exceptions to the correct level ordering occur in the spectrum of  $^8\text{Be}$  above 15 MeV of excitation, and the cluster of five states in a 300 keV window around 6 MeV excitation energy in  $^{10}\text{Be}$ .

Extrapolation uncertainties are considerably smaller for Daejeon16 energies than for the LENPIC  $NN+3N$  energies. This difference arises from two sources. The most important source is the difference in the NCSM basis spaces employed where results for LENPIC  $NN+3N$  are obtained in smaller basis spaces than the Daejeon16 results (see Table 1) due to the increased computational burden of  $3N$  interactions [39, 40]. In addition, the difference in the SRG evolution scales favors the convergence rate for Daejeon16 since Daejeon16 is based on an interaction that has been evolved to a lower momentum scale ( $1.5$  fm $^{-1}$ ) compared to the SRG evolution scale of the LENPIC  $NN+3N$  interaction ( $1.88$  fm $^{-1}$ ).

Proceeding now to nuclei in the upper half of the  $p$ -shell, we see in Fig. 2 that both interactions again give the correct gs spin and parity, with the possible exceptions of the parity inversion in  $^{11}\text{Be}$  and the gs of  $^{12}\text{B}$  with the LENPIC  $\text{N}^2\text{LO}$  interaction. Furthermore, the theoretical level orderings for the low-lying narrow excited states (up to  $^{13}\text{C}$ ) are again in good agreement with experiment to within extrapolation uncertainties, as shown in more detail below.

However, Fig. 2 also reveals the trend towards overbinding that emerges for the LENPIC  $\text{N}^2\text{LO}$  interaction starting at about  $^{12}\text{B}$  and for the Daejeon16 interaction at about  $^{15}\text{N}$ . It had been established from the beginning that Daejeon16 slightly overbinds  $^{12}\text{C}$  by almost 1% and overbinds  $^{16}\text{O}$  by about 3.8 MeV [13]. It is also known that the LENPIC  $\text{N}^2\text{LO}$  interaction overbinds starting around  $A = 12$ : for both  $^{12}\text{B}$  and  $^{12}\text{C}$  this overbinding is only slightly larger than the estimated chiral truncation error, but for  $^{16}\text{O}$  the overbinding is significantly more than the chiral truncation error, and the origin of this overbinding is, as yet, unclear [12]. Note however that the LENPIC interaction is entirely fixed by  $A = 2$  and  $A = 3$  systems,

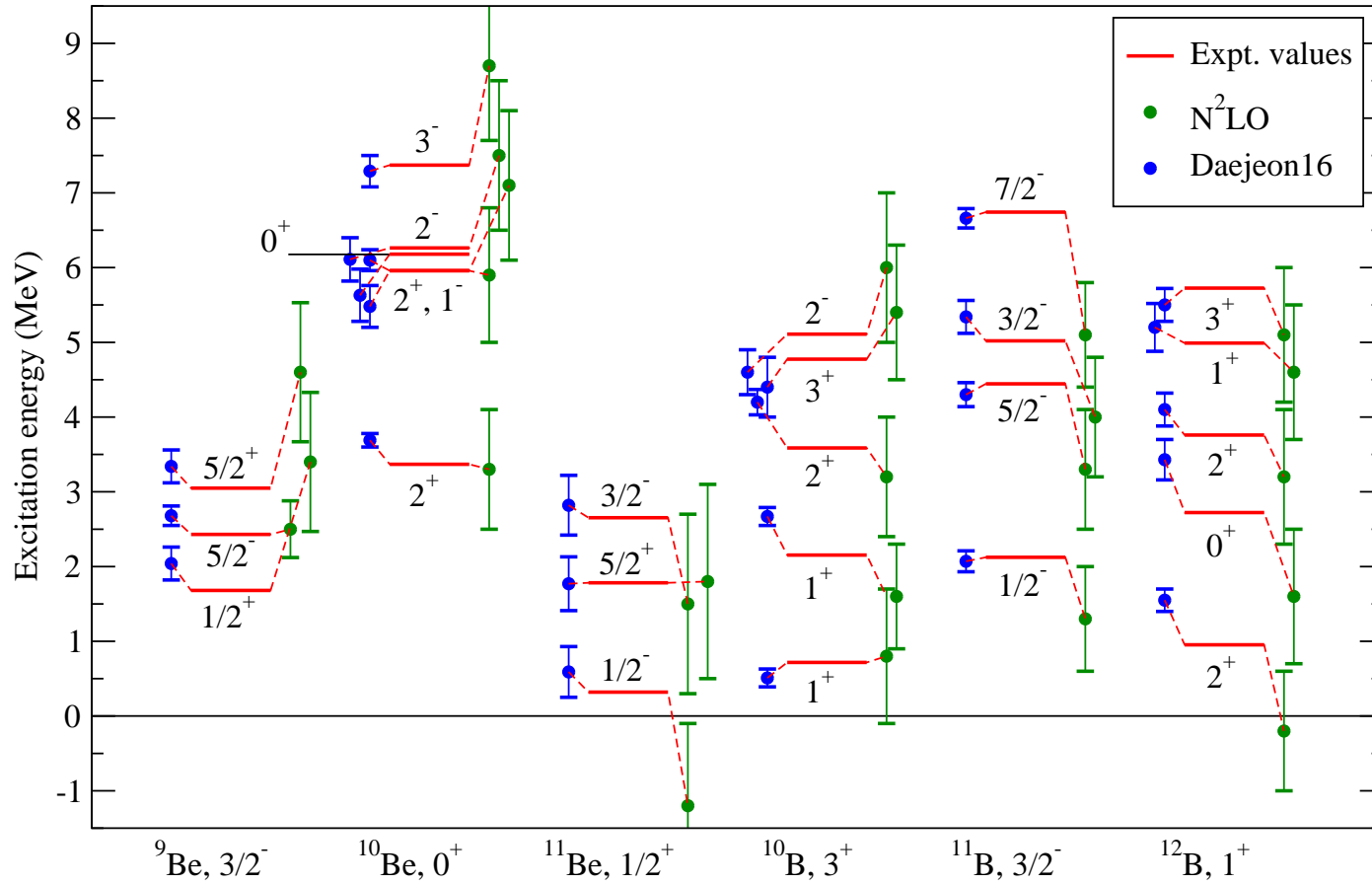


Figure 3: Calculated and experimental excitation energies, spins and parities of selected excited states of six nuclei from  $A = 9$  to  $A = 12$ . Experimental results are taken from Refs. [41–44].

whereas the PET parameters of Daejeon16 were adjusted to fit estimates of  $p$ -shell nuclei including  $^{12}\text{C}$  and  $^{16}\text{O}$ .

In order to examine the low-lying spectroscopy of selected  $A = 9$  to  $A = 12$  nuclei in more detail and to highlight a few exceptional cases, we present their excitation energies on an expanded scale in Fig. 3. To compare with the experimental excitation energies, we have plotted the difference in the independently extrapolated theoretical total energies and treated the the uncertainties of the extrapolated energy of the gs and the excited state as independent; that is, the shown uncertainty is the root-mean-square sum of the extrapolation uncertainties of the gs and the excited state. This should be a conservative estimate of the uncertainty in the excitation energy since NCSM excitation energies are known to be better converged than the total energies [36].

We note the overall good agreement for most states between theoretical and experimental level orderings in Fig. 3 to within extrapolation uncertainties. Even the appearance of low-lying unnatural parity states in these three nuclei appears well-described with one notable and subtle exception, the gs parity of  $^{11}\text{Be}$  with the LENPIC  $\text{N}^2\text{LO}$  interaction discussed below. This overall good agreement indicates that these interactions are successfully encapsulating an important aspect of the cross-shell physics which is becoming important for accurately describing intruder states in the low-lying spectra of light nuclei in the mid  $p$ -shell region.

The experimental gs spin of  $^{10}\text{B}$  has become a celebrated example of the reputed importance of  $3N$  interactions in nuclei [31,45]. The conclusion from calculations with realistic  $NN$  interactions, but without  $3N$  interactions, was, generally, a predicted gs spin of  $1^+$  with a low-lying excited  $3^+$  state. However, the experimental information has that order reversed with a  $3^+$  ground state. The LENPIC  $NN + 3N$  interaction at  $\text{N}^2\text{LO}$  has already been shown to produce the correct level ordering in  $^{10}\text{B}$  [12] concurring with established wisdom since the ordering was found to be incorrect at  $\text{N}^2\text{LO}$  without the  $3N$  interaction [11].

This conventional wisdom on the critical need for a  $3N$  interaction has previously been called into question by the  $^{10}\text{B}$  results with Daejeon16 [13] and also by results with JISP16 [37]. However, the extrapolation uncertainties for the JISP16 results left room for doubt that it was the first interaction to serve as a counterpoint to this conventional wisdom. Here, our extrapolation uncertainties are sufficiently small in Fig. 3 that we confirm the results of Ref. [13] showing Daejeon16 does indeed serve as a clear demonstration that subtle  $3N$  effects can be accommodated in a realistic  $NN$  interaction. This example serves as an important reminder that  $NN$  interactions and their  $3N$  counterparts are not unique and that unitary transformations can, in principle, transform important properties back and forth between them.

Another celebrated example of subtle effects in light nuclei is the parity inversion experimentally observed in  $^{11}\text{Be}$  with a  $J^\pi = \frac{1}{2}^+$  gs. This parity inversion has been attributed to the role of continuum physics [46] which is assumed to be absent in calculations, such as ours, retaining the pure HO basis. Contrary to the claim of the need for explicit continuum physics, we find, as shown in Fig. 3 and discussed by Y. Kim at this meeting [47], that Daejeon16 generates the correct parity-inverted gs for  $^{11}\text{Be}$ . At the same time, the LENPIC  $\text{N}^2\text{LO}$  interaction appears to fail to generate the correct parity-inverted gs. In fact, a closer look at Fig. 3 reveals that all eight (two in  $^9\text{Be}$ , three in  $^{10}\text{Be}$ , two in  $^{11}\text{Be}$ , and one in  $^{10}\text{B}$ ) unnatural-parity states are too high in the spectrum with the LENPIC  $\text{N}^2\text{LO}$  interaction, whereas with

Daejeon16 they are significantly closer to the experimental data, and often within the uncertainty estimates.

Less obvious, but not necessarily less important, is the narrow first excited  $0^+$  state in  $^{10}\text{Be}$  at about 6.2 MeV. With Daejeon16 we do find this state, close to the experimental excitation energy, but with the the LENPIC  $N^2\text{LO}$  interaction we do not find an excited  $0^+$  state in the low-lying spectrum. It is unclear whether this is due to the more limited basis size with the  $3N$  forces, or due to differences in the interactions — to our knowledge, most other interactions, including JISP16, also fail to reproduce this excited  $0^+$  state in  $^{10}\text{Be}$  at the experimental excitation energy.

Finally, let us consider the important case of the lowest two states in  $^{12}\text{B}$ . Daejeon16 produces the correct gs spin ( $1^+$ ) and the first excited state ( $2^+$ ). However, as noted previously [12], the LENPIC  $N^2\text{LO}$  interaction reverses the ordering of these two states and we reaffirm that conclusion in Fig. 3 while noting that extrapolation uncertainties are significant in this case. We also note that the Daejeon16 results for the low-lying states of  $^{12}\text{B}$  all appear to be in good agreement with experiment.

## 4 Summary and Outlook

We have investigated the spectra of light nuclei from  $A = 4$  to  $A = 16$  in the NCFC approach with two recent internucleon interactions, the LENPIC  $NN + 3N$  interaction and the Daejeon16  $NN$  interaction. We have presented extrapolated energies and their uncertainties for 74 states in 22 nuclei including states of both parities, excluding isobaric analog states. The extrapolation uncertainties are shown to be sufficiently small that the theoretical results are found to be in good agreement with experimental data for most states. Both these interactions overbind nuclei at the upper end of the  $p$ -shell which suggests an area for future improvements to the internucleon interactions. Comparing results between Daejeon16 and LENPIC  $NN + 3N$  shows the former interaction to have smaller extrapolation uncertainties and to produce somewhat better agreement with experiment, in particular in the upper half of the  $p$ -shell. The experimental parity inversion in  $^{11}\text{Be}$  and the experimental  $1^+$  gs spin of  $^{12}\text{B}$  provide two examples of subtle effects where the Daejeon16 results agree with experiment while the LENPIC  $NN + 3N$  results appear to be deficient. The better performance of the Daejeon16 interaction should not be too surprising since PETs used in its determination were selected to fit a set of properties of light nuclei.

Overall, we find that the extrapolation uncertainties for the spectroscopy of light nuclei with realistic internucleon interactions have been sufficiently reduced in order to make meaningful detailed comparison between theory and experiment and between different internucleon interactions. As our quantum many-body methods continue to improve and the available computational resources continue to increase, we anticipate providing ever more precise diagnostics of state-of-the-art internucleon interactions and increasingly robust predictive power.

## Acknowledgments

We thank our collaborators on the co-authored papers cited here for insightful discussions and for providing files of interaction matrix elements used in our previously published works cited herein. This work was supported by the US Department of Energy

under Grant Nos. DE-SC0018223 (SciDAC-4/NUCLEI) and DE-FG02-87ER40371, and by the Rare Isotope Science Project of Institute for Basic Science funded by Ministry of Science and ICT and NRF of Korea (2013M7A1A1075764). This research used resources of the National Energy Research Scientific Computing Center (NERSC) and the Argonne Leadership Computing Facility (ALCF), which are US Department of Energy Office of Science user facilities, supported under Contracts No. DE-AC02-05CH11231 and No. DE-AC02-06CH11357, and computing resources provided under the INCITE award ‘Nuclear Structure and Nuclear Reactions’ from the US Department of Energy, Office of Advanced Scientific Computing Research.

## References

- [1] P. Maris, J. P. Vary and A. M. Shirokov, *Phys. Rev. C* **79**, 014308 (2009).
- [2] P. Navrátil, J. P. Vary and B. R. Barrett, *Phys. Rev. Lett.* **84**, 5728 (2000).
- [3] B. R. Barrett, P. Navrátil and J. P. Vary, *Prog. Part. Nucl. Phys.* **69**, 131 (2013).
- [4] <http://www.lenpic.org>.
- [5] S. Weinberg, *Phys. Lett. B* **251**, 288 (1990).
- [6] E. Epelbaum, A. Nogga, W. Gloeckle, H. Kamada, U.-G. Meißner and H. Witala, *Phys. Rev. C* **66**, 064001 (2002).
- [7] E. Epelbaum, H. W. Hammer and U.-G. Meißner, *Rev. Mod. Phys.* **81**, 1773 (2009).
- [8] E. Epelbaum, H. Krebs and U.-G. Meißner, *Eur. Phys. J. A* **51**, 53 (2015).
- [9] E. Epelbaum, H. Krebs and U.-G. Meißner, *Phys. Rev. Lett.* **115**, 122301 (2015).
- [10] S. Binder *et al.* (LENPIC Collaboration), *Phys. Rev. C* **93**, 044002 (2016).
- [11] S. Binder *et al.* (LENPIC Collaboration), *Phys. Rev. C* **98**, 014002 (2018).
- [12] E. Epelbaum *et al.* (LENPIC Collaboration), *Phys. Rev. C* **99**, 024313 (2019).
- [13] A. M. Shirokov, I. J. Shin, Y. Kim, M. Sosonkina, P. Maris and J. P. Vary, *Phys. Lett. B* **761**, 87 (2016).
- [14] D. R. Entem and R. Machleidt, *Phys. Lett. B* **524**, 93 (2002).
- [15] D. R. Entem and R. Machleidt, *Phys. Rev. C* **68**, 041001 (2003).
- [16] R. Machleidt and D. R. Entem, *Phys. Rep.* **503**, 1 (2011).
- [17] Yu. A. Lurie and A. M. Shirokov, *Izv. Ross. Akad. Nauk, Ser. Fiz.* **61**, 2121 (1997) [*Bull. Rus. Acad. Sci., Phys. Ser.* **61**, 1665 (1997)].
- [18] Y. A. Lurie and A. M. Shirokov, *Ann. Phys. (NY)* **312**, 284 (2004).
- [19] A. M. Shirokov, A. I. Mazur, S. A. Zaytsev, J. P. Vary and T. A. Weber, *Phys. Rev. C* **70**, 044005 (2004).

- [20] Yu. A. Lurie and A. M. Shirokov, in *The J-matrix method. Developments and applications*, eds. A. D. Alhaidari, E. J. Heller, H. A. Yamani and M. S. Abdelmonem. Springer, 2008, p. 183.
- [21] P. Maris, *Ab initio calculations of p-shell nuclei up to  $N^2LO$  in chiral Effective Field Theory, to be published in Proc. XLI Brazilian Meeting on Nucl. Phys., 2–6 September 2018, Maresias, SP, Brazil*; arXiv:1906.03703 [nucl-th] (2019).
- [22] S. A. Coon, M. I. Avetian, M. K. G. Kruse, U. van Kolck, P. Maris and J. P. Vary, *Phys. Rev. C* **86**, 054002 (2012).
- [23] R. J. Furnstahl, G. Hagen and T. Papenbrock, *Phys. Rev. C* **86**, 031301 (2012).
- [24] S. N. More, A. Ekström, R. J. Furnstahl, G. Hagen and T. Papenbrock, *Phys. Rev. C* **87**, 044326 (2013).
- [25] K. A. Wendt, C. Forssén, T. Papenbrock and D. Sääf, *Phys. Rev. C* **91**, 061301 (2015).
- [26] I. J. Shin, Y. Kim, P. Maris, J. P. Vary, C. Forssén, J. Rotureau and N. Michel, *J. Phys. G* **44**, 075103 (2017).
- [27] G. A. Negoita *et al.*, *Phys. Rev. C* **99**, 054308 (2019).
- [28] H. M. Aktulga, C. Yang, E. G. Ng, P. Maris and J. P. Vary, *Concurrency Computat.: Pract. Exper.* **26**, 2631 (2014).
- [29] M. Shao, H. M. Aktulga, C. Yang, E. G. Ng, P. Maris and J. P. Vary, *Comput. Phys. Commun.* **222**, 1 (2018).
- [30] A. Nogga, P. Navrátil, B. R. Barrett and J. P. Vary, *Phys. Rev. C* **73**, 064002 (2006).
- [31] P. Navrátil, V. G. Gueorguiev, J. P. Vary, W. E. Ormand and A. Nogga, *Phys. Rev. Lett.* **99**, 042501 (2007).
- [32] D. Gazit, S. Quaglioni and P. Navrátil, *Phys. Rev. Lett.* **103**, 102502 (2009); Erratum: *ibid.* **122**, 029901 (2019).
- [33] S. K. Bogner, R. J. Furnstahl and R. J. Perry, *Phys. Rev. C* **75**, 061001 (2007).
- [34] S. K. Bogner, R. J. Furnstahl, P. Maris, R. J. Perry, A. Schwenk and J. P. Vary, *Nucl. Phys. A* **801**, 21 (2008).
- [35] S. K. Bogner, R. J. Furnstahl and A. Schwenk, *Prog. Part. Nucl. Phys.* **65**, 94 (2010).
- [36] P. Maris and J. P. Vary, *Int. J. Mod. Phys. E* **22**, 1330016 (2013).
- [37] A. M. Shirokov, V. A. Kulikov, P. Maris and J. P. Vary, in *NN and 3N interactions*, eds. L. D. Blokhintsev and I. I. Strakovsky. Nova Science, Hauppauge, NY, 2014, p. 231, <https://novapublishers.com/shop/nn-and-3n-interactions/>.
- [38] A. M. Shirokov, J. P. Vary, A. I. Mazur and T. A. Weber, *Phys. Lett. B* **644**, 33 (2007).

- 
- [39] J. P. Vary, P. Maris, E. Ng, C. Yang and M. Sosonkina, J. Phys. Conf. Ser. **180**, 012083 (2009).
- [40] P. Maris, M. Sosonkina, J. P. Vary, E. G. Ng and C. Yang, Proc. Comput. Sci. **1**, 97 (2010).
- [41] D. R. Tilley, C. M. Cheves, J. L. Godwin, G. M. Hale, H. M. Hofmann, J. H. Kelley, C. G. Sheu and H. R. Weller, Nucl. Phys. A **708**, 3 (2002).
- [42] G. Audi, A. H. Wapstra and C. Thibault, Nucl. Phys. A **729**, 337 (2002).
- [43] D. R. Tilley, J. H. Kelley, J. L. Godwin, D. J. Millener, J. E. Purcell, C. G. Sheu and H. R. Weller, Nucl. Phys. A **745**, 155 (2004).
- [44] J. H. Kelley, J. E. Purcell and C. G. Sheu, Nucl. Phys. A **968**, 71 (2017).
- [45] E. D. Jurgenson, P. Maris, R. J. Furnstahl, P. Navrátil, W. E. Ormand and J. P. Vary, Phys. Rev. C **87**, 054312 (2013).
- [46] A. Calci, P. Navrátil, R. Roth, J. Dohet-Eraly, S. Quaglioni and G. Hupin, Phys. Rev. Lett. **117**, 242501 (2016).
- [47] Y. Kim, I. J. Shin, A. M. Shirokov, M. Sosonkina, P. Maris and J. P. Vary, *see these Proceedings*, p. 15,  
<http://www.ntse.khb.ru/files/uploads/2018/proceedings/Kim.pdf>.

# Continuum Effect in Resonant Excitation Spectra of Weakly-Bound Nuclei

S. J. Dai<sup>a</sup>, F. R. Xu<sup>a</sup>, J. G. Li<sup>a</sup>, B. S. Hu<sup>a</sup> and Z. H. Sun<sup>a,b</sup>

<sup>a</sup>*School of Physics and State Key Laboratory of Nuclear Physics and Technology, Peking University, Beijing 100871, China*

<sup>b</sup>*Physics Division, Oak Ridge National Laboratory, Oak Ridge, Tennessee 37831, USA*

## Abstract

Starting from the CD-Bonn potential, we have performed Gamow shell-model calculations for neutron-rich oxygen isotopes, investigating excitation spectra and their resonant properties. The Gamow shell model is based on the Berggren ensemble, which is capable of treating the continuum effect reasonably in weakly-bound or unbound nuclei. To calculate heavier-mass oxygen isotopes, we choose  $^{16}\text{O}$  as a frozen core in the Gamow shell-model calculations. The first  $2^+$  excitation energies of the even-even O isotopes are calculated, and compared with those obtained by the conventional shell model using the empirical USDB interaction. The continuum effect is proved to play an important role in the shell evolution near the drip line. We discuss also the effect of the Berggren contour choice. We improve the approximation in the contour choice to give more precise calculations of resonance widths.

**Keywords:** *CD-Bonn interaction; Gamow shell model; drip-line nuclei; Berggren ensemble; continuum; resonance*

## 1 Introduction

Thanks to the radioactive isotope beam technique, the exploration of the neutron drip line is no longer unachievable. A recent experiment performed at RIKEN-RIBF investigated the extremely neutron-rich nucleus  $^{26}\text{O}$  by removing a proton from the radioactive secondary beam of  $^{27}\text{F}$  [1]. The decay products,  $^{24}\text{O}$  and two neutrons, were observed. This experiment confirmed that  $^{24}\text{O}$  is the last bound nucleus of neutron-rich oxygen isotopes, and positioned the ground-state resonance of  $^{26}\text{O}$  at about 18 keV above threshold. Another excited state in  $^{26}\text{O}$  was also observed at 1.28 MeV, which is believed to be the first  $2^+$  state [1].

As a powerful method for studying atomic nuclei, including in the medium-mass region, the shell model is very commonly used to investigate oxygen isotopes [2–4]. Shell model calculations using the USDB interaction have been successful in reproducing the observables of *sd*-shell nuclei, such as the binding energies, spectra, and transition rates [5–9]. However, the USDB interaction is constructed in the harmonic

---

*Proceedings of the International Conference ‘Nuclear Theory in the Supercomputing Era — 2018’ (NTSE-2018), Daejeon, South Korea, October 29 – November 2, 2018, eds. A. M. Shirokov and A. I. Mazur. Pacific National University, Khabarovsk, Russia, 2019, p. 183.*

<http://www.ntse.khb.ru/files/uploads/2018/proceedings/FurongXu.pdf>.

oscillator (HO) basis. The HO basis always gives well-localized wave functions of nuclear states. However, these cannot describe the loosely-bound or unbound properties of drip-line nuclei. For the drip-line nucleus  $^{26}\text{O}$ , the HO-basis shell-model calculation with the USDB interaction gives a  $2^+$  excitation energy about 0.8 MeV higher than the experimental data [1]. The three-body model calculations indicate that the two-neutron decay channel may play an important role in the  $^{26}\text{O}$  system [10–12].

In the three-body model calculation, the three-body system  $^{24}\text{O} + n + n$  is correlated by a density-dependent contact pairing interaction. The two-neutron decay channel is taken into account by evolving the initial state, generated by removing a proton from the calculated ground state of the  $^{25}\text{F} + n + n$  system, with the Hamiltonian of the three-body system. The Hamiltonian is based on a one-body Woods–Saxon (WS) potential with a finite depth, and the two-body pairing interaction [10–12]. Using a finite-depth one-body potential is crucial for the model, as it allows the particle emissions.

The three-body model has been successful in reproducing the first  $2^+$  state energy of  $^{26}\text{O}$ , as the decay channel can couple the bound and continuum single particle (s.p.) states [10–12]. For describing the properties of weakly-bound or unbound nuclei near the drip line, the continuum effect has already been proved to be very important [13–19]. In the three-body model, a phenomenological pairing interaction is applied. As was pointed out in Ref. [11], the pairing strength has to be finely tuned to get a precise result. Fitting the pairing strength mixes different effects, like the continuum effect and the three-body force, and the exact contribution from each of them cannot be identified. Another problem is that the three-body model cannot give the decay width directly and the method used to calculate the widths is parameter-dependent [11].

To minimize the obscure mixing effects caused by the fitted interaction, as well as to calculate the decay width self-consistently, we revisit the continuum effect in the oxygen isotopes by the Gamow shell model (GSM) [18, 20, 21] with a realistic nuclear force, the CD-Bonn interaction [22]. The GSM is based on the Berggren ensemble, which is composed of s.p. bound states, resonant states and non-resonant continuums [13, 18, 20, 21]. The continuum states in the Berggren ensemble are analytically extended to the complex plane and discretized along a certain contour. The imaginary parts of the resonant s.p. eigenenergies give the resonance widths of the s.p. states. These s.p. widths integrate to the total widths of the many-body system through the shell model. On the other hand, the CD-Bonn potential describes the nucleon-nucleon interaction with high precision within a very wide range. To accelerate the convergence of many-body calculations, the bare CD-Bonn interaction is renormalized using the  $V_{\text{low-}k}$  procedure [23]. For the shell-model calculation with a frozen core, we adopt the  $Q$ -box folded-diagram perturbation method [24, 25] to construct a realistic effective model-space Hamiltonian, as done in Ref. [21].

As mentioned above, analytically extending the continuum states to the complex plane is essential in the Berggren ensemble, which includes narrow resonant states, and introduces an additional dimension to describe the resonance width. However, a complex contour requires more discretizing points to reach convergence due to the additional dimension. Since it is believed that the non-resonant continuum mainly couples with bound states through the resonances, and the direct coupling is assumed to be less important, in most models based on the Berggren ensemble, only partial waves that include narrow resonances are extended to the complex plane [18, 20, 21, 26–30].

However the accuracy of this approximation is not yet well tested. In this paper, we will discuss the Berggren contour choice in the oxygen chain by expanding the extended partial waves from  $d_{3/2}$  to all  $sd$  partial waves.

In this paper, we perform a realistic-force GSM calculation for the neutron-rich oxygen isotopes  $^{18,20,22,24,25,26}\text{O}$  to study how the continuum effect affects the shell evolution in the drip-line region, as well as to investigate the continuum effect from the non-resonant continuum in partial waves without narrow resonances.

## 2 Theoretical framework

The Berggren ensemble is a s.p. basis specialized for treating the continuum and resonances. The one-body Schrödinger equation in the complex- $k$  space gives the Berggren states,

$$\frac{d^2 u(r)}{dr^2} = \left( \frac{l(l+1)}{r^2} + \frac{2m}{\hbar^2} V_{WS}(r) - k^2 \right) u(r), \quad (1)$$

where  $V_{WS}$  is the WS potential with a spin-orbit coupling,

$$V_{WS}(r) = -V_0 f(r) - 4V_{SO} \frac{1}{r} \frac{df(r)}{dr} l \cdot s, \quad (2)$$

where  $l$  and  $s$  refer to the orbital angular momentum and spin of the particle, respectively, and

$$f(r) = -\frac{1}{1 + e^{\frac{r-r_0 A^{1/3}}{d}}}. \quad (3)$$

The basis states include bound, resonant and continuum states due to the finite depth of the WS potential. In the present calculations, the parameters of the WS potential are  $V_0 = 45.39$  MeV,  $r_0 = 1.347$  fm,  $d = 0.70$  fm, and  $V_{SO} = 18.2$  MeV. The  $sd$ -shell s.p. energies are  $-5.31$  MeV,  $-3.22$  MeV and  $(1.06 - 0.09i)$  MeV for the  $0d_{5/2}$ ,  $1s_{1/2}$  bound states and  $0d_{3/2}$  resonant orbit, respectively. The values are the same as the universal parameters [31], except that the strength  $|V_0|$  is reduced to reproduce the experimental width extracted from  $^{17}\text{O}$  [21].

The completeness relation of the Berggren ensemble can be written as

$$\sum_{n \in \{b, d\}} u_n(r, k_n) u_n(r', k_n) + \int_{L^+} dk v(r, k) v(r', k) = \delta(r - r'), \quad (4)$$

where  $b$  and  $d$  denote the bound states and decaying resonant states respectively, and  $L^+$  denotes the integral contour of the continuum. The contour lies in the complex plain. Only narrow resonances enclosed in the contours are included in the summation of Eq. (4) according to Cauchy's integral theorem. Since the orbital angular momentum in the s.p. Hamiltonian is conserved, the contours of different partial waves may differ. For a partial wave that does not contain narrow resonances, a contour lying on the real-momentum axis is widely used.

The effective interaction in the Berggren ensemble is obtained by performing a  $Q$ -box folded-diagram perturbation based on the CD-Bonn interaction. The matrix elements, which are given originally in the HO basis, are projected to the Berggren ensemble by overlapping the Berggren basis wave functions and those of the HO

basis. In the present work, we are using the truncation  $N_{\text{shell}} = 22$  for the HO basis. The CD-Bonn interaction is renormalized by the  $V_{\text{low-}k}$  procedure before projection to the Berggren ensemble. To minimize the induced three-body force in the  $V_{\text{low-}k}$  renormalization, a hard cutoff of  $\Lambda = 2.6 \text{ fm}^{-1}$  is chosen. In the  $Q$ -box calculation, the starting energy is  $-6 \text{ MeV}$ , which is approximately equal to the average  $sd$ -shell s.p. energy of the one-body Woods-Saxon potential.

With the  $^{16}\text{O}$  core, the model space of the effective interaction is all  $sd$ -shell orbits including bound states  $0d_{5/2}$  and  $1s_{1/2}$ , the narrow resonant state  $0d_{3/2}$ , and the  $d_{3/2}$  non-resonant continuum states on the complex plain. As mentioned above, a real-momentum continuum contour is commonly adopted for partial waves that do not have narrow resonances. Because we are also investigating the continuum effect contributed by partial waves that do not have narrow resonances, the results with different contours in the  $s_{1/2}$  and  $d_{5/2}$  partial waves are compared. We change these contours from the real-momentum axis to the same as that of the  $d_{3/2}$  partial wave. In the calculation, we choose the contour  $\{0.0 \rightarrow 2.2\}$  (in  $\text{fm}^{-1}$ ) in the real axis and discretize it with 20 discrete points. The complex contour is taken as  $\{0.0 \rightarrow (0.48 - 0.20i) \rightarrow 0.62 \rightarrow 2.2\}$  (in  $\text{fm}^{-1}$ ) with 20 discrete points as well.

### 3 Calculations and discussion

The excitation energy of the first  $2^+$  excited state is an indicator of the shell gap in the  $sd$  shell. In this paper, we calculate the  $2_1^+$  excitation energies of oxygen isotopes, shown in Fig. 1. We see that both the CD-Bonn GSM and USDB HO-basis SM calculations give good agreement with experimental  $2_1^+$  excitation energies, especially in the well-bound nuclei  $^{18,20,22}\text{O}$ , where both calculations reproduce the data well. This indicates that, although based on a realistic force, the effective interaction in the GSM has the same precision for the well-bound systems as the empirical USDB interaction which fits the data of bound nuclei. However, for the  $2_1^+$  excitation energy in the unbound  $^{26}\text{O}$ , the USDB interaction gives  $2.11 \text{ MeV}$  which is about  $800 \text{ keV}$  higher than the experimental data. The CD-Bonn GSM improves the results of calculations significantly (see Fig. 1). Since the effective interaction in GSM is as

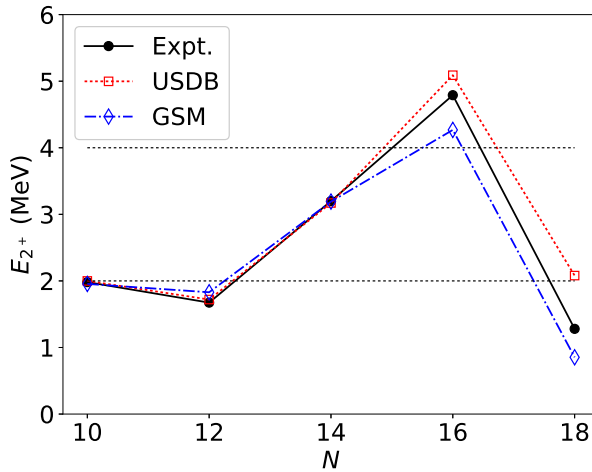


Figure 1: Calculated  $2_1^+$  excitation energies in  $^{18,20,22,24,26}\text{O}$  compared with the experimental data [1, 32] and USDB calculations. The USDB calculation overestimates the  $2^+$  excitation energy in  $^{26}\text{O}$ , while the GSM calculation improves the result by taking the continuum effect into account.

precise as the USDB interaction in the well-bound nuclei, we can thus conclude that the improvement should be mainly due to the inclusion of the continuum.

The calculated  $2^+$  excitations of  $^{24}\text{O}$  and  $^{26}\text{O}$  are lower than the experimental data, which may be partially due to the lacking of the three-body force in the GSM calculations. With an increasing number of valence neutrons, the effect of the three-body force becomes significant. In our previous work [21], we proved that the three-body force introduced by the  $V_{\text{low-}k}$  process is weak when the hard cutoff of  $2.6 \text{ fm}^{-1}$  is used. However, the initial three-body force, which is not considered, would have a non-negligible effect for neutron-rich isotopes with a large number of valence neutrons. In the work studying the oxygen chain using the *ab-initio* coupled cluster method [28], with both two-body and three-body interaction derived from the chiral effective field theory [33], the initial three-body force has an effect of increasing the excitation energies of the  $2^+$  states in the even-even O isotopes. Although the  $2^+$  state in  $^{26}\text{O}$  was not calculated in Ref. [28], the direction of this effect should remain the same. This conclusion supports our result that the  $2^+$  state is lower in energy than the experimental data if no three-body force is considered.

Another purpose of the present work is to investigate the influence of the contour choice. We use different contours for the  $sd$  partial waves to calculate all well-bound as well as weakly-bound and unbound nuclei. For convenience, we use the following notations:

- i)  $C_0$ : the complex contour (i. e., a triangle shape below the real-momentum axis, see Fig. 1 in Ref. [21], our previous paper) with 20 discrete points is employed in the  $d_{3/2}$  channel, which contains a narrow resonance, while the real-momentum contours with only 8 discrete points are used in all other channels (including  $s_{1/2}$  and  $d_{5/2}$  channels), which have no narrow resonances.
- ii)  $C_1$ : the same as  $C_0$  except that the number of discrete points for  $s_{1/2}$  and  $d_{5/2}$  partial waves is increased to 20.
- iii)  $C_2$ : the same as  $C_1$  except that the complex-momentum contour, like that in the  $d_{3/2}$  partial wave, is employed in the  $s_{1/2}$  channel.
- iv)  $C_3$ : the same as  $C_2$  except that the same complex-momentum contour employed also in the  $d_{5/2}$  channel.

Figure 2 displays the results of calculations of low-lying states in  $^{22-26}\text{O}$ . We see that there is no meaningful changes of the results when the number of discretizing points is increased from 8 to 20, except for the  $^{24}\text{O}$  where the energies become slightly lower. An increase in the number of discretizing points leads to a remarkable increase in the model dimension. Therefore, a reasonable but converged number of discretizing points is an issue that one should consider in the GSM calculations. From our calculations for the  $sd$ -shell nuclei, 8 discretizing points should be reasonable in most cases.

From Fig. 2, we can also analyze the results of calculations with different strategies of the contour choice. Overall, the different strategies in the choices of contours give almost the same results, except that  $C_3$  gives slightly higher energies for the  $2^+$  and  $3^+$  states in  $^{22}\text{O}$ . This means that for the partial waves with no narrow resonances, real-momentum contours can be chosen without a loss of accuracy of the calculations. A real-momentum contour with reasonable discretizing points can significantly reduce the computational burden. This means that if there are no narrow resonances in the channel, the continuum states on the real-momentum contour are good enough to describe the continuum effect in the real part of the eigenenergies.

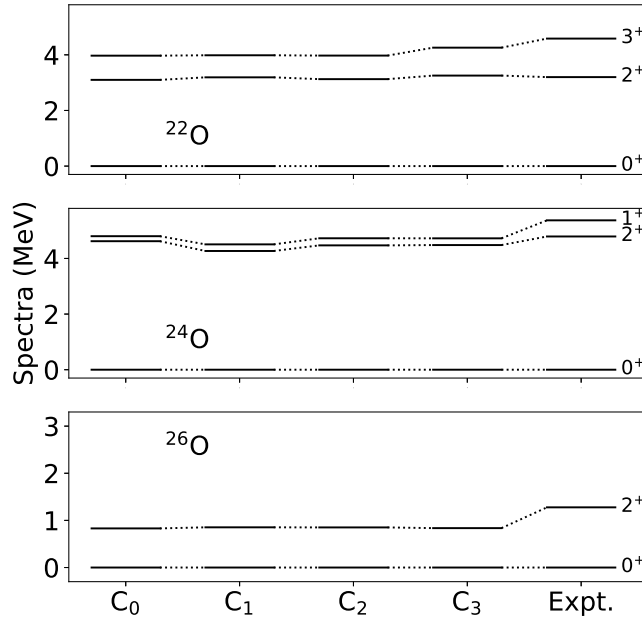


Figure 2: Low-lying states in  $^{22,24,26}\text{O}$ . The experimental data are taken from Refs. [1, 32]. Different strategies of the contour choosing  $C_i$  are defined in the text. The results show that the real parts of the eigenenergies given by GSM do not change meaningfully with the different choices of contours for the channels without narrow resonances.

Figure 3 plots the imaginary parts (i. e., resonance widths) of the obtained eigenenergies of the resonant states in  $^{24,25,26}\text{O}$ , compared with the experimental data available currently [1, 32]. The calculated resonance widths are gently dependent on the prescriptions of contour choice. The widths tend to be slightly smaller with more partial waves taking complex-momentum contours, and closer to the experimental values. However, the GSM calculation with a complex-momentum contour is much more expensive in computation. The new experiment of  $^{26}\text{O}$  [1] mentioned in the

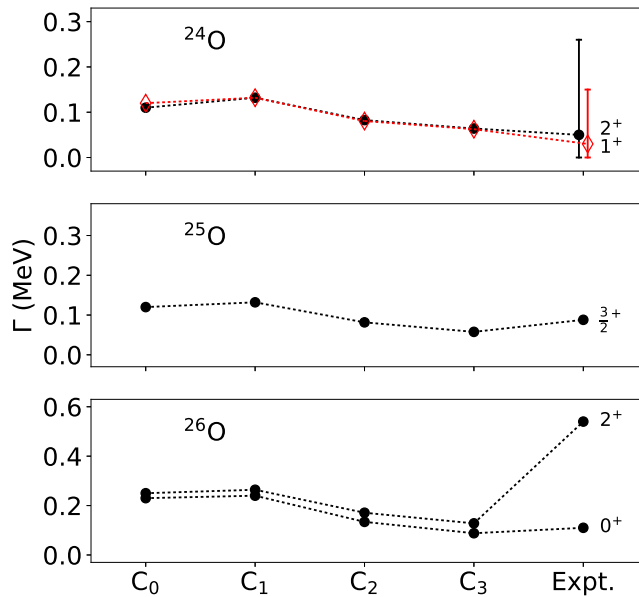


Figure 3: Widths of resonances in  $^{24,25,26}\text{O}$ . The experimental data are taken from Refs. [1, 32].

introduction has also updated the resonance width of the unbound  $^{25}\text{O}$  ground state. The experimental resonance width of the  $2^+$  state in  $^{26}\text{O}$  [1] looks extremely large, much larger than obtained in the GSM calculation. The experimental strength of the  $2^+$  resonant state is relatively weak, and the FWHM is influenced a lot by continuum states around. The present calculation predicts a much smaller resonance width for this state.

In the present paper, we are investigating how to treat the continuum effect in both energy and width of resonances. For the calculation of resonance energy, choosing a real-momentum contour for a partial wave that has no narrow resonance is good enough to give a convergent result. Taking a complex-momentum contour does not change the result. For the calculation of resonance width, however, choosing complex-momentum contours for all partial waves of the model space seems to be more reasonable, and hence recommended. For partial waves belonging to the excluded space, couplings with valence particles are weak, and hence it should be safe to use real-momentum contours for the respective channels.

## 4 Conclusion

In conclusion, we have applied the with-core GSM based on the CD-Bonn potential to neutron-rich oxygen isotopes, investigating the continuum effect on both resonance energy and width. These calculations were motivated with the recent experiment on  $^{26}\text{O}$  beyond the neutron drip line. The calculated  $2^+$  excitation energies were compared with shell-model calculations using the empirical USDB interaction, showing a strong continuum effect in the spectra of drip-line nuclei. By choosing the different prescriptions of contours in the Berggren coordinates for the GSM calculation, we have discussed the convergence of the resonance spectrum. It is suggested that all model-space partial waves, regardless of whether there is a narrow resonance, should take the same complex-momentum contour to obtain a convergent resonance width.

## 5 Acknowledgement

This work has been supported by the National Key R&D Program of China under Grant No. 2018YFA0404401; the National Natural Science Foundation of China under Grants No. 11835001, No. 11575007 and No. 11847203; the China Postdoctoral Science Foundation under Grant No. 2018M630018; and the CUSTIPEN (China-U.S. Theory Institute for Physics with Exotic Nuclei) funded by the U.S. Department of Energy, Office of Science under Grant No. DE-SC0009971.

## References

- [1] Y. Kondo *et al.*, Phys. Rev. Lett. **116**, 102503 (2016).
- [2] E. Caurier, F. Nowacki, A. Poves and J. Retamosa, Phys. Rev. C, **58** 2033 (1998).
- [3] C. R. Hoffman *et al.*, Phys. Rev. Lett. **100**, 152502 (2008).

- 
- [4] C. Yuan, T. Suzuki, T. Otsuka, F. Xu and N. Tsunoda, *Phys. Rev. C* **85**, 064324 (2012).
- [5] B. A. Brown and W. A. Richter, *Phys. Rev. C* **74**, 034315 (2006).
- [6] M. Kowalska, D. T. Yordanov, K. Blaum, P. Himpe, P. Lievens, S. Mallion, R. Neugart, G. Neyens and N. Vermeulen, *Phys. Rev. C* **77**, 034307 (2008).
- [7] R. Kanungo *et al.*, *Phys. Rev. Lett.* **102**, 152501 (2009).
- [8] K. Tshoo *et al.*, *Phys. Rev. Lett.* **109**, 022501 (2012).
- [9] S. R. Stroberg, H. Hergert, J. D. Holt, S. K. Bogner and A. Schwenk, *Phys. Rev. C* **93**, 051301(R) (2016).
- [10] K. Hagino and H. Sagawa, *Phys. Rev. C* **90**, 027303 (2014).
- [11] K. Hagino and H. Sagawa, *Phys. Rev. C* **89**, 014331 (2014).
- [12] L. V. Grigorenko and M. V. Zhukov, *Phys. Rev. C* **91**, 064617 (2015).
- [13] R. Id Betan, R. J. Liotta, N. Sandulescu and T. Vertse, *Phys. Rev. Lett.* **89**, 042501 (2002).
- [14] K. Bennaceur, J. Dobaczewski and M. Płoszajczak, *Phys. Rev. C* **60**, 034308 (1999).
- [15] N. Michel, W. Nazarewicz and M. Płoszajczak, *Phys. Rev. C* **82**, 044315 (2010).
- [16] I. Rotter, *Rep. Prog. Phys.* **54**, 635 (1991).
- [17] A. Volya and V. Zelevinsky, *Phys. Rev. C* **74**, 064314 (2006).
- [18] N. Michel, W. Nazarewicz, M. Płoszajczak and K. Bennaceur, *Phys. Rev. Lett.* **89**, 042502 (2002).
- [19] W. Fritsch, R. Lipperheide and U. Wille, *Nucl. Phys. A* **241**, 79 (1975).
- [20] N. Michel, W. Nazarewicz, M. Płoszajczak and J. Okołowicz, *Phys. Rev. C* **67**, 054311 (2003).
- [21] Z. H. Sun, Q. Wu, Z. H. Zhao, B. S. Hu, S. J. Dai and F. R. Xu, *Phys. Lett. B* **769**, 227 (2017).
- [22] R. Machleidt, *Phys. Rev. C* **63**, 024001 (2001).
- [23] S. Bogner, T. Kuo and A. Schwenk, *Phys. Rep.* **386**, 1 (2003).
- [24] K. Takayanagi, *Nucl. Phys. A* **852**, 61 (2011).
- [25] N. Tsunoda, K. Takayanagi, M. Hjorth-Jensen and T. Otsuka, *Phys. Rev. C* **89**, 024313 (2014).
- [26] N. Michel, W. Nazarewicz and M. Płoszajczak, *Phys. Rev. C* **70**, 064313 (2004).
- [27] Y. Jaganathen, R. M. I. Betan, N. Michel, W. Nazarewicz and M. Płoszajczak, *Phys. Rev. C* **96**, 054316 (2017).

- [28] G. Hagen, M. Hjorth-Jensen, G. R. Jansen, R. Machleidt and T. Papenbrock, *Phys. Rev. Lett.* **108**, 242501 (2012).
- [29] G. Papadimitriou, J. Rotureau, N. Michel, M. Płoszajczak and B. R. Barrett, *Phys. Rev. C* **88**, 044318 (2013).
- [30] I. J. Shin, Y. Kim, P. Maris, J. P. Vary, C. Forssén, J. Rotureau and N. Michel, *J. Phys. G* **44**, 075103 (2017).
- [31] J. Dudek, Z. Szymański and T. Werner, *Phys. Rev. C* **23**, 920 (1981).
- [32] <http://www.nndc.bnl.gov/>.
- [33] R. Machleidt and D. R. Entem, *Phys. Rep.* **503**, 1 (2011).

# Shell-Model Study of Calcium Isotopic Chain Starting from Chiral Two- and Three-Body Potentials

L. Coraggio<sup>a</sup> and Y. Z. Ma<sup>b</sup>

<sup>a</sup>*Istituto Nazionale di Fisica Nucleare, Complesso Universitario di Monte S. Angelo,  
Via Cintia — I-80126 Napoli, Italy*

<sup>b</sup>*School of Physics and State Key Laboratory of Nuclear Physics and Technology, Peking  
University, Beijing I-100871, China*

## Abstract

We have studied neutron-rich calcium isotopes in terms of the nuclear shell model employing a realistic effective interaction derived from realistic two- and three-body potentials built up within the chiral perturbation theory. We focus our attention on the shell-evolution properties of such an isotopic chain, namely on the excitation energy of yrast  $J^\pi = 2^+$  states and two-neutron separation energies of even- $A$  isotopes. The calculated results are in a good agreement with the available experimental data up to  $^{56}\text{Ca}$ , but show different predictions for heavier nuclei when including or not the three-body potential. In this context, the  $N = 40$  shell closure and the location of calcium dripline is also discussed.

**Keywords:** *Nuclear shell model; effective interactions; nuclear forces*

## 1 Introduction

Heavy calcium isotopes with mass number  $A > 48$  are currently the subject of great experimental and theoretical interest. With an  $N/Z$  ratio  $> 1.4$  they lie far from the stability valley and provide a good opportunity to explore the evolution of shell structure when approaching the neutron drip line [1, 2]. In this context, it should be mentioned that the question of the appearance of a shell closure at  $N = 34$  traces back to the work of Beiner and coworkers within the framework of the energy density formalism [3]. A decade ago some shell-model (SM) calculations [4, 5] have revived this issue indicating the existence of a large shell gap at  $N = 34$ , employing the empirical SM Hamiltonian GXPF1A [5]. On the other hand, the results of other SM calculations, obtained with different SM Hamiltonians, did not exhibit any shell closure for  $^{54}\text{Ca}$  [6, 7]. As a matter of fact, a decrease of the experimental  $2_1^+$  excitation energy in  $^{54}\text{Ca}$  with respect the one in  $^{56}\text{Ca}$  was observed in 2013, that evidences a lack of the  $N = 34$  shell closure [8].

---

*Proceedings of the International Conference ‘Nuclear Theory in the Supercomputing Era — 2018’ (NTSE-2018), Daejeon, South Korea, October 29 – November 2, 2018, eds. A. M. Shirokov and A. I. Mazur. Pacific National University, Khabarovsk, Russia, 2019, p. 192.*

<http://www.ntse.khb.ru/files/uploads/2018/proceedings/Coraggio.pdf>.

The contradictory theoretical predictions point to the crucial role played by the SM Hamiltonian, and the weakening of predictive power of an empirical procedure to derive them.

The realistic shell-model provides an approach that may overcome the ambiguity of fitting the SM single-particle (SP) energies and two-body matrix elements (TBME) to a chosen set of observables, namely deriving the effective Hamiltonian by way of the many-body perturbation theory and starting from a realistic nuclear potential [9, 10].

To this end, we have performed a perturbative expansion of a  $fp$ -shell effective Hamiltonian  $H_{\text{eff}}$ , arresting the series at the third order, and starting from a realistic nuclear two-nucleon force (2NF) based on the chiral perturbation theory (ChPT) at next-to-next-to-next-to-leading order ( $N^3\text{LO}$ ) [11]. We also include in our  $H_{\text{eff}}$ , aside the above two-body potential, a chiral  $N^2\text{LO}$  three-body potential [12] whose effects are considered at first-order in perturbation theory.

As mentioned before, we draw our attention to the shell evolution of calcium isotopes, as can be inferred from the behavior of the yrast  $J^\pi = 2^+$  states and ground-state (g.s.) energies. In particular, we want also to stress the role played by three-nucleon forces (3NF) to tackle this issue, so we will report results obtained using realistic SM effective Hamiltonians that include or not 3NF contributions.

The relevance of 3NF for a successful SM description of the evolution of shell closures traces back to the seminal papers of Zuker and coworkers [13, 14], who have investigated the need of modifications of the monopole component of TBME obtained from realistic SM Hamiltonians [15]. They also inferred that this should trace back to the lack of a 3NF in the nuclear realistic potentials employed to derive the  $H_{\text{eff}}$  [16].

Extensive direct investigations about the role of 3NFs in realistic  $H_{\text{eff}}$  have been carried out more recently by Schwenk and coworkers, who have performed studies of calcium [17, 18] isotopic chain starting from nuclear potentials built up within the chiral perturbative expansion and softened by way of  $V_{\text{low-}k}$  technique [19] or the similarity renormalization-group (SRG) approach [20].

This paper is organized as follows. First, a brief description of the derivation of  $H_{\text{eff}}$  within the perturbative approach is reported in Section 2. Section 3 is devoted to the presentation of the results of our calculations of the excitation energy  $E_{2^+}^{\text{exc}}$  of the yrast  $J^\pi = 2^+$  states and two-neutron separation energies  $S_{2n}$  for the calcium isotopes ranging from  $N = 22$  to  $N = 42$ , and compare them with the available data from experiment. In Section 4 we discuss our results and make some concluding remarks.

## 2 Outline of calculations

As mentioned before, we consider as 2NF the chiral  $N^3\text{LO}$  potential derived by Entem and Machleidt in Ref. [11], and as 3NF a chiral  $N^2\text{LO}$  potential, which shares the regulator function of a nonlocal form and some of the low-energy constants (LECs) with the 2NF. It should be stressed that the  $N^2\text{LO}$  3NF is composed of three components, namely the two-pion ( $2\pi$ ) exchange term  $V_{3N}^{(2\pi)}$ , the one-pion ( $1\pi$ ) exchange plus contact term  $V_{3N}^{(1\pi)}$ , and the contact term  $V_{3N}^{(\text{ct})}$ , and, consistently, the LECs  $c_1$ ,  $c_3$ , and  $c_4$  appearing in  $V_{3N}^{(2\pi)}$ , are the same as those in the  $N^3\text{LO}$  2NF.

Besides this, the 3NF  $1\pi$ -exchange and contact terms are own two extra LECs (known as  $c_D$  and  $c_E$ , respectively), which need to be determined by reproducing observables in systems with mass  $A > 2$ .

For our calculations, we adopt the same  $c_D$  and  $c_E$  values as employed in Ref. [21], namely,  $c_D = -1$  and  $c_E = -0.34$ , that have been determined by way of no-core shell model (NCSM) calculations [12].

The details about the calculation of our 3NF matrix elements in the harmonic-oscillator (HO) basis can be found in Appendix of Ref. [21]. The Coulomb potential is explicitly taken into account in our calculations.

In Ref. [21], it can be found also a detailed description of the derivation of our  $H_{\text{eff}}$  for one- and two-valence nucleon systems, starting from 2NF and 3NF, while here we present only a brief summary.

Our  $H_{\text{eff}}$  are derived in the model space spanned by the five orbitals,  $0f_{7/2}$ ,  $0f_{7/2}$ ,  $1p_{3/2}$ ,  $1p_{1/2}$ ,  $0g_{9/2}$ , outside the doubly-closed  $^{40}\text{Ca}$ . We have added the  $0g_{9/2}$  orbital to the standard  $fp$  ones in order to have a sounder description of neutron-rich systems and to investigate the location of neutron dripline in calcium isotopes.

We introduce an auxiliary one-body potential  $U$  to break up the Hamiltonian  $H$  for a system of  $A$  nucleons into a sum of a one-body term  $H_0$ , which describes the independent motion of the nucleons, and a residual interaction  $H_1$ :

$$H = \sum_{i=1}^A \frac{p_i^2}{2m} + \sum_{i<j=1}^A V_{ij}^{2\text{NF}} + \sum_{i<j<k=1}^A V_{ijk}^{3\text{NF}} = T + V^{2\text{NF}} + V^{3\text{NF}}$$

$$= (T + U) + (V^{2\text{NF}} - U) + V^{3\text{NF}} = H_0 + H_1^{2\text{NF}} + H_1^{3\text{NF}}. \quad (1)$$

In our calculation we use the HO potential,  $U = \frac{1}{2}m\omega^2 r^2$ , with the oscillator parameter  $\hbar\omega = 11$  MeV, according to the expression  $\hbar\omega = 45A^{-1/3} - 25A^{-2/3}$  for  $A = 40$ .

Once the  $H_0$  has been introduced, the reduced model space is defined in terms of a finite subset of  $H_0$ 's eigenvectors. The diagonalization of the many-body Hamiltonian in Eq. (1) within the infinite Hilbert space is then reduced to the solution of an eigenvalue problem for an effective Hamiltonian  $H_{\text{eff}}$  in a finite space.

We employ the time-dependent perturbation theory to derive  $H_{\text{eff}}$  [10,22].  $H_{\text{eff}}$  is expressed through the Kuo–Lee–Ratcliff folded-diagram expansion in terms of the vertex function  $\hat{Q}$ -box, which is composed of irreducible valence-linked diagrams [23,24]. We include in the  $\hat{Q}$ -box one- and two-body Goldstone diagrams through the third order in  $H_1^{2\text{NF}}$  and up to the first order in  $H_1^{3\text{NF}}$ . It is worth pointing out that the input chiral 2NF and 3NF have not been modified by way of any renormalization procedure, and the perturbative properties of the  $\hat{Q}$ -box from  $\text{N}^3\text{LO}$  2NF potential have been discussed in Ref. [22]. The folded-diagram series is then summed up to all orders using the Lee–Suzuki iteration method [25].

The  $H_{\text{eff}}$  derived for one valence-nucleon systems contains only one-body contributions which provides the SP energies for the SM calculation, while the two-body matrix elements are obtained from  $H_{\text{eff}}$  derived from the two valence-nucleon systems once the theoretical SP energies are subtracted from its diagonal matrix elements.

We have derived two  $H_{\text{eff}}$ ; one has been obtained calculating  $\hat{Q}$ -box diagrams with 2NF vertices only, and the other has been built up including also  $H_1^{3\text{NF}}$  first-order contributions in the collection of  $\hat{Q}$ -box diagrams (see Fig. 3 in Ref. [21]).

The neutron SP energies calculated with respect to  $0f_{7/2}$  orbital are reported in Table 1.

We observe that the  $\epsilon_{p_{3/2}-f_{7/2}}$  splitting provided by the 2NF only is too small to secure the shell closure of  $^{48}\text{Ca}$ , so, when diagonalizing the SM Hamiltonians, we

Table 1: Theoretical neutron SP energies (in MeV) derived starting from 2NF only (first column), and including 3NF contributions too (second column).

orbital	$\epsilon_{\nu}^{2NF}$	$\epsilon_{\nu}^{2NF+3NF}$
$0f_{7/2}$	0.0	0.0
$0f_{5/2}$	4.6	5.8
$1p_{3/2}$	0.6	2.8
$1p_{1/2}$	2.0	4.3
$0g_{9/2}$	1.9	6.7

consider the same set of SP energies, namely, the one calculated including also the 3NF contributions. We dub the  $H_{\text{eff}}$  with TBME derived with the 2NF only  $H_{\text{eff}}^{2NF}$ , and  $H_{\text{eff}}^{3NF}$  is the one whose SP energies and TBME have been obtained by adding also the 3NF.

### 3 Results

We start our study of calcium isotopes showing in Fig. 1 our results of their  $E_{2^+}^{\text{exc}}$  from  $N = 22$  up to  $N = 42$  (blue triangles and black diamonds), and compare them with available experimental data [8, 26] (red dots).

We observe that the behaviors obtained with both  $H_{\text{eff}}$  are very similar up to  $N = 38$ , the results with  $H_{\text{eff}}^{3NF}$  are in a better agreement with experiment. The shell closure at  $N = 28$  is reproduced, as well as the subshell closure at  $N = 32$  and the slight excitation-energy decrease between  $N = 32$  and  $N = 34$ .

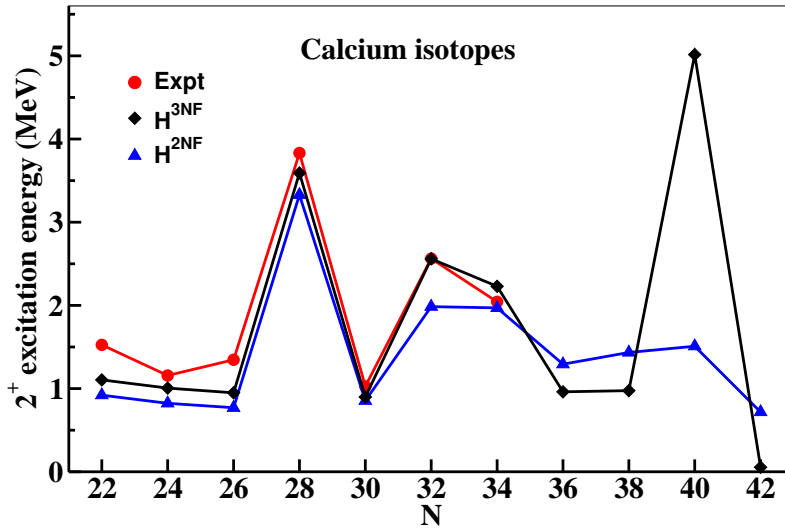


Figure 1: Experimental (red dots) and calculated excitation energies of the yrast  $J^{\pi} = 2^+$  states for calcium isotopes from  $N = 22$  to 42. The results obtained with  $H_{\text{eff}}^{2NF}$  are reported with blue triangles, those with  $H_{\text{eff}}^{3NF}$  are drawn as black diamonds.

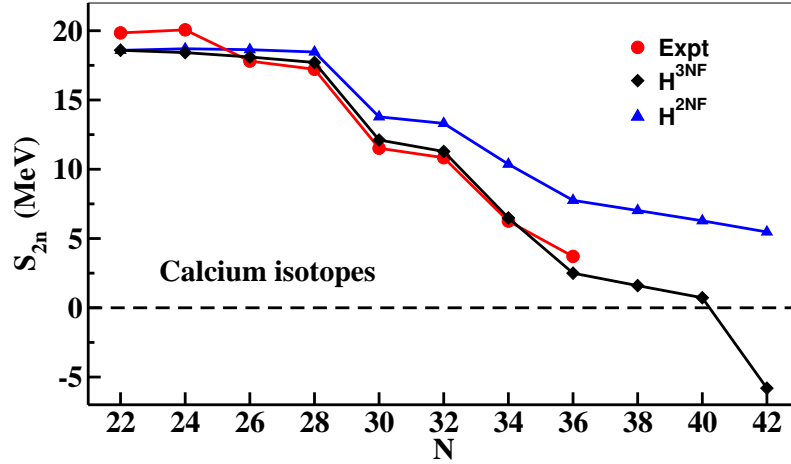


Figure 2: Experimental and calculated two-neutron separation energies for calcium isotopes from  $N = 22$  to 42. See text for details.

The comparison with the data for lighter isotopes are less satisfactory, these systems are largely affected by core-excitation components of  $^{40}\text{Ca}$  that have not been taken explicitly into account.

The larger discrepancy between the results obtained with  $H_{\text{eff}}^{2\text{NF}}$  and  $H_{\text{eff}}^{3\text{NF}}$  appears at  $N = 40$ , where the latter exhibits a strong closure of the  $0f_{5/2}$  orbital. Since both Hamiltonians share the same set of SP energies, this feature traces back to different monopole component of the  $0f_{5/2}, 0g_{9/2}$  configuration. In particular, this monopole component of  $H_{\text{eff}}^{3\text{NF}}$  enhances the energy splitting between the effective single-particle energies [27] of  $0f_{5/2}$  and  $0g_{9/2}$  orbitals when increasing the valence-neutron number, generating a strong shell closure at  $N = 40$ .

These closure properties are also present in the calculation of the two-neutron separation energies that are shown in Fig. 2 for the calcium isotopes up to  $N = 42$ . As before, the results obtained with  $H_{\text{eff}}^{2\text{NF}}$  are reported as blue triangle, while the  $H_{\text{eff}}^{3\text{NF}}$  ones are drawn as black diamonds. Data from experiment [1, 2, 28] are reported with red dots. It should be pointed out that we have shifted the SP energies in Table 1 in order to reproduce the experimental g.s. energy of  $^{41}\text{Ca}$  [28].

We have reported the results up to  $N = 42$  since  $H_{\text{eff}}^{3\text{NF}}$  predicts  $^{60}\text{Ca}$  as the last bound isotope.

As can be seen, both experimental and theoretical  $S_{2n}$  show a rather flat behavior up to  $N = 28$ , then a sudden drop occurs at  $N = 30$  that is a signature of the shell closure due to the  $0f_{7/2}$  filling. Another decrease appears at  $N = 34$  because at that point the valence neutrons start to occupy the  $1p_{1/2}$  and  $0f_{5/2}$  orbitals.

The results obtained with  $H_{\text{eff}}^{3\text{NF}}$  follow closely the behavior of the experimental  $S_{2n}$ , while those obtained with  $H_{\text{eff}}^{2\text{NF}}$  provide a less satisfactory agreement from  $N = 28$  on. This supports the crucial role of 3NF contributions to reproduce the observed shell evolution.

As in the case of the calculated  $E_{2^+}^{\text{exc}}$ , the difference obtained with  $H_{\text{eff}}^{2\text{NF}}$  and  $H_{\text{eff}}^{3\text{NF}}$  between the monopole component of  $0f_{5/2}, 0g_{9/2}$  configuration is responsible for different slopes towards different neutron driplines. As a matter of fact,  $H_{\text{eff}}^{2\text{NF}}$  pro-

vides bound calcium isotopes up to  $N = 50$ , while according to the SM calculations with  $H_{\text{eff}}^{3\text{NF}}$  the calcium dripline should be located at  $^{60}\text{Ca}$ .

## 4 Concluding remarks

We have presented the results of SM calculations for the calcium isotopic chain, which have been performed employing the SM effective Hamiltonian derived from realistic two- and three-body potentials built up within the chiral perturbation theory.

The outcome of our calculation is manifold.

- a) Single-particle energies obtained from the effective SM Hamiltonian starting from the 2NF are not able to provide satisfactory shell-closure properties, especially the one at  $N = 28$ .
- b) The 3NF contributions to the SP energies are crucial to reproduce the  $^{48}\text{Ca}$  shell closure corresponding to the filling of the  $0f_{7/2}$  orbital.
- c) The monopole component associated with the two-body matrix elements are rather different when including or not the 3NF. In particular, when adding the three-body potential to the starting Hamiltonian, we predict a strong shell closure at  $N = 40$ . This is at variance with the case when the effects of the three-body potential are neglected.
- d) The difference observed in the monopole component of the  $0f_{5/2}, 0g_{9/2}$  configuration leads to different predictions for the dripline, which is located at  $N = 40$  when including the contributions of the three-body potential.

The last mentioned feature is quite intriguing, since the recent experimental observation of  $^{60}\text{Ca}$  [29] and a study of the calcium isotopes by way of a Bayesian model averaging analysis [30] have revived the issue of the calcium dripline location.

## References

- [1] F. Wienholtz *et al.*, Nature **498**, 346 (2013).
- [2] S. Michimasa *et al.*, Phys. Rev. Lett. **121**, 022506 (2018).
- [3] M. Beiner, R. J. Lombard and D. Mas, Nucl. Phys. A **249**, 1 (1975).
- [4] M. Honma, T. Otsuka, B. A. Brown and T. Mizusaki, Phys. Rev. C **69**, 034335 (2004).
- [5] M. Honma, T. Otsuka, B. A. Brown and T. Mizusaki, Eur. Phys. J. A **25**, 499 (2005).
- [6] A. Poves, J. Sánchez-Solano, E. Caurier, F. Nowacki, Nucl. Phys. A **694**, 157 (2001).
- [7] E. Caurier, G. Martínez-Pinedo, F. Nowacki, A. Poves, A. P. Zuker, Rev. Mod. Phys. **77**, 427 (2005).
- [8] D. Steppenbeck *et al.*, Nature **502**, 207 (2013).

- 
- [9] B. H. Brandow, *Rev. Mod. Phys.* **39**, 771 (1967).
- [10] T. T. S. Kuo and E. Osnes, *Lecture Notes Phys.* **364**, 1 (1990).
- [11] D. R. Entem and R. Machleidt, *Phys. Rev. C* **66**, 014002 (2002).
- [12] P. Navrátil, V. G. Gueorguiev, J. P. Vary, W. E. Ormand and A. Nogga, *Phys. Rev. Lett.* **99**, 042501 (2007).
- [13] E. Caurier, E. A. P. Zuker, A. Poves and G. Martínez-Pinedo, *Phys. Rev. C* **50**, 225 (1994).
- [14] J. Duflo and A. P. Zuker, *Phys. Rev. C* **59**, 2347 (1999).
- [15] T. T. S. Kuo and G. E. Brown, *Nucl. Phys.* **84**, 40 (1966).
- [16] A. P. Zuker, *Phys. Rev. Lett.* **90**, 042502 (2003).
- [17] J. D. Holt, T. Otsuka, A. Schwenk and T. Suzuki, *J. Phys. G* **39**, 085111 (2012).
- [18] J. D. Holt, J. Menéndez, J. Simonis and A. Schwenk, *Phys. Rev. C* **90**, 024312 (2014).
- [19] S. Bogner, T. T. S. Kuo, L. Coraggio, A. Covello and N. Itaco, *Phys. Rev. C* **65**, 051301 (2002).
- [20] S. K. Bogner, R. J. Furnstahl and R. J. Perry, *Phys. Rev. C* **75**, 061001 (2007).
- [21] T. Fukui, L. De Angelis, Y. Z. Ma, L. Coraggio, A. Gargano, N. Itaco and F. R. Xu, *Phys. Rev. C* **98**, 044305 (2018).
- [22] L. Coraggio, A. Covello, A. Gargano, N. Itaco and T. T. S. Kuo, *Ann. Phys. (NY)* **327**, 2125 (2012).
- [23] T. T. S. Kuo, S. Y. Lee and K. F. Ratcliff, *Nucl. Phys. A* **176**, 65 (1971).
- [24] T. T. S. Kuo, J. Shurpin, K. C. Tam, E. Osnes and P. J. Ellis, *Ann. Phys. (NY)* **132**, 237 (1981).
- [25] K. Suzuki and S. Y. Lee, *Prog. Theor. Phys.* **64**, 2091 (1980).
- [26] <http://www.nndc.bnl.gov/ensdf/>.
- [27] Y. Utsuno, T. Otsuka, T. Mizusaki and M. Honma, *Phys. Rev. C* **60**, 054315 (1999).
- [28] G. Audi, A. H. Wapstra and C. Thibault, *Nucl. Phys. A* **729**, 337 (2003).
- [29] O. B. Tarasov *et al.*, *Phys. Rev. Lett.* **121**, 022501 (2018).
- [30] L. Neufcort, Y. C. Cao, W. Nazarewicz, E. Olsen and F. Viens, *Phys. Rev. Lett.* **122**, 062502 (2019).

# Towards Minkowski Space Solutions of Dyson–Schwinger Equations through un-Wick Rotation

Tobias Frederico<sup>a</sup>, Dyana C. Duarte<sup>a</sup>, Wayne de Paula<sup>a</sup>,  
Emanuel Ydrefors<sup>a</sup>, Shaoyang Jia<sup>b</sup> and Pieter Maris<sup>b</sup>

<sup>a</sup>*Instituto Tecnológico da Aeronáutica, DCTA, 12.228-900 São José dos Campos, Brazil*

<sup>b</sup>*Department of Physics and Astronomy, Iowa State University, Ames, IA 50011, USA*

## Abstract

The fermion self-energy is calculated from the rainbow-ladder truncation of the Dyson–Schwinger equation (DSE) in quantum electrodynamics (QED) for spacelike momenta and in the complex momentum plane close to the timelike region, both using Pauli–Villars regularization. Specifically, the DSE is solved in the complex momentum plane by rotating either the energy component of the four-momentum or the magnitude of Euclidean four-momentum to reach the timelike region in Minkowski space. The coupling constant is appropriately chosen to ensure the singularities of the fermion propagator located in the timelike region while producing significant differences from the perturbative solutions. For simplicity, we choose the Feynman gauge, but the method is applicable in other covariant gauges as well. We demonstrate that the approximate spectral representation based on the fermion self-energy near the timelike region is consistent with the solution of the DSE directly in the Euclidean space.

**Keywords:** *QED; fermion Dyson–Schwinger equation; Minkowski space calculations; rainbow-ladder truncation*

## 1 Motivation

The measurable quantities associated with the structure of a hadron state in the full possible kinematical range, which would be obtained by solving, e. g., quantum chromodynamics (QCD), require the knowledge of matrix elements of physical operators with timelike momenta. This poses a challenge to methods based on a purely Euclidean formulation of QCD, using either discretization methods such as lattice gauge theories, or continuum methods like the Dyson–Schwinger (DSE) and Bethe–Salpeter equations (BSE) [1]. To extract physical observables defined in Minkowski space, these methods have to rely on an analytic continuation from Euclidean space such that, e. g., the momenta of physical hadrons are on-shell (in the timelike region). This is straightforward to do for mesons as bound states of a quark and anti-quark [2, 3],

---

*Proceedings of the International Conference ‘Nuclear Theory in the Supercomputing Era — 2018’ (NTSE-2018), Daejeon, South Korea, October 29 – November 2, 2018, eds. A. M. Shirokov and A. I. Mazur. Pacific National University, Khabarovsk, Russia, 2019, p. 199.*

<http://www.ntse.khb.ru/files/uploads/2018/proceedings/Frederico.pdf>.

and can also be done for baryons. Furthermore, Poincaré-invariant form factors can be obtained [4, 5] in a limited momentum region without any ambiguity. However, starting from a purely Euclidean formulation, it is far from trivial to access observables defined on the light-front, such as the parton distribution functions and their generalizations.

Here we remind the readers that with these continuum methods, it is essential to take into account the nonperturbative dressing of quark propagators and vertices, in particular for light mesons: the pions represent the Goldstone bosons associated with dynamical chiral symmetry breaking, and their Bethe–Salpeter amplitudes are closely related to the self-energies of the light quarks [6]. Thus, if one aims to explore the rich kinematical range associated with observable hadron structure, it is desirable to obtain the solution of the BSE with dressed quark propagators in Minkowski space.

To make progress with the DSEs applied to QCD, it is therefore necessary to obtain the dressed propagators in Minkowski space. The DSE for the fermion self-energy within a QED-like model and rainbow-ladder truncation has been studied extensively. Early investigations based on analytic continuation of the Euclidean DSE suggested the existence of a pair of mass-like singularities at complex-conjugate momenta [7–9]. Subsequently, the DSE was studied in Minkowski metric using the Nakanishi integral representation (NIR) [10] in Refs. [11–13]. Their results showed a complicated analytic structure of the self-energies in the timelike region, which deserves to be studied further. More recently, the solutions for DSE for the fermion propagator in Minkowski space with on-shell renormalization within quenched QED were obtained in Ref. [14].

Efforts in solving the two-boson BSE in Minkowski space with bare particles using the NIR have been undertaken since the pioneering works in Refs. [15, 16], which relied on the uniqueness of the Nakanishi weight function in the nonperturbative domain of bound states. These techniques were further developed by the introduction of the light-front projection allied to the NIR to solve the BSEs for bosons [17–20] and for fermions [21–23]. Recently we obtained the approximate two-boson Minkowski Bethe–Salpeter amplitude from the solution of the Euclidean BSE by numerically ‘un-Wick rotating’ the homogeneous integral equation towards Minkowski space [24]. The solutions found with this new approach reveal the rich analytic structure of the Bethe–Salpeter amplitude, consistent with the one obtained in Minkowski space via the Nakanishi integral representation.

Motivated by the success of the un-Wick rotation method developed for solving the BSE, and the challenge to obtain the self-energy in the timelike region, this approach is extended here to investigate the fermion self-energies both in the spacelike and the timelike regions. We use the rainbow-ladder truncation of the fermion DSE with a massive or massless exchange vector boson. In Section 2, the truncated DSE is presented with its representations both in the Minkowski metric and in the Euclidean metric. Here we restrict ourselves to the Feynman gauge, but the method is applicable in any covariant gauge. We rely on the Pauli–Villars (PV) regularization to eliminate ultraviolet divergences; for simplicity we do not apply any renormalization condition, so our numerical results depend on the PV mass.

We solve the truncated DSE in the complex momentum plane using two different implementations:

1. the complex-rotation of the fourth component of the Euclidean four-momenta towards the zeroth component (energy component) of the four-momenta in the

Minkowski metric (‘un-Wick rotation’);

2. and an analytic continuation of the magnitude of the Euclidean four-momenta to rotate the Euclidean DSE on the spacelike axis towards the pure timelike axis in the Minkowski metric,

as described in Section 3. Both implementations give (within their numerical uncertainty) the same results in a large region of the complex momentum plane. The numerical results for the self-energies are discussed in Section 4. In this preliminary study, the coupling constant is chosen below the critical value for dynamical chiral symmetry breaking, but large enough to allow for nonperturbative effects. We also demonstrate that the obtained results close to the timelike axis can be used as a good approximation to the spectral representation of the self-energy.

## 2 DSE in Minkowski and Euclidean metric

In the Minkowski metric, we can write the inverse fermion propagator  $S^{-1}$  as

$$S^{-1}(p) = \not{p}A(p^2) - B(p^2) = A(p^2)(\not{p} - M(p^2)), \quad (1)$$

with  $M(p^2) = B(p^2)/A(p^2)$ . For convenience we also define  $Z(p^2) = 1/A(p^2)$ . With this notation, the fermion propagator  $S$  can be written as

$$S(p) = \frac{A(p^2)\not{p} + B(p^2)}{A^2(p^2)p^2 - B^2(p^2) + i\epsilon} = Z(p^2)\frac{\not{p} + M(p^2)}{p^2 - M^2(p^2) + i\epsilon}, \quad (2)$$

where we have introduced the  $i\epsilon$  prescription to select the correct Riemann sheet when the denominator in the spectral representation vanishes. For simplicity, however, we will suppress the explicit  $i\epsilon$ 's unless that could cause ambiguities.

Next, consider DSE for the fermion propagator in the rainbow (ladder) truncation by coupling to a vector boson with mass  $\mu$  and PV regularization with mass  $\Lambda$ ,

$$S^{-1}(p) = \not{p} - m_0 - ig^2 \int \frac{d^4k}{(2\pi)^4} \gamma^\mu S(k) \gamma^\nu [D_{\mu\nu}(q; \mu) - D_{\mu\nu}(q; \Lambda)], \quad (3)$$

with the bare fermion mass  $m_0$  and  $q = p - k$ . The (massive) vector boson in the covariant gauge can be written as [25]

$$D_{\mu\nu}(q; m) = \frac{-1}{q^2 - m^2 + i\epsilon} \left[ g_{\mu\nu} - (1 - \xi) \frac{q_\mu q_\nu}{q^2 - \xi m^2 + i\epsilon} \right], \quad (4)$$

where  $\xi$  is the gauge parameter. The Landau gauge is defined by  $\xi = 0$ , while  $\xi = 1$  defines the Feynman gauge. For simplicity, we will only consider Feynman gauge here. Projecting out the equations for  $A$  and  $B$  we arrive at

$$B(p^2) = m_0 + ig^2 \int \frac{d^4k}{(2\pi)^4} \frac{4B(k^2)}{k^2 A^2(k^2) - B^2(k^2)} \frac{\Lambda^2 - \mu^2}{(q^2 - \mu^2)(q^2 - \Lambda^2)}, \quad (5)$$

$$A(p^2) = 1 + ig^2 \int \frac{d^4k}{(2\pi)^4} \frac{2p \cdot k}{p^2} \frac{A(k^2)}{k^2 A^2(k^2) - B^2(k^2)} \frac{\Lambda^2 - \mu^2}{(q^2 - \mu^2)(q^2 - \Lambda^2)}, \quad (6)$$

with implicit  $i\epsilon$  prescriptions for various propagator poles.

Solving the DSE numerically directly in Minkowski space poses the following challenges:

- the integration  $\int d^4k$  in Minkowski metric;
- the known singularities in the denominators  $(q^2 - \mu^2)$  and  $(q^2 - \Lambda^2)$ ;
- the unknown but expected singularity in the denominator  $k^2 A^2(k^2) - B^2(k^2)$ .

The first challenge can be dealt with by integrating over  $k_0$  and  $\vec{k}$  separately:

$$\int \frac{d^4k}{(2\pi)^4} = \int_{-\infty}^{\infty} \frac{dk_0}{2\pi} \int \frac{d^3\vec{k}}{(2\pi)^3}. \quad (7)$$

The latter two could be overcome by using an explicitly nonzero  $i\epsilon$  in the propagator denominators. However, numerically this is not necessarily stable, in particular since the location of the singularity in the fermion propagator is determined by the solution of the DSE.

Indeed, the common practice is to perform a formal Wick rotation to Euclidean space, avoiding the singularities altogether. Of course, the DSE can only be solved for Euclidean momenta after such a procedure, corresponding to spacelike momenta in Minkowski metric. Specifically, after applying the formal Wick rotation, we obtain the fermion DSE using Euclidean four-vectors  $p_E$  and  $k_E$ ,

$$B(-p_E^2) = m_0 + g^2 \int \frac{d^4k_E}{(2\pi)^4} \frac{4 B(-k_E^2)}{k_E^2 A^2(-k_E^2) + B^2(-k_E^2)} \frac{\Lambda^2 - \mu^2}{(q_E^2 + \mu^2)(q_E^2 + \Lambda^2)}. \quad (8)$$

$$A(-p_E^2) = 1 + g^2 \int \frac{d^4k_E}{(2\pi)^4} \frac{A(-k_E^2)}{k_E^2 A^2(-k_E^2) + B^2(-k_E^2)} \frac{2 p_E \cdot k_E (\Lambda^2 - \mu^2)}{p_E^2 (q_E^2 + \mu^2)(q_E^2 + \Lambda^2)}. \quad (9)$$

Note that in the Euclidean metric,  $p_E^2$  runs from 0 to  $+\infty$ , and that results for Euclidean  $p_E^2 \geq 0$  are equivalent to the results for spacelike momenta  $p^2 = -p_E^2 \leq 0$  in Minkowski metric. In the next Section we discuss how one can obtain the solution of the DSE for timelike momenta.

### 3 Solving the DSE numerically

In the Euclidean space, we can perform the integrations using 4-dimensional hyperspherical coordinates:

$$\int \frac{d^4k_E}{(2\pi)^4} = \int_0^\infty \frac{k_E^3 dk_E}{(2\pi)^4} \int_0^\pi \sin^2(\theta) d\theta \int_0^\pi \sin(\phi) d\phi \int_0^{2\pi} d\alpha. \quad (10)$$

The unknown functions  $A$  and  $B$  of the fermion propagator depend only on  $k^2$ , and there is only one nontrivial angle in the integrand, namely the angle between  $k$  and  $p$ . Thus we can perform two of the three angular integrations analytically, with the remaining angular integral to be evaluated numerically

$$\int \frac{d^4k_E}{(2\pi)^4} I(k, p) = 2 \int_0^\infty \frac{k_E^3 dk_E}{(2\pi)^3} \int_0^\pi \sin^2(\theta) d\theta I(k_E^2, p_E^2, \cos(\theta)). \quad (11)$$

This leads to a set of coupled nonlinear integral equations in one dimension for space-like values of  $p_E^2 \geq 0$ ,

$$B(-p_E^2) = m_0 + \frac{2g^2}{(2\pi)^3} \int_0^\infty k_E^3 dk_E \frac{4B(-k_E^2)}{k_E^2 A^2(-k_E^2) + B^2(-k_E^2)} \times \int_0^\pi \sin^2 \theta d\theta \frac{\Lambda^2 - \mu^2}{(q_E^2 + \mu^2)(q_E^2 + \Lambda^2)}, \quad (12)$$

$$A(-p_E^2) = 1 + \frac{2g^2}{(2\pi)^3} \int_0^\infty k_E^3 dk_E \frac{A(-k_E^2)}{k_E^2 A^2(-k_E^2) + B^2(-k_E^2)} \times \int_0^\pi \sin^2 \theta d\theta \frac{2k_E \cos \theta}{p_E} \frac{\Lambda^2 - \mu^2}{(q_E^2 + \mu^2)(q_E^2 + \Lambda^2)}. \quad (13)$$

It is straightforward to solve these coupled nonlinear integral equations iteratively using a suitable discretization of the integrals and an initial guess for the functions  $A$  and  $B$ .

### 3.1 Un-Wick rotating from the Euclidean solution

Instead of using 4-dimensional hyperspherical coordinates, we can also integrate over the fourth (or energy) component separately, and use 3-dimensional spherical coordinates for the remaining 3 dimensions,

$$\int \frac{d^4 k_E}{(2\pi)^4} = \int_{-\infty}^\infty \frac{dk_4}{2\pi} \int \frac{d^3 \vec{k}}{(2\pi)^3} = \frac{1}{(2\pi)^3} \int_{-\infty}^\infty dk_4 \int_0^\infty k_v^2 dk_v \int_0^\pi \sin(\phi) d\phi, \quad (14)$$

where  $k_v = |\vec{k}|$ . In this case, it is convenient to write the inverse of the fermion propagator  $A$  and  $B$  as functions of two variables,  $p_4$  and  $p_v$ . After doing so, we arrive at

$$B(p_4, p_v) = m_0 + \frac{g^2}{(2\pi)^3} \int_{-\infty}^\infty dk_4 \int_0^\infty k_v^2 dk_v \frac{4B(k_4, k_v)}{(k_4^2 + k_v^2) A^2(k_4, k_v) + B^2(k_4, k_v)} \times \int_0^\pi \sin(\phi) d\phi \frac{\Lambda^2 - \mu^2}{(q_E^2 + \mu^2)(q_E^2 + \Lambda^2)}, \quad (15)$$

$$A(p_4, p_v) = 1 + \frac{g^2}{(2\pi)^3} \int_{-\infty}^\infty dk_0 \int_0^\infty k_v^2 dk_v \frac{A(k_4, k_v)}{(k_4^2 + k_v^2) A^2(k_4, k_v) + B^2(k_4, k_v)} \times \int_0^\pi \sin(\phi) d\phi \frac{2(p_4 k_4 + p_v k_v \cos \phi)}{p_4^2 + p_v^2} \frac{\Lambda^2 - \mu^2}{(q_E^2 + \mu^2)(q_E^2 + \Lambda^2)}, \quad (16)$$

where  $q_E^2 = (p_4 - k_4)^2 + (\vec{p} - \vec{k})^2 = p_4^2 - 2p_4 k_4 + k_4^2 + p_v^2 - 2p_v k_v \cos(\phi) + k_v^2$ . We can now solve for  $A$  and  $B$  as functions of two variables,  $p_4$  and  $p_v$ , and up to numerical precision, we should get the same results for  $A(p_4^2 + p_v^2)$  and  $B(p_4^2 + p_v^2)$  as above.

We can now undo the Wick rotation by applying the transformation

$$p_4 \rightarrow e^{-i\delta} p_4, \quad k_4 \rightarrow e^{-i\delta} k_4, \quad dk_4 \rightarrow e^{-i\delta} dk_4, \quad (17)$$

while keeping  $p_4$  and  $k_4$  real, analogous to the method used in Ref. [24] to obtain the Minkowski space Bethe–Salpeter amplitudes from the Euclidean BSE. As long as the contribution from the integral along the arcs at  $|k_4| = \pm\infty$  vanishes, true in the case of PV regularization, we only need to keep the integration over  $k_4$  from  $-\infty$  to  $\infty$ .

In the limit of  $\delta \rightarrow \pi/2$  this transformation becomes

$$p_4 \rightarrow -ip_4 \equiv p_0, \quad k_4 \rightarrow -ik_4 \equiv k_0, \quad dk_4 \rightarrow -idk_4 \equiv dk_0, \quad (18)$$

which recovers the DSEs in the Minkowski metric, for both the spacelike and the timelike region. Indeed, applying this transformation to Eqs. (15) and (16), we obtain

$$B(p_0, p_v) = m_0 + i \frac{g^2}{(2\pi)^3} \int_{-\infty}^{\infty} dk_0 \int_0^{\infty} k_v^2 dk_v \frac{4 B(k_0, k_v)}{(k_0^2 - k_v^2) A^2(k_0, k_v) - B^2(k_0, k_v)} \\ \times \int_0^{\pi} \sin(\phi) d\phi \frac{\Lambda^2 - \mu^2}{(-q_0^2 + q_v^2 + \mu^2)(-q_0^2 + q_v^2 + \Lambda^2)}, \quad (19)$$

$$A(p_0, p_v) = 1 + i \frac{g^2}{(2\pi)^3} \int_{-\infty}^{\infty} dk_0 \int_0^{\infty} k_v^2 dk_v \frac{A(k_0, k_v)}{(k_0^2 - k_v^2) A^2(k_0, k_v) - B^2(k_0, k_v)} \\ \times \int_0^{\pi} \sin(\phi) d\phi \frac{p_0 k_0 - p_v k_v \cos \phi}{p_0^2 - p_v^2} \frac{\Lambda^2 - \mu^2}{(q_0^2 - q_v^2 - \mu^2)(q_0^2 - q_v^2 - \Lambda^2)}, \quad (20)$$

where  $q_0^2 = (p_0 - k_0)^2$  and  $q_v^2 = (\vec{p} - \vec{k})^2$ . Now we can recognize  $p_0^2 - p_v^2$  as  $p^2$  in the Minkowski metric, and similarly for  $k_0^2 - k_v^2$  and  $q_0^2 - q_v^2$ , and thus we arrive at the DSE in Minkowski space, Eqs. (5) and (6). Of course, in these expressions for the DSEs in Minkowski metric for both timelike and spacelike momenta, there are singularities in the propagators under the integral, which are understood in conjunction with  $i\epsilon$  prescription.

With  $\delta \in (0, \pi/2)$ , the transformation given by Eq. (17) acts as the tool to interpolate the DSEs between the Euclidean and Minkowski metrics. In the limit of  $\delta \rightarrow \pi/2$ , the Minkowski space invariant  $p^2 = p_0^2 - p_v^2$  is real and runs from  $-\infty$  to  $+\infty$ . But for  $0 < \delta < \pi/2$  the ‘invariant’  $p^2 = -e^{-2i\delta} p_4^2 - p_v^2$  covers a slice in the upper complex  $p^2$  plane. As  $\delta$  approaches  $\pi/2$ , it covers almost the entire upper complex momentum plane, and ‘collapses’ onto the real axis only in the limit  $\delta \rightarrow \pi/2$ . As long as there are no singularities in the upper complex  $p^2$  plane, we can continuously connect the solution of the DSEs near the timelike region to the solution in the spacelike region. As a consistency check, for any value of  $0 \geq \delta \geq \pi/2$ , we should obtain the same (spacelike) solution for  $p_4 = 0$ .

In Fig. 1 we present solutions of the DSE in the Feynman gauge obtained by un-Wick rotating  $p_4$ . When un-Wick rotating  $p_4$  from the Euclidean metric, we solve the DSE on a slice in the complex  $p^2 = e^{i2\delta} p_4^2 + p_v^2$  plane; the boundaries of this slice are given by  $(p_4 = 0, p_v)$ , which corresponds to the spacelike axis, and by  $(p_4, p_v = 0)$ , which approaches the timelike axis in the limit  $\delta \rightarrow \pi/2$ . The results for  $A(p_4 = 0, p_v)$  and  $B(p_4 = 0, p_v)$ , i. e., on the spacelike axis, are indeed independent of the angle  $\delta$  and purely real, as is shown in the left panel of Fig. 1. In the right panel, we show our results as a function of  $p_4$  for  $p_v = 0$ , in which case we do see a dependence on the angle  $\delta$ , as expected; furthermore, both  $A$  and  $B$  develop an imaginary part, which increases in magnitude with increasing  $\delta$ . However, as we approach  $\delta = \pi/2$ , the numerics becomes unstable due to singularities in the propagators, which prevents us from actually reaching the timelike axis.

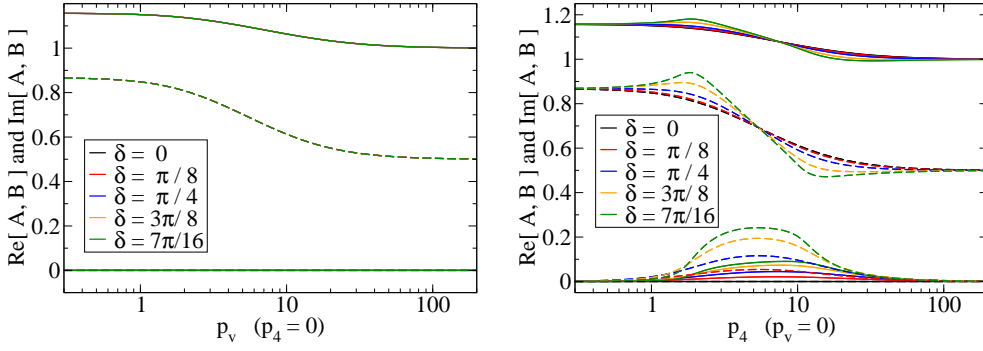


Figure 1: Real and imaginary parts of the inverse propagator functions  $A$  (solid) and  $B$  (dashed) at different angles  $\delta$ , obtained by un-Wick rotating the Euclidean solution as a function of  $p_v$  at  $p_4 = 0$ , corresponding to the spacelike  $p^2$  axis (left) and as a function of  $p_4$  at  $p_v = 0$ , along a line in the complex  $p_4 e^{-i\delta}$  plane (right);  $\delta = \pi/2$  would be the timelike axis. On the right we also show our results of rotating the magnitude of  $p$  from the spacelike region towards the timelike region, which are indistinguishable at the scale shown. Parameters are  $m_0 = 0.5$ ,  $\mu = 1.0$ ,  $\Lambda = 10.0$ , and  $\alpha = 0.5$ .

### 3.2 Rotating the spacelike region to the timelike region

Alternatively, we can rotate the DSE from the Euclidean spacelike axis towards the timelike axis by applying the transformation

$$p \rightarrow e^{-i\delta} p, \quad k \rightarrow e^{-i\delta} k, \quad dk \rightarrow e^{-i\delta} dk \quad (21)$$

on the magnitude of the (Euclidean) four-vectors, while continuing to use 4-dimensional hyperspherical coordinates, as was done in, e. g., Refs. [8,9]. With this technique we keep  $p$  and  $k$  real (and positive), and we retain the 4-dimensional symmetry. As long as the contribution along the arc at  $k = \infty$  vanishes (and with the explicit PV regularization it does), we can neglect the contribution along this arc, and keep only the integration over  $k$  from 0 to  $\infty$ .

In the limit of  $\delta = \pi/2$  this transformation becomes

$$p_E^2 \rightarrow -p_E^2 = p^2, \quad k_E^2 \rightarrow -k_E^2 = k^2, \quad k_E^3 dk_E \rightarrow k_E^3 dk_E = k^3 dk, \quad (22)$$

and effectively this gives us the DSEs on the pure timelike axis with  $p^2 \geq 0$ ,

$$B(p^2) = m_0 - \frac{2g^2}{(2\pi)^3} \int_0^\infty k^3 dk \frac{4B(k^2)}{k^2 A^2(k^2) - B^2(k^2)} \times \int_0^\pi \sin^2 \theta d\theta \frac{\Lambda^2 - \mu^2}{(q^2 - \mu^2)(q^2 - \Lambda^2)}, \quad (23)$$

$$A(p^2) = 1 - \frac{2g^2}{(2\pi)^3} \int_0^\infty k^3 dk \frac{A(k^2)}{k^2 A^2(k^2) - B^2(k^2)} \times \int_0^\pi \sin^2 \theta d\theta \frac{2k \cos \theta}{p} \frac{\Lambda^2 - \mu^2}{(q^2 - \mu^2)(q^2 - \Lambda^2)}. \quad (24)$$

Note, Eqs. (23) and (24) are for timelike momenta only,  $p^2 \geq 0$ ,  $k^2 \geq 0$ , and  $q^2 = (p - k)^2 \geq 0$  — they are different from the DSEs in the Minkowski metric, Eqs. (5) and (6). Again, singularities under the integrals are specified by the  $i\epsilon$  prescription.

For any  $0 < \delta < \pi/2$ , this method gives the DSE along the line from 0 to  $\infty$  in the upper complex  $p^2$  plane, rather than on the slice of the upper complex momentum plane. Furthermore, it remains an integral equation in one variable, rather than in two variables as with the method described in the previous subsection. This method is therefore numerically easier to implement, and leads to a better numerical precision.

In the right panel of Fig. 1, we also include our results obtained with this method. Not surprisingly, the results of the two methods are essentially indistinguishable, at least at the scale shown. However, the method of rotating the magnitude of  $p$  is much more accurate (for a similar numerical effort) than the explicit un-Wick rotation of the fourth component, because when we un-Wick rotate the fourth component, we break the 4-dimensional symmetry by treating the fourth component and the 3-vector components differently. Furthermore, we solve the propagator functions  $A$  and  $B$  as functions of two independent real variables,  $p_4$  and  $p_v$ , for a given angle  $\delta$  (or, equivalently, as a function of one complex variable  $p^2 = p_4^2 e^{i2\delta} + p_v^2$ ), whereas, if we rotate the magnitude of  $p$ , the functions  $A$  and  $B$  remain functions of only one essentially real variable. In particular, as  $\delta$  approaches  $\pi/2$ , in the case of the un-Wick rotation we solve the DSE in the entire upper  $p^2$  plane, whereas, if we rotate the magnitude of  $p$ , we solve the DSE along a line from 0 to  $\infty$  close to the timelike axis. Clearly, the latter approach is more efficient numerically.

## 4 Results for the self-energy in the timelike region

In order to discuss our results as we approach the timelike region, it is more convenient to use  $\theta = \pi/2 - \delta$ ; with this notation the timelike axis corresponds to the limit  $\theta \rightarrow 0$ . For moderate values of the coupling (well below those corresponding to dynamical chiral symmetry breaking), we can achieve accurate results down to  $\theta = \pi/256 \approx 0.7^\circ$  by rotating the magnitude of  $p$ , whereas if we decrease  $\theta$  below about  $\theta = \pi/16 \approx 11^\circ$ , the un-Wick rotation becomes numerically challenging, requiring an efficient implementation on parallel high-performance computing systems.

In Fig. 2 we see that the imaginary parts of  $A(p^2)$  and  $B(p^2)$  become nonzero along the timelike axis. Furthermore, both the real parts and the imaginary parts of  $A(p^2)$  and  $B(p^2)$  develop kinks, that is, discontinuities in their derivatives. The location of these kinks is determined by the physical thresholds for the production of an exchange particle; these kinks occur at  $(m_{\text{phys}} + \mu)^2$  and  $(m_{\text{phys}} + \Lambda)^2$ , where the pole mass  $m_{\text{phys}}$  is determined from the zero of the inverse propagator, at  $M(p^2) = \sqrt{p^2}$ .

These kinks are generally attributed to the integration over the propagator poles in Eqs. (5) and (6), where one (or more) denominator becomes zero. Mathematically, the kinks are caused by a pinch singularity due to the zeros of the exchange boson propagator and the fermion propagator in Eqs. (5) and (6).

### 4.1 Analytic structure and pole mass

In Fig. 3 we show our results for  $M^2(p^2)$  and  $Z(p^2) = 1/A(p^2)$  in the infrared region. The fermion propagator has a singularity at  $p^2 = M^2(p^2) = m_{\text{phys}}^2$  in the

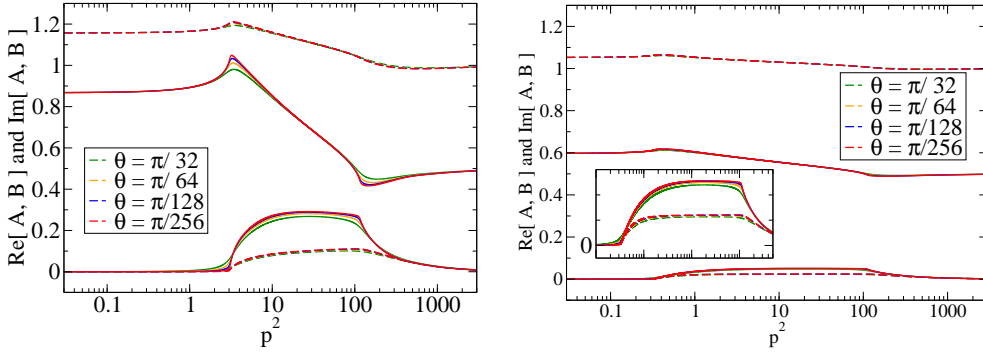


Figure 2: Real and imaginary parts of the inverse propagator functions  $A$  (dashed) and  $B$  (solid) at different angles  $\theta$  close to the timelike axis. Both figures are with  $m_0 = 0.5$  and the PV mass  $\Lambda = 10$ ; the exchange mass  $\mu = 1.0$  and  $\alpha = 0.5$  (left) and the massless vector boson and  $\alpha = 0.1$  (right).

timelike region. With a nonzero mass for the exchange boson, this singularity is a simple mass-pole (at least in the Feynman gauge) — but neither the inverse propagator functions  $A^2(p^2)$  and  $B(p^2)$ , nor the dynamical mass function  $M(p^2)$  shows any discontinuity or kink at this mass-pole.

The first kink or branch-point in the inverse propagator functions is located at  $(m_{\text{phys}} + \mu)^2 \geq m_{\text{phys}}^2$ , as marked by the vertical dotted line in Fig. 3. At this kink, both the propagator itself and the inverse propagator functions have a branch-point, at which point the imaginary part becomes nonzero. With a nonzero exchange mass  $\mu$ , this kink occurs well beyond the mass-pole at  $p^2 = M^2(p^2)$ , and both the propagator and the inverse propagator functions are finite at this branch-point. However, in the limit of  $\mu \rightarrow 0$ , this branch-point coincides with the mass-pole singularity, as can be seen in the right panel of Fig. 3. Consequently, the propagator exhibits a

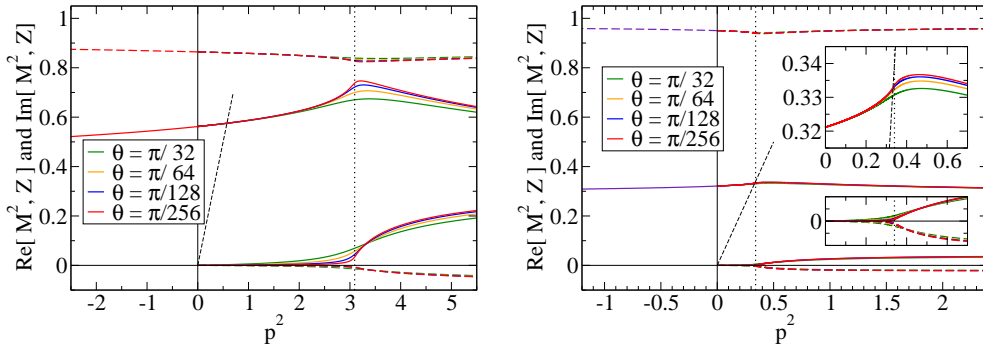


Figure 3: Real and imaginary parts of the dynamical mass squared,  $M^2(p^2)$  (solid), and wave function renormalization,  $Z(p^2) = 1/A(p^2)$  (dashed), in the spacelike and close to the timelike axis, again with  $m_0 = 0.5$  and the PV mass  $\Lambda = 10$ . The extracted pole masses and residues are:  $m = 0.759$  and  $Z(m^2) = 0.82$  for the mass  $\mu = 1.0$  and  $\alpha = 0.5$  (left) and  $m = 0.58$  and  $Z(m^2) = 0.34$  for the massless vector boson and  $\alpha = 0.1$  (right).

more complicated singularity instead of a simple mass-pole, at which point the inverse propagator is zero, and a branch-cut starts along the timelike axis. The sign of the imaginary part is a consequence of the  $i\epsilon$  prescription — or, in the case of the un-Wick rotation, of the direction of the rotation.

Due to the PV regularization, the (inverse) propagator has a second kink along the timelike axis, located at  $(m_{\text{phys}} + \Lambda)^2$ , beyond which the imaginary parts fall off to zero, and the real parts of the (inverse) fermion propagator approach their bare (tree-level) values, see Fig. 2.

## 4.2 Spectral representation of the self-energy

With the PB regularization, the integral representation for the scalar and vector self-energies can be written as

$$B(p^2) = m_0 + \int_0^\infty ds \frac{\rho_B(s)}{p^2 - s + i\epsilon} \quad \text{with } \rho_B(s) = -\text{Im}[B(s)/\pi], \quad (25)$$

$$A(p^2) = 1 + \int_0^\infty ds \frac{\rho_A(s)}{p^2 - s + i\epsilon} \quad \text{with } \rho_A(s) = -\text{Im}[A(s)/\pi], \quad (26)$$

following the standard spectral representation of the propagators [25]. In principle, the spectral functions  $\rho_{A,B}$  fully determine the scalar and vector self-energies, and thus the propagator.

We show in the left panel of Fig. 4 approximations to the spectral functions  $\rho_{A,B}$  obtained from the imaginary parts of  $A$  and  $B$  at different angles  $\theta$  close to the timelike axis. (Note that the angle  $\theta$  is defined as the rotation angle for  $p_0$  or the magnitude of  $p$ ; in terms of the variable  $s$  used in the spectral representation, this corresponds to an angle  $2\theta$ .) The right panel confirms that in the limit of  $\theta \rightarrow 0$ , these approximate spectral functions can indeed reproduce the Euclidean (spacelike) to high accuracy. With a more careful analysis and using a Mellin transformation, we can use these ‘approximate spectral representations’ at nonzero values of  $\theta$  to calculate the self-energies in the entire slice of the upper complex  $p^2$  plane, bounded by the

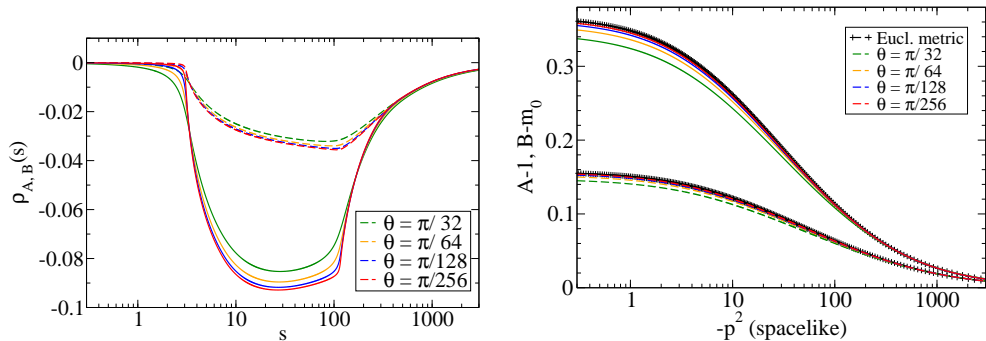


Figure 4: Left: Approximate spectral functions  $\rho_{A,B}$  obtained at different angles  $\theta$  close to the timelike axis for  $m_0 = 0.5$ ,  $\mu = 1.0$ ,  $\Lambda = 10.0$ , and  $\alpha = 0.5$ . Right: Spacelike self-energies obtained from the approximate spectral functions, compared to the Euclidean solution.

real spacelike axis (negative  $p^2$ ) and the line  $p^2 e^{i2\theta}$ . More details will be presented in Ref. [26].

## 5 Conclusion and outlook

This contribution presents a preliminary study of the nonperturbative fermion propagator in both the spacelike and near the timelike regions by investigating the fermion DSE in rainbow-ladder truncation in the Feynman gauge in a QED-like theory. Two methods to solve the Pauli–Villars regulated DSE were implemented to obtain the self-energies near the timelike axis, both relying on an analytic continuation of the Euclidean DSE into the complex momentum plane. In the first approach the energy component of the four-momenta are complex-rotated to bring the Euclidean formulation towards the Minkowski metric, while in the second method the magnitude of the four-vector  $p$  is complex-rotated to rotate the spacelike axis towards the timelike axis. Both methods were used to compute the Dirac scalar and vector self-energies of the fermion near the timelike region. The second method showed to be much more accurate allowing calculations with angles as small as  $\theta = \pi/256 \approx 0.7^\circ$ , quite close to the timelike axis. This is natural as with a fixed angle, in the first method the DSE has to be solved as function of two real variables, while in the second approach the scalar and vector self-energies depend on only one real variable, allowing a finer grid in this one variable.

The coupling constant was chosen sufficiently large for the solutions to allow for noticeably nonperturbative effects, while below the value for the dynamical chiral symmetry breaking. With a massive vector boson, the obtained nonperturbative fermion propagator has a mass-pole at  $p^2 = M^2(p^2) = m_{\text{phys}}^2$  on the timelike axis, followed by a branch-cut starting at  $p^2 = (m_{\text{phys}} + \mu)^2$ . With massless bosons,  $\mu = 0$ , this branch-cut starts at the physical mass, and the mass-pole becomes a more complicated singularity. Finally, the imaginary part of the self-energies along the timelike axis were used to obtain the spectral densities, from which the spacelike self-energies were computed in good agreement with the Euclidean self-energies.

In the future, we intend to explore in more detail the analytic structure of the fermion propagator in the complex plane by, e. g., generalizing the spectral representation with finite  $\theta$  associated with the study the solutions of Laplace equations using Mellin transform [26]; we also plan to extend these investigations to other gauges, in particular the Landau gauge, and to other theories. The next step will be to use these nonperturbative propagators in the Minkowski metric for bound state calculations and to explore hadron structure directly in the Minkowski space.

## Acknowledgments

This work was supported by Fundação de Amparo à Pesquisa do Estado de São Paulo, Brazil (FAPESP) Thematic grants No. 13/26258-4 and No. 17/05660-0, by CAPES, Brazil - Finance Code 001, and by the US Department of Energy under Grants No. DE-FG02-87ER40371 and No. DE-SC0018223 (SciDAC-4/NUCLEI). TF thanks Conselho Nacional de Desenvolvimento Científico e Tecnológico (Brazil), Project INCT-FNA Proc. No. 464898/2014-5, and the Fulbright Visiting Professor Award. DCD thanks FAPESP grant No. 17/26111-4. EY thanks FAPESP grant

No. 016/25143-7. PM thanks the Visiting Researcher Fellowship from FAPESP, grant No. 2017/19371-0. This research used resources of the National Energy Research Scientific Computing Center (NERSC), which is a US Department of Energy Office of Science user facility, supported under Contracts No. DE-AC02-05CH11231.

## References

- [1] G. Eichmann, H. Sanchis-Alepuz, R. Williams, R. Alkofer and C. S. Fischer, *Prog. Part. Nucl. Phys.* **91**, 1 (2016).
- [2] P. Maris and C. D. Roberts, *Phys. Rev. C* **56**, 3369 (1997).
- [3] P. Maris and P. C. Tandy, *Phys. Rev. C* **60**, 055214 (1999).
- [4] P. Maris and P. C. Tandy, *Phys. Rev. C* **62**, 055204 (2000).
- [5] M. S. Bhagwat and P. Maris, *Phys. Rev. C* **77**, 025203 (2008).
- [6] P. Maris, C. D. Roberts and P. C. Tandy, *Phys. Lett. B* **420**, 267 (1998).
- [7] D. Atkinson and D. W. E. Blatt, *Nucl. Phys. B* **151**, 342 (1979).
- [8] P. Maris, *Nonperturbative analysis of the fermion propagator: Complex singularities and dynamical mass generation*. Ph.D. thesis, University of Groningen, Groningen, 1993.
- [9] P. Maris, *Phys. Rev. D* **50**, 4189 (1994).
- [10] N. Nakanishi, *Prog. Theor. Phys. Suppl.* **43**, 1 (1969).
- [11] V. Sauli, *JHEP* **0302**, 001 (2003).
- [12] V. Sauli, *Few-Body Syst.* **39**, 45 (2006).
- [13] V. Sauli, J. Adam, Jr. and P. Bicudo, *Phys. Rev. D* **75**, 087701 (2007).
- [14] S. Jia and M. R. Pennington, *Phys. Rev. D* **96**, 036021 (2017).
- [15] K. Kusaka and A. G. Williams, *Phys. Rev. D* **51**, 7026 (1995).
- [16] K. Kusaka, K. M. Simpson and A. G. Williams, *Phys. Rev. D* **56**, 5071 (1997).
- [17] V. A. Karmanov and J. Carbonell, *Eur. Phys. J. A* **27**, 1 (2006).
- [18] V. Sauli, *Few-Body Syst.* **49**, 223 (2010).
- [19] T. Frederico, G. Salmè and M. Viviani, *Phys. Rev. D* **85**, 036009 (2012).
- [20] T. Frederico, G. Salmè and M. Viviani, *Phys. Rev. D* **89**, 016010 (2014).
- [21] J. Carbonell and V. A. Karmanov, *Eur. Phys. J. A* **46**, 387 (2010).
- [22] W. de Paula, T. Frederico, G. Salmè and M. Viviani, *Phys. Rev. D* **94**, 071901 (2016).

- 
- [23] W. de Paula, T. Frederico, G. Salmè, M. Viviani and R. Pimentel, *Eur. Phys. J. C* **77**, 764 (2017).
  - [24] A. Castro, E. Ydrefors, W. de Paula, T. Frederico, J. H. de Alvarenga Nogueira and P. Maris, *J. Phys. Conf. Ser.* **1291**, 012006 (2019); arXiv:1901.04266 [hep-ph] (2019).
  - [25] C. Itzykson and J.-B. Zuber, *Quantum field theory*. McGraw-Hill, New York, 1985.
  - [26] P. Maris, S. Jia, D. C. Duarte, W. de Paula, E. Ydrefors and T. Frederico, *in preparation*.

# Bound States of Relativistic Nature

V. A. Karmanov<sup>a</sup>, J. Carbonell<sup>b</sup> and H. Sazdjian<sup>b</sup>

<sup>a</sup>*Lebedev Physical Institute, Moscow, Russia*

<sup>b</sup>*Institut de Physique Nucléaire, Orsay, France*

## Abstract

Bethe–Salpeter equation for massless exchange and large fine structure constant  $\alpha > \pi/4$ , in addition to Balmer series, provides another (abnormal) series of energy levels which are not given by the Schrödinger equation. So strong field can be created by a point-like charge  $Z > 107$ . The nuclei with this charge, though available, are far from being point-like that weakens the field. Therefore, the abnormal states of this origin do hardly exist.

We analyze a more realistic case of exchange by a massive particle when the large value of coupling constant is typical for the strong interaction. It turns out that this interaction still generates a series of abnormal relativistic states. The properties of these solutions are studied. Their existence in nature seems to be possible.

**Keywords:** *Bethe–Salpeter equation; massive ladder exchange; relativistic bound states*

## 1 Introduction

The Bethe–Salpeter (BS) equation [1] is a relativistic counterpart of the Schrödinger equation. In the spinless case, for a two-body system, it reads

$$\Phi(k, p) = \frac{i^2}{[(\frac{p}{2} + k)^2 - m^2 + i\epsilon][(\frac{p}{2} - k)^2 - m^2 + i\epsilon]} \int \frac{d^4 k'}{(2\pi)^4} iK(k, k', p) \Phi(k', p), \quad (1)$$

$p$  is the total four-momentum,  $k$  is the relative one. The bound state mass squared is  $M^2 = p^2 = (2m - B)^2$  and  $B$  is the (positive) binding energy. The kernel in Eq. (1) in the case of exchange by a particle with mass  $\mu$  has the form

$$iK(k, k', p) = \frac{i(-ig)^2}{(k - k')^2 - \mu^2 + i\epsilon}. \quad (2)$$

Soon after its derivation, the BS equation was studied by Wick [2] and Cutkosky [3] in the model of two spinless particles interacting by a massless scalar exchange ( $\mu = 0$ ), since known as Wick–Cutkosky model. Solving Eq. (1) in the limit of small binding

---

*Proceedings of the International Conference ‘Nuclear Theory in the Supercomputing Era — 2018’ (NTSE-2018), Daejeon, South Korea, October 29 – November 2, 2018, eds. A. M. Shirokov and A. I. Mazur. Pacific National University, Khabarovsk, Russia, 2019, p. 212.*

<http://www.ntse.khb.ru/files/uploads/2018/proceedings/Karmanov.pdf>.

energies ( $B/m \ll 1$ ), these authors reproduced the Coulomb spectrum, i. e., the Balmer series,

$$B_n = \frac{\alpha^2 m}{4n^2}, \quad (3)$$

given also by the Schrödinger equation with the potential  $V(r) = -\frac{\alpha}{r}$ , where  $\alpha = g^2/(16\pi m^2)$ . (Wick and Cutkosky [2, 3] used another definition of the coupling constant:  $\lambda = \frac{\alpha}{\pi}$ ). According to Ref. [3], when  $\alpha \rightarrow 2\pi$ , the ground state of mass  $M$  determined by Eq. (1) tends to 0. When  $\alpha > 2\pi$ , there is no physical solution for the ground state:  $M^2$  becomes negative.

To solve the BS equation, Cutkosky has represented the BS amplitude for the  $S$ -wave states in the following integral form:

$$\Phi_n(k, p) = \sum_{r=0}^{n-1} \int_{-1}^1 \frac{g_n^r(z) dz}{[m^2 - \frac{1}{4}M^2 - k^2 - p \cdot k z - i\epsilon]^{2+n}}, \quad n = 1, 2, \dots \quad (4)$$

After substituting Eq. (4) into Eq. (1) and some manipulations, one finds that the functions  $g_n^r(z)$  satisfy coupled integral equations with an exception of  $g_n^0$  which satisfies a decoupled homogeneous equation. Other functions  $g_n^r$ ,  $0 < r \leq (n-1)$ , are then determined from  $g_n^0$  through the remaining equations. Denoting henceforth  $g_n^0$  by  $g_n$ , one obtains the equation for  $g_n$ ,

$$g_n''(z) + \frac{2(n-1)z}{(1-z^2)} g_n'(z) - \frac{n(n-1)}{(1-z^2)} g_n(z) + \frac{\alpha}{\pi} \frac{1}{(1-z^2)(1-\eta^2 + \eta^2 z^2)} g_n(z) = 0, \quad (5)$$

where  $\eta = \frac{M}{2m} = 1 - \frac{B}{2m}$  and the boundary conditions are  $g_n(\pm 1) = 0$ . For a given  $n$ , this homogeneous equation has another infinite spectrum  $M_{nk}$  distinct from the ordinary relativistic generalization of the Balmer series, corresponding to bound states  $g_{nk}$  with binding energies  $B_{nk} = 2m - M_{nk}$  depending on the second integer quantum number  $k = 1, 2, 3, \dots$ . In the limit of small binding energies,  $B_{nk}$  is independent of  $n$ , namely:

$$B_{nk} \approx B_k = m \exp\left(-\frac{2\pi^{3/2}k}{\sqrt{\alpha - \pi/4}}\right), \quad (6)$$

For  $k = 0$  and arbitrary  $n$ , the levels are still given by the Balmer series (3) corresponding to the so-called normal ones. The abnormal solutions  $g_{nk}(z)$  have  $k$  nodes in  $z$ . The solutions  $g_{nk}(z)$  are symmetric in  $z \rightarrow -z$  for even  $k$  and antisymmetric for odd  $k$ . The corresponding BS amplitudes in the rest frame are symmetric or antisymmetric relative to  $k_0 \rightarrow -k_0$ . It was shown in Ref. [4] that the antisymmetric solutions do not contribute to the  $S$ -matrix and therefore they are hardly observable. Therefore we will consider the symmetric (normal and abnormal) states only.

To summarize, for the massless exchange, in addition to the Balmer series, the BS equation predicts for each  $n$  another series of states with binding energies  $B_{nk}$  given by Eq. (6) in the limit  $B/m \ll 1$ . These states exist only if  $\alpha > \frac{\pi}{4}$ . Their binding energies tend to zero when  $\alpha \rightarrow \frac{\pi}{4}$ . They are absent in the spectrum of non-relativistic Schrödinger equation, and therefore they were called "abnormal".

Wick and Cutkosky found analytical solutions of Eq. (5) in the limit  $\eta = \frac{M}{2m} \rightarrow 1$ . We solved this equation numerically for arbitrary  $\eta$ . The examples of normal and abnormal symmetric solutions  $g(z)$  are shown in Figs. 1 and 2 respectively. These solutions correspond to  $n = 1$  and differ by the  $k$  values:  $k = 0$  and  $k = 2$ .

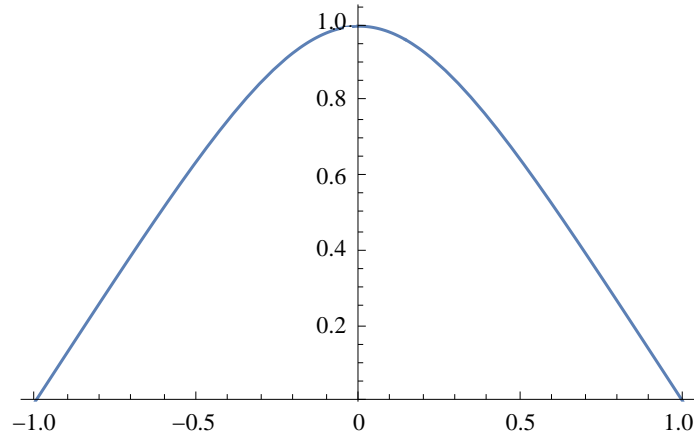


Figure 1: Normal solution  $g(z)$  of Eq. (5) ( $\mu = 0$ ) corresponding to  $n = 1$ ,  $k = 0$ ,  $B = 0.2$ ,  $\alpha = 1.786$ .

The aim of our research is to answer the question: can the abnormal states exist in the nature or not? In the case of the massless exchange considered by Wick and Cutkosky and sketched above, the answer seems to be negative. The required coupling constant  $\alpha > \frac{\pi}{4}$  is too large to be reached in practice. Indeed, since the value  $\alpha = \frac{1}{137}$  corresponds to  $Z = 1$ ,  $\alpha > \frac{\pi}{4}$  corresponds to the charge  $Z > \frac{\pi}{4} / (\frac{1}{137}) \approx 107$ . Nuclei with this and larger charges, though do not exist in nature, were created in a laboratory ( $Z = 107$  corresponds to bohrium). However, they are far from being point-like. Since the charge is distributed in a large volume, the strength of the electric field is reduced. Therefore, to create an abnormal state, one needs even larger (maybe, much larger) value of  $Z$ . This makes the problem unrealistic.

However, the value  $\alpha = \frac{\pi}{4} \approx 0.78$  is normal when dealing with strong interactions. The latters are modeled by a massive particle exchange. Therefore, in our

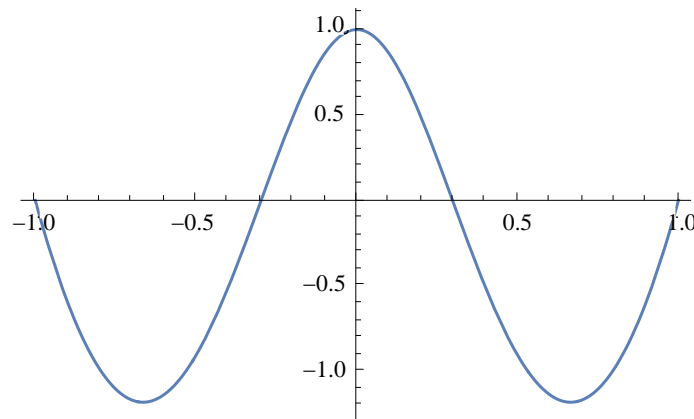


Figure 2: Abnormal symmetric solution  $g(z)$  of Eq. (5) ( $\mu = 0$ ) corresponding to  $n = 1$ ,  $k = 2$ ,  $B = 0.2$ ,  $\alpha = 17.19$ .

research, we will replace the massless exchanged particle by a massive one, and we will study whether or not the abnormal states will still survive. It turns out that the most peculiar properties of the abnormal states in the Wick–Cutkosky model (the existence of the critical coupling constant  $\alpha_c = \frac{\pi}{4}$  determining the existence of the abnormal states; the simultaneous appearance and disappearance of infinite series of levels when the coupling constant crosses the critical value) are a consequence of the zero exchanged mass. One could then expect that these properties do not exist anymore in the massive case. However, this does not forbid the existence of the abnormal states at all, though a definite answer requires some research.

## 2 Non-zero exchanged mass

For solving this problem, it is still convenient to use an integral representation for the BS amplitude similar to Eq. (4), namely:

$$\Phi(k, p) = \int_0^\infty d\gamma \int_{-1}^1 \frac{g(\gamma, z) dz}{[\gamma + m^2 - \frac{1}{4}M^2 - k^2 - p \cdot k z - i\epsilon]^3}. \quad (7)$$

This representation has been proposed by Nakanishi [5]. To simplify the notations, we omit here the indices  $n, k$ . In contrast to Eq. (4) for the massless case, the weight function  $g(\gamma, z)$  in Eq. (7) depends on an additional variable  $\gamma$  and, correspondingly, the integral in Eq. (7) is double. The massless exchange corresponds to a particular situation where the function  $g(\gamma, z)$  can be expressed, concerning its  $\gamma$  dependence, as a superposition of the delta function and  $(n - 1)$  its derivatives in  $\gamma$ :

$$g(\gamma, z) = g_n(\gamma, z) = \sum_{r=0}^{n-1} \delta^{(r)}(\gamma) g_n^r(z), \quad n = 1, 2, \dots \quad (8)$$

Substituting  $\Phi(k, p)$  in the BS equation (1) by its expression (7), one can derive an equation for  $g(\gamma, z)$ . Some properties of the solutions will be still studied analytically whereas the spectrum and corresponding solutions will be found numerically.

For the ladder BS kernel, the equation for the weight function  $g(\gamma, z)$  was firstly derived in Ref. [6], though in a little bit complicated form. For an arbitrary BS kernel, the equation for  $g(\gamma, z)$  was derived in Ref. [7], though in the form containing integrals in both sides of equation. It reads:

$$\int_0^\infty \frac{g(\gamma', z) d\gamma'}{[\gamma' + \gamma + z^2 m^2 + (1 - z^2)\kappa^2]^2} = \int_0^\infty d\gamma' \int_{-1}^1 dz' W(\gamma, z; \gamma', z') g(\gamma', z'), \quad (9)$$

where  $\kappa^2 = m^2 - \frac{1}{4}M^2$ . In the canonical form,

$$g(\gamma, z) = \int_0^\infty d\gamma' \int_{-1}^1 dz' \mathcal{V}(\gamma, z; \gamma', z') g(\gamma', z'), \quad (10)$$

for the ladder BS kernel, the equation for  $g(\gamma, z)$  was derived in Ref. [8]. In this work, the expression for the kernel  $\mathcal{V}(\gamma, z; \gamma', z')$  corresponding to the ladder BS kernel, was found.

It was noticed in Ref. [9] that the l.h.s. of Eq. (9) is the generalized Stieltjes transform which can be inverted analytically. In this way, the equation for  $g(\gamma, z)$  in the canonical form valid for arbitrary BS kernel, was derived. For the ladder BS kernels, the kernels  $\mathcal{V}(\gamma, z; \gamma', z')$  in Eq. (10) found in Ref. [9] and [8], coincide with each other. A useful research of the non-relativistic limit of the BS equation was done in Ref. [10].

We will analyze the equation in the form (10) with the kernel derived in Ref. [8] from the ladder kernel (2). This kernel reads

$$\mathcal{V}(\gamma, z; \gamma', z') = +\frac{\alpha m^2}{2\pi} \times \begin{cases} h(\gamma, -z; \gamma', -z') & \text{if } -1 \leq z' \leq z \leq 1, \\ h(\gamma, z; \gamma', z') & \text{if } -1 \leq z \leq z' \leq 1, \end{cases} \quad (11)$$

with the function

$$h(\gamma, z; \gamma', z') = \theta(\eta) P(\gamma, z, \gamma', z') + Q(\gamma', z'), \quad (12)$$

where

$$P(\gamma, z, \gamma', z') = \frac{B}{\gamma A \Delta} \frac{1+z}{(1+z')} - C(\gamma, z, \gamma', z')$$

with

$$\begin{aligned} A(\gamma', z') &= \frac{1}{4} z'^2 M^2 + \kappa^2 + \gamma', & B(\gamma, z, \gamma', z') &= \mu^2 + \gamma' - \gamma \frac{1+z'}{1+z}, \\ C(\gamma, z, \gamma', z') &= \int_{y_-}^{y_+} \chi(y) dy, & Q(\gamma', z') &= \int_0^\infty \chi(y) dy, \\ \Delta(\gamma, z, \gamma', z') &= \sqrt{B^2 - 4\mu^2 A}. \end{aligned}$$

The functions  $C$  and  $Q$  contain the function

$$\chi(y) = \frac{y^2}{[y^2 + A + y(\mu^2 + \gamma') + \mu^2]^2}$$

and the integration limits in  $C$  are given by  $y_{\pm} = \frac{-B \pm \Delta}{2A}$ . The argument  $\eta$  of the  $\theta$ -function in the first term of Eq. (12) is

$$\eta = -B - 2\mu\sqrt{A} = \gamma \frac{1+z'}{1+z} - \mu^2 - \gamma' - 2\mu\sqrt{\frac{1}{4}z'^2 M^2 + \kappa^2 + \gamma'}.$$

The results of solving numerically Eq. (10) with the parameters  $\mu = 0.15$  and  $B = 0.2$  are displayed in Fig. 3. The coupling constant  $\alpha = 2.1$  and corresponds to the “normal” state. They have been obtained in a recent work [11] by using the same spline techniques as in Ref. [7]. The Nakanishi weight function  $g$  has been computed by several authors in the past either by solving Eq. (9) or its equivalent normal form of Eq. (10). None of them put in evidence a striking behavior of this quantity manifested in Fig. 3 — it is a step-like function on variable  $\gamma$  but has a flat behavior in some domain as a function of variable  $z$ . The numerical difficulties in finding solution appear, on one hand, because of the  $g$  numerical instabilities related to the  $\epsilon$ -trick introduced in Ref. [7], and, on the other hand, because of describing a flat behavior by a Gaussian-like basis expansion employed in Refs. [8, 12–14]. This behavior has been also proved analytically in Ref. [11] and will be discussed below in Section 4.

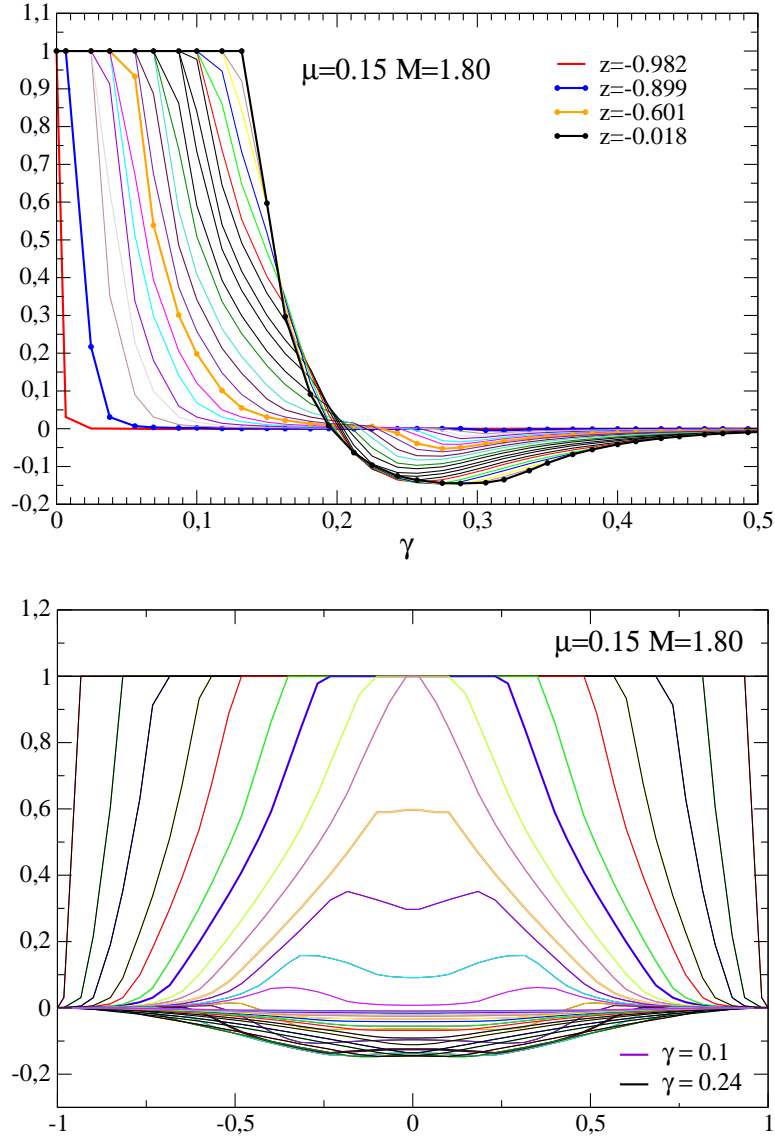


Figure 3: Nakanishi weight function  $g(\gamma, z)$  corresponding to  $m = 1$ ,  $\mu = 0.15$ ,  $B = 0.2$  and  $\alpha = 2.1$  as a function of  $\gamma$  for a fixed  $z$  (top) and as a function of  $z$  for a fixed  $\gamma$  (bottom).

### 3 Non-relativistic limit

The “relativistic world” differs from the non-relativistic one by the existence of the limiting value of speed of any object or signal, which is identified with the speed of light  $c$ . Calculating via a relativistic equation the binding energy corresponding to a normal state and taking the limit  $c \rightarrow \infty$ , we should obtain the non-relativistic

binding energy. The abnormal states, not existing in the non-relativistic limit, should disappear when  $c \rightarrow \infty$ . The relativistic equations presented above implied  $c = 1$ . To study the limit  $c \rightarrow \infty$ , we should now restore the speed of light  $c$  in these equations.

The strategy is the following. We should introduce  $c$  in the parameters which are used as an input in the equation. This, of course, automatically has an influence on the parameters which are the “output” (found from the equation), therefore we should leave their value untouched. This means that we should replace  $m$  by  $mc^2$ . As for the total mass, it is not an independent parameter (not an input), it is expressed as  $M = 2mc^2 - B$ . Therefore one *should not* make the replacement  $M \rightarrow Mc^2$ . The same is valid for  $B$  since it is also not an input, but it is found from the equation (already containing  $mc^2$ ) as an eigenvalue. Therefore one also *should not* make the replacement  $B \rightarrow Bc^2$ , one should keep instead the binding energy  $B$  as it is. Since the coupling constant in QED is  $\alpha = e^2/(\hbar c)$ , the  $c$  value should appear in the coupling explicitly. Therefore  $\alpha$  should be replaced by  $\alpha/c$ .

In the last replacement, there was no any reference to the mass of the exchange particle. Therefore it is valid not only in QED, but also in the Yukawa model with a massive particles exchange. A subtle point is the replacement of the exchanged mass  $\mu$ . The ladder exchange results in the Yukawa potential with the factor  $\sim \exp(-\mu r)$ . Restoring  $c$  in this factor, we get  $\exp\left(-\frac{\mu c^2 r}{\hbar c}\right)$ . We get a zero-range potential in the limit  $c \rightarrow \infty$ , the Yukawa potential shrinks to a delta-function. However, in the present research, we study how the energies found from a relativistic equation are transformed into the energies determined by the Schrödinger equation with a given potential  $V(r)$ , and we are not interested in the effects resulting from the variation of  $V(r)$  with  $c$ . The shrink is avoided if we replace  $\mu \rightarrow \mu c$ , not  $\mu \rightarrow \mu c^2$ .

With these replacements made in the kernel  $\mathcal{V}$ , we solve Eq. (10) numerically and, varying  $c$ , we study the behavior of two energy levels. More precisely, for a fixed binding energy  $B$ , we study the behavior of the coupling constant  $\alpha$  as a function of  $c$  in the interval  $1 \leq c \leq 10$ . We use  $m = 1$ ,  $\mu = 0.15$  and  $B = 0.1$ . For one of the states, which we associate with the “normal” solution, we found  $\alpha(c = 1) \approx 1.45$ . For another state, which we associate with the “abnormal” solution, we found  $\alpha(c = 1) \approx 10$ . The results for  $\alpha(c)$  for these two states are shown in Figs. 4 and 5. These curves have opposite behaviors (decreasing and increasing) as functions of  $c$ .

We see in Fig. 4 that in the non-relativistic limit ( $c \rightarrow \infty$ )  $\alpha$  decreases and tends to the limiting finite value  $\alpha \approx 0.9$ . This value is just the coupling constant of the Yukawa potential providing the binding energy  $B = 0.1$  in the Schrödinger equation. Therefore we associate this solution with the “normal” one which has the non-relativistic limit. The decrease of  $\alpha$  with  $c$  seen at Fig. 4 can be easily explained qualitatively. As it was noticed in many papers, the relativistic effects added to the non-relativistic dynamics, result in an effective repulsion. Therefore, when we go to the non-relativistic limit ( $c$  increases), we decrease this repulsion. Hence, we need a smaller coupling constant  $\alpha$  to keep the fixed value of the binding energy  $B = 0.1$ .

According to the curve  $\alpha(c)$  shown in Fig. 5, the value of  $\alpha$  increases with  $c$ , at least in the interval  $1 \leq c \leq 10$ . The disappearance of the abnormal states as  $c$  increases means that the corresponding energy levels are “pushed out” into the continuum spectrum. That is, they move up and cross the value  $B = 0$ . To prevent this movement and to keep these levels at a constant value, say, at  $B = 0.1$ , like in Fig. 5 at  $c = 1$ , one should increase the attraction. Hence, when  $c$  increases, we need a larger coupling constant  $\alpha$  as is observed in Fig. 5. Therefore we associate this

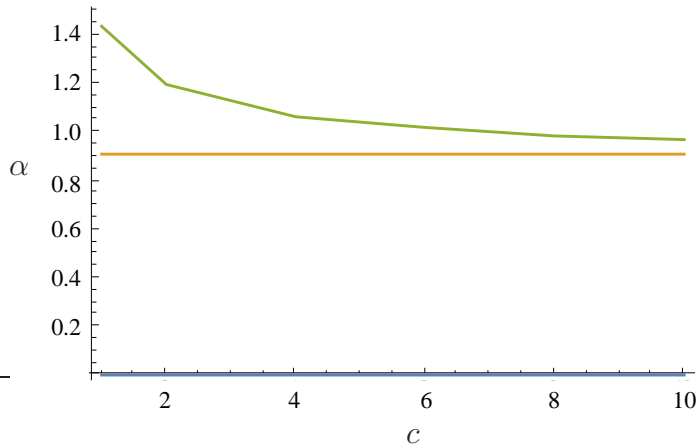


Figure 4: The coupling constant  $\alpha$  vs the speed of light  $c$  for the parameters  $m = 1$ ,  $\mu = 0.15$ ,  $B = 0.1$ . The decreasing line is found from the relativistic Eq. (10) for the “normal” solution; the horizontal line is the limiting value of this decreasing line, the coupling constant for the Yukawa potential in the Schrödinger equation.

solution with the “abnormal” one.

These results demonstrate the existence of the abnormal states in the solution of the BS equation with the massive ladder kernel (we assume that the qualitative behavior of  $\alpha$  as a function of  $c$  can be extrapolated to larger  $c$  values). At least one of them is found and the corresponding  $\alpha(c)$  function is shown in Fig. 5.

Coming back to the zero-mass exchange, we can make the replacements  $m \rightarrow mc^2$  and  $\alpha \rightarrow \alpha/c$  in the Eq. (6) describing the binding energy  $B_k$ . Then, solving this

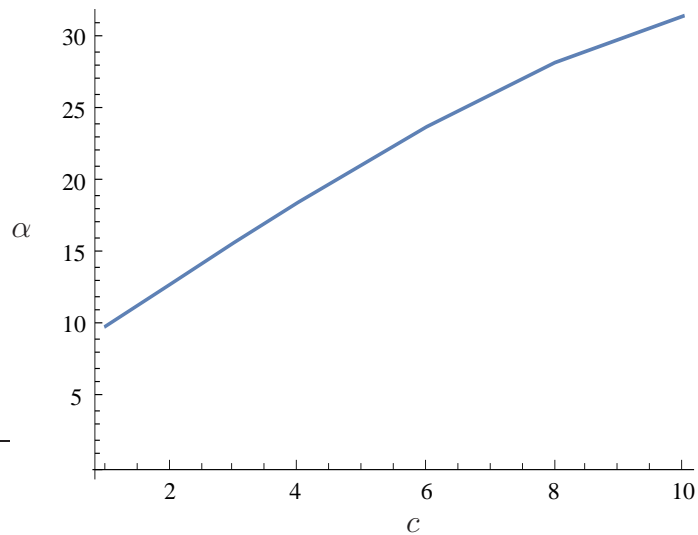


Figure 5: The coupling constant  $\alpha$  vs the speed of light  $c$  for the parameters  $m = 1$ ,  $\mu = 0.15$ ,  $B = 0.1$  for the “abnormal” solution.

equation with respect to  $\alpha$ , we find:

$$\alpha = c \left( \frac{\pi}{4} + \frac{4\pi^3 k^2}{\log^2 \frac{B_k}{mc^2}} \right). \quad (13)$$

This formula gives an analytical example of the dependence  $\alpha(c)$  which has no finite limit at  $c \rightarrow \infty$ , that serves as an undoubted property of the abnormal state.

We remind that for the massless exchange, there exists another criterion to select an abnormal state: it is the existence of nodes in the solution  $g(z)$  (see Fig. 2). Though for distinguishing an abnormal state it is sufficient to fit only one of these two criterions, it is useful to establish both. For the massive exchange, we discussed so far only one criterion for the selection of an abnormal solution: the absence of a finite limit of  $\alpha$  as  $c \rightarrow \infty$ . Below we will formulate another criterion, also based on an analysis of nodes of the solution  $g(\gamma, z)$ .

## 4 Properties of the $z$ -dependence of the solution $g(\gamma, z)$

In the case of massless exchange discussed in Section 1, a normal solution  $g(z)$  has no nodes (see Fig. 1). However, for massive exchange, this property cannot be used to distinguish a normal solution. In Fig. 6 we show the solution  $g(\gamma, x)$  (with the parameters  $m = 1$ ,  $\mu = 0.15$ ,  $B = 0.1$ ,  $\alpha = 1.4375$ ) for the fixed value  $\gamma = 0.17$  as a function of  $x = \frac{1}{2}(1 + z)$ . Instead of  $z$ , we introduced for convenience the new variable  $x$  varying in the limits  $0 \leq x \leq 1$ . This is a normal solution since the dependence  $\alpha(c)$  corresponding to this solution, is shown in Fig. 4.

In spite of the fact that this solution is normal, it has nodes as a function of  $x$  for a fixed  $\gamma$ . However, it turns out that the behavior of  $g(\gamma, x)$  is qualitatively different in different parts of the domain of its definition. There is an area where  $g(\gamma, x) = \text{const}$ .

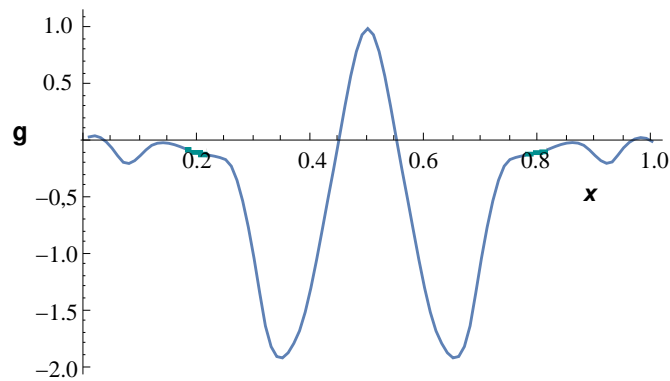


Figure 6: Normal solution  $g(\gamma = 0.17, x)$  of Eq. (10) with the kernel of Eq. (11) vs  $x = \frac{1}{2}(1 + z)$  for the parameters  $m = 1$ ,  $\mu = 0.15$ ,  $B = 0.1$ ,  $\alpha = 1.4375$  at the fixed value of  $\gamma = 0.17$ .

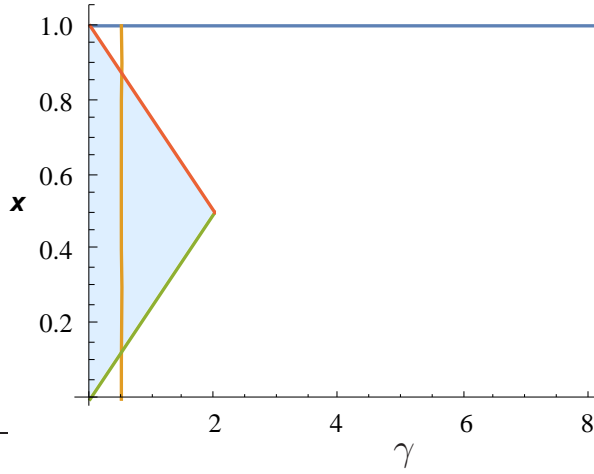


Figure 7: Domain of definition of the function  $g(\gamma, x)$ . Shaded area is the domain defined by Eq. (14) where  $g(\gamma, x) = const.$

This area is defined (up to a factor) by:

$$\gamma \leq \gamma_0(x) \sim \begin{cases} \mu x & \text{if } 0 \leq x \leq \frac{1}{2}, \\ \mu(1-x) & \text{if } \frac{1}{2} \leq x \leq 1. \end{cases} \quad (14)$$

The domain ( $0 \leq \gamma < \infty, 0 \leq x \leq 1$ ) is shown in Fig. 7, the shaded area corresponds to Eq. (14).

Let us fix the  $\gamma = 0.005$  from the area defined by Eq. (14) and consider the  $x$  dependence of  $g(\gamma = fixed, x)$ . This corresponds to the variation of  $x$  along the vertical line crossing the triangle in Fig. 7. Solving numerically Eq. (10) for the normal solution of the type shown in Fig. 6 for  $\gamma = 0.17$ , we now obtain Fig. 8. We see that in the interval  $x_1 < x < x_2$  where the vertical line in Fig. 7 is inside the shaded triangle, the function  $g(\gamma = 0.005, x)$  is indeed constant, as expected. Outside

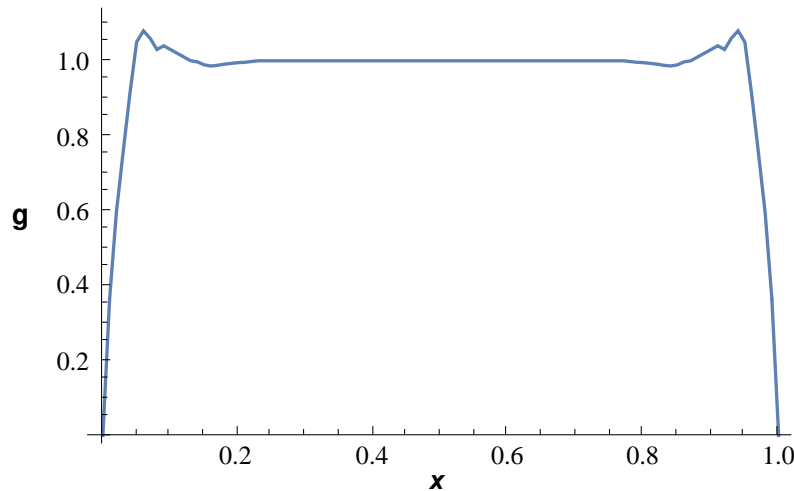


Figure 8: Normal solution  $g(\gamma = 0.005, x)$  of Eq. (10) with the kernel of Eq. (11) vs  $x$  for the same parameters as in Fig. 6.

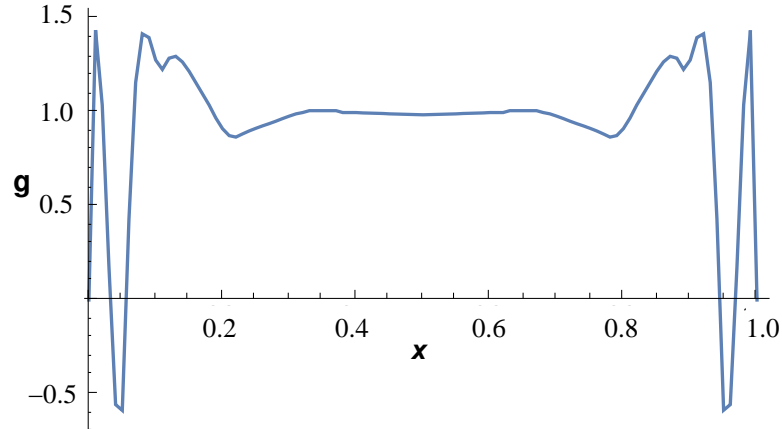


Figure 9: Abnormal symmetric solution  $g(\gamma = 0.005, x)$  of Eq. (10) with the kernel of Eq. (11) vs  $x$  for the same parameters as in Figs. 6 and 8 except  $\alpha = 11.2859$ .

this interval, when  $x$  is close to 0 or to 1,  $g(\gamma = 0.005, x)$  varies. However, it has no nodes. In this respect, the behavior of the normal solution  $g(\gamma = 0.005, x)$  is analogous to the behavior of normal  $g(z)$  for the massless exchange. The latter has nodes nowhere except for the points  $x = 0$  and 1, where the nodes are imposed by the boundary conditions.

The symmetric abnormal solution for the same parameters (though, of course, for a different binding energy) is shown in Fig. 9. It is still constant when  $x$  is inside the domain defined by Eq. (14) and has nodes outside this domain, in contrast to the normal solutions. Like for the massless exchange, this gives us another criterion (in addition to the limit  $\alpha(c \rightarrow \infty)$ ) to distinguish, in the case of the massive exchange, the abnormal solutions from the normal ones.

We emphasize that these results are based on the numerical calculations. It would be useful to derive them analytically.

## 5 Conclusion

Like the Dirac equation predicting antiparticles, the BS equation predicts bound states having a purely relativistic origin: these are the so-called “abnormal” states, not given by the Schrödinger equation.

We have found that such states, previously obtained in the Wick–Cutkosky model (scalar massless exchange) in the case of a large coupling constant, exist also for the interaction provided by massive exchange with values of the coupling constant typical for the strong interaction. It is worth conjecturing that these states could be manifested in some processes in nature. One should analyze from this point of view systems which is difficult to describe as ordinary bound states and which require exotic speculations. Maybe, some of these systems are “abnormal” ones.

For a deeper understanding of the abnormal states, it would be useful to calculate corresponding electromagnetic form factors, to compare them with the “normal” form factors and to calculate also the transition form factors of the type normal  $\leftrightarrow$  abnormal states.

A clarification of the content of the “abnormal” state vector, i. e., of the contributions to its norm of the Fock components with different numbers of particles, is still an intriguing problem. Preliminary results look as follows. For the normal state, when the binding energy tends to zero, the contribution of the two-body sector dominates in the norm of the state vector. On the contrary, for the abnormal state, when the binding energy tends to zero ( $\alpha \rightarrow \frac{\pi}{4}$ ), the contribution of the two-body sector to the norm of the state vector decreases.

## References

- [1] E. E. Salpeter and H. Bethe, Phys. Rev. **84**, 1232 (1951).
- [2] G. C. Wick, Phys. Rev. **96**, 1124 (1954).
- [3] R. E. Cutkosky, Phys. Rev. **96**, 1135 (1954).
- [4] M. Ciafalony and P. Menotti, Phys. Rev. **140**, B929 (1965).
- [5] N. Nakanishi, Phys. Rev. **130**, 1230 (1963); Prog. Theor. Phys. Suppl. **43**, 1 (1969); *Graph theory and Feynman integrals*. Gordon and Breach, New York, 1971.
- [6] K. Kusaka and A. G. Williams, Phys. Rev. D **51**, 7026 (1995); K. Kusaka, K. Simpson and A.G. Williams, *ibid.* **56**, 5071 (1997).
- [7] V. A. Karmanov and J. Carbonell, Eur. Phys. J. A **27**, 1 (2006).
- [8] T. Frederico, G. Salmè and M. Viviani, Phys. Rev. D **89**, 016010 (2014).
- [9] J. Carbonell, T. Frederico, V. A. Karmanov, Phys. Lett. B **769**, 418 (2017).
- [10] G. Wanders, Helv. Phys. Acta **30**, 417 (1957).
- [11] J. Carbonell, V. A. Karmanov and H. Sazdjian, *to be published*.
- [12] T. Frederico, G. Salmè and M. Viviani, Eur. Phys. J. C **75**, 398 (2015).
- [13] M. Viviani, T. Frederico, G. Salmè, Few-Body Syst. **56**, 369 (2015).
- [14] R. Pimentel and W. de Paula, Few-Body Syst. **57**, 491 (2016).

# Dynamical Nucleon-Pion System via Basis Light-Front Quantization

Weijie Du<sup>a</sup>, Yang Li<sup>a,b,c</sup>, Xingbo Zhao<sup>d,e</sup> and James P. Vary<sup>a</sup>

<sup>a</sup>*Department of Physics and Astronomy, Iowa State University, Ames, Iowa 50010, USA*

<sup>b</sup>*Hebei Key Laboratory of Compact Fusion, Langfang 065001, China*

<sup>c</sup>*ENN Science and Technology Development Co., Ltd., Langfang 065001, China*

<sup>d</sup>*Institute of Modern Physics, Chinese Academy of Sciences, Lanzhou 730000, China*

<sup>e</sup>*University of Chinese Academy of Sciences, Beijing 100049, China*

## Abstract

We present the first application of the Basis Light-Front Quantization method to study a simple chiral model of the nucleon-pion system via an *ab initio*, non-perturbative, Hamiltonian approach. As a test problem, we consider the physical proton as a relativistic bound state of the nucleon-pion system. Based on the chiral model of the nucleon-pion system, we construct the mass-squared matrix of the system within our light-front basis representation. We obtain the proton's mass and the corresponding light-front wave function by solving the eigenvalue problem of the mass-squared matrix. With the resulting boost-invariant light-front wave function, we also compute the proton's parton distribution function.

**Keywords:** *Ab initio; non-perturbative; basis light-front quantization; chiral nucleon-pion model*

## 1 Introduction

Developing a relativistic methodology that is broadly applicable to nuclear physics is important. Progress in this direction will be useful for studying high-momentum experiments of nuclear targets using exclusive, nearly exclusive or inclusive processes [1–3]. One of the promising methods for such investigations is the Basis Light-Front Quantization (BLFQ) method [4].

BLFQ is a non-perturbative, *ab initio* method, which treats relativistic quantum field theory via the Hamiltonian approach within the light-front (LF) formalism. BLFQ has been shown to be a promising tool in a range of applications, such as the electron anomalous magnetic moment [5, 6], the positronium spectrum [7], and the heavy quarkonium structure and radiative transitions [8–12]. More recently, BLFQ has been applied successfully to the properties of the light mesons [13], which are then extended to higher scales by QCD evolution [14]. This Hamiltonian approach has also been extended to develop a non-perturbative scattering framework through time-dependent BLFQ (tBLFQ) [15–17].

---

*Proceedings of the International Conference ‘Nuclear Theory in the Supercomputing Era — 2018’ (NTSE-2018), Daejeon, South Korea, October 29 – November 2, 2018, eds. A. M. Shirokov and A. I. Mazur. Pacific National University, Khabarovsk, Russia, 2019, p. 224.*

<http://www.ntse.khb.ru/files/uploads/2018/proceedings/Zhao.pdf>.

The LF quantization procedure for treating a chiral nucleon-pion ( $N\pi$ ) model was first proposed by Miller [18, 19] in studying the  $N\pi$  scattering and the nucleon-nucleon scattering via the perturbative approach. In this work, we present the first non-perturbative, *ab initio* treatment of the same chiral model. As a test problem, we consider the physical proton as the relativistic bound state of the  $N\pi$  system. Using the BLFQ method, we compute the mass-squared matrix element of the  $N\pi$  system within the LF basis representation. We then solve the eigenvalue problem of the resulting mass-squared matrix and obtain the proton's mass and LF wave function (LFWF). The proton's LFWF is boost-invariant and can be directly applied to compute the observables such as the parton distribution function (PDF).

The outline of this paper is the following. We begin with the theory part in Section 2, which introduces the elements of BLFQ, such as the derivation of the LF Hamiltonian density, our choice of the basis construction and truncation schemes, the derivation of the mass-squared matrix element in the basis representation, and the formalism of the observables in this work. We present the results of the proton's mass, LFWF and PDF in Section 3. We conclude in Section 4, where we also discuss our future plans.

## 2 BLFQ approach to a chiral model

### 2.1 Hamiltonian dynamics

The dynamical  $N\pi$  system can be evaluated from the eigenvalue equation

$$P^\mu P_\mu |\Psi\rangle = M^2 |\Psi\rangle, \quad (1)$$

where  $P^\mu$  is the energy-momentum four-vector operator. In the LF coordinates, the mass-squared operator,

$$H_{LC} \equiv P^2 = P^\mu P_\mu = P^+ P^- - (P^\perp)^2, \quad (2)$$

is analogous to the Hamiltonian in non-relativistic quantum mechanics. The details of the LF convention and notation in this work can be found in Refs. [10, 15, 20]. Since  $P^+$  and  $(P^\perp)^2$  are kinematical, the  $P^-$ ,

$$P^- = \frac{(P^\perp)^2 + M^2}{P^+}, \quad (3)$$

is also referred to as LF Hamiltonian that generates the LF time-evolution (dynamics). In principle,  $P^-$  can be obtained from a Lagrangian with a Legendre transformation.

$H_{LC}$  can be numerically evaluated when expressed as a matrix eigenvalue problem in a complete set of basis functions as in BLFQ. In principle, the set of basis functions has an infinite dimension. In practice, one limits the basis size by introducing a truncation scheme(s). The resulting finite-dimensional eigenvalue problem can be evaluated numerically as a function of cutoff(s) in the truncation scheme(s). By extrapolation to the continuum limit, the physical observables can be obtained.

### 2.2 LF Hamiltonian density by Legendre transformation

Treating the chiral Lagrangians via the LF formalism (see, e. g., Refs. [21–24] and references therein) would usually result in the difficulty in solving the constraint

equation of the nucleon field. In order to solve this difficulty, Miller [18, 19] suggested a chiral transformation of the field variables to obtain the chiral Lagrangian of the Gürsey-type linear representation [25]. In this work, we follow Refs. [18, 19] and adopt a chiral model of the  $N\pi$  system. The Lagrangian reads

$$\mathcal{L} = \frac{1}{4}f^2\text{Tr}\left(\partial_\mu U \partial^\mu U^\dagger\right) + \frac{1}{4}M_\pi^2 f^2\text{Tr}\left(U + U^\dagger - 2\right) + \bar{\chi}\left\{\gamma_\mu i\partial^\mu - M_N - M_N(U - 1)\right\}\chi, \quad (4)$$

which is a linear realization of the chiral symmetry.  $f$  is chosen to be the pion decay constant (set as 93 MeV in this work).  $M_N$  and  $M_\pi$  are the nucleon mass and pion mass, respectively.  $\chi$  denotes the bi-spinor field of the nucleon.  $U$  is the unitary matrix for the chiral transformation, in which the pion field is introduced. If one works up to the order of  $1/f^2$ ,  $U$  takes the form [18, 19]

$$U = 1 + i\gamma_5 \frac{\vec{\tau} \cdot \vec{\pi}}{f} - \frac{1}{2f^2}\pi^2 + \mathcal{O}\left(\frac{1}{f^3}\right), \quad (5)$$

where  $\vec{\tau}$  denotes the Pauli matrices  $\tau_a$  ( $a = 1, 2, 3$ ), while  $\vec{\pi}$  represents the scalar pion fields  $\pi_a$  ( $a = 1, 2, 3$ ).

The corresponding constraint equation of the nucleon field is

$$\chi_- = \frac{1}{p^+}\gamma^0\left[\gamma^\perp \cdot p^\perp + M_N U\right]\chi_+, \quad (6)$$

where the kinematic (dynamical) nucleon field component is  $\chi_-$  ( $\chi_+$ ).

By Legendre transformation, we obtain the LF Hamiltonian density from Eq. (4). In this work, we keep only the terms that correspond to the processes of single-pion emission/absorption (up to the order of  $1/f$ ). The resulting LF Hamiltonian density is

$$\begin{aligned} \mathcal{P}^- = & \frac{1}{2}\partial^\perp \pi_a \cdot \partial^\perp \pi_a + \frac{1}{2}M_\pi^2 \pi_a \pi_a + \chi_+^\dagger \frac{(p^\perp)^2 + M_N^2}{p^+} \chi_+ \\ & + \chi_+^\dagger \left[ -\gamma^\perp \cdot i\partial^\perp + M_N \right] \frac{1}{p^+} M_N \left[ i\gamma_5 \frac{\vec{\tau} \cdot \vec{\pi}}{f} \right] \chi_+ \\ & + \chi_+^\dagger M_N \left[ -i\gamma_5 \frac{\vec{\tau} \cdot \vec{\pi}}{f} \right] \frac{1}{p^+} \left[ \gamma^\perp \cdot i\partial^\perp + M_N \right] \chi_+ + \mathcal{O}(1/f^2). \quad (7) \end{aligned}$$

Higher-order contributions to  $\mathcal{P}^-$  are expected to be corrections to the current calculation.

## 2.3 Basis construction and truncation schemes

### 2.3.1 Symmetries

The methodology of constructing the basis for carrying out the matrix eigenvalue solution of the LF mass-squared operator  $H_{LC}$  within a basis representation, BLFQ, is discussed in Refs. [4, 7, 15]. In constructing the basis, we need to pay a specific attention to the symmetries of the LF Hamiltonian  $P^-$ . These symmetries are: (1) the translational symmetry in the longitudinal direction, which results in the conservation of the total longitudinal momentum  $P^+$ ; (2) the rotational symmetry in the

transverse direction, which means that the longitudinal projection of the total angular momentum is conserved; (3) the conservation of the net fermion number; and (4) the transverse boost invariance. In this work, we also assume rotational symmetry in isospin space, where the longitudinal projection of the isospin of the constituent system is conserved. We construct the LF basis set according to these symmetries.

### 2.3.2 Single particle basis

We start with constructing the single-particle (s.p.) basis. In the longitudinal direction, we employ the discretized plane wave basis  $\{|p^+\rangle\}$ . In particular, we constrain a particle in a longitudinal box of length  $x_+ = L$  and apply the periodic (anti-periodic) boundary condition to boson (fermion). The longitudinal momentum is discretized as

$$p^+ = \frac{2\pi}{L}j, \quad (8)$$

where  $j = 1, 2, 3, \dots$  for bosons and  $j = \frac{1}{2}, \frac{3}{2}, \frac{5}{2}, \dots$  for fermions. Note that we exclude the “zero modes” ( $j = 0$ ) for bosons (pions in this work).

It is useful to define the longitudinal momentum fraction  $x$  in terms of the total longitudinal momentum  $P^+$  as

$$x \equiv \frac{p^+}{P^+} = \frac{j}{K}, \quad (9)$$

where the dimensionless parameter  $K$  is related to  $P^+$  via the relation  $P^+ = \frac{2\pi}{L}K$ .

In the transverse direction, we employ the two dimensional harmonic oscillator (2DHO) basis. This choice of basis is useful to insure the transverse boost invariance of the LF kinematics [4, 26]. The generating operator for the 2DHO basis can be expressed as [7]

$$P_+^\Omega = \frac{(p^\perp)^2}{2p^+} + \frac{1}{2}\Omega^2 p^+(r^\perp)^2 = \frac{1}{2}\Omega \left[ \frac{(p^\perp)^2}{xP^+\Omega} + xP^+\Omega(r^\perp)^2 \right], \quad (10)$$

where the oscillator energy  $\Omega$  is related to the energy scale of the 2DHO basis set as

$$b = \sqrt{P^+\Omega}. \quad (11)$$

In the following, we refer to  $b$  as the basis strength.

For the convenience in evaluating integrals involving 2DHO basis, we further introduce the momentum fraction weighted variables [27] as

$$q^\perp \equiv \frac{p^\perp}{\sqrt{x}}, \quad s^\perp \equiv \sqrt{x}r^\perp, \quad (12)$$

where  $[s_i^\perp, q_j^\perp] = i\delta_{ij}$  ( $i, j = 1, 2$ ). The generating operator of the 2DHO basis in terms of the conjugate variables ( $s^\perp, q^\perp$ ) can be rewritten as

$$P_+^\Omega = \frac{1}{2}\Omega \left[ \left( \frac{q^\perp}{\sqrt{P^+\Omega}} \right)^2 + \left( \sqrt{P^+\Omega}s^\perp \right)^2 \right]. \quad (13)$$

In the momentum representation, the 2DHO wave function is

$$\langle q^\perp | nm \rangle = \Psi_n^m(q^\perp) = \frac{1}{b} \sqrt{\frac{4\pi n!}{(n+|m|)!}} \rho^{|m|} e^{-\frac{1}{2}\rho^2} L_n^{|m|}(\rho^2) e^{im\phi}, \quad (14)$$

where the transverse momentum in the complex representation is

$$q^\perp = b\rho e^{i\phi}, \quad (q^\perp)^* = b\rho e^{-i\phi} \quad (15)$$

with  $\phi = \arg q^\perp$ ,  $|q^\perp| = b\rho$ .  $n$ ,  $m$  are the quantum numbers for the radial part and angular part of the wave function, respectively. They are related to the eigenenergy of the corresponding 2DHO wave function

$$E_{nm} = (2n + |m| + 1)\Omega. \quad (16)$$

In addition to the momentum space, we also have the the spin and isospin degrees of freedom for the  $N\pi$  model. The s.p. basis can thus be classified according to the following set of quantum numbers

$$|\alpha\rangle = |x, n, m, s, t\rangle, \quad (17)$$

where  $s$  denotes the helicity and  $t$  denotes the longitudinal projection of the isospin of the particle. It is understood that the nucleons are of spin  $\frac{1}{2}$  and isospin  $\frac{1}{2}$ , while pions are of spin 0 and isospin 1.

### 2.3.3 Multi-particle basis

The multi-particle basis is constructed as a direct product of the s.p. bases functions ( $\otimes|\alpha\rangle$ ). According to the symmetries of  $P^-$  for the  $N\pi$  system, we require the quantum numbers for all the constituent particles (labeled by  $i$ ) in the retained multi-particle basis states to satisfy the following relations:

$$\sum_i p_i^+ = P^+, \quad \sum_i m_i + \sum_i s_i = M_J, \quad \sum_i t_i = T_z, \quad \sum_i n^i = N_f. \quad (18)$$

The first identity requires all the basis states to have the same total longitudinal momentum. It is equivalent to

$$\sum_i j_i = K \quad \text{or} \quad \sum_i x_i = 1 \quad (19)$$

according to Eqs. (8) and (9) for the fixed box-length  $L$  and the total longitudinal momentum  $P^+$ . The second identity in Eq. (18) states the conservation of the longitudinal projection of the total angular momentum  $M_J$ , which is produced by the helicity  $s_i$  and the longitudinal projection of the orbital angular momentum  $m_i$  of each constituent particle. (Note, however, the total angular momentum  $J$  is not a good quantum number in the LF basis states.) The third identity in Eq. (18) states that the longitudinal projection of the total isospin  $T_z$  or, equivalently, total charge for the system is conserved. The last identity in Eq. (18) refers to the conservation of the net fermion number  $N_f$ , with  $n^i = 1$  for a nucleon and  $n^i = 0$  for each pion.

### 2.3.4 Truncation scheme

We apply three truncations in this work. First, the number of Fock sectors for the  $N\pi$  system is truncated at the nucleon plus one-pion sector

$$|N_{\text{phys}}\rangle = a|N\rangle + b|N\pi\rangle, \quad (20)$$

with the amplitudes being  $a = \langle N | N_{\text{phys}} \rangle$  and  $b = \langle N\pi | N_{\text{phys}} \rangle$ . It is also possible to include higher Fock sectors, e. g.,  $|N\pi\pi\rangle$ . However, we will postpone this to future work. According to the Fock sector truncation Eq. (20), we have the net fermion number  $N_f = 1$  for all the basis states.

Second, we cut off the total longitudinal momentum for the many-body basis state

$$K = K_{\text{max}}, \quad (21)$$

which makes the number of the longitudinal modes finite [28]. The longitudinal continuum limit can be approached at the limit of  $K_{\text{max}} \rightarrow \infty$  for a given box length  $L$ .

Third, we truncate the number of the modes in the transverse direction for the many-body basis states by restricting the number of maximal excitation quanta,  $N_{\text{max}}$ , as

$$\sum_i (2n_i + |m_i| + 1) \leq N_{\text{max}}, \quad (22)$$

where  $i$  denotes the constituent particles. By taking  $N_{\text{max}} \rightarrow \infty$ , the continuum limit in the transverse direction is realized.

### 2.3.5 UV and IR cutoffs

There are intrinsic ultraviolet (UV) and infrared (IR) cutoffs imposed by the truncation in the transverse direction. For the 2DHO basis, the UV cutoff in momentum space is around  $p_{\text{max}}^\perp \propto b\sqrt{N_{\text{max}}}$ , while the IR cutoff is around  $p_{\text{min}}^\perp \propto b/\sqrt{N_{\text{max}}}$ .

### 2.3.6 Factorization

The application of the 2DHO s.p. basis in the transverse direction with  $N_{\text{max}}$  truncation admits an exact factorization of the LFWF into the ‘‘intrinsic’’ and the ‘‘center of mass’’ (CM) components [4, 29, 30]. Taking advantage of this factorization, the spurious CM excitation due to the adoption of the 2DHO s.p. basis can be eliminated by the use of a Lagrange multiplier term as explained below. The analogous factorization scheme has been adopted in the studies of nuclear structures (c. f., Ref. [29, 30]), where the three dimensional harmonic oscillator basis is adopted.

## 2.4 Mode expansions

The pion field can be expressed in terms of the creation and annihilation operators

$$\pi_a(x) = \sum_{k^+} \sum_{\lambda=-1}^{\lambda=1} \frac{1}{2\pi\sqrt{2Lk^+}} \int \frac{d^2k^\perp}{(2\pi)^2} [a(k, \lambda) \varepsilon_a(\lambda) e^{-ikx} + a^\dagger(k, \lambda) \varepsilon_a^*(\lambda) e^{ikx}], \quad (23)$$

where we introduce the following polarization vectors to track the isospin degree of freedom of the scalar pion field  $\pi_a$  ( $a = 1, 2, 3$ ):

$$\varepsilon(+1) = \frac{1}{\sqrt{2}} \begin{pmatrix} 1 \\ i \\ 0 \end{pmatrix}, \quad \varepsilon(0) = \begin{pmatrix} 0 \\ 0 \\ 1 \end{pmatrix}, \quad \varepsilon(-1) = \frac{1}{\sqrt{2}} \begin{pmatrix} 1 \\ -i \\ 0 \end{pmatrix}, \quad (24)$$

with  $\varepsilon^\dagger(\lambda_i)\varepsilon(\lambda_j) = \delta_{\lambda_i,\lambda_j}$  and  $\varepsilon(-\lambda) = \varepsilon^*(\lambda)$ . The subscript ‘‘a’’ indicates the component of the polarization vector  $\varepsilon(\lambda)$ ,  $\lambda$  denotes the longitudinal projection of the isospin of the physical pions, i. e.,  $\pi^\pm$  and  $\pi^0$ .

Similar to the pion field, the nucleon field can be represented with the creation and annihilation operators,

$$\chi_+(x) = \sum_{p^+} \sum_{s,t} \frac{1}{2\pi\sqrt{2L}} \zeta(s) T(t) \int \frac{d^2p^\perp}{(2\pi)^2} \left[ b(p, s, t) e^{-ipx} + d^\dagger(p, -s, -t) e^{ipx} \right], \quad (25)$$

where

$$\zeta\left(+\frac{1}{2}\right) = (1, 0, 0, 0)^T, \quad \zeta\left(-\frac{1}{2}\right) = (0, 1, 0, 0)^T, \quad (26)$$

$$T\left(+\frac{1}{2}\right) = (1, 0)^T, \quad T\left(-\frac{1}{2}\right) = (0, 1)^T. \quad (27)$$

With the discretized longitudinal momentum [Eq. (9)], the commutation and anticommutation relations are

$$[a(k, \lambda), a^\dagger(k', \lambda')] = (2\pi)^2 \delta^{(2)}(k_\perp - k'_\perp) \delta_{\lambda,\lambda'} \delta_{x,x'}, \quad (28)$$

$$\{b(p, s, t), b^\dagger(p', s', t')\} = (2\pi)^2 \delta^{(2)}(p_\perp - p'_\perp) \delta_{s,s'} \delta_{t,t'} \delta_{x,x'}, \quad (29)$$

$$\{d(p, s, t), d^\dagger(p', s', t')\} = (2\pi)^2 \delta^{(2)}(p_\perp - p'_\perp) \delta_{s,s'} \delta_{t,t'} \delta_{x,x'}. \quad (30)$$

Note with our Fock space expansion [Eq. (20)], the independent field for the anti-nucleon is not included. The canonical anti/commutation relations of the field operators are

$$[\pi_a(x), \pi_b(y)]_{x^+=y^+} = -\frac{i}{4} \varepsilon(x^- - y^-) \delta^{(2)}(x^\perp - y^\perp) \delta_{ab}, \quad (31)$$

$$\{\chi_+(x), \chi_+^\dagger(y)\}_{x^+=y^+} = \frac{1}{2} \gamma^0 \gamma^+ \delta(x^- - y^-) \delta^{(2)}(x^\perp - y^\perp). \quad (32)$$

$\varepsilon(x) = \theta(x) - \theta(-x)$  is the antisymmetric step function, where the step function is

$$\theta(x) = 0 \text{ for } x \leq 0; \quad \theta(x) = 1 \text{ for } x > 0. \quad (33)$$

The relations  $\frac{\partial \varepsilon(x)}{\partial x} = 2\delta(x)$  and  $|x| = x\varepsilon(x)$  hold. For the representation of the gamma matrices in this work, we follow the convention of Refs. [10, 15, 20].

The creation and annihilation operators in the 2DHO basis with the momentum fraction weighted variables are

$$a(x, k^\perp, \lambda) = \frac{1}{\sqrt{x}} \sum_{n,m} \Psi_n^m\left(\frac{k^\perp}{\sqrt{x}}\right) \alpha(x, n, m, \lambda), \quad (34)$$

$$b(x, p^\perp, s, t) = \frac{1}{\sqrt{x}} \sum_{n,m} \Psi_n^m\left(\frac{q^\perp}{\sqrt{x}}\right) \beta(x, n, m, s, t), \quad (35)$$

with the anti/commutation relations being

$$[\alpha(x, n, m, \lambda), \alpha^\dagger(x', n', m', \lambda)] = \delta_{x,x'} \delta_{n,n'} \delta_{m,m'} \delta_{\lambda,\lambda'}, \quad (36)$$

$$\{\beta(x, n, m, s, t), \beta^\dagger(x', n', m', s', t')\} = \delta_{x,x'} \delta_{n,n'} \delta_{m,m'} \delta_{s,s'} \delta_{t,t'}. \quad (37)$$

## 2.5 Mass-squared operator

The adoption of the 2DHO s.p. basis in the transverse direction results in the inclusion of the spurious CM excitation within the mass spectrum. In order to eliminate the CM excitation in the BLFQ approach, we introduce a Lipkin–Lawson Lagrange multiplier term [31,32] to the mass-squared operator  $H_{LC}$  [Eq. (2)]. The modified mass-squared operator is

$$H = H_{LC} + \Lambda(H_{CM} - 2b^2I), \quad (38)$$

where  $\Lambda > 0$  is the Lagrangian multiplier. The intrinsic motion in the solutions is not influenced by this Lawson term ( $H_{CM} - 2b^2I$ ) due to the factorization of the LFWF in the 2DHO basis with  $N_{\max}$  truncation. Since the mass spectrum of the intrinsic motion is only determined by the intrinsic part of the LFWF, it is independent of  $\Lambda$ . The CM motion is governed by

$$H_{CM} = (P^\perp)^2 + b^4(R^\perp)^2, \quad (39)$$

where the CM momentum and coordinate in the transverse direction are respectively

$$P^\perp = \sum_i p_i^\perp, \quad R^\perp = \sum_i x_i r_i^\perp. \quad (40)$$

In terms of momentum fraction weighted variables [Eq. (12)], these CM variables are

$$P^\perp = \sum_i \sqrt{x_i} q_i^\perp, \quad R^\perp = \sum_i \sqrt{x_i} s_i^\perp. \quad (41)$$

$H_{CM}$  satisfies the eigenequation

$$H_{CM}|nm\rangle = (2n + |m| + 1)2b^2|nm\rangle, \quad (42)$$

where  $|nm\rangle$  is the eigenvector that corresponds to the eigenvalue  $\mathcal{E}_{nm} = (2n + |m| + 1)2b^2$ . Based on Eq. (42), it is easy to see that the states with CM excitation (i. e., states with  $n \neq 0$  and  $m \neq 0$ ) are lifted in the spectrum; only the states with the lowest CM mode (i. e., states with  $n = m = 0$ ) remain unshifted [27]. In general, the spectrum of  $H$  is a set of equally spaced approximate copies<sup>1</sup> (named as subspectra), with the spacing characterized by  $2\Lambda b^2$  for every additional excitation quanta in the CM degree of freedom. In practice, we choose  $\Lambda$  to be sufficiently large such that the subspectra with different CM modes are well separated.

Making use of the LF Hamiltonian density  $\mathcal{P}^-$  [Eq. (7)] and the mode expansions for pion and nucleon fields [Eqs. (23) and (25)], we calculate the LF Hamiltonian  $P^-$  and hence the mass-squared operator [Eq. (2)] as

$$H_{LC} = P^+ \underbrace{(P_{KE_N}^- + P_{KE_\pi}^- + P_{\text{int}}^-)}_{P^-} - (P^\perp)^2, \quad (43)$$

where  $P_{KE_N}^-$  and  $P_{KE_\pi}^-$  are the contributions from a free nucleon and a free pion, respectively.  $P_{\text{int}}^-$  is the interaction term that describes the contributions from the one-pion absorption and emission processes.

---

<sup>1</sup>These copies are not the exact copies since the addition of available quanta to the CM motion means the loss of available quanta in the relative motion.

## 2.6 Observables

In terms of the LF basis set  $\{|\xi\rangle\} \equiv \{|x_N, n_N, m_N, s_N, t_N; x_\pi, n_\pi, m_\pi, s_\pi=0, t_\pi \equiv \lambda\rangle\}$ , the matrix of the modified mass-squared operator for the  $N\pi$  system (Eq. (38)) can be constructed. By solving the eigenequation (via numerical matrix diagonalization)

$$H|\Psi_i\rangle = M_i^2|\Psi_i\rangle, \quad (44)$$

we obtain the eigenmass  $M_i$  and the corresponding eigenvector

$$|\Psi_i\rangle \equiv \sum_{\xi} C_i(\xi) |\xi\rangle, \quad (45)$$

with  $C_i(\xi) = \langle \xi | \Psi_i \rangle$  being the LF amplitude corresponding to the basis state  $|\xi\rangle$ . The summation is taken over the LF basis set  $\{|\xi\rangle\}$ . The LFWF is made up by the LF amplitudes  $\{\langle \xi | \Psi_i \rangle\}$ .

We can apply the LFWF to compute observables for the hadronic structure, such as the PDF, the elastic electric and magnetic form factors, and the spin decomposition. As an illustration, we calculate the PDF in this work. The investigation of other observables will be presented in the future work.

### 2.6.1 PDF

The probability to find a constituent nucleon with the longitudinal momentum fraction  $x_N$  in the current  $N\pi$  model is

$$f(x_N) = \sum' C^*(\xi) C(\xi), \quad (46)$$

where it is understood that  $x_\pi = 1 - x_N$  due to the conservation of the longitudinal momentum. The primed sum in Eq. (46) denotes that the sum is over all quantum numbers except  $x_N$ .

## 3 Results and discussions

In this work, we adopt the Fock-sector-dependent renormalization (FSDR) [33–36] scheme. We numerically diagonalize the matrix of the modified mass-squared operator  $H$  [Eq. (38)], in which process the bare nucleon mass is tuned in the matrix elements within the single nucleon sector. This process is iterative and continues until the square-root of the eigenvalue of the ground state (identified as the physical proton) matches the mass of the physical proton (taken as 938 MeV in this work).

The mass counterterm is introduced only to the single-nucleon sector. In the FSDR scheme, we expect the mass counterterm to compensate for the mass correction due to the radiative processes: the quantum fluctuation from the single-nucleon sector to the  $N\pi$  sector and back again. On the other hand, the nucleon mass in the  $N\pi$  sector remains as the physical value. We fix the pion mass at 137 MeV in the FSDR procedure.

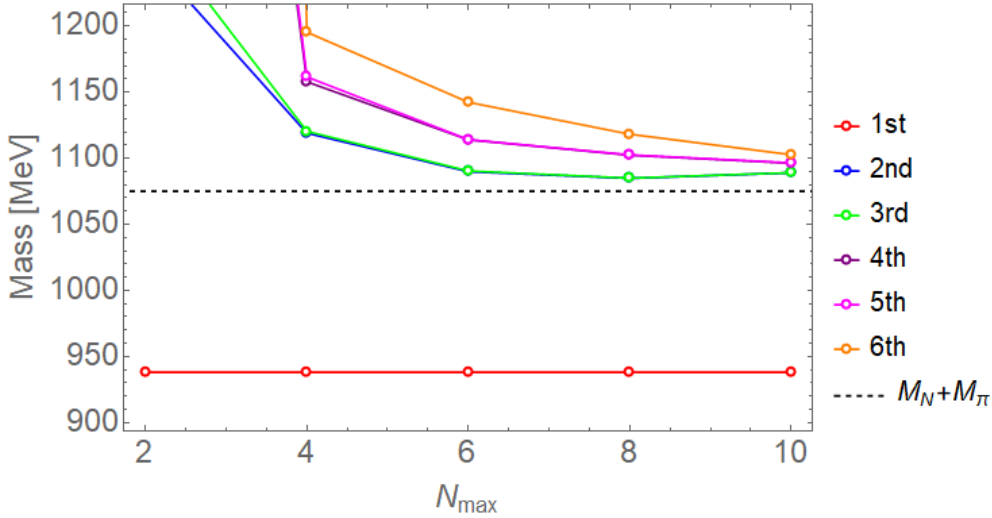


Figure 1: Model space dependence of the spectrum of the  $N\pi$  system computed via the BLFQ approach. The masses corresponding to the lowest 6 eigenstates are plotted as functions of  $N_{\max}$  (set to be  $K_{\max} - \frac{1}{2}$ ). The basis strength is fixed as  $b = 250$  MeV. The dashed line (at 1075 MeV) shows the threshold of the continuum of the  $N\pi$  system. The ground (bound) state is identified as the physical proton.

### 3.1 Mass spectrum of the $N\pi$ system

We first study the dependence of the mass spectrum of the  $N\pi$  system on the model space, which is determined by the truncation parameters,  $N_{\max}$  and  $K_{\max}$ , and the basis strength,  $b$ . For convenience, we set  $K_{\max}$  to be  $N_{\max} + 1/2$  throughout this work.

In Fig. 1, we show the lowest 6 states in the mass spectrum of the  $N\pi$  system as functions of  $N_{\max}$ , where we choose  $b = 250$  MeV as an example. We identify the ground (and also bound) state as the physical proton, of which the eigenvalue has been renormalized to 938 MeV by the FSDR procedure. The corresponding LFWF is boost invariant; it encodes all the information of the intrinsic structure of the proton. The other states appear to be the scattering states and their eigenvalues lie above the threshold of the continuum, which is the sum of the physical pion and proton masses adopted in this work (i. e., 1075 MeV).

We find all the eigenenergies of these 6 states seem to converge as  $N_{\max}$  increases. The proof of the convergence is complicated and demanding in computing power; we will save the proof for the future work. As  $N_{\max}$  increases, a better representation of the scattering states of the  $N\pi$  system is anticipated. This can be inferred from the increasing level density of the scattering states as  $N_{\max}$  increases.

### 3.2 Proton's LFWF

To compute the proton's LFWF, we need to fix the basis strength  $b$  besides fixing the bare nucleon mass via the FSDR procedure for each choice of  $N_{\max}$  ( $K_{\max} = N_{\max} + 1/2$  as a reminder). This is achieved by varying  $b$  to fit the r.m.s. charge radius of a

Table 1: Model space parameters employed to obtain the proton’s LFWFs. Note, we set  $N_{\max} = K_{\max} - \frac{1}{2}$ .

$N_{\max}$	6	8	10
$b$ [MeV]	176.95	245.54	279.55

proton  $\sqrt{\langle r_{p,E}^2 \rangle}$ , which is 0.844 fm (see, e. g., Ref. [37]). Overall, we fit for each  $N_{\max}$  both the mass and the r.m.s. charge radius to respective physical values in order to determine the mass counterterm and  $b$  in computing the proton’s LFWF. In Table 1, we list the resulting model space parameters ( $N_{\max}$  and  $b$ ) to obtain the proton’s LFWFs in this work.

### 3.3 Proton’s PDF

We apply the proton’s LFWF to compute its PDF, which encodes the distribution of the longitudinal momentum carried by its constituents. In this work, such PDF also represents the probability that the proton fluctuates into the constituent nucleon (of the longitudinal momentum fraction  $x_N$ ) and pion (of the longitudinal momentum fraction  $x_\pi$ ).

In Fig. 2, the proton’s PDF,  $f(x_N)$ , is shown as a function of  $x_N$  and the model space (with parameter settings shown in Table. 1). Note, we rescale the the  $x$ -axis as  $x_\pi = 1 - x_N$  in the plot. We do not show the results for  $f(x_N = 1)$  in Fig. 2, which represents the probability to find a bare nucleon in the physical proton. For the cases with  $N_{\max} = 6, 8$  and  $10$ , such probabilities are 0.83, 0.69, and 0.62, respectively.

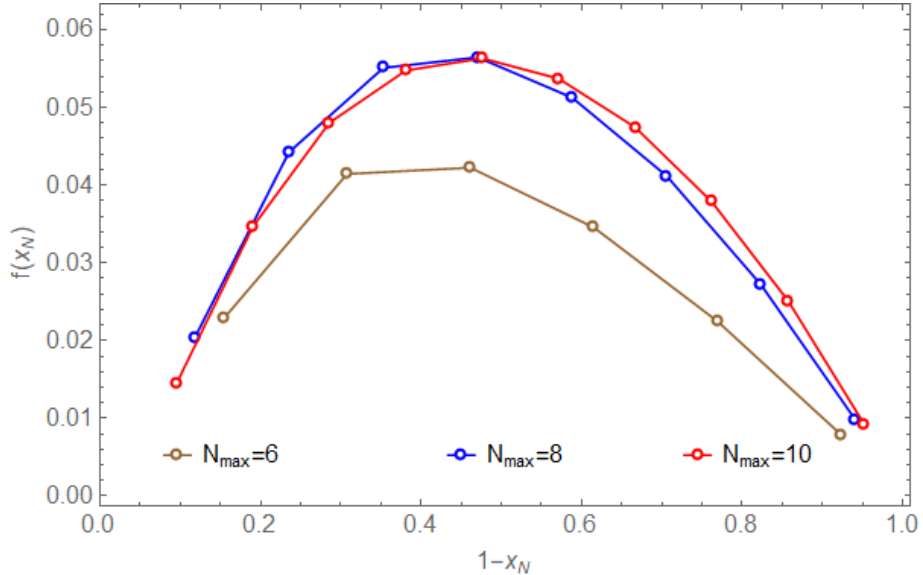


Figure 2: The proton’s PDF,  $f(x_N)$ , as a function of the longitudinal momentum fraction of the constituent nucleon  $x_N$  (note, we rescale the  $x$ -axis as  $1 - x_N = x_\pi$  in the plot) and of the model space (defined by  $N_{\max}$  and  $b$ ). See text for details.

For each  $N_{\max}$ , we verified that  $f(x_N)$  satisfies both the normalization condition and the momentum sum rule. As  $N_{\max}$  increases,  $f(x_N)$  seems to converge (as indicated by the spacing between the curves and the positions of the peaks in the plot). Our results of  $f(x_N)$  peak at about  $x_\pi = 0.45$  (or  $x_N = 0.55$ ) for the model spaces with  $N_{\max} = 8$  and 10. In the future, we plan to study  $f(x_N)$  where large/complete model spaces and high Fock sectors are applied. Also, the internal degrees of freedom of the constituents will be included to study the flavor asymmetry of the proton [38–41].

## 4 Conclusions and outlook

In this work, we apply, for the first time, the Basis Light-Front Quantization (BLFQ) method [4] to study a chiral model of the nucleon-pion ( $N\pi$ ) system via an *ab initio* non-perturbative Hamiltonian approach. We demonstrate the approach with a test problem, in which the physical proton is treated as a relativistic bound state of the  $N\pi$  system.

Starting from the Lagrangian density for the chiral model of the  $N\pi$  system [18,19], we proceed with a Legendre transformation to obtain the corresponding light-front (LF) Hamiltonian density. In this work, we keep only the Fock sectors  $|N\rangle$  and  $|N\pi\rangle$ . Correspondingly, we restrict the interaction terms in the LF Hamiltonian density and keep only the terms that correspond to the single-pion emission and absorption processes.

We then show the construction and truncation schemes of our LF basis. As for the basis set in the momentum space, we employ the discretized plane wave basis in the longitudinal direction and the two dimensional harmonic oscillator basis in the transverse direction. Besides, we also discuss our basis construction in the spin and isospin degrees of freedom. We prune and truncate our basis according to the symmetry principles of our test problem.

We compute the matrix element of the mass-squared operator within our choice of the LF basis representation, where we decouple the center of mass excitation by the Lipkin–Lawson method [31,32]. We obtain the mass spectrum of the  $N\pi$  system and the corresponding boost-invariant light-front wave function (LFWF) by solving the eigenvalue problem of the resulting mass-squared matrix, in which process the mass counterterm is incorporated by the Fock-sector-dependent renormalization (FSDR) scheme [33–36].

The mass spectrum of the  $N\pi$  system in our solution includes both the bound and the scattering states. We study the model space dependence of this spectrum. In particular, we investigate the eigenvalues of the lowest 6 states as a function of the model space, which is determined by the truncation parameters  $N_{\max}$ ,  $K_{\max}$ , basis strength  $b$ , and the choice of Fock sectors. With increasing model space dimension, all the eigenvalues of these 6 states seem to converge, while the scattering states of the  $N\pi$  system produce improving representations of the continuum. Meanwhile, the eigenvalue of the ground state produces the physical proton mass for each model space with proper choice of the mass counterterm; such ground state is identified as the (physical) proton state. Note that larger Fock space would be necessary in order to verify the real convergence. We will postpone this verification to the future work.

To study the proton’s parton distribution function (PDF), we compute the proton’s LFWFs in a sequence of model spaces where both the proton’s mass and its r.m.s. charge radius are fitted to respective physical values. For the resulting PDF,

we investigate its dependencies on the model space and on the longitudinal momentum fraction of the constituent nucleon ( $x_N$ ). We find that the proton's PDF seems to converge with increasing model space dimension (scaled by  $N_{\max}$ ). For the model spaces with  $N_{\max} = 8$  and 10, the computed PDFs peak at about  $x_N = 0.55$  (or  $x_\pi = 0.45$ ). Further inclusion of the quark distribution functions of the constituent nucleon and pion could reveal the pion cloud's role in the light quark flavor asymmetry of the proton (see, e. g., Ref. [41]).

This work can progress into multiple paths in the future. We attempt to connect the current chiral model to the modern chiral effective theory (see, e. g., [42, 43] and references therein). This work is currently ongoing. After this connection is accomplished, we plan to extend the current calculation (up to next-to-leading Fock sector) to incorporate systematically the contributions from higher Fock sectors, where we will examine the basis space dependence as well as the convergence of the Fock-sector expansion [44, 45]. We expect such investigations to be demanding in computing power. We plan to incorporate the technology of high performance computing (see Ref. [46] and references therein).

The current framework can be straightforwardly extended to investigate more nucleonic observables of great experimental interest, such as the transverse momentum distribution, and various categories of form factors. In addition, this framework can be extended to study more complicated nuclear systems, such as the deuteron, where the role of the relativistic dynamics is important but still unclear.

## Acknowledgments

We acknowledge valuable discussions with G. A. Miller, A. W. Thomas, E. Epelbaum, C. Weiss, M. Burkardt, P. Maris, T. Frederico, L. Geng, S. Jia, X. Ren and S. Tang. This work was supported by the U.S. Department of Energy (DOE) under grant No. DE-FG02-87ER40371. X. Zhao is supported by new faculty startup funding from the Institute of Modern Physics, Chinese Academy of Sciences.

## References

- [1] O. Hen, G. A. Miller, E. Piasetzky and L. B. Weinstein, *Rev. Mod. Phys.* **89**, 045002 (2017).
- [2] J. J. Aubert *et al.* (European Muon Collaboration), *Phys. Lett. B* **123**, 275 (1983).
- [3] H. Cheng and T. Wu, *Expanding protons: Scattering at high energies*. MIT Press, Cambridge, 1987.
- [4] J. P. Vary, H. Honkanen, J. Li, P. Maris, S. J. Brodsky, A. Harindranath, G. F. de Teramond, P. Sternberg, E. G. Ng and C. Yang, *Phys. Rev. C* **81**, 035205 (2010).
- [5] H. Honkanen, P. Maris, J. P. Vary and S. J. Brodsky, *Phys. Rev. Lett.* **106**, 061603 (2011).

- [6] X. Zhao, H. Honkanen, P. Maris, J. P. Vary and S. J. Brodsky, Phys. Lett. B **737**, 65 (2014).
- [7] P. Wiecki, Y. Li, X. Zhao, P. Maris and J. P. Vary, Phys. Rev. D **91**, 105009 (2015).
- [8] J. P. Vary, L. Adhikari, G. Chen, S. Jia, M. Li, Y. Li, P. Maris, W. Qian, J. R. Spence, S. Tang, K. Tuchin, A. Yu and X. Zhao, Few-Body Syst. **59**, 56 (2018).
- [9] Y. Li, P. Maris, X. Zhao and J. P. Vary, Phys. Lett. B **758**, 118 (2016).
- [10] Y. Li, P. Maris and J. P. Vary, Phys. Rev. D **96**, 016022 (2017).
- [11] S. Tang, Y. Li, P. Maris and J. P. Vary, Phys. Rev. D **98**, 114038 (2018).
- [12] M. Li, Y. Li, P. Maris and J. P. Vary, Phys. Rev. D **98**, 034024 (2018).
- [13] S. Jia and J. P. Vary, Phys. Rev. C **99**, 035206 (2019).
- [14] J. Lan, C. Mondal, S. Jia, X. Zhao and J. P. Vary, Phys. Rev. Lett. **122**, 172001 (2019).
- [15] X. Zhao, A. Ilderton, P. Maris and J. P. Vary, Phys. Rev. D **88**, 065014 (2013).
- [16] X. Zhao, A. Ilderton, P. Maris and J. P. Vary, Phys. Lett. B **726**, 856 (2013).
- [17] G. Chen, X. Zhao, Y. Li, K. Tuchin and J. P. Vary, Phys. Rev. D **95**, 096012 (2017).
- [18] G. A. Miller, Phys. Rev. C **56**, 2789 (1997).
- [19] G. A. Miller, Prog. Part. Nucl. Phys. **45**, 83 (2000).
- [20] A. Harindranath, *Light front QCD: Lecture notes*. Saha Institute of Nuclear Physics, 2005 (*unpublished*).
- [21] N. A. Tsirova, V. A. Karmanov and J.-F. Mathiot, Phys. Atom. Nucl. **73**, 1952 (2010).
- [22] J.-F. Mathiot and N. A. Tsirova, Phys. Atom. Nucl. **76**, 1387 (2013).
- [23] C. R. Ji, W. Melnitchouk and A. W. Thomas, Phys. Rev. D **80**, 054018 (2009).
- [24] C. R. Ji, W. Melnitchouk and A. W. Thomas, Phys. Rev. D **88**, 076005 (2013).
- [25] P. Chang and F. Gürsey, Phys. Rev. **164**, 1752 (1967).
- [26] S. J. Brodsky, H. C. Pauli and S. S. Pinsky, Phys. Rep. **301**, 299 (1998).
- [27] P. Maris, P. Wiecki, Y. Li, X. Zhao and J. P. Vary, Acta Phys. Polon. Supp. **6**, 321 (2013).
- [28] K. Hornbostel, S. J. Brodsky and H. C. Pauli, Phys. Rev. D **41**, 3814 (1990).
- [29] B. R. Barrett, P. Navratil and J. P. Vary, Prog. Part. Nucl. Phys. **69**, 131 (2013).

- [30] M. A. Caprio, P. Maris and J. P. Vary, *Phys. Rev. C* **86**, 034312 (2012).
- [31] H. J. Lipkin, *Phys. Rev.* **109**, 2071 (1958).
- [32] D. H. Gloeckner and R. D. Lawson, *Phys. Lett. B* **53**, 313 (1974).
- [33] J. R. Hiller and S. J. Brodsky, *Phys. Rev. D* **59**, 016006 (1999).
- [34] V. A. Karmanov, J.-F. Mathiot and A. V. Smirnov, *Phys. Rev. D* **77**, 085028 (2008).
- [35] V. A. Karmanov, J.-F. Mathiot and A. V. Smirnov, *Phys. Rev. D* **82**, 056010 (2010).
- [36] V. A. Karmanov, J.-F. Mathiot and A. V. Smirnov, *Phys. Rev. D* **86**, 085006 (2012).
- [37] J. M. Alarcón, D. W. Higinbotham, C. Weiss and Z. Ye, *Phys. Rev. C* **99**, 044303 (2019).
- [38] C. A. Aidala *et al.* (SeaQuest Collaboration), arXiv:1706.09990 [physics.ins-det] (2017).
- [39] R. S. Towell *et al.* (NuSea Collaboration), *Phys. Rev. D* **64**, 052002 (2001).
- [40] E. A. Hawker *et al.* (NuSea Collaboration), *Phys. Rev. Lett.* **80**, 3715 (1998).
- [41] M. Alberg and G. A. Miller, arXiv:1712.05814 [nucl-th] (2017).
- [42] D. R. Entem and R. Machleidt, *Phys. Rev. C* **68**, 041001 (2003).
- [43] E. Epelbaum, H. W. Hammer and U.-G. Meißner, *Rev. Mod. Phys.* **81**, 1773 (2009).
- [44] Y. Li, V. A. Karmanov, P. Maris and J. P. Vary, *Few-Body Syst.* **56**, 495 (2015).
- [45] Y. Li, V. A. Karmanov, P. Maris and J. P. Vary, *Phys. Lett. B* **748**, 278 (2015).
- [46] J. P. Vary, R. Basili, W. Du, M. Lockner, P. Maris, D. Oryspayev, S. Pal, S. Sarker, H. M. Aktulga, E. Ng, M. Shao and C. Yang, in *Proc. Int. Conf. Nucl. Theor. Supercomputing Era (NTSE-2016), Khabarovsk, Russia, September 19–23, 2016*, eds. A. M. Shirokov and A. I. Mazur. Pacific National University, Khabarovsk, Russia, 2018, p. 15, <http://www.ntse-2016.khb.ru/Proc/Vary.pdf>; arXiv:1803.04101 [nucl-th] (2018).

# Nucleon Form Factors from Basis Light-Front Quantization

Chandan Mondal<sup>a</sup>, Siqu Xu<sup>a</sup>, Jiangshan Lan<sup>a,b</sup>, Xingbo Zhao<sup>a,b</sup>,  
Yang Li<sup>c</sup>, Henry Lamm<sup>d</sup> and James P. Vary<sup>c</sup>

<sup>a</sup>*Institute of Modern Physics, Chinese Academy of Sciences, Lanzhou 730000, China*

<sup>b</sup>*University of Chinese Academy of Sciences, Beijing 100049, China*

<sup>c</sup>*Department of Physics and Astronomy, Iowa State University, Ames, IA 50011, USA*

<sup>d</sup>*Department of Physics, University of Maryland, College Park, Maryland 20742, USA*

## Abstract

We investigate the electromagnetic form factors of the nucleon in the framework of basis light-front quantization. We compute the form factors using the light-front wavefunctions obtained by diagonalizing the effective Hamiltonian consisting of the holographic QCD confinement potential, the longitudinal confinement, and a one-gluon exchange interaction with fixed coupling. The nucleon electromagnetic radii are also computed.

**Keywords:** *Form factors; light-front quantization; nucleon*

## 1 Introduction

Electromagnetic form factors are critical to understanding nucleon structure. There are many experiments and theoretical studies on these form factors and they remain a very active field of research. We refer to the articles [1–5] for detailed reviews. It is well known that the matrix element of electromagnetic current for the nucleon requires two form factors, namely, Dirac and Pauli form factors,

$$J_{had}^\mu(q^2) = \bar{u}(p') \left( \gamma^\mu F_1(q^2) + \frac{i\sigma^{\mu\nu} q_\nu}{2M} F_2(q^2) \right) u(p), \quad (1)$$

where  $q^2 = (p' - p)^2 = -2p' \cdot p + 2M^2 = -Q^2$  is the square of the momentum transferred to the nucleon and  $M$  is the nucleon mass. The normalizations of the form factors are given by  $F_1^p(0) = 1$ ,  $F_2^p(0) = \kappa_p = 1.793$  for the proton and  $F_1^n(0) = 0$ ,  $F_2^n(0) = \kappa_n = -1.913$  for the neutron. Cates *et al.* [6] first decomposed the nucleon form factors into their flavor components. Writing the hadronic current as the sum of quark currents one can decompose the nucleon electromagnetic form factors into flavor-dependent form factors. Neglecting the strange quark contribution, the hadronic matrix element for electromagnetic current can be expressed as

$$J_{had}^\mu(q^2) = \langle N(p') | (e_u \bar{u} \gamma^\mu u + e_d \bar{d} \gamma^\mu d) | N(p) \rangle, \quad (2)$$

---

*Proceedings of the International Conference ‘Nuclear Theory in the Supercomputing Era — 2018’ (NTSE-2018), Daejeon, South Korea, October 29 – November 2, 2018, eds. A. M. Shirokov and A. I. Mazur. Pacific National University, Khabarovsk, Russia, 2019, p. 239.*

<http://www.ntse.khb.ru/files/uploads/2018/proceedings/Mondal.pdf>.

where  $e_u$  and  $e_d$  are the charges of  $u$  and  $d$  quarks in the units of positron charge ( $e$ ). Under the charge and isospin symmetry  $\langle p|\bar{u}\gamma^\mu u|p\rangle = \langle n|\bar{d}\gamma^\mu d|n\rangle$ , it is straightforward to write down the flavor form factors in term of the nucleon form factors as

$$\begin{aligned} F_i^u(Q^2) &= 2F_i^p(Q^2) + F_i^n(Q^2), \\ F_i^d(Q^2) &= F_i^p(Q^2) + 2F_i^n(Q^2), \quad (i = 1, 2), \end{aligned} \quad (3)$$

with the normalizations  $F_1^u(0) = 2$ ,  $F_2^u(0) = \kappa_u$  and  $F_1^d(0) = 1$ ,  $F_2^d(0) = \kappa_d$ , where the anomalous magnetic moments for the up and the down quarks are  $\kappa_u = 2\kappa_p + \kappa_n = 1.673$  and  $\kappa_d = \kappa_p + 2\kappa_n = -2.033$ . It was shown in Ref. [6] that though the ratio of Pauli and Dirac form factors for the proton  $F_2^p/F_1^p \propto 1/Q^2$ , the  $Q^2$  dependence above 1 GeV<sup>2</sup> is almost constant for the ratio of the quark form factors  $F_2/F_1$  for both  $u$  and  $d$ . The Sachs form factors for the nucleon are written in terms of Dirac and Pauli form factors as

$$G_E^N(Q^2) = F_1^N(Q^2) - \frac{Q^2}{4M^2} F_2^N(Q^2), \quad (4)$$

$$G_M^N(Q^2) = F_1^N(Q^2) + F_2^N(Q^2), \quad (5)$$

and the electromagnetic radii are defined by

$$\langle r_E^2 \rangle^N = -6 \frac{dG_E^N(Q^2)}{dQ^2} \Big|_{Q^2=0}, \quad (6)$$

$$\langle r_M^2 \rangle^N = -\frac{6}{G_M^N(0)} \frac{dG_M^N(Q^2)}{dQ^2} \Big|_{Q^2=0}. \quad (7)$$

The basis light-front quantization (BLFQ) approach has been developed for solving many-body bound state problems in quantum field theories [7–10]. It is a Hamiltonian formalism incorporating the advantages of the light-front dynamics [11, 12]. This formalism has been successfully applied to quantum electrodynamics (QED) systems including the electron anomalous magnetic moment [10] and the strong coupling bound-state positronium problem [8]. It has also been applied to heavy quarkonia [13] and  $B_c$  mesons [14] as QCD bound states. Recently, the BLFQ approach using a Hamiltonian that includes the color singlet Nambu–Jona–Lasinio interaction to account for the chiral dynamics has been applied to the light mesons [15, 16]. In this work, we study the electromagnetic form factors of the nucleon using the light-front wavefunctions (LFWFs) obtained by diagonalizing the effective light-front Hamiltonian in the constituent valence quark representation with the potential including the light-front holographic QCD in the transverse direction [17], longitudinal confinement [9], and one-gluon exchange interaction with a fixed coupling in the framework of BLFQ.

## 2 Effective light-front Hamiltonian

The structures of the bound states are encoded in the LFWFs which are obtained as the eigenfunctions of the light-front Schrödinger equation,

$$H_{\text{eff}}|\Psi\rangle = M^2|\Psi\rangle, \quad (8)$$

where  $H_{\text{eff}}$  is the effective Hamiltonian of the system with the mass squared,  $M^2$ , eigenvalue. In general,  $|\Psi\rangle$  is the eigenvector in the Hilbert space spanned by all Fock sectors. In the valence Fock sector, the effective Hamiltonian for the nucleon wavefunctions that we adopt is given by

$$H_{\text{eff}} = \sum_a \frac{\vec{k}_{a\perp}^2 + m_a^2}{x_a} + \frac{1}{2} \sum_{a,b} \left[ \kappa_T^4 x_a x_b (\vec{r}_{a\perp} - \vec{r}_{b\perp})^2 - \frac{\kappa_L^4}{(m_a + m_b)^2} \partial_{x_a} (x_a x_b \partial_{x_b}) \right] \\ + \frac{1}{2} \sum_{a,b} \frac{C_F 4\pi \alpha_s (Q_{ab}^2)}{Q_{ab}^2} \bar{u}_{s'_a}(k'_a) \gamma^\mu u_{s_a}(k_a) \bar{u}_{s'_b}(k'_b) \gamma^\nu u_{s_b}(k_b) d_{\mu\nu}, \quad (9)$$

where  $\sum_a x_a = 1$  and  $\sum_a \mathbf{k}_{a\perp} = 0$ ;  $m_{a/b}$  is the mass of the quark and  $\kappa_L$  ( $\kappa_T$ ) is the strength of the longitudinal (transverse) confinement;  $\vec{\zeta}_\perp \equiv \sqrt{x_a x_b} \vec{r}_\perp$  is the holographic variable [17], where  $\vec{r}_\perp = \vec{r}_{a\perp} - \vec{r}_{b\perp}$  is the transverse separation between two quarks,  $\partial_x f(x, \vec{\zeta}_\perp) = \partial f(x, \vec{\zeta}_\perp) / \partial x |_{\vec{\zeta}}$ ;  $Q_{ab}^2 = -q^2 = -(1/2)(k'_a - k_a)^2 - (1/2)(k'_b - k_b)^2$  is the average momentum transfer squared;  $C_F = -2/3$  is the color factor;  $d_{\mu\nu}$  is the gluon polarization tensor which reduces to the metric tensor  $g_{\mu\nu}$  by summing over the dynamical one-gluon exchange and the instantaneous gluon exchange, and  $\alpha_s$  is the running coupling which can be replaced by a constant for simplicity. Note that we use different quark masses in the kinetic energy term and in the one-gluon exchange interaction of the effective light-front Hamiltonian to simulate the effects of higher Fock components and the other QCD interactions. Upon diagonalization of the resulting effective Hamiltonian matrix in a chosen basis representation, one obtains the mass spectrum and the corresponding wavefunctions of the system.

In the BLFQ, Eq. (8) is expressed in a truncated basis representation of the valence Fock space, and the resulting finite-dimensional matrix is diagonalized numerically. The choice of basis is arbitrary as long as it is orthogonal and normalized. We choose the two-dimensional harmonic oscillator (2D-HO) basis in the transverse direction and the discretized plane-wave basis in the longitudinal direction [7–10]. Each single-particle basis state can be identified using four quantum numbers,  $\bar{\alpha} = \{k, n, m, \lambda\}$ . The longitudinal momentum of the particle is characterized by the first quantum number  $k$ . In the longitudinal direction  $x^-$ , we constrain the system to a box of length  $2L$ , and impose (anti-) periodic boundary conditions on (fermions) bosons. As a result, the longitudinal momentum  $p^+ = 2\pi k/L$  is discretized, where the dimensionless quantity  $k = 1, 2, 3, \dots$  for bosons and  $k = \frac{1}{2}, \frac{3}{2}, \frac{5}{2}, \dots$  for fermions. The zero mode for bosons is neglected. In the many-body basis, all basis states are selected to have the same total longitudinal momentum  $P^+ = \sum_i p_i^+$ , where the sum is over the particles in a particular basis state. One then parameterizes  $P^+$  using a dimensionless variable  $K = \sum_i k_i$  such that  $P^+ = \frac{2\pi}{L} K$ . For a given particle  $i$ , the longitudinal momentum fraction  $x$  is defined as

$$x_i = \frac{p_i^+}{P^+} = \frac{k_i}{K}. \quad (10)$$

$K$  determines the “resolution” in the longitudinal direction, and thus the resolution of parton distribution functions. The longitudinal continuum limit corresponds to the limit  $L, K \rightarrow \infty$ . The next two quantum numbers,  $n$  and  $m$ , denote radial excitation and angular momentum projection, respectively, of the particle within the 2D-HO basis in the transverse direction. The choice of the 2D-HO basis for BLFQ is made

because the HO potential is a confining potential, and therefore its wavefunctions should form an ideal basis for systems subjected to QCD confinement. Since we assume harmonic confinement in the transverse direction, these transverse basis states are also computationally convenient.

In order to numerically diagonalize  $H_{\text{eff}}$ , the infinite dimensional basis must be truncated down to a finite dimension. In BLFQ, two levels of the truncation scheme are implemented. First, the number of Fock sectors in the basis is restricted. This truncation is based on physical as well as practical considerations. For instance, the nucleon is expected to be fairly well described by the lowest few sectors. For example, the nucleon state can be expressed schematically as

$$|N\rangle_{\text{phys}} = a|qqq\rangle + b|qqqg\rangle + c|qqqq\bar{q}\rangle + \dots \quad (11)$$

In this work, we limit ourselves to the leading Fock sector  $|qqq\rangle$  only.

Second, within each Fock sector, further truncation is still needed to reduce the basis to a finite dimension. We introduce a truncation parameter  $K_{\text{max}}$  on the longitudinal direction such that  $\sum_l k_l \leq K_{\text{max}}$ , where  $k_l$  is the longitudinal momentum quantum number of  $l$ -th particle in the basis state. Note that systems with larger  $K_{\text{max}}$  have simultaneously higher ultra-violet (UV) and lower infra-red (IR) cutoffs in the longitudinal direction. In the transverse direction, we require that the total transverse quantum number  $N_\alpha = \sum_l (2n_l + |m_l| + 1)$  for multi-particle basis state  $|\alpha\rangle$  satisfies  $N_\alpha \leq N_{\text{max}}$ , where  $N_{\text{max}}$  is a chosen truncation parameter. The transverse continuum limit corresponds to  $N_{\text{max}} \rightarrow \infty$ . The 2D-HO basis may be defined by two parameters, mass  $M$  and frequency  $\Omega$ . We adopt a single HO parameter  $b = \sqrt{M\Omega}$ , since our transverse modes depend only on  $b$  rather than on  $M$  and  $\Omega$  individually. Here, we choose the value of  $b = 0.45$  GeV, the same as the confining strength  $\kappa_L$  ( $\kappa_T$ ).  $N_{\text{max}}$  and  $b$  define both the transverse IR and UV regulator in BLFQ. In addition, our many body states have well defined values of the total angular momentum projection  $M_J = \sum_i (m_i + \lambda_i)$ , where  $\lambda$  is the fourth quantum number which corresponds the helicity of the particle.

### 3 Electromagnetic form factors in BLFQ

In the light-front formalism for a spin  $\frac{1}{2}$  composite system, the Dirac and Pauli form factors  $F_1(q^2)$  and  $F_2(q^2)$  are identified with the helicity-conserving and helicity-flip matrix elements of the  $J^+$  current [18],

$$\left\langle P + q, \uparrow \left| \frac{J^+(0)}{2P^+} \right| P, \uparrow \right\rangle = F_1(q^2), \quad (12)$$

$$\left\langle P + q, \uparrow \left| \frac{J^+(0)}{2P^+} \right| P, \downarrow \right\rangle = -(q^1 - iq^2) \frac{F_2(q^2)}{2M}, \quad (13)$$

where  $M$  is the nucleon mass and the arrow indicates the helicity of the nucleon. The physical nucleon state with momentum  $P$  can be expanded in terms of multi-particle

light-front wavefunctions [19]:

$$|P, S_z\rangle = \sum_n \int \prod_{i=1}^n \frac{dx_i d^2k_{\perp i}}{16\pi^3 \sqrt{x_i}} 16\pi^3 \delta\left(1 - \sum_{i=1}^n x_i\right) \delta^2\left(\sum_{i=1}^n k_{\perp i}\right) \times \psi_n^{S_z}(x_i, k_{\perp i}, \lambda_i) |n, x_i P^+, x_i P_{\perp} + k_{\perp i}, \lambda_i\rangle. \quad (14)$$

Here  $x_i = k_i^+/P^+$  and  $k_{\perp i}$  represent the relative transverse momentum of the  $i$ -th constituent and  $n$  is the number of particles in a Fock state; the physical transverse momenta are  $p_{\perp i} = x_i P_{\perp} + k_{\perp i}$ ;  $\lambda_i$  and  $S_z$  are the light-cone helicities of the quark and nucleon, respectively; the boost invariant light-front wave functions  $\psi_n$  depend only on  $x_i$  and  $k_{\perp i}$  and are independent of the total momentum of the state  $P^+$  and  $P_{\perp}$ . In the overlap representation, the electromagnetic form factors are then expressed as

$$F_1^q(q^2) = \sum_{n, \lambda_i} \int \prod_{i=1}^n \frac{dx_i d^2k_{\perp i}}{16\pi^3} 16\pi^3 \delta\left(1 - \sum_j x_j\right) \delta^2\left(\sum_{j=1}^n k_{\perp j}\right) \times \psi_n^{\dagger*}(x'_i, k'_{\perp i}, \lambda_i) \psi_n^{\dagger}(x_i, k_{\perp i}, \lambda_i), \quad (15)$$

$$\frac{-(q^1 - iq^2)}{2M} F_2^q(q^2) = \sum_{n, \lambda_i} \int \prod_{i=1}^n \frac{dx_i d^2k_{\perp i}}{16\pi^3} 16\pi^3 \delta\left(1 - \sum_j x_j\right) \delta^2\left(\sum_{j=1}^n k_{\perp j}\right) \times \psi_n^{\dagger*}(x'_i, k'_{\perp i}, \lambda_i) \psi_n^{\perp}(x_i, k_{\perp i}, \lambda_i), \quad (16)$$

where for the struck parton  $x'_1 = x_1$ ,  $k'_{\perp 1} = k_{\perp 1} + (1 - x_1)q_{\perp}$  and  $x'_i = x_i$ ,  $k'_{\perp i} = k_{\perp i} - x_i q_{\perp}$  for the spectators ( $i = 2, \dots, n$ ). We consider the frame where  $q = (0, 0, \mathbf{q}_{\perp})$ , thus  $Q^2 = -q^2 = \mathbf{q}_{\perp}^2$ . Since we restrict ourselves to the leading Fock sector, the nucleon basis state can be written as

$$|N_{\text{phys}}^{S_z}\rangle = |k_{q_1}, n_{q_1}, m_{q_1}, \lambda_{q_1}\rangle \otimes |k_{q_2}, n_{q_2}, m_{q_2}, \lambda_{q_2}\rangle \otimes |k_{q_3}, n_{q_3}, m_{q_3}, \lambda_{q_3}\rangle. \quad (17)$$

We obtain the light-front wavefunctions numerically by diagonalizing the effective Hamiltonian given in Eq. (9) with the basis representation given by Eq. (17). Using the resulting light-front wavefunctions  $\psi_n$ , we evaluate the electromagnetic form factors of the nucleon. The parameters are tuned to fit the electromagnetic properties of the nucleons. Following the convention of Ref. [20], we fix the normalizations of the Dirac and the Pauli form factors as

$$F_1^q(Q^2) = n_q \frac{F_1^{(\text{BLFQ})q}(Q^2)}{F_1^{(\text{BLFQ})q}(0)}, \quad F_2^q(Q^2) = \kappa_q \frac{F_2^{(\text{BLFQ})q}(Q^2)}{F_2^{(\text{BLFQ})q}(0)}, \quad (18)$$

so that  $F_1^q(0) = n_q$  and  $F_2^q(0) = \kappa_q$ , where  $n_u = 2$ ,  $n_d = 1$  and the anomalous magnetic moments for the  $u$  and  $d$  quarks are  $\kappa_u = 1.673$  and  $\kappa_d = -2.033$ . The advantage of the modified formulae in Eq.(18) is that, irrespective of the values of the parameters, the normalization conditions for the form factors are automatically satisfied.

In Fig. 1, we show the  $Q^2$  dependence of the Dirac and the Pauli form factors of  $u$  and  $d$  quark. We set the confining strengths  $\kappa_L = \kappa_T = 0.45$  GeV in both the

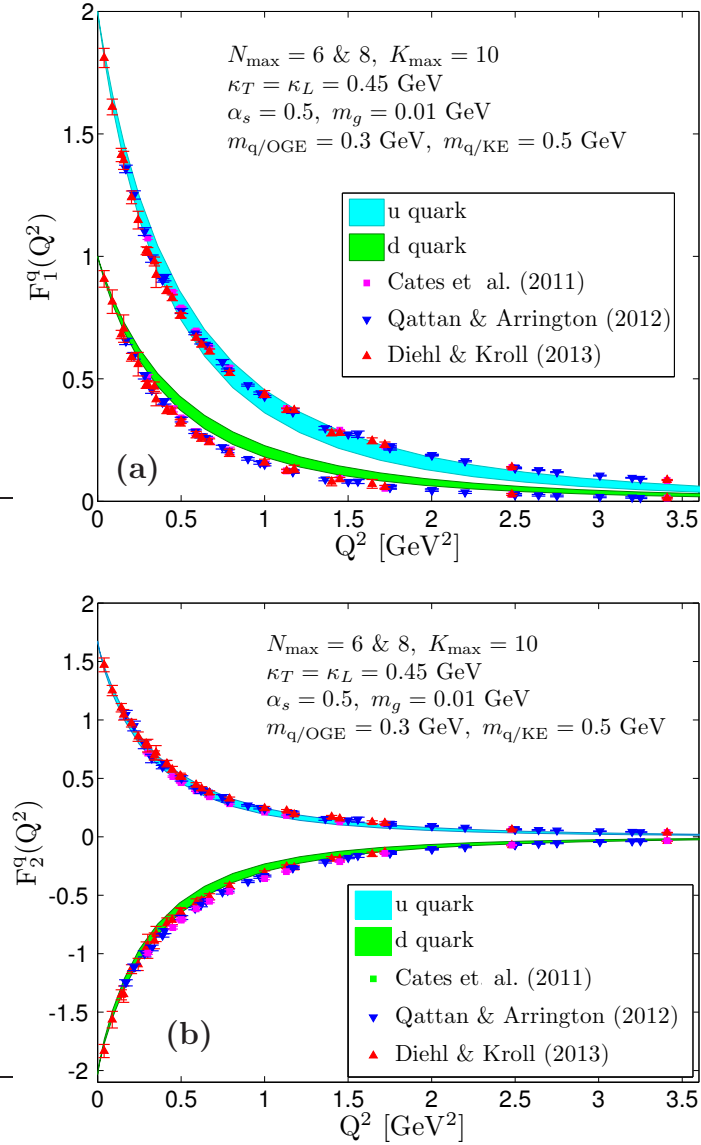


Figure 1: BLFQ results for the Dirac (a) and Pauli (b) form factors of  $u$  and  $d$  quarks with confining strength  $\kappa_L = \kappa_T = 0.45$  GeV and fixed coupling  $\alpha_s = 0.5$ . The quark mass in the kinetic energy term is  $m_{q/\text{KE}} = 0.5$  GeV, whereas the quark mass in the one-gluon-exchange interaction is  $m_{q/\text{OGE}} = 0.3$  GeV. The bands correspond to the range for  $N_{\max} = 6-8$  with  $K_{\max} = 10$ . We choose the value of the HO parameter  $b$  the same as  $\kappa_L(\kappa_T)$ , i. e.,  $b = 0.45$  GeV.  $m_g (= 0.01$  GeV) is a small gluon mass regulator used for numerical convenience. The experimental data are taken from Refs. [6, 21, 22].

longitudinal and transverse confinements and the coupling constant  $\alpha_s = 0.5$ . The bands represent the range of our results due to increasing the basis from  $N_{\max} = 6$  to  $N_{\max} = 8$  with  $K_{\max} = 10$ . We use different quark masses, i. e., in the kinetic

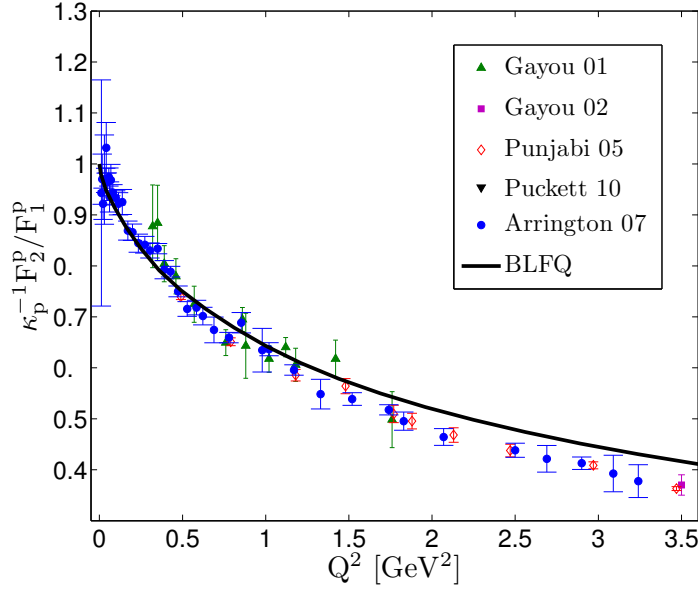


Figure 2: The ratio of the Pauli and Dirac form factors of the proton with the same parameters as mentioned in Fig. 1 and with basis truncation  $N_{\max} = 8$  and  $K_{\max} = 10$ . The ratio is divided by  $\kappa_p$ . The experimental data are taken from Refs. [23–27].

energy term  $m_{q/\text{KE}} = 0.5$  GeV and in the one-gluon exchange interaction  $m_{q/\text{OGE}} = 0.3$  GeV in order to minimize the effect of higher Fock component and the other QCD interactions. Figure 1 shows that the BLFQ results for the flavor Pauli form factors are in reasonable agreement with the experimental data. The Dirac form factor for the  $u$  quark is also in reasonable agreement with the data. However, the theoretical  $d$  quark form factor is somewhat over estimated compared to the data.

The nucleon form factors can be obtained from the flavor dependent form factors. The ratio of Pauli and Dirac form factors of the proton for  $N_{\max} = 8$  and  $K_{\max} = 10$  is shown in Fig. 2. We find that at low  $Q^2$  our result agrees well with the experimental data. The Sachs form factors for the proton are presented in Fig. 3 where we find a good agreement between theory and experiment. In Fig. 4, we show the Sachs form factors for the neutron. Our results for the neutron magnetic form factor are in a reasonable agreement with experimental data, however, for the charge form factor is overestimated as compared to the data. The deviations of the neutron charge form factor from the experimental data can be attributed to the fact that the  $d$  quark form factor  $F_1^d$  does not have the correct behavior in this model. From the Sachs form factors we also compute the electromagnetic radii of the nucleons. We quote the radii in Table 1, the experimental values are taken from the Ref. [37]. Here again, we find a reasonable agreement with experiment.

## 4 Conclusions

The electromagnetic form factors for the nucleon and their flavor decomposition have been presented using the BLFQ approach. The form factors have been evaluated from

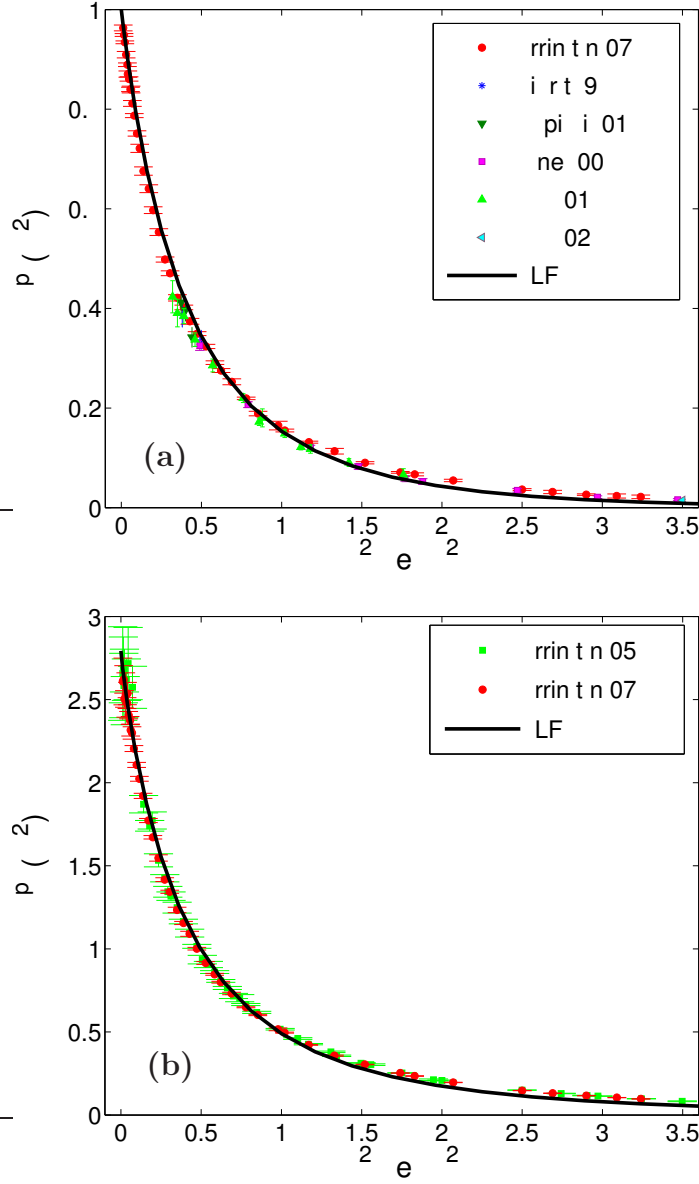


Figure 3: BLFQ results for the Sachs form factors  $G_E(Q^2)$  (a) and  $G_M(Q^2)$  (b) of the proton with the same parameters as mentioned in Fig. 1 and with the basis truncation  $N_{\max} = 8$  and  $K_{\max} = 10$ . The experimental data are taken from Refs. [23–25, 28–30] and Refs. [25, 31], respectively.

Table 1: Electromagnetic radii of nucleons.

Quantity	BLFQ	Measured data [37]
$r_E^p$	0.804 fm	$0.877 \pm 0.005$ fm
$r_M^p$	0.917 fm	$0.777 \pm 0.016$ fm
$\langle r_E^2 \rangle^n$	$-0.1214$ fm <sup>2</sup>	$-0.1161 \pm 0.0022$ fm <sup>2</sup>
$r_M^n$	1.007 fm	$0.862^{+0.009}_{-0.008}$ fm

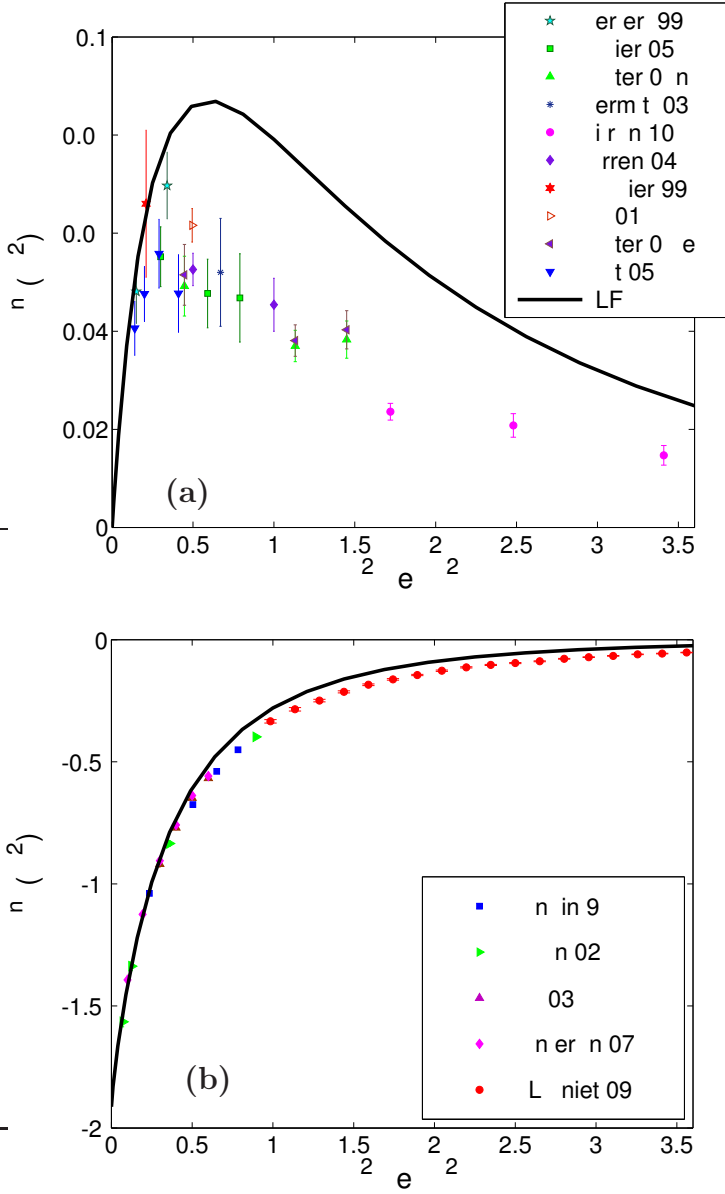


Figure 4: BLFQ results for the Sachs form factors  $G_E(Q^2)$  (a) and  $G_M(Q^2)$  (b) of the neutron with the same parameters as mentioned in Fig. 1 and with basis truncation  $N_{\max} = 8$  and  $K_{\max} = 10$ . The experimental data are taken from Refs. [23–25, 28–30] and Refs. [32–36], respectively.

the overlaps of the light-front wavefunctions which were obtained by diagonalizing the effective Hamiltonian. In our model, we consider the holographic QCD confinement potential, longitudinal confinement, and a one-gluon exchange interaction with fixed coupling in the effective light-front Hamiltonian. We observed a reasonable agreement of our results for the proton and  $u$  quark form factors with the experimental data, however, the Dirac form factor of  $d$  quark and the neutron charge form factors deviate from the data for the basis truncation  $N_{\max} = 8$  and  $K_{\max} = 10$ . We also presented the electromagnetic radii for the nucleon.

## Acknowledgments

CM is supported by the China Postdoctoral Science Foundation (CPSF) under the Grant No. 2017M623279 and the National Natural Science Foundation of China (NSFC) under the Grant No. 11850410436. The work of XZ is supported by new faculty startup funding by the Institute of Modern Physics, Chinese Academy of Sciences under the Grant No. Y632030YRC. HL is supported by the U.S. Department of Energy under the Award No. DE-FG02-93ER-40762. The work of JPV is supported by the U.S. Department of Energy under Grants Nos. DE-FG02-87ER40371, DE-SC0018223 (SciDAC4/NUCLEI) and DE-SC0015376 (DOE Topical Collaboration in Nuclear Theory for Double-Beta Decay and Fundamental Symmetries).

## References

- [1] H. Y. Gao, *Int. J. Mod. Phys. E* **12**, 1 (2003).
- [2] C. E. Hyde-Wright and K. de Jager, *Ann. Rev. Nucl. Part. Sci.* **54**, 217 (2004).
- [3] C. F. Perdrisat, V. Punjabi and M. Vanderhaeghen, *Prog. Part. Nucl. Phys.* **59**, 694 (2007).
- [4] D. Chakrabarti and C. Mondal, *Eur. Phys. J. C* **73**, 2671 (2013).
- [5] C. Mondal, *Phys. Rev. D* **94**, 073001 (2016).
- [6] G. D. Cates, C. W. de Jager, S. Riodian and B. Wojtsekhowski, *Phys. Rev. Lett.* **106**, 252003 (2011).
- [7] J. P. Vary *et al.*, *Phys. Rev. C* **81**, 035205 (2010).
- [8] P. Wiecki, Y. Li, X. Zhao, P. Maris and J. P. Vary, *Phys. Rev. D* **91**, 105009 (2015).
- [9] Y. Li, P. Maris, X. Zhao and J. P. Vary, *Phys. Lett. B* **758**, 118 (2016).
- [10] X. Zhao, H. Honkanen, P. Maris, J. P. Vary and S. J. Brodsky, *Phys. Lett. B* **737**, 65 (2014).
- [11] S. J. Brodsky, H. C. Pauli and S. S. Pinsky, *Phys. Rep.* **301**, 299 (1998).
- [12] J. R. Hiller, *Prog. Part. Nucl. Phys.* **90**, 75 (2016).
- [13] Y. Li, P. Maris and J. P. Vary, *Phys. Rev. D* **96**, 016022 (2017).
- [14] S. Tang, Y. Li, P. Maris and J. P. Vary, *Phys. Rev. D* **98**, 114038 (2018).
- [15] S. Jia and J. P. Vary, *Phys. Rev. C* **99**, 035206 (2019).
- [16] J. Lan, C. Mondal, S. Jia, X. Zhao and J. P. Vary, *Phys. Rev. Lett.* **122**, 172001 (2019).
- [17] S. J. Brodsky, G. F. de Teramond, H. G. Dosch and J. Erlich, *Phys. Rep.* **584**, 1 (2015).

- [18] S. J. Brodsky and S. D. Drell, *Phys. Rev. D* **22**, 2236 (1980).
- [19] S. J. Brodsky, M. Diehl, D. S. Hwang, *Nucl. Phys. B* **596**, 99 (2001).
- [20] C. Mondal and D. Chakrabarti, *Eur. Phys. J. C* **75**, 261 (2015).
- [21] I. A. Qattan and J. Arrington, *Phys. Rev. C* **86**, 065210 (2012).
- [22] M. Diehl and P. Kroll, *Eur. Phys. J. C* **73**, 2397 (2013).
- [23] O. Gayou *et al.*, *Phys. Rev. C* **64**, 038202 (2001).
- [24] O. Gayou *et al.*, *Phys. Rev. Lett.* **88**, 092301 (2002).
- [25] J. Arrington, W. Melnitchouk and J. A. Tjon, *Phys. Rev. C* **76**, 035205 (2007).
- [26] V. Punjabi *et al.*, *Phys. Rev. C* **71**, 055202 (2005).
- [27] A. Puckett *et al.*, *Phys. Rev. Lett.* **104**, 242301 (2010).
- [28] T. Pospischil *et al.*, *Eur. Phys. J. A* **12**, 125 (2001).
- [29] B. D. Milbrath *et al.*, *Phys. Rev. Lett.* **80**, 452 (1998).
- [30] M. K. Jones *et al.*, *Phys. Rev. Lett.* **84**, 1398 (2000).
- [31] J. Arrington, *Phys. Rev. C* **71**, 015202 (2005).
- [32] H. Anklin *et al.*, *Phys. Lett. B* **428**, 248 (1998).
- [33] G. Kubon *et al.*, *Phys. Lett. B* **524**, 26 (2002).
- [34] W. Xu *et al.*, *Phys. Rev. C* **67**, 012201 (2003).
- [35] B. Anderson *et al.*, *Phys. Rev. C* **75**, 034003 (2007).
- [36] J. Lachniet *et al.*, *Phys. Rev. Lett.* **102**, 192001 (2009).
- [37] J. Beringer *et al.* (Particle Data Group), *Phys. Rev. D* **86**, 010001 (2012).

# Robust *Ab Initio* Predictions for Nuclear Rotational Structure in the Be Isotopes

M. A. Caprio<sup>a</sup>, P. J. Fasano<sup>a</sup>, J. P. Vary<sup>b</sup>, P. Maris<sup>b</sup>  
and J. Hartley<sup>a,c,\*</sup>

<sup>a</sup>Department of Physics, University of Notre Dame, Notre Dame, Indiana 46556, USA

<sup>b</sup>Department of Physics and Astronomy, Iowa State University, Ames, Iowa 50011, USA

<sup>c</sup>Department of Chemistry and Physics, Erskine College, Due West, South Carolina 29639, USA

## Abstract

No-core configuration interaction (NCCI) calculations for  $p$ -shell nuclei give rise to rotational bands, identified by strong intraband  $E2$  transitions and by rotational patterns for excitation energies, electromagnetic moments, and electromagnetic transitions. However, convergence rates differ significantly for different rotational observables and for different rotational bands. The choice of internucleon interaction may also substantially impact the convergence rates. Consequently, there is a substantial gap between simply observing the *qualitative* emergence of rotation in *ab initio* calculations and actually carrying out detailed *quantitative* comparisons. In this contribution, we illustrate the convergence properties of rotational band energy parameters extracted from NCCI calculations, and compare these predictions with experiment, for the isotopes  $^{7-11}\text{Be}$ , and for the JISP16 and Daejeon16 interactions.

**Keywords:** Nuclear rotation; no-core configuration interaction (NCCI); Be isotopes

## 1 Introduction

*Ab initio* nuclear theory aims to describe nuclei, with quantitative precision, from the underlying internucleon interactions. Light nuclei are known to display rotational band structure (see, e. g., Refs. [1–4]). Therefore, we should at least aspire for *ab initio* theory to be able to predict rotational band structure. However, there are challenges to obtaining converged calculations of the relevant observables, both energies and electromagnetic transition strengths [5–8].

There are thus a few basic questions to be asked about the emergence of rotation in *ab initio* calculations of light nuclei:

---

\*Present address: Department of Physics and Astronomy, Michigan State University, East Lansing, MI 48824, USA.

---

*Proceedings of the International Conference ‘Nuclear Theory in the Supercomputing Era — 2018’ (NTSE-2018), Daejeon, South Korea, October 29 – November 2, 2018, eds. A. M. Shirokov and A. I. Mazur. Pacific National University, Khabarovsk, Russia, 2019, p. 250.*

<http://www.ntse.khb.ru/files/uploads/2018/proceedings/Caprio.pdf>.

(1) Is there a *qualitative emergence* of rotational “features” in the calculated results? These features include rotational energy patterns and transition patterns.

(2) Can robust *quantitative predictions* be made for rotational observables? These observables include rotational band energy parameters or intrinsic matrix elements. Here we must have good convergence of the results of the many-body calculation, at which point we can then explore the robustness of the predictions across possible internucleon interactions.

(3) Once the *ab initio* description for nuclear rotation is solidly established, what can it tell us about the structure of these rotational states? This understanding may come in the form of identifying, e. g., many-body symmetries [9–12] or cluster structure [2, 4, 13] underlying the rotation.

Regarding the first, qualitative question, no-core configuration interaction (NCCI) [14] calculations for *p*-shell nuclei give rise to rotational bands, identified by strong intraband *E2* transitions and by rotational patterns for excitation energies, electromagnetic moments, and electromagnetic transitions [15, 16] (see also Ref. [17] for a pedagogical review). However, convergence rates differ significantly for different rotational observables and for different rotational bands, as well as in calculations based on different internucleon interactions [17]. Consequently, there is a substantial gap between simply observing the *qualitative* emergence of rotation in *ab initio* calculations and actually obtaining detailed *quantitative* predictions for comparison with experiment.

In this contribution, we focus on quantitative predictions of rotational band energy parameters. We first illustrate the convergence properties of rotational parameters extracted from NCCI calculations, taking  $^{11}\text{Be}$  as an example (Section 2). We then obtain *ab initio* predictions for rotational band parameters across the isotopes  $^{7-11}\text{Be}$ . We explore the robustness of these predictions with respect to the choice of internucleon interaction (JISP16 [18] and Daejeon16 [19]) and compare these predictions with experiment (Section 3).

## 2 Illustration: Rotational bands in $^{11}\text{Be}$

### 2.1 Excitation spectrum and bands

To illustrate the nature of the rotational bands obtained in NCCI calculations, let us take  $^{11}\text{Be}$  as an example. In this nucleus, we encounter bands with qualitatively different termination and convergence properties.

A calculated eigenvalue spectrum for  $^{11}\text{Be}$  is shown in Fig. 1.<sup>1</sup> The detailed results depend upon the particular choice of the internucleon interaction (here, JISP16 [18] plus Coulomb interaction between protons) and truncated space (here, up to  $N_{\text{max}} = 8$  excitation quanta, and with oscillator basis length scale given by  $\hbar\omega = 20$  MeV), as we shall explore in subsequent Sections, but the example calculation in Fig. 1 provide a representative illustration of the general rotational features.

Band members are expected to have energies following the rotational formula  $E(J) = E_0 + AJ(J + 1)$ , where the rotational energy constant  $A \equiv \hbar^2/(2\mathcal{J})$  is inversely related to the moment of inertia  $\mathcal{J}$  of the rotational intrinsic state, and the intercept parameter  $E_0 = E_K - AK^2$  is related to the energy  $E_K$  of the rotational

<sup>1</sup>The NCCI calculations shown here are obtained using the code MFDn [20–22].

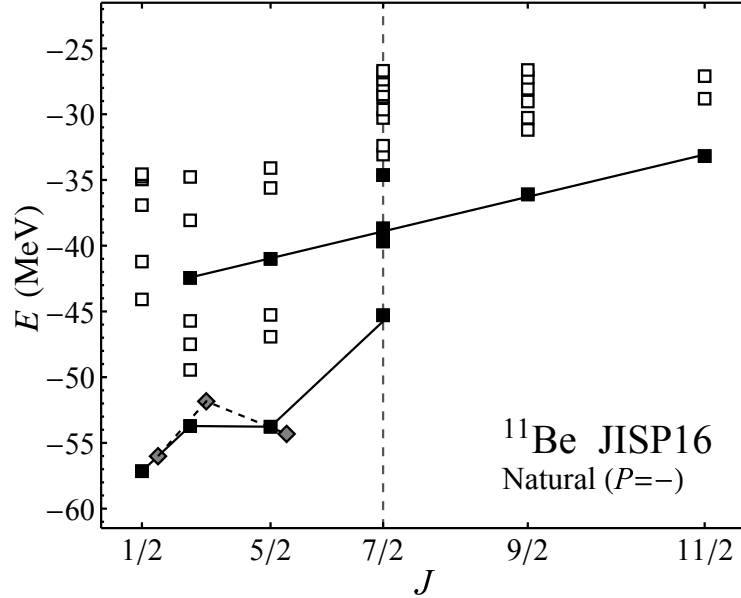


Figure 1: Calculated energy eigenvalues (squares) for states in the natural (negative) parity space of  $^{11}\text{Be}$ , with the JISP16 interaction; the three lowest calculated unnatural (positive) parity states are also shown (diamonds, displaced horizontally for clarity). Energies are plotted with respect to angular momenta scaled as  $J(J+1)$ . Solid symbols indicate band members, as identified by strong  $E2$  transitions and other supporting observables. Lines indicate rotational fits (1) to the calculated energies of the band members. Calculated with  $N_{\text{max}} = 8$  (or  $N_{\text{max}} = 9$  for unnatural parity) at  $\hbar\omega = 20$  MeV.

intrinsic state [23, 24].<sup>2</sup> The level energies in Fig. 1 are therefore plotted against angular momenta scaled as  $J(J+1)$ , so that the energies within a band follow a linear pattern. For  $K = 1/2$  bands, the Coriolis contribution to the kinetic energy significantly modifies this pattern, yielding an energy staggering which is given, in first-order perturbation theory, by

$$E(J) = E_0 + A[J(J+1) + a(-)^{J+1/2}(J + \frac{1}{2})], \quad (1)$$

where the Coriolis decoupling parameter  $a$  depends upon the structure of the rotational intrinsic state.

Rotational band members are shown in Fig. 1 by filled symbols. These identifications are based not simply on the level energies, but rather on strong  $E2$  connections (for illustration, see Figs. 6, 10, and 14 of Ref. [17]).

The lowest filling of harmonic oscillator shells possible for  $^{11}\text{Be}$ , consistent with Pauli exclusion, has an odd number of nucleons in the negative-parity  $p$  shell. Thus, the “natural” parity for  $^{11}\text{Be}$ , as would be obtained in a traditional  $0\hbar\omega$  shell model description or an  $N_{\text{max}} = 0$  NCCI calculation, is negative. In Fig. 1, we focus on the

<sup>2</sup>Under the assumption of axial symmetry, each band is characterized by a projection  $K$  of the angular momentum on the intrinsic symmetry axis, and the rotational band members have angular momenta  $J \geq K$ .

natural (negative) parity states (indicated by squares) and show only the lowest three “unnatural” (positive) parity states for comparison (diamonds).

In this particular calculation (Fig. 1), the lowest positive parity state ( $1/2^+$ ) lies slightly above the lowest negative parity state ( $1/2^-$ ). However, experimentally, the ground state of  $^{11}\text{Be}$  is  $1/2^+$ , lying 0.320 MeV below a  $1/2^-$  excited state [25]. (Such a reversal of the ground state parity relative to the natural parity is known as *parity inversion*.) Different rates of convergence between the natural and unnatural parity states makes it challenging to predict the level ordering when the separation of energies is so small.

The lowest negative-parity band has  $K^P = 1/2^-$  and apparently terminates with the  $7/2^-$  state. This angular momentum  $J = 7/2$  (indicated by the dashed vertical line in Fig. 1) is the highest which can be obtained in a  $p$ -shell description of  $^{11}\text{Be}$ , that is, in the shell model  $0\hbar\omega$  valence space or in an NCCI  $N_{\text{max}} = 0$  calculation.

On the other hand, the excited negative-parity  $K^P = 3/2^-$  band extends past the maximal valence angular momentum. The  $J \leq 7/2$  band members lie in a region of the excitation spectrum with a comparatively high level density and are thus subject to mixing with the “background” non-rotational states. Such mixing occurs when an approximate accidental degeneracy of the rotational state and background states leads to a small energy denominator for mixing. Since we found that the energies of these states converge differently with  $N_{\text{max}}$  and  $\hbar\omega$ , mixing for any given rotational state might arise in one truncated calculation but not the next. For instance, in the particular calculation shown here, the  $E2$  strengths suggest that the excited  $7/2^-$  band member is actually fragmented over three states, as indicated by the filled symbols. Starting with  $J = 9/2$ , this band becomes yrast, and the band members are comparatively well-isolated.

The lowest calculated positive parity states are the  $1/2^+$ ,  $3/2^+$ , and  $5/2^+$  members of a  $K^P = 1/2^+$  band. This band continues to much higher angular momentum than shown here, as may be seen in Fig. 3(e) of Ref. [16].

## 2.2 Dependence of the calculated bands on $N_{\text{max}}$ truncation

While Fig. 1 illustrates the qualitative features of the rotational patterns which arise in NCCI calculations, it represents an approximate calculation of the spectrum, as obtained in a truncated space. It is thus only an unconverged “snapshot”, along the path towards the true results which would be obtained if the many-body problem could be solved in the full, untruncated many-body space.

To see how the rotational pattern evolves, as we progress through calculations truncated to successively higher numbers of oscillator excitations, let us focus on the rotational band members in the negative parity space of  $^{11}\text{Be}$ . We trace out the energies obtained for  $N_{\text{max}} = 6, 8,$  and  $10$  in Fig. 2 (top). These energies are far from converged. Each level moves downward by several MeV for each step in  $N_{\text{max}}$ .

However, the energies of levels within a band move downward nearly in lockstep. Thus, if we look instead at *excitation* energies, as in Fig. 2 (bottom), here taken relative to the lowest ( $1/2^-$ ) negative parity state, the energies of the  $K^P = 1/2^-$  band members are comparatively stable. In fact, only the excitation energy of the terminating  $7/2^-$  band member changes noticeably at an MeV scale.

The  $K^P = 3/2^-$  band is still converging downward relative to the  $K^P = 1/2^-$

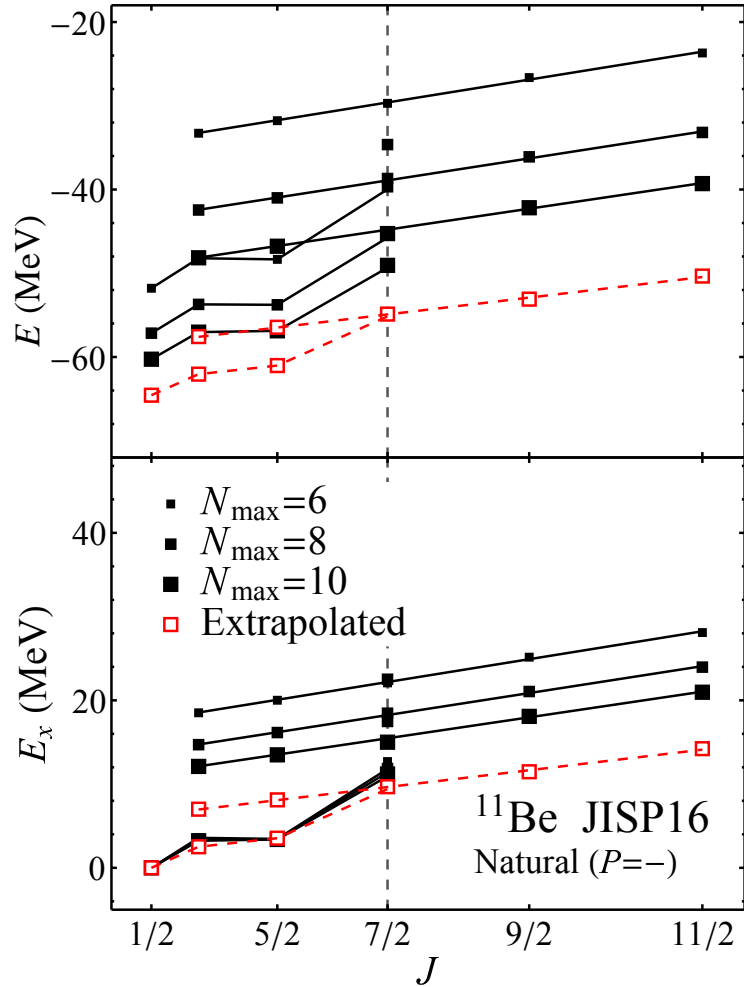


Figure 2: Convergence of calculated energy eigenvalues (top) and excitation energies (bottom) with  $N_{\max}$ , for rotational band members in the natural (negative) parity space of  $^{11}\text{Be}$ . Successively larger symbols indicate successively higher  $N_{\max}$  values ( $N_{\max} = 6, 8,$  and  $10$ ). The open symbols indicate exponentially extrapolated level energies. Lines indicate rotational fits (1) to the calculated (or extrapolated) energies of these band members. Calculated with the JISP16 interaction at  $\hbar\omega = 20$  MeV.

band with increasing  $N_{\max}$ , reflected in the decreasing excitation energies in Fig. 2 (bottom). It is not obvious where we could expect these excitation energies to settle, if we could solve the nuclear many-body problem in the full, untruncated space.

However, we can attempt to *estimate* the full-space result by assuming a functional form for the convergence of the calculated energy eigenvalues. For instance, the sequence of eigenvalues computed at successive  $N_{\max}$  appears to follow a roughly geometric convergence pattern, suggestive of a decaying exponential in  $N_{\max}$  [6,26,27]:

$$E(N_{\max}) = c_0 + c_1 \exp(-c_2 N_{\max}). \quad (2)$$

Since calculated energies at three  $N_{\max}$  values are required to fix the three parameters in Eq. (2), this functional form provides a three-point extrapolation formula for energies, giving the estimate  $E \rightarrow c_0$  as  $N_{\max} \rightarrow \infty$ . This is only an *ad hoc* phenomenological prescription, but it provides an idea of what might be plausible for the full-space results.

Extrapolated energies for the  $^{11}\text{Be}$  band members are shown in Fig. 2 (open symbols): as eigenvalues (top), and then as excitation energies, taken relative to the extrapolated  $1/2^-$  eigenvalue (bottom). While the extrapolated energies of the  $K^P = 3/2^-$  band members still lie above those of the  $K^P = 1/2^-$  band at lower angular momenta, the lower slope of the excited band, combined with the Coriolis staggering of the  $K^P = 1/2^-$  band members, leads to nearly degenerate extrapolated energies for the  $7/2^-$  members of these two bands. If such a degeneracy were to arise, we could expect significant two-state mixing to occur between the two rotational configurations in the  $7/2^-$  band members (similar to the mixing of the excited  $7/2^-$  with the background states seen already at higher excitation energy, in Fig. 1). The level repulsion induced by this mixing would be highly non-perturbative and would thus frustrate any simple attempt at extrapolating the energies from low- $N_{\max}$  calculations where the mixing is not yet in effect.

### 2.3 Stability of calculated rotational energy parameters

Rotational energy parameters extracted from calculations for the  $^{11}\text{Be}$  bands are examined, as functions of  $N_{\max}$  and  $\hbar\omega$  and for different interactions, in Figs. 3–5. There are several questions to be answered for these extracted parameter values:

- (1) Are the calculated values stable against the parameters  $N_{\max}$  and  $\hbar\omega$  of the truncated space?
- (2) If so, are the predictions consistent across the different internucleon interactions?
- (3) How do these predictions then compare to experiment?

Recall that these parameters are the inertial (or slope) parameter  $A$ , energy (or intercept) parameter  $E_0$ , and Coriolis decoupling (or staggering) parameter  $a$  (for  $K = 1/2$ ). The excitation energy  $E_x$  of bands relative to each other is then measured by the difference in their band energy parameters  $E_0$  (we use the  $K^P = 1/2^-$  band as our reference for excitation energies).<sup>3</sup>

It is instructive to examine and compare the convergence behaviors of the parameters  $A$ ,  $a$ , and  $E_x$  for the various bands, and subject to different interactions. Successive curves in each plot in Figs. 3–5 represent calculations at successively higher  $N_{\max}$ , obtained for different oscillator basis length scales given by  $\hbar\omega$ .<sup>4</sup> Each

<sup>3</sup>Translating differences of band energy parameters into differences in intrinsic excitation energies would require that we also take into account the correction  $\propto K^2$  (Section 2.1).

<sup>4</sup>These rotational parameters are extracted from the energies of the “cleanest” band members, least subject to mixing with nearby states. Thus, the parameters for the  $K^P = 1/2^-$  band in Fig. 3 are extracted from the three lowest-energy band members ( $1/2^-$ ,  $3/2^-$ , and  $5/2^-$ ), and similarly for the  $K^P = 1/2^+$  band in Fig. 5. On the other hand, for the  $K^P = 3/2^-$  band, the lower-energy band members are in a region of higher level density and subject to mixing with background states, which can perturb their energies and make it more difficult to trace their evolution across calculations with different  $N_{\max}$  and  $\hbar\omega$ . Therefore, we take energy parameters defined by a straight line through the  $9/2^-$  and  $11/2^-$  band members for the analysis in Fig. 4 (the rotational fit lines in Figs. 1 and 2 were instead obtained as a combined fit to the  $3/2^-$ ,  $5/2^-$ ,  $9/2^-$  and  $11/2^-$  band members).

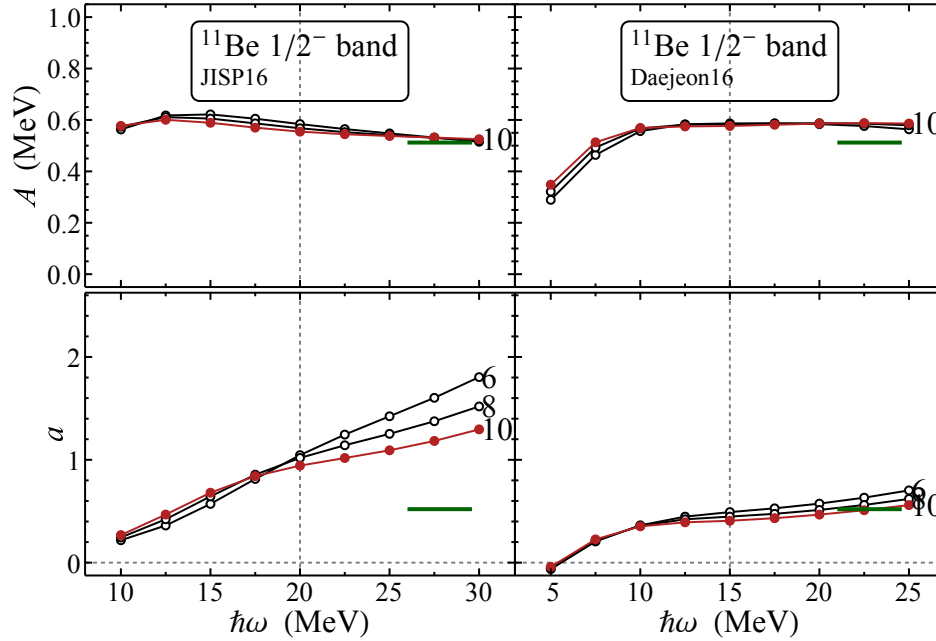


Figure 3: Dependence of the extracted rotational energy parameters, for the  $K^P = 1/2^-$  band of  $^{11}\text{Be}$ , on the truncation parameters  $N_{\text{max}}$  and  $\hbar\omega$  of the NCCI space in which the calculations are carried out. Successive curves are for successively higher  $N_{\text{max}}$  values ( $N_{\text{max}} = 6, 8,$  and  $10$ , noted alongside curve). Experimental values (horizontal lines) are shown for comparison ( $A = 0.51$  MeV and  $a = 0.52$ ). The vertical dashed lines indicate the approximate location of the variational energy minimum, in  $\hbar\omega$ , of the calculated ground state energy (see text).

figure then includes results based on the JISP16 (left) and Daejeon16 (right) interactions.<sup>5</sup> The  $\hbar\omega$  range is centered on the approximate location of the variational energy minimum for the computed ground state energy, which occurs at  $\hbar\omega \approx 20$  MeV for JISP16 and  $\hbar\omega \approx 15$  MeV for Daejeon16 (vertical dotted lines). Experimental values for the rotational band parameters [29], extracted from the observed level energies, are shown for comparison (horizontal lines).<sup>6</sup>

<sup>5</sup>The JISP16 interaction [18] is a two-body interaction derived from nucleon-nucleon scattering data by  $J$ -matrix inverse scattering, then adjusted via a phase-shift equivalent transformations to better describe light nuclei with  $A \leq 16$ . The Daejeon16 interaction [19] is instead obtained from the Entem–Machleidt (EM)  $N^3\text{LO}$  chiral interaction [28], softened via a similarity renormalization group (SRG) transformation to enhance convergence, and then likewise adjusted via a phase-shift equivalent transformation to better describe light nuclei with  $A \leq 16$ .

<sup>6</sup>The experimental band parameter values for the bands in  $^{11}\text{Be}$  are based on fits of the rotational energy formula to the experimental levels, as summarized in Table III of Ref. [29]: for the  $1/2^-$  band, the  $1/2^-$  at 0.320 MeV,  $3/2^-$  at 2.654 MeV, and  $5/2^-$  at 3.889 MeV; for the  $3/2^-$  band, the  $3/2^-$  at 3.955 MeV and  $5/2^-$  at 5.255 MeV; for the  $1/2^+$  band, the  $1/2^+$  ground state,  $3/2^+$  at 3.400 MeV, and  $5/2^+$  at 1.783 MeV. These assignments of levels to bands in  $^{11}\text{Be}$  follow Refs. [3, 30], while energies are from Ref. [25]. However, there are conflicting spin-parity assignments in the literature. For instance, the level at 3.4 MeV was assigned as  $3/2^-$  in  $(t, p)$  [31],  $(3/2^-)$  in  $\beta$  decay [32], and  $(3/2, 5/2)^+$  in breakup [33], and is evaluated as  $(3/2^-, 3/2^+)$  [25]. The level at 3.9 MeV, was assigned as  $3/2^+$  in  $(t, p)$  [31] but as  $5/2^-$  in  $\beta$  decay [32], corroborated as negative parity in transfer reactions [34], and evaluated as  $5/2^-$  [25].

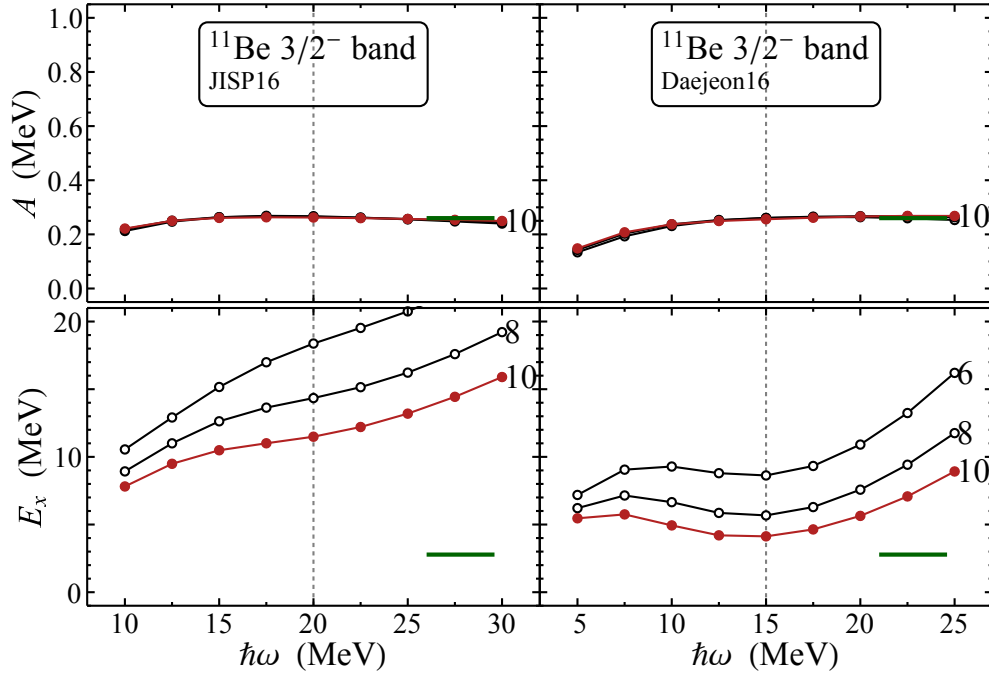


Figure 4: Dependence of the extracted rotational energy parameters, for the excited  $K^P = 3/2^-$  band of  $^{11}\text{Be}$ , on the truncation parameters  $N_{\text{max}}$  and  $\hbar\omega$  of the NCCI space in which the calculations are carried out. Successive curves are for successively higher  $N_{\text{max}}$  values ( $N_{\text{max}} = 6, 8,$  and  $10$ , noted alongside curve). The band excitation energy  $E_x$  is taken relative to the  $K^P = 1/2^-$  band. Experimental values (horizontal lines) are shown for comparison ( $A = 0.26$  MeV and  $E_x = 2.77$  MeV). The vertical dashed lines indicate the approximate location of the variational energy minimum, in  $\hbar\omega$ , of the calculated ground state energy (see text).

The slope parameter  $A$  follows entirely from relative energies within a band, which were already seen from Figs. 1 and 2 to be comparatively well-converged. From the top panels in Figs. 3–5, the calculated  $A$  parameter is essentially converged for the Daejeon16 calculations (in the vicinity of the variational minimum  $\hbar\omega$ ), while there is still some residual dependence on  $N_{\text{max}}$  (at the few-percent level) and  $\hbar\omega$  for the JISP16 calculations. There is remarkable consistency across these two interactions, as well as with the experimental values. A shallower slope corresponds in the rotational picture to a larger moment of inertia. Note that the excited  $K^P = 3/2^-$  band, by this measure, has a moment of inertia roughly twice that of the  $K^P = 1/2^-$  band, both in calculations and experiment (this greater moment of inertia may be understood in terms of  $\alpha$  cluster structure and the molecular orbitals occupied by the neutrons [13]).

Even though the Coriolis decoupling parameter  $a$  [Figs. 3 (bottom) and 5 (middle)] is likewise determined only from relative energies within a band, it is found to be much more sensitive to the truncation of the calculation. (This parameter is extracted essentially as a second difference in level energies, and numerical second derivatives are known to be sensitive to uncertainties or fluctuations in the inputs.) For instance, in the JISP16 calculations for the  $K^P = 1/2^-$  band [Fig. 3 (bottom, left)], although

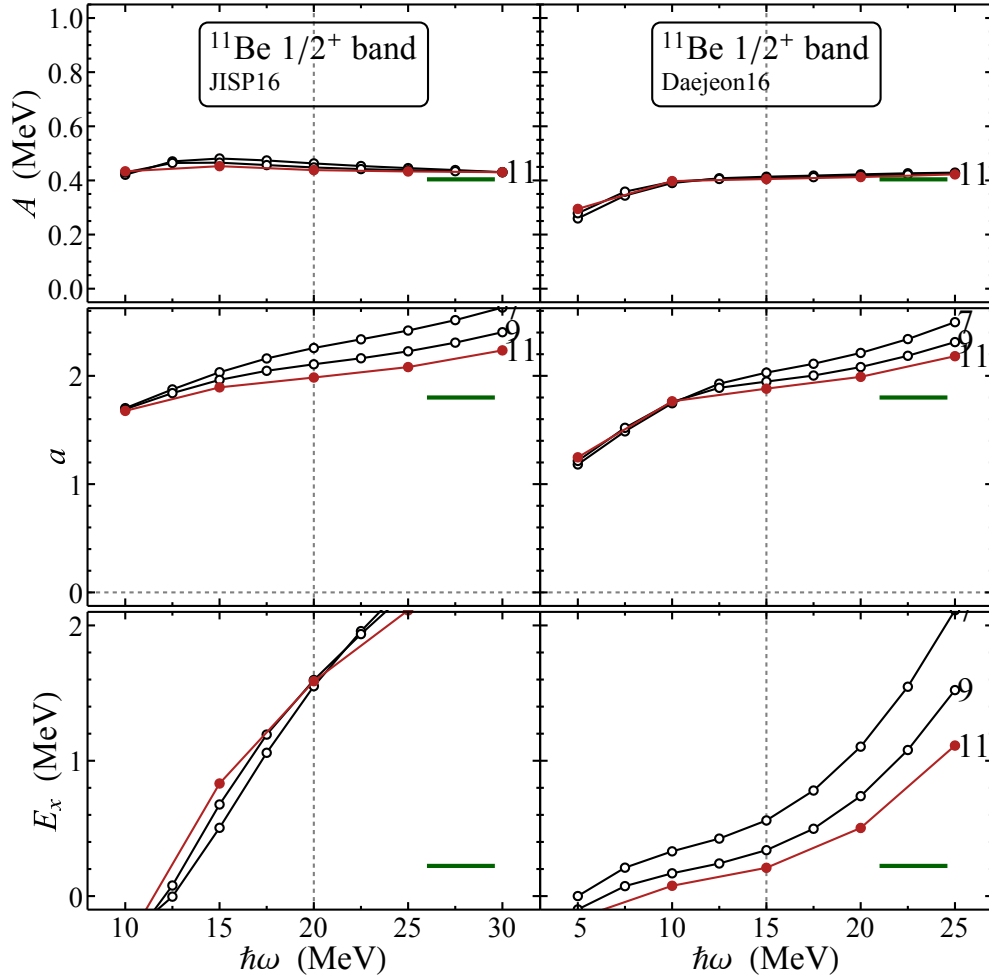


Figure 5: Dependence of the extracted rotational energy parameters, for the unnatural-parity  $K^P = 1/2^+$  band of  $^{11}\text{Be}$ , on the truncation parameters  $N_{\text{max}}$  and  $\hbar\omega$  of the NCCI space in which the calculations are carried out. Successive curves are for successively higher  $N_{\text{max}}$  values ( $N_{\text{max}} = 7, 9$ , and  $11$ , noted alongside curve). The band excitation energy  $E_x$  is taken relative to the  $K^P = 1/2^-$  band. Experimental values (horizontal lines) are shown for comparison ( $A = 0.40$  MeV,  $a = 1.80$ , and  $E_x = 0.22$  MeV). The vertical dashed lines indicate the approximate location of the variational energy minimum, in  $\hbar\omega$ , of the calculated ground state energy (see text).

the Coriolis decoupling parameter is deceptively independent of  $N_{\text{max}}$  at  $\hbar\omega = 20$  MeV (vertical dashed line), there is still a strong  $\hbar\omega$  dependence, which means that it is not yet possible to extract a converged value. On the other hand,  $a$  seems to be comparatively well converged in the Daejeon16 calculations for this same band [Fig. 3 (bottom, right)] and in close agreement with experiment ( $a \approx 0.5$ ). For the  $K^P = 1/2^+$  band, although the  $a$  parameter obtained for both interactions is developing a plateau (or shoulder) as a function of  $\hbar\omega$ , indicative of convergence [Fig. 5 (middle)], there is

still  $N_{\max}$  dependence at about the 10% level. The calculated values are consistent with the much larger decoupling parameter ( $a \approx 1.8$ ) experimentally found for this band.

Finally, the excitation energy of the  $K^P = 3/2^-$  band [Figs. 4 (bottom)] is poorly converged, as already found in Section 2.2. The excitation energy of the unnatural parity  $K^P = 1/2^+$  band [Figs. 5 (bottom)] is still highly  $\hbar\omega$ -dependent (though again deceptively  $N_{\max}$  independent at  $\hbar\omega = 20$  MeV) for the JISP16 interaction, while the excitation energy obtained in the Daejeon16 calculation is approaching convergence at the  $\sim 0.1$ – $0.2$  MeV level and appears consistent with experiment. More detailed comparisons must rely upon extrapolation, as considered in the following discussion of band parameters along the Be isotopic chain (Section 3).

### 3 Rotational energy parameters for the Be isotopes

A variety of rotational bands were identified across the Be isotopes in Ref. [16]. These include examples of “short” bands (terminating at the maximal valence angular momentum) and “long” (non-terminating) bands, as well as unnatural parity bands, akin to those discussed above for  $^{11}\text{Be}$  (Section 2).

We survey the rotational energy parameters extracted from *ab initio* calculations in Fig. 6. While the calculations in Ref. [16] made use of the JISP16 interaction without Coulomb contribution, and thus could not be directly compared to experiment, the present JISP16 and Daejeon16 calculations include Coulomb interaction and thus may be directly compared to experiment, convergence permitting. We do not attempt to display the sensitivity of the extracted parameters to the basis parameter  $\hbar\omega$ , but rather confine ourselves to the values obtained at the approximate variational energy minimum in  $\hbar\omega$ . However, we do show the sequence of extracted values for four successive  $N_{\max}$  truncations, as a more limited indicator of convergence. We also show the band parameters obtained from exponentially extrapolated energies.

The first notable feature of the predicted band parameters in Fig. 6 is the overall global consistency between predictions with the JISP16 and Daejeon16 interactions, across the set of bands considered. Despite the caveat that significant remaining  $\hbar\omega$ -dependence of some of the extracted band parameters leaves their converged values in doubt (see Section 2.3), the values for both the  $A$  and  $a$  parameters obtained at the variational minimum in  $\hbar\omega$  are generally largely  $N_{\max}$ -independent at the MeV scale considered here. In contrast, relative excitation energies of different bands are poorly converged, but even here the extrapolated energies are largely consistent across interactions.

The overall pattern of rotational band parameters closely matches experiment. Where discrepancies arise, the tendency is for the *ab initio* calculations to be consistent with each other rather than with experiment. Here it should be noted that there can be significant ambiguities in identification of the experimental band members (see, e. g., footnote 6), as well as fundamental uncertainties in comparing energies obtained in a bound-state formalism, such as NCCI, with those from experimental resonant scattering analysis.

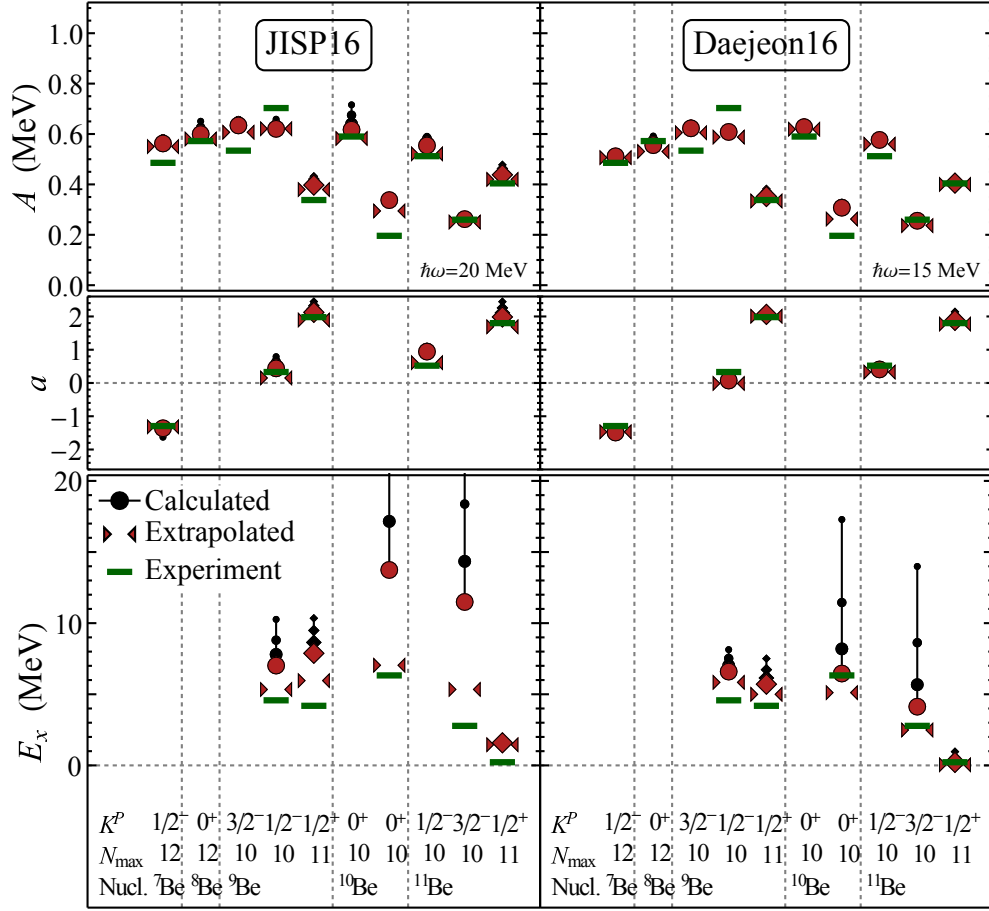


Figure 6: Band energy parameters for  ${}^7\text{--}11\text{Be}$ , extracted from calculated energy eigenvalues: rotational constant  $A$  (top), Coriolis decoupling parameter  $a$  (middle), and band excitation energy  $E_x$  (bottom), for the JISP16 (left) and Daejeon16 (right) internucleon interactions. Successively larger symbols indicate successively higher  $N_{\max}$  values. Parameter values are also shown based on exponentially extrapolated level energies (paired triangles). Experimental values for the band energy parameters (horizontal lines) are shown for comparison [29]. The nuclide, band ( $K^P$ ), and highest  $N_{\max}$  value calculated are noted at the bottom of the plot. Results are obtained from calculations at  $\hbar\omega = 20$  MeV for JISP16 and  $\hbar\omega = 15$  MeV for Daejeon16.

## 4 Conclusion

We have explored the dependences of rotational band energy parameters on the truncation parameters of an oscillator-basis NCCI calculation for the illustrative case of  ${}^{11}\text{Be}$  (Figs. 3–5) and, more generally, across the Be isotopes (Fig. 6). We find that *ab initio* calculations can provide quantitatively robust predictions for rotational band energy parameters in light ( $p$ -shell) nuclei. Even subject to the present limitations on *ab initio* many-body calculations, numerically robust predictions can be made for

rotational band parameters in the Be isotopes. The results obtained with two interactions of significantly different pedigree (the JISP16 interaction from  $J$ -matrix inverse scattering and the Daejeon16 interaction originating from chiral perturbation theory) yield highly consistent results. These results are also, overall, remarkably consistent with the experimentally observed band parameters.

## Acknowledgements

We thank Jie Chen, Jakub Herko, and Anna McCoy for comments on the manuscript. This material is based upon work supported by the U.S. Department of Energy, Office of Science, under Award Numbers DE-FG02-95ER-40934, DESC00018223 (SciDAC/NUCLEI), and DE-FG02-87ER40371, and by the U.S. National Science Foundation under Award Number NSF-PHY05-52843. This research used computational resources of the University of Notre Dame Center for Research Computing and of the National Energy Research Scientific Computing Center (NERSC), a U.S. Department of Energy, Office of Science, user facility supported under Contract DE-AC02-05CH11231.

## References

- [1] J. D. Rogers, *Annu. Rev. Nucl. Sci.* **15**, 241 (1965).
- [2] W. von Oertzen, *Z. Phys. A* **354**, 37 (1996).
- [3] W. von Oertzen, *Z. Phys. A* **357**, 355 (1997).
- [4] M. Freer, *Rep. Prog. Phys.* **70**, 2149 (2007).
- [5] M. Pervin, S. C. Pieper and R. B. Wiringa, *Phys. Rev. C* **76**, 064319 (2007).
- [6] S. K. Bogner, R. J. Furnstahl, P. Maris, R. J. Perry, A. Schwenk and J. Vary, *Nucl. Phys. A* **801**, 21 (2008).
- [7] C. Cockrell, J. P. Vary and P. Maris, *Phys. Rev. C* **86**, 034325 (2012).
- [8] P. Maris and J. P. Vary, *Int. J. Mod. Phys. E* **22**, 1330016 (2013).
- [9] T. Dytrych, K. D. Sviratcheva, C. Bahri, J. P. Draayer, and J. P. Vary, *Phys. Rev. C* **76**, 014315 (2007).
- [10] T. Dytrych, K. D. Launey, J. P. Draayer, P. Maris, J. P. Vary, E. Saule, U. Catalyurek, M. Sosonkina, D. Langr and M. A. Caprio, *Phys. Rev. Lett.* **111**, 252501 (2013).
- [11] C. W. Johnson, *Phys. Rev. C* **91**, 034313 (2015).
- [12] A. E. McCoy, M. A. Caprio and T. Dytrych, *Ann. Acad. Rom. Sci. Ser. Chem. Phys. Sci.* **3**, 17 (2018).
- [13] Y. Kanada-En'yo, M. Kimura and A. Ono, *Prog. Exp. Theor. Phys.* **2012**, 01A202 (2012).

- [14] B. R. Barrett, P. Navrátil and J. P. Vary, *Prog. Part. Nucl. Phys.* **69**, 131 (2013).
- [15] M. A. Caprio, P. Maris and J. P. Vary, *Phys. Lett. B* **719**, 179 (2013).
- [16] P. Maris, M. A. Caprio and J. P. Vary, *Phys. Rev. C* **91**, 014310 (2015); Erratum: *ibid.* **99**, 029902(E) (2019).
- [17] M. A. Caprio, P. Maris, J. P. Vary and R. Smith, *Int. J. Mod. Phys. E* **24**, 1541002 (2015).
- [18] A. M. Shirokov, J. P. Vary, A. I. Mazur and T. A. Weber, *Phys. Lett. B* **644**, 33 (2007).
- [19] A. M. Shirokov, I. J. Shin, Y. Kim, M. Sosonkina, P. Maris and J. P. Vary, *Phys. Lett. B* **761**, 87 (2016).
- [20] P. Maris, M. Sosonkina, J. P. Vary, E. Ng and C. Yang, *Procedia Comput. Sci.* **1**, 97 (2010).
- [21] H. M. Aktulga, C. Yang, E. G. Ng, P. Maris and J. P. Vary, *Concurrency Computat.: Pract. Exper.* **26**, 2631 (2014).
- [22] M. Shao, H. M. Aktulga, C. Yang, E. G. Ng, P. Maris and J. P. Vary, *Comput. Phys. Commun.* **222**, 1 (2018).
- [23] P. Ring and P. Schuck, *The nuclear many-body problem*. Springer-Verlag, New York, 1980.
- [24] D. J. Rowe, *Nuclear collective motion: Models and theory*. World Scientific, Singapore, 2010.
- [25] J. Kelley, E. Kwan, J. E. Purcell, C. G. Sheu and H. R. Weller, *Nucl. Phys. A* **880**, 88 (2012).
- [26] C. Forssen, J. P. Vary, E. Caurier and P. Navratil, *Phys. Rev. C* **77**, 024301 (2008).
- [27] P. Maris, J. P. Vary and A. M. Shirokov, *Phys. Rev. C* **79**, 014308 (2009).
- [28] D. R. Entem and R. Machleidt, *Phys. Rev. C* **68**, 041001 (2003).
- [29] P. Maris, M. A. Caprio and J. P. Vary, *Phys. Rev. C* **91**, 014310 (2015).
- [30] H. G. Bohlen, W. von Oertzen, R. Kalpakchieva, T. N. Massey, T. Corsch, M. Milin, C. Schulz, Tz. Kokalova and C. Wheldon, *J. Phys. Conf. Ser.* **111**, 012021 (2008).
- [31] G.-B. Liu and H. T. Fortune, *Phys. Rev. C* **42**, 167 (1990).
- [32] Y. Hirayama, T. Shimoda, H. Izumi, A. Hatakeyama, K. P. Jackson, C. D. P. Levy, H. Miyatake, M. Yagi and H. Yanoa, *Phys. Lett. B* **611**, 239 (2005).
- [33] N. Fukuda *et al.*, *Phys. Rev. C* **70**, 054606 (2004).
- [34] H. G. Bohlen *et al.*, *Nucl. Phys. A* **722**, 3c (2003).

# Isospin-Symmetry Breaking Correction to Superaligned $0^+ \rightarrow 0^+$ $\beta$ -Decay

Nadezda A. Smirnova<sup>a</sup> and Latsamy Xayavong<sup>a,b</sup>

<sup>a</sup>*CENBG (Université de Bordeaux - CNRS/IN2P3), 33175 Bordeaux-Gradignan, France*

<sup>b</sup>*Physics Department, Faculty of Sciences, National University of Laos, 7322 Dongdok, Vientiane Capital, Lao PDR*

## Abstract

Superaligned  $0^+ \rightarrow 0^+$  nuclear  $\beta$ -decay provides an important test of fundamental symmetries underlying the Standard Model of particle physics, namely, the conserved vector-current (CVC) hypothesis and the unitarity of the Cabibbo–Kobayashi–Maskawa (CKM) quark-mixing matrix. These applications require theoretical corrections to  $\beta$ -decay rates, accounting for electroweak interactions between emitted leptons and hadrons (*radiative* corrections) and for the loss of the analogue symmetry between the parent and the daughter states (*isospin-symmetry breaking* correction).

In this work, we present large-scale shell-model calculations of the isospin-symmetry breaking correction to  $0^+ \rightarrow 0^+$   $\beta$ -decay in the  $p$ ,  $sd$  and  $pf$ -shell. We exploit accurate charge-dependent Hamiltonians and evaluate Fermi transition matrix elements using spherical Woods–Saxon (WS) radial wave functions. Calculations are performed beyond the closure approximation, which requires a large number of intermediate states. We address the question of convergence of nuclear charge radii and of the radial-overlap part of the correction as a function of intermediate states, testing, in particular, the splitting of the correction into two terms (the so-called separation ansatz). We show that the developed adjustment procedure, under available experimental constraints, leads to a rather consistent set of corrections for different shell-model interactions and WS parameterizations. The results are compared to previous studies within the shell model. Their implication for the CVC hypothesis of the Standard Model is discussed.

**Keywords:** *Nuclear shell model, isospin-symmetry breaking correction, super-aligned beta decay, Standard Model*

## 1 Introduction

The superaligned  $0^+ \rightarrow 0^+$  nuclear  $\beta$ -decay has been attracting attention of physicists already for a number of decades [1]. Since these transitions are governed uniquely by the vector part of the weak current, the constancy of the so-called absolute  $Ft$ -values for various emitters can serve to test the CVC hypothesis. These  $Ft$  values

---

*Proceedings of the International Conference ‘Nuclear Theory in the Supercomputing Era — 2018’ (NTSE-2018), Daejeon, South Korea, October 29 – November 2, 2018, eds. A. M. Shirokov and A. I. Mazur. Pacific National University, Khabarovsk, Russia, 2019, p. 263.*

<http://www.ntse.khb.ru/files/uploads/2018/proceedings/Smirnova.pdf>.

are obtained from the experimentally deduced  $ft$  values, where  $t$  is the experimental partial half-life of the transition and  $f$  is the statistical rate function, as given by the following master formula [1, 2]:

$$Ft^{0^+ \rightarrow 0^+} \equiv ft^{0^+ \rightarrow 0^+}(1 + \delta'_R)(1 + \delta_{NS} - \delta_C) = \frac{K}{|M_F^0|^2 G_V^2 (1 + \Delta_R)}. \quad (1)$$

Here  $K = 2\pi^3 \hbar \ln 2 (\hbar c)^6 / (m_e c^2)^5$ ,  $G_V$  is the vector coupling constant for a semi-leptonic decay,  $|M_F^0| = \sqrt{T(T+1) - T_{zi}T_{zf}}$  is the absolute value of the Fermi matrix element in the isospin-symmetry limit,  $T$  and  $T_z$  are the isospin and its projection of the initial  $i$  and final  $f$  states. Besides, Eq. (1) contains  $\Delta_R$ ,  $\delta'_R$ ,  $\delta_{NS}$ , which are transition independent, transition-dependent and nuclear-structure dependent *radiative* corrections, respectively, and  $\delta_C$  is the *isospin-symmetry breaking* correction.

If the CVC hypothesis holds ( $Ft$  is obtained to be constant), from Eq. (1) one can deduce  $G_V$  and use it, combined with the fundamental Fermi coupling constant  $G_F$  extracted from a purely leptonic muon decay, to get the absolute value of the  $V_{ud}$  matrix element of the CKM matrix:  $|V_{ud}| = G_V/G_F$ . This is important for the unitarity tests of the CKM matrix, for example, one can check the normalization condition of its first row:

$$|V_u|^2 = |V_{ud}|^2 + |V_{us}|^2 + |V_{ub}|^2.$$

Other potential possibilities to extract  $V_{ud}$  are provided by the neutron decay, pion decay and transitions between mirror  $T = 1/2$  partners [1, 3]. The neutron decay is free from the nuclear structure correction, however, one needs to determine the Gamow–Teller/Fermi branching ratio and thus one needs to measure an additional parameter, such as the  $\beta$ -asymmetry,  $\nu$ -asymmetry or  $e\nu$ -correlation coefficient [1]. This increases experimental uncertainty on the extracted  $Ft$  value. Similar uncertainties arise for the mirror  $T = 1/2$  decays, where, in addition to the correlation parameters, one has to evaluate the isospin-symmetry breaking correction (see Ref. [3] for details). The pion  $\beta$ -decay offers the possibility, but this branch is very weak and, thus, the experimental uncertainty is large. It follows that the  $0^+ \rightarrow 0^+$   $\beta$ -decay is by far more advantageous compared to other decays and this is why it is worth to put efforts into it.

At present, the  $ft$ -values of 14 best-known  $T = 1$  emitters are obtained with a precision better than 0.4% [2]. They include  $^{10}\text{C}$ ,  $^{14}\text{O}$ ,  $^{22}\text{Mg}$ ,  $^{26m}\text{Al}$ ,  $^{34}\text{Cl}$ ,  $^{34}\text{Ar}$ ,  $^{38m}\text{K}$ ,  $^{38}\text{Ca}$ ,  $^{42}\text{Sc}$ ,  $^{46}\text{V}$ ,  $^{50}\text{Mn}$ ,  $^{54}\text{Co}$ ,  $^{62}\text{Ga}$  and  $^{74}\text{Rb}$ . The corresponding  $ft$ -values are deduced from the measured decay  $Q$ -values and partial half-lives. While nuclear masses are measured nowadays with high precision, the experimental uncertainty on the  $ft$  values is dominated by the error in the Fermi decay branching ratio [2]. In particular, the  $ft$  values of light  $N = Z$  emitters are known with the best precision due to the fact that they are dominated by the Fermi branch at more than 90%.

In this contribution, we focus on the isospin-symmetry breaking correction,  $\delta_C$ , which appears due to the lack of the analogue symmetry between the parent and daughter nuclear states. It is defined as a deviation of the realistic Fermi matrix element squared from its isospin-symmetry value:

$$|M_F|^2 = |M_F^0|^2(1 - \delta_C). \quad (2)$$

This correction should be evaluated within a nuclear-structure model able to account for the broken isospin symmetry in nuclear states. In spite of the recent progress

in microscopic many-body theory and nuclear forces, the precise description of the isospin-symmetry breaking is still a challenge. Existing predictions from various theoretical approaches are not in agreement (see Refs. [2, 4] and references therein). In particular, based on the compatibility with the CVC hypothesis, in their latest survey [2] Hardy and Towner retained only their own results for the  $|V_{ud}|$  evaluation from Ref. [5].

However, the fact that a calculation is consistent with the conservation of the vector current, does not provide any constraint onto the magnitude of the  $Ft$  value. Hence, alternative calculations would be of use. In addition, new experimental measurements or theoretical developments may emerge. For example, adopting a recently re-evaluated  $\Delta_R$  [6], with a reduced uncertainty and slightly modified central value, and keeping all other values as in Ref. [2], the normalization condition for the CKM upper row clearly shows some tensions.

In this work we present calculations of the isospin-symmetry breaking correction to the  $0^+ \rightarrow 0^+$  decay rates for a number of  $p$ -,  $sd$ - and  $pf$ -shell emitters, using the nuclear shell-model with isospin-nonconserving (INC) Hamiltonians and realistic WS radial wave functions. Performing large-scale computations beyond the closure approximation, we address the question of convergence of matrix elements of operators as a function of the number of intermediate states. In particular, we test the validity of the separation of  $\delta_C$  into two parts (the isospin-mixing and radial overlap parts) by an exact calculation of the Fermi matrix element for lighter emitters. Investigation of the role of core-excited configurations is in progress and will be published elsewhere.

## 2 Formalism

Within the shell model, the nuclear eigenstates are obtained from diagonalization of an effective one- plus two-body Hamiltonian, in a many-body spherically-symmetric basis (typically, in the harmonic-oscillator basis). The Fermi matrix element can be expressed as a sum over valence space orbitals of one-body transition densities (OBTDs) times single-particle matrix elements of the isospin operator [7–9]:

$$M_F = \langle f | \hat{T}_+ | i \rangle = \sum_{\alpha} \langle f | a_{\alpha_n}^{\dagger} a_{\alpha_p} | i \rangle \langle \alpha_n | \hat{t}_+ | \alpha_p \rangle. \quad (3)$$

Here  $|i\rangle$  and  $|f\rangle$  are initial and final nuclear states obtained from the diagonalization of a shell-model Hamiltonian in a valence space,  $\hat{T}_+ = \sum_k \hat{t}_+(k)$  is the isospin raising operator for valence nucleons,  $a_{\alpha}^{\dagger}$  and  $a_{\alpha}$  are the creation and annihilation operators for neutrons or protons, with  $\alpha = (n_{\alpha}, l_{\alpha}, j_{\alpha}, m_{\alpha})$  denoting a complete set of spherical quantum numbers.

If the nuclear Hamiltonian is isospin-invariant, then the Fermi matrix element given by Eq. (3) reduces to a model-independent isospin-symmetry value,  $M_F^0$ . The absolute value of the realistic Fermi matrix element is slightly smaller than  $|M_F^0|$  because of the violation of the isospin symmetry. Usually two sources of the isospin-symmetry breaking are considered. First, the effective valence-space shell-model Hamiltonian should contain INC terms, such as the Coulomb interaction between protons and charge-dependent terms of nuclear origin. In this case, the initial and final nuclear states, obtained from the shell-model diagonalization in a chosen model space, will not be exactly analogue states. The resulting OBTDs,  $\langle f | a_{\alpha_n}^{\dagger} a_{\alpha_p} | i \rangle$ , will be different from their isospin-symmetry limit, denoted as  $\langle f | a_{\alpha_n}^{\dagger} a_{\alpha_p} | i \rangle^T$ .

Another source of the isospin-symmetry breaking arises from the single-particle matrix element,  $\langle \alpha_n | \hat{t}_+ | \alpha_p \rangle$ , which is just an overlap between a proton and a neutron radial wave functions,

$$\langle \alpha_n | \hat{t}_+ | \alpha_p \rangle = \int_0^\infty R_{k_\alpha, n}(r) R_{k_\alpha, p}(r) r^2 dr = \Omega_{k_\alpha} \equiv \Omega_\alpha, \quad (4)$$

with  $k_\alpha = (n_\alpha, l_\alpha, j_\alpha)$ . If the harmonic-oscillator basis is used, those overlaps are all equal to unity. However, they will differ from unity when the proton and neutron single-particle wave functions are obtained from a realistic single-particle potential with charge-dependent terms. We remark that as soon as we renounce the use of the harmonic-oscillator basis, the most right-hand-side expression for the Fermi matrix element in Eq. (3) becomes approximate in the valence space. As was recalled by Miller and Schwenk [10,11], acting on the single-particle bases, different for protons and neutrons, the exact isospin operator would connect single-particle states from the valence space to those which are outside the valence space. However, an existing calculation for  $^{10}\text{C}$  decay within the No-Core Shell Model [12], which exploits the exact Fermi operator, does not report on essential differences with a phenomenological calculation in the valence space with an approximate isospin operator. As far as no evidence exists on the impact of the exact operator, we follow previous studies [1, 2, 13, 14] and use the standard approximation for the isospin operator, truncating it to a given valence space.

It can be shown [7–9] that within the shell model, the  $\delta_C$  correction can be split into two parts, according to the two sources of the isospin-symmetry breaking mentioned above. Let us denote by  $\Delta_\alpha$  a difference between OBTDs obtained from the INC and the isospin-symmetric shell-model Hamiltonians:

$$\Delta_\alpha = \langle f | a_{\alpha_n}^\dagger a_{\alpha_p} | i \rangle^T - \langle f | a_{\alpha_n}^\dagger a_{\alpha_p} | i \rangle. \quad (5)$$

Then, in the closure approximation, one can express the matrix element  $M_F$  in terms of  $\Delta_\alpha$  and  $\Omega_\alpha$  as

$$\begin{aligned} M_F &= \sum_\alpha (\langle f | a_{\alpha_n}^\dagger a_{\alpha_p} | i \rangle^T - \Delta_\alpha) \Omega_\alpha \\ &= \sum_\alpha (\langle f | a_{\alpha_n}^\dagger a_{\alpha_p} | i \rangle^T - \Delta_\alpha) [1 - (1 - \Omega_\alpha)] \\ &= M_F^0 \left[ 1 - \frac{1}{M_F^0} \sum_\alpha \Delta_\alpha + \frac{1}{M_F^0} \sum_\alpha \Delta_\alpha (1 - \Omega_\alpha) \right. \\ &\quad \left. - \frac{1}{M_F^0} \sum_\alpha \langle f | a_{\alpha_n}^\dagger a_{\alpha_p} | i \rangle^T (1 - \Omega_\alpha) \right]. \quad (6) \end{aligned}$$

Retaining only the leading-order (linear) terms in small terms, we can express  $M_F^2$  as

$$|M_F|^2 = |M_F^0|^2 \left[ 1 - \frac{2}{M_F^0} \sum_\alpha \Delta_\alpha - \frac{2}{M_F^0} \sum_\alpha \langle f | a_{\alpha_n}^\dagger a_{\alpha_p} | i \rangle^T (1 - \Omega_\alpha) + \mathcal{O}(\zeta^2) \right], \quad (7)$$

where  $\zeta$  denotes  $(1 - \Omega_\alpha)$  or  $\Delta_\alpha$ . Comparing Eq. (7) with Eq. (2), we observe that the total correction  $\delta_C$  to a good approximation is given by a sum of two parts,

$$\delta_C = \delta_{IM} + \delta_{RO}, \quad (8)$$

which are the *isospin-mixing* part,

$$\delta_{IM} = \frac{2}{M_F^0} \sum_{\alpha} \Delta_{\alpha}, \quad (9)$$

and the *radial-overlap* part,

$$\delta_{RO} = \frac{2}{M_F^0} \sum_{\alpha} \langle f | a_{\alpha_n}^{\dagger} a_{\alpha_p} | i \rangle^T (1 - \Omega_{\alpha}). \quad (10)$$

Within the closure approximation this separation ansatz is thus almost exact, that can be easily verified numerically. The neglected terms are of the order of the product of two corrections and can be skipped with confidence. However, as we will explain later, in practice, the  $\delta_{RO}$  is evaluated beyond the closure approximation. We discuss this issue in Section 5 and propose a numerical verification of the separation ansatz in small model spaces.

In the present contribution, we summarize results obtained for a series of *p*-, *sd*- and *pf*-shell nuclei,  $^{10}\text{C}$ ,  $^{14}\text{O}$ ,  $^{22}\text{Mg}$ ,  $^{26m}\text{Al}$ ,  $^{26}\text{Si}$ ,  $^{30}\text{S}$ ,  $^{34}\text{Cl}$ ,  $^{34}\text{Ar}$ ,  $^{38m}\text{K}$ ,  $^{38}\text{Ca}$ ,  $^{46}\text{V}$ ,  $^{46}\text{Cr}$ ,  $^{50}\text{Mn}$ ,  $^{50}\text{Fe}$ ,  $^{54}\text{Co}$ ,  $^{54}\text{Ni}$  and  $^{62}\text{Ga}$ . The shell-model calculations have been performed with NuShellX@MSU code [15], using the Cohen–Kurath effective Hamiltonians [16, 17] for  $A = 10, 14$ , the interactions of the ZBM-type [18–20] for  $A = 14, 22$ , USD/USDA/USDB [21, 22] for nuclei with  $26 \leq A \leq 38$ , KB3G [23], GXPF1A [24] and FPD6 [25] for nuclei with  $A = 46, 50, 54$ , and JUN45 [26] and MRG [27] for  $^{62}\text{Ga}$ . There are strong indications [5] that decays of  $A = 38, 42, 46$  have to be considered in the enlarged  $s_{1/2}d_{3/2}f_{7/2}p_{3/2}$  model space. We work on this issue, however, in the present study we present preliminary results for  $A = 38$  from the *sd*-shell and for  $A = 46$  from the *pf*-shell.

The isospin-mixing part of the correction has been obtained from INC versions of the cited above Hamiltonians, as will be described in the next Section. The radial-overlap part has been estimated beyond the closure approximation using thoroughly adjusted WS radial wave functions. Then, we present calculations of  $\delta_C$  obtained directly from the calculation of the Fermi matrix element beyond the closure approximation and confirm the use of the separation ansatz, at least, in small model spaces. In the last Section, we discuss the consistency of our preliminary results with the CVC hypothesis.

### 3 Isospin-mixing correction

To get the isospin-mixing part of the correction,  $\delta_{IM}$ , according to Eq. (9), we have performed calculations with INC Hamiltonians designed for each model space. These Hamiltonians have been constructed using the method worked out in Refs. [28, 29]. One starts from a well-established isospin-conserving Hamiltonian, whose eigenstates form degenerate isobaric multiplets. Then, one introduces an INC term,  $V_{INC}$ , consisting of isovector single-particle energies, the two-body Coulomb interaction between protons and effective two-body charge-symmetry breaking and charge-independence breaking components of nuclear origin. Those two latter terms can be modeled by the Yukawa pion or rho-meson exchange potential or simply by a  $T = 1$  term of the original isospin-conserving Hamiltonian. The resulting  $V_{INC}$  is thus a superposition

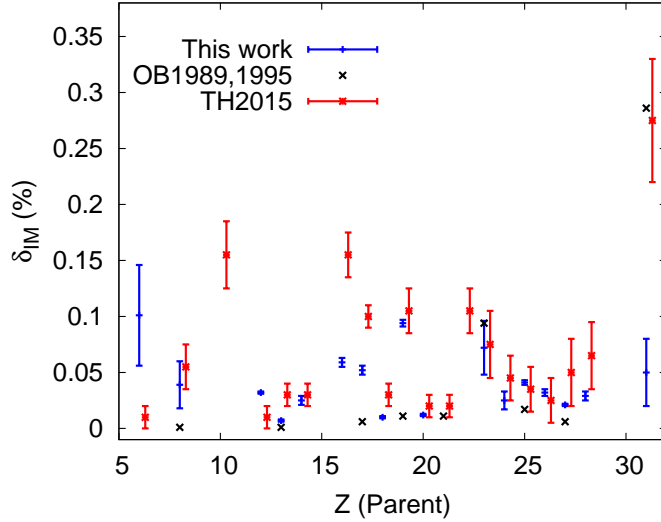


Figure 1: Isospin-mixing part of the correction for selected *sd*- and *pf*-shell nuclei: present results are compared with previous works of Towner and Hardy [2] and Ormand and Brown [14].

of an isoscalar, an isovector and an isotensor operators. Evaluating within perturbation theory the splitting of the isobaric multiplets due to the expectation values of the non-isoscalar terms, one gets for a mass excess an expression quadratic in  $T_z$ , known as the Wigner's isobaric-multiplet mass equation [30]:

$$M(\eta, T, T_z) = a(\eta, T) + b(\eta, T)T_z + c(\eta, T)T_z^2. \quad (11)$$

Here  $\eta = (A, J^\pi, N_{exc}, \dots)$  denotes all other quantum numbers (except for  $T$ ), which are required to label a quantum state of an isobaric multiplet, whereas  $a$ ,  $b$  and  $c$  are coefficients. The unknown strengths of the isovector and isotensor terms are found by a fit to experimental  $b$  and  $c$  coefficients for ground and excited states in a given model space (experimental databases can be found in Refs. [31,32]). Having established the unknown strength parameters, we add  $V_{INC}$  to the original isospin-conserving effective Hamiltonian  $H$ :  $H_{INC} = H + V_{INC}$ . Obviously,  $H_{INC}$  does not commute with the many-body isospin operator anymore. We diagonalize it in the proton-neutron formalism and get states of a slightly mixed isospin.

Since the isospin is not conserved, calculations of  $\beta$ -decays between  $0^+$  isobaric analogue states show that a fraction of the Fermi strength is split among many non-analogue states in the daughter nuclei, producing contributions to  $\delta_C$  from the model space (or  $\delta_{IM}$ ). One can distinguish two main sources of isospin impurities in the parent and daughter states [14]. The first is due to mixing with other non-analogue  $0^+$ ,  $T = 1$  states. Besides, in  $N = Z$  nuclei, high-lying  $0^+$ ,  $T = 0$  states may provide certain admixtures as well. In the first order perturbation theory, the isospin-impurity amplitude is inversely proportional to the energy difference between the two admixed  $0^+$  states,  $\Delta E$ . Therefore, the corresponding contribution to the isospin-mixing correction behaves as  $\sim 1/(\Delta E)^2$ . We estimate the isospin-mixing correction from the splitting of the Fermi states over about 100 excited  $0^+$  states. To improve the accuracy, we scale the theoretical values with experimental energy differences when available (typically, for a few lowest  $0^+$  states).

In the present work we used the charge-dependent versions of the above cited effective Hamiltonians in the  $p$ ,  $p_{1/2}d_{5/2}s_{1/2}$ ,  $sd$ ,  $pf$  and  $f_{5/2}pg_{9/2}$  shell-model spaces from Refs. [14, 15, 28]. The resulting  $\delta_{IM}$  corrections are summarized in Fig. 1 in

Table 1: Preliminary values of  $\delta_{IM}$ ,  $\delta_{RO}$  and  $\delta_C$  with their uncertainties obtained in this work, in comparison with the results of Towner and Hardy from [2, 33]. The present results for  $A = 38$  are obtained in the  $sd$ -shell, while the results for  $A = 46$  are obtained in the  $pf$ -shell.

Parent	This work			Towner, Hardy (2015)		
	$\delta_{IM}(\%)$	$\delta_{RO}(\%)$	$\delta_C(\%)$	$\delta_{IM}(\%)$	$\delta_{RO}(\%)$	$\delta_C(\%)$
$^{10}\text{C}$	0.102 (45)	0.203 (24)	0.304 (51)	0.010 (10)	0.165 (15)	0.175 (18)
$^{14}\text{O}$	0.039 (21)	0.271 (25)	0.309 (33)	0.055 (20)	0.275 (15)	0.330 (25)
$^{22}\text{Mg}$	0.032 ( 1)	0.313 (30)	0.345 (30)	0.010 (10)	0.370 (20)	0.380 (22)
$^{26}\text{Al}$	0.007 ( 1)	0.249 (16)	0.255 (16)	0.030 (10)	0.280 (15)	0.310 (18)
$^{26}\text{Si}$	0.025 ( 4)	0.360 (28)	0.386 (28)	0.030 (10)	0.405 (25)	0.435 (27)
$^{30}\text{S}$	0.059 ( 4)	0.656 (31)	0.715 (31)	0.155 (20)	0.700 (20)	0.855 (28)
$^{34}\text{Cl}$	0.052 ( 4)	0.616 (30)	0.668 (30)	0.100 (10)	0.550 (45)	0.650 (46)
$^{34}\text{Ar}$	0.010 ( 1)	0.662 (52)	0.672 (52)	0.030 (10)	0.665 (55)	0.695 (56)
$^{38}\text{K}$	0.094 ( 3)	0.582 (99)	0.676 (99)	0.105 (20)	0.565 (50)	0.670 (54)
$^{38}\text{Ca}$	0.012 ( 1)	0.773 (83)	0.785 (83)	0.020 (10)	0.745 (70)	0.765 (71)
$^{46}\text{V}$	0.072 (24)	0.338 (46)	0.410 (52)	0.076 (30)	0.545 (55)	0.620 (63)
$^{46}\text{Cr}$	0.025 ( 8)	0.450 (70)	0.475 (70)	0.045 (20)	0.715 (85)	0.760 (87)
$^{50}\text{Mn}$	0.041 ( 2)	0.458 (16)	0.499 (16)	0.035 (20)	0.610 (50)	0.645 (54)
$^{50}\text{Fe}$	0.032 ( 3)	0.428 (76)	0.460 (76)	0.025 (20)	0.635 (45)	0.660 (50)
$^{54}\text{Co}$	0.021 ( 1)	0.632 (72)	0.652 (72)	0.050 (30)	0.720 (60)	0.770 (67)
$^{54}\text{Ni}$	0.029 ( 4)	0.601 (71)	0.629 (72)	0.065 (30)	0.725 (60)	0.790 (67)
$^{62}\text{Ga}$	0.050 (30)	0.961(181)	1.010 (184)	0.275 (55)	1.20 (20)	1.48 (21)

comparison with previous works [2, 14], while the numerical values can be found in Table 1. The uncertainties of our results stem from the use of different INC Hamiltonians for the same nucleus in the same model space. We observe that our results are in agreement with the calculations of Towner and Hardy [2] for a number of  $sd$ - and  $pf$ -shell emitters. The value of  $\delta_{IM}$  for  $^{10}\text{C}$  is much larger in our calculation than that of Towner and Hardy. This comes partly from a larger mixing matrix element and partly from a higher position of the second  $0^+$  state in  $^{10}\text{B}$ . At the same time, our values for  $^{22}\text{Mg}$ ,  $^{26}\text{Al}$  and  $^{62}\text{Ga}$  are much smaller than the results of Towner and Hardy. For the latter one, we exceptionally use the  $pf$  shell for this calculation, because the construction of an accurate INC Hamiltonian in the model space beyond the  $^{56}\text{Ni}$  core is still in progress. We notice that there is an agreement of both results for  $A = 46$  and 50, although we have used the  $pf$ -shell model space, while Towner and Hardy used the  $s_{1/2}d_{3/2}f_{7/2}p_{3/2}$  one.

We conclude by saying that, as seen from Fig. 1,  $\delta_{IM}$  is very sensitive to the details of the shell-model interaction and, in particular, to the charge-dependent term. However, the  $\delta_{IM}$  contribution is no more than 10% to the total correction, and hence it slightly affects final  $\delta_C$  values.

## 4 Radial-overlap correction

The radial overlap correction,  $\delta_{RO}$ , is the major part of the isospin-symmetry breaking correction. To go beyond the closure approximation of Eq. (10), one has to insert the summation over intermediate states in the  $(A - 1)$  nucleus [7, 8],

$$\delta_{RO} = \frac{2}{M_F^0} \sum_{\alpha, \pi} \langle f | a_{\alpha_n}^\dagger | \pi \rangle^T \langle i | a_{\alpha_p}^\dagger | \pi \rangle^T (1 - \Omega_\alpha^\pi), \quad (12)$$

where the matrix elements  $\langle f | a_{\alpha_n}^\dagger | \pi \rangle^T$  and  $\langle i | a_{\alpha_p}^\dagger | \pi \rangle^T$  are related to the spectroscopic amplitudes for the neutron and proton pick-up, respectively. In the angular momentum coupled formalism, we can rewrite this expression as

$$\delta_{RO} = \frac{2}{M_F^0} \sum_{k, \pi} S_{k_n}^{T\pi} S_{k_p}^{T\pi} (1 - \Omega_k^\pi), \quad (13)$$

with  $k \equiv k_\alpha$  for simplicity and

$$S_{k_n}^{T\pi} = \frac{\langle \Psi(A) J_f | a_{k_n}^\dagger | \Psi(A-1) J_\pi \rangle^T}{\sqrt{2J_f + 1}}, \quad S_{k_p}^{T\pi} = \frac{\langle \Psi(A) J_i | a_{k_p}^\dagger | \Psi(A-1) J_\pi \rangle^T}{\sqrt{2J_f + 1}}.$$

Again, the label  $T$  means that the nuclear eigenstates  $\Psi(A)$  and  $\Psi(A-1)$  are obtained in the isospin-symmetry limit. The radial integrals  $\Omega_{k_\alpha}^\pi \equiv \Omega_k^\pi$  depend on  $\pi$  via

$$\Omega_k^\pi = \int_0^\infty R_{k_n}^\pi(r) R_{k_p}^\pi(r) r^2 dr. \quad (14)$$

The notations  $R_k^\pi(r)$  means that these radial wave functions are extracted from a potential for which one nucleon separation energies correspond to  $S_p + E_\pi$ . Thus, for each excitation energy  $E_\pi$  we fit the potential in order to reproduce experimental proton and neutron separation energies separately. For every transition, we take up to 200 excited states of each spin and parity of the intermediate nucleus and check that the  $\delta_{RO}$  is well converged. We also remark that the summation in Eq. (13) is incoherent, thus the consistency of signs of the spectroscopic amplitudes is very important.

In our study, we have explored two different parameterizations of the WS potential: one being close to that of Ref. [34] ( $BM_m$ ), while the other, referred to as SWV, being based on Ref. [35]. The details of these parameterizations and the role of each term are discussed extensively in Refs. [4, 9]. Briefly speaking, we use the WS potential of the standard form,

$$V(r) = V_0 f(r, R_0, a_0) + V_s \left( \frac{r_s}{\hbar} \right)^2 \frac{1}{r} \frac{d}{dr} [f(r, R_s, a_s)] (\mathbf{l} \cdot \boldsymbol{\sigma}) + V_c(r), \quad (15)$$

where

$$f(r, R_i, a_i) = \frac{1}{1 + \exp\left(\frac{r-R_i}{a_i}\right)}, \quad (16)$$

with  $i$  denoting either 0 for the central term or  $s$  for the spin-orbit term. The radius is modeled in a standard way as  $R_i = r_i(A-1)^{1/3}$ , while the diffuseness parameters,  $a_i$ , are kept fixed. In general, the spin-orbit length parameter,  $r_s$ , is smaller than

that of the volume term,  $r_0$ , because of a very short range of the two-body spin-orbit interaction [34]. The one-body Schrödinger equation is solved in relative coordinates for a particle of mass  $\mu = m(A-1)/A$ , where  $m$  is the nucleon mass and  $A$  is the mass number of the composite nucleus. The isovector terms of the WS potential, which provide the difference between the proton and neutron wave functions, are most crucial for the radial-overlap correction. Their global parameterization is not accurate enough. This is why we consider only the Coulomb term, while all other possible isovector contributions are taken into account by adjustment of a specific potential parameter (a potential depth or a surface term) to match either the proton or the neutron separation energy. The Coulomb radius parameter is related to the root-mean-charge radius of the parent nucleus. The WS length parameter is varied to insure that the charge density constructed from the proton radial wave functions yields a root-mean-charge radius in agreement with the experimental value measured by the electron scattering [36] or by the isotope-shift estimation [37].

Contrary to all previous works, we have calculated the nuclear radii beyond the closure approximation [4, 9]. The square of the charge radius (relative to the inert core) is given by the expectation value of the operator  $r_{sm}^2$  in the ground state of the parent nucleus:

$$\langle r^2 \rangle_{sm} = \langle i | r_{sm}^2 | i \rangle = \frac{1}{Z} \sum_{\alpha} \langle \alpha_p | r^2 | \alpha_p \rangle \langle i | a_{\alpha_p}^\dagger a_{\alpha_p} | i \rangle. \quad (17)$$

Inserting the complete sum over intermediate states  $\sum_{\pi} |\pi\rangle \langle \pi|$  into this equation, we convert the proton occupation numbers,  $\langle i | a_{\alpha_p}^\dagger a_{\alpha_p} | i \rangle$ , into a sum of the spectroscopic factors over intermediate states. Taking into account that the radial wave functions depend on  $\pi$ , we get the following expression:

$$\langle r^2 \rangle_{sm} = \frac{1}{Z} \sum_{\alpha, \pi} \langle i | a_{\alpha_p}^\dagger | \pi \rangle^2 \langle \alpha_p | r^2 | \alpha_p \rangle^{\pi}, \quad (18)$$

with the single-particle matrix element being

$$\langle \alpha_p | r^2 | \alpha_p \rangle^{\pi} = \int_0^{\infty} r^4 |R_{k_p}^{\pi}(r)|^2 dr. \quad (19)$$

The convergence of the expression (18) is quite fast. We found out that it results in slightly smaller values of the charge radii, requiring thus larger values of the length parameter  $r_0$ .

The adjustment procedure can be summarized as follows. For a given value of  $a$ , we vary two parameters, the potential depth  $V_0$  and the length parameter,  $r_0$ , in a way to reproduce known experimental observables — the one-nucleon separation energies and the radius of the parent nucleus. The fit is performed either by a modification of the central part depth  $V_0$  or by an addition of a separate surface term,

$$V_g(r) = \left( \frac{\hbar}{m_{\pi} c} \right)^2 \frac{V_g}{a_s r} \exp\left( \frac{r - R_s}{a_s} \right) [f(r, R_s, a_s)]^2, \quad (20)$$

and by a modification of the  $V_g$  parameter. As we have found out for the  $sd$  shell [4], the procedure involving the variation of  $V_0$  removes essentially the dependence on a particular parameterization: the  $BM_m$  and SWV results are very similar. The fit of

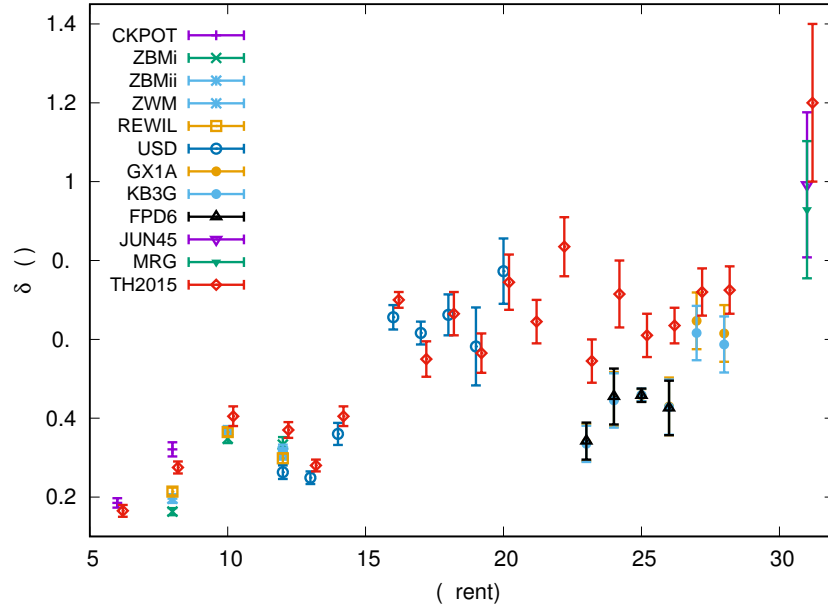


Figure 2: Radial-overlap corrections obtained from the shell model with WS radial wave functions ( $BM_m$  parameterizations). The results of Towner and Hardy [37] are shown for comparison.

the surface term results in larger differences between the results from two parameterizations and we keep this in our analysis. Figure 2 shows our results for  $\delta_{RO}$  obtained in the  $p$ ,  $p_{1/2}d_{5/2}s_{1/2}$ ,  $sd$ ,  $pf$  and  $f_{5/2}pg_{9/2}$  shell-model spaces, being the average from  $BM_m$  and SWV parameterizations and two different methods of the fit (volume or surface term). For comparison we show the latest calculations of Towner and Hardy [2,5]. Again, our  $sd$ -shell values for  $A = 26, 30$  and  $34$  are in a good agreement with the results of Ref. [2]. The values obtained for  $A = 38$  look to be close to the values of Towner and Hardy, however, we should remember that our calculation uses a small  $sd$ -shell model space. We also remark that Towner and Hardy [5] used different model spaces for  $A = 46$  and  $50$ , which causes major differences in these cases (our  $pf$ -shell values are systematically smaller). We remark that three different  $pf$ -shell interactions, KB3G, GX1A and FPD6, give almost identical values for  $A = 46$  and  $50$ . Calculations for  $A = 38, 42$  and  $46$  in the model space around  $^{40}\text{Ca}$  are in progress and will be published elsewhere. The dominant part of the uncertainty is systematic due to experimental uncertainties of nuclear radii (see Ref. [4] for details). The use of different shell-model interactions for a given model space is considered as a source of statistical uncertainty. Its contribution is minor. It is seen that, except for a few cases, our uncertainties are similar to those deduced by Towner and Hardy.

## 5 Beyond the separation ansatz

In this section we present calculations of the nuclear structure correction without the separation ansatz. First, let us derive the expression for the  $\delta_C$  beyond the

closure approximation. In this case, the summation over intermediate states has to be included in the expression of the Fermi matrix element,

$$M_F = \sum_{\alpha} \langle f | a_{\alpha_n}^{\dagger} a_{\alpha_p} | i \rangle \langle \alpha_n | \hat{t}_+ | \alpha_p \rangle = \sum_{\alpha} \sum_{\pi} \langle f | a_{\alpha_n}^{\dagger} | \pi \rangle \langle i | a_{\alpha_p}^{\dagger} | \pi \rangle \Omega_{k\alpha}^{\pi}. \quad (21)$$

In the  $J$ -coupled form, this expression becomes

$$M_F = \sum_{k,\pi} S_{k_p}^{\pi} S_{k_n}^{\pi} \Omega_k^{\pi}. \quad (22)$$

Denoting the deviations of the spectroscopic amplitudes from their isospin-symmetry limits as

$$S_{k_p}^{T\pi} - S_{k_p}^{\pi} = D_{k_p}^{\pi}, \quad (23)$$

$$S_{k_n}^{T\pi} - S_{k_n}^{\pi} = D_{k_n}^{\pi}, \quad (24)$$

we can rewrite the Fermi matrix element as

$$M_F = \sum_{k,\pi} \left( S_{k_p}^{T\pi} - D_{k_p}^{\pi} \right) \left( S_{k_n}^{T\pi} - D_{k_n}^{\pi} \right) [1 - (1 - \Omega_k^{\pi})] \quad (25a)$$

$$= \sum_{k,\pi} \left[ \underbrace{S_{k_p}^{T\pi} S_{k_n}^{T\pi}}_{M_F^0} - \underbrace{S_{k_p}^{T\pi} S_{k_n}^{T\pi} (1 - \Omega_k^{\pi})}_{O(\zeta)} - \underbrace{\left( S_{k_p}^{T\pi} S_{k_n}^{T\pi} - S_{k_p}^{\pi} S_{k_n}^{\pi} \right)}_{O(\zeta)} \right] \quad (25b)$$

$$+ \left[ \underbrace{\left( S_{k_p}^{T\pi} D_{k_n}^{\pi} + S_{k_n}^{T\pi} D_{k_p}^{\pi} \right) (1 - \Omega_k^{\pi})}_{O(\zeta^2)} - \underbrace{D_{k_p}^{\pi} D_{k_n}^{\pi} (1 - \Omega_k^{\pi})}_{O(\zeta^3)} \right]. \quad (25c)$$

Line (25b) contains the Fermi matrix element in the isospin-symmetry limit and leading-order (linear) contributions to the correction  $\delta_C$  expressed by  $\delta_{RO} + \delta_{IM}$ , while the terms shown on line (25c) represent the corrections of the second and third orders. Again, we can wish to keep only linear terms in small quantities and therefore to use an approximate expression:

$$M_F = M_F^0 \left[ 1 - \frac{1}{M_F^0} \sum_{k,\pi} \left( S_{k_p}^{T\pi} S_{k_n}^{T\pi} - S_{k_p}^{\pi} S_{k_n}^{\pi} \right) - \frac{1}{M_F^0} \sum_{k,\pi} S_{k_p}^{T\pi} S_{k_n}^{T\pi} (1 - \Omega_k^{\pi}) + O(\zeta^2) \right]. \quad (26)$$

Taking this expression squared, we get

$$|M_F|^2 = |M_F^0|^2 \left[ 1 - \frac{2}{M_F^0} \sum_{k,\pi} \left( S_{k_p}^{T\pi} S_{k_n}^{T\pi} - S_{k_p}^{\pi} S_{k_n}^{\pi} \right) - \frac{2}{M_F^0} \sum_{k,\pi} S_{k_p}^{T\pi} S_{k_n}^{T\pi} (1 - \Omega_k^{\pi}) + O(\zeta^2) \right]. \quad (27)$$

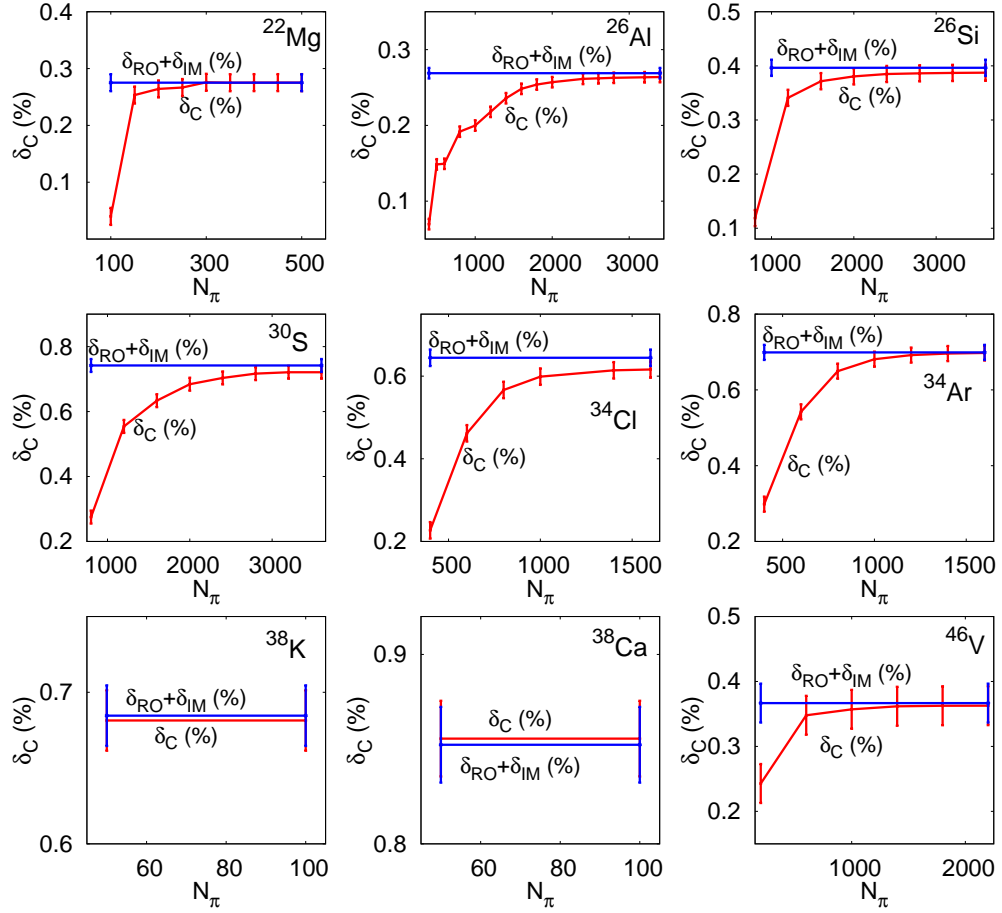


Figure 3: The isospin-symmetry breaking correction obtained from the exact calculation,  $\delta_C$ , and from the sum  $\delta_{IM} + \delta_{RO}$  as a function of the number of intermediate states of each angular momentum and parity.

Again, we observe that the correction splits into two parts,  $\delta_C \approx \delta_{IM} + \delta_{RO}$ , with  $\delta_{RO}$  defined by Eq. (13) and the isospin-mixing part given by Eq. (9), which we can rewrite as

$$\delta_{IM} = \frac{2}{M_F^0} \sum_{k,\pi} \left( S_{k_p}^{T\pi} S_{k_n}^{T\pi} - S_{k_p}^\pi S_{k_n}^\pi \right). \quad (28)$$

Although the approximation seems to be good, we have performed the exact calculation of the Fermi matrix element using Eq. (21) and compared between the result and the approximation given by the sum  $\delta_{IM} + \delta_{RO}$ . The expression in Eq. (21) converges very slowly as a function of the number of intermediate states  $\pi$ : up to a few thousand intermediate states are often required, which is not easily doable in large model spaces. Thus, we have used for verification only the *sd*-shell emitters and  $^{46}\text{V}$  in the *pf*-shell. Figure 3 shows the values of  $\delta_C$  from the exact calculation of the Fermi matrix element and from the separation ansatz according to Eq. (27) as a function of the number of intermediate states of each angular momentum and parity. We remark

that, while the  $\delta_{IM} + \delta_{RO}$  is converged when about 100 intermediate states are used, to get the  $\delta_C$  converged we need at least 2000 excited states for nuclei from the middle of the  $sd$  shell. The results shown in Fig. 3 are obtained from the INC version of USD (for the  $sd$ -shell emitters) and the INC version of GXPF1A for  $A = 46$  [15], but we checked that the results are similar for other interactions in the same model spaces. Uncertainties correspond to the systematic errors due to experimental uncertainties of the measured charge radii. For all cases considered, it is seen that the separation ansatz represents a robust approximation to the exact value of  $\delta_C$ .

At the same time, the intermediate state procedure has still to be checked on the effect of orthogonality of the single-particle states, as well as possible center-of-mass contributions. These are open problems to be addressed in future.

## 6 Consistency with the CVC hypothesis

Our preliminary  $\delta_C$  values obtained by now are summarized in Table I and can be also found in Fig. 4 in comparison with the latest results by Towner and Hardy [2].

To estimate the quality of our preliminary results, we perform the confidence-level test proposed recently by Towner and Hardy [38]. Based on the assumption that the CVC hypothesis is valid to at least  $\pm 0.03\%$  and adopting the values of  $ft$ ,  $\delta'_R$ ,  $\delta_{NS}$  from Ref. [2], we check whether our set of corrections produce a statistically consistent set of  $\mathcal{F}t$  values.

If we assume that the CVC hypothesis is satisfied ( $\mathcal{F}t$  is constant), without regarding the CKM unitarity, we can convert the experimental  $ft$  values into experimental values for structure-dependent corrections and compare the results of the calculation. Defining pseudo-experimental values of the isospin-symmetry breaking correction as

$$\delta_C^{exp} = 1 + \delta_{NS} - \frac{\mathcal{F}t}{ft(1 + \delta'_R)}, \quad (29)$$

we can test a set of  $\delta_C$  for  $N$  superallowed transitions, using the method of least squares with  $\mathcal{F}t$  as the adjustable parameter. To characterize the quality of the fit,

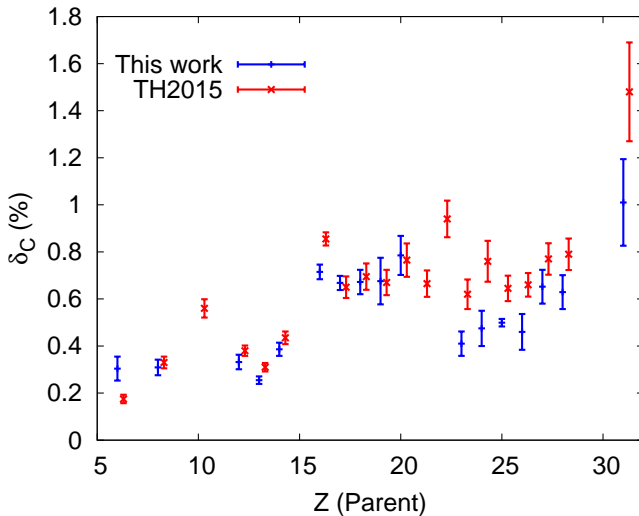


Figure 4: Isospin-symmetry breaking correction obtained from the INC shell-model with WS radial wave functions. The results of Towner and Hardy [2] are shown for comparison.

we use the optimized value for  $\chi^2/\nu$  ( $\nu = N - 1$ ):

$$\chi^2/\nu = \frac{1}{N-1} \sum_{i=1}^N \frac{[\delta_C(i) - \delta_C^{exp}]^2}{\sigma_i^2}. \quad (30)$$

In the present test we consider 10 transitions:  $^{10}\text{C}$ ,  $^{14}\text{O}$ ,  $^{22}\text{Mg}$ ,  $^{26m}\text{Al}$ ,  $^{26}\text{Si}$ ,  $^{34}\text{Cl}$ ,  $^{34}\text{Ar}$ ,  $^{50}\text{Mn}$ ,  $^{54}\text{Co}$  and  $^{62}\text{Ga}$ . An improved measurement of the branching ratio of  $^{26}\text{Si}$  decay has been reported recently [39], resulting in  $ft = 3051.5(57)$  s, so we have included this transition in our analysis. However, we do not use our preliminary *sd*-shell results for  $A = 38$  and *pf*-shell results for  $A = 46$ , since those decays should be evaluated in a more adequate *sdpf* shell-model space. The obtained optimized value of  $\chi^2/\nu = 1.75$  is encouraging and the corresponding  $\mathcal{F}t = 3074.0$  sec is in fair agreement with the latest evaluation by Towner and Hardy [2]. A more complete comparison will be done when we get results for all of 14 best known emitters.

## 7 Conclusions

In this contribution we present new shell-model calculations of the isospin-symmetry breaking correction to the superallowed  $0^+ \rightarrow 0^+$   $\beta$ -decay. The main goal of our study is to reexamine the previous work within the nuclear shell model making advantage of the remarkable progress in the state-of-the-art description of nuclear properties within a large-scale diagonalization technique. We find that the isospin-mixing part of the correction is very sensitive to a particular parameterization of the charge-dependent term of the Hamiltonian. However, representing a small part of the correction, it does not affect much the final values. The radial-overlap part of the correction is the dominant part. We have performed calculations for 13 emitters from *p*,  $p_{1/2}sd_{5/2}$ , *sd*, *pf* and  $f_{5/2}pg_{9/2}$  model spaces without truncations and taking into account up to 200 excited states of each relevant spin and parity of the intermediate nucleus. Two different parameterizations of a spherical WS potential have been investigated. Our adjustment procedure, relying on the experimental nuclear radii and nucleon separation energies, largely removes the dependence of the results on the WS potential parameters. The calculation of nuclear radii have been performed beyond the closure approximation. In general, the results stay consistent with previous studies, although the final  $Ft$  value may deviate from the presently accepted value. A further work on nuclei of the masses  $A = 38, 42, 46, 74$  is needed to accomplish the study.

The preliminary implications of our new results for electroweak tests lead to a slightly different average  $Ft$  value with an overall good agreement with CVC. Calculations for a larger set of emitters are in progress.

## Acknowledgments

We are grateful to B. A. Brown for providing us with the NuShellX@MSU shell-model code, we thank M. Bender for numerous enlightening discussions and B. Blank for his motivating interest to this study and clarification of experimental aspects of the measurements under consideration, as well as for his comments on the present manuscript. L. Xayavong thanks CENBG for the hospitality and financial support during his 3-week stay. The work is supported by IN2P3/CNRS, France, in the

framework of the “Isospin-symmetry breaking” project. Large-scale calculations have been performed at Mésocentre de Calcul Intensif Aquitain (MCIA), Bordeaux.

## References

- [1] I. S. Towner and J. C. Hardy, Rep. Prog. Phys. **74**, 046301 (2010).
- [2] J. C. Hardy and I. S. Towner, Phys. Rev. C **91**, 025501 (2015).
- [3] O. Naviliat-Cuncic and N. Severijns, Phys. Rev. Lett. **102**, 142302 (2009).
- [4] L. Xayavong and N. A. Smirnova, Phys. Rev. C **97**, 024324 (2018).
- [5] I. S. Towner and J. C. Hardy, Phys. Rev. C **77**, 025501 (2008).
- [6] C.-Y. Seng, M. Gorchtein, H. H. Patel and M. Ramsey-Musolf, Phys. Rev. Lett. **121**, 241804 (2018).
- [7] I. S. Towner, J. C. Hardy, M. Harvey, Nucl. Phys. A **284** 269 (1977).
- [8] W. E. Ormand and B. A. Brown, Nucl. Phys. A **440**, 274 (1985).
- [9] L. Xayavong, Ph. D. thesis, University of Bordeaux, Bordeaux, 2016.
- [10] G. A. Miller and A. Schwenk, Phys. Rev. C **78**, 035501 (2008).
- [11] G. A. Miller and A. Schwenk, Phys. Rev. C **80**, 064319 (2009).
- [12] E. Caurier, P. Navrátil, W. E. Ormand and J. P. Vary, Phys. Rev. C **66**, 024314 (2002).
- [13] W. E. Ormand and B. A. Brown, Phys. Rev. Lett. **62**, 866 (1989).
- [14] W. E. Ormand and B. A. Brown, Phys. Rev. C **52**, 2455 (1995).
- [15] B. A. Brown and W. D. M. Rae, Nucl. Data Sheets **120**, 115 (2014).
- [16] S. Cohen and D. Kurath, Nucl. Phys. **73**, 1 (1965).
- [17] S. Cohen and D. Kurath, Nucl. Phys. **101**, 1 (1967).
- [18] A. P. Zuker, B. Buck and McGrory, Phys. Rev. Lett. **21**, 39 (1968).
- [19] A. P. Zuker, Phys. Rev. Lett. **23**, 983 (1969).
- [20] B. S. Reehal and B. H. Wildenthal, Part. Nucl. **6**, 137 (1973).
- [21] B. H. Wildenthal, Prog. Part. Nucl. Phys. **11**, 5 (1984).
- [22] B. A. Brown and W. A. Richter, Phys. Rev. C **74**, 034315 (2006).
- [23] A. Poves, J. Sánchez-Solano, E. Caurier and F. Nowacki, Nucl. Phys. A **694**, 157 (2001).
- [24] M. Honma, T. Otsuka, B. A. Brown and T. Mizusaki, Phys. Rev. C **69**, 034335 (2004).

- 
- [25] W. A. Richter, M. G. van der Merwe, R. E. Julies and B. A. Brown, Nucl. Phys. A **523**, 325 (1990).
- [26] M. Honma, T. Otsuka, T. Mizusaki and M. Hjorth-Jensen, Phys. Rev. C **80**, 064323 (2009).
- [27] E. Caurier, F. Nowacki, A. Poves and J. Retamosa, Phys. Rev. Lett. **77**, 1954 (1996).
- [28] W. E. Ormand and B. A. Brown, Nucl. Phys. A **491**, 1 (1989).
- [29] Y. H. Lam, N. A. Smirnova and E. Caurier, Phys. Rev. C **87**, 054304 (2013).
- [30] E. P. Wigner, in *Proc. of the Robert A. Welch Foundation Conf. on Chemical Research, 1957*, ed. W. O. Milligan. Welch Foundation, Houston, 1958, Vol. 1, p. 86.
- [31] Y. H. Lam, B. Blank, N. A. Smirnova, J. B. Bueb and M. S. Antony, At. Data Nucl. Data Tables **99**, 680 (2013).
- [32] M. MacCormick and G. Audi, Nucl. Phys. A **925**, 61 (2014).
- [33] I. S. Towner and J. C. Hardy, Phys. Rev. C **92**, 055505 (2015).
- [34] A. Bohr and B. R. Mottelson, *Nuclear structure, vol. 1*. W. A. Benjamin, 1969.
- [35] N. Schwierz, I. Wiedenhöver and A. Volya, arXiv:0709.3525 [nucl-th] (2007).
- [36] I. Angeli and K. P. Marinova, At. Data Nucl. Data Tables **99**, 69 (2013).
- [37] I. S. Towner and J. C. Hardy, Phys. Rev. C **66**, 035501 (2002).
- [38] I. S. Towner and J. C. Hardy, Phys. Rev. C **82**, 065501 (2010).
- [39] M. Bencomo *et al.*, Phys. Rev. C **100**, 015503 (2019).

# Symmetry-Adapted No-Core Shell-Model Calculations for Probing the Structure of Atomic Nuclei

J. P. Draayer<sup>a</sup>, K. D. Launey<sup>a</sup>, T. Dytrych<sup>a,b</sup>, R. B. Baker<sup>a</sup>,  
A. C. Dreyfuss<sup>a</sup>, D. Kekejian<sup>a</sup> and G. H. Sargsyan<sup>a</sup>

<sup>a</sup>*Department of Physics and Astronomy, Louisiana State University, Baton Rouge, LA 70803-4001, USA*

<sup>b</sup>*Nuclear Physics Institute, 250 68 Řež, Czech Republic*

## Abstract

The use of symmetries to unmask simplicity within complexity in atomic nuclei is examined within its historical context and the evolving *ab initio* no-core shell model (NCSM) approaches that typically rely heavily on high-performance computing and applied math methods. Some examples — old and new — that demonstrate the important role symmetries plays in this evolution, are noted. Further, an extension of the symmetry adapted no-core shell model (SA-NCSM), one that incorporates deformation from the onset, is proffered as a potential path forward for further reducing the combinatorial growth of model-space sizes that are required to track collective phenomena in a non-deformed theory. This feature suggests a means for extending *ab initio* methods to even heavier nuclei.

**Keywords:** *Ab initio theory; no-core shell model (NCSM); symmetry-adapted NCSM; symplectic model; deformed configurations; many-particle Nilsson model*

## 1 Introduction

This contribution is organized into five sections: 1) A short ‘Introduction’ (i. e., this paragraph) that lays out the structure of this report, 2) A brief ‘Historical overview’ of efforts — old and new — focused on expanding shell-model spaces to reproduce collective and clustering features (principal co-author A. Dreyfuss), 3) Some recent ‘Exemplary results’ which show that special symmetries can be used to tame the combinatorial growth of NCSM model spaces while extending their reach, and to reproduce observed enhanced  $B(E2)$  transition strengths without the use of effective charges (principle co-authors R. Baker and G. Sargsyan), 4) How ‘Canonical transformations’ from non-deformed to deformed many-particle configurations that preserve these special symmetries can be used to gain further reductions in model space sizes — essentially an interacting many-particle Nilsson model (principal co-author D. Kekejian), and 5) A ‘Conclusion’ that looks beyond the current landscape to more novel

---

*Proceedings of the International Conference ‘Nuclear Theory in the Supercomputing Era — 2018’ (NTSE-2018), Daejeon, South Korea, October 29 – November 2, 2018, eds. A. M. Shirokov and A. I. Mazur. Pacific National University, Khabarovsk, Russia, 2019, p. 279.*

<http://www.ntse.khb.ru/files/uploads/2018/proceedings/Draayer.pdf>.

notions that just as special symmetries carry one from the NCSM to its symmetry-adapted extension, SA-NCSM, should enable use of *ab initio* methods in studies of heavier nuclei.

## 2 Historical overview

The independent-particle model of Mayer and Jensen [1, 2], with its reproduction of the ‘magic’ numbers of nuclei, can arguably be called the first microscopic theory of nuclear structure. Its success inspired the development of various follow-on models of increasing levels of sophistication across the second half of the last century. However, testing these theories against experimental data was limited by meager computational resources, up until about the last decade or so of that period. The advent of truly high-performance computational resources in the 90s enabled the development and testing of so-called no-core shell model (NCSM) concepts [3, 4] (see, e. g., Refs. [5–7]), which to date have been used to describe the structure of low-lying states of *s*- and *p*-shell nuclei, starting from *ab initio* principles.

The NCSM preserves exact symmetries like time reversal invariance, parity conservation, and translational invariance within an overarching many-particle framework that respects particle number conservation and statistics; that is, the NCSM is a fully microscopic many-fermion theory of nuclear structure that uses realistic interactions between and among nucleons that reside in properly anti-symmetrized bases states built from single-particle states of the three-dimensional harmonic oscillator (3D-HO), where the energy scale of the latter is set by the  $\hbar\Omega$  parameter of the oscillator.

Within the NCSM framework, the complete model space is organized into the horizontal slices of the HO, each separated in energy from its neighbors by  $\hbar\Omega$ , with interactions among particles within a slice as well as between particles in neighboring slices accounted for, up to some  $N_{\max}$  cutoff which is the maximum total number of oscillator quanta above the lowest HO configuration for a given nucleus, thereby reducing the infinite model space to a truncated subspace of the full space, one capped by the  $N_{\max}\hbar\Omega$  cutoff limit imposed on the theory. In the  $N_{\max}\hbar\Omega \rightarrow \infty$  limit, the theory encompasses the entire shell-model space.

While the independent-particle model approach was being developed, there was a complementary push towards models that describes the observed strongly collective features found in nuclei. Some notable early models that reproduce collective features are the Bohr–Mottelson Model (BMM) for collective nuclear motion [8], the Geometrical Collective Model (GCM) of the Greiner school [9, 10], and of particular relevance to this report, the Elliott SU(3) Model [11, 12]. Specifically, the Elliott model captures the importance of the SU(3) symmetry in describing — from a microscopic perspective — the deformed structures in light to intermediate-mass nuclei. A similar approach using pseudo-spin symmetry and its pseudo-SU(3) complement has been used to describe deformation in the upper *pf* and lower *sdg* shells, and in particular, in strongly deformed nuclei of the rare-earth and actinide regions [13], as well as in many other studies (e. g., see Ref. [14]). The collective symplectic model developed by Rowe and Rosensteel [15, 16], with the  $\text{Sp}(3, \mathbb{R})$  underpinning symmetry, intersects with these collective approaches. In one limit, the symplectic model can be shown to be a microscopic realization of the Bohr–Mottelson theory, and, in another, a multi-shell generalization of the Elliott model, with SU(3) being a subgroup of  $\text{Sp}(3, \mathbb{R})$ .

**First-principles SA-NCSM** — Building on the foundations of particle-driven models, such as the NCSM, and the use of symmetries to reproduce collectivity, as in the collective symplectic model, the *ab initio* symmetry-adapted no-core shell model (SA-NCSM) is a no-core shell model with a symmetry-adapted basis that is either  $SU(3)$ -coupled or  $Sp(3, \mathbb{R})$ -coupled. In the  $SU(3)$ -coupled realization, basis states are organized with respect to the physically relevant, deformation-related  $SU(3)_{(\lambda\mu)} \supset^{\kappa} SO(3)_L$  subgroup chains. In a given complete  $N_{\max}$  model space, results for the SA-NCSM and NCSM coincide exactly, for the same interaction. The use of symmetries to guide SA-NCSM model space selection allows for the consideration of only the most physically-relevant subspace of a complete  $N_{\max}$  model space. The SA-NCSM uses a very general intrinsic non-relativistic Hamiltonian

$$H = T_{\text{rel}} + V_{\text{NN}} + V_{3\text{N}} + \dots + V_{\text{Coul}}, \quad (1)$$

where  $T_{\text{rel}}$  is the relative kinetic energy, and the nucleon-nucleon,  $V_{\text{NN}}$ , and possibly 3-nucleon,  $V_{3\text{N}}$ , interactions are included along with the Coulomb interaction,  $V_{\text{Coul}}$ , between the protons.

First-principles studies of  $p$ -shell nuclei computed in the *ab initio* SA-NCSM show the emergence of a simple pattern that favors large deformation and low spin (Fig. 1). For example, the SA-NCSM wave function for the  $1^+$  ground state of  ${}^6\text{Li}$  computed in an  $N_{\max} = 10$  model space with the bare JISP16 nucleon-nucleon ( $NN$ ) interaction is dominated by the deformed  $0\hbar\Omega (2\ 0)$  irreducible representation (irrep) and its symplectic excitations (e. g.,  $2\hbar\Omega (4\ 0)$ ,  $4\hbar\Omega (6\ 0)$ , etc.). This pattern is seen in studies of other  $p$ -shell nuclei, including  ${}^6\text{He}$ ,  ${}^8\text{Be}$ , and  ${}^{12}\text{C}$ , using various realistic  $NN$  interactions, including chiral interactions. This universality of this emergent feature underlines the importance of the  $SU(3)$  and  $Sp(3, \mathbb{R})$  symmetries in describing nuclear structure.

**No-core Symplectic Shell Model (NCSpM)** — The symplectic  $Sp(3, \mathbb{R})$  symmetry applied in a microscopic framework is directly related to the particle position and momentum coordinates, and naturally describes rotations and vibrations of an equilibrium deformation [17, 18]. By exploiting this emergent symmetry, the microscopic no-core symplectic shell model (NCSpM) [19] makes use of a schematic interaction to approach model spaces beyond what is currently within reach of *ab initio* theories. The NCSpM is a fully microscopic no-core shell model based on the physically relevant symplectic  $Sp(3, \mathbb{R})$  group [15, 16] and its  $SU(3)$  subgroup [11, 12, 20]. In the same complete  $N_{\max}$  model space and using the same interaction, the NCSM and NCSpM results are identical. In analogy to the NCSM horizontal slices of the complete model space, the NCSpM organizes the complete space into a series of vertical ‘cones’ within the HO well, which are irreps of  $Sp(3, \mathbb{R})$ , included up to some  $N_{\max}$ . Each of these irreps described a single equilibrium deformation and its rotations and vibrations. By including only a few of these cones, the model space is greatly reduced, which allows extension to higher  $N_{\max}$  model spaces beyond the current NCSM limits, giving access to the spaces needed to probe clustering in nuclei.

The microscopic NCSpM uses a many-body Hamiltonian that includes a collective piece that enters through the quadrupole-quadrupole interaction, as described in Ref. [19, 21]:

$$H = T_{\text{rel}} + V_{\text{NN}} + V_{\text{mN}}^{\text{eff}} + \dots + V_{\text{Coul}}. \quad (2)$$

The  $V_{\text{NN}}$  is taken to be the bare JISP16 nucleon-nucleon interaction, which is turned

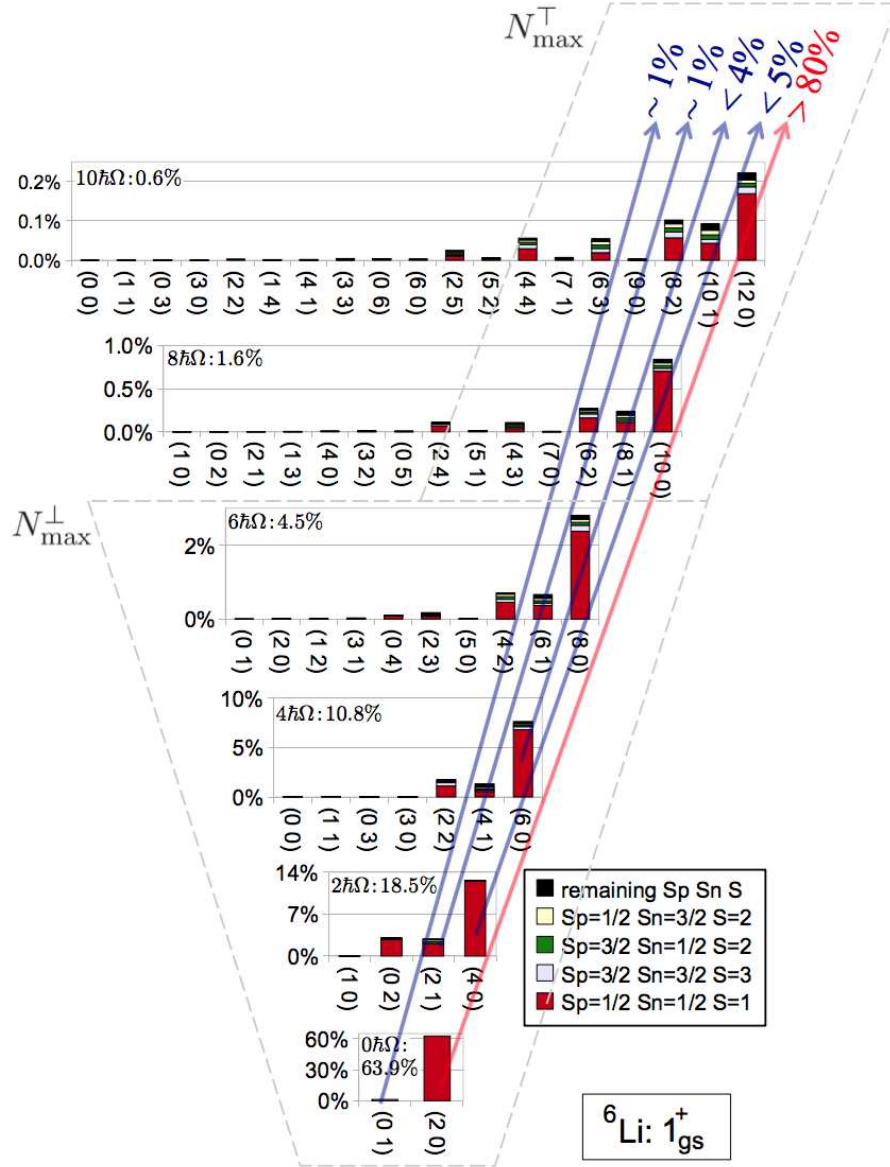


Figure 1: Probability distributions for proton, neutron, and total intrinsic spin components ( $S_p S_n S$ ) across the Pauli-allowed deformation-related ( $\lambda\mu$ ) values for the  $1^+$  ground state of  ${}^6\text{Li}$ , calculated in 12 HO shells with the JISP16 bare interaction ( $\hbar\Omega = 20$  MeV). The most deformed configurations ( $\lambda\mu$ ) are at the right of each HO shell subspace, where the strengths are concentrated indicating the dominance of collectivity. A symmetry-guided model-space selection takes advantage of this emergent property by including the full space up through  $N_{\text{max}}^\perp$ , but then selecting a subset of configurations with high deformation and low spin up through  $N_{\text{max}}^\top$ . A model space constructed in this way is labeled  $\langle N_{\text{max}}^\perp \rangle N_{\text{max}}^\top$ . The projection onto symplectic vertical slices (with probability  $\geq 1\%$ ) is schematically illustrated by arrows and clearly reveals the preponderance of a single symplectic irrep. Adapted from Ref. [17].

on only among bandheads of symplectic irreps, introducing horizontal mixing of all the states (up through the  $N_{\max}$  cutoff) within the symplectic vertical slices. The effective many-nucleon interaction is taken to be  $V_{\text{mN}}^{\text{eff}} = \sum_{i=1}^A \frac{m\Omega^2 \mathbf{r}_i^2}{2} + \frac{\chi}{2} \frac{(e^{-\gamma(Q \cdot Q)} - 1)}{\gamma}$ . The symplectic  $\text{Sp}(3, \mathbb{R})$  symmetry is preserved by the HO potential and  $T_{\text{rel}}$ , and the important quadrupole-quadrupole interaction  $\frac{1}{2} Q \cdot Q = \frac{1}{2} \sum_i q_i \cdot (\sum_j q_j)$ , which introduces the interaction of each particle with the total quadrupole moment of the system.<sup>1</sup> The value of  $\chi$  is fixed using self-consistent arguments [22] by the estimate used in an  $\text{Sp}(3, \mathbb{R})$ -based study of cluster-like states of  $^{16}\text{O}$  [23], and the strength of the HO potential is fixed using the empirical estimate  $\hbar\Omega \approx 41/A^{1/3}$ . The only adjustable parameter in the model is  $\gamma$ . The  $H_\gamma$  potential term introduces many-body interactions hierarchically, controlled by  $\gamma < 1$ , such that higher-order terms in the exponential of  $Q \cdot Q$  become negligible. For example, we find that for the  $^{12}\text{C}$  ground state, all terms in the expansion beyond  $(Q \cdot Q)^2$  contribute negligibly to the wave function. However, the  $^{12}\text{C}$  Hoyle state band, requires the inclusion of terms up through  $(Q \cdot Q)^4$  (or the third order in  $\gamma$ ) [19].

The energy spectrum for  $^{12}\text{C}$ , computed in the NCSpm with  $N_{\max} = 20$  and  $\hbar\Omega = 18$  MeV down-selected to only 5 symplectic irreps, agrees remarkably well with experiment (Fig. 2). We find that the lowest  $0^+$ ,  $2^+$ , and  $4^+$  states of the two  $0p-0h$  irreps [ $0p-0h$  (4 0) and  $0p-0h$  (1 2)] reproduce the ground state rotational band. The lowest  $0^+$  state of the  $4p-4h$  (12 0) irrep coincides with the experimental Hoyle state, and the lowest  $0^+$  state of the  $2p-2h$  (6 2) irrep coincides with the third  $0^+$  in  $^{12}\text{C}$ . The low-lying  $3^-$  state is reproduced using the  $1p-1h$  (3 3) irrep. The one-body (matter) densities shown in Fig. 2 (right) indicate a donut-like shape for the  $^{12}\text{C}$  ground state, while the  $0_2^+$  state shows peaks in the probability density aligned along the  $z$ -axis, indicating overlapping clusters spatially extended along this axis. While a smaller  $N_{\max}$  model space is sufficient for convergence of the ground state rotational band, the wave function for the  $0_2^+$  state of  $^{12}\text{C}$  has significant contributions from highly deformed configurations [e. g., (12 0), (14 0), (16 0), etc.] and requires a much larger  $N_{\max}$  model space in order for the collectivity of the state to fully develop and for the energy to reach convergence.

In addition to the energy spectrum, the NCSpm reproduces observables such as  $B(E2)$  transition strengths (Fig. 2), matter rms radii, and electric quadrupole moments, and has been used to investigate the nature of the giant monopole and quadrupole resonances in selected light- and intermediate-mass nuclei [25]. This model has also been applied to studies of other nuclei, including  $^8\text{Be}$ , as well as various  $sd$ -shell nuclei without the need to adjust the  $\gamma$  strength parameter [26, 27]. Its ability to reproduce energy spectra as well as collective features in various nuclei indicates that the NCSpm captures important components of the underlying nuclear physics.

### 3 Exemplary results

*Ab initio* SA-NCSM calculations have now been extended into and beyond the intermediate mass region as shown in Fig. 3, including odd- $A$  nuclei and their negative parity states (e. g.,  $^{19}\text{Ne}$  in 12 HO major shells [28]) and nuclei near the dripline (e. g.,

<sup>1</sup>Note, the average value of  $Q \cdot Q$  within an oscillator shell introduces a major renormalization of the HO shell structure, so, as is normally done, this average is removed; that is,  $Q \cdot Q \rightarrow (Q \cdot Q - \langle Q \cdot Q \rangle)$ , where the average  $\langle Q \cdot Q \rangle$  has a simple universal operator form that applies to a HO shell.



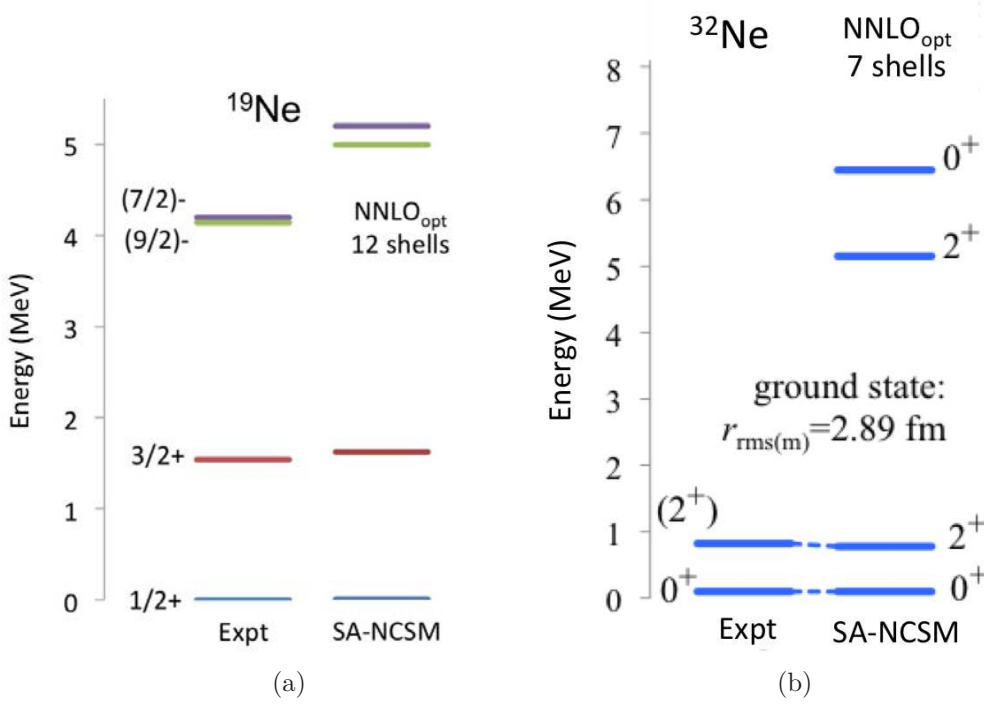


Figure 3: *Ab initio* SA-NCSM calculations using the chiral  $\text{NNLO}_{\text{opt}}$   $NN$  interaction [31] for excitation spectra in (a)  $^{19}\text{Ne}$  with 12 HO major shells and (b)  $^{32}\text{Ne}$  with 7 HO major shells. Simulations are performed on the Blue Waters system.

$^{32}\text{Ne}$  in 7 HO major shells [29]). Further, medium mass nuclei (e. g.,  $^{48}\text{Ti}$  in 8 HO major shells [29]) are now within the reach of the SA-NCSM. All of these results utilize realistic chiral interactions and were able to incorporate contributions from higher HO major shells than previously achievable in order to allow the development of the most important configurations in each nucleus. The results show good agreement with experiment, especially as related to collectivity, a traditionally challenging feature for *ab initio* models to reproduce. For example, the quadrupole moment for the first  $2^+$  state in  $^{48}\text{Ti}$  from experiment is known to be  $-17.7 e \cdot \text{fm}^2$  [30] and SA-NCSM calculations show a value of  $-19.3 e \cdot \text{fm}^2$  based on the chiral  $\text{NNLO}_{\text{opt}}$   $NN$  interaction [31] in 8 HO major shells with no effective charges. This indicates that the symmetry-adapted basis is capable of allowing the necessary collectivity to develop while also controlling the combinatorial growth associated with standard NCSM model spaces.

To further study the collectivity, especially with respect to the isospin symmetry breaking effects in mirror nuclei, we carry forward a systematic study of  $B(E2)$  values in mirror nuclei. Traditionally the isospin symmetry breaking has been studied by comparing the level energies in mirror nuclei or their masses. To advance the understanding of isospin symmetry breaking effects, a range of spectroscopic data is required, including the  $B(E2)$  values, in addition to the energies of excited states. For example, Fig. 4 shows *ab initio* SA-NCSM calculation results for  $^{21}\text{Mg}$  and  $^{21}\text{F}$  mirror nuclei. Calculations of  $B(E2)$  strengths were performed using various symmetry-based selections of the SA-NCSM model space and  $\hbar\Omega$  values, and only the results with

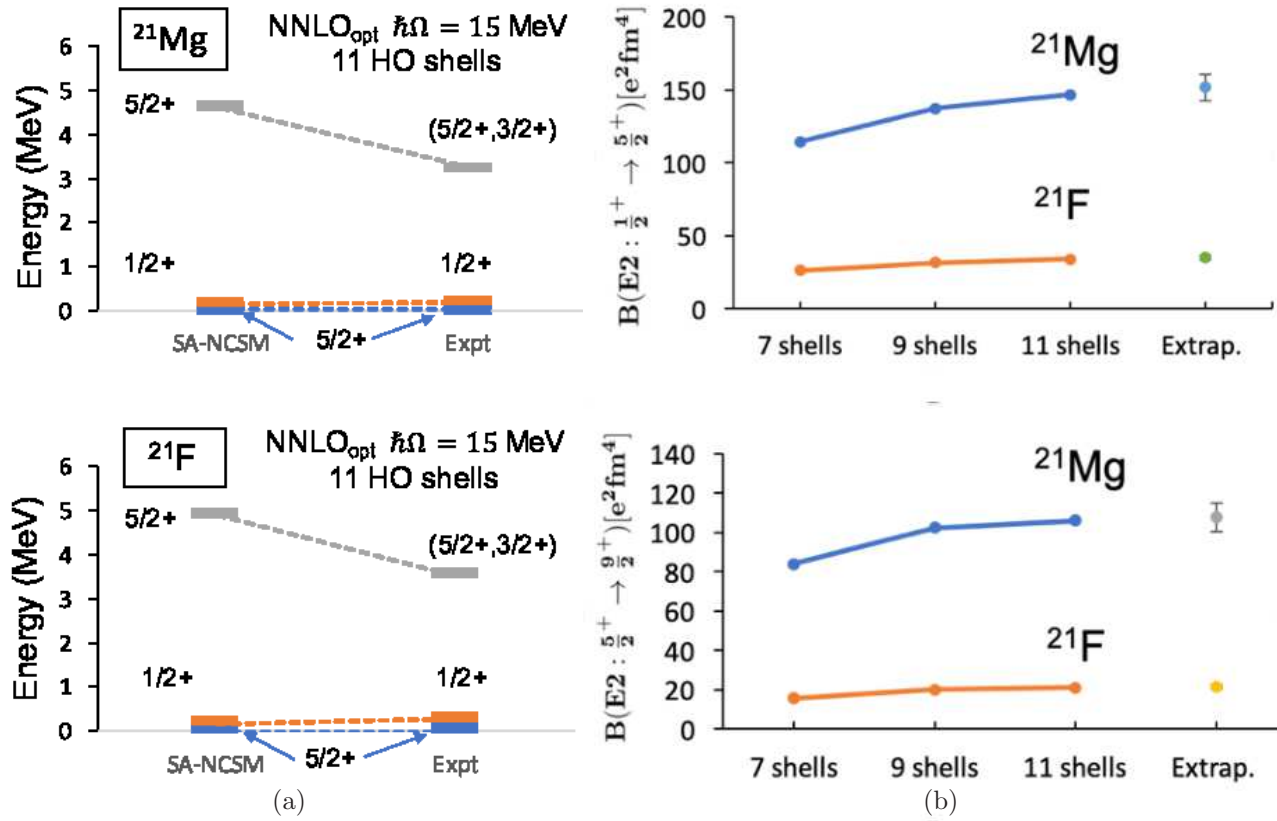


Figure 4: *Ab initio* SA-NCSM calculations using the chiral NNLO<sub>opt</sub> *NN* interaction [31] in ultra-large model spaces ( $\hbar\Omega = 15$  MeV). (a) Energy spectrum of  $^{21}\text{Mg}$  and  $^{21}\text{F}$  in 11 HO major shells, and (b) convergence of the  $B(E2 : \frac{1}{2}^+ \rightarrow \frac{5}{2}^+)$  (top) and  $B(E2 : \frac{5}{2}^+ \rightarrow \frac{9}{2}^+)$  (bottom) strengths with increasing model space, and the extrapolated values with uncertainties from model space and  $\hbar\Omega$  variance. Simulations are performed on the Blue Waters system. Experimental values for the  $B(E2)$  are available in Ref. [32].

the most optimal parameters that show the fastest convergence trend are depicted in Fig. 4. The variance of the model spaces and HO parameter  $\hbar\Omega$  is accounted for the extrapolated values and their uncertainties. These results compare to the recent experimental values [32] reasonably well, demonstrating the SA-NCSM capability to describe collectivity in these challenging mirror nuclei.

## 4 Canonical transformations

The symplectic  $\text{Sp}(3, \mathbb{R})$  group is the group of linear canonical transformations in phase space [33]. We use this fact to define a linear unitary canonical transformation that maps the generators of the  $\text{sp}(3, \mathbb{R})$  algebra into a deformed equivalent set while preserving the symplectic symmetry. We expect that the associated deformed basis states can capture the dominant physics of deformed systems in smaller model spaces, which, in turn, reduces the computational resource requirements.

In classical mechanics, canonical transformations are a set of transformations that preserve the Poisson brackets between generalized coordinates and momenta,

$$\{q_i, p_j\} = \{\tilde{q}_i, \tilde{p}_j\} = \delta_{ij}. \quad (3)$$

The generalization of this definition to the quantum mechanical case is achieved if one replaces the Poisson brackets with commutation relations between the coordinate and momentum operators.

$$[q_i, p_j] = [\tilde{q}_i, \tilde{p}_j] = i\delta_{ij}. \quad (4)$$

Furthermore, the canonical transformations in classical mechanics are always unitary transformations. However, this is not necessarily the case in quantum mechanics [34]. In quantum mechanics, a canonical transformation can be unitary or non-unitary [35, 36]. For the purpose of constructing a deformed basis, we will limit ourselves to unitary transformations. Now we define the following unitary canonical transformations:

$$\begin{aligned} \tilde{q}_i &= \frac{1}{\sqrt{\epsilon_i}} q_i, \\ \tilde{p}_i &= \sqrt{\epsilon_i} p_i, \end{aligned} \quad (5)$$

where ‘ $\sim$ ’ denotes the quantities in the canonically deformed space, and the  $\epsilon_i$ ’s are the deformation parameters (real positive quantities) that define the specifics of the transformation. The physical implication of  $\epsilon_i$  depends on the system being studied. If we choose  $\epsilon_i = \omega/\omega_i$  where  $\omega_i$  is the HO frequency in the  $i$ -th direction, then  $\epsilon_i$  could be interpreted as a deformation parameter that transforms the non-deformed canonical set  $(q_i, p_i)$  into the deformed canonical set  $(\tilde{q}_i, \tilde{p}_i)$ . It is important to note that these canonical transformations not only preserve the Heisenberg algebra, but also preserve the symplectic algebra such that it closes under commutation just as the non-deformed algebra does [37].

Using the canonical transformations defined above, we construct the deformed harmonic oscillator creation and annihilation operators in terms of non-deformed

ones,

$$\begin{aligned}\tilde{b}_{in}^+ &= \frac{1}{2} \left( \frac{1}{\sqrt{\epsilon_i}} (b_{in}^+ + b_{in}) + \sqrt{\epsilon_i} (b_{in}^+ - b_{in}) \right), \\ \tilde{b}_{in} &= \frac{1}{2} \left( \frac{1}{\sqrt{\epsilon_i}} (b_{in}^+ + b_{in}) - \sqrt{\epsilon_i} (b_{in}^+ - b_{in}) \right).\end{aligned}\tag{6}$$

It is easy to see that the canonical transformations in Eqs. (6) are equivalent to Eqs. (5), and therefore

$$[b_{in}, b_{jn}^+] = [\tilde{b}_{in}, \tilde{b}_{jn}^+] = \delta_{ij},\tag{7}$$

which are equivalent to Eq. (4).

The canonical transformations defined in Eqs. (5) are symmetric with respect to inverse transformations. The inverse transformations are achieved if one removes ‘ $\sim$ ’ from the deformed quantities and adds it to the non-deformed quantities and then flips the deformation coefficients. To demonstrate this, we apply this procedure of inverse transformation to Eq. (5) by making the substitution ( $\tilde{q}_i \rightarrow q_i, \tilde{p}_i \rightarrow p_i$ ), then flipping the coefficients  $\frac{1}{\sqrt{\epsilon_i}} \rightarrow \sqrt{\epsilon_i}$ ,  $\sqrt{\epsilon_i} \rightarrow \frac{1}{\sqrt{\epsilon_i}}$ , and we get

$$\begin{aligned}q_i &= \sqrt{\epsilon_i} \tilde{q}_i, \\ p_i &= \frac{1}{\sqrt{\epsilon_i}} \tilde{p}_i,\end{aligned}\tag{8}$$

which are the inverse transformations.

Using the canonical transformations, we express the many-body HO Hamiltonian in terms of the deformed symplectic operators in  $\hbar\omega$  units,

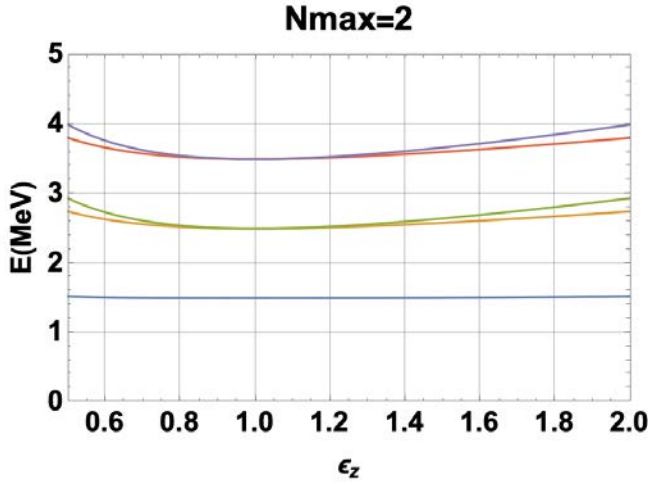
$$H = \sum_i C_{ii} = \frac{1}{4} \left( \epsilon_i (\tilde{A}_{ii} + \tilde{B}_{ii} + 2\tilde{C}_{ii}) + \frac{1}{\epsilon_i} (-\tilde{A}_{ii} - \tilde{B}_{ii} + 2\tilde{C}_{ii}) \right),\tag{9}$$

where, for simplicity,  $\epsilon_x = \epsilon_y$  has been chosen with the constraint  $\epsilon_x \epsilon_y \epsilon_z = 1$  which implies volume conservation of the system. Then Eq. (9) reduces to

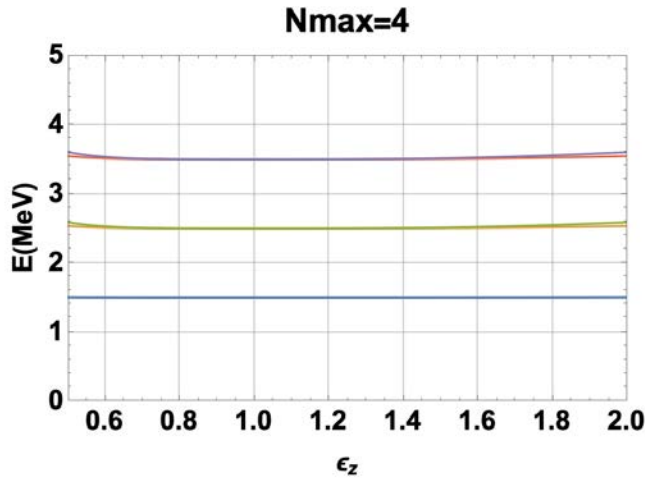
$$H = \frac{1}{4} \left( \left( \epsilon_z - \frac{1}{\epsilon_z} \right) (\tilde{A}_{zz} + \tilde{B}_{zz}) + 2 \left( \sqrt{\epsilon_z} + \frac{1}{\sqrt{\epsilon_z}} \right) (\tilde{C}_{xx} + \tilde{C}_{yy}) + 2 \left( \epsilon_z + \frac{1}{\epsilon_z} \right) \tilde{C}_{zz} \right).\tag{10}$$

Diagonalizing the Hamiltonian in Eq. (10) for a single particle within a model space of  $N_{\max} = 2$  and  $N_{\max} = 4$  we get results shown in Fig. 5. We expected to see all the eigenvalues independent of  $\epsilon_z$ , however Fig. 5 shows a slight dependence of the eigenvalues on  $\epsilon_z$ . This is because we are attempting to map from an infinite Hilbert space onto a finite Hilbert space, which one can only do approximately by going to higher and higher  $N_{\max}$  values; that is, the transformation from the non-deformed to deformed set of operators is not truly a unitary one. To get a unitary transformation, that will be independent of  $\epsilon_z$ , one has to map it onto infinite deformed basis states which is not possible, but as the figures show, with increasing  $N_{\max}$  the results seem to converge very nicely to the low-lying eigenvalues by the time  $N_{\max} = 4$ .

Note that when we applied the canonical transformations to the harmonic oscillator Hamiltonian in Eq. (9), the operator  $C_{ii}$  includes the zero point energy or the so-called vacuum energy in its definition. It is usually common practice in quantum mechanics and quantum field theories to renormalize the energy by discarding the



(a)



(b)

Figure 5: The eigenvalues (in  $\hbar\omega$  units) of a 3D spherical HO as a function of  $\epsilon_z$  in the deformed model spaces of  $N_{\max}=2$  (a) and  $N_{\max}=4$  (b) where  $\epsilon_x = \epsilon_y$  and the  $\epsilon_x \epsilon_y \epsilon_z = 1$  constraint applies.

vacuum contribution to the energy since it has no physical meaning. However, the vacuum term should be included when applying canonical transformations because it is part of the symplectic algebra  $\text{sp}(3, \mathbb{R})$ . In order to unitarily map the symplectic operators to their deformed counterparts, one also needs to map the vacuum to its deformed counterpart. After the mapping one could renormalize the energy by throwing away the deformed vacuum. The vacuum term in  $C_{ii}$  for a single particle is  $\frac{3}{2}$  which, after applying the canonical transformation becomes  $6(\sqrt{\epsilon_z} + \frac{1}{\sqrt{\epsilon_z}}) + 3(\epsilon_z + \frac{1}{\epsilon_z})$  for  $\epsilon_x = \epsilon_y$  and  $\epsilon_x \epsilon_y \epsilon_z = 1$ .

## 5 Conclusions

A short ‘Historical overview’ of multi-shell-model efforts to understand observed features of light nuclei is given in Section 2. The focus is on ‘open-shell’ methods —

commonly called the NCSM, where nucleons are allowed to occupy any and all valence shells of a 3D HO that include excited configurations up to an aggregated  $N_{\max}$  value coupled with the use of *ab initio* rather than schematic interactions within that space. These concepts, introduced around the turn of the last century, serves as a demarkation between ‘old’ and ‘new’ in the evolution of the shell-model for reproducing and predicting nuclear phenomena. Our focus within this framework is on the use of symmetries to tame the exponential grow of model spaces, which otherwise await the availability of ever larger and faster high-performance computing resources and/or various extrapolation procedures for further advances within this NCSM framework.

Section 3 gives some examples of how one can beat back the exponential growth of NSCM spaces through the recognition and use of special symmetries that track with dominant modes in nuclei. A dominant feature that stands above all others is strong  $B(E2)$  transition strengths between members of rotational bands. This feature, which is correlated with the emergence of coherent states that organizes the NSCM landscape into various shapes, which was foreshadowed by early successes of collective models like that of Bohr and Mottelson [8] as well as that of Nilsson [38] and the so-called Geometrical Collective Model of Greiner and associates [9, 10], which extend to odd- $A$  nuclei with an uncoupled nucleon residing within the collective geometrical shape defined by that of the others. This collusion among nucleons that leads to collective configurations, which can be characterized as a co-existence of geometrical shapes, tracks with Elliott’s SU(3) Model [11, 12] within a single shell and its multi-shell extension, the symplectic shell model, Sp(3,  $\mathbb{R}$ ) [19] that in its most rudimentary form can be envisioned as the addition HO quanta (via particle excitations) of the monopole and quadrupole type to the simplest of  $N_{\max} = 0$  configurations.

What this picture suggests, as it did in the earliest days via the Nilsson Model [38], is moving to a deformed geometry from the onset might define a smarter path forward. In Section 4 we show results which suggest that this can be achieved while simultaneously maintaining all the advantages of the symplectic shell-model picture through exploitation of a canonical transformation away from spherical symmetry to a deformed geometry that preserves commutation relations of the symplectic algebra while maintaining the unitarity of the transformation. From a practical perspective this means that everything learned and developed for a spherical symplectic picture can be brought forward into a deformed symplectic picture. As suggested above, this can be seen as an interacting many-particle generalization of the Nilsson Model. While additional work remains to be done, the underlying feature of this evolving picture look promising for its overarching simplicity; namely, the accommodation of what requires high  $N_{\max}$  values within a spherical geometry within lower  $\tilde{N}_{\max}$  model spaces of a deformed geometry. It also suggests that the development and application of a deformed symmetry-adapted NCSM for nuclei may soon be within reach.

## Acknowledgements

Support from the U.S. National Science Foundation (OIA-1738287 and ACI-1713690) and the U.S. Department of Energy (DE-SC0005248), as well as those from Louisiana State University, especially computational resources under the Louisiana Optical Network Initiative, and the Southeastern Universities Research Association are all gratefully acknowledged.

## References

- [1] M. G. Mayer, Phys. Rev. C **75**, 1969 (1949).
- [2] O. Haxel, J. H. D. Jensen and H. E. Suess, Phys. Rev. **75**, 1766 (1949).
- [3] P. Navrátil, J. P. Vary and B. R. Barrett, Phys. Rev. Lett. **84**, 5728 (2000).
- [4] B. Barrett, P. Navrátil and J. Vary, Prog. Part. Nucl. Phys. **69**, 131 (2013).
- [5] P. Navrátil, S. Quaglioni, I. Stetcu and B. R. Barrett, J. Phys. G **36**, 083101 (2009).
- [6] R. Roth and P. Navrátil, Phys. Rev. Lett. **99**, 092501 (2007).
- [7] T. Abe, P. Maris, T. Otsuka, N. Shimizu, Y. Utsuno and J. Vary, Phys. Rev. C **86**, 054301 (2012).
- [8] A. Bohr and B. R. Mottelson, *Nuclear structure*. Benjamin, New York, 1969.
- [9] G. Gneuss, U. Mosel and W. Greiner, Phys. Lett. B **30**, 397 (1969).
- [10] J. Eisenberg and W. Greiner, *Nuclear theory I: Nuclear collective models*. North-Holland, Amsterdam, 1987.
- [11] J. P. Elliott, Proc. Roy. Soc. A **245**, 128 (1958).
- [12] J. P. Elliott and M. Harvey, Proc. Roy. Soc. A **272**, 557 (1962).
- [13] C. Bahri, J. Draayer and S. Moszkowski, Phys. Rev. Lett. **68**, 2133 (1992).
- [14] A. Zuker, J. Retamosa, A. Poves and E. Caurier, Phys. Rev. C **52**, R1741 (1995).
- [15] G. Rosensteel and D. J. Rowe, Phys. Rev. Lett. **38**, 10 (1977).
- [16] D. J. Rowe, Rep. Prog. Phys. **48**, 1419 (1985).
- [17] K. D. Launey, T. Dytrych and J. P. Draayer, Prog. Part. Nucl. Phys. **89**, 101 (2016).
- [18] D. Rowe, AIP Conf. Proc. **1541**, 104 (2013).
- [19] A. C. Dreyfuss, K. D. Launey, T. Dytrych, J. P. Draayer and C. Bahri, Phys. Lett. B **727**, 511 (2013).
- [20] T. Dytrych, K. D. Sviratcheva, J. P. Draayer, C. Bahri and J. P. Vary, J. Phys. G **35**, 123101 (2008).
- [21] K. D. Launey, A. C. Dreyfuss, J. P. Draayer, T. Dytrych and R. B. Baker, J. Phys. Conf. Ser., **569**, 012061 (2014).
- [22] D. J. Rowe, Phys. Rev. **162**, 866 (1967).
- [23] D. J. Rowe, G. Thiamova and J. L. Wood, Phys. Rev. Lett. **97**, 202501 (2006).

- [24] A. C. Dreyfuss, J. P. Draayer, K. D. Launey, T. Dytrych and R. B. Baker, in *Proc. 6th Int. Conf. on Fission and Properties of Neutron-Rich Nucl. — ICFN6, November 6–12, 2016, Sanibel Island, Florida, USA*, eds. J. H. Hamilton, A. V. Ramayya and P. Talou. World Scientific, Singapore, 2017.
- [25] A. C. Dreyfuss, K. D. Launey, T. Dytrych, J. P. Draayer, R. B. Baker, C. M. Deibel and C. Bahri, *Phys. Rev. C* **95** (2017).
- [26] K. D. Launey, T. Dytrych, J. P. Draayer, G. K. Tobin, M. C. Ferriss, D. Langr, A. C. Dreyfuss, P. Maris, J. P. Vary and C. Bahri, in *Proc. 5th Int. Conf. on Fission and Properties of Neutron-Rich Nucl. — ICFN5, November 4–10, 2012, Sanibel Island, Florida, USA*, eds. J. H. Hamilton and A. V. Ramayya. World Scientific, Singapore, 2013.
- [27] G. K. Tobin, M. C. Ferriss, K. D. Launey, T. Dytrych, J. P. Draayer and C. Bahri, *Phys. Rev. C* **89**, 034312 (2014).
- [28] J. P. Draayer, K. D. Launey, T. Dytrych, A. C. Dreyfuss, G. H. Sargsyan and R. B. Baker, in *Walter Greiner memorial volume*, eds. P. O. Hess and H. Stöcker. World Scientific, Singapore, 2018, p. 97.
- [29] K. D. Launey, A. Mercenne, G. H. Sargsyan, H. Shows, R. B. Baker, M. E. Miora, T. Dytrych and J. P. Draayer, *AIP Conf. Proc.* **2038**, 020004 (2018).
- [30] J. W. Lightbody, Jr., *Phys. Lett. B* **38**, 475 (1972).
- [31] A. Ekström, G. Baardsen, C. Forssén, G. Hagen, M. Hjorth-Jensen, G. R. Jansen, R. Machleidt, W. Nazarewicz, T. Papenbrock, J. Sarich and S. M. Wild, *Phys. Rev. Lett.* **110**, 192502 (2013).
- [32] P. Ruotsalainen *et al.*, *Phys. Rev. C* **99**, 051301(R) (2019).
- [33] M. Moshinsky and C. Quesne, *J. Math. Phys.* **12**, 1772 (1971).
- [34] A. Anderson, *Ann. Phys. (NY)* **232**, 292 (1994).
- [35] P. A. Mello and M. Moshinsky, *J. Math. Phys.* **16**, 2017 (1975).
- [36] J. Deenen, M. Moshinsky and T. Seligman, *Ann. Phys. (NY)* **127**, 458 (1980).
- [37] J. P. Draayer, *Retrospective Theses and Dissertations* 3731 (1968).
- [38] S. G. Nilsson, *Dan. Mat. Fys. Medd.* **29**, 16 (1955).

# Convergence in the Symplectic No-Core Configuration Interaction Framework

Anna E. McCoy<sup>a,b</sup>, Mark A. Caprio<sup>b</sup> and Tomáš Dytrych<sup>c,d</sup>

<sup>a</sup>TRIUMF, Vancouver, British Columbia V6T 2A3, Canada

<sup>b</sup>Department of Physics, University of Notre Dame, Notre Dame, Indiana 46556, USA

<sup>c</sup>Nuclear Physics Institute, Academy of Sciences of the Czech Republic, 250 68 Řež, Czech Republic

<sup>d</sup>Department of Physics and Astronomy, Louisiana State University, Louisiana 70803, USA

## Abstract

The symplectic no-core configuration interaction (SpNCCI) framework for *ab initio* nuclear structure predictions carries out calculations in a correlated many-body basis which encodes an approximate  $\text{Sp}(3, \mathbb{R})$  symplectic symmetry of the nucleus. This framework opens up the possibility of identifying and restricting the many-body space to include only the basis states which dominantly contribute to the nuclear wavefunctions of interest. We examine the convergence of  ${}^3\text{He}$  binding energy and matter radius in a basis truncated according to a simple scheme based on the symplectic symmetry.

**Keywords:** *Symplectic no-core configuration interaction (SpNCCI); symmetry adapted basis; ab initio nuclear physics*

## 1 Introduction

In no-core configuration interaction (NCCI) approaches to solving the nuclear many-body problem, one of the biggest challenges is tied to the necessity of describing both short and long range correlations within the chosen basis. In the harmonic oscillator basis, this translates to the need to include oscillator configurations (distributions of particles over harmonic oscillator shells) with many oscillator quanta. However, the basis grows rapidly as the number of oscillator quanta increases, and the size of the resulting basis quickly exceeds current computational limits. So, we must look to methods which allow us to reduce the necessary size of the basis while still capturing the relevant physics. In the symplectic no-core configuration interaction (SpNCCI) framework, the many-body problem is solved in a basis consisting of highly correlated states which have definite  $\text{Sp}(3, \mathbb{R})$  symmetry. The goal is then to use the approximate symplectic symmetry of the nucleus [1–6] to significantly reduce the basis size.

Truncation of the many-body basis by symplectic symmetry is well-suited for long range observables that are sensitive to the tail of the wavefunction, e. g., nuclear radii and  $E2$  transition strengths. The need to include highly excited configurations in the

---

*Proceedings of the International Conference ‘Nuclear Theory in the Supercomputing Era — 2018’ (NTSE-2018), Daejeon, South Korea, October 29 – November 2, 2018, eds. A. M. Shirokov and A. I. Mazur. Pacific National University, Khabarovsk, Russia, 2019, p. 293.*

<http://www.ntse.khb.ru/files/uploads/2018/proceedings/McCoy.pdf>.

nuclear wavefunction is largely due to the kinetic energy term of nuclear Hamiltonian. The nuclear interaction dominates the Hamiltonian at for low number of oscillator quanta, whereas the kinetic energy dominates for highly excited states. Since the symplectic symmetry is conserved by the kinetic energy [7, 8], the SpNCCI basis is broken into subspaces, or irreducible representations (irreps), which are not connected by the kinetic energy. Moreover, while the nuclear interaction does mix states within different symplectic irreps, it has been observed [1–6] that the interaction only strongly mixes states belonging to a relatively small number of symplectic irreps. Thus, identifying the relatively small number of symplectic irreps containing the dominantly contributing low-lying states also provides a selection criteria for the “important” high-lying states. The overall effect is that more of the the highly excited basis states necessary for describing the tail of the wavefunction are included in the basis than would have been possible with the traditional  $N_{\max}$  truncated many-body basis [9].

In this paper, we briefly present the SpNCCI basis (Section 2) and computational framework (Section 3). In Section 4, we then discuss convergence behaviour in a symplectic truncated basis using the  $^3\text{He}$  binding energy and matter radius to illustrate.

## 2 The symplectic basis

The SpNCCI many-body basis is composed of states with definite  $\text{Sp}(3, \mathbb{R})$  symmetry. These states can be thought of as linear combinations of the harmonic oscillator configurations (or Slater determinants) that form the traditional NCCI [or no-core shell model (NCSM)] basis [9]. In this sense, the SpNCCI basis states build in single-particle correlations. However, in actual calculations, the SpNCCI basis states are never explicitly expressed in terms of Slater determinants, as discussed in Section 3.

In the symplectic basis, the states are first organized into irreducible representations (irreps) of  $\text{Sp}(3, \mathbb{R})$  [7, 8]. Within each symplectic irrep, the basis states are then organized into irreps of  $\text{U}(3)$ . That is, the basis reduces the subgroup chain  $\text{Sp}(3, \mathbb{R}) \supset \text{U}(3)$ . The  $\text{U}(3)$  group factorizes into  $\text{U}(3) \sim \text{U}(1) \times \text{SU}(3)$ , where  $\text{U}(1)$  is the group of the harmonic oscillator Hamiltonian, for which the quantum number is the total number  $N$  of oscillator quanta, and  $\text{SU}(3)$  is Elliott’s  $\text{SU}(3)$  group, generated by orbital angular momentum and quadrupole operators [10, 11]. Thus, basis states within the  $\text{U}(3)$  irrep are characterized by definite  $\text{U}(3)$  symmetry  $\omega = N_\omega(\lambda_\omega, \mu_\omega)$ . In other words, the basis states have definite total number of oscillator quanta  $N_\omega$ , as in traditional NCCI calculations, as well as definite Elliott  $\text{SU}(3)$  symmetry  $(\lambda_\omega, \mu_\omega)$ .

Each symplectic irrep is then labeled according to the single  $\text{U}(3)$  irrep with the fewest number of oscillator quanta in the symplectic irrep. This irrep is referred to as the *lowest grade irrep* (LGI). An LGI can be identified as the states which are annihilated by the symplectic lowering operator  $B^{(0,2)}$ . The remaining states in the symplectic irrep are obtained by repeatedly acting on the LGI with the symplectic raising operator  $A^{(2,0)}$ . Each raising operation adds two oscillator quanta. Thus, a single symplectic irrep contains states with oscillator quanta  $N_\omega = N_\sigma, N_\sigma + 2, \dots$ . The laddering operator can be applied infinitely many times, so the symplectic irrep is, in principle, unbound. However, the SpNCCI framework requires a finite basis, so each irrep must be truncated, e. g., to some finite number of oscillator quanta.

### 3 Calculations in symplectic basis

In the SpNCCI framework, the matrix elements of the nuclear Hamiltonian (and other observables) are obtained directly in the symplectic basis via recurrence. Such an approach was first proposed for a symplectic shell model by Reske, Suzuki and Hecht [12–14]. These methods are extended in the SpNCCI framework to accommodate general spin and isospin-dependent nonlocal nuclear interactions for *ab initio* calculations [5].

In this recurrence, the matrix elements between high-lying SpNCCI basis states (with many oscillator quanta) are expressed in terms of states with fewer number of oscillator quanta. This expression is obtained by making use of commutation relation of the Hamiltonian operator with the symplectic ladder operator, which relate states with different number of oscillator quanta [5]. The recurrence starts with the matrix elements between the lowest lying states in each symplectic irrep (between LGIs). The matrix elements between LGIs are obtained by expanding the LGIs in terms of SU(3) coupled configurations and then using the existing symmetry adapted no-core shell model (SA-NCSM) code `LSU3Shell` [15] to compute the matrix elements.

The expansion of the LGIs in terms of SU(3) coupled configurations is obtained by solving for the simultaneous null space of the Sp(3,  $\mathbb{R}$ ) lowering operator  $B^{(0,2)}$  and the center-of-mass oscillator number operator  $N_{\text{cm}}^{(0,0)}$ , in the SA-NCSM basis. The resulting states are fully antisymmetric by construction with zero center-of-mass excitations [center-of-mass free (CMF)]. The intrinsic symplectic raising operator preserves both the antisymmetrization and CMF nature of the states. Consequently, the basis state obtained by acting on the LGI with the raising operator are likewise both antisymmetrized and CMF.

### 4 Convergence

The efficacy of the SpNCCI framework depends on how well we can obtain converged values for nuclear observables in a symplectic truncated basis. Before we can develop effective truncation schemes, we need first to understand the convergence behaviour of these observables. As a simple example, we consider the convergence behaviour of the  ${}^3\text{He}$  binding energy (Fig. 1) and matter radius (Fig. 2) obtained using the code `spncci` [17].

For this illustration, we simply restrict the basis to symplectic irreps generated from LGIs with oscillator quanta less than or equal to some fixed number. We quote this number in terms of excitation quanta  $N_{\text{ex}}$ , i. e., number of oscillator quanta above the lowest Pauli allowed number of quanta  $N_0$  for the given nucleus. Thus the restriction on the LGI is given by  $N_{\sigma,\text{ex}} \leq N_{\sigma,\text{max}}$  where  $N_{\sigma,\text{ex}} = N_{\sigma} - N_0$ . Each of the panels in Fig. 1 and Fig. 2 correspond to a different value of  $N_{\sigma,\text{max}}$ . For example, the calculations in Fig. 1(a) are carried out in a symplectic basis which includes only the symplectic irreps with  $N_{\sigma,\text{ex}} \leq 2$ , i. e., in an  $N_{\sigma,\text{max}} = 2$  truncated basis.

Within each  $N_{\sigma,\text{max}}$  truncated space, each of the symplectic irreps in the basis must be truncated to some finite number of states. Here we include only the states in each irrep with number of excitation quanta ( $N_{\text{ex}} = N_{\omega} - N_0$ ) less than some maximum value  $N_{\text{max}}$ , i. e.,  $N_{\text{ex}} \leq N_{\text{max}}$ . Each of the curves shown in the panel corresponds to successively higher maximum allowed excitation quanta ( $N_{\text{max}} = 2, 4, \dots, 16$ ). A

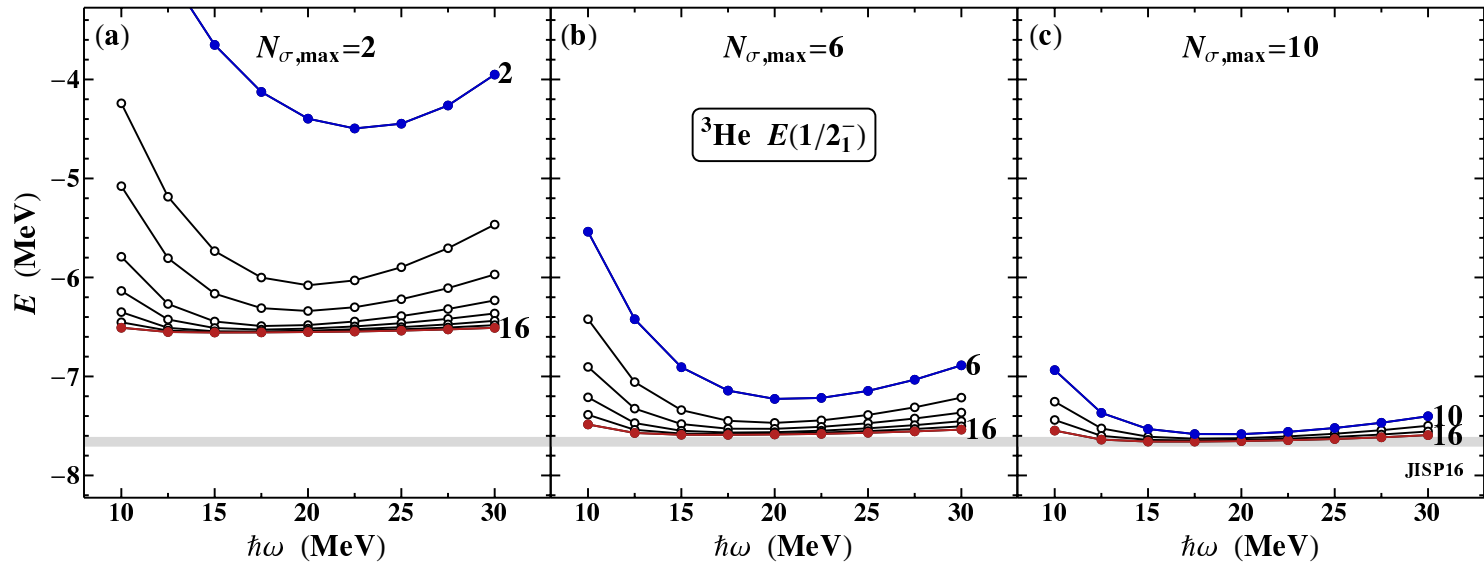


Figure 1: Convergence of the binding energy of  ${}^3\text{He}$  in the SpNCCI framework. The set of symplectic irreps included in the calculation is given by (a)  $N_{\sigma,\text{max}} = 2$ , (b)  $N_{\sigma,\text{max}} = 6$ , or (c)  $N_{\sigma,\text{max}} = 10$ . Each curve is labeled by the  $N_{\text{max}} = N_{\sigma,\text{max}}, N_{\sigma,\text{max}} + 2, \dots, 16$  truncation used within these irreps. The gray band indicates the approximate full-space value. These calculations are based on the JISP16 internucleon interaction [16].

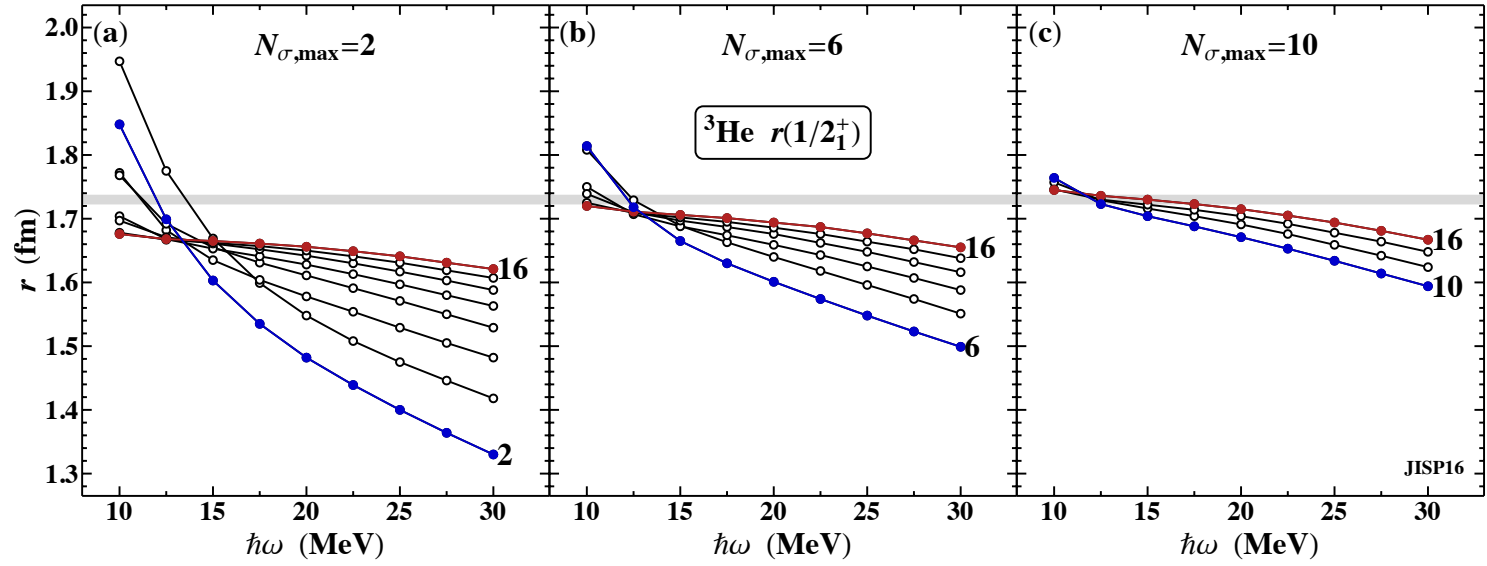


Figure 2: Convergence of the  ${}^3\text{He}$  r.m.s. matter radius in the SpNCCI framework. The set of symplectic irreps included in the calculation is given by (a)  $N_{\sigma,\text{max}} = 2$ , (b)  $N_{\sigma,\text{max}} = 6$ , or (c)  $N_{\sigma,\text{max}} = 10$ . Each curve is labeled by the  $N_{\text{max}} = N_{\sigma,\text{max}}, N_{\sigma,\text{max}} + 2, \dots, 16$  truncation used within these irreps. The gray band indicates the approximate full-space value. These calculations are based on the JISP16 internucleon interaction [16].

truncated basis in which  $N_{\sigma,\max} = N_{\max}$  (blue curve) will yield identical results to those obtained in the traditional NCCI framework in an  $N_{\max}$  truncated basis.

Let us first consider the binding energy of  ${}^3\text{He}$  shown in Fig. 1. When convergence is achieved, the results obtained no longer depend on the choice of many-body basis. In the SpNCCI framework, this means that convergence is signalled when results no longer depend on the length scale of the oscillator basis (results are independent of  $\hbar\omega$ ) and when they no longer change as additional basis states are included in the basis (as  $N_{\max}$  and  $N_{\sigma,\max}$  increase). In Fig. 1(a), the results for  $N_{\max} = N_{\sigma,\max} = 2$  (blue curve) vary significantly for different values of  $\hbar\omega$ . However, with each successive  $N_{\max}$ , the curves begin to flatten, signalling the results are approaching convergence with respect to  $\hbar\omega$ . Similarly, with increasing  $N_{\max}$ , the curves fall closer together, indicating that the values are approaching convergence with respect to  $N_{\max}$ . By  $N_{\max} = 16$  (red curve) the results are comparatively independent of  $\hbar\omega$  and  $N_{\max}$ .

However, the convergence within an  $N_{\sigma,\max}$  space is not the same as convergence within the full space (all symplectic irreps included). Note that the converged value obtained in the  $N_{\sigma,\max} = 2$  space [Fig. 1(a)] is not the same as value obtained in the full many-body basis<sup>1</sup> (gray line). Thus, the results are not yet converged with respect to the number of symplectic irreps included, i. e., with respect to  $N_{\sigma,\max}$ . In Fig. 1(b), the energies obtained in the space including the  $N_{\sigma,\max} = 6$  irreps are, again, converging with respect to  $\hbar\omega$  and  $N_{\max}$ . However, now they are converging to a different value. Similarly, in Fig. 1(c), the energies converge within the  $N_{\sigma,\max} = 10$  space with increasing  $N_{\max}$ , but, again, to a different value. However, the difference between the  $N_{\max} = 16$  curve for  $N_{\sigma,\max} = 6$  and  $N_{\max} = 10$  is significantly smaller than the difference between the  $N_{\sigma,\max} = 2$  and  $N_{\sigma,\max} = 6$  curves. This relatively small shift of the energy curves at fixed  $N_{\max}$  between  $N_{\sigma,\max} = 6$  and  $N_{\sigma,\max} = 10$  indicates that the results are nearing convergence with respect to  $N_{\sigma,\max}$ .

Let us now take a look at the r.m.s radius of  ${}^3\text{He}$ . In traditional NCCI calculations, which corresponds here to the  $N_{\sigma,\max} = N_{\max}$  calculations, we see a strong dependence on the length scale  $\hbar\omega$  [20, 21]. However, within an  $N_{\sigma,\max}$  truncated space, as more and more excited configurations are included in the basis (increasing  $N_{\max}$ ), the values for the radius converge with respect to both  $N_{\max}$  and  $\hbar\omega$ , just as they did for the energy. The effect of including additional  $\text{Sp}(3, \mathbb{R})$  irreps (increasing  $N_{\sigma,\max}$ ) is then to simply shift the value of the radius obtained at large  $N_{\max}$ .

This behaviour suggests that a reasonable approximate value may be obtained within a comparatively small subspace composed of a relatively small number of symplectic irreps. In this example, the inclusion of just the higher  $N_{\text{ex}}$  states belonging to the  $N_{\sigma,\max} = 2$  irreps is sufficient to obtain a value for the radius which is converged with respect to  $\hbar\omega$  and  $N_{\max}$  and which is within 0.1 fm of the full space value. For  $N_{\max} = 16$ , the largest calculation shown for  $N_{\sigma,\max} = 2$  in Fig. 2(a), the dimension of the space for  $J = 1/2$  is 217 where as the full  $M$ -scheme space (basis for traditional NCCI calculations) at  $N_{\max} = 16$  with angular momentum projection  $M = 1/2$  has dimension 392 039, which is more than three orders of magnitude larger than that of the corresponding symplectic basis.

---

<sup>1</sup> The approximate full space values are obtained using the NCCI code `MFDn` [18, 19].

## 5 Conclusion

Carrying out calculations in a symplectic basis opens up the possibility obtaining accurate predictions in a much smaller basis than possible in the traditional NCCI framework, particularly for long range observables. The simple  $N_{\sigma, \max}$  truncation scheme used in the results shown in Fig. 1 and Fig. 2 barely begins to touch on the potential uses of the symplectic symmetry as a means of defining efficient truncation schemes. The challenge is to identify the relevant symplectic irreps by, e. g., a perturbative approach similar to the method employed in the importance truncated no-core-shell model (IT-NCSM) [22].

## Acknowledgements

We thank David J. Rowe for invaluable assistance with the  $\text{Sp}(3, \mathbb{R})$  formalism and Chao Yang, Pieter Maris, Calvin W. Johnson, and Patrick J. Fasano for discussions of the computational implementation.

This material is based upon work supported by the U.S. Department of Energy, Office of Science, Office of Nuclear Physics, under Award Number DE-FG02-95ER-40934, by the U.S. Department of Energy, Office of Science, Office of Workforce Development for Teachers and Scientists, Graduate Student Research (SCGSR) program, under Contract Number DE-AC05-06OR23100, by the Research Corporation for Science Advancement, under a Cottrell Scholar Award. TRIUMF receives federal funding via a contribution agreement with the National Research Council of Canada.

This research used computational resources of the University of Notre Dame Center for Research Computing.

## References

- [1] T. Dytrych, K. D. Sviratcheva, C. Bahri and J. P. Draayer, Phys. Rev. Lett. **98**, 1 (2007).
- [2] T. Dytrych, K. D. Sviratcheva, C. Bahri and J. P. Draayer, Phys. Rev. C **76**, 014315 (2007).
- [3] T. Dytrych, K. D. Sviratcheva, C. Bahri, J. P. Draayer and J. P. Vary, J. Phys. G **35**, 095101 (2008).
- [4] T. Dytrych, K. D. Sviratcheva, J. P. Draayer, C. Bahri and J. P. Vary, J. Phys. G **35**, 123101 (2008).
- [5] A. E. McCoy, *Ab initio multi-irrep symplectic no-core configuration interaction calculations*, Ph.D. thesis. University of Notre Dame, 2018; <https://curate.nd.edu/show/pz50gt57p16>.
- [6] A. E. McCoy, M. A. Caprio and T. Dytrych, Ann. Acad. Rom. Sci. Ser. Chem. Phys. Sci. **3**, 17 (2018).
- [7] G. Rosensteel and D. J. Rowe, Ann. Phys. (NY) **126**, 343 (1980).
- [8] D. J. Rowe, Rep. Prog. Phys. **48**, 1419 (1985).

- 
- [9] B. R. Barrett, P. Navrátil and J. P. Vary, *Prog. Part. Nucl. Phys.* **69**, 131 (2013).
- [10] J. P. Elliott, *Proc. Roy. Soc. (London) A* **245**, 128 (1958).
- [11] M. Harvey, *Adv. Nucl. Phys.* **1**, 67 (1968).
- [12] E. J. Reske, *Sp(6,R) symmetry and the giant quadrupole resonance in  $^{24}\text{Mg}$* , *Ph.D. thesis*. University of Michigan, 1984.
- [13] Y. Suzuki and K. T. Hecht, *Nucl. Phys. A* **455**, 315 (1986).
- [14] Y. Suzuki and K. T. Hecht, *Progr. Theor. Phys.* **77**, 190 (1987).
- [15] T. Dytrych *et al.*, *LSU3shell: Ab initio no-core shell model in SU(3)-scheme basis*, <http://sourceforge.net/projects/lsu3shell>.
- [16] A. M. Shirokov, J. P. Vary, A. I. Mazur and T. A. Weber, *Phys. Lett. B* **644**, 33 (2007).
- [17] A. E. McCoy and M. A. Caprio, *Computer code spncci*, <http://github.com/nd-nuclear-theory/spncci>.
- [18] P. Maris, M. Sosonkina, J. P. Vary, E. Ng and C. Yang, *Procedia Comput. Sci.* **1**, 97 (2010).
- [19] H. M. Aktulga, C. Yang, E. G. Ng, P. Maris and J. P. Vary, *Concurrency Computat.: Pract. Exper.* **10**, 3129 (2013).
- [20] S. K. Bogner *et al.*, *Nucl. Phys. A* **801**, 21 (2008).
- [21] P. Maris and J. P. Vary, *Int. J. Mod. Phys. E* **22**, 1330016 (2013).
- [22] R. Roth and P. Navrátil, *Phys. Rev. Lett.* **99**, 092501 (2007).

# Alpha-cluster Structure from No-Core Monte Carlo Shell Model

Takashi Abe<sup>a</sup>

<sup>a</sup> Center for Nuclear Study, the University of Tokyo, 2-1 Hirosawa, Wako, Saitama 351-0198, Japan

## Abstract

Owing to recent computational and methodological advancements, *ab initio* approaches in nuclear structure physics have been largely developed. The no-core Monte Carlo shell model (MCSM) is one of these methods to investigate nuclear structure in light nuclei. With this method, it is currently capable to calculate physical observables up to around lower *sd*-shell region. As one of physics investigations with the no-core MCSM, the  $\alpha$ -cluster structure of Be isotopes and  $^{12}\text{C}$  nucleus is focused on and qualitatively discussed from an *ab initio* point of view.

**Keywords:** *Alpha-cluster structure; Monte Carlo shell model; no-core shell model*

## 1 Introduction

Nowadays, there are many approaches to solve nuclear many-body problems. One of successful methods is the shell-model approach [1–3]. The shell-model calculations have provided much of theoretical understanding of nuclear structure based on the single-particle picture. In these calculations, the energy eigenvalues and eigenfunctions are obtained by the diagonalization of sparse real symmetric matrices using the Lanczos method to describe several low-lying states. The limitation of this approach is directly related to the size of Hamiltonian matrices to be diagonalized. In the case of no-core shell model, the current limit is around  $10^{10}$  *M*-scheme dimensions [4]. The dimension of Hamiltonian matrices in the single-particle truncation is illustrated in Fig. 1. Now the mass region of interest has been extended to heavier and/or neutron-rich nuclei to investigate various exotic phenomena, and is located at the area beyond the scope of this standard approach with the Lanczos method.

Under these circumstances, there are some variants of shell-model approaches aiming to go beyond the standard approach. One of them is the Monte Carlo shell model (MCSM) [5–7]. Here, we provide a brief overview of the MCSM, especially for the no-core calculations, and the study on the  $\alpha$ -cluster structure using this method. The outline of this contribution is as follows. In Section 2, the formulation of the

---

*Proceedings of the International Conference ‘Nuclear Theory in the Supercomputing Era — 2018’ (NTSE-2018), Daejeon, South Korea, October 29 – November 2, 2018, eds. A. M. Shirokov and A. I. Mazur. Pacific National University, Khabarovsk, Russia, 2019, p. 301.*

<http://www.ntse.khb.ru/files/uploads/2018/proceedings/Abe.pdf>.

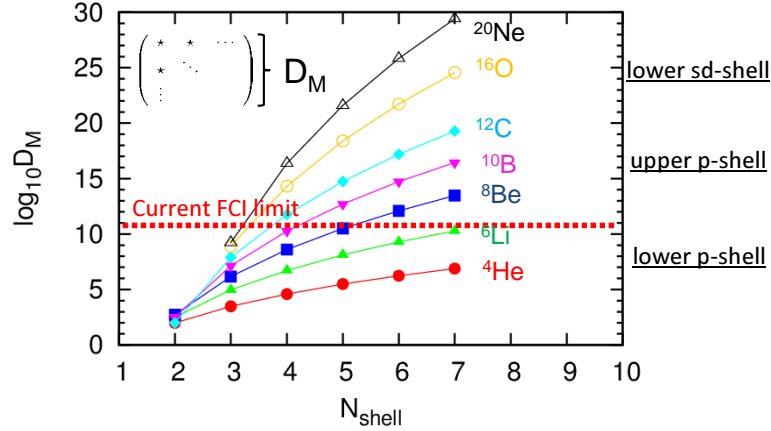


Figure 1: The  $M$ -scheme dimensions as a function of the size of basis space for several light nuclei.

MCSM is briefly introduced. In Section 3, the current status of the MCSM for no-core calculations is shown. As one of physics investigations by the no-core MCSM, we discuss  $\alpha$ -clustering phenomena in Be isotopes and  $^{12}\text{C}$  nucleus in Section 4. The summary is given in Section 5.

## 2 Monte Carlo Shell Model

In the Monte Carlo shell model (MCSM), the Hamiltonian comprises one- and two-body terms, and is written in the second quantized form as

$$\hat{H} = \sum_{ij} t_{ij} \hat{c}_i^\dagger \hat{c}_j + \frac{1}{4} \sum_{ijkl} \bar{v}_{ijkl} \hat{c}_i^\dagger \hat{c}_j^\dagger \hat{c}_l \hat{c}_k, \quad (1)$$

with the creation and annihilation operators,  $\hat{c}^\dagger$  and  $\hat{c}$ , respectively. The indices,  $i, j, k$ , and  $l$ , stand for the single-particle states. The one- and two-body matrix elements are described as  $t_{ij}$  and  $\bar{v}_{ijkl}$ . Here, the two-body matrix elements are antisymmetrized as  $\bar{v}_{ijkl} = -\bar{v}_{jikl} = -\bar{v}_{ijlk} = \bar{v}_{jilk}$ .

With this Hamiltonian, the MCSM wave function is expressed as a linear combination of total-angular-momentum- and parity-projected deformed Slater determinants,

$$|\Psi_{IM\pi}^{(N_b)}\rangle = \sum_{n=1}^{N_b} \sum_{K=-I}^I f_{nK}^{(N_b)} \hat{P}_{MK}^{I\pi} |\phi_n\rangle, \quad (2)$$

with the total-angular-momentum- and parity-projection operator,  $\hat{P}_{MK}^{I\pi} = \hat{P}_{MK}^I \hat{P}^\pi$ . The number of deformed Slater determinants is  $N_b$ . The amplitude  $f_{nK}^{(N_b)}$  is the coefficient of each basis function. The deformed Slater determinant reads

$$|\phi\rangle = \prod_{\alpha=1}^{N_f} \sum_{i=1}^{N_{sp}} D_{i\alpha} \hat{c}_i^\dagger |-\rangle, \quad (3)$$

with the numbers of nucleons  $N_f$  and single-particle states  $N_{sp}$ . Note that the particle vacuum is described as  $|-\rangle$ . The complex matrix  $D$  characterizes the deformation from the spherical harmonic-oscillator Slater determinants.

In Eq. (3), the matrix elements of  $D$  are determined by minimizing the energy eigenvalues in stochastic and deterministic ways following the variational principle. The stochastic sampling of bases is done in a way similar to the auxiliary-field Monte Carlo technique, introducing auxiliary fields by the Hubbard–Stratonovich transformation. Candidates of basis function are generated by the imaginary-time evolution. Among these generated candidates, we take the one which gives the lowest energy eigenvalue. Then, we further minimize the energy eigenvalue by optimizing the matrix  $D$  in a deterministic way with the conjugate gradient method.

Concerning the actual computational procedure, we start with one basis, usually the Hartree–Fock basis. We increase the number of bases by repeating the basis search in stochastic and deterministic ways as described above until the energy eigenvalues sufficiently converge. The typical number of bases becomes finally around 100, so that we reduce the diagonalization problem of a large and sparse Hamiltonian matrix into a dense Hamiltonian matrix with about 100 linear dimension. At each step of the basis search, the energy eigenvalues  $E$  and coefficients of eigenvector  $f_{nK}$  are obtained by solving the following generalized eigenvalue problem,

$$\sum_{nK} \langle \phi_m | \hat{H} \hat{P}_{MK}^{I\pi} | \phi_n \rangle f_{nK} = E \sum_{nK} \langle \phi_m | \hat{P}_{MK}^{I\pi} | \phi_n \rangle. \quad (4)$$

In order to evaluate the energy eigenvalues more precisely, we also compute the energy variance and extrapolate our MCSM results towards vanishing energy variances where the exact eigenvalue of original Hamiltonian matrix exists. For more details, see the reviews of MCSM in Refs. [5–7].

### 3 *Ab initio* no-core MCSM

One of the major challenges in nuclear physics is to understand nuclear structure and reactions from the first principles. For this purpose, a number of *ab initio* studies have become actively done these days, mainly due to a rapidly growing computational power and refinement of *ab initio* techniques for quantum many-body calculations (see review articles, for example, Ref. [8] and references therein).

In the *ab initio* approaches, all nucleon degrees of freedom are activated and nuclear forces from two- and three-nucleon interactions fitted to  $NN$ -scattering data and deuteron properties (applying some soften procedures of original interactions) are used as an input of many-body calculations. Typically, the cost for these calculations tends to be computationally expensive. Therefore, an alternate way to reduce the computational cost is awaited. For instance, in the case of no-core shell model, a couple of methods have been proposed and are providing new insights into *ab initio* nuclear structure calculations, such as the importance-truncated no-core shell model [9, 10] and symmetry-adapted no-core shell model [11]. The no-core MCSM is one of the variants pursuing this direction [12, 13].

For the application of the no-core MCSM, we have employed the JISP16  $NN$  interaction due to the limitation of handling explicit  $3N$  interactions at present. This is the  $J$ -matrix inverse scattering potential (JISP), one of the realistic nonlocal  $NN$

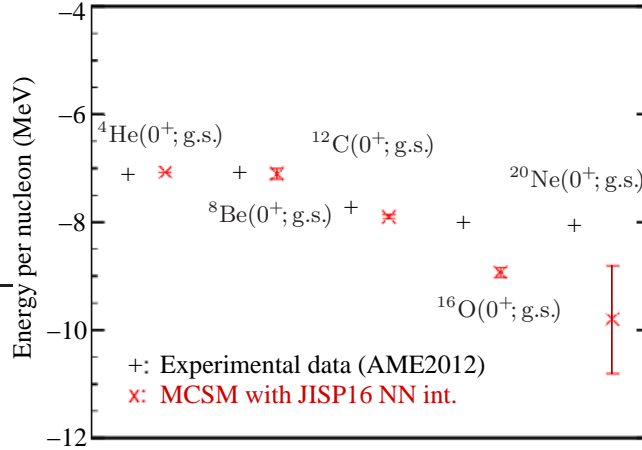


Figure 2: Comparison of binding energies for light nuclei between MCSM calculations and experimental data. The error bars denote estimated uncertainties for the extrapolation of MCSM results.

interactions constructed through phase-equivalent transformations [14]. This interaction is fitted not only to the two-nucleon scattering data and deuteron properties but also to the properties of light nuclei up to  ${}^{16}\text{O}$ . Although we treat only  $NN$  interactions in the calculations, it is sufficient to prove the capability of the MCSM technique for no-core shell-model calculations.

With the JISP16  $NN$  interaction, we have calculated the ground-state energies and root-mean-square point-nucleon radii of  ${}^4\text{He}$ ,  ${}^8\text{Be}$ ,  ${}^{12}\text{C}$ ,  ${}^{16}\text{O}$  and  ${}^{20}\text{Ne}$  nuclei as shown in Figs. 2 and 3, respectively, including the nuclei in which the standard no-core shell-model calculations are hardly performed to obtain converged results due to huge dimensionality of Hamiltonian matrices. From our recent no-core MCSM computation on the K computer, the JISP16  $NN$  interaction provides the binding energies consistent with experimental data up to around  ${}^{12}\text{C}$ , but overbinds nuclei as  $A$  increases. In a similar way, the radii are consistent with experiment up to around  $A \sim 8$ , but are clearly underestimated for  $A$  larger than 12. Our results infer the necessity of explicit inclusion of  $3N$  potentials for heavier nuclei above the upper  $p$ -shell region even with a non-local potential such as the JISP16  $NN$  interaction.

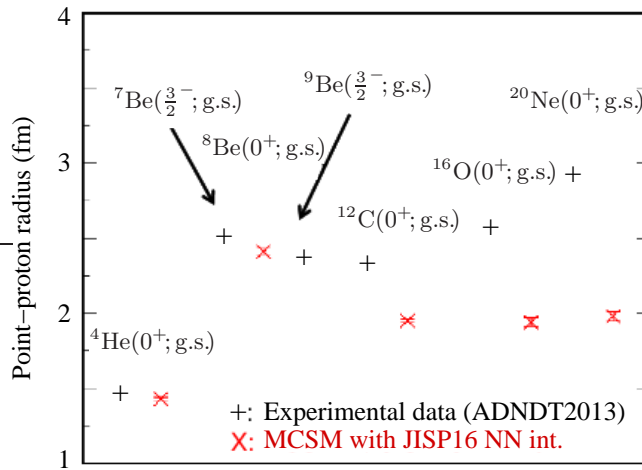


Figure 3: Comparison of radii for light nuclei between MCSM calculations and experimental data. Note that the experimental data for neighboring Be isotopes are plotted as a reference of the MCSM calculation for  ${}^8\text{Be}$ .

However, a new non-local  $NN$  interaction, the Daejeon16  $NN$ , is expected to give better results than those with the JISP16  $NN$  interaction [15, 16]. It is interesting to see how well the results of no-core MCSM calculations can be improved with this interaction and to what extent the off-shell properties of such kind of nonlocal  $NN$  interactions can absorb the effects of explicit  $3N$  interactions beyond the  $p$ -shell region.

## 4 Alpha-cluster structure from the no-core MCSM

For physics applications of the no-core MCSM, the  $\alpha$ -cluster structure has been recently investigated focusing on two- (three-)  $\alpha$ -cluster structure of Be (C) isotopes. The  $\alpha$ -cluster structure in light nuclei is one of the fundamental aspects in nuclear many-body system, and has been studied intensively for a long time. Up to present, there are a number of studies on  $\alpha$ -cluster physics from the first principles as well as those based on cluster models. The purpose for the investigation by the no-core MCSM is to understand the mechanism of appearance and disappearance of  $\alpha$ -cluster structures in the intrinsic density of nuclei utilizing the nature of deformed Slater determinants in the MCSM wave functions.

As an exploratory study, a proof-of-principle calculation by the no-core MCSM has been done for the low-lying states of  $^{10,12}\text{Be}$  nuclei with the AV18 and N3LO  $\chi\text{EFT}$   $NN$  potentials transformed by the unitary correlation operator method [17]. Physical observables of low-lying states of  $^{10}\text{Be}$  are reasonably well reproduced. Following this exploratory study of Be isotopes, the no-core MCSM has been further applied to the study of intrinsic shape of these exotic nuclei [18–21]. The no-core MCSM calculations with JISP16  $NN$  interaction have been performed to construct intrinsic densities of ground and some excited states in Be isotopes in order to better understand the  $\alpha$ -cluster and molecular-orbital structure of Be isotopes. For a visualization of intrinsic structure of nuclei, we superpose the deformed Slater determinants in the MCSM wave function before the angular-momentum and parity projections so as to obtain the density distribution in the body-fixed frame by aligning the orientation of each deformed Slater determinant in terms of quadrupole deformation.

From our investigation, we have obtained some promising results as shown in Fig. 4. First, we have observed the emergence of two- $\alpha$ -cluster structure in the  $^8\text{Be}$  ground state without any assumption of the  $\alpha$ -cluster structure. This fact indicates that the  $\alpha$  clusters can be described efficiently with deformed Slater determinants. Second, we can identify in the ground and first excited  $0^+$  states of  $^{10}\text{Be}$  nuclei the molecular-orbital structures formed by two valence neutrons (equal to the total number of neutrons minus the number of protons) on top of two  $\alpha$  clusters. For the ground state (the first excited  $0^+$  state), two valence neutrons give  $\pi$ - ( $\sigma$ -) orbit of molecular orbital states. In addition, we can observe four valence neutrons forming some mixture of the  $\pi$ - and  $\sigma$ -orbital structures in the  $^{12}\text{Be}$  ground state. Third, we can see the fading of intrinsic shape of the  $\alpha$  clusters as the number of neutrons increases. This structure change cannot be obtained by cluster models, which assume the  $\alpha$  cluster as a fundamental degree of freedom. This finding implies a way to investigate the deformation of  $\alpha$  clusters.

In addition to the investigation of intrinsic structure of Be isotopes, we also extend our analysis to three  $\alpha$  clusters in the  $^{12}\text{C}$  nucleus. In the analysis of the intrinsic shape of  $^{12}\text{C}$ , we introduce the cluster analysis in the statistics. We define the distance

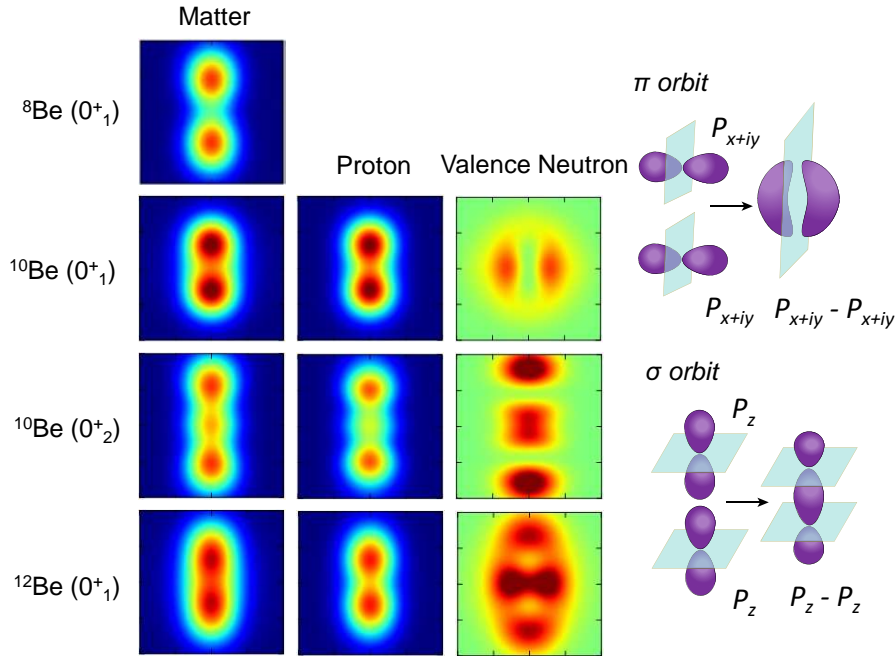


Figure 4: Schematic intrinsic density illustrating the  $\alpha$ -cluster and molecular-orbital structure of Be isotopes obtained by the no-core MCSM.

measured in the Euclidean space which gauges the similarity of densities and categorize the groups of similar shape. For the first application, we divide our deformed Slater determinants, which amount around 100 basis states, into 15 groups. By separating the deformed Slater determinants into these groups, we have calculated overlap probability of deformed Slater determinants in each group with the total MCSM wave function. The results are shown in Fig. 5. From this analysis, we have obtained the  $0^+$  ground state of  ${}^{12}\text{C}$  mainly composed by the group of the compact (shell-model-like) shape and that of three  $\alpha$  clusters. For the second  $0^+$  state, the overlap probability is distributed among all 15 groups on an equal footing. It indicates that this state is a gas-like state, which is proposed by the study with the THSR wave functions [22] as the Bose–Einstein condensation of the  $\alpha$  gas.

## 5 Summary

We shortly outlined the Monte Carlo shell model (MCSM) from its formalism to some numerical results, focusing on recent application of this method to *ab initio* no-core calculations. The essence of the MCSM is the importance truncation. The size of the original large sparse Hamiltonian matrix spanned by harmonic-oscillator Slater determinants is reduced to a smaller dense one spanned by stochastically selected bases. With this method, one can perform large-scale shell-model calculations even in the case that the standard shell-model approaches with the Lanczos method cannot handle. Most of the physics of interest usually lies on the forefront of and even beyond the current computational limit.

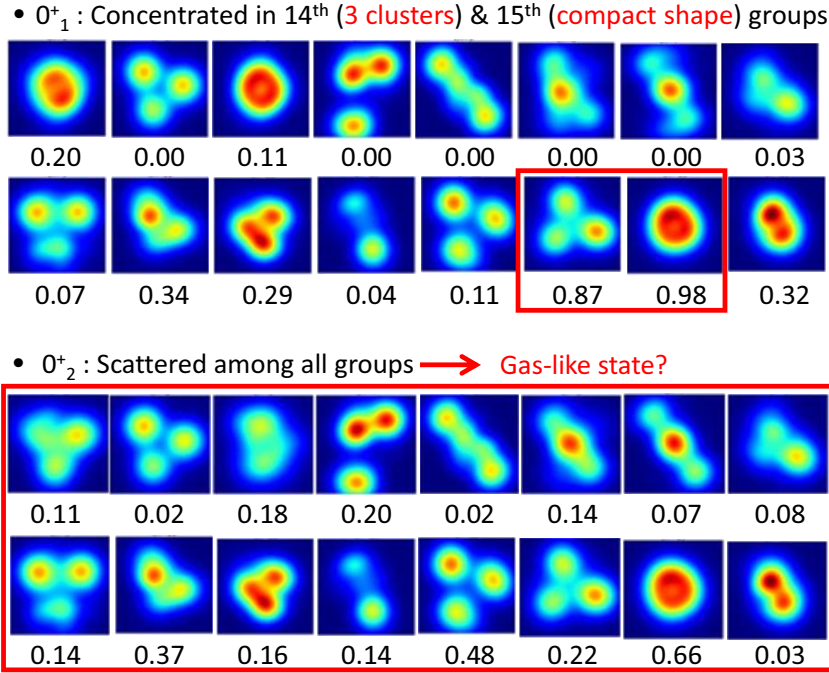


Figure 5: Cluster analysis of the  $^{12}\text{C}$  nucleus in the no-core MCSM.

In this contribution, the MCSM has been presented focusing on the no-core shell-model calculations. It is found that the no-core MCSM results for light nuclei up to  $A \leq 20$  with a  $NN$  potential can be extrapolated to the limit of infinite basis space and provide *ab initio* solutions with evaluated theory uncertainties. The JISP16  $NN$  interaction gives good agreement with experimental data up to around 12-nucleon system even without handling explicit three-nucleon interactions. As one of physics applications, an exploratory study of the  $\alpha$  cluster phenomena has been provided with the visualization of intrinsic density obtained from the MCSM wave functions before spin- and parity-projections. We found the emergence of two- $\alpha$ -cluster structure in the  $^8\text{Be}$  ground state without any assumption of  $\alpha$  clusters. We also identified the molecular orbital states of valence neutrons in neutron-rich Be isotopes. The deformation of  $\alpha$  clusters was seen in the ground states of Be isotopes with increasing the number of neutrons. Following the study of the Be isotopes, the analysis of the intrinsic shape of  $^{12}\text{C}$  was briefly discussed. The intrinsic density of the ground state of  $^{12}\text{C}$  is mainly composed of compact shell-model-like and three- $\alpha$ -cluster shapes, while the overlap probability for the second  $0^+$  state is distributed among various configurations which indicates a gas-like state.

For future perspectives, the no-core MCSM calculations with the Daejeon16  $NN$  interaction are necessary for providing some insights on how far such kind of nonlocal  $NN$  interactions can be applied to a heavier mass region. Also, a quantitative analysis of the  $\alpha$ -cluster structures based on intrinsic densities is expected to be done in the near future.

## Acknowledgments

This work is supported by MEXT and JICFus Priority Issue 9 Tackled by Using Post K Computer “Elucidation of the Fundamental Laws and Evolution of the Universe”. T. A. thanks T. Otsuka, Y. Utsuno, N. Shimizu, T. Yoshida, Y. Tsunoda, P. Maris, and J. P. Vary for the collaboration related to the no-core MCSM. The MCSM calculations were performed on K computer at RIKEN AICS (hp140210, hp150224, and hp160211, hp170230, hp180179).

## References

- [1] B. A. Brown, *Prog. Part. Nucl. Phys.* **47**, 517 (2001).
- [2] E. Caurier, G. Martinez-Pinedo, F. Nowacki, A. Poves and A. P. Zuker, *Rev. Mod. Phys.* **77**, 427 (2005).
- [3] B. R. Barrett, P. Navrátil and J. P. Vary, *Prog. Part. Nucl. Phys.* **69**, 131 (2013).
- [4] C. Forssén, B. D. Carlsson, H. T. Johannsson, D. Sääf, A. Bansal, G. Hagen and T. Papenbrock, *Phys. Rev. C* **97**, 034328 (2018).
- [5] T. Otsuka, M. Honma, T. Mizusaki, N. Shimizu and Y. Utsuno, *Prog. Part. Nucl. Phys.* **47**, 319 (2001).
- [6] N. Shimizu, T. Abe, Y. Tsunoda, Y. Utsuno, T. Yoshida, T. Mizusaki, M. Honma and T. Otsuka, *Prog. Theor. Exp. Phys.* **2012**, 01A205 (2012).
- [7] N. Shimizu, T. Abe, M. Honma, T. Otsuka, T. Togashi, Y. Tsunoda, Y. Utsuno and T. Yoshida, *Phys. Scr.* **92**, 063001 (2017).
- [8] W. Leidemann and G. Orlandini, *Prog. Part. Nucl. Phys.* **68**, 158 (2013).
- [9] R. Roth and P. Navrátil, *Phys. Rev. Lett.* **99**, 092501 (2007).
- [10] R. Roth, *Phys. Rev. C* **79**, 064324 (2009).
- [11] T. Dytrych, K. D. Launey, J. P. Draayer, P. Maris, J. P. Vary, E. Saule, U. Catalyurek, M. Sosenkina, D. Langr and M. A. Caprio, *Phys. Rev. Lett.* **111**, 252501 (2013).
- [12] T. Abe, P. Maris, T. Otsuka, N. Shimizu, Y. Utsuno and J. P. Vary, *AIP Conf. Proc.* **1355**, 173 (2011).
- [13] T. Abe, P. Maris, T. Otsuka, N. Shimizu, Y. Utsuno and J. P. Vary, *Phys. Rev. C* **86**, 054301 (2012).
- [14] A. M. Shirokov, J. P. Vary, A. I. Mazur and T. A. Weber, *Phys. Lett. B* **644**, 33 (2007).
- [15] A. M. Shirokov, I. J. Shin, Y. Kim, M. Sosenkina, P. Maris and J. P. Vary, *Phys. Lett. B* **761** 87 (2016).
- [16] I. J. Shin, Y. Kim, P. Maris, J. P. Vary, C. Forssén, J. Rotureau and N. Michel, *J. Phys. G* **44**, 075103 (2017).

- 
- [17] L. Liu, T. Otsuka, N. Shimizu, Y. Utsuno and R. Roth, *Phys. Rev. C* **86**, 014302 (2012).
  - [18] T. Yoshida, N. Shimizu, T. Abe and T. Otsuka, *Few-Body Syst.* **54**, 1465 (2013).
  - [19] T. Yoshida, N. Shimizu, T. Abe and T. Otsuka, *EPJ Web Conf.* **66**, 02113 (2014).
  - [20] T. Yoshida, N. Shimizu, T. Abe and T. Otsuka, *J. Phys. Conf. Ser.* **569**, 012063 (2014).
  - [21] T. Yoshida, N. Shimizu, T. Abe and T. Otsuka, *JPS Conf. Proc.* **6**, 030028 (2015).
  - [22] A. Tohsaki, H. Horiuchi, P. Schuck and G. Röpke, *Phys. Rev. Lett.* **87**, 192501 (2001).

# Elastic $n-{}^6\text{He}$ Scattering and ${}^7\text{He}$ Resonant States in the No-Core Shell Model

I. A. Mazur<sup>a,b</sup>, A. M. Shirokov<sup>b,c,d</sup>, I. J. Shin<sup>e</sup>, A. I. Mazur<sup>b</sup>,  
Y. Kim<sup>e</sup>, P. Maris<sup>d</sup> and J. P. Vary<sup>d</sup>

<sup>a</sup>Center for Extreme Nuclear Matters, Korea University, Seoul 02841, Republic of Korea

<sup>b</sup>Department of Physics, Pacific National University, Khabarovsk 680035, Russia

<sup>c</sup>Skobeltsyn Institute of Nuclear Physics, Lomonosov Moscow State University, Moscow 119991, Russia

<sup>d</sup>Department of Physics and Astronomy, Iowa State University, Ames, IA 50011-3160, USA

<sup>e</sup>Rare Isotope Science Project, Institute for Basic Science, Daejeon 305-811, Republic of Korea

## Abstract

We present results of calculations of  $n-{}^6\text{He}$  elastic scattering phase shifts and resonances in  ${}^7\text{He}$ . The calculations utilize the SS-HORSE method combined with *ab initio* no-core shell model calculations of the  ${}^7\text{He}$  and  ${}^6\text{He}$  nuclei with Daejeon16 and the JISP16  $NN$  interactions.

**Keywords:** *Nucleon-nucleus scattering; resonances; SS-HORSE method; no-core shell model*

## 1 Introduction

A modern trend of nuclear theory is a development of methods for describing nuclear states in the continuum, resonances in particular, as well as the boundaries of nuclear stability and nuclei beyond the drip lines. Obviously, *ab initio* (“first-principles”) approaches in this field are of primary importance. The only input for *ab initio* theoretical studies is the nucleon-nucleon ( $NN$ ) and, if needed, three-nucleon ( $3N$ ) interactions.

Currently there are a number of reliable methods for *ab initio* description of nuclear bound states (see, e. g., the review [1]). Prominent methods include the Green function’s Monte Carlo [2], the no-core shell model (NCSM) [3], the coupled cluster method [4], etc. The NCSM calculations are utilized in this paper. The NCSM is a modern version of the nuclear shell model which does not introduce an inert core and includes the degrees of freedom of all nucleons of a given nucleus. The multi-particle wave function is expanded in a series of basis many-body oscillator functions (Slater determinants) which include all many-body oscillator states with total excitation quanta less or equal to some given value defined in terms of  $N_{\text{max}}$ . This makes it

---

*Proceedings of the International Conference ‘Nuclear Theory in the Supercomputing Era — 2018’ (NTSE-2018), Daejeon, South Korea, October 29 – November 2, 2018, eds. A. M. Shirokov and A. I. Mazur. Pacific National University, Khabarovsk, Russia, 2019, p. 310.*

<http://www.ntse.khb.ru/files/uploads/2018/proceedings/MazurI.pdf>.

possible to separate completely the center-of-mass motion. The number of basis states increases very rapidly with number of nucleons  $A$  and with  $N_{\max}$ . The achievement of a reasonable accuracy of the NCSM calculations is primarily limited by the memory of available modern leadership-class supercomputers. Currently, NCSM applications are obtained for nuclei with the number of nucleons of about 20. As  $A$  increases, due to computational limits restricting basis space sizes, there is a greater need for extrapolations to estimate converged results.

However, the NCSM cannot be directly applied to the description of resonant states. Energies of resonant states are positive with respect to some threshold so that one needs to consider decay modes. Special methods taking into account the continuum are therefore needed for the description of resonances.

There are well-developed methods for *ab initio* description of continuum spectrum states based on Faddeev and Faddeev–Yakubovsky equations that are successfully applied in nuclear physics for systems with  $A \leq 5$  nucleons (see, e. g., the review [1] and Ref. [5]). A very important breakthrough in developing *ab initio* theory of nuclear reactions in systems with total number of nucleons  $A > 4$  was achieved by combining the NCSM and the resonating group method to built the so-called NCSM with continuum (NCSMC) approach [6] which has been applied to description of several nuclear systems with up to 11 [7] and very recently up to 12 nucleons [8]. Nuclear resonances can be considered also in the no-core Gamow shell model (GSM) [9]. However, these methods bring forth additional challenges for a numerical realization and the respective calculations become very demanding.

Recently we proposed the SS-HORSE method [10–14], which generalizes the NCSM to the continuum spectrum states. The SS-HORSE allows one to calculate the single-channel  $S$ -matrix and resonances by a simple analysis of NCSM eigenenergy behavior as a function of parameters of the many-body oscillator basis. The SS-HORSE extension of the NCSM was successfully applied to the calculation of the neutron- $\alpha$  and proton- $\alpha$  scattering and resonant states in the  ${}^5\text{He}$  and  ${}^5\text{Li}$  nuclei in Refs. [10, 14]; a generalization of this approach to the case of the democratic decay provided a description of a resonance in the system of four neutrons (tetra-neutron) [15].

A brief review of the SS-HORSE method is presented in Section 2. Results for a single-channel neutron scattering by the  ${}^6\text{He}$  nucleus and resonances in the  ${}^7\text{He}$  nucleus are presented in Section 3.

## 2 SS-HORSE method

Consider a channel of neutron scattering by a nucleus with  $A$  nucleons. The phase shift calculations within the SS-HORSE approach start from the calculation of the set of the NCSM eigenenergies  $E_i^{A+1}$  with some set of the NCSM basis parameters  $N_{\max}^i$  and  $\hbar\Omega^i$  for the whole  $(A+1)$ -particle system, as well as of the ground state energies  $E_i^A$  of the target nucleus with the same  $\hbar\Omega^i$  and the excitation quanta  $N_{\max}^i$  or  $N_{\max}^i - 1$  depending of the parity of the states of interest of the  $(A+1)$ -particle system. The respective relative motion energy is the difference

$$E_i = E_i^{A+1} - E_i^A. \quad (1)$$

The phase shifts  $\delta_\ell(E_i)$  at the eigenenergies  $E_i$  in the partial wave with the orbital

momentum  $\ell$  in the case of neutral particle scattering are calculated as [10–12]

$$\tan \delta_\ell(E_i) = -\frac{S_{N^i+2,\ell}(E_i)}{C_{N^i+2,\ell}(E_i)}. \quad (2)$$

Here  $S_{n,\ell}(E)$  and  $C_{n,\ell}(E)$  are the regular and irregular oscillator solutions for the free motion, their analytical expressions can be found in Refs. [16–18]; the oscillator quanta of the relative motion

$$N^i = N_{\max}^i + N_{\min}^{A+1} - N_{\min}^A, \quad (3)$$

where  $N_{\max}^i$  is the excitation quanta in the  $(A+1)$ -particle system in the current calculation,  $N_{\min}^{A+1}$  and  $N_{\min}^A$  are the minimal total oscillator quanta consistent with the Pauli principle in the  $(A+1)$ - and  $A$ -particle systems, respectively. The energies  $E_i$  depend, of course, on the NCSM basis parameters,  $N_{\max}^i$  and  $\hbar\Omega^i$ . Therefore by varying these parameters (note,  $\hbar\Omega$  appears in the definition of the functions  $S_{n,\ell}$  and  $C_{n,\ell}$ ) we can calculate the phase shifts in some energy interval. Next we perform the phase shift parameterization which makes it possible to calculate the  $S$ -matrix and its poles including those associated with the resonant states in the  $(A+1)$ -body system.

The phase shifts can be parameterized using the effective range function,

$$K(E) = \left(\sqrt{2\mu E}/\hbar\right)^{2\ell+1} \cot \delta_\ell(E), \quad (4)$$

where  $\mu$  is the reduced mass of scattered particles. The function (4) has good analytical properties and may be expanded in Taylor series of energy  $E$  (the so-called effective range expansion),

$$K(E) = -\frac{1}{a_\ell} + \frac{\mu r_\ell}{\hbar^2} E + cE^2 + \dots, \quad (5)$$

where  $a_\ell$  is the scattering length and  $r_\ell$  is the effective range. The expansion (5) works well at low energies, however in a larger energy interval, in particular, in the region of a resonance, it may be inadequate since the phase shift may take the values of  $0, \pm\pi, \pm 2\pi, \dots$ , when the effective range function  $K(E)$ , according to Eq. (4), tends to infinity. Therefore we express the effective range function as a Padé approximant,

$$K(E) = \frac{-1 + w_1^{(n)} E + w_2^{(n)} E^2 + \dots}{a_\ell + w_1^{(d)} E + w_2^{(d)} E^2 + \dots}. \quad (6)$$

Clearly, at low energies the Padé approximant (6) unambiguously transforms into the effective range expansion (5).

With any set of parameters  $w_1^{(n)}, w_2^{(n)}, \dots, a_\ell, w_1^{(d)}, w_2^{(d)}, \dots$  parametrizing the effective range function  $K(E)$  we can easily calculate the phase shifts  $\delta_\ell(E)$  in the energy interval of interest and calculate the energies  $E_i^{th}$  using Eq. (2) for any combination of the NCSM parameters  $N_{\max}^i$  and  $\hbar\Omega^i$ . These energies  $E_i^{th}$  are compared with the set of energies  $E_i$  obtained in the NCSM calculations; the optimal values of  $w_1^{(n)}, w_2^{(n)}, \dots, a_\ell, w_1^{(d)}, w_2^{(d)}, \dots$ , parametrizing the effective range function, are found

by minimizing the sum of squares of deviation of the sets of  $E_i^{th}$  and  $E_i$  with weights enhancing the contribution of energies obtained with larger  $N_{\max}$  values,

$$\Xi_w = \sqrt{\frac{1}{p} \sum_{i=1}^p \left( (E_i^{th} - E_i)^2 \left( \frac{N_{\max}^i}{N_M} \right)^2 \right)}. \quad (7)$$

Here  $p$  is the number of energy values and  $N_M$  is the largest value of  $N_{\max}^i$  used in the fit. With the optimal set of the fit parameters  $w_1^{(n)}, w_2^{(n)}, \dots, a_\ell, w_1^{(d)}, w_2^{(d)}, \dots$  we can use Eq. (4) and (2) to obtain a parametrization of the  $\hbar\Omega$  dependencies of the eigenenergies  $E_i$  in any basis space  $\mathbb{N}^i$ .

The  $S$ -matrix and the effective range function  $K(E)$  are related by a simple analytic formula. Therefore, after obtaining an accurate parametrization of  $K(E)$ , one can search numerically for the  $S$ -matrix poles in the complex energy plain. Some tricks useful to design a stable and fast numerical algorithm for the pole searches at complex energies, are described in Ref. [14]. By locating the  $S$ -matrix poles, we obtain energies  $E_r$  and widths  $\Gamma$  of resonances in the many-body nuclear system.

### 3 $n-{}^6\text{He}$ scattering

We start from the NCSM calculations of the  ${}^6\text{He}$  ground state energies  $E_i^6$  with the Daejeon16 [19] and JISP16 [20]  $NN$  interactions with  $N_{\max}$  up to 16 and  $\hbar\Omega$  ranging from 8 to 50 MeV. Next we calculate the lowest eigenenergies  $E_i^7$  of the  $3/2^-, 1/2^-, 5/2^-$  and  $1/2^+$  states in the  ${}^7\text{He}$  nucleus with  $N_{\max}$  up to 17 with the same interactions and the same  $\hbar\Omega$  values.

We first consider calculations performed with the Daejeon16  $NN$  interaction. The set of the relative motion energies  $E_i$  is calculated using Eq. (1). As an example, we present in the left panel of Fig. 1 the set of relative motion energies  $E_i$  in the  $3/2^-$

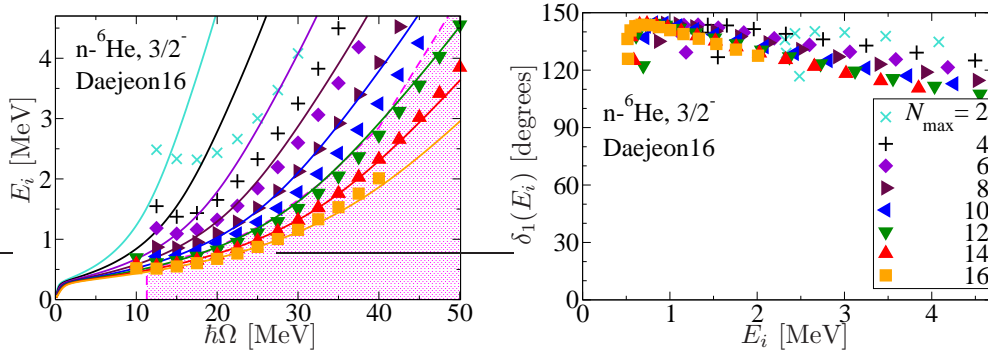


Figure 1: Left panel: Symbols are the energies of the relative motion  $E_i$  in the  $3/2^-$  scattering state obtained in the NCSM with the Daejeon16  $NN$  interaction; the energies used for the SS-HORSE parametrization are taken from the shaded area and the results of the SS-HORSE parametrization of energies for each  $N_{\max}$  are shown by solid curves of respective colors. Right panel: The phase shifts calculated using Eq. (2) at the energies from the left panel.

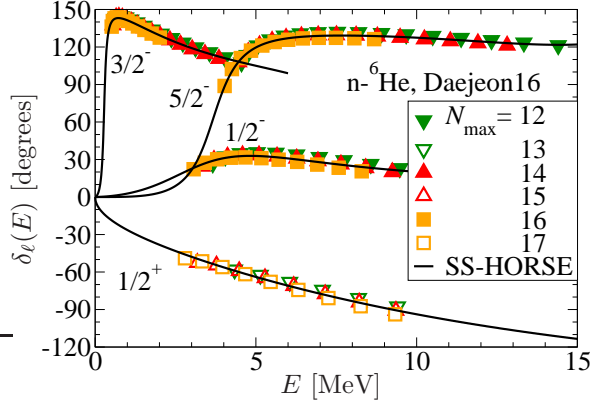


Figure 2: The phase shifts in the  $3/2^-$ ,  $1/2^-$ ,  $5/2^-$  and  $1/2^+$  scattering states obtained with the Daejeon16  $NN$  interaction. Symbols are the selected phase shifts  $\delta_\ell(E_i)$ ; the SS-HORSE fit of the phase shifts is presented by black curves.

state. The right panel of the same figure presents the set of the phase shifts  $\delta_\ell(E_i)$  at these energies calculated using Eq. (2).

As stated in Refs. [10–15], we cannot use all energies  $E_i$  obtained by the NCSM for the further SS-HORSE analysis. The set of acceptable energies  $E_i$  should be selected for the SS-HORSE. In particular, the SS-HORSE equations are consistent only with those energies obtained at any given  $N_{\max}$  which increase with  $\hbar\Omega$ , i. e., for any given  $N_{\max}$  we should have  $\frac{dE}{d\hbar\Omega} > 0$ . In other words, from the set of energies  $E_i^{N_{\max}}$  obtained by NCSM with any  $N_{\max}$  we should select only those which are obtained with  $\hbar\Omega > \hbar\Omega_{\min}^{N_{\max}}$ , where  $\hbar\Omega_{\min}^{N_{\max}}$  corresponds to the minimum of the  $\hbar\Omega$  dependence of the relative motion energies  $E_i^{N_{\max}}$ .

Next, for the effective range function parametrization, we should select only the results obtained with large enough  $N_{\max}$  and in the ranges of  $\hbar\Omega$  values for each  $N_{\max}$  where the phase shifts converge, at least, approximately. The phase shift convergence means that the phase shifts  $\delta_\ell(E_i)$  obtained with different  $N_{\max}$  and  $\hbar\Omega$  values form a single smooth curve as a function of energy. In the right panel of Fig. 1, we see that the phase shifts  $\delta_\ell(E_i)$  tend to form a smooth curve as  $N_{\max}$  increases in a range of moderate energies which correspond to moderate  $\hbar\Omega$  values. The phase shifts  $\delta_\ell(E_i)$  obtained with small enough  $N_{\max}$  deviate significantly from this single curve in large energy intervals. Correspondingly, the phase shifts obtained even with large  $N_{\max}$  at small energies corresponding to small  $\hbar\Omega$  values before the minima of the  $\hbar\Omega$  dependences of  $E_i^{N_{\max}}$  also deviate from the phase shift curve formed by the NCSM results from other  $N_{\max}$  values.

The energies selected for the SS-HORSE fit are shown by the shaded area in the left panel of Fig. 1. The solid curves in this panel show the parametrization of the NCSM energies through the function (6) with a set of fitted parameters. The selected energies produce a set of the phase shifts  $\delta_1(E_i)$  forming a smooth single curve, as is seen in Fig. 2, where we also present the SS-HORSE  $3/2^-$  phase shifts accurately describing the set of the selected phase shifts  $\delta_1(E_i)$ .

We note that we perform a few alternative selections of energies  $E_i$ , e. g., we exclude from the selection some large energies  $E_i$  which lie far from the resonance. These alternative energy selections are used for estimating uncertainties of our predictions for the parameters of the resonance and low-energy scattering. The resonance energies  $E_r$  (relative to the  $n + {}^6\text{He}$  threshold) and widths  $\Gamma$  of resonances in the  ${}^7\text{He}$  nucleus obtained by a numerical location of the  $S$ -matrix poles are presented in

Table 1: Energies  $E_r$  (relative to the  $n + {}^6\text{He}$  threshold) and widths of negative parity resonant states in  ${}^7\text{He}$  nucleus and parameters of low-energy scattering  $n-{}^6\text{He}$  in positive and negative parity states, scattering lengths  $a_\ell$  and effective ranges  $r_\ell$ , obtained with Daejeon16 and JISP16  $NN$  interactions. Our estimate of the uncertainties of the quoted results are in presented parentheses. The available results of the GSM calculations [21] and of the NCSMC calculations [22, 23] with SRG-evolved  $\text{N}^3\text{LO}$  chiral  $NN$  force together with experimental data are presented for comparison.

	Daejeon16	JISP16	GSM	NCSMC	Experiment		
$3/2^-$					[24]		
$E_r$ , MeV	0.27(1)	0.70(2)	0.39	0.71	0.430(3)		
$\Gamma$ , MeV	0.12(1)	0.60(2)	0.178	0.30	0.182(5)		
$a_1$ , fm <sup>3</sup>	-170(10)	-66(2)					
$r_1$ , fm <sup>-1</sup>	-1.10(3)	-0.88(1)					
$1/2^-$					[25]	[26]	[27]
$E_r$ , MeV	2.7(1)	2.8(1)		2.39	3.03(10)	3.53	1.0(1)
$\Gamma$ , MeV	4.2(1)	5.02(2)		2.89	2	10	0.75(8)
$a_1$ , fm <sup>3</sup>	-4.0(1)	-4.5(2)					
$r_1$ , fm <sup>-1</sup>	-4.4(2)	-3.1(1)					
$5/2^-$					[28]		
$E_r$ , MeV	3.65(2)	4.37(4)	3.47(2)	3.13	3.35(10)		
$\Gamma$ , MeV	1.37(1)	1.55(2)	2.25(28)	1.07	1.99(17)		
$a_3$ , fm <sup>7</sup>	-274(4)	-119(4)					
$r_3$ , fm <sup>-5</sup>	-0.0122(4)	-0.040(1)					
$1/2^+$							
$a_0$ , fm	2.1(2)	3.2(5)					
$r_0$ , fm	2.1(2)	1.1(6)					

Table 1 as well as the low-energy scattering parameters, the scattering length  $a_\ell$  and the effective range  $r_\ell$ , together with their estimated uncertainties. For comparison, we present in Table 1 also the resonance parameters from the GSM studies of Ref. [21] and the NCSMC studies of Refs. [22, 23] with SRG-evolved  $\text{N}^3\text{LO}$  chiral  $NN$  forces together with available experimental data. Our results for the  $3/2^-$  resonance are seen to be consistent with the GSM results and experiment.

The same approach is used to examine the  $1/2^-$  and  $5/2^-$  resonances in the  ${}^7\text{He}$  nucleus. The results for the phase shifts together with selected phase shifts  $\delta_1(E_i)$  are also shown in Fig. 2 while the resonance and low-energy scattering parameters are presented in Table 1.

We note that the convergence of the  $1/2^-$  phase shifts, where we obtain a wide resonance, is slower than in the case of the  $3/2^-$  state. As a result, our predictions for the  $1/2^-$  resonance energy and width tend to have larger uncertainties. The predictions for the low-energy scattering parameters for the  $1/2^-$  case appear to have uncertainties comparable to the resonance parameter uncertainties.

The experimental situation for the  $1/2^-$  resonance is not clear. While the resonant energies of Refs. [25, 26] are comparable, the widths are very different. Our results are in fair agreement with the NCSMC results and the neutron pickup and proton-removal reaction experiments [25] and definitely do not support the interpretation of experimental data on one-neutron knockout from  ${}^8\text{He}$  of Ref. [27] advocating a

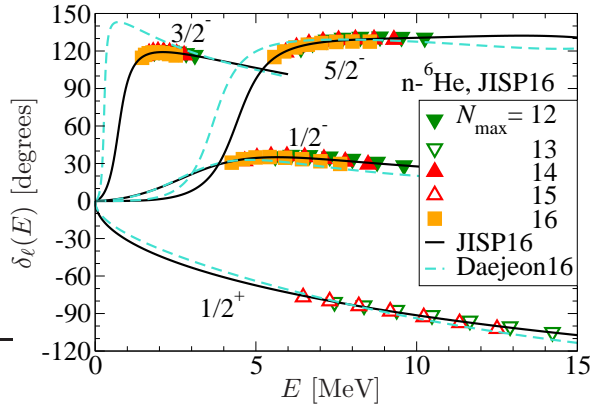


Figure 3: The phase shifts in the  $3/2^-$ ,  $1/2^-$ ,  $5/2^-$  and  $1/2^+$  scattering states obtained with the JISP16  $NN$  interaction in comparison with those obtained with the Daejeon16 (red dashed curves). See Fig. 2 for other details.

low-lying ( $E_r \sim 1$  MeV) narrow ( $\Gamma \leq 1$  MeV)  $1/2^-$  resonance in  ${}^7\text{He}$ .

In the case of the  $5/2^-$  scattering, the phase shifts convergence is similar to that of the  $3/2^-$  state. The resonance energy and width presented in Table 1 are seen to be reasonably close to the experimental data, GSM and NCSMC results.

We analyze also the scattering in the  $1/2^+$  state in our NCSM-SS-HORSE approach. The  $1/2^+$  scattering phase shifts shown in Fig. 2 monotonically decrease without any signal of a resonant state. This result is in an agreement with the experimental data and the GSM predictions of Ref. [21] and NCSMC predictions [22, 23].

The phase shifts obtained with the JISP16  $NN$  interaction are compared with those from Daejeon16 in Fig. 3. The only difference in getting these JISP16 results is that we avoided the expensive  $N_{\max} = 17$  calculations for the positive-parity states since there is no experimental evidence for the positive-parity resonances in  ${}^7\text{He}$  and we do not see any indication of such resonances in our phase shift calculations. The JISP16 and Daejeon16  $1/2^+$  scattering phase shifts are seen to be very close as are the respective low-energy scattering parameters listed in Table 1. The  $3/2^-$  and  $5/2^-$   ${}^7\text{He}$  resonances are generated by the JISP16 at slightly higher energies; the  $1/2^-$  resonance appears approximately at the same energy, however its width is somewhat larger in the JISP16 results compared with the Daejeon16 results.

## 4 Summary and conclusions

We performed a study of the  $n + {}^6\text{He}$  continuum states within the single-channel SS-HORSE extension of the *ab initio* NCSM with JISP16 and Daejeon16  $NN$  interactions. No resonance was found in the  $1/2^+$  state consistent with the GSM [21], NCSMC [22, 23] studies and experimental situation. The  $1/2^-$  resonance is predicted by both interactions to be wide enough and at the energy in a reasonable agreement with the NCSMC [22, 23] calculations and results of experiments of Refs. [25, 26] and clearly contradicts with the hypothesis of a low-lying narrow resonant state suggested in Ref. [27]. We note however that this as well as other  ${}^7\text{He}$  resonances are known from the experiment with weak spin-parity assignment arguments. Our results for the narrow  $3/2^-$  and wide  $5/2^-$  resonances are in a reasonable agreement with experiment and with results quoted in the GSM [21] and NCSMC [22, 23] studies. However, JISP16 overestimates the width of the  $3/2^-$  and the energy of the  $5/2^-$  resonances.

## Acknowledgements

This work is supported in part by the National Research Foundation of Korea (NRF) grant funded by the Korea government (MSIT) (No. 2018R1A5A1025563), by the Russian Science Foundation under Grant No. 16-12-10048, by the U.S. Department of Energy under Grants No. DESC00018223 (SciDAC/NUCLEI) and No. DE-FG02-87ER40371, by the Rare Isotope Science Project of the Institute for Basic Science funded by Ministry of Science and ICT and National Research Foundation of Korea (2013M7A1A1075764). Computational resources were provided by the National Energy Research Scientific Computing Center (NERSC), which is supported by the Office of Science of the U.S. Department of Energy under Contract No. DE-AC02-05CH11231, and by the National Supercomputing Center of Korea with supercomputing resources including technical support (KSC-2018-COL-0002).

## References

- [1] W. Leidemann and G. Orlandini, *Prog. Part. Nucl. Phys.* **68**, 158 (2013).
- [2] S. C. Pieper and R. B. Wiringa, *Ann. Rev. Nucl. Part. Sci.* **51**, 53 (2001).
- [3] B. R. Barrett, P. Navrátil and J. P. Vary, *Prog. Part. Nucl. Phys.* **69**, 131 (2013).
- [4] H. Kümmela, K. H. Lührmann and J. Zabolitzky. *Phys. Rep.* **36**, 1 (1978).
- [5] R. Lazauskas, *Phys. Rev. C* **97**, 044002 (2018).
- [6] P. Navrátil, S. Quaglioni, G. Hupin, C. Romero-Redondo and A. Calci, *Phys. Scr.* **91**, 053002 (2016).
- [7] A. Calci, P. Navrátil, R. Roth, J. Dohet-Eraly, S. Quaglioni and G. Hupin, *Phys. Rev. Lett.* **117**, 242501 (2016).
- [8] P. Navrátil, *Nuclear structure and dynamics from chiral forces*, talk given at the Int. Conf. ‘Nuclear Theory in the Supercomputing Era — 2018’ (NTSE-2018), October 29 – November 2, 2018, Daejeon, South Korea, <http://ntse.khb.ru/files/uploads/2018/presentations/Navratil.pdf>.
- [9] G. Papadimitriou, J. Rotureau, N. Michel, M. Płoszajczak and B. R. Barrett, *Phys. Rev. C* **88**, 044318 (2013).
- [10] A. M. Shirokov, A. I. Mazur, I. A. Mazur and J. P. Vary, *Phys. Rev. C* **94**, 064320 (2016).
- [11] I. A. Mazur, A. M. Shirokov, A. I. Mazur and J. P. Vary, *Phys. Part. Nucl.* **48**, 84 (2017).
- [12] L. D. Blokhintsev, A. I. Mazur, I. A. Mazur, D. A. Savin and A. M. Shirokov, *Yad. Fiz.* **80**, 102 (2017) [*Phys. Atom. Nucl.* **80**, 226 (2017)].
- [13] L. D. Blokhintsev, A. I. Mazur, I. A. Mazur, D. A. Savin and A. M. Shirokov, *Yad. Fiz.* **80**, 619 (2017) [*Phys. Atom. Nucl.* **80**, 1093 (2017)].

- [14] A. M. Shirokov, A. I. Mazur, I. A. Mazur, E. A. Mazur, I. J. Shin, Y. Kim, L. D. Blokhintsev and J. P. Vary, *Phys. Rev. C* **98**, 044624 (2018).
- [15] A. M. Shirokov, G. Papadimitriou, A. I. Mazur, I. A. Mazur, R. Roth and J. P. Vary, *Phys. Rev. Lett.* **117**, 182502 (2016).
- [16] H. A. Yamani and L. J. Fishman, *J. Math. Phys.*, **16**, 410 (1975).
- [17] S. A. Zaytsev, Yu. F. Smirnov and A. M. Shirokov, *Teor. Mat. Fiz.* **117**, 227 (1998) [*Theor. Math. Phys.* **117**, 1291 (1998)].
- [18] J. M. Bang, A. I. Mazur, A. M. Shirokov, Yu. F. Smirnov and S. A. Zaytsev, *Ann. Phys. (NY)* **280**, 299 (2000).
- [19] A. M. Shirokov, I. J. Shin, Y. Kim, M. Sosonkina, P. Maris and J. P. Vary, *Phys. Lett. B* **761**, 87 (2016).
- [20] A. M. Shirokov, J. P. Vary, A. I. Mazur and T. A. Weber, *Phys. Lett. B* **644**, 33 (2007).
- [21] Y. Jaganathen, R. M. Id Betan, N. Michel, W. Nazarewicz and M. Płoszajczak, *Phys. Rev. C* **96**, 054316 (2017).
- [22] S. Baroni, P. Navrátil and S. Quaglioni, *Phys. Rev. Lett.* **110**, 022505 (2013).
- [23] S. Baroni, P. Navrátil and S. Quaglioni, *Phys. Rev. C* **87**, 034326 (2013).
- [24] Z. X. Cao *et al.*, *Phys. Lett. B* **707**, 46 (2012).
- [25] A. H. Wuosmaa *et al.*, *Phys. Rev. C* **72**, 061301 (2005).
- [26] P. Boutachkov *et al.*, *Phys. Rev. Lett.* **95**, 132502 (2005).
- [27] M. Meister *et al.*, *Phys. Rev. Lett.* **88**, 102501 (2002).
- [28] D. R. Tilley *et al.*, *Nucl. Phys. A* **708**, 3 (2002).

## Alphabetic list of the NTSE-2018 participants

- **Takashi Abe**, The University of Tokyo, Japan.....301
- **Shung-Ichi Ando**, Sunmoon University, Korea ..... —
- **Carlo Barbieri**, University of Surrey, UK ..... —
- **Nir Barnea**, The Hebrew University of Jerusalem, Israel ..... —
- **Bruce R. Barrett**, University of Arizona, USA ..... —
- **Mark A. Caprio**, University of Notre Dame, USA ..... 250, 293
- **Myung Ki Cheoun**, Soongsil University, Korea ..... —
- **Kihyeon Cho**, Korea Institute of Science and Technology Information,  
Korea ..... —
- **Luigi Coraggio**, Istituto Nazionale di Fisica Nucleare, Italy ..... 192
- **Jerry Draayer**, Louisiana State University, USA ..... 73, 279
- **Andreas Ekström**, Chalmers University of Technology, Sweden ..... —
- **Charlotte Elster**, Ohio University, USA ..... —
- **Evgeny Epelbaum**, Ruhr-Universität Bochum, Germany ..... 150
- **Kevin Fosse**, Michigan State University, USA ..... —
- **Tobias Frederico**, Instituto Tecnológico de Aeronautica, Brazil ..... 199
- **Hana Gil**, Kyungpook National University, Korea ..... —
- **Gaute Hagen**, Oak Ridge National Laboratory, USA..... —
- **Kyoungsu Heo**, Soongsil University, Korea ..... —
- **Seung-Woo Hong**, Sungkyunkwan University, Korea ..... —
- **Chang Ho Hyun**, Daegu University, Korea ..... —
- **EunJin In** Sungkyunkwan University, Korea..... —
- **Vladimir Karmanov**, Lebedev Physical Institute, Russia ..... 212
- **Seonghyun Kim**, Soongsil University, Korea ..... —

- **Youngman Kim**, Institute for Basic Science, Korea ..... 15, 310
- **Kyujin Kwak**, Ulsan National Institute of Science and Technology, Korea —
- **Young Kwan Kwon**, Rare Isotope Science Project, Institute for Basic Science, Korea ..... —
- **Rimantas Lazauskas**, IPHC, France ..... —
- **Dean Lee**, Michigan State University, USA ..... 45
- **Jounghwa Lee**, Korea Atomic Energy Research Institute, Korea ..... —
- **Ruprecht Machleidt**, University of Idaho, USA ..... 21, 64
- **Alexander Mazur**, Pacific National University, Russia ..... 310
- **Igor Mazur**, Pacific National University, Russia ..... 310
- **Anna McCoy**, TRIUMF, Canada ..... 293
- **Ulf-G. Meißner**, Universität Bonn, Germany ..... 28
- **Chandan Mondal**, Institute of Modern Physics, China ..... 239
- **Alexander Motovilov**, Joint Institute for Nuclear Research, Russia ..... 127
- **Myeong-Hwan Mun**, Korea Atomic Energy Research Institute, Korea ... —
- **Petr Navrátil**, TRIUMF, Canada ..... —
- **Witold Nazarewicz**, Michigan State University, USA ..... —
- **Thomas Neff**, GSI Helmholtzzentrum für Schwerionenforschung GmbH, Germany ..... —
- **Esmond G. Ng**, Lawrence Berkeley National Laboratory, USA ..... —
- **Andreas Nogga**, Forschungszentrum Jülich, Germany ..... —
- **Feng Pan**, Liaoning Normal University, China ..... 73
- **Chong Qi**, KTH Royal Institute of Technology, Sweden ..... 83
- **Dmitry Rodkin**, Dukhov Research Institute for Automatics, Russia ..... —
- **Mario Sánchez**, CENBG, France ..... —
- **Francesca Sammarruca**, University of Idaho, USA ..... 64
- **Kimiko Sekiguchi**, Tohoku University, Japan ..... 108

- 
- **Noritaka Shimizu**, The University of Tokio, Japan ..... —
  - **Ik Jae Shin**, Rare Isotope Science Project, Institute for Basic Science,  
Korea ..... 15, 168, 310
  - **Andrey Shirokov**, Moscow State University, Russia ..... 15, 310
  - **Roman Skibiński**, Jagiellonian University, Poland ..... 115, 122
  - **Nadezda Smirnova**, University of Bordeaux/CENBG, France ..... 263
  - **Ionel Stetcu**, Los Alamos National Laboratory, USA ..... 91
  - **Yurii Tchuvil'sky**, Moscow State University, Russia ..... —
  - **Jun Terasaki**, Institute of Experimental and Applied Physics,  
Czech Republic ..... 100
  - **Kacper W. Topolnicki**, Marian Smoluchowski Institute of Physics,  
Jagiellonian University, Poland ..... 115, 122
  - **James Vary**, Iowa State University, USA ..... 15, 168, 224, 239, 250, 310
  - **Alexander Volya**, Florida State University, USA ..... —
  - **Stefan Wild**, Argonne National Laboratory, USA ..... —
  - **Furong Xu**, Peking University, China ..... 183
  - **Sergey Yakovlev**, Saint Petersburg State University, Russia ..... 137
  - **Xingbo Zhao**, Institute of Modern Physics, China ..... 224, 239
  - **Wei Zuo**, Institute of Modern Physics, China ..... 52

**NUCLEAR THEORY  
IN THE SUPERCOMPUTING ERA – 2018  
(NTSE-2018)**

*International Conference Proceedings*

Daejeon, Republic of Korea,  
October 29 – November 2, 2018

Printing date: 30.12.19. Format 70x108 1/16.  
Writing paper. “Computer modern” font. Digital printing.  
Quire 28,1. Number of copies 60. Order number 398.

**Publisher:** Pacific National University,  
136 Tikhookeanskaya street, Khabarovsk 680035, Russia.